Mechanisms affecting liquefaction screening of Non-Plastic silty soils using Cone Penetration Resistance

USGS Award Number: 07HQGR0113

Final Report

October 2014

S. Thevanayagam
Principal Investigator
&
V. Veluchamy and Q. Huang
Research Assistants

University at Buffalo
State University of New York
Department of Civil, Struct. & Env. Eng.
212 Ketter Hall, Buffalo, NY 14260

Tel: 716-645-4376; theva@buffalo.edu

Program Element: III

Key Words: Liquefaction, sand, silty sand, Cone Penetration Resistance

"*Research supported by the U.S. Geological Survey (USGS), Department of the Interior, under USGS award number (07HQGR0113). The views and conclusions contained in this document are those of the authors and should not be interpreted as necessarily representing the official policies, either expressed or implied, of the U.S. Government.*"

Abstract

Effect of non-plastic fines on the cone resistance and cyclic resistance of sands and silty sands remains an unresolved problem. This study focuses on: (a) cone penetrometer experiment study on penetration resistance of sands and silty sands at 15 and 25% silt content, (b) numerical study on the effect of permeability and compressibility (representing the effect of silt content), diameter of cone (d_c) and penetration rate (v) on cone resistance in sands and silty sands, (c) comparative analysis of the results from (a) and (b) of the effect of silt content on cone resistance through a non-dimensional parameter T_o ($=vd_c/c_v$, where v is the penetration rate, d_c is the cone diameter and c_v is the coefficient of consolidation) for all soils at the same equivalent inter-granular relative void ratio [$(e_c)_{eq}$] or relative density [$(D_{rc})_{eq}$], and (d) relationship between cyclic resistance and cone penetration resistance and the non-dimensional parameter T_o, and its utility for liquefaction screening.

In both experimental and numerical studies for saturated sands and silty sands, the normalized cone resistance (q_{c1N}) decreased with an increase in silt content, at the same [$(D_{rc})_{eq}$], from 0 to 25%. However this influence of silt content on penetration resistance was absent for dry sands and silty sands at the same [$(D_{rc})_{eq}$]. The difference of cone resistance in saturated sands and silty sands, is thought to be due to partial drainage occurring in saturated silty sands whereas the penetration process is thought to be nearly drained in saturated sands. In the case of dry soils, this pore pressure influence is absent and hence the same penetration resistance is observed in sands and silty sands.

This indicates the important influence of pore pressures and its dissipation rates, depending on the silt content, on cone resistance.

Both experimental data and numerical results indicate that for the same $(D_{rc})_{eq}$, q_{c1N} decreases as T_o increases, which implies a decrease in c_v (or increase in silt content), because of the penetration process transition from drained to partially drained or even undrained condition. In addition, the numerical analysis shows that v and d_c also influence q_{c1N} in silty sands. q_{c1N} decreases as v increase or d_c increases (T_o increases) in the partially drained condition.

Since fines content is not the only factor affecting cone resistance, a T_o dependent relationship between cyclic resistance ratio (CRR) and q_{c1N} for sands and silty sands is proposed for liquefaction screening. Further research is needed to evaluate and validate such a procedure using further cone penetration tests in a large chamber setup, refined numerical simulations, and cyclic tests on the same soils as those used in chamber tests, field data from liquefaction and non-liquefaction sites, and physical model liquefaction tests and cone penetration tests using laminar box shaking facilities. The data and initial analyses presented herein are part of continuing research by the investigators. This report presents a snap shot of the present state of this research. A number of publications have already been made. More concise and definitive conclusions and findings from this research will be disseminated in future publications in the literature.

Table of contents

Abstract iiii
Table of contents ivv
List of Figures ix
List of Tables.....xxii
Notations…… xxiv

Chapter 1. Introduction 1
1.1. Background and statement of problem 1
1.2. Scope of research 2
1.3. Organization of dissertation 3
Chapter 2. Literature review 6
2.1. Introduction.....6
2.2. Liquefaction screening using CPT for sands and silty sands.....7
2.3. Effect of fines on mechanical behavior in silty sands.....13
2.3.1. Framework of inter-granular contact density indices of silty sands 14
2.3.2. Example on the inter-granular contact density index.....18
2.4. Effect of fines on permeability and coefficient of consolidation in silty sands ...19
2.5. Normalized penetration rate-T_o.....22
2.6. Effect of Drainage conditions on cone resistance and liquefaction screening in sands and silty sands 23
2.6.1. Laboratory study 23
2.6.2. Finite element method.....28
2.7. Summary 32
Chapter 3. Design of CPT testing chamber 34
3.1. Introduction.....34
3.2. Design concepts of testing chamber 34
3.2.1. Boundary conditions 35
3.2.2. Chamber size effect.....38
3.2.3. Design consideration of testing chamber system.....39
3.3. Design of testing chamber system 40
3.3.1. Reaction frame and pushing system 41
3.3.2. CPT chamber (Cell) 42
3.3.3. Miniature cone 45
3.3.4. Instrumentation and data acquisition system (DAQ/DAS).....47
3.3.5. Chamber compliance 51
3.4. Summary 53
Chapter 4. CPT chamber tests and analysis: Sands and silty sands 54
4.1. Introduction.....54

4.2. Test procedures 55
4.2.1. Sample preparation and saturation 55
4.2.2. Sample consolidation 56
4.2.3. Cone penetration 56
4.2.4. Disassemble of sample 57
4.3. Analysis of chamber test results 57
4.3.1. Dry sand-silt mix 60
4.3.2. Saturated sand-silt mixture 67
4.3.3. Summary of experimental results 77
4.4. Summary 81
Chapter 5. Numerical simulation of CPT: Procedures 82
5.1. Introduction 82
5.2. Introduction of constitutive models 84
5.2.1. Linear Drucker-Prager (DP) model 84
5.2.2. Modified Drucker-Prager (cap) model 86
5.3. Simulation of monotonic undrained triaxial test 90
5.3.1. Abaqus modeling and simulation steps 92
5.3.2. Validation with monotonic undrained triaxial tests 93
5.3.3. Summary of section 5.3 105
5.4. Simulation of one-dimensional consolidation 106
5.5. Simulation of CPT 109
5.5.1. Simulation procedures 109
5.5.2. Model setup 109
5.5.3. Validation of CPT simulation 120
5.5.4. Conclusion of this section 134
5.6. Summary 134
Chapter 6. Parametric study of cone resistance: Sands and silty sands 136
6.1. Introduction 136
6.2. Effect of permeability on q_{c1N} and $\Delta u/\sigma_{vo}'$ 136
6.2.1. $(D_{rc})_{eq}$=10% 137
6.2.2. $(D_{rc})_{eq}$=41% 142
6.2.3. $(D_{rc})_{eq}$=60% 145
6.2.4. $(D_{rc})_{eq}$=80% 148
6.3. Effect of penetration rate on q_{c1N} and $\Delta u/\sigma_{vo}'$ 151
6.4. Effect of cone diameter on q_{c1N} and $\Delta u/\sigma_{vo}'$ 156
6.5. Effect of T_o on q_{c1N} and $\Delta u/\sigma_{vo}'$ 160
6.6. Summary 164
Chapter 7. 1-g Full scale laminar box: Sand liquefaction tests 165
7.1. Introduction 165
7.2. Full scale laminar box shaking system 165

7.2.1. Laminar box 165
7.2.2. Base shaker and actuators 171
7.2.3. Bracing frame system 172
7.3. Instrumentation for liquefaction test series-LG1 173
7.3.1. Instrumentation plan 173
7.3.2. Summary of sensor working conditions after liquefaction experiments 179
7.4. Hydraulic filling 184
7.4.1. Bucket density tests 185
7.4.2. Sand settlement during filling 187
7.5. CPTs and shear wave velocity tests 192
7.6. Liquefaction experiments 196
7.7. Summary 199
Chapter 8. 1-g Full scale laminar box: Sand liquefaction analysis 200
8.1. Introduction 200
8.2. Liquefaction tests- Shaking series 1 200
8.2.1. Base shaking 200
8.2.2. Acceleration response 202
8.2.3. Excess pore water pressure (Δu) response 208
8.2.4. Horizontal displacement response 214
8.2.5. Ground settlement response 219
8.2.6. Stress-strain response 221
8.2.7. Cone resistance, shear wave velocity and liquefaction resistance 232
8.2.8. Liquefaction analysis 234
8.3. Liquefaction tests- Shaking series 2 240
8.3.1. Base shaking 241
8.3.2. Acceleration response 243
8.3.3. Excess pore water pressure (Δu) response 249
8.3.4. Horizontal displacement response 256
8.3.5. Ground settlement response 263
8.3.6. Stress-strain response 264
8.4. CPT and shear wave velocity results 273
8.5. CPT-based and V_s-based liquefaction analysis 276
8.6. Summary 284
Chapter 9. CPT-based liquefaction screening of sands and silty sands 285
9.1. Introduction 285
9.2. $(CRR)_{field}$ and q_{c1N} versus $(D_{rc})_{eq}$ 285
9.3. $(CRR)_{field}$ versus q_{c1N} 289
9.4. Summary 291
Chapter 10. Conclusion and future work 292
10.1. Conclusion and findings 292

10.2. Suggestions for future research 293
Reference….. 295
Appendix A CPT simulation using FLAC 310
A.1 Undrained triaxial test simulation 310
A.2 One dimensional consolidation simulation 311
A.3 CPT simulation 312
A.3.1 Model setup 313
A.3.2 Results 314
A.4 Recommended Further study 315
Appendix B Parametric study of cap model and monotonic triaxial simulation using Abaqus……. 317
B.1 Parametric study 317
B.1.1 Elastic modulus (E) study 317
B.1.2 Eccentricity parameter (R) study 318
B.1.3 Initial cap yield surface position ($\varepsilon_{vol}^{pl}|_0$) study 319
B.1.4 Transition parameter (α) study 320
B.2 Simulation of OS F55 sand-silt mix 321
B.2.1 C_F=0% 322
B.2.2 C_F=7% 335
B.2.3 C_F=15% 340
B.2.4 C_F=25% 345
Appendix C Optimization of CPT simulation and effect of k on q_{c1N} using Drucker-Prager Model in Abaqus 348
C.1 Study on convergence 348
C.2 Study on discretization types of cone penetrometer 350
C.3 Study on geometric variation of soil medium in the symmetric axis 351
C.4 Study on friction between soil and cone 353
C.5 Study on effect of k on q_{c1N} using Drucker-Prager (DP) model 354
C.5.1 $(D_{rc})_{eq}$=10% 356
C.5.2 $(D_{rc})_{eq}$=41% 359
C.5.2 $(D_{rc})_{eq}$=60% 361
Appendix D Determination of friction coefficient of ball bearings 363
D.1 Introduction 363
D.2 Test results 364
Appendix E Liquefaction experiments of LG1 366
E.1 Liquefaction tests-shaking series 3 366
E.1.1 Base shaker 366
E.1.2 Acceleration response 368
E.1.3 Excess pore water pressure (Δu) response 374
E.1.4 Horizontal displacement response 381

E.1.5 Ground settlement response 385
E.1.6 Stress-strain response 387
E.2 Liquefaction tests-shaking series 4 395
E.2.1 Base shaker 395
E.2.2 Acceleration response 396
E.2.3 Excess pore water pressure (Δu) response 400
E.2.4 Horizontal displacement 404
E.2.5 Ground settlement 406
E.2.6 Stress-strain response 407
E.3 Liquefaction tests-shaking series 5 413
E.3.1 Base shaker 413
E.3.2 Acceleration response 414
E.3.3 Excess pore water pressure (Δu) response 418
E.3.4 Horizontal displacement 422
E.3.5 Ground settlement 424
E.3.6 Stress-strain response 425
E.4 Liquefaction tests-shaking series 6 431
E.4.1 Base shaker 431
E.4.2 Acceleration response 432
E.4.3 Excess pore water pressure (Δu) response 436
E.4.4 Horizontal displacement 440
E.4.5 Ground settlement 442
E.4.6 Stress-strain response 443
E.5 Liquefaction tests-shaking series 7 449
E.5.1 Base shaker 449
E.5.2 Acceleration response 450
E.5.3 Excess pore water pressure (Δu) response 454
E.5.4 Horizontal displacement 458
E.5.5 Ground settlement 460
E.5.6 Stress-strain response 461
E.6 Liquefaction tests-shaking series 8 467
E.6.1 Base shaker 467
E.6.2 Acceleration response 468
E.6.3 Excess pore water pressure (Δu) response 472
E.6.4 Horizontal displacement 475
E.5.6 Ground settlement 477
E.5.6 Stress-strain response 478
E.7 Raw data for shear wave velocity tets 484

List of Figures

Fig. 1.1 Field based liquefaction screening chart using cone resistance (Robertson and Wride, 1998) 1
Fig. 2.1 Liquefaction potential evaluation charts for sands/silty sands using CPT 9
Fig. 2.2 Reduction factor to estimate the variation of cyclic shear stress with depth below level or gently sloping ground surface (Youd and Idriss, 2001) 13
Fig. 2.3 Inter-granular soil mix classification (Thevanayagam et al., 2003) 15
Fig. 2.4 Granular Mix Classifications for OS F55 sand-silt mix (Thevanayagam, 2007a) .. 16
Fig. 2.5 Determination of b_{mon} and b_{cyc} for Fitzgerald bridge mixture when $C_F<C_{Fth}$ 19
Fig. 2.6 Variation of k and C_v versus C_F (Shenthan 2001, Thevanayagam and Martin 2002) 20
Fig. 2.7 Effect of C_F on C_v (Thevanayagam and Martin 2002) 21
Fig. 2.8 $(CRR)_{7.5}$ vs q_{c1N} for different fines contents for 15 and 20 cycles at double strain for 5% (Carraro et al., 2003) 24
Fig. 2.9 Schematic view of miniature cone penetrometer in a triaxial chamber (Kumar and Baju, 2009) 25
Fig. 2.10 Cross-section of modified triaxial test apparatus (Kokusho et al., 2012) 27
Fig. 2.11 Relationship between CSR and peak cone resistance (Kokusho et al., 2012) 28
Fig. 2.12 Variation of cone resistance with respect to permeability (Markauskas et al. , 2005) 30
Fig. 2.13 q_{c1N} versus T_o with different $(D_{rc})_{eq}$ (Ecemis, 2008) 31
Fig. 2.14 Proposed $(CRR)_{7.5}$ versus q_{c1N} for different T_o (Ecemis, 2008) 32
Fig. 3.1 Configurations of boundary conditions in calibration chamber 37
Fig. 3.2 Schematic diagram of complete testing chamber system 41
Fig. 3.3 Snap shot of CPT testing chamber system 41
Fig. 3.4 Snapshot of reaction frame and pushing system 42
Fig. 3.5 Overview of testing chamber (Unit: mm in blankets) 43
Fig. 3.6 Dimension of cylindrical chamber 44
Fig. 3.7 Snapshot of pressure panel 45
Fig. 3.8 Design of miniature cone penetrometer 46
Fig. 3.9 Calibration of cone tip and shaft 47
Fig. 3.10 Snapshot of cone penetrometer 47
Fig. 3.11 Depth measurement gauge 48
Fig. 3.12 Locations of piezometer duct (unit:mm in blankets) 49
Fig. 3.13 Components of piezometer duct 49
Fig. 3.14 Saturation of piezometer duct 50
Fig. 3.15 System expansion due to pressurization 53

Fig. 4.1 Gradation of OS F55 sand-silt mixtures (Thevanayagam et al. 2003) 54
Fig. 4.2 Typical penetration rate fed by pneumatic jack 57
Fig. 4.3 Empirical correlation between q_c and D_r for NC silicesous sand (Digitized from Schmertmann, 1976) 60
Fig. 4.4 Experimental correlation D_r-q_c-σ_{vo}' for mainly NC sands of different compressibility (Digitized from Lancellotta, 1983; Garizio, 1997) 61
Fig. 4.5 Cone tip resistance of dry sands at different D_r 62
Fig. 4.6 Sleeve friction of dry sands at different D_r 63
Fig. 4.7 Comparison of q_{c1N} -D_r between experiments and empirical equations of dry sands 63
Fig. 4.8 Normalized friction ratio with respect to D_r of dry sands 64
Fig. 4.9 q_c and f_s of C_F=25% at $(D_{rc})_{eq}$≈75% under v=0.4 cm/s 65
Fig. 4.10 q_c and f_s of C_F=25% at $(D_{rc})_{eq}$=75% under two penetration rates (CC-12 and CC-13) 66
Fig. 4.11 q_c and f_s of C_F=25% at $(D_{rc})_{eq}$=76% under two penetration rates (CC-16 and CC-17) 66
Fig. 4.12 q_c and f_s of C_F=25% at $(D_{rc})_{eq}$=66% under two penetration rates (CC-18 and CC-19) 66
Fig. 4.13 Variation of k versus C_F (After Shenthan, 2001, Thevanayagam and Martin 2002) 68
Fig. 4.14 Variation of m_v with C_F for virgin loading (After Shenthan, 2001) 70
Fig. 4.15 Variation of c_v with C_F for virgin loading (After Shenthan, 2001)..... 70
Fig. 4.16 q_c, f_s and Δu of C_F=0 at $(D_{rc})_{eq}$=60~70% 73
Fig. 4.17 q_c, f_s and Δu of C_F=15% at $(D_{rc})_{eq}$=73/85% (CC-8) 74
Fig. 4.18 q_c and Δu of C_F=25% at $(D_{rc})_{eq}$=27/48% (CC-10) 75
Fig. 4.19 q_c, f_s and Δu of C_F=25% at $(D_{rc})_{eq}$=67/79% under two penetration rates (CC-14 and CC-15)..... 76
Fig. 4.20 q_c, f_s and Δu of C_F=25% at $(D_{rc})_{eq}$=72/84% under two penetration rates (CC-20 and CC-21)..... 77
Fig. 4.21 q_{c1N} versus $(D_{rc})_{eq}$ at two C_F under v=0.4 cm/s 78
Fig. 4.22 q_{c1N} versus $(D_{rc})_{eq}$ from CPT chamber tests 79
Fig. 5.1 Yield surface for linear Drucker-Prager model (Abaqus 6.10 Manual) 85
Fig. 5.2 Drucker-Prager hardening (Abaqus 6.10 Manual) 86
Fig. 5.3 Yield surface of Cap model (Abaqus 6.10 Manual) 87
Fig. 5.4 Projection of the modified cap yield/flow surfaces on the Π-plane (Abaqus 6.10 Manual) 87
Fig. 5.5 A typical hardening curve for cap model (Abaqus 6.10 Manual)..... 88
Fig. 5.6 Flow potential of Cap Model in p-t plane (Abaqus 6.10 Manual) 89
Fig. 5.7 Comparison of $C_c/[1+(e_{0c})_{eq}]$ versus $(D_{rc})_{eq}$ between empirical and experimental data

..... 91
Fig. 5.8 Model setup of monotonic undrained triaxial test 93
Fig. 5.9 E, ϕ', p_0'/p_f', $\varepsilon_{vol}^{in}|_0$ and R versus $(D_{rc})_{eq}$ under isotropic stress of 100 kPa for different soils 95
Fig. 5.10 Dilation angle versus $(D_{rc})_{eq}$ for OS F55 sand-silt mix (Ecemis, 2008) 95
Fig. 5.11 Simulation of M31 [$(D_{rc})_{eq}$=10%] 99
Fig. 5.12 Simulation of M12 [$(D_{rc})_{eq}$=41%] 100
Fig. 5.13 Simulation of M01 [$(D_{rc})_{eq}$=60%] 101
Fig. 5.14 Simulation of M20 [$(D_{rc})_{eq}$=80%] 102
Fig. 5.15 Simulation of of Monterey sand at D_r=45% under different σ_c' 103
Fig. 5.16 Simulation of Monterey sand at D_r=65% under different σ_c' 104
Fig. 5.17 Simulation of Monterey sand at D_r=85% under σ_c'=100 kPa 104
Fig. 5.18 Simulation of of Toyoura sand at different D_r under σ_c'=100 kPa 105
Fig. 5.19 Numerical simulation of one-dimensional consolidation using cap model 106
Fig. 5.20 Comparison of one-dimensional consolidation between Abaqus and Terzaghi solution using Drucker-Prager model 108
Fig. 5.21 Comparison of one-dimensional consolidation between Abaqus and Terzaghi solution using cap model 108
Fig. 5.22 Geometry and optimized FEM model of cone penetrometer 111
Fig. 5.23 Geometry of soil medium in Abaqus 113
Fig. 5.24 Boundary conditions applied in Abaqus with various configurations at symmetric axis 114
Fig. 5.25 Cone-soil interface 115
Fig. 5.26 Relocation of a node during a mesh sweep 118
Fig. 5.27 Comparison of deformed mesh with/without ALE around cone tip 119
Fig. 5.28 Discretiaztion of cone and soil medium in Abaqus 120
Fig. 5.29 Comparison of q_{c1N} between numerical results of of various Young's moduli and experiments 123
Fig. 5.30 Comparison of chamber test and numerical result of CC-14 123
Fig. 5.31 Comparison of chamber test and numerical result of CC-15 124
Fig. 5.32 Comparison of chamber test and numerical result of CC-20 125
Fig. 5.33 Comparison of chamber test and numerical result of CC-21 125
Fig. 5.34 Comparison of chamber test and numerical results using dry OS F55 sand 129
Fig. 5.35 Comparison of q_{c1N} between experiment and Abaqus using dry OS F55 sand ... 129
Fig. 5.36 Comparison of q_c versus D/d_c between calibration chamber and Abaqus using dry Monterey No. 0/30 sand 131
Fig. 5.37 Comparison of q_c between experimental and numerical results of dry Monterey No. 0/30 sand 132
Fig. 5.38 Comparison of q_{c1N} obtained using abaqus and empirical equations at drained and

undrained conditions 133
Fig. 6.1 Meshes of soil medium around the cone tip before and after penetration 137
Fig. 6.2 q_{c1N} with respect to D/d_c at $(D_{rc})_{eq}$=10% with different permeabilities 138
Fig. 6.3 $\Delta u/\sigma_{vo}'$ with respect to D/d_c at $(D_{rc})_{eq}$=10% with different permeabilities 139
Fig. 6.4 q_{c1N} and $\Delta u/\sigma_{vo}'$ at $(D_{rc})_{eq}$=10% with different permeabilities 140
Fig. 6.5 EPWP distribution at $(D_{rc})_{eq}$=10% with different permeabilities (Unit:kPa) 141
Fig. 6.6 q_{c1N} with respect to D/d_c at $(D_{rc})_{eq}$=41% with different permeabilities 142
Fig. 6.7 q_{c1N} and $\Delta u/\sigma_{vo}'$ at $(D_{rc})_{eq}$=41% with different permeabilities 143
Fig. 6.8 EPWP distribution at $(D_{rc})_{eq}$=41% with different permeabilities (Unit:kPa) 144
Fig. 6.9 q_{c1N} with respect to D/d_c at $(D_{rc})_{eq}$=60% with different permeabilities 145
Fig. 6.10 q_{c1N} and $\Delta u/\sigma_{vo}'$ at $(D_{rc})_{eq}$=60% with different permeabilities 146
Fig. 6.11 EPWP distribution at $(D_{rc})_{eq}$=60% with different permeabilities (Unit:kPa) 147
Fig. 6.12 q_{c1N} with respect to D/d_c at $(D_{rc})_{eq}$=80% with different permeabilities 148
Fig. 6.13 q_{c1N} and $\Delta u/\sigma_{vo}'$ at $(D_{rc})_{eq}$=80% with different permeabilities 149
Fig. 6.14 EPWP distribution at $(D_{rc})_{eq}$=80% with different permeabilities (Unit:kPa) 150
Fig. 6.15 q_{c1N} with respect to D/d_c at $(D_{rc})_{eq}$=10% with different penetration rates 151
Fig. 6.16 $\Delta u/\sigma_{vo}'$ with respect to D/d_c at $(D_{rc})_{eq}$=10% with different penetration rates 152
Fig. 6.17 q_{c1N} and $\Delta u/\sigma_{vo}'$ at $(D_{rc})_{eq}$=10% with different penetration rates 153
Fig. 6.18 Variation of q_{c1N} and $\Delta u/\sigma_{vo}'$ with respect to T_o at $(D_{rc})_{eq}$=10% 154
Fig. 6.19 Comparison of changing k and v on $\Delta u/\sigma_{vo}'$ response for different T_o of soil at $(D_{rc})_{eq}$=10% 155
Fig. 6.20 Variation of q_{c1N} and $\Delta u/\sigma_{vo}'$ with respect to T_o at $(D_{rc})_{eq}$=41% 156
Fig. 6.21 Variation of q_{c1N} and $\Delta u/\sigma_{vo}'$ with respect to T_o at $(D_{rc})_{eq}$=60% 156
Fig. 6.22 Variation of q_{c1N} and $\Delta u/\sigma_{vo}'$ of different $(D_{rc})_{eq}$ at different k using two d_c 157
Fig. 6.23 Variation of q_{c1N} and $\Delta u/\sigma_{vo}'$ with respect to T_o at $(D_{rc})_{eq}$=10% for two d_c 158
Fig. 6.24 Variation of q_{c1N} and $\Delta u/\sigma_{vo}'$ with respect to T_o at $(D_{rc})_{eq}$=41% for two d_c 159
Fig. 6.25 Variation of q_{c1N} and $\Delta u/\sigma_{vo}'$ with respect to T_o at $(D_{rc})_{eq}$=60% for two d_c 159
Fig. 6.26 $q_{c1N}/q_{c1N\text{-}ref}$ versus T_o for different sand-silt mixes 162
Fig. 6.27 q_{c1N} versus T_o for soils with different $(D_{rc})_{eq}$ for Ottawa F55 sand-silt mix 162
Fig. 6.28 $\Delta u/\sigma_{vo}'$ versus T_o for Ottawa F55 sand-silt mix with different $(D_{rc})_{eq}$ 163
Fig. 7.1 Schematic details of laminar box 167
Fig. 7.2 Layout of ball bearings and internal angles distribution 167
Fig. 7.3 Internal restraint angles 168
Fig. 7.4 Snapshot of laminar box 168
Fig. 7.5 Protective membrane and membrange bags 170
Fig. 7.6 Bottom layout of laminar box 171
Fig. 7.7 Connection of actuators to base shaker 172
Fig. 7.8 Plan view of bracing system 173
Fig. 7.9 Instrumentation plan 177

Fig. 7.10 Sensors in laminar box 178
Fig. 7.11 Captured views from digital cameras 179
Fig. 7.12 Setup of close loop hydraulic filling..... 184
Fig. 7.13 Sand and water level during hydraulic filling 185
Fig. 7.14 Plan view-bucket density test locations..... 186
Fig. 7.15 Settlement plate components 188
Fig. 7.16 Activation of settlement plate 189
Fig. 7.17 Settlement plate data..... 190
Fig. 7.18 σ_v' computation diagram 191
Fig. 7.19 ε_v and e versus σ_{vo}' of settlement plates..... 192
Fig. 7.20 Corrected relative density of bucket density samples 192
Fig. 7.21 Device of CPT and shear wave velocity test 193
Fig. 7.22 CPT/shear wave velocity test location..... 194
Fig. 7.23 q_c, u_2 and V_s versus depth of C0 195
Fig. 7.24 Planned input base motions 196
Fig. 8.1 Base shaker of T1 (a_{max}=0.015 g/5 cyc) 201
Fig. 8.2 Base shaker of T2 (a_{max}=0.03 g/15 cyc) 201
Fig. 8.3 Base shaker of T3 (a_{max}=0.1 g/15 cyc) 202
Fig. 8.4 x-acceleration at different depths and base of T1 (a_{max}=0.015 g/5 cyc)..... 203
Fig. 8.5 Amplification factor profile of T1 (a_{max}=0.015 g/5 cyc) 204
Fig. 8.6 x-acceleration at different depths and base of T2 (a_{max}=0.03 g/15 cyc)..... 205
Fig. 8.7 Amplification factor profile of T2 (a_{max}=0.03 g/15 cyc) 206
Fig. 8.8 x-acceleration at different depths and base of T3 (a_{max}=0.1 g/15 cyc)..... 207
Fig. 8.9 Amplification factor profile of T3 (a_{max}=0.1 g/15 cyc) 208
Fig. 8.10 Time history of r_u and base acceleration of T1 (a_{max}=0.015 g/5 cyc)..... 209
Fig. 8.11 Time history of Δu of T1 (a_{max}=0.015 g/5 cyc)..... 210
Fig. 8.12 EPWP profiles of T1 (a_{max}=0.015 g/5 cyc)..... 210
Fig. 8.13 Time history of r_u and base acceleration of T2 (a_{max}=0.03 g/15 cyc).....211
Fig. 8.14 Time history of Δu of T2 (a_{max}=0.03 g/15 cyc) 212
Fig. 8.15 EPWP profiles of T2 (a_{max}=0.03 g/15 cyc)..... 212
Fig. 8.16 Time history of r_u and base acceleration of T3 (a_{max}=0.10 g/15 cyc)..... 213
Fig. 8.17 Time history of Δu of T3 (a_{max}=0.10 g/15 cyc) 214
Fig. 8.18 EPWP profiles of T3 (a_{max}=0.10 g/15 cyc)..... 214
Fig. 8.19 Time history of horizontal displacement of T1 (a_{max}=0.015 g/5 cyc)..... 215
Fig. 8.20 Peak inter-ring drift profile of T1 (a_{max}=0.015 g/5 cyc) 216
Fig. 8.21 Time history of horizontal displacement of T2 (a_{max}=0.03 g/15 cyc)..... 217
Fig. 8.22 Peak inter-ring drift profile of T2 (a_{max}=0.03 g/15 cyc) 217
Fig. 8.23 Time history of horizontal displacement of T3 (a_{max}=0.10 g/15 cyc)..... 218
Fig. 8.24 Peak inter-ring drift profile of T3 (a_{max}=0.10 g/15 cyc) 219

Fig. 8.25 Time history of incremental ground settlement in shaking series 1 220
Fig. 8.26 Conditions of V1,V2 and V3 before and after shaking series 1 221
Fig. 8.27 Locations and free body diagram of shear stress-shear strain estimation 222
Fig. 8.28 Time history of shear stress of T1 (a_{max}=0.015 g/5 cyc)..... 224
Fig. 8.29 Time history of shear strain of T1 (a_{max}=0.015 g/5 cyc)..... 225
Fig. 8.30 Shear stress- strain loop of T1 (a_{max}=0.015 g/5 cyc) 226
Fig. 8.31 Time history of shear stress of T2 (a_{max}=0.03 g/15 cyc)..... 227
Fig. 8.32 Time history of shear strain of T2 (a_{max}=0.03 g/15 cyc)..... 228
Fig. 8.33 Shear stress- strain loop of T2 (a_{max}=0.03 g/15 cyc) 229
Fig. 8.34 Time history of shear stress of T3 (a_{max}=0.10 g/15 cyc)..... 230
Fig. 8.35 Time history of shear strain of T3 (a_{max}=0.10 g/15 cyc)..... 231
Fig. 8.36 Shear stress- strain loop of at different depths of T3 (a_{max}=0.10 g/15 cyc)..... 232
Fig. 8.37 Field based liquefaction screening chart using cone resistance (Robertson and Wride, 1998) 233
Fig. 8.38 Field based liquefaction screening chart using shear wave velocity (Andrus and Stokoe, 2000) 233
Fig. 8.39 Correlation between q_{c1N} and CSR/CRR, Vs1 and CSR/CRR for T2 and T3..... 240
Fig. 8.40 Base shaker of T4 (a_{max}=0.03 g/5 cyc) 241
Fig. 8.41 Base shaker of T8 (a_{max}=0.03 g/5 cyc) 242
Fig. 8.42 Base shaker of T9 (a_{max}=0.03 g/15 cyc) 242
Fig. 8.43 Base shaker of T10 (a_{max}=0.10 g/15 cyc) 243
Fig. 8.44 x-acceleration at different depths and base of T4 and T8 (a_{max}=0.03g/5 cyc)..... 244
Fig. 8.45 Amplification factor profiles of T4 and T8 (a_{max}=0.03 g/5 cyc)..... 245
Fig. 8.46 x-acceleration at different depths and base of T9 (a_{max}=0.03 g/15 cyc)..... 246
Fig. 8.47 Amplification factor profile of T9 (a_{max}=0.03 g/15 cyc) 247
Fig. 8.48 x-acceleration at different depths and base of T10 (a_{max}=0.10 g/15 cyc)..... 248
Fig. 8.49 Amplification factor profile of T10 (a_{max}=0.10 g/15 cyc) 249
Fig. 8.50 Time history of r_u and base acceleration of T4 and T8 (a_{max}=0.03 g/5 cyc)..... 250
Fig. 8.51 Time history of Δu of T4 (a_{max}=0.03 g/5 cyc) 251
Fig. 8.52 Time history of Δu of T8 (a_{max}=0.03 g/5 cyc) 251
Fig. 8.53 EPWP profiles of T4 (a_{max}=0.03 g/5 cyc)..... 252
Fig. 8.54 EPWP profiles of T8 (a_{max}=0.03 g/5 cyc)..... 252
Fig. 8.55 Time history of r_u and base acceleration of T9 (a_{max}=0.03 g/15 cyc)..... 253
Fig. 8.56 Time history of Δu of T9 (a_{max}=0.03 g/15 cyc) 254
Fig. 8.57 EPWP profiles of T9 (a_{max}=0.03 g/15 cyc)..... 254
Fig. 8.58 Time history of r_u and base acceleration of T10 (a_{max}=0.10 g/15 cyc)..... 255
Fig. 8.59 Time history of Δu of T10 (a_{max}=0.10 g/15 cyc) 256
Fig. 8.60 EPWP profiles of T10 (a_{max}=0.10 g/15 cyc)..... 256
Fig. 8.61 Time history of horizontal displacement of T4 (a_{max}=0.03 g/5 cyc)..... 257

Fig. 8.62 Time history of horizontal displacement of T8 (a_{max}=0.03 g/5 cyc)..... 258
Fig. 8.63 Peak inter-ring drift profile of T4 (a_{max}=0.03 g/5 cyc) 259
Fig. 8.64 Peak inter-ring drift profile of T8 (a_{max}=0.03 g/5 cyc) 259
Fig. 8.65 Time history of horizontal displacement of T9 (a_{max}=0.03 g/15 cyc)..... 260
Fig. 8.66 Peak inter-ring drift profile of T9 (a_{max}=0.03 g/15 cyc) 261
Fig. 8.67 Time history of horizontal displacement of T10 (a_{max}=0.10g/15cyc)..... 262
Fig. 8.68 Peak inter-ring drift profile of T10 (a_{max}=0.10 g/15 cyc) 262
Fig. 8.69 Conditions of V1,V2 and V3 before and after shaking series 2 263
Fig. 8.70 Time history of incremental ground settlement in shaking series 2 264
Fig. 8.71 Time history of shear stress of T4 and T8 (a_{max}=0.03 g/5 cyc) 265
Fig. 8.72 Time history of shear strain of T4 and T8 (a_{max}=0.03 g/5 cyc) 266
Fig. 8.73 Shear stress- strain loop of T4 (a_{max}=0.03 g/5 cyc) 267
Fig. 8.74 Shear stress- strain loop of T8 (a_{max}=0.03 g/5 cyc) 267
Fig. 8.75 Time history of shear stress of T9 (a_{max}=0.03 g/15 cyc)..... 268
Fig. 8.76 Time history of shear strain of T9 (a_{max}=0.03 g/15 cyc)..... 269
Fig. 8.77 Shear stress- strain loop of T9 (a_{max}=0.03 g/15 cyc) 270
Fig. 8.78 Time history of shear stress of T10 (a_{max}=0.10 g/15 cyc)..... 271
Fig. 8.79 Time history of shear strain of T10 (a_{max}=0.10 g/15 cyc)..... 272
Fig. 8.80 Shear stress- strain loop of T10 (a_{max}=0.10 g/15 cyc) 273
Fig. 8.81 Profiles of q_c, u_2 and V_s of different CPTs 274
Fig. 8.82 Profiles of q_{c1N}, $\Delta u_2/\sigma_{vo}'$ and V_{s1} of different CPTs 275
Fig. 8.83 q_{c1N} and V_{s1} versus CPT test number at selected depths 276
Fig. 8.84 Correlation between q_{c1N} and CSR, V_{s1} and CSR in LG1-Method I..... 277
Fig. 8.85 Correlation between q_{c1N} and CSR, V_{s1} and CSR in LG1-Method II 278
Fig. 8.86 Correlation between q_{c1N} and CSR, V_{s1} and CSR in LG1-Method III 279
Fig. 9.1 $(CRR)_{tx}$ versus $(D_{rc})_{eq}$ at $C_F<C_{Fth}$..... 286
Fig. 9.2 $(CRR)_{field}$ versus $(D_{rc})_{eq}$ at $C_F<C_{Fth}$..... 287
Fig. 9.3 q_{c1N} versus $(D_{rc})_{eq}$ at different T_o of Ottawa F55 sand-silt mix..... 289
Fig. 9.4 Comparison between proposed T_o dependent $(CRR)_{field}$–q_{c1N} and numerical and laboratory data 290
Fig. 9.5 Comparison between proposed T_o dependent $(CRR)_{field}$–q_{c1N} and field based correlation 291

Fig.A. 1 Simulation of M31 using FLAC 311
Fig.A. 2 Simulation of M47 using FLAC 311
Fig.A. 3 Simulation of M08 using FLAC 311
Fig.A. 4 Simulation of one dimensional consolidation using FLAC..... 312
Fig.A. 5 Model setup and boundary conditions in FLAC..... 313
Fig.A. 6 q_{c1N} and $\Delta u/\sigma_{vo}'$ at different permeabilities of soil at $(D_{rc})_{eq}$=10% using FLAC... 315

Fig.A. 7 q_{c1N} and $\Delta u/\sigma_{vo}'$ at different permeabilities of soil at $(D_{rc})_{eq}$=98% using FLAC... 315

Fig.B. 1 Stress path and stress- and pore pressure-strain curve of M20 with E changing.. 318
Fig.B. 2 Stress path and stress- and pore pressure-strain curve of M20 with R changing . 319
Fig.B. 3 Stress path and stress- and pore pressure-strain curve of M20 with $\varepsilon_{vol}^{pl}|_0$ changing 320
Fig.B. 4 Stress path and stress- and pore pressure-strain curve of M20 with α changing .. 321
Fig.B. 5 Simulation of M08 [$(D_{rc})_{eq}$=102%]..... 322
Fig.B. 6 Simulation of M14 [$(D_{rc})_{eq}$=99%]..... 323
Fig.B. 7 Simulation of M20 [$(D_{rc})_{eq}$=80%]..... 324
Fig.B. 8 Simulation of M05 [$(D_{rc})_{eq}$=79%]..... 325
Fig.B. 9 Simulation of M11 [$(D_{rc})_{eq}$=70%]..... 326
Fig.B. 10 Simulation of M15 [$(D_{rc})_{eq}$=67%]..... 327
Fig.B. 11 Simulation of M10 [$(D_{rc})_{eq}$=65%]..... 328
Fig.B. 12 Simulation of M01 [$(D_{rc})_{eq}$=60%]..... 329
Fig.B. 13 Simulation of M21 [$(D_{rc})_{eq}$=41%]..... 330
Fig.B. 14 Simulation of M12 [$(D_{rc})_{eq}$=41%]..... 331
Fig.B. 15 Simulation of M07 [$(D_{rc})_{eq}$=27%]..... 332
Fig.B. 16 Simulation of M17 [$(D_{rc})_{eq}$=26%]..... 333
Fig.B. 17 Simulation of M09 [$(D_{rc})_{eq}$=17%]..... 334
Fig.B. 18 Simulation of M28 [$(D_{rc})_{eq}$=81%]..... 335
Fig.B. 19 Simulation of M23 [$(D_{rc})_{eq}$=60%]..... 336
Fig.B. 20 Simulation of M26[$(D_{rc})_{eq}$=40%]..... 337
Fig.B. 21 Simulation of M22[$(D_{rc})_{eq}$=22%]..... 338
Fig.B. 22 Simulation of M24[$(D_{rc})_{eq}$=18%]..... 339
Fig.B. 23 Simulation of M37[$(D_{rc})_{eq}$=102%]..... 340
Fig.B. 24 Simulation of M36[$(D_{rc})_{eq}$=45%]..... 341
Fig.B. 25 Simulation of M32[$(D_{rc})_{eq}$=40%]..... 342
Fig.B. 26 Simulation of M31[$(D_{rc})_{eq}$=10%]..... 343
Fig.B. 27 Simulation of M34[$(D_{rc})_{eq}$=8%]..... 344
Fig.B. 28 Simulation of M48[$(D_{rc})_{eq}$=66%]..... 345
Fig.B. 29 Simulation of M47[$(D_{rc})_{eq}$=38%]..... 346
Fig.B. 30 Simulation of M45[$(D_{rc})_{eq}$=18%]..... 347

Fig.C. 1 Two FEM meshes used in CPT simulation 349
Fig.C. 2 Comparison of q_{c1n} of different soils between two meshes 350
Fig.C. 3 Cone penetrometer represented by different discretizations..... 350
Fig.C. 4 Comparison of q_{c1N} of different soils between two different discretizations on cone 351

Fig.C. 5 Comparison of q_{c1N} of different soils between R_h=0 and R_h=0.13cm 352
Fig.C. 6 Comparison of $\Delta u/\sigma_{vo}'$ of different soils between R_h=0 and R_h=0.13cm..... 352
Fig.C. 7 Comparison of q_{c1N} of different soils between different interface friction angles.354
Fig.C. 8 q_{c1N} with respect to D/d_c for different permeabilities at $(D_{rc})_{eq}$=10% using DP ... 356
Fig.C. 9 $\Delta u/\sigma_{vo}'$ with respect to D/d_c for different permeabilities at $(D_{rc})_{eq}$=10% using DP 357
Fig.C. 10 q_{c1N} and $\Delta u/\sigma_{vo}'$ at different permeabilities of soil at $(D_{rc})_{eq}$=10% using DP 357
Fig.C. 11 EPWP distribution of Soil at $(D_{rc})_{eq}$=40% with different permeabilities using DP (Unit:kPa)..... 358
Fig.C. 12 q_{c1N} with respect to D/d_c for different permeabilities at $(D_{rc})_{eq}$=41% using DP . 359
Fig.C. 13 q_{c1N} and $\Delta u/\sigma_{vo}'$ at different permeabilities of soil at $(D_{rc})_{eq}$=41% using DP 359
Fig.C. 14 EPWP distribution of Soil at $(D_{rc})_{eq}$=41% with different permeabilities using DP (Unit:kPa)..... 360
Fig.C. 15 q_{c1N} with respect to D/d_c for different permeabilities at $(D_{rc})_{eq}$=60% using DP . 361
Fig.C. 16 q_{c1N} and $\Delta u/\sigma_{vo}'$ at different permeabilities of soil at $(D_{rc})_{eq}$=60% using DP 361
Fig.C. 17 EPWP distribution of Soil at $(D_{rc})_{eq}$=60% with different permeabilities using DP (Unit:kPa)..... 362

Fig.D. 1 Number of laminates used to define the friction coefficient 364
Fig.D. 2 Force versus time during the manual pulling process 364

Fig.E. 1 Base shaker of T11 (a_{max}=0.03 g/5 cyc) 366
Fig.E. 2 Base shaker of T15 (a_{max}=0.03 g/5 cyc)..... 367
Fig.E. 3 Base shaker of T16 (a_{max}=0.03 g/15 cyc)..... 367
Fig.E. 4 Base shaker of T17 (a_{max}=0.10 g/15 cyc)..... 368
Fig.E. 5 x-acceleration at different depths and base of T11 and T15 (a_{max}=0.03g/5 cyc)... 369
Fig.E. 6 Amplification factor profiles of T11 and T15 (a_{max}=0.03 g/5 cyc) 370
Fig.E. 7 x-acceleration at different depths and base of T16 (a_{max}=0.03g/15 cyc)..... 371
Fig.E. 8 Amplification factor profile of T16 (a_{max}=0.03 g/15 cyc)..... 372
Fig.E. 9 x-acceleration at different depths and base of T17 (a_{max}=0.10 g/15 cyc)..... 373
Fig.E. 10 Amplification factor profile of T17 (a_{max}=0.10 g/15 cyc)..... 374
Fig.E. 11 Time history of r_u and base acceleration of T11 and T15 (a_{max}=0.03 g/5 cyc).... 375
Fig.E. 12 Time history of Δu of T11 (a_{max}=0.03 g/5 cyc) 376
Fig.E. 13 Time history of Δu of T15 (a_{max}=0.03 g/5 cyc) 376
Fig.E. 14 EPWP profiles of T11 (a_{max}=0.03 g/5 cyc) 377
Fig.E. 15 EPWP profiles of T15 (a_{max}=0.03 g/5 cyc) 377
Fig.E. 16 Time history of r_u and base acceleration of T16 (a_{max}=0.03 g/15 cyc)..... 378
Fig.E. 17 Time history of Δu of T16 (a_{max}=0.03 g/15 cyc) 379
Fig.E. 18 EPWP profiles of T16 (a_{max}=0.03 g/15 cyc) 379

Fig.E. 19 Time history of r_u and base acceleration of T17 (a_{max}=0.10 g/15 cyc)..... 380
Fig.E. 20 Time history of Δu of T17 (a_{max}=0.10 g/15 cyc) 381
Fig.E. 21 EPWP profiles of T17 (a_{max}=0.10 g/15 cyc) 381
Fig.E. 22 Time history of horizontal displacement of T11 (a_{max}=0.03 g/5 cyc) 382
Fig.E. 23 Time history of horizontal displacement of T15 (a_{max}=0.03 g/5 cyc) 383
Fig.E. 24 Time history of horizontal displacement of T16 (a_{max}=0.03 g/15 cyc) 384
Fig.E. 25 Time history of horizontal displacement of T17 (a_{max}=0.10 g/15 cyc) 385
Fig.E. 26 Time history of incremental ground settlement in shaking series 3 386
Fig.E. 27 Time history of shear stress of T11 and T15 (a_{max}=0.03 g/5 cyc) 387
Fig.E. 28 Time history of shear strain of T11 and T15 (a_{max}=0.03 g/5 cyc) 388
Fig.E. 29 Shear stress- strain loop of T11 (a_{max}=0.03 g/5 cyc) 389
Fig.E. 30 Shear stress- strain loop of T15 (a_{max}=0.03 g/5 cyc)..... 389
Fig.E. 31 Time history of shear stress of T16 (a_{max}=0.03 g/15 cyc) 390
Fig.E. 32 Time history of shear strain of T16 (a_{max}=0.03 g/15 cyc) 391
Fig.E. 33 Shear stress- strain loop of T16 (a_{max}=0.03 g/15 cyc)..... 392
Fig.E. 34 Time history of shear stress of T17 (a_{max}=0.10 g/15 cyc) 393
Fig.E. 35 Time history of shear strain of T17 (a_{max}=0.10 g/15 cyc) 394
Fig.E. 36 Shear stress- strain loop of T17 (a_{max}=0.10 g/15 cyc)..... 395
Fig.E. 37 Base shaker of T23 (a_{max}=0.03 g/15 cyc)..... 396
Fig.E. 38 Base shaker of T24 (a_{max}=0.10 g/15 cyc)..... 396
Fig.E. 39 x-acceleration at different depths and base of T23 (a_{max}=0.03g/15 cyc) 397
Fig.E. 40 Amplification factor profile of T23 (a_{max}=0.03 g/15 cyc)..... 398
Fig.E. 41 x-acceleration at different depths and base of T24 (a_{max}=0.10 g/15 cyc) 399
Fig.E. 42 Amplification factor profile of T24 (a_{max}=0.10 g/15 cyc)..... 400
Fig.E. 43 Time history of r_u and base acceleration of T23 (a_{max}=0.03 g/15 cyc)..... 401
Fig.E. 44 Time history of Δu of T23 (a_{max}=0.03 g/15 cyc) 402
Fig.E. 45 EPWP profiles of T23 (a_{max}=0.03 g/15 cyc) 402
Fig.E. 46 Time history of r_u and base acceleration of T24 (a_{max}=0.10 g/15 cyc)..... 403
Fig.E. 47 Time history of Δu of T24 (a_{max}=0.10 g/15 cyc) 404
Fig.E. 48 EPWP profiles of T24 (a_{max}=0.10 g/15 cyc) 404
Fig.E. 49 Time history of horizontal displacement of T23 (a_{max}=0.03 g/15 cyc) 405
Fig.E. 50 Time history of horizontal displacement of T24 (a_{max}=0.10 g/15 cyc) 406
Fig.E. 51 Time history of incremental ground settlement in shaking series 4 407
Fig.E. 52 Time history of shear stress of T23 (a_{max}=0.03 g/15 cyc) 408
Fig.E. 53 Time history of shear strain of T23 (a_{max}=0.03 g/15 cyc) 409
Fig.E. 54 Shear stress- strain loop of T23 (a_{max}=0.03 g/15 cyc)..... 410
Fig.E. 55 Time history of shear stress of T24 (a_{max}=0.10 g/15 cyc) 411
Fig.E. 56 Time history of shear strain of T24 (a_{max}=0.10 g/15 cyc) 412
Fig.E. 57 Shear stress- strain loop of T24 (a_{max}=0.10 g/15 cyc)..... 413

Fig.E. 58 Base shaker of T30 (a_{max}=0.03 g/15 cyc) 414
Fig.E. 59 Base shaker of T31 (a_{max}=0.10 g/15 cyc) 414
Fig.E. 60 x-acceleration at different depths and base of T30 (a_{max}=0.03g/15 cyc) 415
Fig.E. 61 Amplification factor profile of T30 (a_{max}=0.03 g/15 cyc) 416
Fig.E. 62 x-acceleration at different depths and base of T31 (a_{max}=0.10 g/15 cyc) 417
Fig.E. 63 Amplification factor profile of T31 (a_{max}=0.10 g/15 cyc) 418
Fig.E. 64 Time history of r_u and base acceleration of T30 (a_{max}=0.03 g/15 cyc) 419
Fig.E. 65 Time history of Δu of T30 (a_{max}=0.03 g/15 cyc) 420
Fig.E. 66 EPWP profiles of T30 (a_{max}=0.03 g/15 cyc) 420
Fig.E. 67 Time history of r_u and base acceleration of T31 (a_{max}=0.10 g/15 cyc) 421
Fig.E. 68 Time history of Δu of T31 (a_{max}=0.10 g/15 cyc) 422
Fig.E. 69 EPWP profiles of T31 (a_{max}=0.10 g/15 cyc) 422
Fig.E. 70 Time history of horizontal displacement of T30 (a_{max}=0.03 g/15 cyc) 423
Fig.E. 71 Time history of horizontal displacement of T31 (a_{max}=0.10 g/15 cyc) 424
Fig.E. 72 Time history of incremental ground settlement in shaking series 5 425
Fig.E. 73 Time history of shear stress of T30 (a_{max}=0.03 g/15 cyc) 426
Fig.E. 74 Time history of shear strain of T30 (a_{max}=0.03 g/15 cyc) 427
Fig.E. 75 Shear stress- strain loop of T30 (a_{max}=0.03 g/15 cyc) 428
Fig.E. 76 Time history of shear stress of T31 (a_{max}=0.10 g/15 cyc) 429
Fig.E. 77 Time history of shear strain of T31 (a_{max}=0.10 g/15 cyc) 430
Fig.E. 78 Shear stress- strain loop of T31 (a_{max}=0.10 g/15 cyc) 431
Fig.E. 79 Base shaker of T37 (a_{max}=0.03 g/15 cyc) 432
Fig.E. 80 Base shaker of T38 (a_{max}=0.10 g/15 cyc) 432
Fig.E. 81 x-acceleration at different depths and base of T37 (a_{max}=0.03g/15 cyc) 433
Fig.E. 82 Amplification factor profile of T37 (a_{max}=0.03 g/15 cyc) 434
Fig.E. 83 x-acceleration at different depths and base of T38 (a_{max}=0.10 g/15 cyc) 435
Fig.E. 84 Amplification factor profile of T38 (a_{max}=0.10 g/15 cyc) 436
Fig.E. 85 Time history of r_u and base acceleration of T37 (a_{max}=0.03 g/15 cyc) 437
Fig.E. 86 Time history of Δu of T37 (a_{max}=0.03 g/15 cyc) 437
Fig.E. 87 EPWP profiles of T37 (a_{max}=0.03 g/15 cyc) 438
Fig.E. 88 Time history of r_u and base acceleration of T38 (a_{max}=0.10 g/15 cyc) 439
Fig.E. 89 Time history of Δu of T38 (a_{max}=0.10 g/15 cyc) 440
Fig.E. 90 EPWP profiles of T38 (a_{max}=0.10 g/15 cyc) 440
Fig.E. 91 Time history of horizontal displacement of T37 (a_{max}=0.03 g/15 cyc) 441
Fig.E. 92 Time history of horizontal displacement of T38 (a_{max}=0.10 g/15 cyc) 442
Fig.E. 93 Time history of incremental ground settlement in shaking series 6 443
Fig.E. 94 Time history of shear stress of T37 (a_{max}=0.03 g/15 cyc) 444
Fig.E. 95 Time history of shear strain of T37 (a_{max}=0.03 g/15 cyc) 445
Fig.E. 96 Shear stress- strain loop of T37 (a_{max}=0.03 g/15 cyc) 446

Fig.E. 97 Time history of shear stress of T38 (a_{max}=0.10 g/15 cyc) 447
Fig.E. 98 Time history of shear strain of T38 (a_{max}=0.10 g/15 cyc) 448
Fig.E. 99 Shear stress- strain loop of T38 (a_{max}=0.10 g/15 cyc)..... 449
Fig.E. 100 Base shaker of T44 (a_{max}=0.03 g/15 cyc)..... 450
Fig.E. 101 Base shaker of T45 (a_{max}=0.10 g/15 cyc)..... 450
Fig.E. 102 x-acceleration at different depths and base of T44 (a_{max}=0.03g/15 cyc)..... 451
Fig.E. 103 Amplification factor profile of T44 (a_{max}=0.03 g/15 cyc)..... 452
Fig.E. 104 x-acceleration at different depths and base of T45 (a_{max}=0.10 g/15 cyc)..... 453
Fig.E. 105 Amplification factor profile of T45 (a_{max}=0.10 g/15 cyc)..... 454
Fig.E. 106 Time history of r_u and base acceleration of T44 (a_{max}=0.03 g/15 cyc)..... 455
Fig.E. 107 Time history of Δu of T44 (a_{max}=0.03 g/15 cyc) 456
Fig.E. 108 EPWP profiles of T44 (a_{max}=0.03 g/15 cyc) 456
Fig.E. 109 Time history of r_u and base acceleration of T45 (a_{max}=0.10 g/15 cyc)..... 457
Fig.E. 110 Time history of Δu of T45 (a_{max}=0.10 g/15 cyc) 458
Fig.E. 111 EPWP profiles of T45 (a_{max}=0.10 g/15 cyc)..... 458
Fig.E. 112 Time history of horizontal displacement of T44 (a_{max}=0.03 g/15 cyc) 459
Fig.E. 113 Time history of horizontal displacement of T45 (a_{max}=0.10 g/15 cyc) 460
Fig.E. 114 Time history of incremental ground settlement in shaking series 7 461
Fig.E. 115 Time history of shear stress of T44 (a_{max}=0.03 g/15 cyc) 462
Fig.E. 116 Time history of shear strain of T44 (a_{max}=0.03 g/15 cyc) 463
Fig.E. 117 Shear stress- strain loop of T44 (a_{max}=0.03 g/15 cyc)..... 464
Fig.E. 118 Time history of shear stress of T45 (a_{max}=0.10 g/15 cyc) 465
Fig.E. 119 Time history of shear strain of T45 (a_{max}=0.10 g/15 cyc) 466
Fig.E. 120 Shear stress- strain loop of T45 (a_{max}=0.10 g/15 cyc)..... 467
Fig.E. 121 Base shaker of T51 (a_{max}=0.03 g/15 cyc)..... 468
Fig.E. 122 Base shaker of T52 (a_{max}=0.10 g/15 cyc)..... 468
Fig.E. 123 x-acceleration at different depths and base of T51 (a_{max}=0.03g/15 cyc)..... 469
Fig.E. 124 Amplification factor profile of T51 (a_{max}=0.03 g/15 cyc)..... 470
Fig.E. 125 x-acceleration at different depths and base of T52 (a_{max}=0.10 g/15 cyc)..... 471
Fig.E. 126 Amplification factor profile of T52 (a_{max}=0.10 g/15 cyc)..... 472
Fig.E. 127 Time history of r_u and base acceleration of T51 (a_{max}=0.03 g/15 cyc)..... 473
Fig.E. 128 Time history of Δu of T51 (a_{max}=0.03 g/15 cyc) 473
Fig.E. 129 EPWP profiles of T51 (a_{max}=0.03 g/15 cyc) 474
Fig.E. 130 Time history of r_u and base acceleration of T45 (a_{max}=0.10 g/15 cyc)..... 474
Fig.E. 131 Time history of Δu of T52 (a_{max}=0.10 g/15 cyc) 475
Fig.E. 132 EPWP profiles of T52 (a_{max}=0.10 g/15 cyc) 475
Fig.E. 133 Time history of horizontal displacement of T51 (a_{max}=0.03 g/15 cyc) 476
Fig.E. 134 Time history of horizontal displacement of T52 (a_{max}=0.10 g/15 cyc) 477
Fig.E. 135 Time history of incremental ground settlement in shaking series 8 478

Fig.E. 136 Time history of shear stress of T51 (a_{max}=0.03 g/15 cyc) 479
Fig.E. 137 Time history of shear strain of T51 (a_{max}=0.03 g/15 cyc) 480
Fig.E. 138 Shear stress- strain loop of soil at different depths of T51 (a_{max}=0.03 g/15 cyc) 481
Fig.E. 139 Time history of shear stress of T52 (a_{max}=0.10 g/15 cyc) 482
Fig.E. 140 Time history of shear strain of T52 (a_{max}=0.10 g/15 cyc) 483
Fig.E. 141 Shear stress- strain loop of T52 (a_{max}=0.10 g/15 cyc) 484
Fig.E. 142 Arrival times of shear wave of C0 484
Fig.E. 143 Arrival times of C3 485
Fig.E. 144 Arrival times of shear wave of C29 485
Fig.E. 145 Arrival times of shear wave of C31 486
Fig.E. 146 Arrival times of shear wave of C38 486
Fig.E. 147 Arrival times of shear wave of C50 487

List of Tables

Table 2.1 Various MSF proposed by investigators (Youd and Noble 1997)..... 12
Table 2.2 properties of soil and test type used for evaluation..... 19
Table 2.3 Reported T_o for drained and undrained conditions during cone penetration 23
Table 2.4 Percentage increase in q_c at penetration rate of 0.1 mm/s with respect to corresponding value at 0.02 mm/s (Kumar and Baju, 2009) 26
Table 3.1 Currently available calibration chambers in the world (After Hsu and Huang, 1999) 35
Table 3.2 Configurations of boundary conditions in calibration chamber..... 36
Table 4.1 Properties of OS F55 sand-silt mixtures (Thevanayagam et al. 2003) 54
Table 4.2 Characteristics of CPT chamber tests using OS F55 sand-silt mix..... 59
Table 4.3 CPT chamber test results of dry OS-00..... 62
Table 4.4 CPT chamber test results of dry OS-25..... 65
Table 4.5 k, m_v, c_v of different C_F from chamber tests 69
Table 4.6 Compressibility data for various sands (after Kulhawy and Mayne, 1990)..... 72
Table 4.7 CPT chamber test results of saturated OS F55 sand-silt mix..... 72
Table 4.8 Summary of q_{c1N} of Ottawa F55 sand-silt mix..... 80
Table 5.1 Typical consolidation properties of saturated normally consolidated sandy soils at various relative densities (Coduto, 2001) 90
Table 5.2 Drucker-Prager model parameters s for different soils 97
Table 5.3 Cap Plasticity model parameters of Ottawa F55 sand-silt mix..... 98
Table 5.4 Parameters of Monterey sand used in the undrained triaxial tests and CPT simulation..... 103
Table 5.5 Elastic and plastic parameters of Toyoura sand used in the cap model 105
Table 5.6 q_{c1N} between numerical results of various Young's moduli and experiments..... 122
Table 5.7 Comparison of experimental and numerical results of q_{c1N} of dry clean sand ... 127
Table 5.8 Boundary conditions and results using Monterey No 0/30 sand 130
Table 6.1 Summary of numerical CPT results using Ottawa F55 sand-silt mix..... 161
Table 7.1 Number of ball bearings per location..... 169
Table 7.2 Instrumentation summary 174
Table 7.3 Instrumentation locations (Cameras not included) 175
Table 7.4 Working conditions of piezometers..... 181
Table 7.5 Working conditions of potentiometers, temposonics and SAAs..... 182
Table 7.6 Working conditions of accelerometers..... 183
Table 7.7 Bucket density data 187
Table 7.8 Input motion of liquefaction test in laminar box..... 198
Table 8.1 Ground settlement of shaking series 1 220

Table 8.2 Estimated $(CSR)_{LB}$ and CSR at D=2.03 m of T3 using different methods 237
Table 8.3 q_{c1N} V_{s1} and CSR/CSR for T2 and T3 239
Table 8.4 Ground settlement of liquefaction tests-shaking series 2..... 264
Table 8.5 Summary of q_{c1N}, V_{s1} and CSR for IM2 and IM3..... 280
Table 9.1 $(D_{rc})_{eq}$ versus $(CRR)_{tx}$ and $(CRR)_{field}$ used in CPT simulation..... 288

Table A. 1 Soil parameters used in the FLAC (After Ecemis, 2008)..... 310

Table C. 1 Summary of numerical results using Drucker Prager 355

Table D. 1 Summary of friction coefficient of each test..... 365

Table E. 1 Ground settlement of liquefaction tests-shaking series 3 386
Table E. 2 Ground settlement of liquefaction tests-shaking series 4 407
Table E. 3 Ground settlement of liquefaction tests-shaking series 5 425
Table E. 4 Ground settlement of liquefaction tests-shaking series 6 443
Table E. 5 Ground settlement of liquefaction tests-shaking series 7 461
Table E. 6 Ground settlement of liquefaction tests-shaking series 8 478

Notations

a: Radius of the circular plate.

$a_{max\text{-}ground}$: Peak ground surface acceleration

a_{max}: Peak input base acceleration

α: Small constant to smoothen the transition between linear shear failure surface and cap yield surface

A: Cross section area of soil

ALE: Arbitrary Lagragian Eulerian

A_0: Non-dimensional empirical correlation factor

b: Parameter determining the contribution of fine grains

B_0: Non-dimensional empirical correlation factor

BC: Boundary condition

β: shape factor in the cap plasticity model

c_v: Coefficient of consolidation

c_{v0}: Coefficient of consolidation for clean sand

C: Courant number

C_0,C_1,C_2: Non-dimensional empirical correlation factor

C_c: Compression index

C_r: Recompression index

C_F: Fines content

C_{Fth}: Threshold fines content

C_{Fl}: Limit fines content

C_Q: Factor to correct the initial effective overburden stress

C_{uc}: Coefficient of uniformity of coarse grain

C_{uf}: Coefficient of uniformity of fine grain

CPT: Cone penetration test

CSR: Cyclic stress ratio

CRR: Cyclic resistance ratio

$(CRR)_{7.5}$: Cyclic resistance ratio for 7.5 magnitude earthquake

$(CRR)_{field}$: Cyclic resistance ratio obtained from field tests

$(CSR)_{LB:}$ Cyclic resistance ratio obtained from liquefaction test in laminar box

$(CRR)_{tx}$:Cyclic resistance ratio obtained from triaxial tests to cause liquefaction in 15 cycles

$(CRR)_{tx-20:}$ Cyclic resistance ratio obtained from triaxial tests to cause liquefaction in 20 cycles

d: Cohesion of material

d_c: Cone diameter

d_{50}: The mean grain size

d_p: Diameter of fine grain

D: Depth/penetration depth

D_0: Flexural rigidity of the plate

DAQ/DAS: Data acquisition system

D_{50}: Mean coarse grain size

D_c: Diameter of calibration chamber

D_L: Calibration chamber size ratio

D_p: Diameter of coarse grain

$(D_{rc})_{eq}$: Equivalent inter-granular relative density

$(D_{rf})_{eq}$: Equivalent inter-fine relative density

δ: Total ground settlement

$\Delta\delta$: Incremental ground settlement

$\Delta\delta_{ave.}$: Average Incremental ground settlement

Δt: Time step

Δu: Excess pore water pressure

Δx_i: Length interval in x_i axis

e: Global void ratio

e_0: Initial void ratio

e_1: Location of initial consolidation state

e_c: Inter-granular void ratio

$(e_c)_{eq}$: Equivalent inter-granular void ratio

e_f: Inter-fine void ratio

$(e_f)_{eq}$: Equivalent inter-fine void ratio

$e_{max,HC}$: Maximum void ratio of host grain

$e_{min,HC}$: Minimum void ratio of host grain

$e_{max,HF}$: Maximum void ratio of host fine

$e_{min,HF}$: Minimum void ratio of host fine

ε_a: Axial strain

$\varepsilon_{vol}^{in}|_0$: Initial cap yield surface position

ε_{vol}^{pl}: Volumetric plastic strain

ε_{vol}^{cr}: Volumetric creep strain

E: Young's modulus

EPWP: Excess pore water pressure

$f_{s:}$ Measured side friction

F_I: Total inertial force in analysis

FEM: Finite element method

FS_L: Factor of safety for liquefaction

ϕ': friction angle of material

g: Acceleration of gravity

G: Potential flow

G_{max}: Maximum shear modulus at small-amplitude of shear strain

h: Thickness of the plate

H_0: Settlement plate placed elevation

H_1: Sand filling elevation

H_{dr}: Drainage path length

γ: Shear strain

γ_{sat}: Unite weight of saturated soil

γ_w: Unite weight of water

ID: Inner diameter

IM: Input motion

k: Permeability

K: The ratio of the flow stress in triaxial tension to the flow stress in triaxial compression

K_b: Bulk modulus

K_0: Coefficient of lateral earth pressure at rest

L_F: Laminate factor

m: Parameter determining the reinforcement factor of coarse grain

m_v: Coefficient of volume compressibility

MSF: Magnitude scaling factor

M_j: The total mass in analysis

M_w: Magnitude

n: Exponent different with soil types

nn: dimension, nn=1, 2, or 3

N: Total normal force acting on the soil body

N_L: Number of cycles to induce liquefaction

p: Mean normal stress

p': Mean effective stress

p_a: Evolution parameter in cap model

p_b: hydrostatic compression yield stress

p_0': initial hydrostatic compression stress

P_{at}: Atmospheric pressure

P_L: Probability of liquefaction

q: Deviatoric stress

q_0:Distributed load

q_c: Measured cone resistance

q_{c1N} ($q_{c1}/_{Pa}$) : Normalized cone resistance

q_{c1}: Corrected cone penetration resistance for overburden pressure

θ: Lode angle

r: Radial distances of points in the middle plance of the circular plate

r_d: Stress reduction factor

r_u: Normalized excess pore water pressure

R: Material parameter controlling the elliptical shape of cap

R_d: Size disparity ratio of coarse grain over fine grain

R_h: Radius of hole away from symmetric axis in numerical analysis

γ': Buoyant unit weight of soil

γ_{sat}: Saturated unit weight of soil

γ_w: Unit weight of water

S: Nearest distance from the center of cone penetrometer to the boundary of chamber

SAA: ShapeAccelArray sensors

SSL: Steady state line

S_{ij}: Deviatoric stress component

σ: Normal stress

σ_c':Initial mean effective stress

σ_v': Effective vertical stress

σ_v: Total vertical stress

σ_{ho}': Initial effective horizontal stress

σ_{vo}: Initial total vertical stress

σ_{vo}': Initial effective vertical stress

t: Time

T: Tangential force exerted on the soil body

T_o: Normalized penetration rate

T_v: Time factor

τ: Average shear stress of soil

u_1: Pore water pressure at tip

u_2: Pore water pressure behind tip

Δu_1: Excess pore water pressure at tip

Δu_2: Excess pore water pressure behind tip

U_{ave}: Average degree of consolidation

ν: Poisson's ratio

v: Penetration rate

v_{xi}: Advection velocity in x_i axis

V: Volume

V_s: Measured shear wave velocity

V_{s1}: Normalized shear wave velocity

ω: Deflection of the points of the circular plate

W: Total weight of soil plus laminates in analysis

ψ: Dilation angle

z_c The vertical distance between cone shoulder/face and pore water pressure sensor location

Chapter 1. Introduction

1.1. Background and statement of problem

Liquefaction is one of the common phenomena that occurres during earthquake, causing severe damage to waterfront structures and lifelines. It is due to the fact that saturated loose sands and silty sands deposit experiences a loss of shear strength and become liquid-like material when subject to shaking.

Thanks to the ability of continuous recording of soil profile, cone penetration test (CPT) has been utilized to characterize the liquefaction potential of soils by relating the normalized cone tip resistance-q_{c1N} to the cyclic resistance ratio (CRR) - Fig. 1.1.

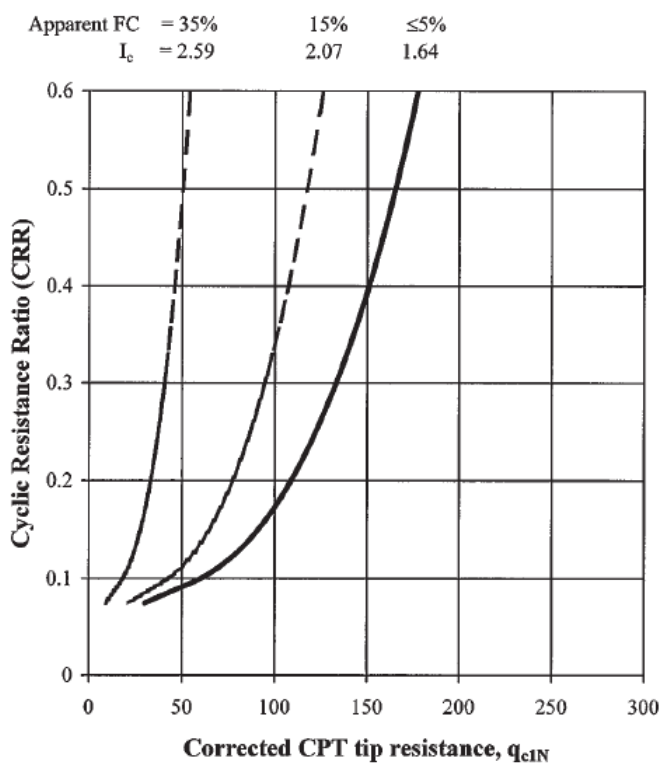

Fig. 1.1 Field based liquefaction screening chart using cone resistance (Robertson and Wride, 1998)

Recognizing the occurrence of liquefaction in silty sands, researchers began to study the effect of fines on liquefaction resistance (Singh, 1996; Carraro et al, 2003; Thevanayagam et al., 2003). It is reported that the mechanical behaviors of clean sand and silty sand are very similar at a given 'equivalent' inter-granular relative density $(D_{rc})_{eq}$ (Thevanayagam et al., 2002; Ni et al., 2004; Fu, 2006; Hazirbaba and Rathje, 2009).

However, the permeability (k) and coefficient of consolidation (c_v) of the sand and silty sand are very different at a given $(D_{rc})_{eq}$ (Shenthan, 2001, Thevanayagam and Martin, 2002). As a result, at a given $(D_{rc})_{eq}$, the effect of fines on the cone resistance is reflected in the coefficient of consolidation c_v via the normalized penetration rate T_o ($T_o=vd_c/c_v$, where v is the penetration velocity, d_c is the diameter of cone) (Finnie and Randolph 1994; House et al. 2001; Randolph and Hope 2004). Although studies have been carried out to examine the effect of T_o on the cone resistance, they are limited to clayed soil (Randolph and Hope, 2004; Chung et al., 2006; Kim et al. 2008; Yi et al., 2012). Recently, investigators (Carraro et al., 2003; Ecemis, 2008; Kumar and Baju, 2009; Kokusho et al., 2012) began to study the effect of T_o on the cone resistance and liquefaction resistance in silty sands using both experimental and numerical approaches. However, a convergent model was yet to be found and in this regard, a thorough study of the effect of T_o on the cone resistance in silty sands covering full range of $(D_{rc})_{eq}$ is in great need.

1.2. Scope of research

The objectives of research are presented as follows:

- Design a new chamber testing system, capable of simulating the condition of constant

vertical stress and zero lateral strain (ideally)-BC3. Conduct CPTs using Ottawa F55 saturated sand-silt mix at different fines contents (0,15 and 25%) to examine the effect of fines on the cone resistance at different fines content (0, 15 and 25%).

- Incorporate the Arbitrary Lagrangian Eulerian (ALE) mesh technique into the modified Drucker-Prager model (cap plasticity model) to thoroughly examine the effect of T_o on cone resistance in silty sands with $(D_{rc})_{eq}$ ranged from very loose to very dense.
- Carry out a series of liquefaction experiments along with cone penetration tests and shear wave velocity tests in a large scale laminar box system to examine the mechanisms and physics of the liquefaction phenomenon.
- Correlate the T_o dependent q_{c1N} to the measured CRR for the same soil used in the numerical analysis. Compare the relationship with the experiments performed in the testing chamber as well as in the laminar box.

1.3. Organization of the report

Chapter 2 presents a literature review on current research of the mechanical behaviors of silty sands, and on the experimental and numerical studies on the effects of fines and penetration rate on the cone resistance.

Chapter 3 details the design of the CPT testing chamber, and chapter 4 summarizes the CPT chamber test results.

Chapter 5 describes the calibration of the cap plasticity model through monotonic undrained triaxial tests and verification of the one-dimensional consolidation solution. The model setup for

the CPT in Abaqus and the validation of the simulation using the experimentals tests tests isintroduced.

Chapter 6 presents the parametric study of cone resistance in silty sand. The effect of permeability, penetration rate and cone diameter on the cone resistance is examined at different $(D_{rc})_{eq}$.

Chapter 7 introduces a new geotechnical facility- full scale laminar box at UB. Instrumentation for level ground test (LG1), sand preparation procedures using clean sands, input base motion are introduced as well. Chapter 8 analyses the experimental data and correlates the CPT/shear wave velocity data to CSR from LG1.

Chapter 9 proposes a T_o dependent relationship between CRR and q_{c1N} and compares the proposed relationship with miniature CPT tests conducted in the testing chamber and in the laminar box, as well as the existing field-based CPT liquefaction screening method.

Chapter 10 summarizes the finding in this dissertation and proposes future research endeavors.

In appendix A, the preliminary simulation of CPT using FLAC is presented.

In appendix B, the parametric study on key parameters of cap plasticity model using Abaqus is presented. Additional monotonic undrained triaxial tests using Ottawa F55 sand-silt mix are simulated.

In appendix C, the parametric study to optimize the numerical model of CPT simulation using Abaqus is described. The numerical examination of the effect of permeability on the cone resistance at different $(D_{rc})_{eq}$ using Drucker-Prager model is presented.

In appendix D, the setup and determination of the coefficient of friction of the ball bearings

used in LG1 is covered.

In appendix E, an additional analysis of liquefaction tests is presented and the raw data of performed shear wave velocity tests are shown as well.

Chapter 2. Literature review

2.1. Introduction

Liquefaction is thoroughly brought to the attention of engineers and researchers after two main earthquakes, 1964 Niigata earthquake and 1964 Alaska earthquake, as it caused severe damage to waterfront structures, lifelines and claimed hundreds of thousands of human lives (Seed and Idriss, 1967). The reason that liquefaction occurs is due to the fact that saturated loose sand deposit loses its shear strength and becomes liquid-like material when subject to seismic loading. It is reported that loose sand is more prone to liquefy than dense sand (Seed, 1979). To identify the liquefaction potential of sands and silty sands, in-situ tests results from standard penetration test (SPT), cone penetration test (CPT) and shear wave velocity test have been correlated to the cyclic resistance ratio (CRR) for different fines contents (Robertson and Campanella 1985; Seed and De Alba 1986; Stark and Olson 1995, Robertson and Wride, 1998; Stokoe et al., 1985). Generally, the liquefaction evaluation procedure uses an empirical correlation between the CRR and the field test results according to field observations. This CRR correlation basically provides a clean sand base curve and a suggested procedure to account for the fines content for sands with fines. However, the liquefaction screening methods do not give the essence of how fines affect the liquefaction potential assessment, which leads to researchers to explore the unknowns.

In this chapter, the liquefaction screening method using CPT is covered. Then a framework explaining the dependence of mechanical behavior of silty sands on the fines content proposed by researchers (Mitchell, 1993; Thevanayagam, 1998; Thevanayagam et al., 2002) is introduced.

Then the effect of fines on permeability and coefficient of consolidation is discussed. A summary on current experimental and numerical researches of the effect of normalized penetration rate (T_o) on the cone resistance in silty or clayed soil is presented. Finally, the objective of this research is brough up.

2.2. Liquefaction screening using CPT for sands and silty sands

Current approaches to evaluate the liquefaction potential are SPT, CPT and shear wave velocity measurement. CPT has gained much attention thanks to the ability of continuous recording of soil profile without missing potential thin layers and the repeatability of test results.

The first liquefaction potential evaluation using CPT was converted from SPT based liquefaction potential assessment for earthquake with magnitude equal to 7.5 (Robertson and Campanella, 1985; Seed and De Alba, 1986)-Fig. 2.1(a). Shibata and Teparaksa (1988) related the CRR to the normalized cone resistance (q_{c1N}) based upon CPT in-situ data [Fig. 2.1(b)]. Mitchell and Tseng (1990), using calibration chamber test results for various clean sands, calibrated a penetration resistance theory and applied it to calculate field cone resistance for soil states at which liquefaction occurred in laboratory liquefaction tests for 15 loading cycles, obtaining the curves shown in Fig. 2.1(b). Stark and Olson (1995) and Robertson and Wride (1998) established CPT-based correlations in Fig. 2.1(c). Idriss and Boulanger (2008) proposed a methodology to account for the effect of non-plastic fines on penetration and liquefaction resistance [Fig. 2.1(d)]. All of the proposed liquefaction assessments showed that the presence of fines causes the $(CRR)_{7.5}$-q_{c1N} curve shift to the left. This indicated the contribution of fines in liquefaction resistance is agreed

among the investigators.

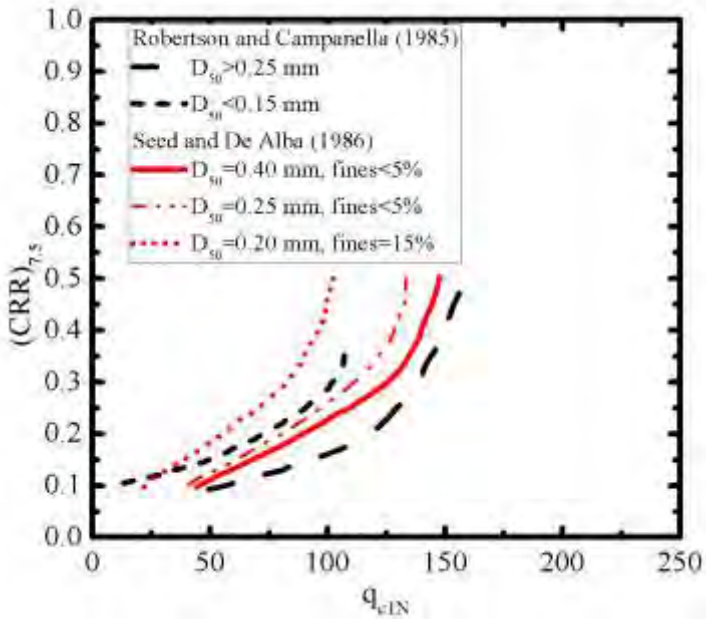

(a)

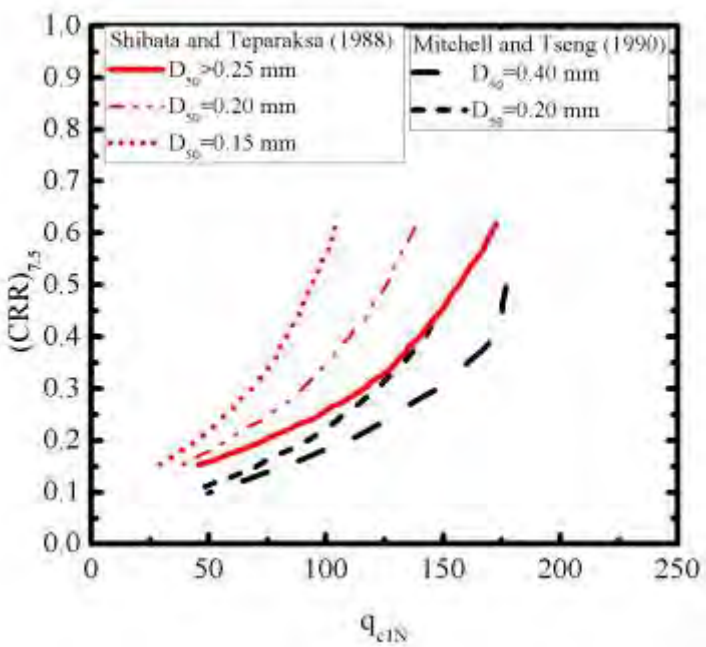

(b)

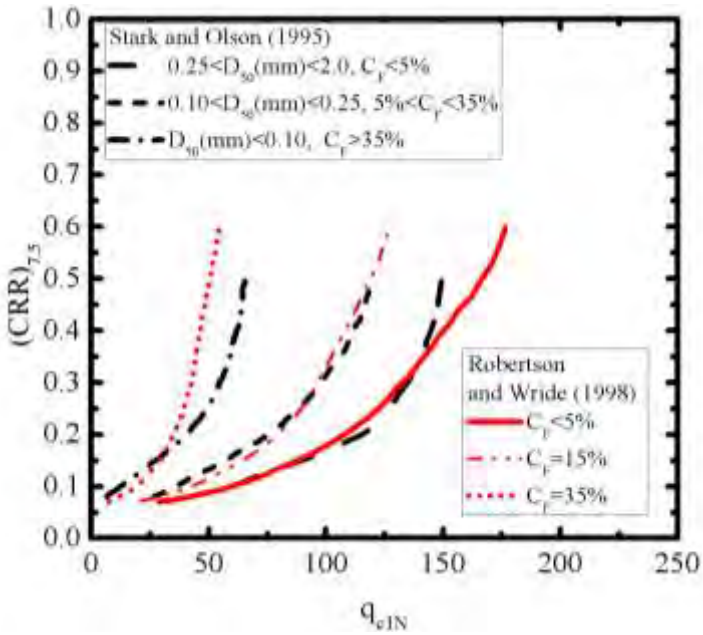

(c)

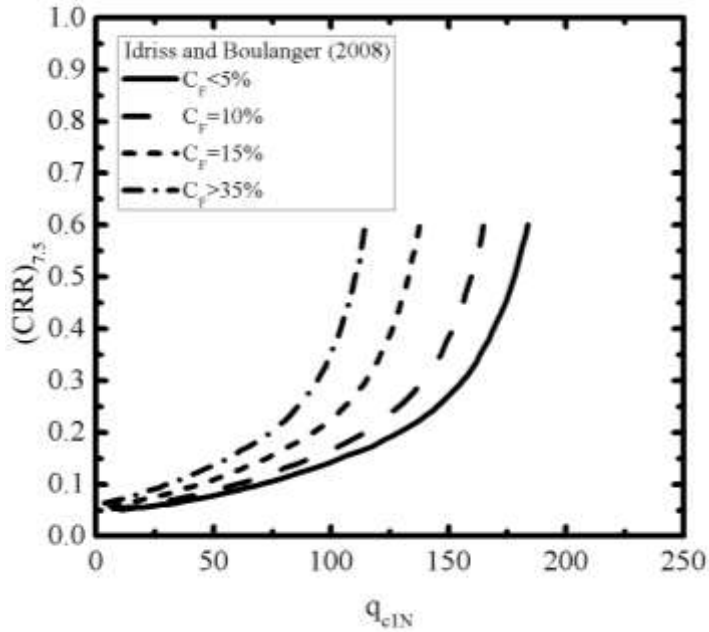

(d)

Fig. 2.1 Liquefaction potential evaluation charts for sands/silty sands using CPT

It shall be noticed that the above mentioned liquefaction potential assessments are relating the CRR at earthquake magnitude of 7.5 to the normalized cone resistance q_{c1N} as:

$$q_{c1N} = \frac{q_{c1}}{P_{at}} = C_Q(\frac{q_c}{P_{at}}) \qquad \text{(Eq. 2.1)}$$

Where q_c is the field cone penetration resistance, P_{at} is the atmospheric pressure and C_Q is the factor to correct the initial effective overburden stress (σ_{vo}'), and defined by Stark and Olson (1995) as

$$C_Q = \frac{1.8}{0.8 + (\sigma_{vo}' / P_{at})} \qquad \text{(Eq. 2.2)}$$

or Youd and Idriss (2001) as

$$C_Q = \left(\frac{P_{at}}{\sigma_{vo}'}\right)^n \leq 1.7 \qquad \text{(Eq. 2.3)}$$

Where n is exponent that differs with soil type and is recommended as 0.5 for clean sand.

It is pointed out that if the magnitude of earthquake is other than 7.5, a magnitude scaling factor (MSF) shall be employed to correct the effect.

Table 2.1 summarizes MSF values defined by various researchers.

Table 2.1 Various MSF proposed by investigators (Youd and Idriss 2001)

Magnitude	Seed and Idriss (1982)	Idriss (1995)	Ambraseys (1988)	Arango (1996)		Andrus and Stoke (1997)	Youd and Noble (1997)		
M_w				Distance based	Energy based		P_L[1]<20%	P_L<32%	P_L<50%
5.5	1.43	2.20	2.86	3.00	2.20	2.80	2.86	3.42	4.44
6.0	1.32	1.76	2.20	2.00	1.65	2.10	1.93	2.35	2,92
6.5	1.19	1.44	1.69	1.60	1.40	1.60	1.34	1.66	1.99
7.0	1.08	1.19	1.30	1.25	1.10	1.25	1.00	1.20	1.39
7.5	1.00	1.00	1.00	1.00	1.00	1.00	-	-	1.00
8.0	0.94	0.84	0.67	0.75	0.85	0.80?[2]	-	-	0.73?
8.5	0.89	0.72	0.44	-	-	0.65?	-	-	0.56?

The factor of safety (FS_L) is employed to evaluate the initiation of liquefaction potential of a given site at give a depth using the charts provided in Fig. 2.1:

$$FS_L = \frac{(CRR)_{7.5}}{CSR} MSF \qquad \text{(Eq. 2.4)}$$

Where

$$CSR = 0.65 \frac{a_{\max-ground}}{g} \sigma_v r_d / \sigma'_{vo} \qquad \text{(Eq. 2.5)}$$

Where CSR is the cyclic stress ratio, $a_{max\text{-}ground}$ is the peak ground surface acceleration, g the acceleration of gravity, σ_v the total vertical stress and r_d the value of a stress reduction factor at depth of interest (Fig. 2.2).

[1] P_L: The probability that liquefaction occurs

[2] ?: Uncertain proposed MSF value

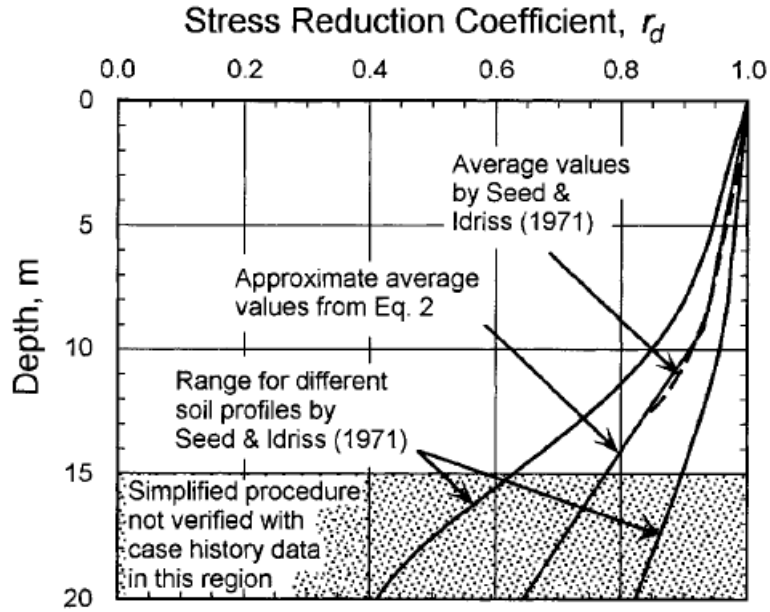

Fig. 2.2 Reduction factor to estimate the variation of cyclic shear stress with depth below level or gently sloping ground surface (Youd and Idriss, 2001)

Although investigators proposed CPT-based liquefaction assessment for sands as well as silty sands, the understanding of how fines affect the liquefaction resistance and cone resistance in silty sands remained unclear.

2.3. Effect of fines on mechanical behavior in silty sands

Attention is drawn to silty sands as liquefaction is observed on this type of soil mixtures (Ishihara, 1985; Troncoso and Verdugo, 1985; Chang, 1987). Extensive experiments and case studies have been carried out to examine the effect of fine grains on the SSL (Ni et. al., 2004; Naeini et al., 2004; Yang et. al., 2006; Murthy et al., 2007; Rahman et al., 2008) and liquefaction resistance (Polito and Martin II, 2001; Carraro et al., 2003; Xenaki et al., 2003; Cubrinovski and Rees, 2008; Hazirbaba and Rathje, 2009; Papadopoulou and Tika, 2008; Stamatopoulos, 2010) in silty sands. However, the essence of how the fines affect the mechanical behavior in silty sands is

not revealed. Recently, a framework (Mitchell, 1993; Thevanayagam, 1998; Thevanayagam et al., 2002) is developed to relate the fines content to the mechanical behavior of silty sands through a contact density index. This section presents a brief summary of this work, and shows an example to support this approach.

2.3.1. Framework of inter-granular contact density indices of silty sands

Void ratio is introduced as a state variable to evaluate the monotonic as well as cyclic response in soils. Previous laboratory tests showed that the global void ratio (e) is a poor index for soil mixtures, because the presence of fine grains contributed to the mechanic behavior such as steady state, shear strength, modulus and cyclic resistance (Salgado et al., 2000; Carraro et al. 2003; Xenaki et al. 2003; Thevanayagam et al. 2003). Mitchell (1993) firstly developed an equation to determine the inter-granular void ratio ignoring the active participation of fine or coarse grains in the force chain. Thevanayagam et al. (2002) introduced parameters b and m to quantify the degree of force chain that fine or coarse grains involved in the mixture.

The classification of whether or not and how fine or coarse-grained particles contribute to the force chain can be seen in Fig. 2.3 based on the fines content C_F and the threshold fines content C_{Fth}:

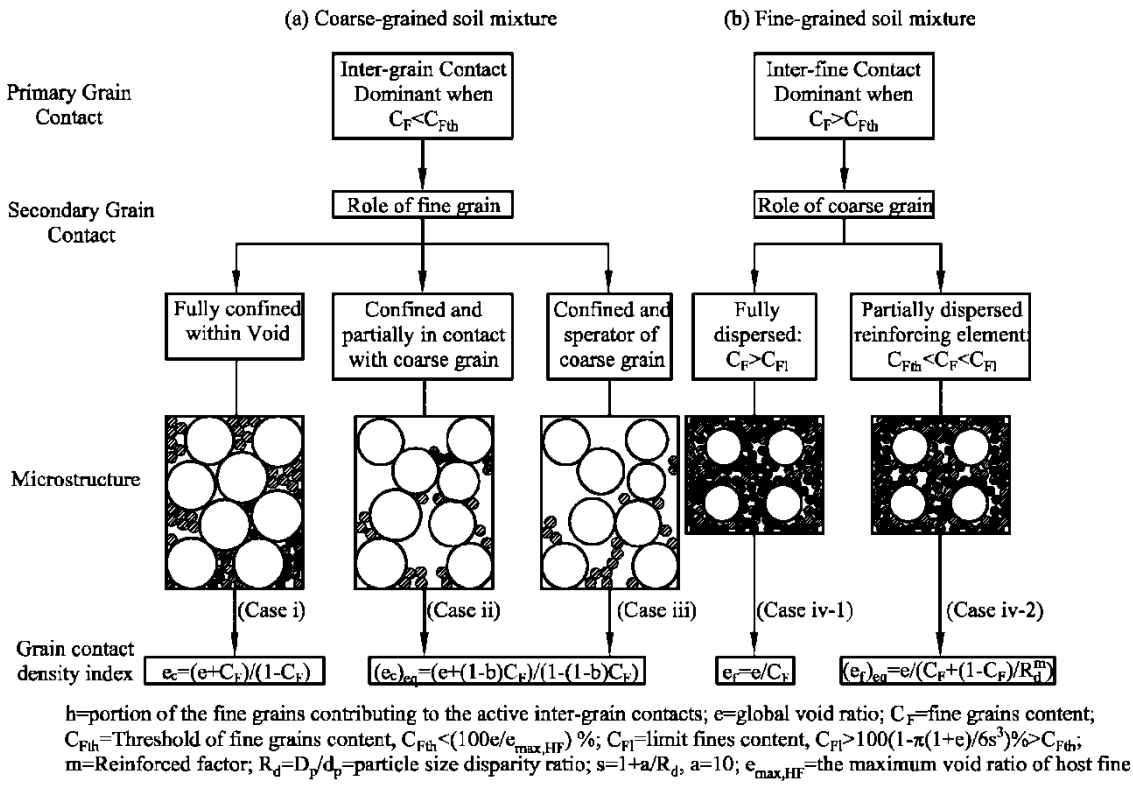

Fig. 2.3 Inter-granular soil mix classification (Thevanayagam et al., 2003)

Fig. 2.4 presents a conceptual diagram of the regions to which case i through case iv belong as well as transition boundaries, limit of minimum void ratio e_{min}, maximum void ratio e_{max}, threshold fines content C_{Fth} and limit fines content C_{Fl} using Ottawa F55 (OS F55) sand-silt mixture.

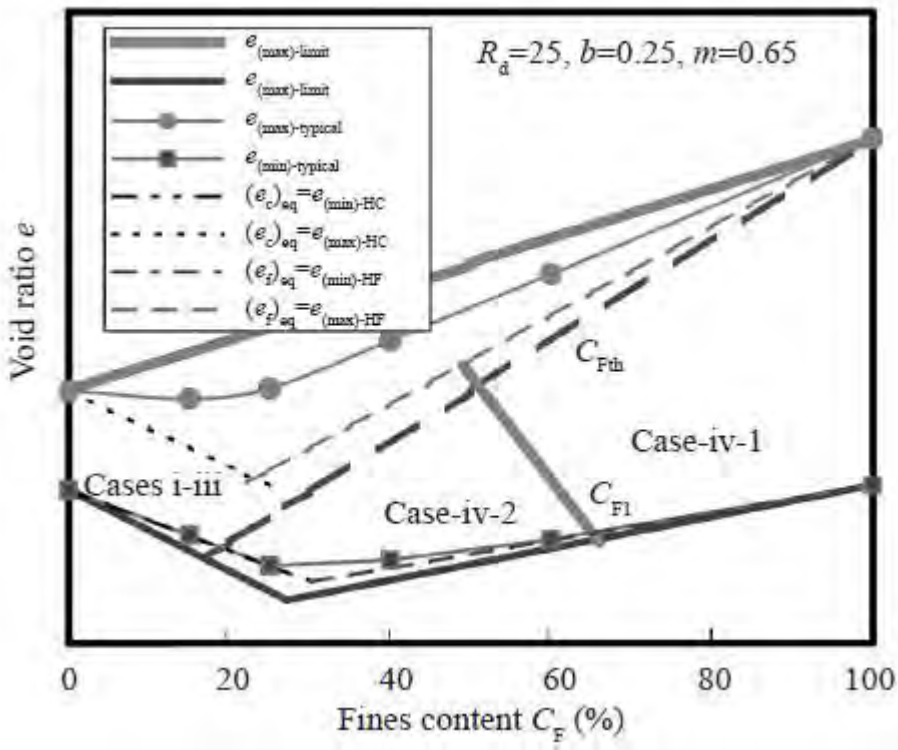

Fig. 2.4 Granular Mix Classifications for OS F55 sand-silt mix (Thevanayagam, 2007a)

2.3.1.1. C_F<C_{Fth} (case i, ii and iii)

There are three cases falling into this category, namely, case i, case ii and case iii, in which coarse grains are the host particles. In case i, when the fine grains are fully confined in the void space of coarse grains, there is no contribution of fine grains to the force chain in soil mixtures. This would result from very large particle size disparity ($R_d = D_p/d_p >> 6.5$) and very low fine content ($C_F << C_{Fth}$) (Thevanayagam, 2007a). In case ii and iii, the coarse-grained particles are separated by some fine-grained particles while the other fine-grained particles remain in the void of coarse-grained particles. Thus the active fine-grained particles separating coarse-grained particles contribute to the internal force chain. The parameter-b, which quantifies the portion of contribution of fine grains in the force chain, is defined to determine the equivalent inter-granular void ratio $(e_c)_{eq}$:

$$(e_c)_{eq} = \frac{e + (1-b)C_F}{1-(1-b)C_F} \qquad \text{(Eq. 2.6)}$$

where e is the global void ratio

0≤b≤1 for non-plastic fines, b=0 indicates zero contribution of fine-grains in the inter-granular force chain, Eq. 2.6 can be express as:

$$(e_c)_{eq} = \frac{e + C_F}{1-C_F} \qquad \text{(Eq. 2.7)}$$

b=1 represents full participation of fine-grained in the inter-granular force chain, and Eq. 2.6 can be rewritten as :

$$(e_c)_{eq} = e \qquad \text{(Eq. 2.8)}$$

When compared the behavior of soil mixtures to host coarse grains, the equivalent inter-granular relative density of soil mixtures $(D_{rc})_{eq}$ shall be used as follows:

$$(D_{rc})_{eq} = \frac{e_{\max,HC} - (e_c)_{eq}}{e_{\max,HC} - e_{\min,HC}} \qquad \text{(Eq. 2.9)}$$

where $e_{max,HC}$ and $e_{min,HC}$ are the maximum and minimum void ratio of the host coarse grain.

2.3.1.2. $C_F > C_{Fth}$ (case iv-1 and iv-2)

When the fines content C_F is greater than the threshold of fines content C_{Fth}, fine grains become the host particles and there are two conditions for this category. The equivalent inter-fine void ratio $[(e_f)_{eq}]$ replacing global void ratio (e) can be determined by introducing a reinforced factor m as :

$$(e_f)_{eq} = \left[\frac{e}{C_F + \frac{(1-C_F)}{R_d^m}} \right] < e_f \le e_{\max,HF} \qquad \text{(Eq. 2.10)}$$

0<m<1, if R_d is very large then Eq. 2.10 can be expressed as:

$$(e_f)_{eq} = \frac{e}{C_F} \qquad \text{(Eq. 2.11)}$$

if R_d =1, then Eq. 2.10 can be rewritten as:

$$(e_f)_{eq} = e \qquad \text{(Eq. 2.12)}$$

So when compared the behavior of soil mixtures to host fine grains, the equivalent inter-fine relative density of soil mixtures $(D_{rf})_{eq}$ shall be used as follows:

$$(D_{rf})_{eq} = \frac{e_{\max,HF} - (e_c)_{eq}}{e_{\max,HF} - e_{\min,HF}} \qquad \text{(Eq. 2.13)}$$

Where $e_{max,HF}$ and $e_{min,HF}$ are the maximum and minimum void ratio of host fine.

Further information on microstructure of soil mixture can be referred to (Thevanayagam, 2007 a and b).

2.3.2. Example on the inter-granular contact density index

An example is shown by interpreting monotonic and cyclic undrained triaxial tests conducted by Curbrinovski and Rees (2008). The soil sample was Fitzgerald bridge mixture from Christchurch, New Zealand. The properties of each soil are tabulated in Table 2.2. Soil samples were isotropically consolidated to an initial mean effective stress of 100 kPa and then for monotonic and cyclic undrained triaxial tests. As can be found from Fig. 2.5, a unique SSL in monotonic tests in terms of $(e_c)_{eq}$ and a unique correlation between $(e_c)_{eq}$ and CSR in cyclic tests are established by incorporating the parameter-b. This indicate that, when compared at the same $(e_c)_{eq}$ or $(D_{rc})_{eq}$, the mechanical behavior such as stress-strain relationship and liquefaction resistance of sands and silty sands are the same.

Table 2.2 properties of soil and test type used for evaluation

Coarse-grain	Fine-grain	C_{uc}	C_{uf}	R_d
Fitzgerald bridge mixture		2.1	18.0	10.9

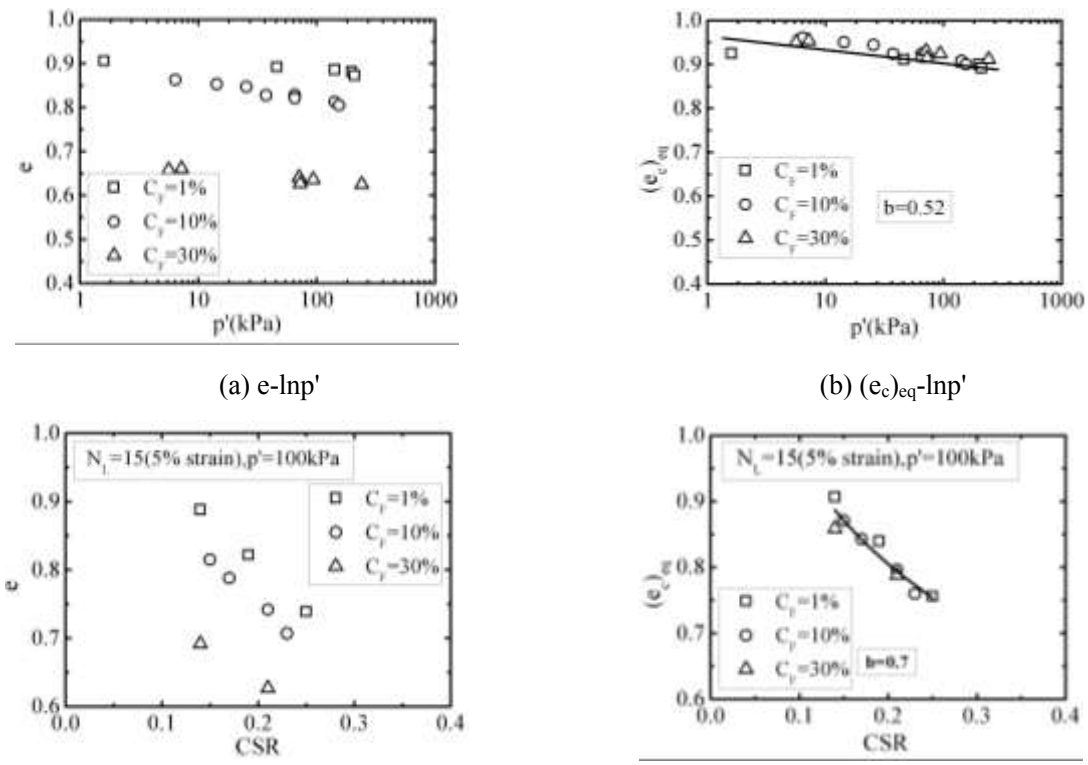

(a) e-lnp'

(b) $(e_c)_{eq}$-lnp'

(c) e-CSR

(d) $(e_c)_{eq}$-CSR

Fig. 2.5 Determination of b_{mon} and b_{cyc} for Fitzgerald bridge mixture when $C_F<C_{Fth}$ (After Curbrinovski and Rees, 2008)

2.4. Effect of fines on permeability and coefficient of consolidation in silty sands

As discussed in section 2.3, at a given $(D_{rc})_{eq}$, sands and silty sands would exhibit at least similar, if not identical, stress-stain relationship and liquefaction resistance. However, available experimental results suggested that even at a given of $(D_{rc})_{eq}$, the permeability (k) and the coefficient of consolidation (c_v) of clean sand and silty sand are very different. k and c_v decrease drastically as silt content increases (Shenthan, 2001; Thevanayagam and Martin 2002).

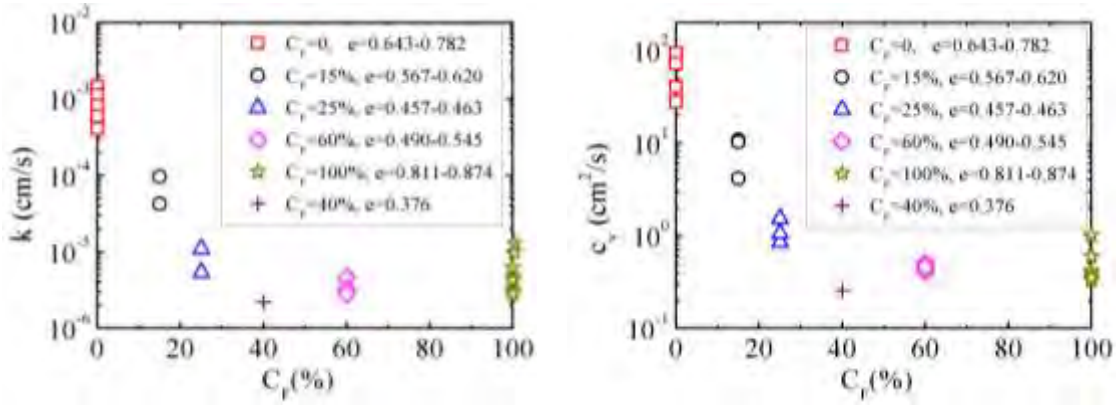

(a) k versus C_F (b) c_v versus C_F

Fig. 2.6 Variation of k and C_v versus C_F (Shenthan 2001, Thevanayagam and Martin 2002)

Fig. 2.6 compares the k and c_v at different C_F for the Ottawa F55 (OS F55) sand mixed with non-plastic fines. The notation 'C_F=25%, e=0.457-0.463' in the figure denotes the fines content is at 25% and the void ratio is ranged from 0.457 to 0.463. For each fines content, both k and c_v vary in a small range due to the difference in void ratio. However, k and c_v decrease rapidly (approximately one order) as C_F increases from 0% to 15%, 15% to 25% and 25% to 40% (up to threshold fines content C_{Fth}). The significant drop in k and c_v value with the increase of C_F up to C_{Fth} is mainly due to the reduced pore size. The k value of the soil specimens is ranged from 0.6 to 1.3x10^{-3} cm/s for C_F=0%, 4-9x10^{-5} cm/s for C_F=15%, 0.6 to 1.2x10^{-5} cm/s for C_F=25%. The corresponding c_v value for C_F=0%, 15% and 25% are 28-93, 4-11, 0.9-1.5 cm^2/s, respectively. However, the k and c_v value slightly increase with increase of fines content after C_F>C_{Fth}. This is attributive to the effect of void ratio. The k value is 3 to 5x10^{-5} cm/s for C_F=60% and 100% and the corresponding c_v values for C_F=60% and 100% are 0.3 to 0.5 and 0.3 to 1 cm^2/s.

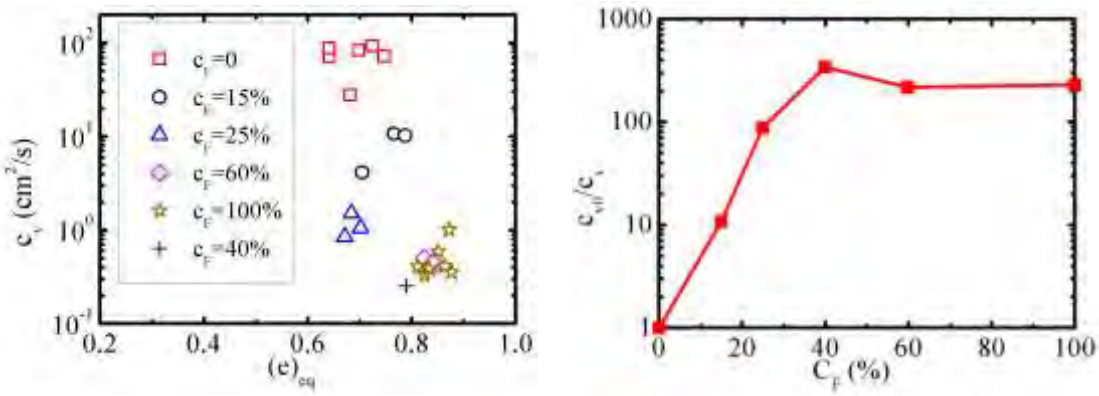

(a) c_v versus $(e)_{eq}$ (b) $(c_v)_0/c_v$ versus C_F

Fig. 2.7 Effect of C_F on C_v (Thevanayagam and Martin 2002)

Fig. 2.7(a) plots c_v versus $(e)_{eq}$ [$(e_c)_{eq}$ for $C_F<C_{Fth}$, $(e_f)_{eq}$ for $C_F>C_{Fth}$]. Contrast to the observation from chapter 3 that a unique SSL and a unique relationship between liquefaction resistance versus $(e)_{eq}$ can be obtained for a soil mixture, there is no correlation between c_v and $(e)_{eq}$. Fig. 2.7(b) shows the normalized (c_{v0}/c_v) versus C_F at nearly the same $(e)_{eq}$, where c_{v0} and c_v are the coefficient of consolidation of clean sand and sand-silt mixture, respectively. The (c_{v0}/c_v) increases significantly with increase of C_F up to about C_{Fth} and is less influenced by the C_F when $C_F>C_{Fth}$. It is argued that at the same contact density, the increase of fines content greatly affects the pore size and permeability, leading to the reduction in c_v. However, when the fines content exceeds the threshold fines content ($C_F>C_{Fth}$), the influence of C_F on the changing of pore size is less apparent compare to that at $C_F<C_{Fth}$. It is noticed that although the absolute magnitude of (c_{v0}/c_v) versus C_F in Fig. 2.7(b) is only for the Ottawa sand-silt mixture, the overall trend for other soil mixtures is expected to be similar.

Based on the observation of the effect of fines on k and c_v, it is noticed that both k and c_v of silty sand differ from clean sand even compared at the same $(e_c)_{eq}$ or $(D_{rc})_{eq}$. k and c_v of silty sand are much smaller than clean sand. The difference of c_v between clean sand and silty sand would

lead to the variation of dissipation time of induced excess pore water pressure as cone penetrates into the soil, hence results in the difference of drainage condition, which plays an important role in the cone resistance.

2.5. Normalized penetration rate-T_o

As mentioned previously, the semi-empirical correlations of q_{c1N}-CRR proposed to evaluate the liquefaction potential does not reveal the essence of fines effect in the cone resistance. The remaining unknown sparks investigations of the effect of fines on the cone resistance in silty sands and other soil mixtures.

It is believed that one of the reasons that the cone resistance differs in soils lies in the various drainage conditions when the cone penetrometer is advancing into different soils. For example, the clean sand, having high permeability, undergoes drained condition and consolidates due to fast dissipation of the excess pore water pressure as the cone penetrates. Hence, it has higher cone resistance when compared to low permeability soils given that all other parameters are identical. The penetration rate (v) and the diameter of cone (d) are also both non-soil-property-related factors contributive to the cone resistance. Thus, a non-dimensional penetration rate T_o (Finnie and Randolph 1994; House et al. 2001; Randolph and Hope 2004) was introduced to probe the degree of consolidation during penetration as follows:

$$T_o = \frac{vd_c}{c_v} \qquad \text{(Eq. 2.14)}$$

Where T_o is the normalized penetration rate,

v is the cone penetration rate,

d_c is the diameter of cone

c_v is the coefficient of consolidation.

Current researches on quantifying the limit value of T_o for drained and undrained conditions during cone penetration were mainly in clayed soils using various penetration rates. (Randolph and Hope, 2004; Chung et al., 2006; Schneider et al., 2007; Kim et al. 2008, Jaeger et al, 2010; Yi et al., 2012). Table 2.3 summarizes the reported limit values of T_o for drained and undrained conditions for various soils.

Table 2.3 Reported T_o for drained and undrained conditions during cone penetration

Test type	Soil type	Undrained	Drained	Reference
Centrifuge	Sand	T_o>30	T_o<0.01	Finnie and Randolph, 1994
Centrifuge	-	T_o>30	-	Randolph and Hope, 2004
Centrifuge	OC and NC clay	T_o>100	-	Schneider et al., 2007
In-situ	Clayed sand	T_o>30	-	Kim et al., 2008
Calibration chamber	Clayed sand	T_o>10	T_o<0.05	Kim et al., 2008
Numerical	Silty sand	T_o>6	T_o<0.01	Ecemis, 2008
Centrifuge	Clayed sand	T_o>20	T_o<0.01	Jaeger et al, 2010
Centrifuge	Clayed soil	T_o>70	T_o<1	Oliveira et al, 2011
Numerical	Fine-grained soil	T_o>10	T_o<0.1	Yi et al., 2012

2.6. Effect of Drainage conditions on cone resistance and liquefaction screening in sands and silty sands

Laboratory testing and numerical examination are the two major approaches to study the effect of T_o on the cone resistance and liquefaction screening among the limited researches.

2.6.1. Laboratory study

Carraro et al. (2003) proposed a correlations between $(CRR)_{7.5}$ and q_{c1N} of sands and silty sands from the help of Ottawa sand with non-plastic silt. The correlation was based on the cyclic

undrained triaxial tests and a cone resistance analysis developed by Salgado using CONPOINT (Fig. 2.8). The cone resistance was computed at the effective overburden stress σ_{vo}'=100 kPa and at the coefficient of lateral earth pressure at rest of 0.40 for each fines content. The theoretical values of cone resistance were calculated for the same relative densities for which the CRR values for 15(20) cycles were determined in the laboratory testing program.

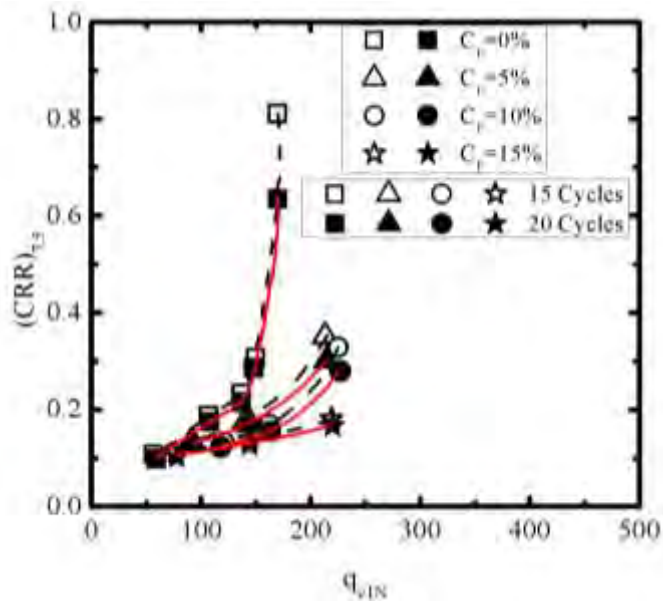

Fig. 2.8 $(CRR)_{7.5}$ vs q_{c1N} for different fines contents for 15 and 20 cycles at double strain for 5% (Carraro et al., 2003)

They found that the liquefaction resistance of clean sand was not much affected by the selection of liquefaction criteria while it shifted up for sands containing different fines contents as the liquefaction criterion changed from 5% double-amplitude axial strain at 20 cycles to 5% double amplitude axial strain at 15 cycles. Contrast to the field based $(CRR)_{7.5}$-q_{c1N} correlation proposed by other researchers (Fig. 2.1), they reported that the cone resistance increased at a faster rate with respect to fines content than cyclic resistance for a given relative density and this phenomenon directly led the $(CRR)_{7.5}$ vs q_{c1N} curve of sands with fines to the right of clean sand. Salgado et al.

(2000) attributed the behavior to the fundamental changes of the fabric of the material when silt content was gradually increased. The reported T_o for soil mixtures of C_F=15% at D_r=31% is approximately 0.75.

Kumar and Baju (2009) accommodated a miniature cone penetrometer with 19.5 mm in diameter to a large triaxial chamber with diameter of 140 mm (chamber size ratio of 140/19.5=7.8). Three types of soil, namely clean sand, sand with silt content of 15% and 25%, were examined in this apparatus with different penetration rates (0.01 mm/s to 0.1mm/s) under various confining stresses (100 and 300 kPa).

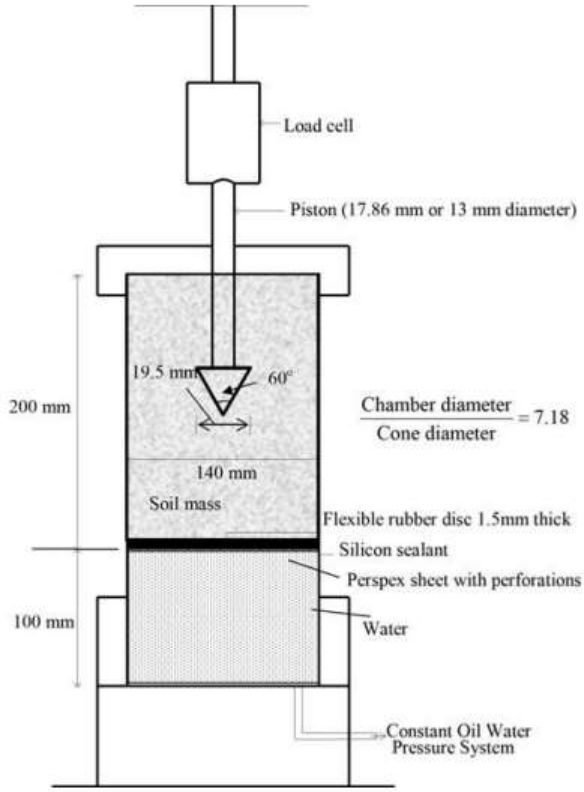

Fig. 2.9 Schematic view of miniature cone penetrometer in a triaxial chamber (Kumar and Baju, 2009)

As seen in Fig. 2.9, the load cell was located at top of penetrometer instead of cone tip. Hence, the cone resistance was calculated based on the measured data subtracted by the sleeve friction

contributed by the shrunken diameter piston. They assumed the K_0 state of soil surrounding piston shaft and suggested the interface friction angle between the shaft and soil being half of the friction angle of the soil to estimate the skin friction from the piston shaft. It was argued that the contribution from the shaft only accounted for less 10% in the total cone resistance.

According to the calculated cone resistance, Table 2.4 summarized the comparison of q_c between penetration rate at 0.1 mm/s and 0.02 mm/s. As can be found in this table, it was reported that the q_c increased with penetration rate. It is possible that the maximum penetration rate (0.1 mm/s) applied in this research is not large enough to trigger the transition of drainage condition (i.e. from drained to partially drained, or even to undrained condition) and hence the entire variation of penetration rate yet remained at drained condition. Faster penetration rate such as standard penetration rate of 20 mm/s is needed to validate the conclusion proposed in this paper.

Table 2.4 Percentage increase in q_c at penetration rate of 0.1 mm/s with respect to corresponding value at 0.02 mm/s (Kumar and Baju, 2009)

Soil Type	Relative density					
	Loose		Medium dense		Dense	
	σ_{vo}'=100 kPa	σ_{vo}'=300 kPa	σ_{vo}'=100 kPa	σ_{vo}'=300 kPa	σ_{vo}'=100 kPa	σ_{vo}'=300 kPa
Clean sand	12.7	8.4	8.2	6.3	7.6	6.4
Sand with 15% silt	10.5	8.0	8.8	7.0	6.5	7.2
Sand with 25% silt	15.9	14.9	13.2	11.8	10.0	7.5

Kokusho et al. (2012) incorporated a miniature cone with 6 mm in diameter and 115.2 mm in height (Fig. 2.10) into a conventional triaxial test apparatus in the attempt of performing CPTs and undrained triaxial tests in the same specimen (100 mm in diameter and 200 mm in height). A series of CPTs and cyclic undrained triaxial tests were completed to examine the effect of non/low-fines on the cone resistance and liquefaction resistance. The host sands was Futtsu beach sand while the

fine particles consisted of silty and clayey soils with low plasticity index about 6. The penetration rate in the sand with different fines content was initiated at about 0.2 cm/s. They noticed that the cone resistance as well as liquefaction resistance decreased with the increase of fines content irrelevant to the relative density and the fines content, and developed a unique relationship between $(CRR)_{tx\text{-}20}$ required to cause liquefaction in 20 cycles and cone resistance shown in Fig. 2.11. It was attributive to that the experimental data points fell into a narrow area. It shall be noticed that the unique relationship, contracted with current liquefaction evaluation charts presented in Fig. 2.1, was that cone resistance increased as the result of increase of fines content. It shall be noted that the diameter of the cone is about one sixth of the 3.57 cm diameter cone and the penetration rate is one tenth of the standard penetration rate (2 cm/s), which may lead to partially drained or even drained condition even the CPT is performed at the highest fines content of 30%.

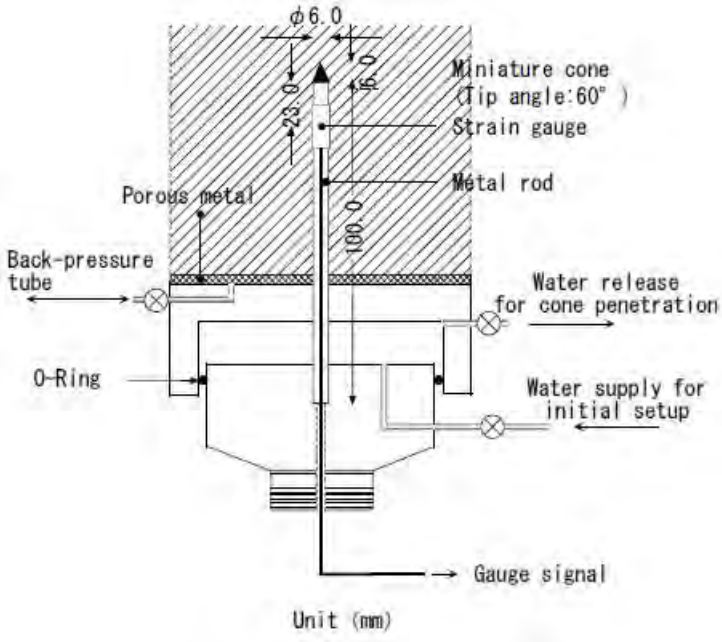

Fig. 2.10 Cross-section of modified triaxial test apparatus (Kokusho et al., 2012)

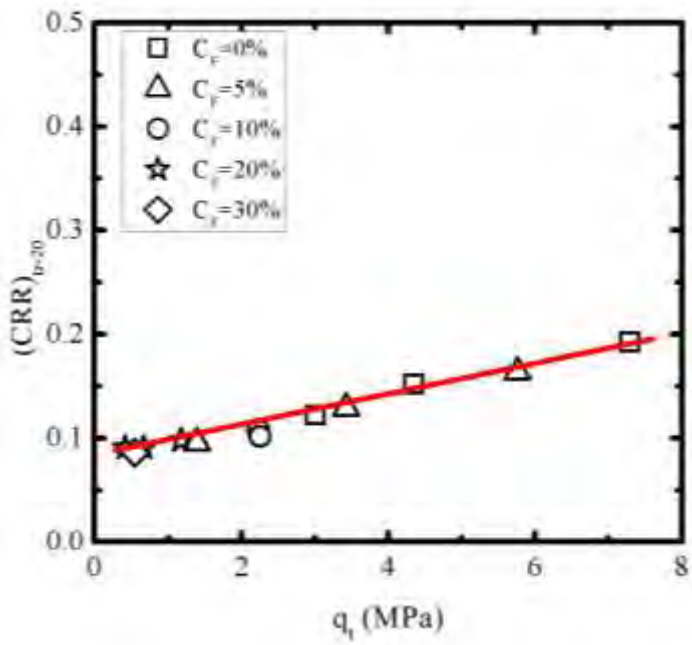

Fig. 2.11 Relationship between CSR and peak cone resistance (Kokusho et al., 2012)

In view of the above, it is found that non-soil-property-related factors such as the penetration rate were often omitted or not fully considered when experimentally examining the effect of fines on silty sands.

2.6.2. Finite element method

Finite element method has been widely applied to study the CPT in either sand for drained condition or clay for undrained condition at the ASTM standard rate of 2 cm/s. Small strain and large strain analysis are the two commonly used techniques of simulating CPT in FEM. A pre-drilled hole in which the cone is placed before penetration is a necessity if the small strain analysis is to be used (Griffiths 1982; De Borst and Verweer, 1984). Arbitrary Lagrangian Eulerian (ALE) formulation and adaptive remeshing strategies based on a Lagrangian formulation are major means in the large strain approach. ALE, uncoupling the evolution of the mesh and material particles and restraining the mesh evolution to bypass heavily mesh distortion, was firstly employed to tackle

this locally heavily distorted problem by Van Den Berger (1994). Susila and Susila and Hryciw (2003) also applied this technique to simulate the CPT in sand using explicit algorithm. Adaptive remeshing strategy, on the other hand, applies Lagrangian formulation and adapts a special remeshing technique as distortion occurs.

The normalized penetration depth D/d_c (D denotes the penetration depth and d_c represents the cone diameter) is used to quantify the penetration depth required to reach steady state of cone resistance. Kiousis (1988) reported a steady state of tip resistance is almost reached when $D/d_c=1/3$ using modified Drucker-Prager (cap) plasticity model to study the cone resistance in clay. The steady state of cone resistance in clayed using Modified Cam-clay model was achieved at $D/d_c \approx 2$ investigated by Voyiadjis and Abu-Farsakh (1997). Wei (2004) reported the value of D/d_c slightly larger than 0.5 yielded converged cone resistance when the effect of inclination on the cone resistance is examined in clayed soil using a user developed constitutive model. All of the above-mentioned examination adopted a pre-bored hole geometry in which the cone was installed at certain depth underneath surface.

Currently, most of the numerical simulations of CPT are either using sand (drained condition) (Van Den Berger, 1994; Susila and Hryciw, 2003; Huang et. al., 2004; Tolooiyan and Gavin, 2011) or clay (undrained condition). Recently, researchers began to take into the consolidation effect in the numerical examination when studying the effect of T_o on the cone resistance in clayed soil. Markauskas et al. (2005) investigated the effect of permeability on the cone resistance in clayed soil using a remeshing technique combined with the cap model (d_c=3.56 cm and v=2cm/s). Fig. 2.12 showed that the drained condition occurred at $k=10^{-5}$ m/s with corresponding T_o=0.25 while

the undrained condition happened at $k=10^{-9}$ m/s with corresponding T_o=2500. Yi el al. (2012) studied the effect of penetration rate on the cone resistance in fine-grained soil using updated Lagrangian formulation. The Drucker-Prager model with no dilation as well as cap model was utilized to perform the study. The penetration rate varied from 1 mm/s to 1×10^{-6} mm/s and the cone diameter was 1 m. T_o for drained and undrained conditions were reported to be 0.1 and 10, respectively.

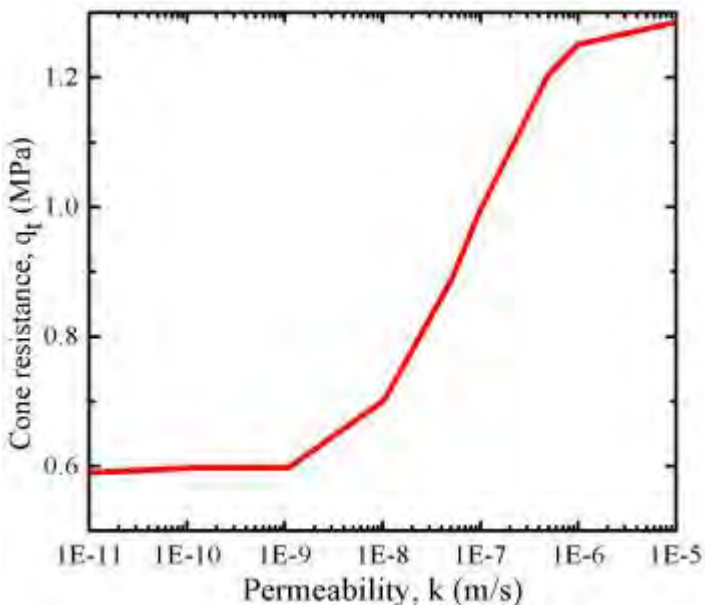

Fig. 2.12 Variation of cone resistance with respect to permeability (Markauskas et al. , 2005)

Ecemis (2008) numerically examined the effect of permeability and compressibility on liquefaction assessment in silty sands using standard cone of 4.37 cm in diameter and standard penetration rate of 2 cm/s. Ottawa F55 sand mixed with various fines contents were the research targets. Undrained monotonic triaxial tests on the sand-silt mixtures performed by Thevanayagam et al. (2003) were employed to calibrate the Drucker-Prager model used in CPT simulation. Numerical values of q_{c1N} were then obtained from the soil mixture with different $(D_{rc})_{eq}$ at various

permeabilities. The investigation showed that for a given $(D_{rc})_{eq}$, q_{c1N} decreased as T_o transited from drained to undrained condition and stabilized when T_o reached the threshold value of undrained condition. As shown in Fig. 2.13, the reported T_o for drained and undrained conditions are about 0.01 and 6, respectively. T_o value ranged from 0.01 to 6 indicates partially drained condition. Fig. 2.14 shows the proposed the correlation between $(CRR)_{7.5}$ and q_{c1N} based upon experimental results reported by Thevanayagam et al. (2003) and the numerical results. It was reported that when T_o increased the correlation curves shifted to the left due to the changing of drainage condition. However, it is noticed that the D/d_c used to calculate q_{c1N} in this analysis was smaller than 1/3 due to some numerical issues. It is also found in this study that the induced excess pore water pressure at cone tip of dense sand-silt mix (dilative material) at low permeability is considerably negative, which is not reported from field observation.

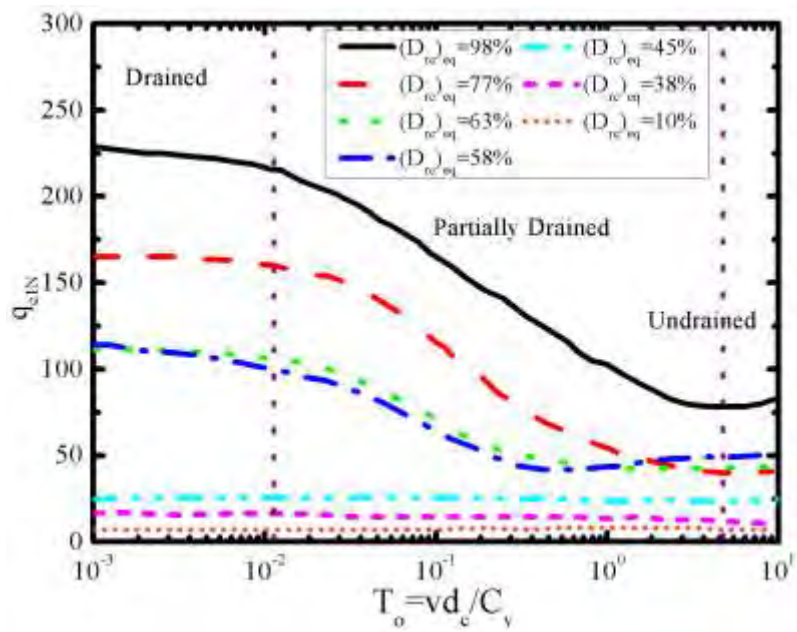

Fig. 2.13 q_{c1N} versus T_o with different $(D_{rc})_{eq}$ (Ecemis, 2008)

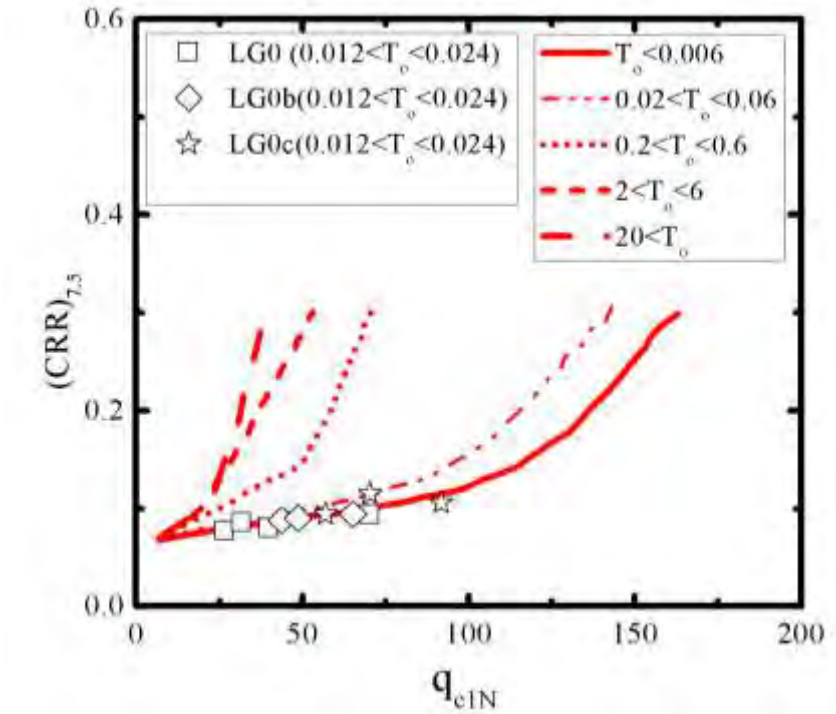

Fig. 2.14 Proposed $(CRR)_{7.5}$ versus q_{c1N} for different T_o (Ecemis, 2008)

In view of this, it is necessary to propose a robust numerical model to performe the parametric study of cone resistance in both loose (contractive) and dense (dilative) silty sands at large penetration depth (e.g. $D/d_c>1$).

2.7. Summary

Based upon the literature review, the effect of fines plays important roles in cone resistance through the following manners: (1) Affecting the stress-strain relationship as well as liquefaction resistance through contact density index. At a given equivalent inter-granular void ratio $[(e_c)_{eq}]$ instead of global void ratio (e), the clean sand and silty sand would exhibit at least similar, if not the same, mechanical behavior such as stress-strain relationship and liquefaction resistance. (2) Affecting the drainage condition through the normalized penetration rate T_o by the coefficient of consolidation c_v ($T_o=vd_c/c_v$). At a given $(e_c)_{eq}$ or $(D_{rc})_{eq}$, c_v decreases significantly as fines content

increases when $C_F<C_{Fth}$. In addition, the non-soil-property-related factor such as penetration rate shall be taken into account as well.

Among the limited experimental researches in the silty sands, there is divergence on how the non-plastic fines affect the cone resistance and liquefaction screening. The effect of penetration rate or cone diameter on the cone resitance is often ignored, which may lead to erroneous conclusions when examining the effect of fines on the cone resistance.

In addition, current numerical study on the effect of T_o on the cone resistance is limited to non-dilative material or is limited to shallow penetration ($D/d_c<0.3$). Thus it is in need to

1) Experimentally, examine the effect of fines on the cone resistance in silt sands at various C_F.
2) Numerically, employee an appropriate numerical model applicable for both contractive (loose) and dilative (dense) materials and capable of simulating large strain problem to thoroughly examine the effect of T_o (fines content, penetration rate and cone diameter) on the cone resistance in silty sands.
3) Proposed a T_o instead of fines content dependent CRR-q_{c1N} for liquefaction evaluation.

Chapter 3. Design of CPT testing chamber

3.1. Introduction

Compared to an in-situ test, a chamber test could provide a relatively homogeneous specimen and the knowledge of stress history. Therefore, a testing chamber is designed and developed to study the effect of fines and penetration rate on the cone resistance in silty sands. In this chapter, a literature review on factors affecting the CPT in testing chamber is presented followed by the introduction of designing a CPT testing chamber.

3.2. Design concepts of testing chamber

Table 3.1 presents a summary of the currently available calibration chambers in the world, most of which are designed as flexible wall chambers. Two main factors affect the CPT performed in the calibration chamber: the boundary conditions applied to the calibration chamber and the chamber size ratio: the diameter ratio of the chamber to the penetrometer ($D_L=D_c/d_c$).

Table 3.1 Currently available calibration chambers in the world (After Hsu and Huang, 1999)

Calibration chamber (Owner, Location)	Specimen diameter	Specimen height	Boundary conditions		
	(m)	(m)	Radial	Bottom	Top
Country Roads Board, Australia	0.76	0.91	Flexible	Cushion	Rigid
University of Florida, U.S.A	1.20	1.20	Flexible	Cushion	Rigid
Monash University, Australia	1.20	1.80	Flexible	Cushion	Rigid
Norwegian Geotechnical Institute	1.20	1.50	Flexible	Cushion	Rigid
ENEL-CRIS, Milano, Italy	1.20	1.50	Flexible	Cushion	Rigid
ISMES, Bergamo, Italy	1.20	1.50	Flexible	Cushion	Rigid
University of California, Berkely, U.S.A	0.76	0.80	Flexible	Rigid	Rigid
University of Texas, at Austin, U.S.A	Cube 2.1x2.1x2.1		Flexible	Flexible	Flexible
University of Houston, U.S.A	0.76	2.54	Flexible	Cushion	Cushion
North Carolina State University, U.S.A	0.94	1.00	Flexible	Rigid	Cushion
Louisiana State University, U.S.A	0.55	0.80	Flexible	Flexible	Rigid
Golder Associate, Calgary, Canada	1.40	1.00	Flexible	Rigid	Cushion
Viginia Polytechnic Institute and State University, U.S.A	1.50	1.50	Flexible	Rigid	Rigid
University of Grenoble, France	1.20	1.50	Flexible	Cushion	Cushion
Oxford University, U.K.	0.90	1.10	Flexible	Cushion	Rigid
University of Tokyo, Japan	0.90	1.10	Flexible	Rigid	Rigid
University of Sheffield, U.K.	0.79	1.00	Flexible	Rigid	Flexible
Cornell University, U.S.A	2.10	2.90	Flexible	Rigid	Rigid
Waterways Experiment Station, U.S.A.	0.80-3.00	Variable	Flexible	Rigid	Rigid
National Chiao-Tung University, Taiwan	0.51	0.76	Flexible	Rigid	Rigid
National Chiao-Tung University, Taiwan	0.79	1.60	Flexible	Flexible	Flexible
The University of Oklahoma Calibration Chamber, USA (Tan, 2005)	0.61	0.45-1.42	Flexible	Rigid	Rigid
Korea University Calibration Chamber Laboratory, Korea, (Kim et al., 2008)	1.20	1.00	Flexible	Rigid	Rigid
The University of New South Wales, Sydney, Australia (Pournaghiazar et al., 2011)	0.46	0.84	Flexible	Rigid	Rigid

3.2.1. Boundary conditions

A typical cavity-wall calibration chamber is capable of creating four types of boundary conditions as listed in Fig. 3.1 and Table 3.2. The variation of these four types of boundary

conditions depends on whether stress or displacement is applied on the top, bottom and circumferential (lateral) surfaces of the specimen. Been et al. (1988) indicated that boundary conditions on the top and bottom of the chamber specimen have little effect on CPT test results. Parkin (1988) found that of the four boundary conditions, the most significant are BC1 and BC3. Houlsby and Hitchman (1988) stated that the cone resistance (q_c) has no consistent correlation when the initial effective stress (σ_{vo}') is applied in the chamber under BC1 conditions. Most calibration chamber tests so far have been undertaken using BC1 because BC2 and BC3 were not practically achievable in the flexible wall chambers. In general, if all other factors are identical, the q_c obtained from BC1 and BC4 (both corresponding to a constant circumferential/lateral stress) yield similar results while the q_c determined using BC2 and BC3 (related to zero lateral displacement) do not deviate much from each other.

Table 3.2 Configurations of boundary conditions in calibration chamber

Type of boundary conditions	Top and bottom boundary		Lateral boundary	
	Stress	Strain	Stress	Strain
BC1	Constant	-	Constant	-
BC2	-	0	-	0
BC3	Constant	-	-	0
BC4	-	0	Constant	-

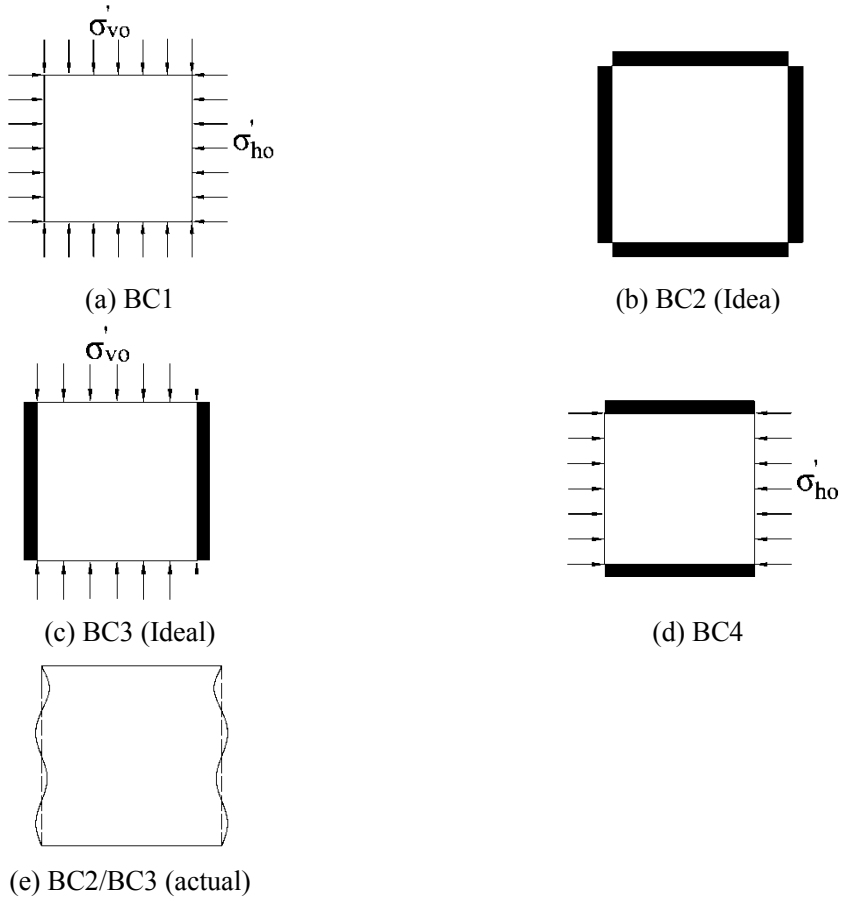

Fig. 3.1 Configurations of boundary conditions in calibration chamber

However, none of the aforementioned boundary conditions perfectly simulate the free field conditions. The discrepancy of the boundary conditions between calibration chamber and free field results in different q_c values given that all other parameters such as soil properties and cone diameter are the same. But the difference can be largely reduced if the calibration chamber size ratio (D_L=D_c/d_c) increases. It is important to note that the q_c obtained in BC1 is often lower than in the field, because the constant lateral stress during penetration underestimate the value that will develop during penetration in the field. In contrast, ideal BC3 condition with a perfectly rigid lateral wall, would lead to a higher q_c than measured in the field (Salgado et al., 1998).

3.2.2. Chamber size effect

As noticed previously, the chamber size ratio plays an important role in the CPT using calibration chamber in that it determines whether the boundary conditions of the calibration chamber can model the in-situ free field conditions. Mayne and Kulhawy (1991) recommended that a D_L of 70 can simulate free field conditions regardless of the initial relative density and stress state. Nonetheless, q_c asymptotically reaches free field penetration resistance as D_L tends to be infinite at the rate related to factors such as the relative density and stress state of the specimen.

Puppala (1993) performed a series of CPTs using dry sand specimens at three different D_r (45%, 65% and 85%) under three confining stresses (100, 200 and 300 kPa) at D_L of 42. It was pointed out that the chamber size ratio of 42 had insignificant influence on the obtained cone resistance even in dense sands, indicating that the chamber size effect can be greatly reduced at this chamber size ratio.

Gui et al. (1998) proposed the design guidelines of calibration chamber in sands based on the CPTs carried out in five European centrifugal laboratories. It was reported that the cone resistance (q_c) did not change much as D_L exceeded 21 while it decreased drastically as D_L increased from 8.85 to 21, and the ratio of penetrometer diameter to d_{50} (d_c/d_{50}) shall exceed 20 to reduce the error of obtaining realistic cone resistance. Moreover, the effect of penetration location was studied through a dimensionless parameter-S/d_c (S is the nearest distance from the center of cone penetrometer to the boundary of chamber). It was shown that there was no much deviation in q_{c1n} as S/d surpassed 11 in circular as well as rectangular chamber. But the q_c was prone to increase as S/d went larger in circular chamber while the opposite trend was found in rectangular chamber.

A comprehensive series of CPTs were conducted in calibration chambers at ENEL-CRIS and ISMES reported by Salgado et al. (1998) to clarify boundary conditions and chamber size effects. Four cone penetrometers with different diameters (3.57 cm, 2.54 cm, 2 cm and 1 cm) were advanced in one calibration chamber of 120 cm in diameter. Most of the tests were carried out using three larger diameter penetrometers. The specimen with the relative densities from loose to dense, the vertical stresses from 50 to 700 kPa and the overconsolidation ratio differing from 1 to about 15 were investigated. However, the number of tests for any given set of initial conditions (approximately the same relative density and stress state) and different cone sizes was limited and did not cover the full range of chamber size ratios even hundreds of tests were performed. In this regard, Salgado et al. (1998) numerically examined the boundary conditions as well as chamber size effect in clean sands based upon a theory proposed by Salgado et al. (1997b). Cavity expansion is the foundation of this theory, to which a computer program called CONPOINT was incorporated. A general expression of this numerical analysis can be formed as:

$$q_c = f(D_r,\ \sigma'_{ho},\ \mathrm{D_c/d_c},\ \mathrm{BC}) \qquad \text{(Eq. 3.1)}$$

Where σ_{ho}' is the initial lateral effective stress BC is the type of boundary conditions in calibration chamber.

Based upon the experimental and numerical examination, it was proposed that the chamber size ratio ranged from 25 to 120 would give the ratio of chamber to free field penetration resistance varying from 0.5 to 0.9 for heavily dilatant samples and 0.8 to 0.98 for compressive samples.

3.2.3. Design consideration of testing chamber system

In view of the above and the existing rigid wall chamber at UB, a testing chamber with inner

diameter of 50.8 cm and height of 49 cm is modified and developed. This chamber is only capable of simulating BC3 condition [constant vertical stress and zero lateral strain (ideally)]. In addition, a penetrometer with diameter (d_c) of 1.27 cm is fabricated, which gives the chamber size ratio (D_c/d_c) of 40 and the ratio of cone size to soil grain size (d_c/d_{50}) around 65 for clean sand.

It shall be noticed that the maximum penetration rate used in this research is 0.4 cm/s, which is one fifth of the standard penetration rate (2 cm/s) and the cone diameter is 1.27 cm, which is about one third of the standard cone (d_c=3.57 or 4.37 cm). This would result in that the T_o of CPT performed in the current system would be about 1/15 of that conducted in the field for the same soil using Eq. 2.14. For a given soil, the drainage condition during penetration process would be different in field from this study. In this regard, the study provides a qualitative rather than quantitative understanding of how the effect of fines influences the cone resistance in silty sands.

3.3. Design of testing chamber system

A complete CPT testing chamber system in this research consists of the following parts (Fig. 3.2 and Fig. 3.3):

1. A self-balance reaction frame and a pushing system;
2. A testing chamber to maintain the specimen and to apply desired boundary conditions;
3. A penetrometer to measure tip resistance and sleeve friction;
4. A data acquisition system (DAS/DAQ) and instrumentation;

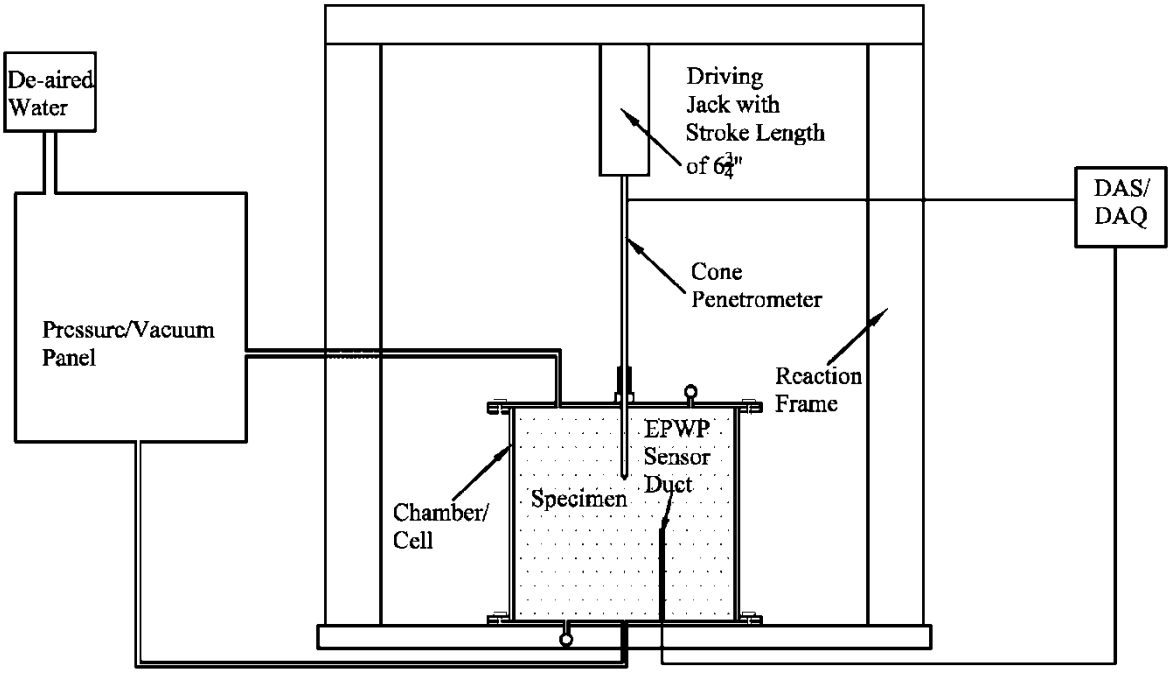

Fig. 3.2 Schematic diagram of complete testing chamber system

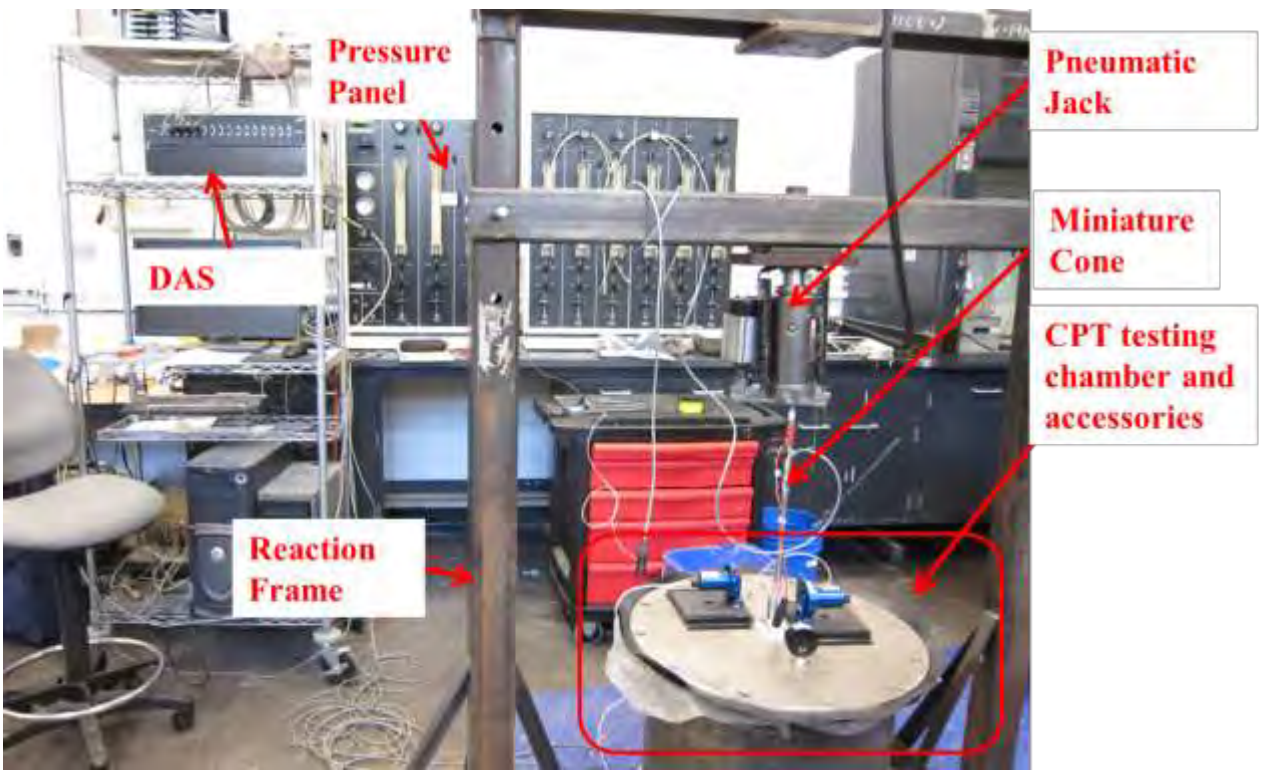

Fig. 3.3 Snap shot of CPT testing chamber system

3.3.1. Reaction frame and pushing system

Fig. 3.4 shows the designed self-balanced steel reaction frame. The height for the pneumatic

jack connection can be adjusted at three locations (123.2, 138.4 and 143.6 cm). The pneumatic jack is capable of applying up to 108 kN (12 ton) force and the maximum achievable penetration rate of the jack is about 0.4 cm/s. The stroke of this jack is 17.1 cm (6.75 inch). As a result, the penetrometer is placed in the specimen prior to penetration to minimize the shallow depth effect. The cone tip is about $14d_c$ from the top of specimen when the penetrometer is placed in the specimen.

Fig. 3.4 Snapshot of reaction frame and pushing system

3.3.2. CPT chamber (Cell)

The CPT testing chamber is modified from an existing single-walled aluminum cylinder (rigid-wall testing chamber). This means that only zero strain (ideally) in the lateral direction is

possible in this chamber (BC3). Fig. 3.5(a) and (b) schematically shows the detail of testing chamber when assembled for saturation and for consolidation and CPT, respectively. A chamber (Fig. 3.6) with inner diameter of 50.8 cm (20 inch), height of 49 cm (19.3 inch) and thickness of 1.0 cm (0.375 inch) is connected to the top and bottom caps through twelve bolts with 1.0 cm (0.375 inch) in diameter.

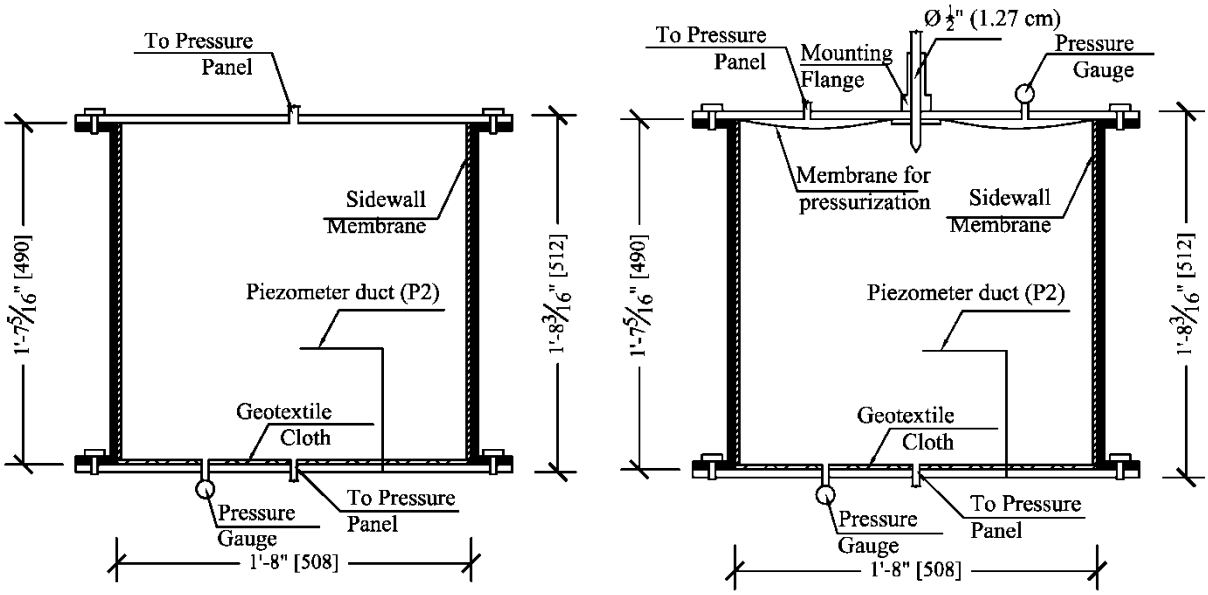

(a) For saturation (b) For consolidation and penetration

Fig. 3.5 Overview of testing chamber (Unit: mm in blankets)

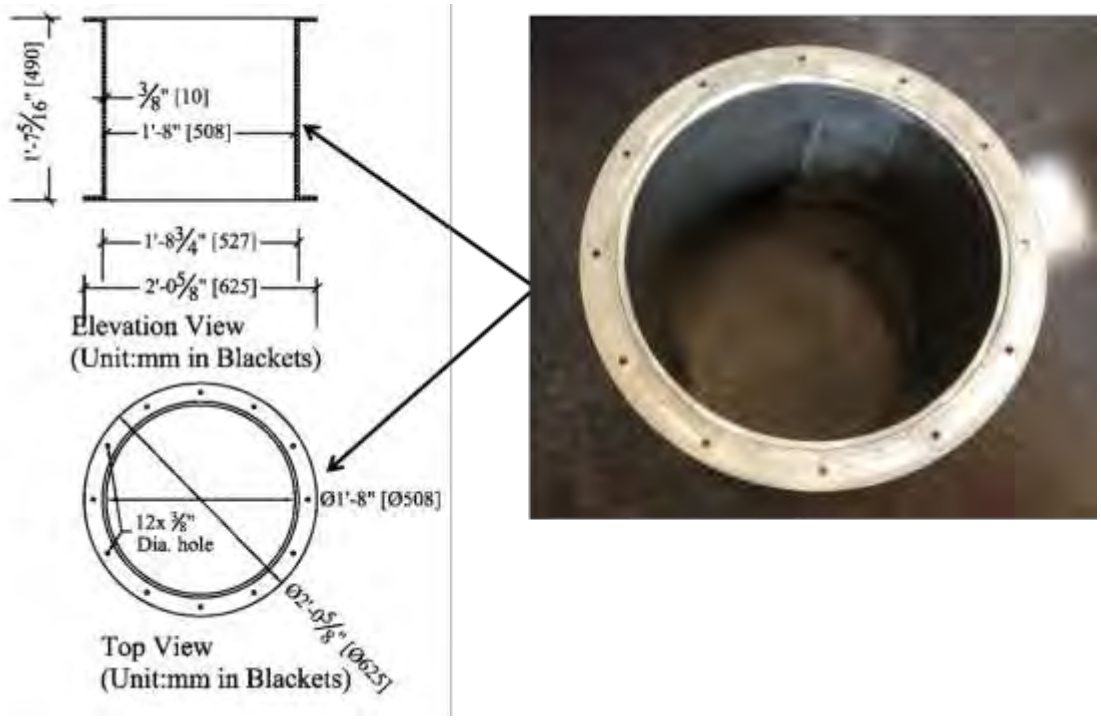

Fig. 3.6 Dimension of cylindrical chamber

Two top caps are used in the testing chamber, the first one for specimen saturation and the second one for specimen consolidation and CPT. The top caps are 62.5 cm in diameter and 1.0 cm in thickness. Fig. 3.5(b) shows the secone top cap assembled to the chamber. It is connected to a pressure panel (Fig. 3.7) to apply the pressure of up to 138 kPa (20 psi) to the specimen through a pressurization membrane. The top cap also provides one location for the CPT at the center of chamber. As can be seen in Fig. 3.5(b), a mounting flange with 1.27 cm (0.5 inch) shaft diameter made by Thompson Inc. is bolted to the center of top cap, aiming at guiding the penetrometer as well as sealing the water at the penetration location when the penetrometer is in position. A pressure gauge is installed at the top cap to monitor the pressure exerted to the specimen.

The bottom cap has the same size as the top cap and is accommodated for the pore pressure

sensor installation, saturation/back pressure application and back pressure measurement.

A membrane wrap made of 0.1 mm thick polythene in order to minimize the friction development between the wall and the specimen is placed against the inner wall of chamber before sample preparation. Lubricant is sprayed around the inner wall as well as the polythene membrane before sample preparation to reinforce this purpose.

Fig. 3.7 presents that a conventional pressure panel is served as the water pressure or suction supply and saturation system for the specimen. The desired vertical stress or suction is achieved by controlling the regulator and is feed through a small diameter tube to the chamber.

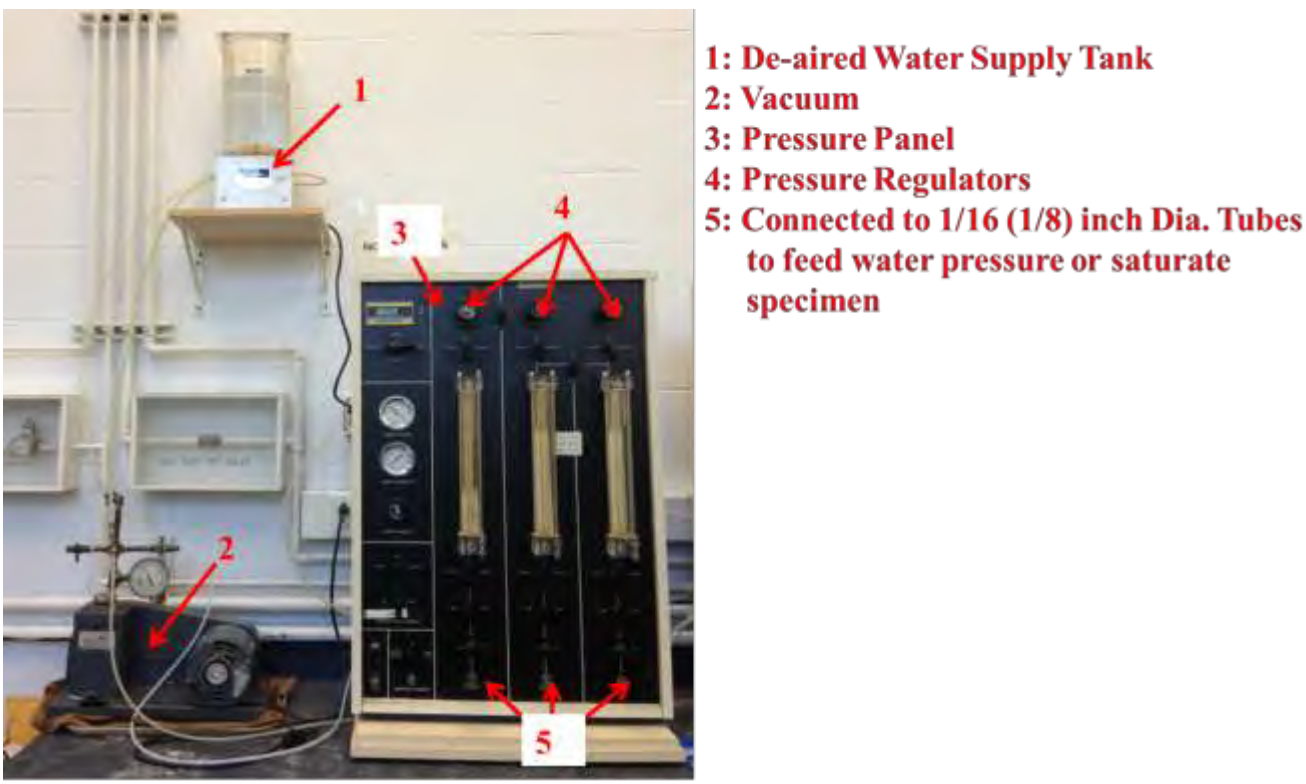

Fig. 3.7 Snapshot of pressure panel

3.3.3. Miniature cone

A miniature cone penetrometer with 1.27 cm in diameter (0.5 inch) is designed to minimize the boundary effect. The chamber size ratio D_c/d_c is about 40, indicating that the free field can be

simulated in this testing chamber and the ratio of d_c/d_{50} is about 65 for clean sands.

Fig. 3.8 details the design concept of miniature cone penetrometer. A 69.9 cm (27.5 inch) long cone shaft is made of a hollow steel rod with outer diameter of 1.27 cm (0.5 inch). A 1.27 cm (0.5 inch) diameter cone with projection area of 1.27cm^2 is welded to a 1.0 cm (0.375 inch) diameter solid steel rod with five pre-drilled holes for the cone and shaft connection. Five pins with 3.18 mm (0.125 inch) in diameter connect the shaft and cone, leaving a small clearance between the lower end of cone shaft and the cone tip. The clearance gap is sealed with silicone glue as to prevent water leakage.

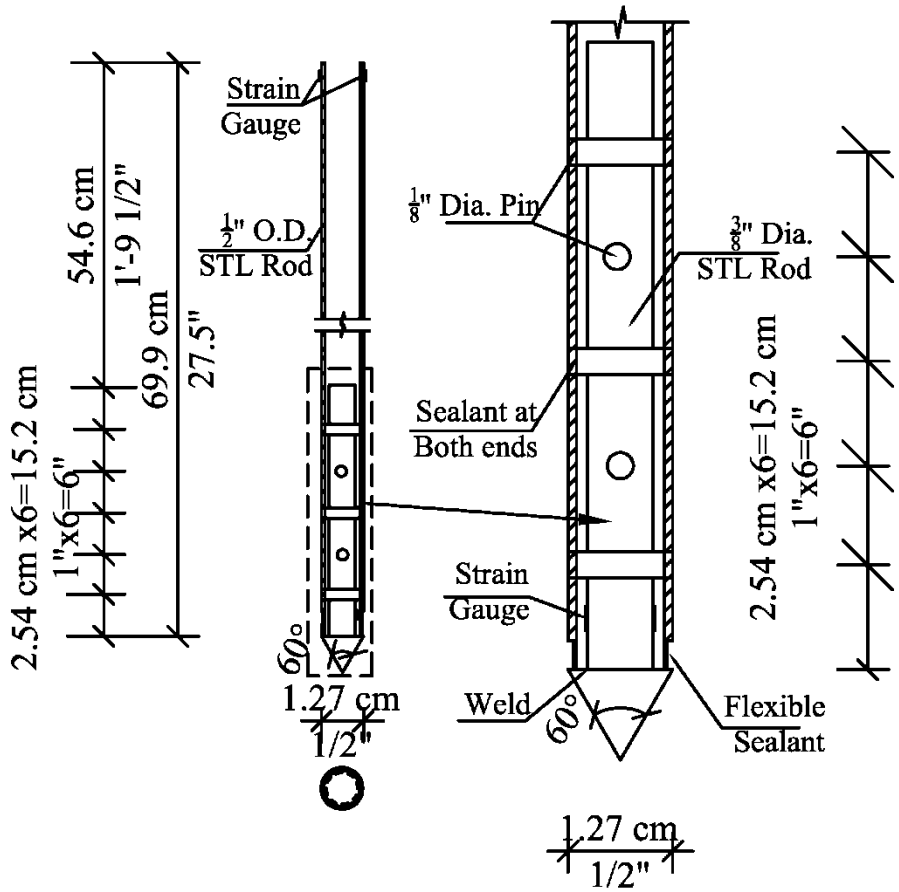

Fig. 3.8 Design of miniature cone penetrometer

Two load cells are located at the cone tip and the top end of shaft. The load cell location to

measure the sleeve friction of this miniature cone differs from that of a standard cone because of the size and space limitation. Fig. 3.9 compares the applied load and the measured loads at cone tip and cone shaft.

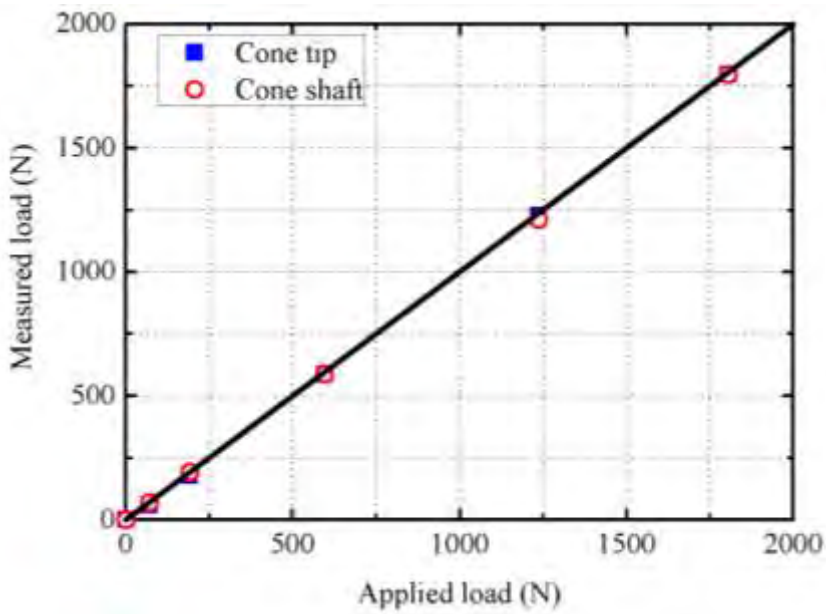

Fig. 3.9 Calibration of cone tip and shaft

A snapshot of the manufactured miniature cone penetrometer is shown in Fig. 3.10.

Fig. 3.10 Snapshot of cone penetrometer

3.3.4. Instrumentation and data acquisition system (DAQ/DAS)

PI-660-6000 (Pacific Instruments, Inc., CA) is used to collect and record experimental data with sample rate of 50 Hz.

Fig. 3.11 shows the penetration depth measurement device in the system. Two potentiometers

are mounted at the top cap and attached to the bottom of pneumatic jack.

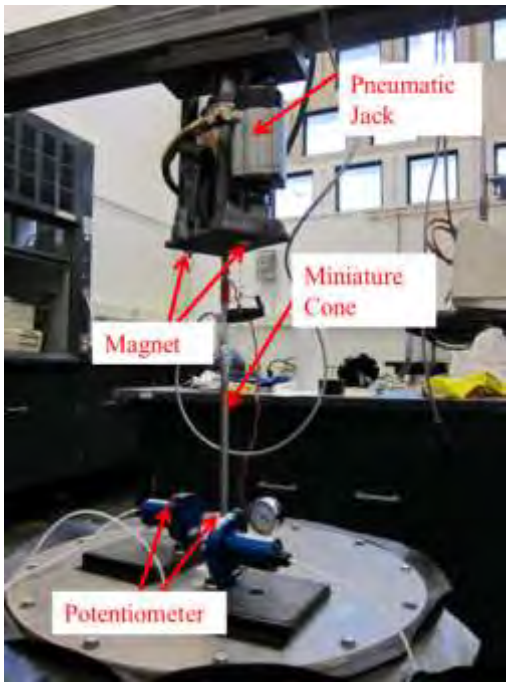

Fig. 3.11 Depth measurement gauge

A piezometer duct is employed to monitor the pore pressure variation around cone tip during penetration. The tentative location of the piezometers duct (u_2) is shown in Fig. 3.12, which is 3mm (0.125 inch)-1/4d_c horizontally away from the penetrometer. However, the piezometer duct is located at tip face (final position, u_1) of some tests (CC-14, 15, 20 and 21). Fig. 3.13 shows the assembly of piezometer duct. The piezometer duct consists of a bendable stainless needle with 1.2 mm inside diameter, a set of coupling and an accommodated piezometer (Kulite XCL-11-250-50A).

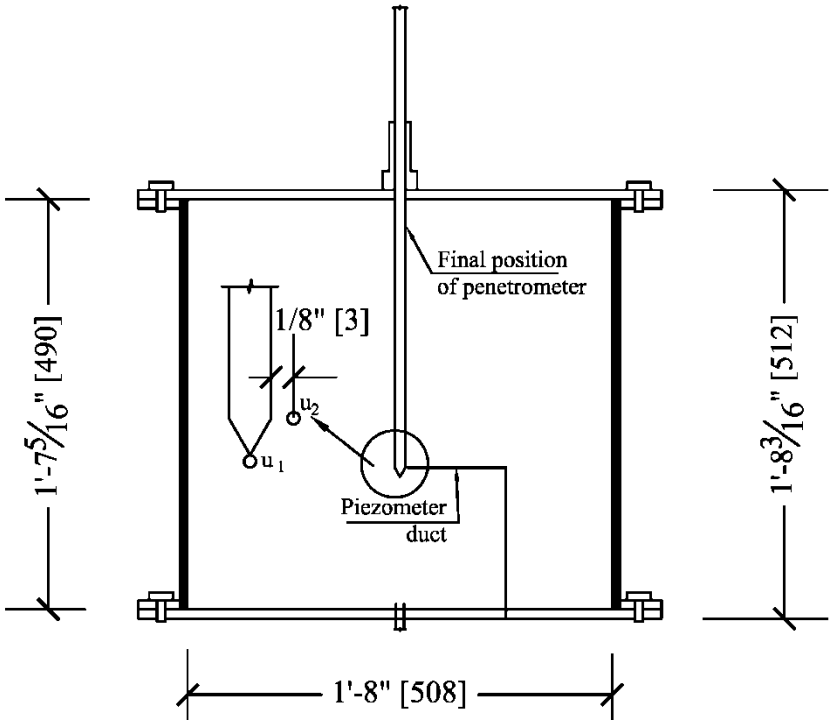

Fig. 3.12 Locations of piezometer duct (unit:mm in blankets)

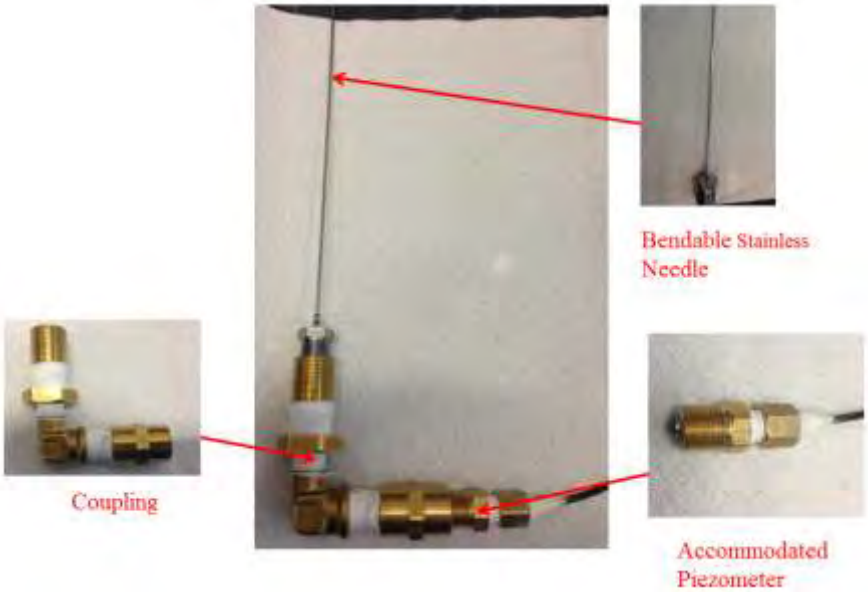

Fig. 3.13 Components of piezometer duct

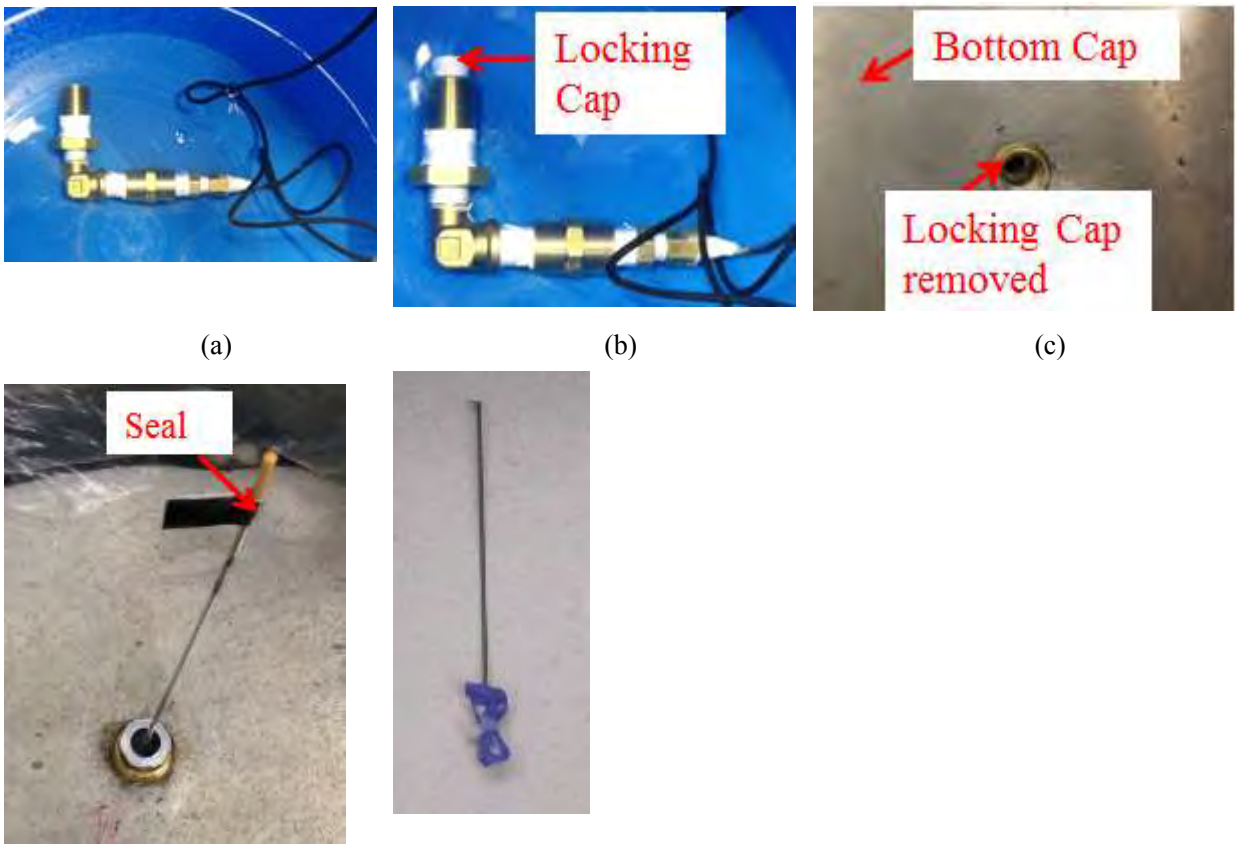

(a) (b) (c)

(d) (e)

Fig. 3.14 Saturation of piezometer duct

Fig. 3.14(a)-(e) illustrates the saturation process of the piezometer duct. Both the accommodated piezometer and coupler are submerged into de-aired water and they are jointed together through one end of the coupling [Fig. 3.14(a)]. A locking cap is threaded to the other end of coupling after the saturation for the piezometer is completed [Fig. 3.14(b)]. The piezometer together with coupling is installed through bottom cap to the testing chamber as shown in Fig. 3.14(c). Then de-aired water is percolated through a bottom outlet. The locking cap is removed and replaced by the stainless needle in the chamber when the desired water level is reached. The other end of the stainless needle is sealed to preserve the saturation of the piezometer after it is made at the desired location. Then water is empty for dry pluviation of the specimen [Fig. 3.14(d)].

The sealing at the end of stainless needle is replaced with a plastic filter as the desired sand level is reached [Fig. 3.14(e)].

3.3.5. Chamber compliance

The testing chamber expands when it is assembled and under pressure. The system expansion under pressure is taken into account because the volume of water going in or out through the chamber is used to determine the compressibility of the specimen. To determine the compliance of the system, the chamber is filled with water firstly and the top cap is locked. Then water pressure is applied through the bottom of chamber at several increments. At each pressure increment, the amount of water going into the system is recorded, which equals to the expansion of the system (mostly on top and bottom cap, the volume expansion due to radial expansion is negligibly small). Timonshenko and Woinowsy-Krieger (1959) analytically examined the symmetric bending of circular plates due to uniformly distributed load. The deflection (ω) of the plate at any point can be determined as below:

For circular plate with clamped edges

$$\omega = \frac{q_0 (a^2 - r^2)^2}{64 D_0} \qquad \text{(Eq. 3.2)}$$

For circular plate with supported edges

$$\omega = \frac{q_0 (a^2 - r^2)}{64 D_0} \left(\frac{5+\upsilon}{1+\upsilon} a^2 - r^2 \right) \qquad \text{(Eq. 3.3)}$$

Where q_0 is the distributed load, υ is the Poisson's ratio, a is the radius of the plate and r is the radial distance from center to the point of interst.

D_0 is the flexural rigidity of the plate, can be determined from

$$D_0 = \frac{Eh^3}{12(1-\upsilon^2)} \qquad \text{(Eq. 3.4)}$$

Where E is the Young's modulus of the plate and h is the thickness of the plate, from Eq. 3.2 and Eq.3.3, we can compute the volume expansion due to distributed load exerted on the bottom or top cap as:

For circular plate with clamped edges

$$V = \int_0^a 2\pi r\omega dr = \int_0^a \pi \frac{q_0(a^2-r^2)^2}{64D_0} dr^2 = \frac{\pi q_0 a^6}{192D_0} \qquad \text{(Eq. 3.5)}$$

For circular plate with supported edges

$$V = \int_0^a 2\pi r\omega dr = \int_0^a \pi \frac{q_0(a^2-r^2)}{64D_0}\left(\frac{5+\upsilon}{1+\upsilon}a^2 - r^2\right)dr^2 = \frac{\pi q_0 a^6}{D_0}\left(\frac{1}{32(1+\upsilon)} + \frac{1}{192}\right) \qquad \text{(Eq. 3.6)}$$

For the current aluminum made testing chamber, E=70GPa, υ=0.3, h=0.95 cm, a=28.80 cm (The diameter is taken as the distance between bolt center and bolt center).

Fig. 3.15 shows the volume expansion due to applied pressure in the chamber as well as from analytical solutions. A regression line is then obtained to estimate the compliance of the system. When the specimen is consolidated, half of the expansion coefficient deterimined from Fig. 3.15 is applied to correct the amount of water flowing out of the system at each pressure increment.

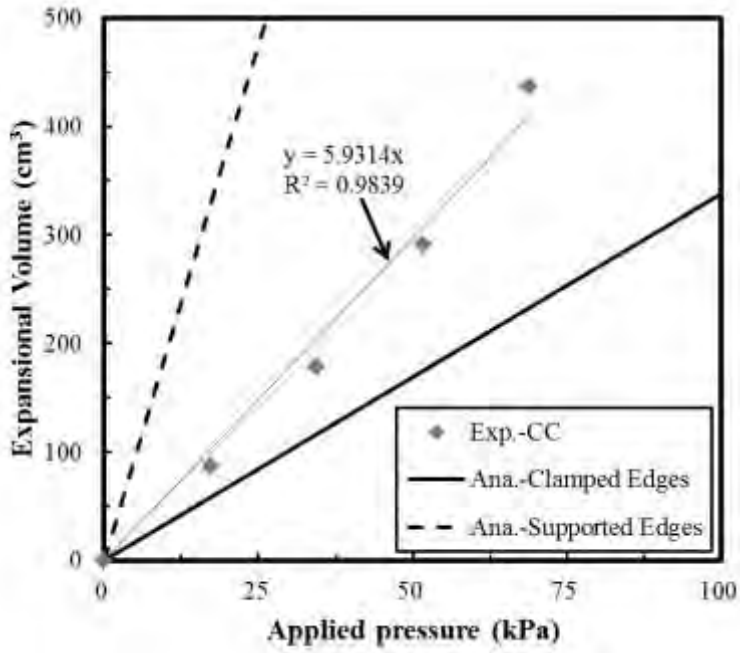

Fig. 3.15 System expansion due to pressurization

3.4. Summary

In this chapter, four commonly used boundary conditions in the calibration chamber are presented and the effect of calibration chamber size ratio is discussed. Secondly, a new chamber testing system for CPT and a miniature cone penetrometer are designed and fabricated with BC3 condition (constant stress in vertical direction and zero strain in horizontal direction). The chamber size ratio of about 40 indicates that the free field condition of CPT can be simulated in this testing chamber. However, the maximum achievable penetration rate used in this study is 0.4 cm/s, which is only one fifth of the standard penetration rate.

Chapter 4. CPT chamber tests and analysis: Sands and silty sands

4.1. Introduction

Table 4.1 and Fig. 4.1 present the information of Ottawa F55 sand (OS F55 sand) and sand-silt mixtures prepared by mixing OS F55 sand with non-plastic silt [Sil co sil # 40 (GSF#40)] (Thevanayagam et al. 2003) used in the CPT chamber tests. The sand-silt mixtures at silt (fines) contents of 0%, 15%, 25% and 100% by dry weight are termed as OS-00, OS-15, OS-25, OS-100, respectively.

Table 4.1 Properties of OS F55 sand-silt mixtures (Thevanayagam et al. 2003)

Soil Type	C_F (%)	e_{max}	e_{min}	d_{50} (mm)	C_u
OS-00	0	0.800	0.608	0.250	1.69
OS-15	15	0.750	0.428	0.235	13.61
OS-25	25	0.860	0.309	0.230	28.24
OS-100	100	2.100	0.627	0.010	10.00

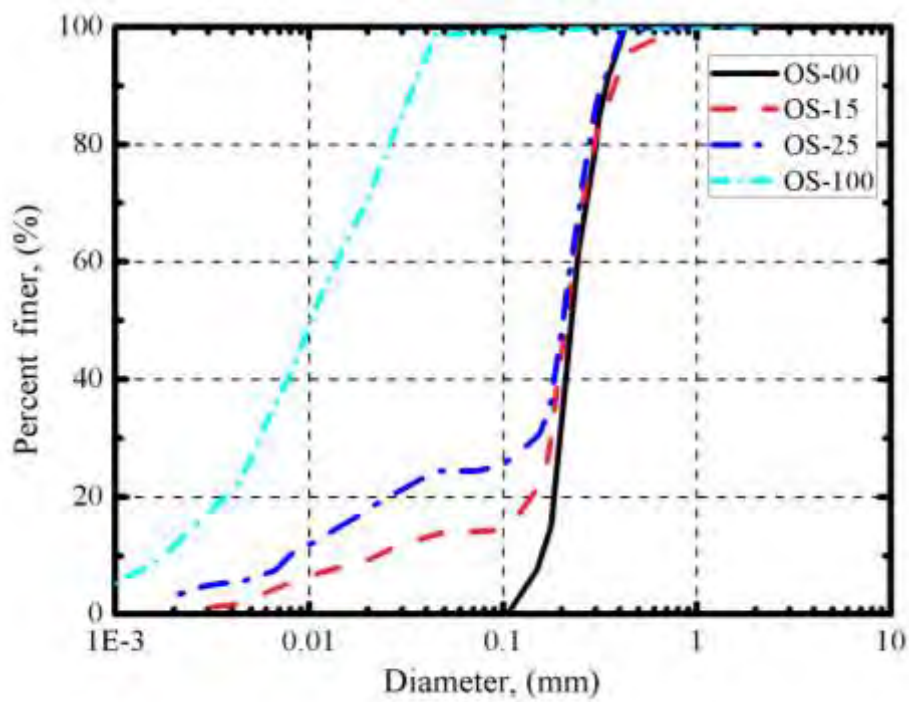

Fig. 4.1 Gradation of OS F55 sand-silt mixtures (Thevanayagam et al. 2003)

In this chapter, the testing chamber system developed was firstly tested for its functionality using dry clean sands (OS F55 sand). Secondly, a series of CPT chamber tests were performed to examine the effect of fines and penetration rate on the cone resistance in silty sands.

4.2. Test procedures

The entire CPT in the testing chamber is divided into four stages, which are sample preparation, sample consolidation, penetrating into sample and disassemble of sample, respectively.

4.2.1. Sample preparation and saturation

Dry pluviation is usually applied to form the clean sand or silty sand samples inside the chamber. The 49 cm high chamber is divided into 14 sub-layers in order to prepare a relatively uniform specimen. The weight of each sub-layer is calculated based on the dimension of the chamber at a targeted void ratio, and it is necessary to start with a slightly higher void ratio to allow for possible densification during wetting, saturation, and consolidation. To achieve a soil mix with desired fines content, the weights of fine and coarse grains are computed based upon the dry weight. Then both soils are placed into a container, and mixed thoroughly until there is no obvious color difference and no segregation to have a relatively uniform soil mix.

The saturation of sample is followed after the dry specimen is formed. Carbon dioxide is firstly slowly introduced into the specimen for about five to six hours from the bottom cap [Fig. 3.5(a)]. Meanwhile, a suction of about 5 to 10 kPa is applied through the top cap. Then the de-aired water is allowed to flow from the pressure panel through the bottom cap into the sample after the percolation of carbon dioxide. Almost twice the amount of de-air water wetting the sample is

circulated through bottom cap to ensure the saturation of sample and the suction is continuously supplied through the top cap to extract the remaining air in the sample. The top cap for saturation is removed and replaced by the top cap for consolidation and CPT after saturation [Fig. 3.5(b)]. The entire volume of water introduced into and out of the sample is recorded to determine the void ratio of sample. B check is performed after the saturation is completed.

4.2.2. Sample consolidation

The sample is connected to pressure panel for consolidation after it is carefully prepared in the chamber. The targeted water pressure is applied through the regulator located on the pressure panel. The pressure is increased at a 17.3 kPa (2.5 psi) increment up to 103.5 kPa (15 psi). The amount of water flowing into pressure panel, together with the chamber expansion correction, is used to calculate the volume change of soil at each consolidation stage.

4.2.3. Cone penetration

The penetrometer is driven by the pneumatic jack into the sample at a constant rate after the consolidation is completed. Fig. 4.2 shows the relationship between penetration depth versus time at the no load condition, giving the penetration rate of 0.46 cm/s. The maximum feed rate is 0.40 cm/s when the cone is penetrating into the sample, which is one fifth of the ASTM standard penetration rate (2 cm/s).

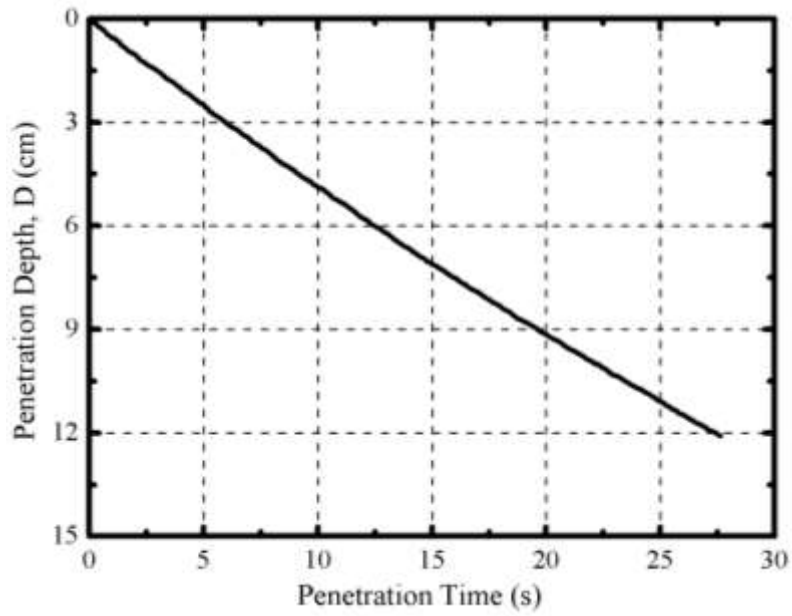

Fig. 4.2 Typical penetration rate fed by pneumatic jack

The penetration depth, pore water pressure, cone resistance and sleeve friction are recorded through a data acquisition system as the cone penetrometer advances into the sample.

4.2.4. Disassemble of sample

This process involves relieving the applied pressure, unconnecting the chamber from pressure panel, removing the cone penetrometer, unplugging the instrumentation and emptying the chamber for the next experiment.

4.3. Analysis of chamber test results

This section analyzes the CPTs carried out in the testing chamber using OS F55 sand-silt mix. A total of 19 CPT chamber tests were performed in this study. Five tests were performed using dry clean sands (OS-00) at two D_r (about 40% and 65%) under v=0.4 cm/s to test the effectiveness of the developed chamber testing system. Seven tests were performed using dry OS-25 at different penetration rates and seven tests were performed using saturated sand-silt mix of C_F=0, 15 and

25%. Table 4.2 lists the characteristics of conducted CPTs. The void ratio is evaluated based on two approaches for saturated samples. The first approach is based on the dimension of sample, which is the only approach to obtain the void ratio of dry sample. The second approach is to use the water content of sample. It shall be noticed that vacuum was not applied through top cap during CO_2 percolation and water circulation was not performed for the sample saturation in CC-7 (C_F=0%) and CC-8 (C_F=15%), and the B check was not performed after the saturation was done. Moreover, the saturation process took several weeks for CC-7 due to the smaller diameter tube used for saturation and some unexpected issues. The B value was 0.70 after the specimen was prepared for CC-10 while the B values were greater than 0.95 for both CC-14(15) and CC-20(21).

Table 4.2 Characteristics of CPT chamber tests using OS F55 sand-silt mix

Test No.	Sample type	C_F	Based on water content				Based on sample dimension				σ_{vo}'	BC Type	v	B-value
			e	$(e_c)_{eq}$	D_r	$(D_{rc})_{eq}$	e	$(e_c)_{eq}$	D_r	$(D_{rc})_{eq}$				
		(%)			(%)	(%)			(%)	(%)	(kPa)		(cm/s)	
CC-2	Dry	0	-	-	-	-	0.714	0.714	45	45	50	BC3	0.4	-
CC-4	Dry	0	-	-	-	-	0.718	0.718	42	42	50	BC3	0.4	-
CC-3	Dry	0	-	-	-	-	0.688	0.688	59	59	50	BC3	0.4	-
CC-5	Dry	0	-	-	-	-	0.671	0.671	67	67	50	BC3	0.4	-
CC-6	Dry	0	-	-	-	-	0.671	0.671	67	67	50	BC3	0.4	-
CC-11	Dry	25	-	-	-	-	0.325	0.651	97	78	50	BC3	0.4	-
CC-12	Dry	25	-	-	-	-	0.329	0.657	96	75	50	BC3	0.16	-
CC-13													0.4	
CC-16	Dry	25	-	-	-	-	0.327	0.654	97	76	50	BC3	0.09	-
CC-17													0.4	
CC-18	Dry	25	-	-	-	-	0.342	0.673	94	66	50	BC3	0.1	-
CC-19													0.4	
CC-7	Saturated	0	0.680	0.680	62	62	0.687	0.687	59	59	50	BC3	0.4	N/A
CC-8	Saturated	15	0.443	0.637	95	85	0.464	0.660	89	73	50	BC3	0.4	N/A
CC-10	Saturated	25	0.370	0.707	89	48	0.403	0.748	84	27	75	BC3	0.4	0.70
CC-14	Saturated	25	0.323	0.648	98	79	0.332	0.672	94	67	50	BC3	0.09	0.96
CC-15													0.4	
CC-20	Saturated	25	0.314	0.638	99	84	0.333	0.661	96	72	50	BC3	0.09	0.98
CC-21													0.4	

4.3.1. Dry sand-silt mix

4.3.1.1. OS-00 (C_F=0%)

Two sets of CPTs using dry OS F55 sand at two relative densities ($D_r \approx$40 and 65%) were carried out under the vertical effective stress (σ_{vo}') of about 50 kPa. The empirical correlations between q_c and D_r were employed to compare the experimental results.

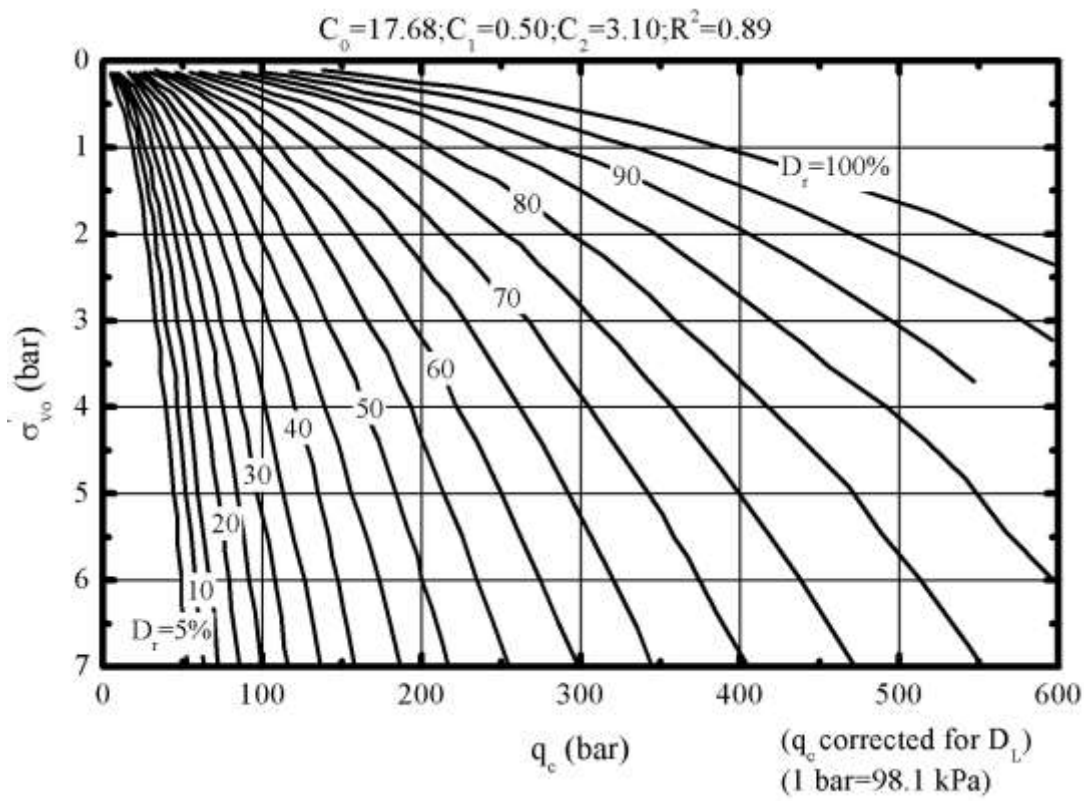

Fig. 4.3 Empirical correlation between q_c and D_r for NC silicesous sand (Digitized from Schmertmann, 1976)

Schmertmann (1976) firstly proposed the correlation between q_c and D_r based upon CPTs conducted in the calibration chambers. The soil samples used in the tests were normally consolidated (NC) fine to medium unaged dry sands with the correlation shown as follows:

$$D_r = \frac{1}{C_2} \ln\left[\frac{q_c / p_{at}}{C_0 (\sigma_{vo}' / p_{at})^{C_1}}\right] \qquad \text{(Eq. 4.1)}$$

Where D_r is in decimal unit, p_{at} is the atmospheric pressure (expressed in the same unit system of stress and penetration resistance), σ_{vo}' is the initial vertical effective stress and the non-dimensional factors C_0, C_1 and C_2 are 17.68, 0.50 and 3.10 respectively. The correlation between q_c and D_r at different σ_{vo}' can be obtained using Fig. 4.3 as well.

Lacellotta (1983) introduced the equation correlating q_c to D_r as:

$$D_r = A_0 + B_0 \ln\left[\frac{q_c}{\left(\sigma_{vo}'\right)^{\alpha}}\right] \qquad \text{(Eq. 4.2)}$$

Where q_c and σ_{vo}' are in kPa, and the empirical correlation factors A_0, B_0 and α are -1.292, 0.268 and 0.52, regressed by Jamiolkowki et al. (2001), based upon the CPTs from calibration chamber (Fig. 4.4).

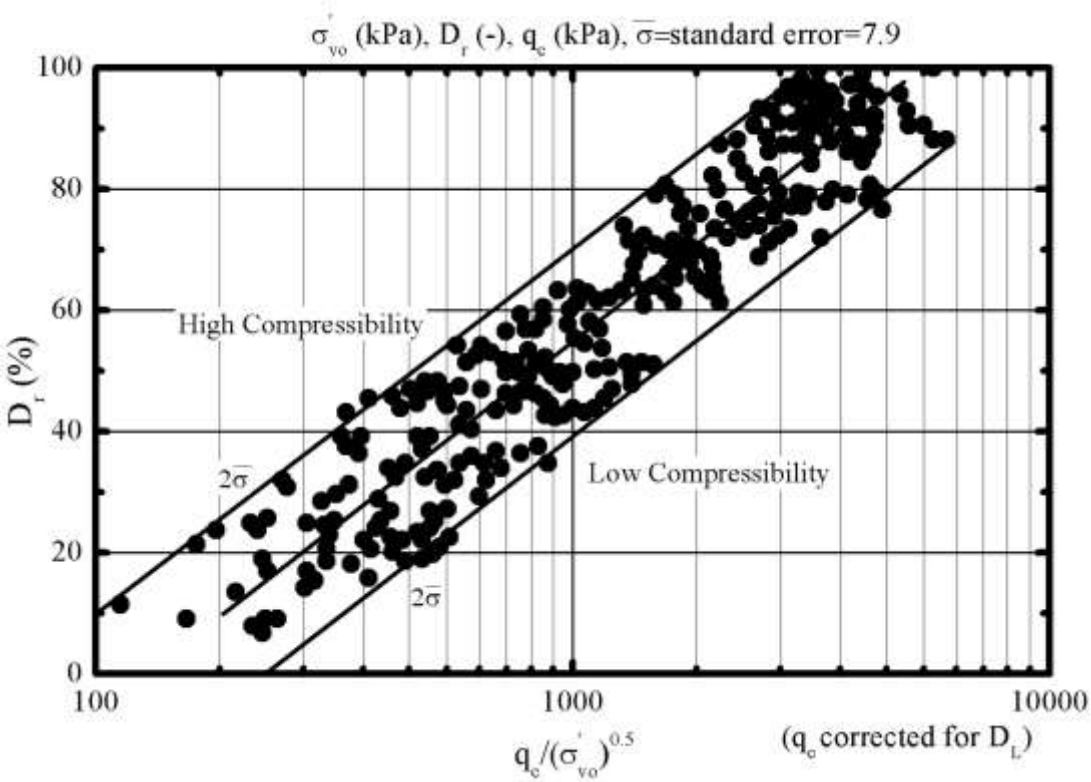

Fig. 4.4 Experimental correlation D_r-q_c-σ_{vo}' for mainly NC sands of different compressibility (Digitized from Lancellotta, 1983; Garizio, 1997)

Table 4.3 summarizes the CPT chamber test results using dry sands. Fig. 4.5 and Fig. 4.6 plot the experimental results of cone resistance (q_c) and sleeve friction (f_s) versus penetration depth for different relative densities.

Table 4.3 CPT chamber test results of dry OS-00

Test No.	$D_r[(D_{rc})_{eq}]$	C_F	q_c	v	f_s	f_s/q_c
	(%)	(%)	(MPa)	(cm/s)	(kPa)	(%)
CC-2	45	0	1.5	0.40	14	0.9
CC-4	42	0	1.5	0.40	14	0.9
CC-3	59	0	5.5	0.40	23	0.4
CC-5	67	0	7.7	0.40	24	0.3
CC-6	67	0	6.7	0.40	40	0.6
CC-1	39	0	-	-	-	-

As discussed in Chapter 3, the measured sleeve friction is based upon the in-soil length of cone shaft. The stabilized q_c for D_r=42, 45, 59 and 67% are 1.5, 1.5, 5.5, 7.7 (6.7) MPa, respectively. The average f_s for D_r=42, 45, 59 and 67% are 14, 14, 23, 24 (40) kPa, respectively.

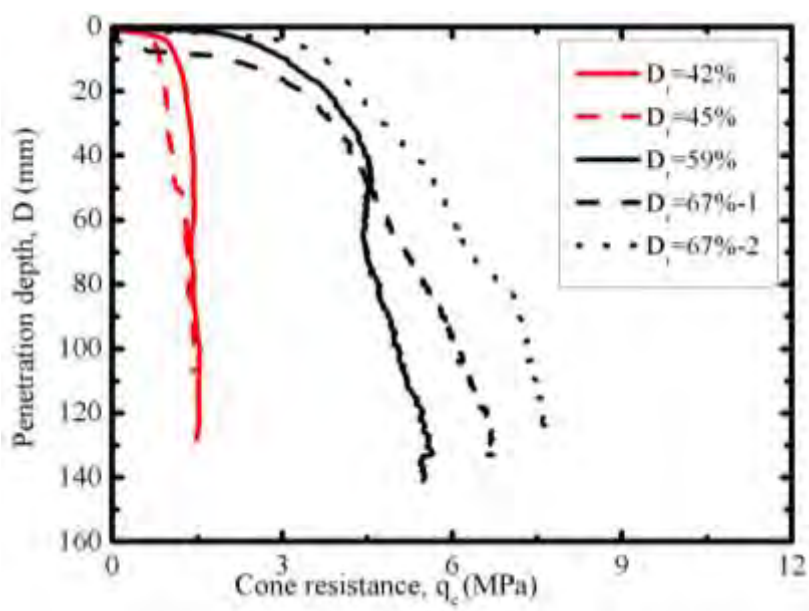

Fig. 4.5 Cone tip resistance of dry sands at different D_r

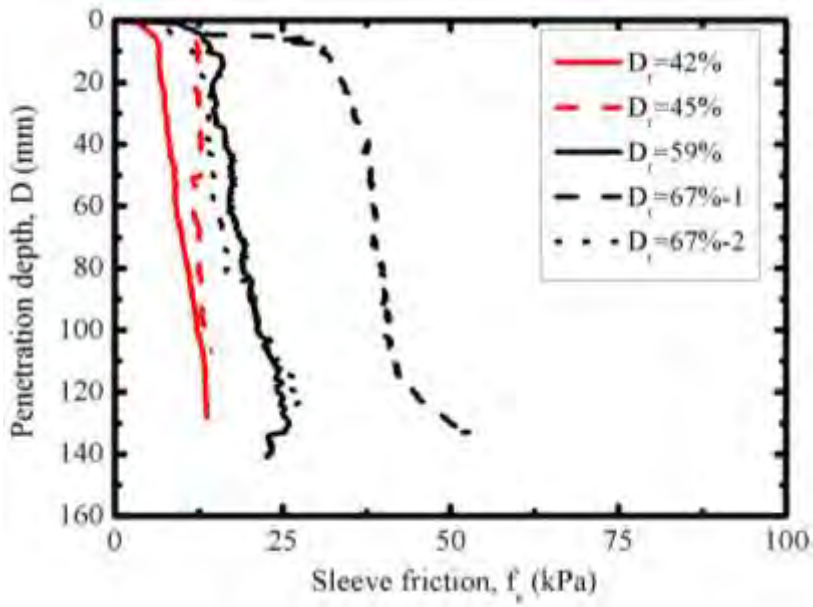

Fig. 4.6 Sleeve friction of dry sands at different D_r

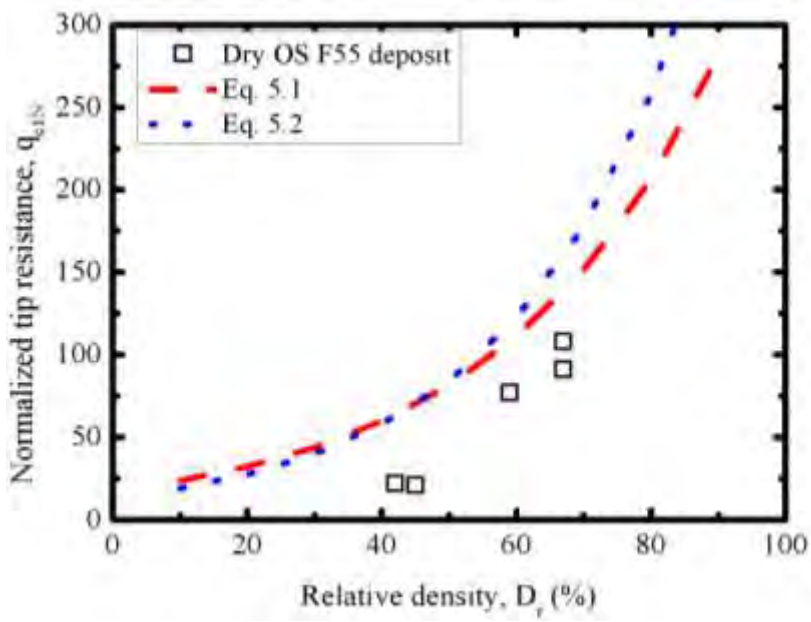

Fig. 4.7 Comparison of q_{c1N} -D_r between experiments and empirical equations of dry sands

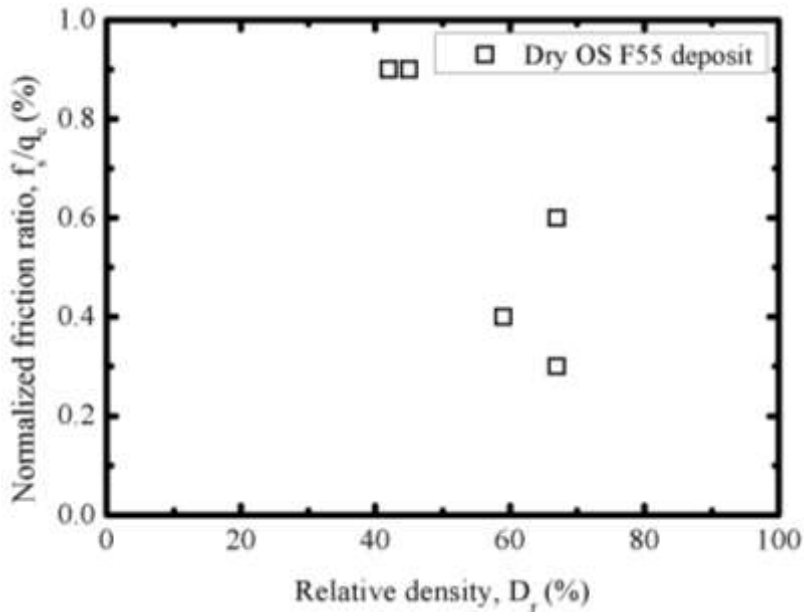

Fig. 4.8 Normalized friction ratio with respect to D_r of dry sands

Fig. 4.7 compares the normalized tip resistance (q_{c1N}) between experimental results and empirical equations. The experimental results fall into reasonable regions when compared to the empirical equations. The normalized friction ratio (f_s/q_c) with respect to relative density (D_r) is displayed in Fig. 4.8. The f_s/q_c for D_r=42%, 45%, 59% and 67% are 0.9%, 0.9%, 0.4% and 0.3% (0.6%), respectively.

It has been reported that the q_c does not deviate much when the CPT is performed in dry and saturated sands at the ASTM standard penetration rate of 2 cm/s given other parameters are identical (Sharp et al., 2010; Pournaghiazar et al., 2011). It is because that the penetration process is in drained condition as the cone penetrometer advances into sands. As a result, the q_{c1N} obtained using dry sands in the testing chamber can be used to correlate the relationship between q_{c1N} and CRR for saturated sands.

4.3.1.2. OS-25 (C_F=25%)

Seven experiments carried out using dry OS-25 are aiming to examine the repeatability of

silty sand sample preparation method and to study the effect of penetration rate under 'drained' condition. Table 4.4 summarizes the experimental results of each test. CC-11 is the test performed using maximum penetration depth the jack can provide. CC-12 and CC-13 (CC-16 and CC-17, CC-18 and CC-19) are carried out in one specimen with two penetration rates.

Table 4.4 CPT chamber test results of dry OS-25

Test No.	D_r	$(D_{rc})_{eq}$	C_F	v	q_c	f_s	f_s/q_c
	(%)	(%)	(%)	(cm/s)	(MPa)	(kPa)	(%)
CC-11	97	78	25	0.4	11.9	80	0.7
CC-12	96	75	25	0.16	9.4	43	0.5
CC-13	96	75	25	0.4	9.4	45	0.5
CC-16	97	76	25	0.09	9.4	42	0.4
CC-17	97	76	25	0.4	9.9	48	0.5
CC-18	94	66	25	0.1	7.6	33	0.4
CC-19	94	66	25	0.4	7.9	33	0.4

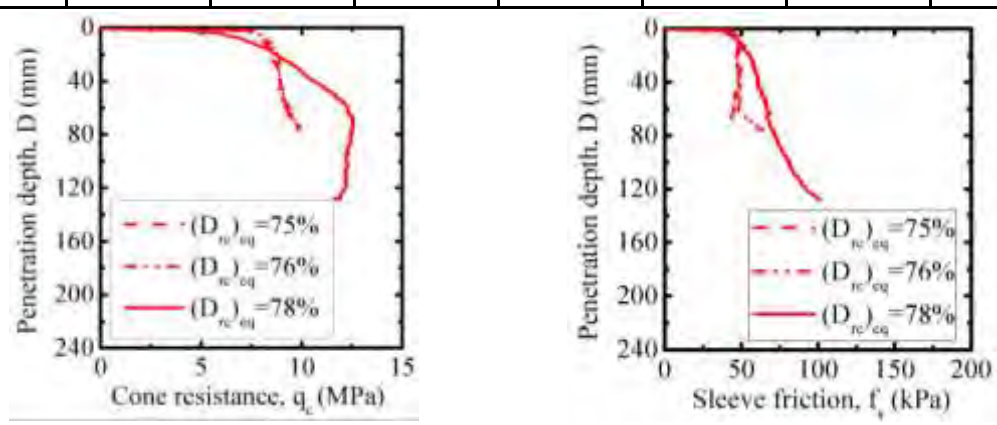

(a) q_c (b) f_s

Fig. 4.9 q_c and f_s of C_F=25% at $(D_{rc})_{eq}$≈75% under v=0.4 cm/s

Fig. 4.9 presents the q_c and f_s of OS-25 at nearly the same D_r [$(D_{rc})_{eq}$] under the same penetration rate of 0.40 cm/s. The q_c and f_s of $(D_{rc})_{eq}$=75% (CC-13), 76% (CC-17) and 78% (CC-11), are 9.4 MPa and 45 kPa, 9.9 MPa and 48 kPa, 11.9 MPa and 80 kPa, respectively, which indicates the repeatability of sample preparation method used for the sand-silt mixture. Fig. 4.9 also displays that the q_c stabilizes at the penetration depth of about 60 to 70 mm (D/d_c=4.7 to 5.5)

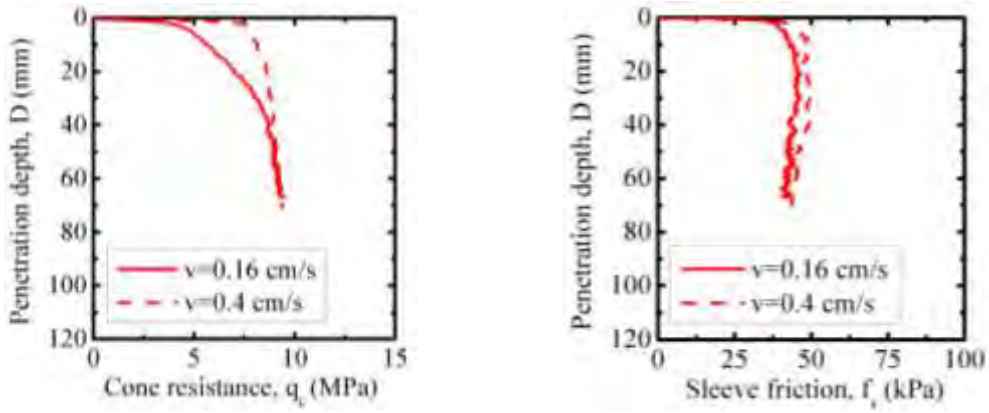

(a) q_c (b) f_s

Fig. 4.10 q_c and f_s of C_F=25% at $(D_{rc})_{eq}$=75% under two penetration rates (CC-12 and CC-13)

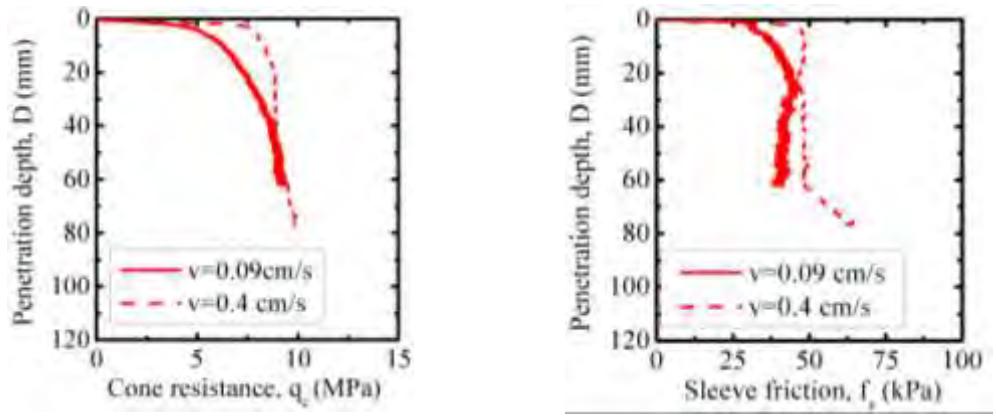

(a) q_c (b) f_s

Fig. 4.11 q_c and f_s of C_F=25% at $(D_{rc})_{eq}$=76% under two penetration rates (CC-16 and CC-17)

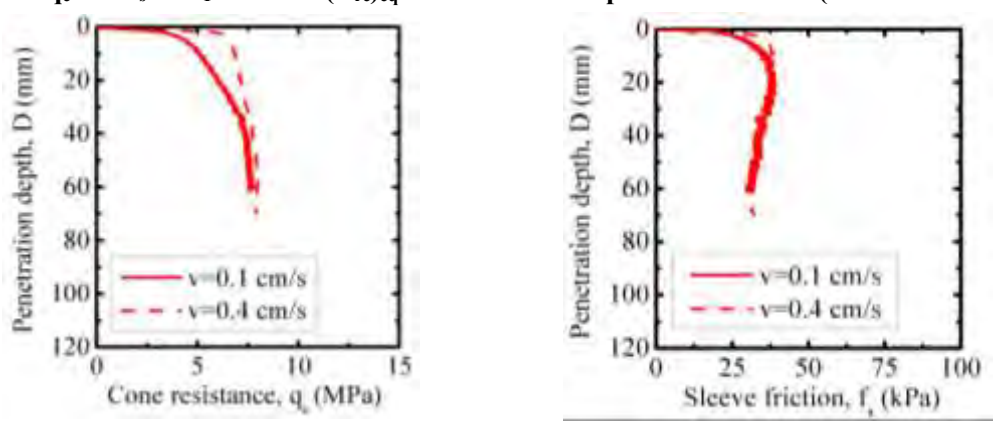

(a) q_c (b) f_s

Fig. 4.12 q_c and f_s of C_F=25% at $(D_{rc})_{eq}$=66% under two penetration rates (CC-18 and CC-19)

Fig. 4.10 plots the q_c and f_s of OS-25 at $(D_{rc})_{eq}$=75% with two penetration rates (CC-12 and CC-13). The q_c and f_s at v=0.16 and 0.4 cm/s are 9.4 MPa and 43 kPa, and 9.4 MPa and 45 kPa, respectively. Fig. 4.11 plots the q_c and f_s of OS-25 at $(D_{rc})_{eq}$=76% with two penetration rates (CC-

16 and CC-17). The q_c and f_s at v=0.09 and 0.4 cm/s are 9.4 MPa and 42 kPa, and 9.9 MPa and 48 kPa, respectively. Fig. 4.12 plots the q_c and f_s of OS-25 at $(D_{rc})_{eq}$=66% with two penetration rates (CC-18 and CC-19). q_c and f_s at v=0.1 and 0.4 cm/s are 7.6 MPa and 33 kPa, and 7.9 MPa and 33 kPa, respectively. Fig. 4.10 through Fig. 4.12 suggest that the effect of penetration rates on the cone resistance is insignificantly small when the tests are performed in 'drained' condition, which was also reported by Gui et al. (1998).

4.3.2. Saturated sand-silt mixture

4.3.2.1. Effect of fines on $(D_{rc})_{eq}[(e_c)_{eq}]$, k, m_v, c_v

As presented previously in chapter 2, the effect of fines on $(D_{rc})_{eq}$ $[(e_c)_{eq}]$ can be quantified through a contact index b for a sand-silt mixture when $C_F<C_{Fth}$. The stress-strain relationship and the cyclic stress ratio of clean sand and silty sand are, if not the same, at least similar when compared at a given $(D_{rc})_{eq}$. However, available experimental data suggested that the permeability k and coefficient of consolidation c_v of clean sand and silty sand are not the same even at the same $(D_{rc})_{eq}$. k and c_v decrease significantly with an increase in fines content (Shenthan 2001, Thevanayagam and Martin 2002). Table 4.5 summarizes the permeability (k), coefficient of volume compressibility (m_v) and coefficient of consolidation (c_v) of OS F55 sand-silt from chamber tests. The permeabilities reported by Shenthan (2001) for C_F=0% and 15% are used in this study since hydraulic conductivity tests were not performed at CC-7 (C_F=0) and CC-8 (C_F=15%).

Fig. 4.13 compares the k at different C_F of OS F55 sand-silt mix. The notation 'C_F=25%, e=0.457-0.463' in the figure denotes the fines content is at 25% and the void ratio is ranged from

0.457 to 0.463. For each fines content, k varies in a small range due to the difference in void ratio. However, k decreases rapidly (approximately one order) as C_F increases from 0% to 15%, 15% to 25% and 25% to 40% (up to threshold fines content C_{Fth}), respectively. The significant drop in k with the increase of C_F up to C_{Fth} is mainly due to the reduced pore size. The k value of the soil specimens is ranged from 0.6 to 1.3×10^{-3} cm/s for C_F=0%, $4\text{-}9 \times 10^{-5}$ cm/s for C_F=15%, 0.6 to 1.2×10^{-5} cm/s for C_F=25% reported by Shenthan (2001) in the undrained trixial tests. The k value of the soil specimens used in the testing chamber for C_F=25% agrees well with the values reported by Shenthan (2001), which is 0.7 to 1.2×10^{-5} cm/s.

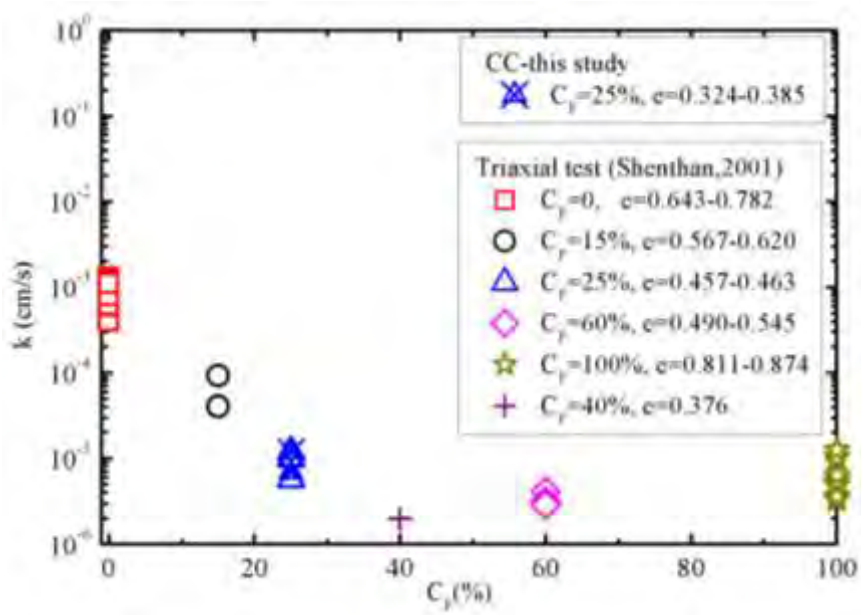

Fig. 4.13 Variation of k versus C_F (After Shenthan, 2001, Thevanayagam and Martin 2002)

Table 4.5 k, m_v, c_v of different C_F from chamber tests

C_F	e	$(e_c)_{eq}$	D_r	$(D_{rc})_{eq}$	k[3]	$m_{v\text{-virgin}}$			$c_{v\text{-virgin}}$		
						σ_{vo}'= 26 kPa	σ_{vo}'= 43 kPa	σ_{vo}'=63 kPa	σ_{vo}'= 26 kPa	σ_{vo}'= 43 kPa	σ_{vo}'= 63 kPa
(%)			(%)	(%)	(cm/s)	(kPa^{-1})	(kPa^{-1})	(kPa^{-1})	(cm^2/s)	(cm^2/s)	(cm^2/s)
0	0.680/0.687	0.680/0.687	62/59	62/59	1.3E-03	1.00E-04	8.30E-05	-	132.7	159.8	-
15	0.443/0.464	0.637/0.660	95/89	85/73	9.3E-05	9.10E-05	7.60E-05	-	10.4	12.5	-
25	0.370/0.400	0.700/0.744	89/82	48/29	7.0E-06	1.34E-04	8.70E-05	8.80E-05	0.5	0.8	0.8
25	0.323/0.342	0.648/0.672	98/94	79/67	1.0E-05	9.50E-05	9.60E-05	-	1.1	1.1	-
25	0.314/0.333	0.638/0.661	99/96	84/72	1.2E-05	9.10E-05	6.90E-05	-	1.3	1.8	-

[3] The permeability for C_F=0% and 15% are adopted from Shenthan (2001)

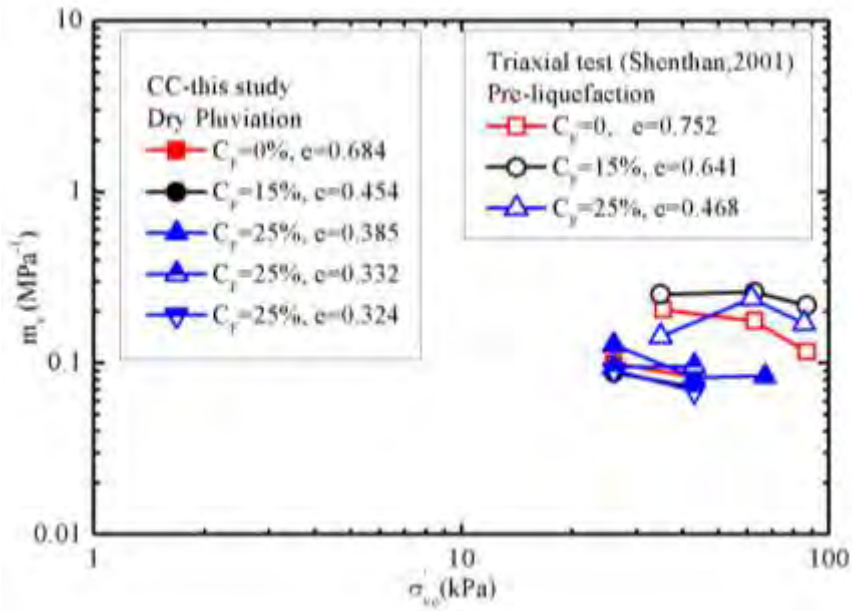

Fig. 4.14 Variation of m_v with C_F for virgin loading (After Shenthan, 2001)

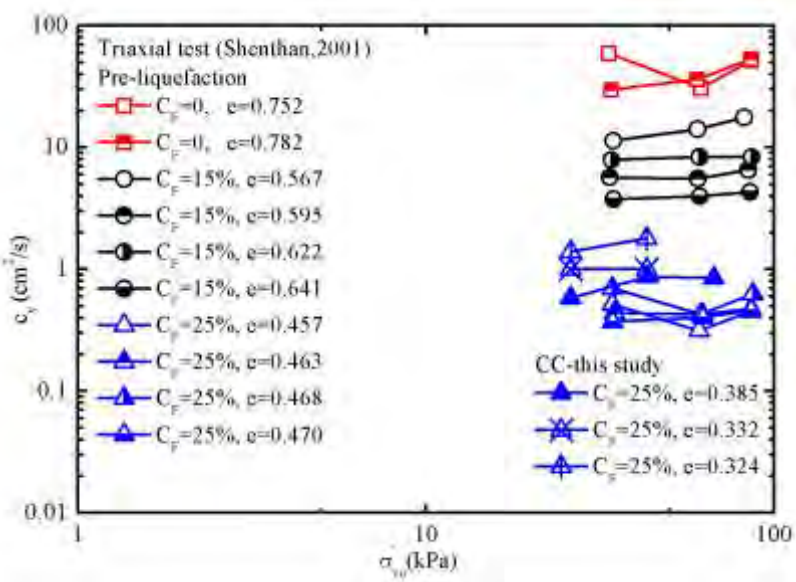

Fig. 4.15 Variation of c_v with C_F for virgin loading (After Shenthan, 2001)

Fig. 4.14 plots m_v versus σ_{vo}' at different C_F for virgin loading reported by Shenthan (2001) and obtained from testing chamber. It can be seen from the figure that m_v of different C_F fall into narrow bands for either triaxial or chamber specimens. Fig. 4.15 plots c_v versus σ_{vo}' at different C_F for virgin loading reported by Shenthan (2001) and obtained from testing chamber. It is observed

that c_v decreases approximately one order when C_F increases from 0 to 15%, and from 15 to 25%.

Based on the observation of the effect of fines on k and c_v, it is noticed that both k and c_v of silty sands differ from clean sands even compared at the same $(e_c)_{eq}$ or $(D_{rc})_{eq}$. k and c_v of silty sands are much smaller than clean sands. The difference of c_v between clean sands and silty sands would lead to the variation of dissipation time of induced excess pore water pressure (EPWP) as cone penetrates into the soil, hence results in the difference of drainage condition. It is noted that c_v obtained from testing chamber and triaxial test is corresponding to compression ratio and c_v related to recompression ratio is the controlling factor affecting the dissipation of EPWP around cone tip during cone penetration (Baligh and Levadoux, 1986a and b). Hence, c_v related to recompression ratio is converted from that corresponding to compression ratio by multiplying the ratio of C_c/C_r (where C_c is the compression index and C_r is the recompression index). For saturated overconsolidated sands, C_c/C_r is typically 3 (Coduto, 2001). Kulhawy and Mayne (1990) reported compressibility data for six sands shown in Table 4.6. In considering the above, C_c/C_r is assumed to be 3.5 to compute the T_o in chamber tests.

Table 4.6 Compressibility data for various sands (after Kulhawy and Mayne, 1990)

Sand	e_o	C_c		C_r	C_c/C_r	
		σ_{vo}'/P_{at}=1~3	σ_{vo}'/P_{at}=20~30		σ_{vo}'/P_{at}=1~3	σ_{vo}'/P_{at}=20~30
Monterey 0	0.854	0.021	0.085	0.006	3.5	14.2
	0.782	0.018	0.090	0.007	2.6	12.9
Ticino	0.917	0.025	0.130	0.007	3.6	18.6
	0.827	0.026	0.085	0.006	4.3	14.2
Hokksund	0.870	0.024	0.095	0.005	4.8	19.0
	0.790	0.018	0.056	0.005	3.6	11.2
Ottawa	0.760	0.025	0.030	0.007	3.6	4.3
	0.560	0.005	0.010	0.003	1.7	3.3
Reid-Bedford	0.900	0.013	0.090	0.005	2.6	18.0
	0.650	0.005	0.019	0.003	1.7	6.3
Hilton Mine	0.950	0.038	0.210	0.009	4.2	23.3
	0.732	0.022	0.100	0.006	3.7	16.7

4.3.2.2. CPT results

The targeted $(D_{rc})_{eq}$ of the sand-silt mix at different C_F were 60 to 80% and the final vertical effective stress is around 50 kPa or 75 kPa (CC-10). Table 4.7 summarizes the stabilized q_c, the average f_s and the corresponding f_s/q_c.

Table 4.7 CPT chamber test results of saturated OS F55 sand-silt mix

Test No.	D_r	$(D_{rc})_{eq}$	C_F	σ_{vo}'	v	q_c	f_s	f_s/q_c
	(%)	(%)	(%)	(kPa)	(cm/s)	(MPa)	(kPa)	(%)
CC-7	62/59	62/59	0	50	0.40	5.9	35	0.6
CC-8	95/89	85/73	15	50	0.40	10.7	50	0.5
CC-10	89/82	48/29	25	75	0.40	1.4	-	-
CC-14	98/94	79/67	25	50	0.09	4.8	17	0.3
CC-15	98/94	79/67	25	50	0.40	4.3	15	0.3
CC-20	99/96	84/72	25	50	0.09	8.2	25	0.3
CC-21	99/96	84/72	25	50	0.40	7.5	25	0.3
CC-9	-	-	25	-	-	-	-	-

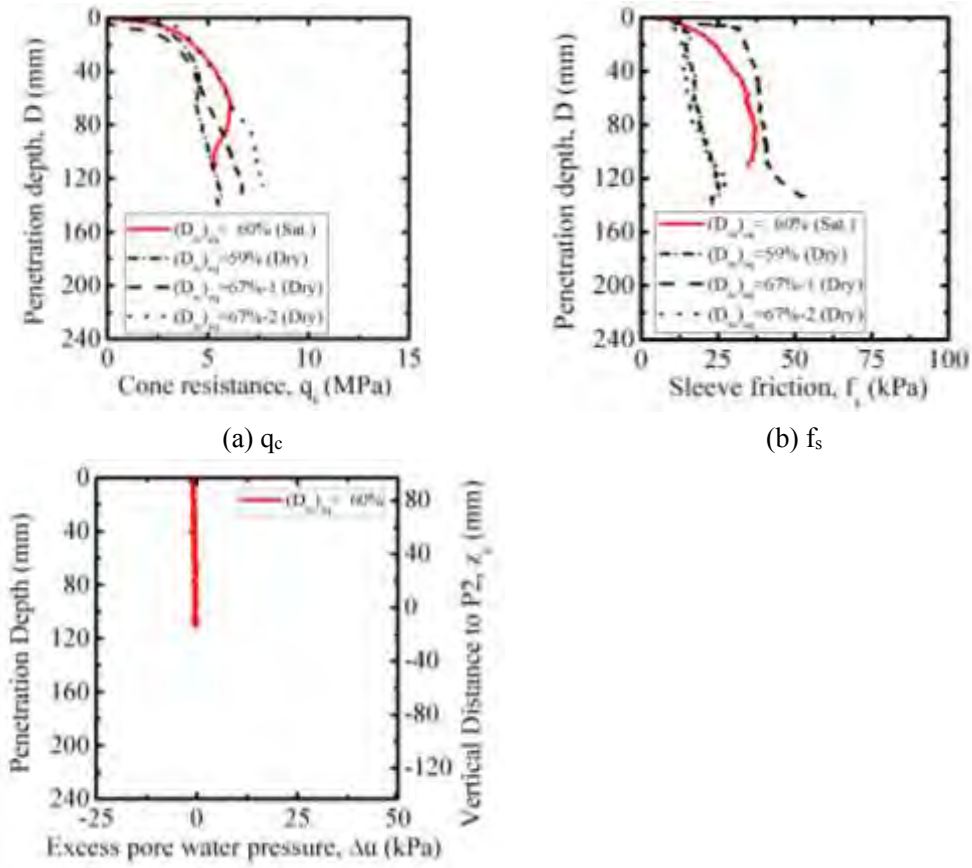

(a) q_c (b) f_s

(c) Δu

Fig. 4.16 q_c, f_s and Δu of C_F=0 at $(D_{rc})_{eq}$=60~70%

Fig. 4.16(a)-(c) plots the profiles of cone resistance q_c, sleeve friction f_s and excess pore water pressure Δu behind cone tip of saturated and dry clean sands (C_F=0%) at $(D_{rc})_{eq}$=60%~70% under v=0.40 cm/s. The comparison of q_c and f_s between dry and saturated sands is presented in Fig. 4.16(a) and (b). q_c of saturated clean sand at $(D_{rc})_{eq}$=58/62% is 5.8 MPa, agreeing well with dry specimens as expected. There is small discrepancy of f_s between dry and saturated specimen, the average f_s for saturated clean sand of $(D_{rc})_{eq}$≈60% is 35 kPa while the average f_s for dry clean sands of $(D_{rc})_{eq}$=59% and 67% are 23 and 24(40) kPa, respectively. Negligible development of Δu behind cone tip during the cone penetration process implies the drained condition of penetration. Overall, the experimental results (e.g. q_c and f_s) obtained using saturated clean sand are consistent with

those obtained using dry clean sands at nearly the same $(D_{rc})_{eq}$≈60%.

Fig. 4.17(a)-(c) presents the profiles of cone resistance q_c, sleeve friction f_s and excess pore water pressure Δu behind cone tip of C_F=15% at $(D_{rc})_{eq}$=73/85% under v=0.40 cm/s (CC-8). The stabilized q_c and Δu_2 are 10.7 MPa and -9 kPa, respectively. The measured negative Δu_2 behind cone tip indicates the dilation of soil during penetration. The average f_s is 50 kPa, giving the ratio of f_s/q_c equal to 0.5%.

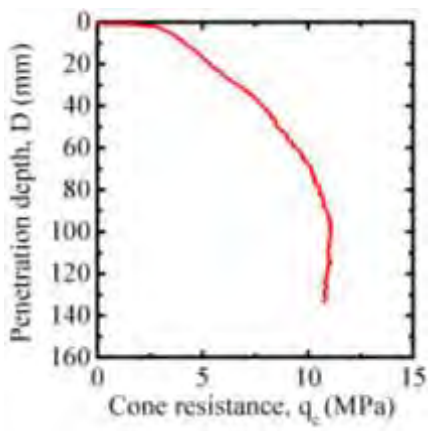

(a) q_c

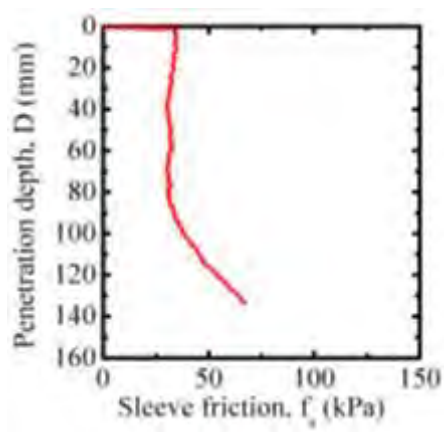

(b) f_s

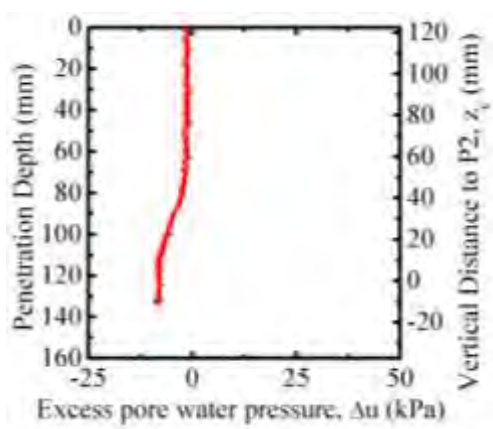

(c) Δu

Fig. 4.17 q_c, f_s and Δu of C_F=15% at $(D_{rc})_{eq}$=73/85% (CC-8)

Fig. 4.18(a) and (b) shows the profiles of cone resistance q_c and excess pore water pressure Δu behind cone tip profiles of C_F=25% at $(D_{rc})_{eq}$=27/48% under v=0.40 cm/s (CC-10). It was found

that the load cell located at the top of shaft malfunctioned during penetration and hence the sleeve friction was not computed in this test. The stabilized q_c and Δu are 1.4 MPa and 2 kPa, respectively.

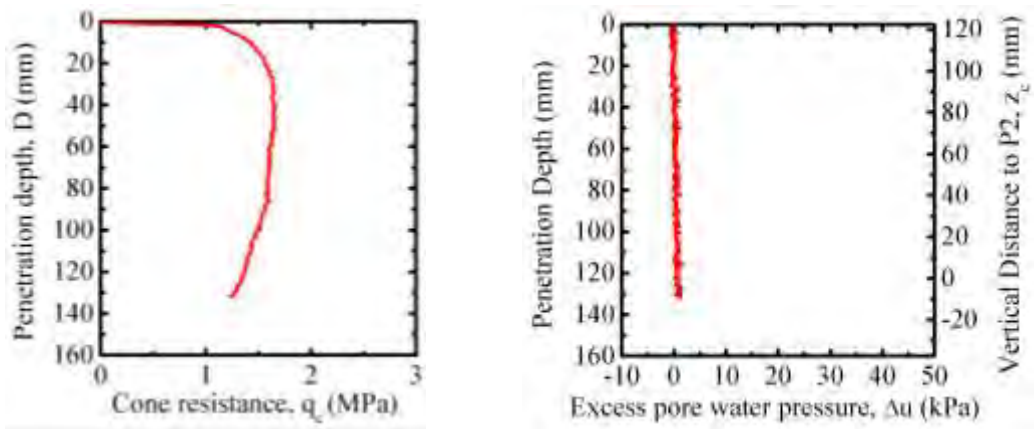

(a) q_c (b) Δu

Fig. 4.18 q_c and Δu of C_F=25% at $(D_{rc})_{eq}$=27/48% (CC-10)

Fig. 4.19(a)-(c) shows the profiles of cone resistance q_c, sleeve friction f_s and excess pore water pressure Δu of C_F=25% at $(D_{rc})_{eq}$=67/79% under v=0.09 and 0.40 cm/s (CC-14 and CC-15). It is noticed that the lateral location of piezometer duct is corresponding to cone tip face at these two tests. The stabilized q_c decreases from 4.8 to 4.3 MPa when penetration rate increases from 0.09 to 0.40 cm/s. The average f_s for v=0.09 and 0.40 cm are 17 and 15 kPa, respectively. There is no much excess pore water pressure build up (maximum of 2 kPa) during cone advancement for the test performed at v=0.09 cm/s. However, for the test conducted at 0.4 cm/s, the measured Δu initially negatively increases (0 to -18 kPa) as the cone approaches to the piezometer duct (z_c/d_c from 5 to 3), then positively increases to a maximum positive value (-18 to 11 kPa) as the cone further advances (z_c/d_c from 3 to 0).

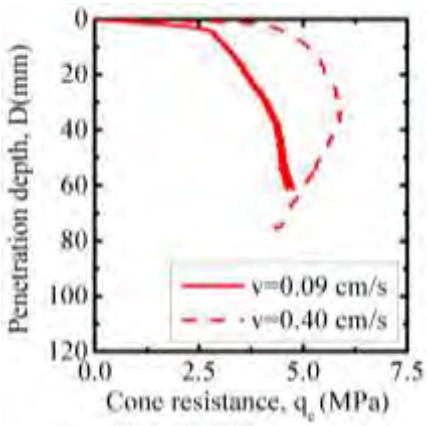

(a) q_c

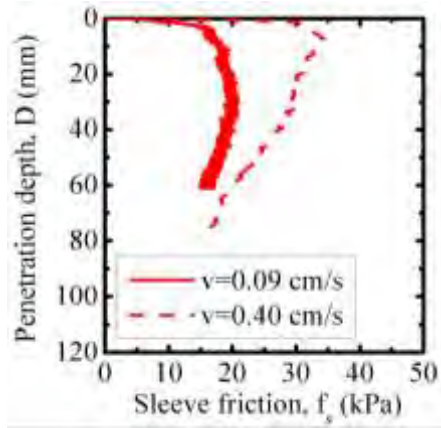

(b) f_s

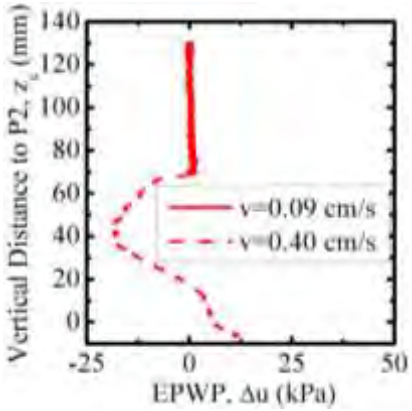

(c) Δu_1

Fig. 4.19 q_c, f_s and Δu of C_F=25% at $(D_{rc})_{eq}$=67/79% under two penetration rates (CC-14 and CC-15)

Fig. 4.20(a)-(c) shows the profiles of cone resistance q_c, sleeve friction f_s and excess pore water pressure Δu of C_F=25% at $(D_{rc})_{eq}$=72/84% under v=0.09 and 0.40 cm/s (CC-20 and CC-21). It is noticed that the lateral location of piezometer duct is corresponding to cone tip face at these two tests. The stabilized q_c decreases from 8.2 to 7.5 MPa when penetration rate increases from 0.09 to 0.40 cm/s. The average f_s for v=0.09 and 0.40 cm are 25 and 25 kPa, respectively. There is no much excess pore water pressure build up (maximum of 6 kPa) during cone advancement for the test performed at v=0.09 cm/s. However, for the test conducted at 0.4 cm/s, the measured Δu initially negatively increases (0 to -28 kPa) as the cone approaches to the piezometer duct (z_c/d_c from 5 to 3), then positively increases to a maximum positive value (-28 to 1 kPa) as the cone

further advances (z_c/d_c from 3 to 0).

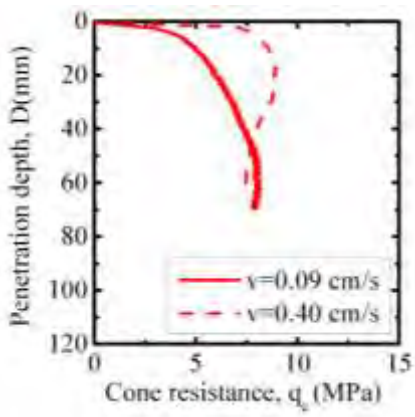

(a) q_c

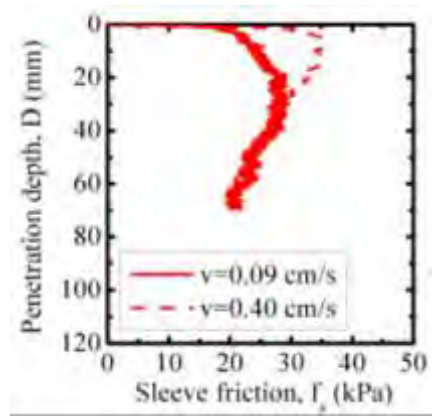

(b) f_s

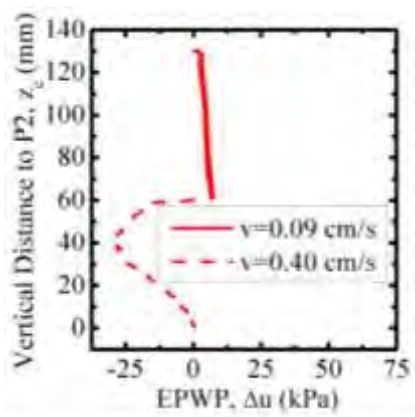

(c) Δu_1

Fig. 4.20 q_c, f_s and Δu of C_F=25% at $(D_{rc})_{eq}$=72/84% under two penetration rates (CC-20 and CC-21)

Fig. 4.19 and Fig. 4.20 show that the cone resistance slightly deceases as penetration rate increases from 0.09 to 0.4 cm/s. It indicates the penetration rate also influence the cone resistance. Nonetheless, more experiments performed at higher penetration rates (such as 2 cm/s or higher) are needed to further validate the findings.

4.3.3. Summary of experimental results

Table 4.8 summarizes the q_{c1N} and $(CRR)_{field}$ (see section 9.2 for details) of OS F55 sand-silt mix. The corresponding T_o of each experiment are also presented in this table.

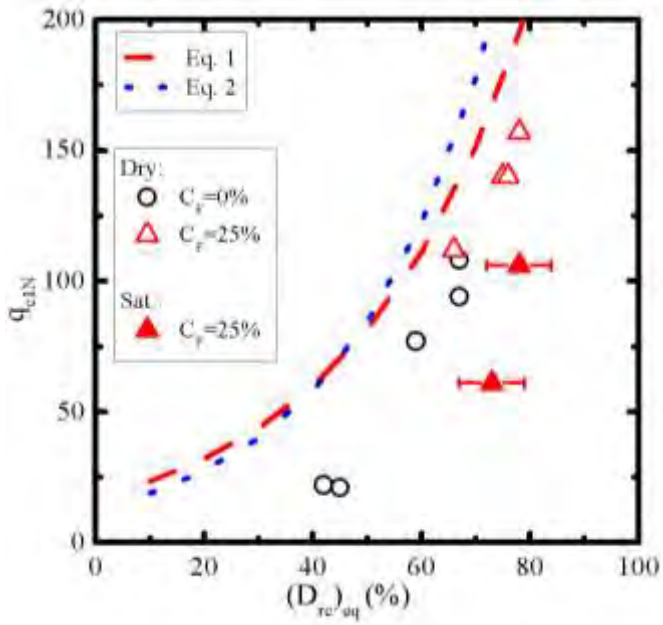

Fig. 4.21 q_{c1N} versus $(D_{rc})_{eq}$ at two C_F under v=0.4 cm/s

Fig. 4.21 presents the relationship between q_{c1N} and $(D_{rc})_{eq}$ from testing chamber at v=0.4 cm/s as well as empirical equations. The q_{c1N} decreases with an increase in silt content, at the same $[(D_{rc})_{eq}]$, from 0 to 25%. However this influence of silt content on penetration resistance is absent for dry sands and silty sands at the same $[(D_{rc})_{eq}]$. The difference of penetration resistance in saturated sands and silty sands, is thought to be due to partial drainage occurring in saturated silty sands whereas the penetration process is thought to be nearly drained in saturated sands. In the case of dry soils, this pore pressure influence is absent and hence the same penetration resistance is observed in sands and silty sands.

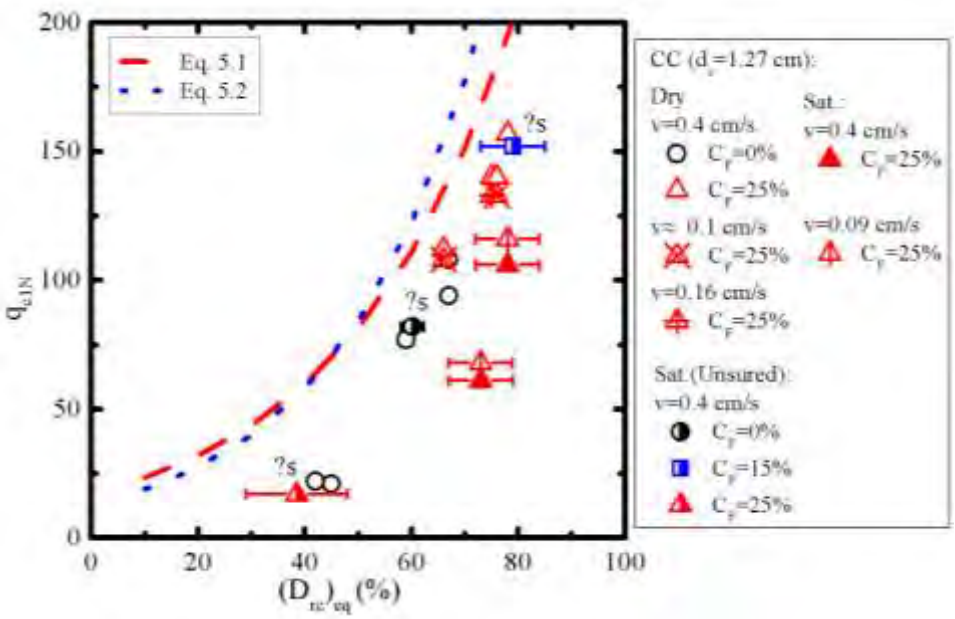

Fig. 4.22 q_{c1N} versus $(D_{rc})_{eq}$ from CPT chamber tests

Fig. 4.22 presents the relationship between q_{c1N} and $(D_{rc})_{eq}$ from testing chamber as well as empirical equations. In addition to the finding from Fig. 4.21, it is found that as penetration rate increases, q_{c1N} decreases in saturated silty sands whereas it remains the same in dry silty sands.

Table 4.8 Summary of q_{c1N} of Ottawa F55 sand-silt mix

Test No.	Sample type	C_F (%)	e	$(e_c)_{eq}$	D_r (%)	$(D_{rc})_{eq}$ (%)	T_o	q_{c1N}	$q_{c1N\text{-}aver}$	$(CRR)_{field\text{-}ave}$
CC-2	Dry	0	0.714	0.714	45	45	-	21	21	0.109
CC-4	Dry	0	0.718	0.718	42	42	-	21		
CC-3	Dry	0	0.688	0.688	59	59	-	77	77	0.150
CC-5	Dry	0	0.671	0.671	67	67	-	108	101	0.177
CC-6	Dry	0	0.671	0.671	67	67	-	94		
CC-11	Dry	25	0.325	0.651	97	78	-	168	147	0.215
CC-12	Dry	25	0.329	0.657	96	75	-	133		
CC-13	Dry	25	0.329	0.657	96	75	-	140		
CC-16	Dry	25	0.327	0.654	97	76	-	133		
CC-17	Dry	25	0.327	0.654	97	76	-	140		
CC-18	Dry	25	0.342	0.673	94	66	-	108	110	0.174
CC-19	Dry	25	0.342	0.673	94	66	-	112		
CC-7	Saturated	0	0.680/0.687	0.680/0.687	62/59	62/59	0.0015	82	82	0.155
CC-8	Saturated	15	0.443/0.464	0.637/0.660	95/89	85/73	0.01	152	152	0.254
CC-10	Saturated	25	0.370/0.403	0.707/0.748	89/84	48/27	0.2	17	20	0.098
CC-14	Saturated	25	0.323/0.342	0.648/0.672	98/94	79/67	0.02	68	68	0.202
CC-15	Saturated	25	0.323/0.342	0.648/0.672	98/94	79/67	0.1	61	61	0.202
CC-20	Saturated	25	0.314/0.333	0.638/0.661	99/96	84/72	0.01	116	116	0.252
CC-21	Saturated	25	0.314/0.333	0.638/0.661	99/96	84/72	0.06	106	106	0.252

4.4. Summary

This chapter introduces the soil samples used in the chamber, details the experimental procedures and summarizes and analyzes the experimental results of CPT chamber tests.

A number of CPTs were carried out in the speciemens at fines content of 0, 15 and 25%. It is shown that in the saturated specimens of the same $(D_{rc})_{eq}$, the q_{c1N} decreases as C_F increases from 0 to 25%. However, the effect of C_F is absent in dry specimens. The difference of penetration resistance in saturated sands and silty sands is thought to be due to partial drainage occurring in saturated silty sands whereas the penetration process is thought to be nearly drained in saturated sands. In the case of dry soils, this pore pressure influence is absent and hence the same penetration resistance is observed in sands and silty sands. It is also found that the penetration rate influence the cone resistance in saturated silty sands. For a given $(D_{rc})_{eq}$, the q_{c1N} decreases with an increase in penetration.

It is noticed that the maximum penetration rate achievable in this study is 0.4 cm/s, which is one fifth of the standard penetration rate and the cone diameter is 1.27 cm. For a given specimen, the T_o obtained from this study at the fastest penetration rate would be about 1/15 of that determined from field using the standard cone (d_c=3.56 or 4.37 cm) at the standard penetration rate (v=2 cm/s). Hence, more CPTs performed under faster penetration rates (e.g. v=2 cm/s or higher) at various $(D_{rc})_{eq}$ are needed to further validate the findings.

Chapter 5. Numerical simulation of CPT: Procedures

5.1. Introduction

A Preliminary analysis was performed using a finite difference scheme based software-FLAC^{2D} 6.0 (Appendix A) and a finite element scheme based software-Abaqus 6.10 to simulate the CPT. For Flac, the contituitvie model used is Mohr-Coulomb model since it only supports Mohr-Coulomb material and elastic material in the stress-balance step (the first step of CPT simulation) when the vertical stress gradient is considered. Moreover, instead of driving the cone into the soil, the penetration step is altered by applying the designated vertical displacement on the soil nodes along the cone path. Hence the interaction between soil and cone is absent. For Abaqus, it supports several constitutive models in the stress-balance step and the cone-soil interface can be modelled using Coulomb friction criteria. As a result, Abaqus is selected to perform the CPT simulation and the parametric study of cone resistance after comparison.

Since the soil around cone tip exhibits plastic behavior during cone penetration it is important to incorporate an appropriate plastic model into the numerical analysis. Among the plasticity models available in Abaqus, Mohr-Coulomb, Drucker-Prager and modified Drucker-Prager (cap) models are the most used constitutive models for cohesionless materials in CPT simulation. Mohr-Coulomb and Drucker-Prager model are often resorted to simulate the drained condition of CPT in sands (i.e. neglecting excess pore water generation at standard penetration rate of 2 cm/s) (Van Den Berger 1994; Susila and Hyrciw, 2003; Huang et. al., 2004; Tolooiyan and Gavin, 2011). However, it is unrealistic and impractical to ignore the generation and dissipation of excess pore

water pressure around cone tip when the cone is penetrating into the silty sand at a standard penetration rate. Ecemis (2008) employed the Drucker-Prager model to examine the effect of permeability and compressibility on the cone resistance. It was found that for the CPT simulation, the Drucker-Prager model used in the dilative material at low permeabilities (e.g. $k<10^{-8}$ m/s) under a large penetration depth (e.g. $D/d_c>1$) would yield considerably negative excess pore water pressure around the cone tip (Appendix C). The Preliminary analysis also showed similar issues using the Mohr-Coulomb model. With this regard, a suitable constitutive model is in need to carry out the consolidation coupled analysis in the CPT simulation for a better understanding of the effect of T_o on cone resistance in silty sands. Recently, the cap model was used in contractive soils to study the effect of T_o on the cone resistance (Markauskas et al., 2005; Yi et al., 2012). However, there is still lack of application of the cap model for dense silty sands (dilative materials) in the cone penetration simulation coupled with consolidation analysis. The large strain as well as heavy distortion of soil elements around cone tip induced by cone penetration process is another numerical issue to be considered.

In view of the above, this chapter addresses the application of the cap plasticity model in combination with the arbitrary Lagrangian Eulerian (ALE) mesh technique provided in Abaqus to simulate the CPT.

Firstly, motonic undrained triaxial tests reported by Thevanayagam et al. (2003) are simulated and compared using Drucker-Prager and cap plasticity model. The parameters of Drucker-Prager model are adopted from Ecemis (2008) except Young's modulus. The parameters used in the cap plasticity model are calibrated through a series of monotonic undrained triaxial tests with different

equivalent relative densities $(D_{rc})_{eq}$. The validation of cap model is also performed in the monotonic triaxial tests reported by other researchers (Puppala, 1993; Verdugo and Ishihara, 1996). Then the verification is performed through a one-dimensional consolidation problem using both constitutive models since the coefficient of consolidation (c_v) is the paramount factor among the soil-related properties affecting the cone resistance in sands and silty sands.

Cap plasticity model is selected as the constitutive model for numerical simulation in this study after comparison. Finally the arbitrary Lagrangian Eulerian (ALE) mesh technique is incorporated into cap plasticity model to carry out the coupled consolidation finite element analyses in CPT. A number of CPT chamber tests are used to validate the numerical model. In addition, the numerical examination of effect of permeability on the cone resistance using Drucker-Prager model is presented in Appendix C.

5.2. Introduction of constitutive models

5.2.1. Linear Drucker-Prager (DP) model

The extended Drucker-Prager can be used to model frictional materials such as granular-like soils and rock and allow material to harden and/or soften isotropically.

5.2.1.1. Yield function

There are three types of yield surfaces provided in Abaqus, which are linear, hyperbolic and exponent yield surface, respectively. Fig. 5.1 shows the yield surface for linear Drucker-Prager model in meridional plane.

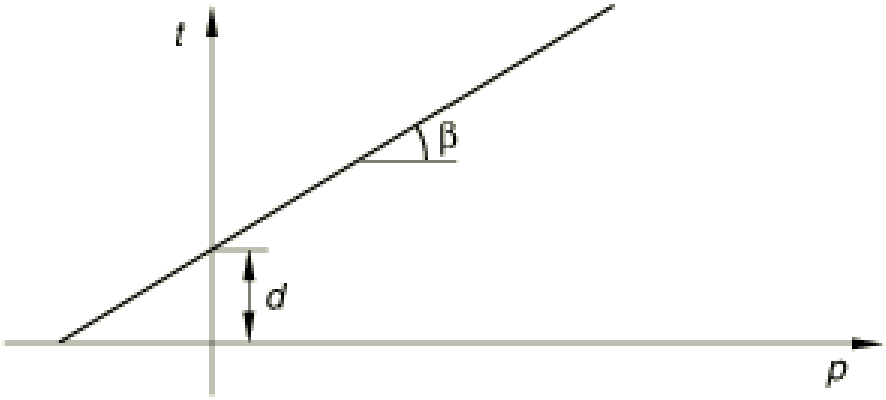

Fig. 5.1 Yield surface for linear Drucker-Prager model (Abaqus 6.10 Manual)

The yield function for linear Drucker-Prager model can be expressed as:

$$t - p\tan\beta - d = 0 \qquad \text{(Eq. 5.1)}$$

where

p is the mean normal stress, $p = \frac{1}{3}\sigma_{ii}$

$t = \frac{1}{2}q\left[1 + \frac{1}{K} - \left(1 - \frac{1}{K}\right)\left(\frac{r}{q}\right)^3\right]$, K is the ratio of the yield stress in triaxial tension to yield stress in triaxial compression. $r = \left(\frac{9}{2}S_{ij}S_{jk}S_{ki}\right)^{\frac{1}{3}}$

q is the deviatoric stress, $q = \sqrt{\frac{3}{2}S_{ij}S_{ji}}$ and $S_{ij} = \sigma_{ij} - \delta_{ij}p$, δ_{ij} is the Kronecker delta

β is the slope of the linear yield surface in the p–t stress plane and is commonly referred to the friction angle of the material.

d is the cohesion of material.

5.2.1.2. Hardening and flow rule

Associate flow and nonassociate flow are both available in linear Drucker-Prage model (Fig. 5.2).

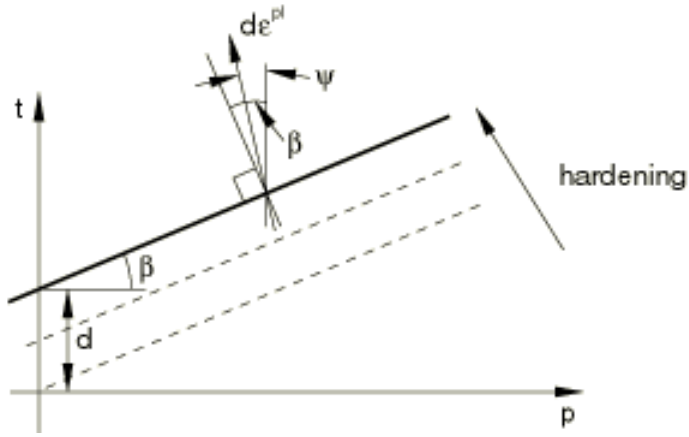

Fig. 5.2 Drucker-Prager hardening (Abaqus 6.10 Manual)

5.2.2. Modified Drucker-Prager (cap) model

The cap plasticity model is based on the linear Drucker-Prager model by adding an end 'cap' to it The main advantages of the cap model over the linear Drucker-Prager model are that the excessive amount of plastic dilation at yielding due to the normality rule used can be limited (Chen and Baladi, 1985) and the failure of material can be either in compression or in shear.

5.2.2.1. Yield function

The cap model consists of two parts (Fig. 5.3): an ultimate failure envelope which serves to limit the maximum shear stresses attainable by material (linear Drucker-Prager shear failure line) and an elliptically shaped strain-hardening yield surface that produces plastic volumetric and shear strain as it moves.

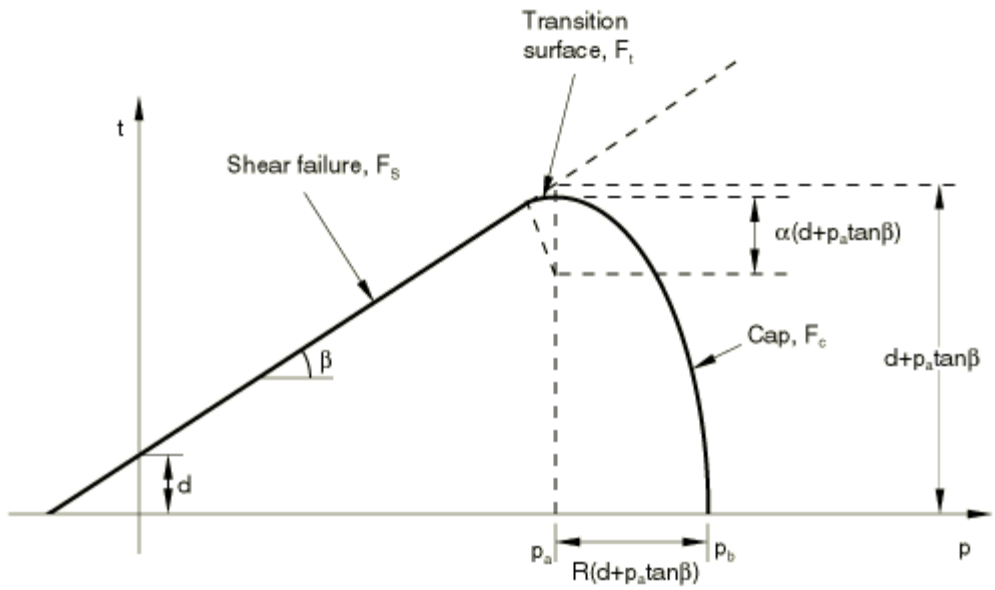

Fig. 5.3 Yield surface of Cap model (Abaqus 6.10 Manual)

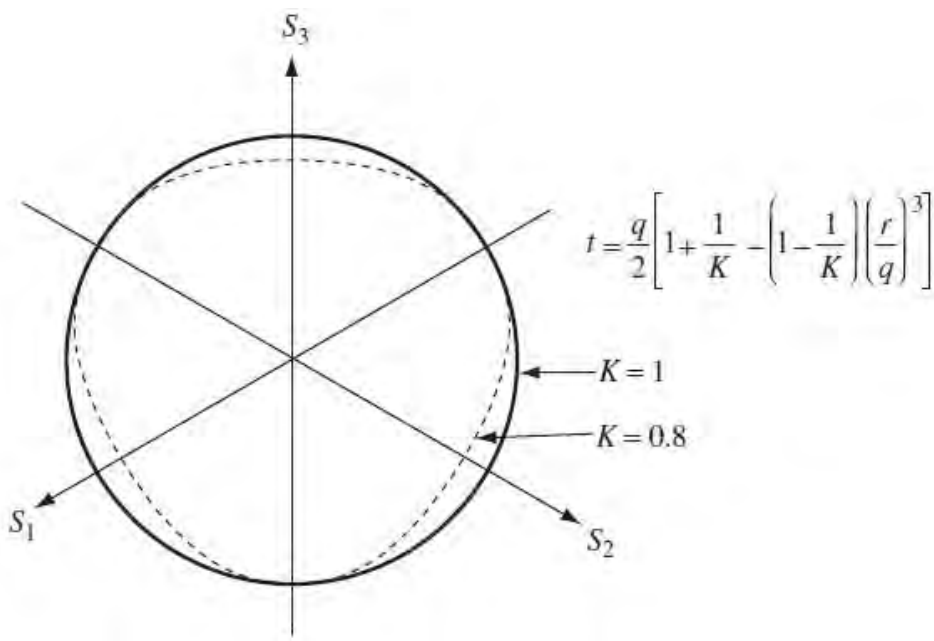

Fig. 5.4 Projection of the modified cap yield/flow surfaces on the Π-plane (Abaqus 6.10 Manual)

The shear failure yield function is the same as linear Drucker-Prager and can be expressed as:

$$t - p\tan\beta - d = 0 \qquad \text{(Eq. 5.2)}$$

and the cap yield function can be written as:

$$\sqrt{(p-p_a)^2+\left[\frac{Rt}{(1+\alpha-\alpha/\cos\beta)}\right]^2}-R(d+p_a\tan\beta)=0 \qquad \text{(Eq. 5.3)}$$

where

R is the material parameter controlling the elliptical shape of cap.

α is a small constant to smoothen the transition between linear shear failure surface and cap yield surface.

P_a is the evolution parameter that represents the volumetric plastic strain driven hardening/softening.

The transition yield surface is taken as:

$$\sqrt{(p-p_a)^2+\left[t-(1-\frac{\alpha}{\cos\beta})(d+p_a\tan\beta)\right]^2}-\alpha(d+p_a\tan\beta)=0 \qquad \text{(Eq. 5.4)}$$

5.2.2.2. Hardening and flow rule

The hardening law is a user-defined piecewise linear function relating the hydrostatic compression yield stress (p_b) and the corresponding volumetric inelastic strain (Fig. 5.5). It shall be noticed that the piecewise linear function shall include all values of effective pressure stress that the material will be subjected to during the analysis (Abaqus 6.10 user's manual, 2010).

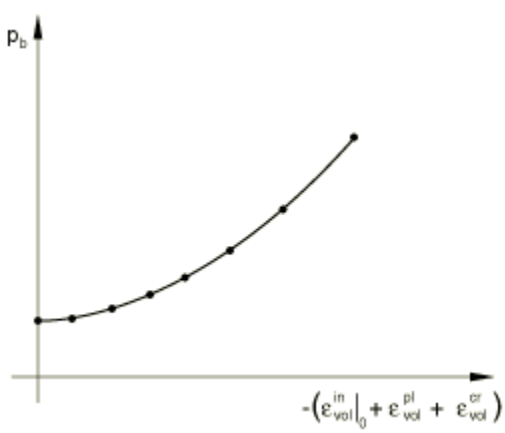

Fig. 5.5 A typical hardening curve for cap model (Abaqus 6.10 Manual)

The evolution parameter p_a can derived from be Fig. 5.3 as

$$p_a = \frac{p_b - R\,d}{(1 + R\ \tan\beta)} \qquad \text{(Eq. 5.5)}$$

The hardening curve can be determined (excluding the creep effect) as follows if the compression index C_c and the recompression index C_r are known from an isotropic compression test:

$$\varepsilon_{vol}^{pl} = \frac{C_c - C_r}{1 + e_0} \log\left(\frac{p'}{p'_0}\right) \qquad \text{(Eq. 5.6)}$$

where e_0 is the initial void ratio, p_0' and p' is the initial and final hydrostatic pressure, respectively

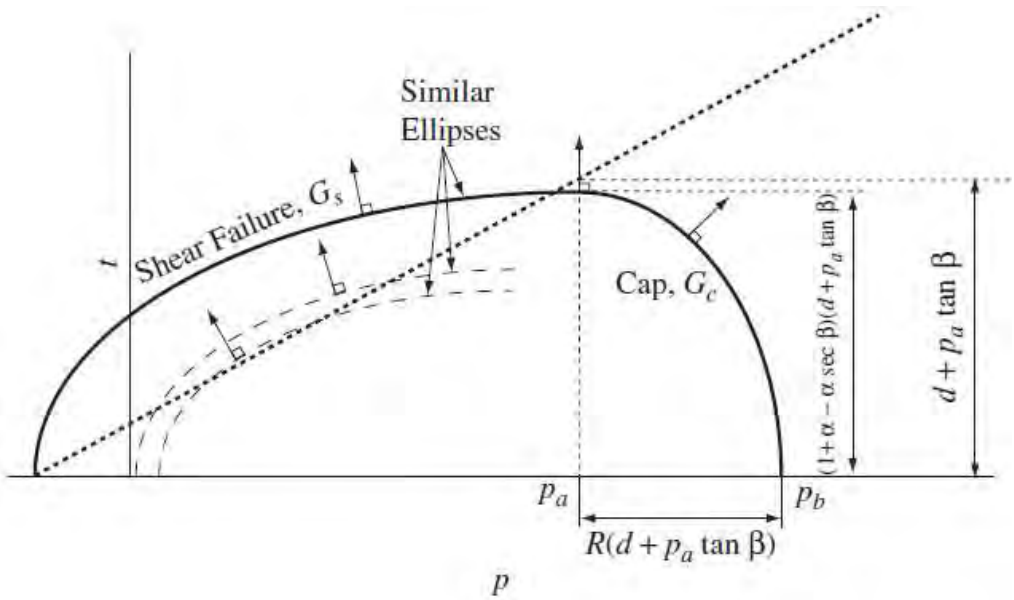

Fig. 5.6 Flow potential of Cap Model in p-t plane (Abaqus 6.10 Manual)

The flow rule of the linear shear failure yield surface and transition yield surface is defined as nonassociated while it is defined as associated in the cap yield surface (Fig. 5.6).

The flow potential in cap yield surface (G_c) is expressed as:

$$\sqrt{(p-p_a)^2+\left[\frac{Rt}{(1+\alpha-\alpha/\cos\beta)}\right]^2} \qquad \text{(Eq. 5.7)}$$

while the flow potential in shear failure and transition yield surface (G_s) is written as:

$$\sqrt{(p_a-p)\tan\beta+\left[\frac{t}{1+\alpha-\alpha/\cos\beta}\right]^2} \qquad \text{(Eq. 5.8)}$$

5.3. Simulation of monotonic undrained triaxial test

Compression index (C_c) is assumed using the table shown below for different relative densities from Coduto (2001).

Table 5.1 Typical consolidation properties of saturated normally consolidated sandy soils at various relative densities (Coduto, 2001)

Soil type	$C_c/(1+e_0)$					
	D_r=0%	D_r=20%	D_r =40%	D_r =60%	D_r =80%	D_r =100%
Medium to coarse sand	0.010	0.008	0.006	0.005	0.003	0.002
Fine to coarse sand	0.011	0.009	0.007	0.005	0.003	0.002
Fine to medium sand	0.013	0.010	0.008	0.006	0.004	0.003

Fig. 5.7 compares the empirical $C_c/[1+(e_{0c})_{eq}]$ proposed by Coduto (2001) and experimental $C_c/[1+(e_{0c})_{eq}]$ reported by Shenthan (2001) as well as laminar box data in section 7.4. The experimental values are bit larger than the empirical ones at a given $(D_{rc})_{eq}$.

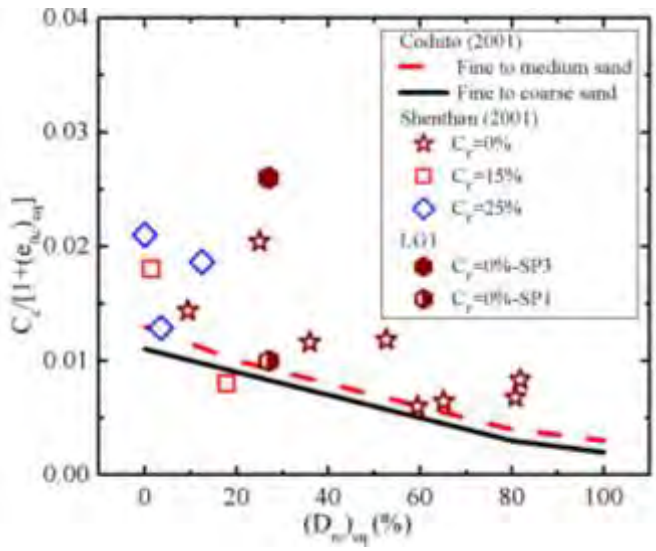

Fig. 5.7 Comparison of $C_c/[1+(e_{0c})_{eq}]$ versus $(D_{rc})_{eq}$ between empirical and experimental data

A parametric study (Appendix B) is carried out to investigate the key parameters in cap plasticity model to better understand the effect of each parameter on the stress path and stress-strain response of silty sands used in the numerical study. It is noticed that the combination of eccentricity parameter (R), initial yield surface position ($\varepsilon_{vol}^{in}|_0$) and hardening curve determines the dilation or contraction of soil and how much softening or hardening the soil would experience. From the study on the Young's modulus, it is found that larger elastic modulus leads soil to reaching steady state faster in terms of axial strain. It is noticed that influence of α on the stress path and stress stain of the monotonic undrained triaxial test is insignificant and hence it is set to 0 for the entire analysis. However, it is noteworthy that the initial hydrostatic compression stress p_0' is a key parameter in simulating dilative materials such as dense sands or heavily overconsolidated clays. It is found in the simulation that the ratio of p_0'/p_f' (p_f' is the mean effective stress at failure or steady state) in the range of 2 to 3 would give reasonable results when compared to experimental monotonic undrained triaxial tests under the eccentricity parameter (R) of 1. For contractive material, p_0' is the initial mean effective stress in all simulations. Although the

eccentricity parameter R is having influence on the stress path and stress-strain relationship and it is suggested to be from 0.001 to 1000 (Abaqus user's manual, 2010), the effect of R can be adjusted by the other parameters such as p_0'. In addition, the R value is equal to 1/tan(β) when using critical state model (Fig. 5.9 (f)). In consideration of the above, R is set to 1 in the entire analysis. To simplify the determination of $\varepsilon_{vol}^{in}|_0$, we assume that $\varepsilon_{vol}^{in}|_0=0$. This means that the dilative material yields the moment the stress path hits the shear failure envelope and behaves elatroplastically until failure while the contractive material yields at the moment of loading and behaves elatroplastically unitil failure.

5.3.1. Abaqus modeling and simulation steps

An axisymmetric two-dimensional model is used to resolve this problem. The model is shown in Fig. 5.8(a) after applying the symmetric boundary conditions, which is (1) the displacement in vertical direction (u_z) at bottom end (z=0) is zero. (2) the displacement in radial direction (u_r) at left end (r=0) is zero. A 4-node axisymmetric quadrilateral, bilinear displacement, bilinear pore pressure (CAX4P) element is used in the undrained triaxial tests simulation. The reason that the first order element is favored over the second order element is for the upcoming simulation of CPT, which would be discussed in section 5.5.2.1.

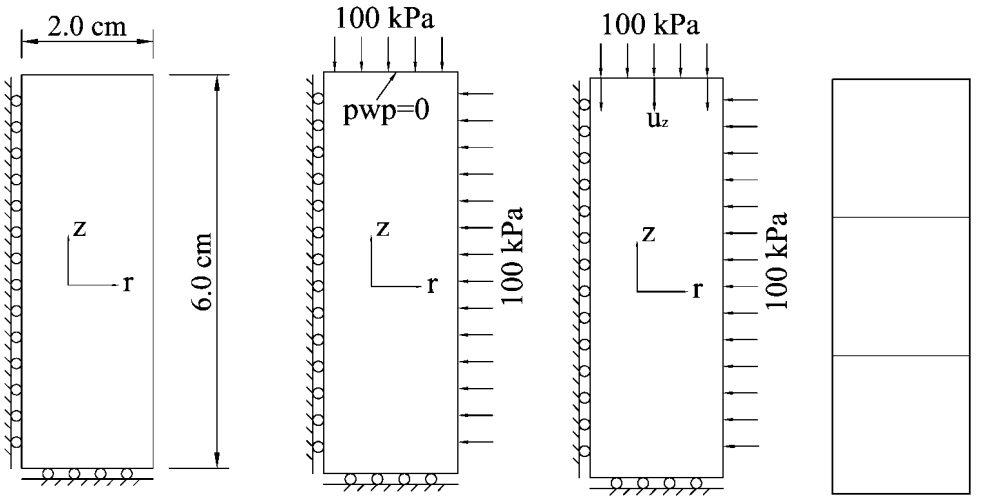

(a) Geometry (b) consolidation (c) shearing (d) 3-ele. mesh

Fig. 5.8 Model setup of monotonic undrained triaxial test

Consolidation step [Fig. 5.8(b)] and undrained shearing step [Fig. 5.8(c)] are involved in the simulation. The consolidation step is achieved by applying the 100 kPa confining stress at both z- and r-direction while allowing drainage on top surface. The undrained shearing step comes after the consolidation step is finished. The strain rate of this step is set to match experimental conditions. Fig. 5.8(d) gives the meshes used in the simulations of triaxial tests.

5.3.2. Validation with monotonic undrained triaxial tests

In this section, monotonic undrained triaxial tests from previous literatures (Thevanayagam et al., 2003; Puppala, 1993; Verdugo and Ishihara, 1996) are resorted to examine the effectiveness of cap model.

Young's modulus (E), ratio of E/E_{max}, frciton angle (ϕ'), initial hydrostatic compression stress (p_0'), initial cap yield surface position ($\varepsilon_{vol}^{in}|_0$) and eccnetricity parameter (R) in the simulation under isotropic stress of 100 kPa for differet soils are plotted in Fig. 5.9. E_{max} is estimated using the equation proposed by Hardin and Drneivich (1972) below:

$$E_{\max} = 2(1+\upsilon)G_{\max}$$
$$G_{\max} = 1230\frac{(2.97-e)^2}{1+(e_c)_{eq}}\sigma_c^{'0.5} \qquad \text{(Eq. 5.9)}$$

Where E_{max} and G_{max} are the maximum Young's and shear moduli at small strain level, respectively. υ is the Poisson's ratio, $(e_c)_{eq}$ is the equivalent inter-granular void ratio, $\sigma_c^{'}$ is the initial mean effective stress, in psi unit.

It shall be noticed that the Young's modulus used throughout the entire analysis is assumed to be constant although the modulus of soil varies significantly with strain. The application of constant Young's modulus would yield practical and reasonable idealization of a complex soil for engineering purpose and avoid numerical instability for large strain analysis.

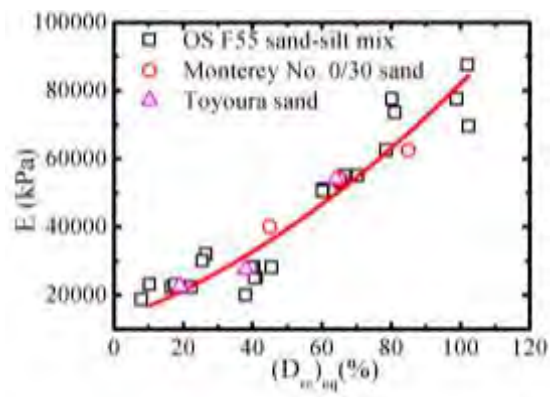

(a) E vs $(D_{rc})_{eq}$

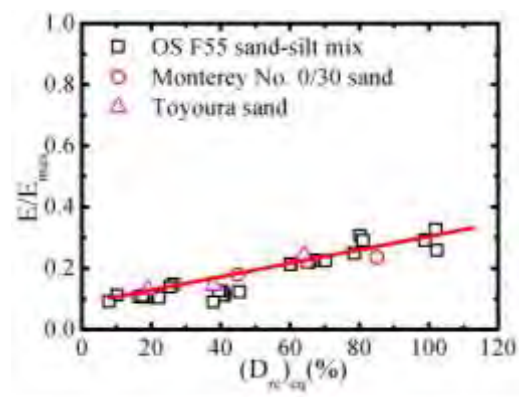

(b) E/E_{max} vs $(D_{rc})_{eq}$

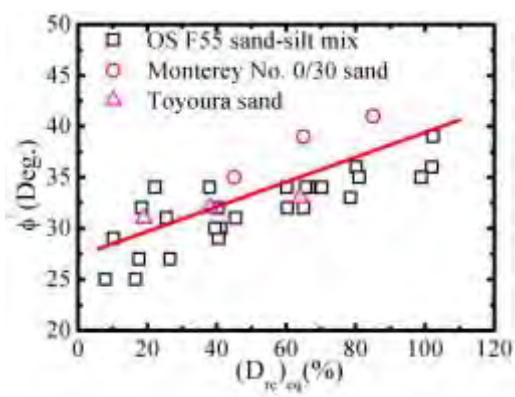

(c) $\phi^{'}$ vs $(D_{rc})_{eq}$

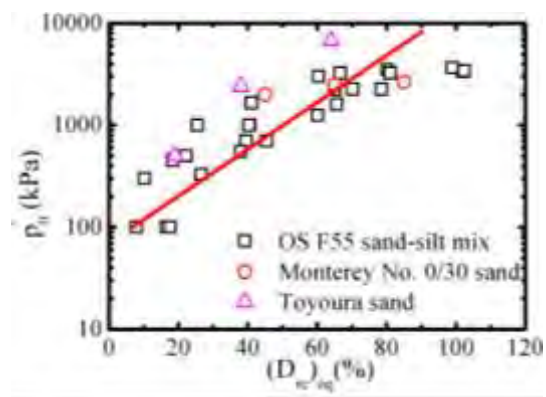

(d) $p_0^{'}$ vs $(D_{rc})_{eq}$

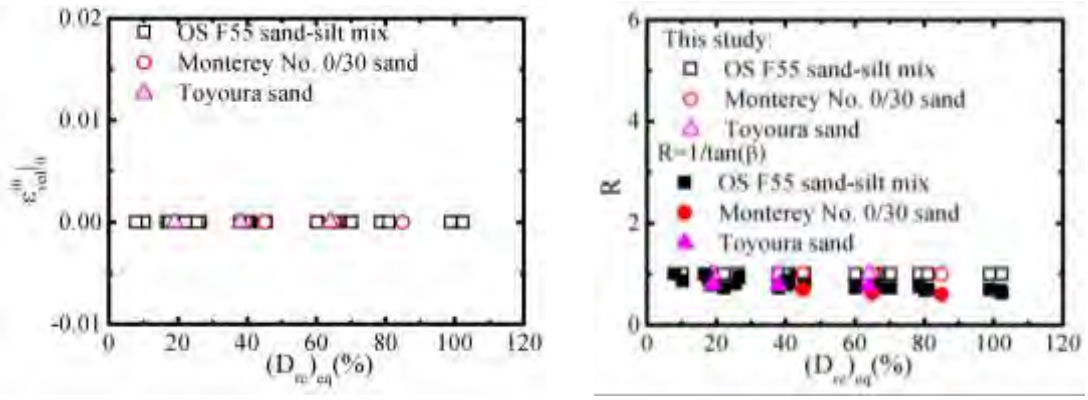

(e) $\varepsilon_{vol}^{in}|_0$ vs $(D_{rc})_{eq}$ (f) R vs $(D_{rc})_{eq}$

Fig. 5.9 E, ϕ', p_0'/p_f', $\varepsilon_{vol}^{in}|_0$ and R versus $(D_{rc})_{eq}$ under isotropic stress of 100 kPa for different soils

5.3.2.1. Comparison with experiments using Ottawa F55 sand-silt mix

In this section, the comparison of numerical simulation using Drucker-Prager model and cap model are both compared with the experimental data using OS F55 sand-silt mix reported by Thevanayagam et al. (2003). The undrained monotonic triaxial tests are performed at stain rate of 0.6%/min (0.01%/s) under confining stress of 100 kPa.

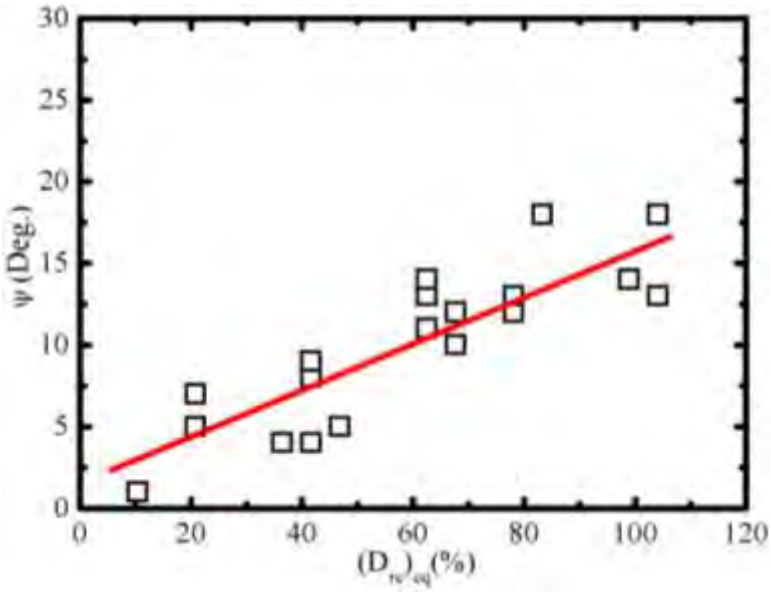

Fig. 5.10 Dilation angle versus $(D_{rc})_{eq}$ for OS F55 sand-silt mix (Ecemis, 2008)

The parametric study of Drucker-Prager model was fully discussed by Ecemis (2008). Fig. 5.10 presents the correlation between dilation angle used in the simulation and $(D_{rc})_{eq}$. Four

different soils ranging from very loose to very dense are used to test the effectiveness of selected cap plasticity model in this section, which are M31 [$(D_{rc})_{eq}$ =10%], M12 [$(D_{rc})_{eq}$ =41%], M01 [$(D_{rc})_{eq}$=60%], and M20 [$(D_{rc})_{eq}$ =80%], respectively. Soil parameters for each test are summarized in Table 5.2 (Drucker-Prager model) and Table 5.3 (cap model). Parameters of other soils simulated in appendix B.2 using cap model are also presented in Table 5.3. Fig. 5.11 to Fig. 5.14 present the comparison between numerical and experimental results of these four soils using two constitutive models. For the Drucker-Prager model, the main difference between numerical and experimental results lies in the fact that the unlimited dilation continues without reaching steady state for dilative soils, which would lead to unrealistic pore water pressure response and development of effective stress around cone tip during penetration (Appendix C). It shall also be noticed that the soil always behaves ealsitcally when it is within the shear failure envelop. For the cap model, the numerical simulation can reasonably capture all monotonic undrained triaxial tests in general although some discrepancy exists. The variations are partially attributed to constant elastic modulus used in the simulation (e.g., soil M12) and the limitation that the cap model in Abaqus cannot identify the transformation phase of soil from contraction to dilation, i.e. a cap model would only allow either contraction or dilation in the plastic stage (e.g. soil M31).

Cap plasticity model is adopted as the constitutive model. However, the numerical examination of effect of permeability on the cone resistance using Drucker-Prager model is presented in Appendix C.

Table 5.2 Drucker-Prager model parameters s for different soils

Soil type	Fine Content	Void Ratio	Equivalent Void Ratio	Relative Density	Equivalent granular relative density	Per.	Elastic Modulus		Poisson Ratio	Friction Angle	Friction Angle	Dilation angle	Dilation angle	Flow ratio
	C_F	e	$(e_c)_{eq}$	D_r	$(D_{rc})_{eq}$	k	This study	Ecemis (2008)	υ	ϕ	β	ψ	ψ*	K
	(%)			(%)	(%)	m/s	(kPa)	(kPa)		(Deg.)	(Deg.)	(Deg.)	(Deg.)	
M31	15	0.58	0.78	54	10	2.97E-06	23100	29107	0.2	29	49	1	2	1
M12	0	0.722	0.722	41	41	7.67E-06	25000	48128	0.2	29	49	4	8	1
M01	0	0.684	0.684	60	60	1.06E-05	50958	50958	0.2	32	52	13	26	1
M20	0	0.646	0.646	80	80	1.36E-05	77500	38000	0.2	36	56	12	24	1

Table 5.3 Cap Plasticity model parameters of Ottawa F55 sand-silt mix

Soil type	Fines Content	Void Ratio	Equivalent Void Ratio	Relative Density	Equivalent granular relative density	Per.	Elastic Modulus	Poisson Ratio	Friction Angle	Friction Angle	K	R	α	Ini. Yield Position	Ini. Hydrostatic stress	p_o'/p_f'	Final/Steady state stress
	C_F	e	$(e_c)_{eq}$	D_r	$(D_{rc})_{eq}$	k	E	υ	ϕ'	β				$\varepsilon_{vol}^{pl}\|_0$	p_o'		p_f'
	(%)			(%)	(%)	m/s	(kPa)		(Deg.)	(Deg.)					(kPa)		(kPa)
M08	0	0.604	0.604	102	102	1.70E-05	87500	0.2	36	56	1	1	0	0.000	3350	2.8	1215
M14	0	0.610	0.610	99	99	1.65E-05	77500	0.2	35	55	1	1	0	0.000	3650	2.6	1397
M20	0	0.646	0.646	80	80	1.36E-05	77500	0.2	36	56	1	1	0	0.000	3500	2.8	1239
M05	0	0.649	0.649	79	79	1.34E-05	62500	0.2	33	53	1	1	0	0.000	2250	2.4	920
M11	0	0.665	0.665	70	70	1.21E-05	55000	0.2	34	54	1	1	0	0.000	2250	2.5	900
M15	0	0.672	0.672	67	67	1.30E-05	55000	0.2	34	54	1	1	0	0.000	3250	2.4	1345
M10	0	0.675	0.675	65	65	1.13E-05	53500	0.2	32	52	1	1	0	0.000	2250	2.4	928
M01	0	0.684	0.684	60	60	1.06E-05	50958	0.2	32	52	1	1	0	0.000	3000	2.8	1073
M21	0	0.721	0.721	41	41	7.59E-06	25000	0.2	30	50	1	1	0	0.000	1650	2.4	696
M12	0	0.722	0.722	41	41	7.67E-06	25000	0.2	29	49	1	1	0	0.000	1000	2.2	452
M07	0	0.749	0.749	27	27	6.20E-06	32000	0.2	27	47	1	1	0	0.000	330	2.1	155
M17	0	0.751	0.751	26	26	6.00E-06	30000	0.2	31	51	1	1	0	0.000	1000	2.4	412
M09	0	0.768	0.768	17	17	5.00E-06	22300	0.2	25	45	1	1	0	0.000	100	2.0	49
M28	7	0.558	0.644	-	81	2.07E-05	73500	0.2	35	55	1	1	0	0.000	3250	2.7	1218
M23	7	0.596	0.684	-	60	1.77E-05	50500	0.2	34	54	1	1	0	0.000	1250	2.4	521
M26	7	0.632	0.722	-	40	7.00E-06	28100	0.2	32	52	1	1	0	0.000	1000	2.4	424
M22	7	0.665	0.757	-	22	1.21E-05	22300	0.2	34	54	1	1	0	0.000	500	2.2	230
M24	7	0.672	0.765	-	18	1.40E-05	22300	0.2	32	52	1	1	0	0.000	450	2.2	209
M37	15	0.423	0.603	-	102	1.48E-05	69500	0.2	39	58	1	1	0	0.000	3400	2.7	1266
M36	15	0.520	0.713	1	45	7.54E-06	28100	0.2	31	51	1	1	0	0.000	700	2.3	302
M32	15	0.530	0.724	1	40	6.69E-06	28000	0.2	30	50	1	1	0	0.000	700	2.2	315
M31	15	0.580	0.780	1	10	2.97E-06	23100	0.2	29	49	1	1	0	0.000	300	2.4	123
M34	15	0.584	0.785	1	8	9.30E-05	18700	0.2	25	45	1	1	0	0.000	100	2.3	43
M48	25	0.360	0.674	1	66	1.35E-06	53000	0.2	34	54	1	1	0	0.000	1600	2.3	690
M47	25	0.403	0.727	1	38	8.10E-07	20000	0.2	34	54	1	1	0	0.000	550	2.3	240
M45	25	0.435	0.766	1	18	1.00E-07	23100	0.2	27	47	1	1	0	0.000	100	1.2	84

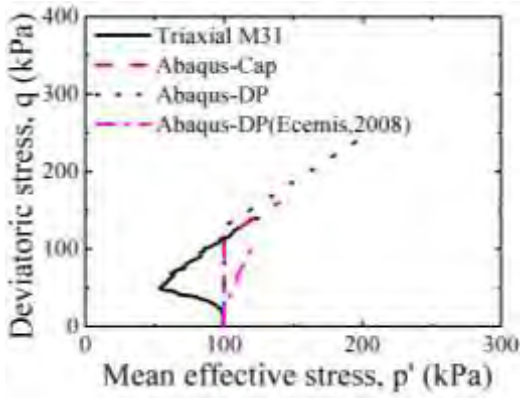

(a)q-p' plot

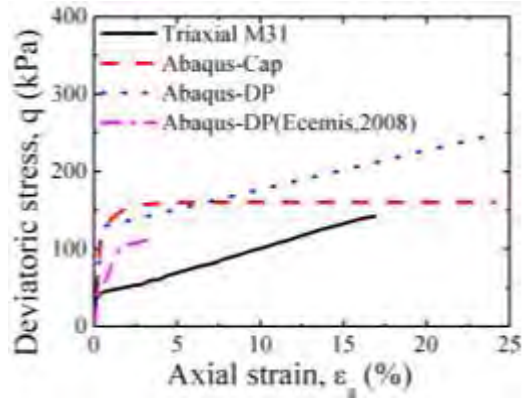

(b) q-ε_a plot

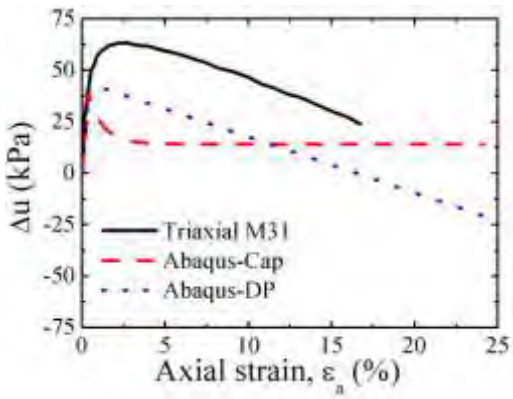

(c) Δu-ε_a plot

Fig. 5.11 Simulation of M31 [$(D_{rc})_{eq}$=10%]

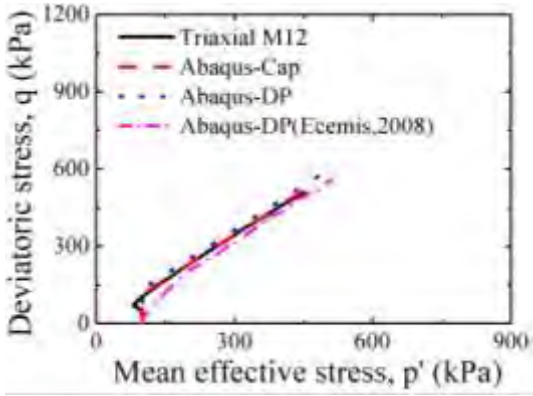

(a)q-p' plot

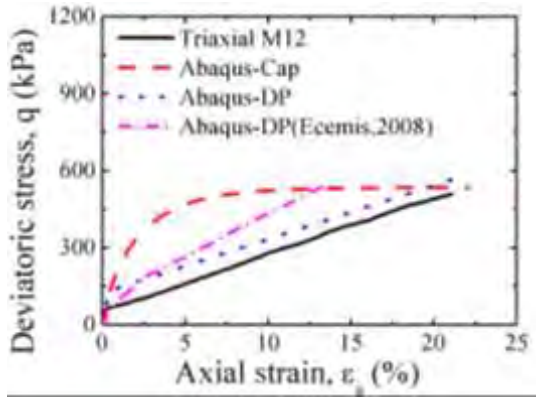

(b) q-ε_a plot

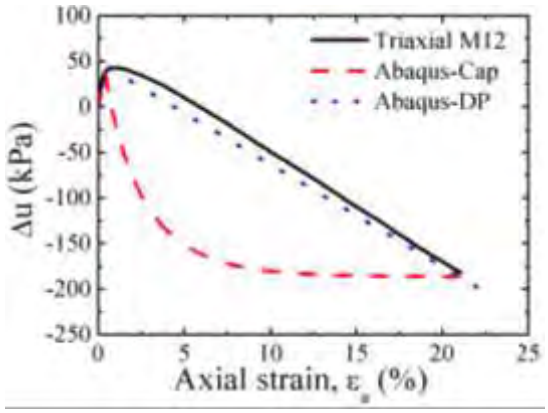

(c) Δu-ε_a plot

Fig. 5.12 Simulation of M12 [$(D_{rc})_{eq}$=41%]

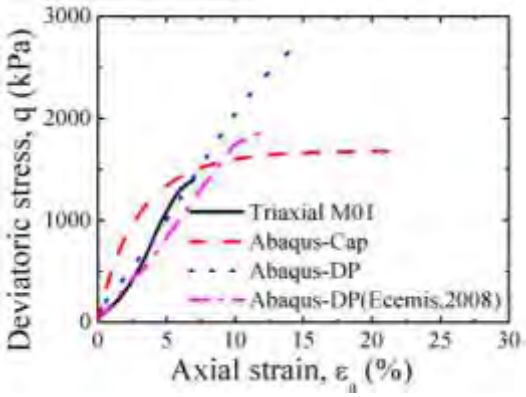

(a)q-p' plot

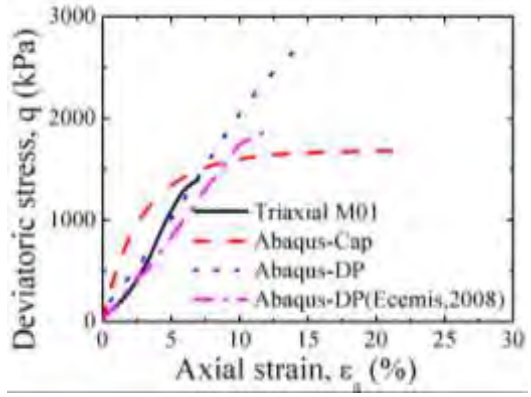

(b) q-ε_a plot

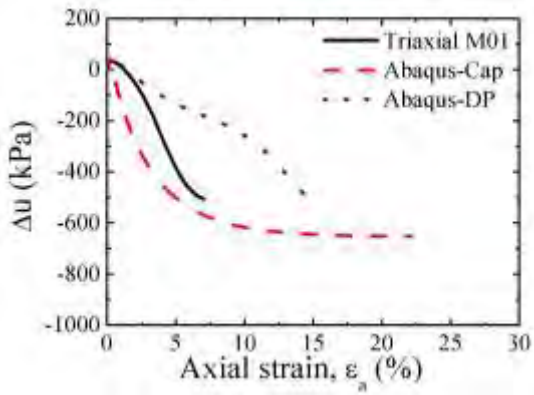

(c) Δu-ε_a plot

Fig. 5.13 Simulation of M01 [$(D_{rc})_{eq}$=60%]

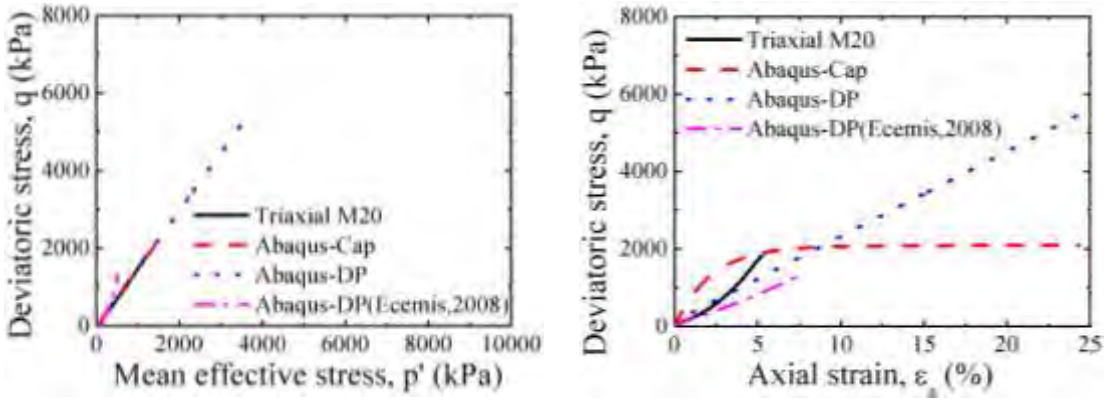

(a)q-p' plot (b) q-ε_a plot

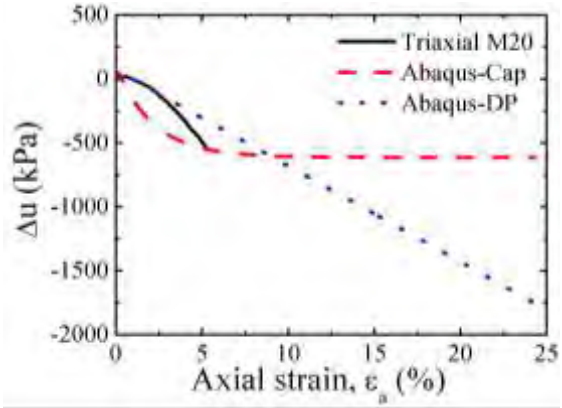

(c) Δu-ε_a plot

Fig. 5.14 Simulation of M20 [$(D_{rc})_{eq}$=80%]

5.3.2.2. Comparison with experiments using Monterey No. 0/30 sand

Puppala (1993) performed a series of miniature CPTs (dry specimens) in calibration chamber as well as monotonic undrained triaxial tests using Monterey No. 0/30 sand at different D_r (45, 65 and 85%) under various isotropic stresses (100, 200 and 300 kPa). The undrained triaxial tests are used to calibrate both elastic and plastic parameters of the cap plasticity model and the CPT test results are employed to examine the effectiveness of numerical model used in this work. The samples used in the triaxial tests were about 7 cm in diameter and 15 cm in height and the loading rate of triaxial test is 0.05 mm/min.The related elastic and plastic parameters of soils used in the simulations are summarized in Table 5.4. Fig. 5.15 through Fig. 5.17 show that the numerical

simulation using cap plasticity model can accurately predict the behavior of Monterey sand across a wide range of relative densities and confining stresses.

For CPTs performed in the calibration chamber, the cross section area of cone was 1.27 cm^2 and the calibration chamber was 0.53 m in diameter and 0.70~0.73 in height, giving the calibration chamber size ratio D_L=42. The penetration rate was 2 cm/s.

Table 5.4 Parameters of Monterey sand used in the undrained triaxial tests and CPT simulation

D_r	$(D_{rc})_{eq}$	E	υ	ϕ'	β	R	α	$\varepsilon_{vol}{}^{pl}\|_0$	p_0'	σ_c'
(%)	(%)	(kPa)		(Deg.)	(Deg.)				(kPa)	(kPa)
45	45	40000	0.2	35	55	1	0	0	2000	100
45	45	56000	0.2	35	55	1	0	0	2250	200
45	45	68000	0.2	35	55	1	0	0	2250	300
65	65	54000	0.2	39	58	1	0	0	2500	100
65	65	76500	0.2	39	58	1	0	0	2500	200
65	65	94000	0.2	39	58	1	0	0	2550	300
85	85	62500	0.2	41	59	1	0	0	2650	100

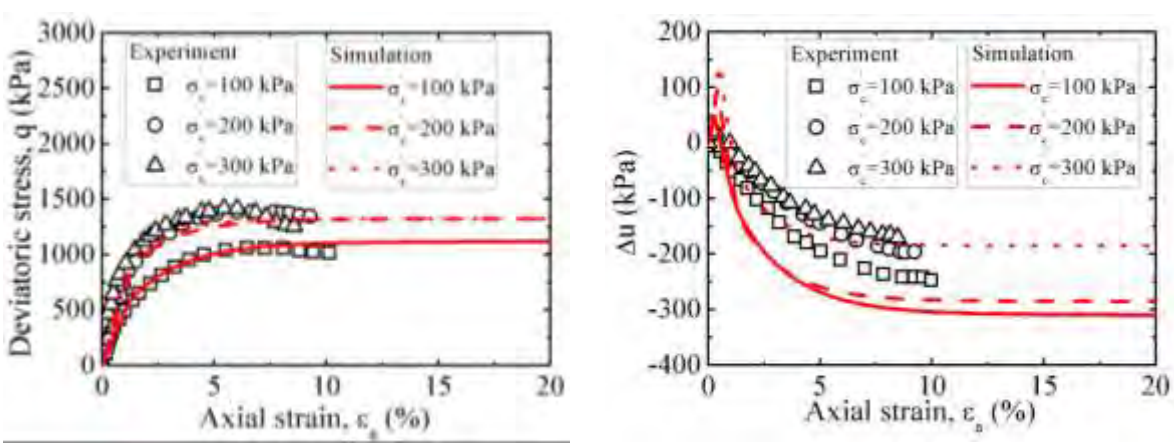

(a) q-ε_a (b) Δu-ε_a

Fig. 5.15 Simulation of of Monterey sand at D_r=45% under different σ_c'

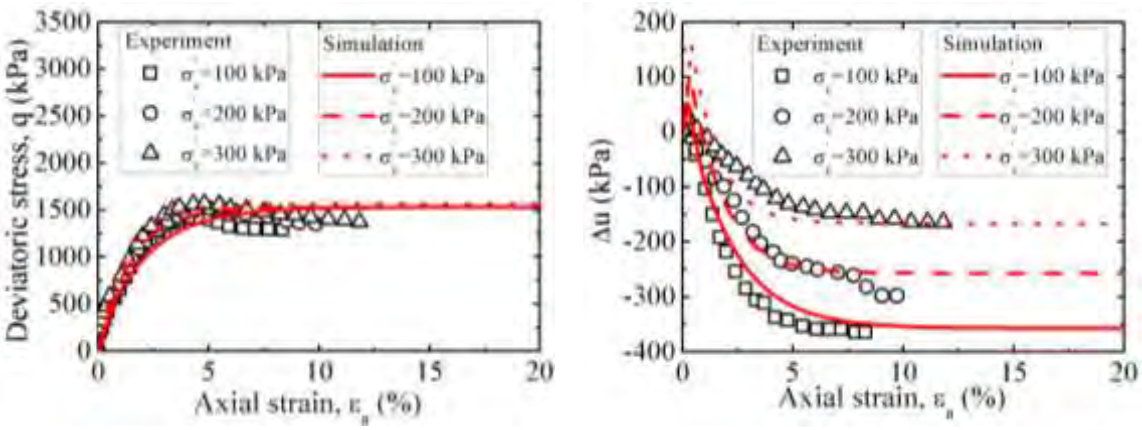

(a) q-ε_a (b) Δu-ε_a

Fig. 5.16 Simulation of Monterey sand at D_r=65% under different σ_c'

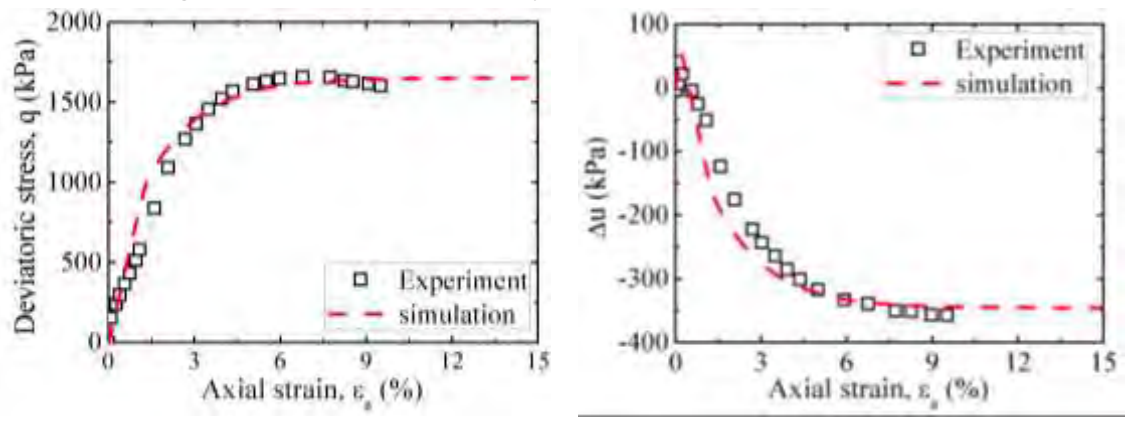

(a) q-ε_a (b) Δu-ε_a

Fig. 5.17 Simulation of Monterey sand at D_r=85% under σ_c'=100 kPa

5.3.2.3. Comparison with experiments using Toyoura sand

Another set of monotonic undrained triaxial tests under 100 kPa using Toyoura sand at various relative densities under σ_c'=100 kPa reported by Verdugo and Ishihara (1996) is resorted to test the effectiveness of cap model. The samples were 5 cm in diameter and 10 cm in height and the deformation rate was 1 mm/min. The elastic and plastic properties of soils are tabulated in Table 5.5. Reasonable prediction of experimental data is achieved by the numerical simulation as shown in Fig. 5.18.

Table 5.5 Elastic and plastic parameters of Toyoura sand used in the cap model

D_r	$(D_{rc})_{eq}$	E	υ	ϕ'	β	R	α	$\varepsilon_{vol}^{in}\|_0$	p_0'
(%)	(%)	(kPa)		(Deg.)	(Deg.)				(kPa)
19	19	22500	0.2	31	51	1	0	0	500
38	38	27500	0.2	32	52	1	0	0	2400
64	64	54000	0.2	33	53	1	0	0	6750

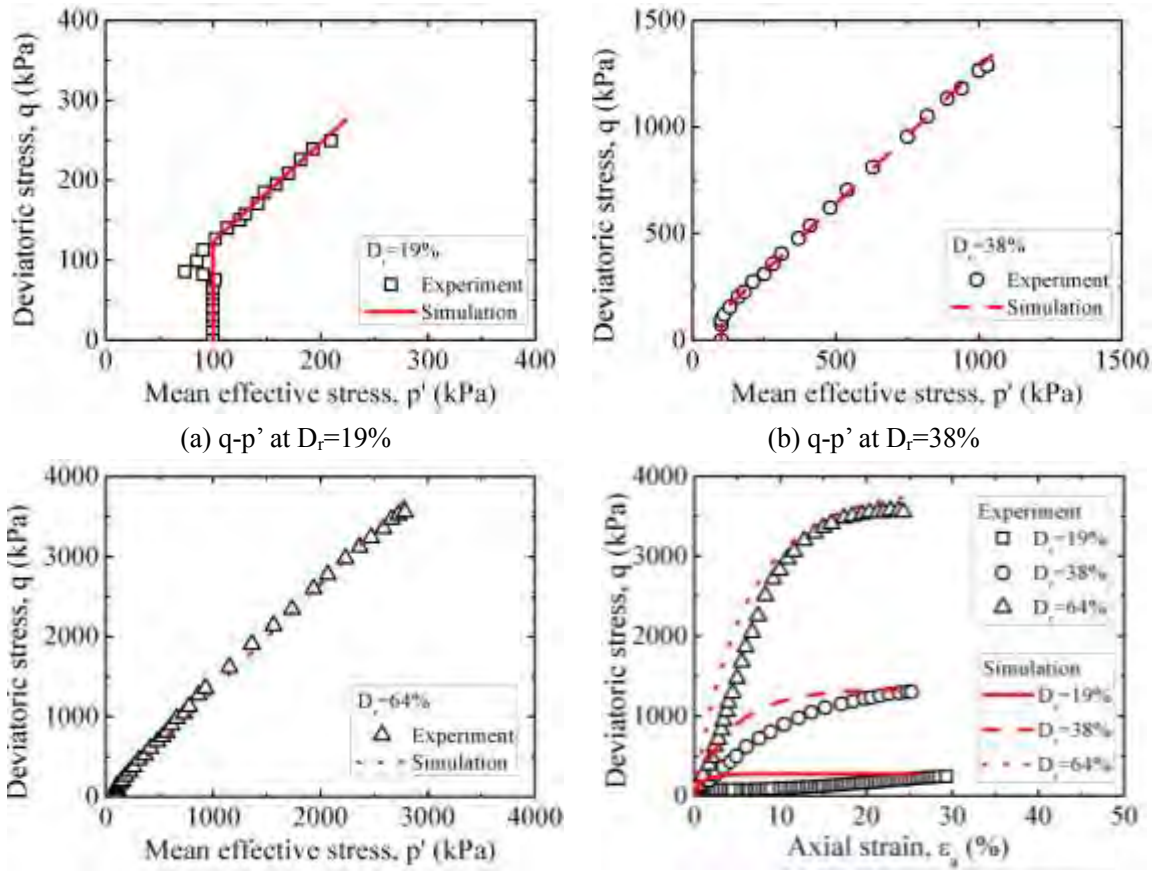

(a) q-p' at D_r=19% (b) q-p' at D_r=38%

(c) q-p' at D_r=64% (d) q-ε_a

Fig. 5.18 Simulation of of Toyoura sand at different D_r under σ_c'=100 kPa

5.3.3. Summary of section 5.3

In this section, the montonic undrained triaxial tests of three soils are simulated in the Abaqus using cap model. The numerical results, in general, show reasonable agreement with the experimental data for soil exhibiting either contractive or dilative behavior although some discrepancy exists. The difference may be attributed to the constant modulus instead of strain-

dependent modulus used in the simulation and the lack of ability to capture the phase transition zone in Abaqus.

5.4. Simulation of one-dimensional consolidation

In this section, a soil column with 10 m in height and 1 m in width is modeled to simulate the one-dimensional consolidation problem with one way drainage (Fig. 5.19). Soil parameters (M20) are obtained from Table 5.2 and Table 5.3 except permeability. Element CAX4P is used in the numerical verification.

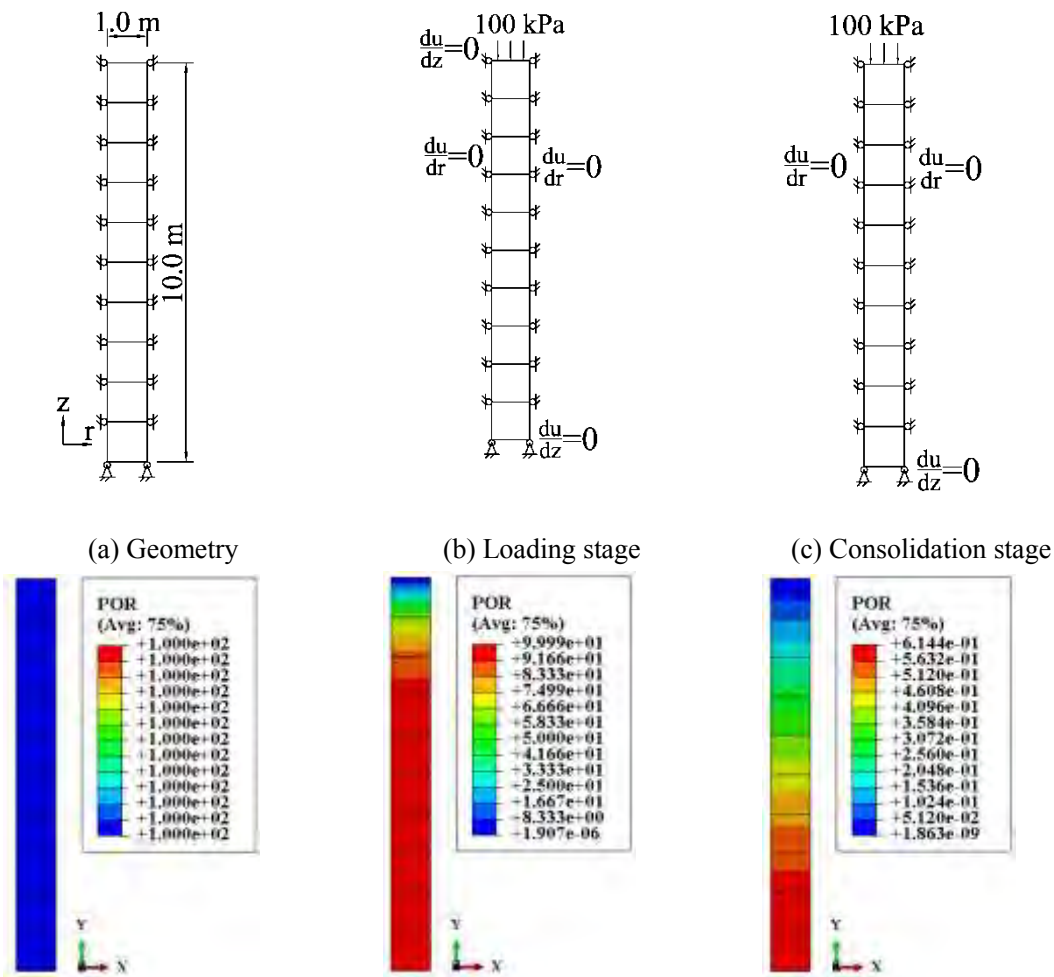

(a) Geometry (b) Loading stage (c) Consolidation stage

(d) EPWP at the end of loading -Unit (kPa) (e) EPWP at the start of loading-Unit (kPa) (f) EPWP at the end of consolidation -Unit (kPa)

Fig. 5.19 Numerical simulation of one-dimensional consolidation using cap model

Horizontal displacement is restrained at both sides and vertical displacement is restrained at bottom [Fig. 5.19(a)]. Loading and consolidation step are the two simulation steps. In the loading step [Fig. 5.19(b)], a distributed load of 100 kPa is applied at top of soil column in a very short time period (0.001s) to simulate an instant surcharge. Then the drainage at top surface is allowed to simulate the one-way drainage of consolidation [Fig. 5.19(c)]. Fig. 5.19(d) to (e) presents the excess pore pressure response when the instant loading is applied, when one-way drainage at top surface is activated and when the final consolidation is completed, respectively.

The time factor T_v is expressed as

$$T_v = \frac{c_v t}{H_{dr}^2} \qquad \text{(Eq. 5.10)}$$

where

H_{dr} is the drainage path length

t is the time

c_v is the coefficient of consolidation, can be determined from

$$c_v = \frac{k}{\gamma_w m_v} \qquad \text{(Eq. 5.11)}$$

k is the permeability of soil, γ_w is the unit weight of water and m_v is the coefficient of volume compressibility, can be derived from oedometer test as

$$m_v = \frac{1}{E}\left(1 - 2\frac{\nu^2}{1-\nu}\right) = \frac{(1+\nu)(1-2\nu)}{(1-\nu)E} \qquad \text{(Eq. 5.12)}$$

while from triaxial cell, m_v can be determined as

$$m_v = \frac{3(1-2\nu)}{E} \qquad \text{(Eq. 5.13)}$$

Fig. 5.20(a) and (b) compare the numerical solutions using Drucker-Prager model at three different permeabilities ($k=10^{-5}$m/s, 10^{-7} m/s, 10^{-9} m/s) to Terzaghi's solution using two computed c_v. Well agreement is achieved between numerical and analytical solution using Drucker-Prager model when Eq.5.12 [Fig. 5.20(a)] is used to compute c_v while small discrepancy exists between numerical and analytical solution when Eq.5.13 [Fig. 5.20(b)] is used.

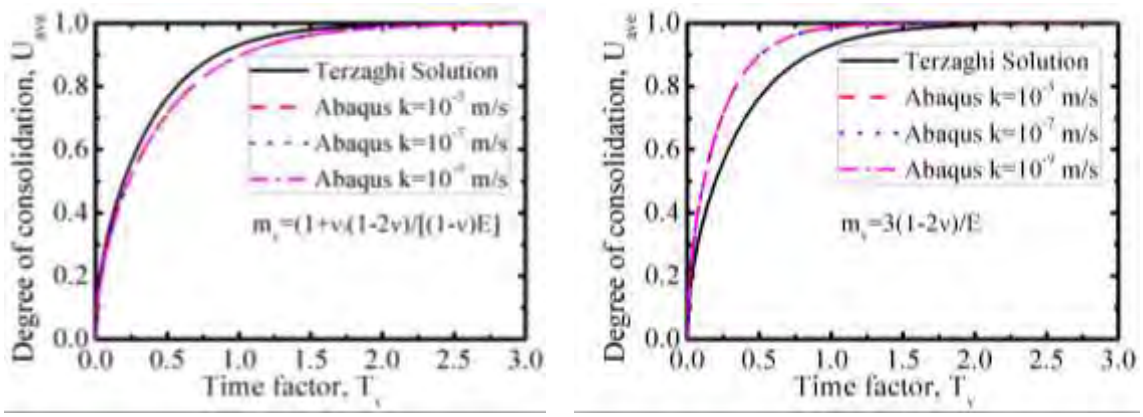

(a) (b)

Fig. 5.20 Comparison of one-dimensional consolidation between Abaqus and Terzaghi solution using Drucker-Prager model

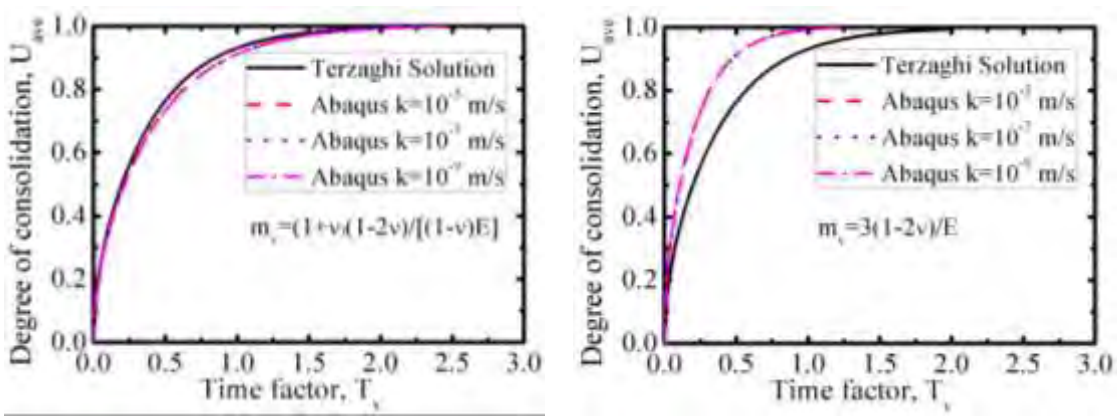

(a) (b)

Fig. 5.21 Comparison of one-dimensional consolidation between Abaqus and Terzaghi solution using cap model

Fig. 5.21(a) and (b) compare the numerical solutions using cap model at three different permeabilities ($k=10^{-5}$m/s, 10^{-7} m/s, 10^{-9} m/s) to Terzaghi's solution using two computed c_v. Similar to the numerical results obtained using Drucker-Prager model, well agreement is achieved between

numerical and analytical solution using cap model when using Eq.5.12 [Fig. 5.21(a)] to compute c_v while small discrepancy exists between numerical and analytical solution when using Eq.5.13 [Fig. 5.21(b)]. Hence, c_v obtained from Eq.5.12 is selected to computed the T_o in the numerical simulation.

It may conclude that numerical simulation using either Drucker-Prager or cap model compares well with the analytical one-dimensional consolidation problem when using Eq.5.12.

5.5. Simulation of CPT

In this section, the geometry, the discretization of cone and soil and the simulation procedures of CPT using Abaqus are introduced. In addition, the arbitrary Lagrangian Eulerian (ALE) mesh technique provided by Abaqus is presented. The ALE mesh technique is aiming at alleviating the element distortion around the cone tip as the cone advances into soil. The established numerical model is validated with a number of CPT chamber tests.

5.5.1. Simulation procedures

Geostatic step and penetration step comprise the CPT simulation. The purpose of geostatic step is to balance the initial stress of soil medium. This is a step to achieve stress equilibrium and almost zero displacement when the computation of this step is completed. The penetration step after geostatic step is to drive the cone penetrometer at a designated rate into the soil medium until the cone resistance reaches steady state. In this study, the steady state of cone resistance is achieved when the normalized penetration depth D/d_c is in the range of 1.5 to 3.2.

5.5.2. Model setup

A two-dimensional geometry is adopted in the numerical analysis since the cone and soil can

be modeled in the axisymmetric domain.

5.5.2.1. Geometry in CPT using Abaqus

The cone diameter (d_c) is 4.37 cm (in some cases 1.27 cm) with the projection area of 15 cm^2 (in some cases 1.27 cm^2) and the cone tip angle is 60° [Fig. 5.22(a)]. The idealized round cone tip demonstrated in Fig. 5.22(b) is to avoid sharp geometry connection and it is argued that this idealization can give sufficient accuracy obtaining the pore pressure response around the cone (Aubeny, 1992). Only half of the cone is simulated due to symmetry.

The cone penetrometer can be modeled using either deformable element (Susila and Hryciw, 2003; Wei, 2004; Ecemis, 2008) to which the properties of steel is assigned or analytical rigid element (Markauskas 2005; Yi, 2012). Two types of cone discretization, namely, the CAX4R element and analytical rigid body, are studied in Appendix C.2. Well agreement of q_{c1N} between these two discretization methods of cone was achieved. One distinct advantage of the analytical rigid body discretization compared to the non-rigid cone discretization lies in that Abaqus is not performing computation on this part and hence it is cost effective in terms of computation time. Thus the analytical rigid cone representation (rigid cone) is adopted in this study.

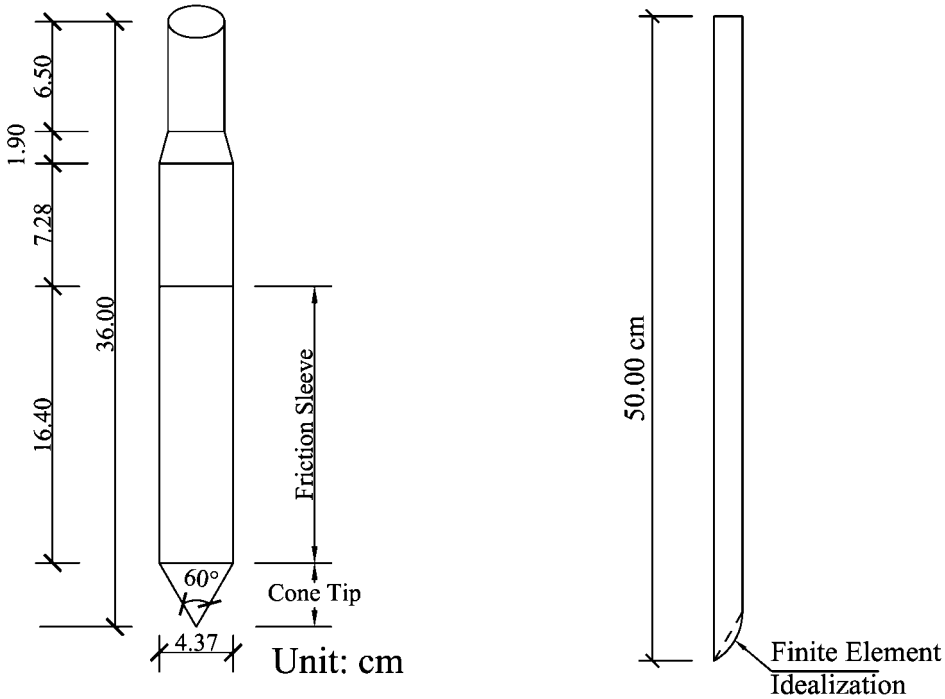

(a) geometry of cone (b) FEM model of cone

Fig. 5.22 Geometry and optimized FEM model of cone penetrometer

The geometry of the numerical model usded for 4.37 cm diameter cone is shown in Fig. 5.23. The analytical rigid cone is placed into a pre-drilled hole with depth of 11 d_c to avoid the shallow penetration and boundary effect. The dimension of uni-layered soil medium is 1.8 m (180 cm) in height and 0.8 m (80 cm) in length, aiming at creating a relatively 'infinite' medium. The geometry of soil for 1.27 cm diameter cone simulation is scaled down by a ratio of 4.37/1.27=3.44. The chamber size ratio D_L is 37, nearly the same as that of testing chamber introduced in Chapter 3. CAX4P element is employed to form the soil medium. It is found in the preliminary analysis that there is almost no deviation of q_{c1N} as well as $\Delta u/\sigma_{vo}'$ around cone tip when the soil medium is discretized by different elements [i.e. 4-node element CAX4P and higher order element CAX8RP (An 8-node axisymmetric quadrilateral, biquadratic displacement, bilinear pore pressure, reduced integration)] at small normalized penetration depth (D/d_c<1). However, the computational time to

carry out the analysis is reduced using 4-node elements (CAX4P) compared to higher order elements (CAX8RP) given that all other parameters are identical. It was also reported that the 4-node element is more numerically stable in the coupled-consolidation analysis involving large sliding movements at the cone/soil interface (Wei, 2004; Yi et al, 2012). In addition, the higher-order-node element is not supported by ALE technique in coupled solid-fluid analysis in Abaqus.

The vertical effective stress in the soil medium is assumed to be 100 kPa everywhere since the main interest is the development of stress and excess pore water pressure of soil around the cone tip area and the gradient of vertical stress of soil is of secondary consideration. The 100 kPa vertical stress is applied on soil surface and the initial lateral effective stress σ_{ho}' is applied as $K_0\sigma_{vo}'$, where K_0=1-sinϕ'.

Some investigators (Mahutka et al., 2006; Ecemis, 2008; Yi et al., 2012) reported the restraint (i.e., zero lateral displacement) of soil at symmetric axis was unrealistic since it prevented soil elements around the cone tip zone from 'flowing' as soil is under penetration. A tiny cavity (with radius of R_h, R_h=0 indicating zero cavity) around the symmetric axis (CL) shall be introduced to offset the limitation. In this regard, the effect of variation of geometry around the symmetric axis (R_h=0 and R_h=0.13 cm) on the cone resistance is examined in Appendix C.3. q_{c1N} using these two geometries well agrees with each other in the numerical analysis. Moreover, the $\Delta u/\sigma_{vo}'$ at and behind cone tip for these two geometries are compared well. The geometry with R_h=0 cm is adopted in the numerical model since it denotes the real in-situ boundary conditions.

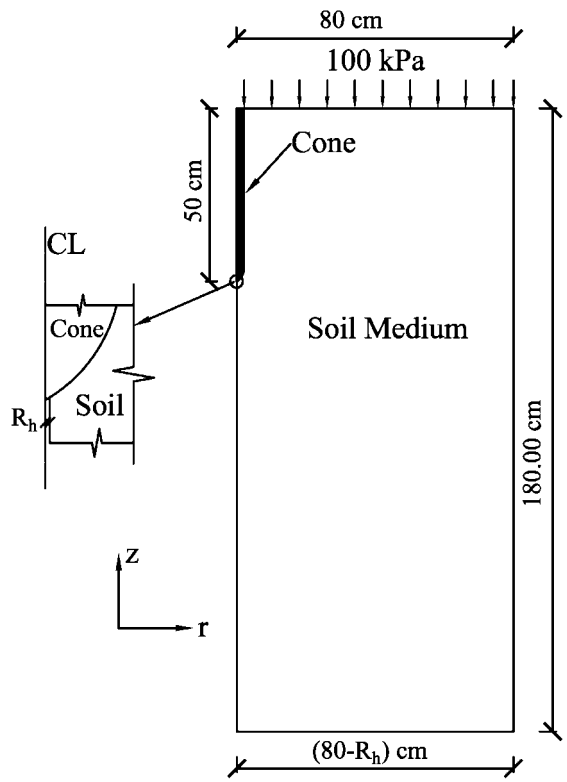

Fig. 5.23 Geometry of soil medium in Abaqus

5.5.2.2. Boundary conditions

Displacement/velocity field and fluid flow/pore pressure field are the two sets of boundary conditions applied to the numerical model. For the displacement/velocity field of soil medium, both displacement in r and z direction are constrained at bottom end and only displacement in r direction at right end is restrained in geostatic and penetration step (Fig. 5.24). For the left bottom side, the displacement in r direction is restrained for R_h=0 while it is freed for $R_h \neq 0$. However, a pressure of $K_0\sigma_{vo}'$ is imposed at left bottom side for $R_h \neq 0$. At the stance of cone, the displacement field in all directions of the cone is restrained in the geostatic step while a designated penetration rate [vertical (z direction) velocity] is assigned to the cone in the penetration step.

For the flow fluid field/pore pressure of soil medium, all of boundaries are considered as undrained except the top side boundary. And there is no pore pressure induced across the interface

between the soil medium and cone penetrometer.

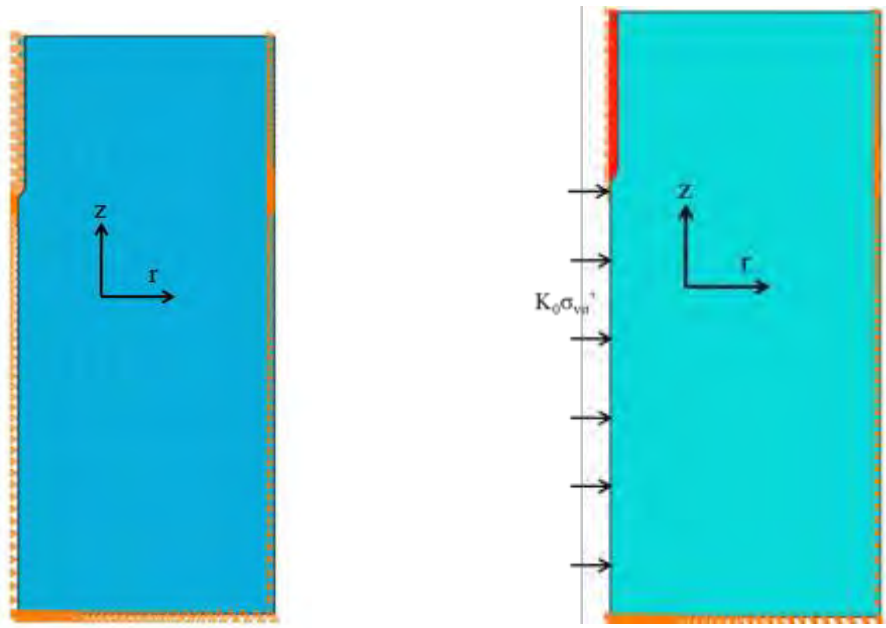

(a) R_h=0 (a) $R_h \neq 0$

Fig. 5.24 Boundary conditions applied in Abaqus with various configurations at symmetric axis

5.5.2.3. Friction between cone and soil

The cone-soil interaction is achieved through the friction between these two materials. The effect of friction coefficient has been studied by several researchers (Durgunoglu and Mitchell 1975a and b, Voyiadjis and Abu-Farsakh, 1997). The contact surface is represented in Fig. 5.25 with finite sliding formulation and surface to surface discretization method and the master-slave relationship is defined such that the cone is the master and the soil is the slave. The friction coefficient between cone and soil is studied ranged from zero to the tangent of the friction angle of soil [tan(ϕ')] in Appendix C.4.

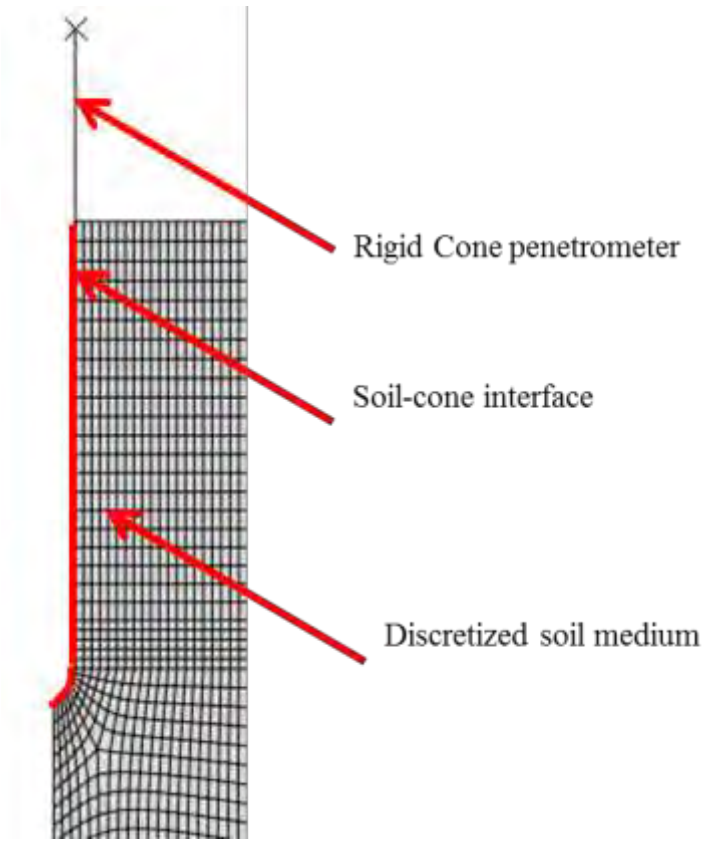

Fig. 5.25 Cone-soil interface

In this study, it is noticed that the friction coefficient being tan(0.5ϕ') would yield relatively reasonable numerical results in terms of q_{c1N} as well as $\Delta u/\sigma_{vo}'$ in both clean sands and silty sands when compared to experimental data. The selected friction of tan(0.5ϕ') between cone and soil medium interaction is also adopted by other researchers in the CPT simulation of sands (Susila and Hryciw, 2003; Tolooiyan and Gavin, 2011). Coduto (2001) suggested the ratio of interface friction angle over soil friction angle would be 0.5~0.7 for the interaction between smooth steel and soil to compute the side friction of pile foundation.

5.5.2.4. Arbitrary Lagrangian Eulerian (ALE) mesh

The Lagrangian formulation, in which the mesh nodes move with material nodes, is accurate for small deformation related problems. The Lagrangian formulation allows an easy tracking of

free surfaces and interfaces between different materials and history dependent materials. However, the instability of following the large distortions in the computational domain of this formulation makes the numerical results unfavorable when dealing with large deformation problems (Gadala and Wang, 1998). Eulerian formulation, in which the mesh is fixed and the material moves with respect to mesh, can be applied to handle the large distortion problems. Nonetheless, the accurate interface between materials, free boundaries and simulation of the material deformation history cannot be guaranteed (Gadala and Wang, 1998). As a result, the Arbitrary Lagrangian-Eulerian (ALE) formulation was developed to overcome the limitations of pure Lagrangian and pure Eulerian formulations.

Lagrangian Eulerian (ALE) mesh technique provided by Abaqus is used in the simulation in the attempt of reducing the element distortion around the cone tip area and meanwhile providing accurate and reliable numerical results in the cone penetration process. As a combination of conventional Lagrangian or Eulerian mesh technique, the ALE adaptive meshing makes a high-quality mesh throughout an analysis possible, even when large deformation occurs, by allowing the mesh to move independently of the material. Sweeping (mesh smoothing) and advection are the two critical tasks consisting the ALE mesh technique after Lagrangian phase. Sweeping is the process of creating a new mesh while advection is the process of remapping solution variables from the old mesh to the new mesh. The adaptive meshing in Abaqus/Standard uses an operator split method wherein each analysis increment consists of a Lagrangian phase followed by an Eulerian phase. The Lagrangian phase is the typical Abaqus/Standard solution increment where neither mesh sweeps nor advection occurs. Once the equilibrium equations have converged,

sweeping is applied to smooth the mesh. Following the adjustment of nodes through the mesh sweeping process, material point quantities are advected in an Eulerian phase to account for the revised meshing of the model in its current configuration.

The sweeping (smoothing) process is performed after the Lagrangian phase, in order to reduce the element distortion. During each mesh sweep, nodes in the domain are relocated based on the positions of neighboring nodes obtained during the previous mesh sweep. The displacements applied during sweeps are not associated with mechanical behavior. There are two sweeping algorithms in Abaqus available, which are original configuration projection and volume smoothing, respectively. Original configuration projection determines the weight function from a least squares minimization procedure that minimizes node displacement in a projection of the mesh back to the original configuration. This method of smoothing affects only deformations of the mesh and not the original mesh. Volume smoothing determines the weight function by computing a volume-weighted average of the element centers in the elements surrounding the node. In Fig. 5.26, the new position of node M is determined by a volume-weighted average of the positions of the element centers, C, of the four surrounding elements. The volume weighting will tend to push the node away from element center C1 and toward element center C3, thus reducing element distortion. These two sweeping algorithms can be applied together by using assigning weight factors to each algorithm with sum of the factors equal to 1.

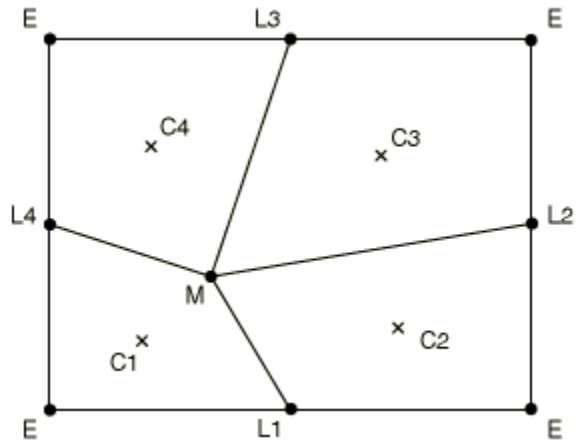

Fig. 5.26 Relocation of a node during a mesh sweep

Abaqus/Standard applies an explicit method, based on the Lax-Wendroff method, to integrate the advection equation. The update scheme is second-order accurate and provides some upwinding. Nodal quantities are advected by first converting them to the material point quantities. Advection of the material quantities will generally result in loss of equilibrium, for two main reasons. The first reason is the errors in the advection process itself. To minimize the errors in advection, Abaqus/Standard imposes restrictions on the magnitude of the advection velocity by requiring that the Courant number for every element in the adaptive domain be less than one. In cases where the Courant number is greater than one the programmer will be informed and Abaqus/Standard will generate multiple advection passes per increment. The Courant number is defines as

$$C = \Delta t \sum_{i=1}^{nn} \frac{v_{xi}}{\Delta x_i} \qquad \text{(Eq. 5.14)}$$

Where C is the Courant number, Δt is the time step, nn is the dimension, v_{xi} and are the advection velocity and length interval in x_i axis, respectively.

The second reason for the loss of equilibrium is changes in the representation of the underlying material quantities by the changed mesh. These sources of error in equilibrium are

significant only when the mesh is too coarse to provide a good solution and mesh smoothing is carried out with such small frequency that the mesh motion is larger than the average element size. In practical applications these errors are typically insignificant, the resulting loss of equilibrium is generally small, and the residuals generated by the loss of the equilibrium fall within the limits of the Abaqus/Standard convergence criterion. Any loss of equilibrium is not propagated since equilibrium will again be satisfied at the end of the Lagrangian phase of the next increment.

Fig. 5.27(a) and (b) compares the soil elements around cone tip when the normalized penetration depth D/d_c reaches 2.3 with/without ALE mesh technique, respectively. It can be clearly seen that no severe distortion of elements around the cone tip is observed using ALE mesh technique while the severe distortion occurs without applying ALE mesh technique is spotted. The steady state of q_c reaches when D/d_c is in range of 1.5 to 3.2 in this study.

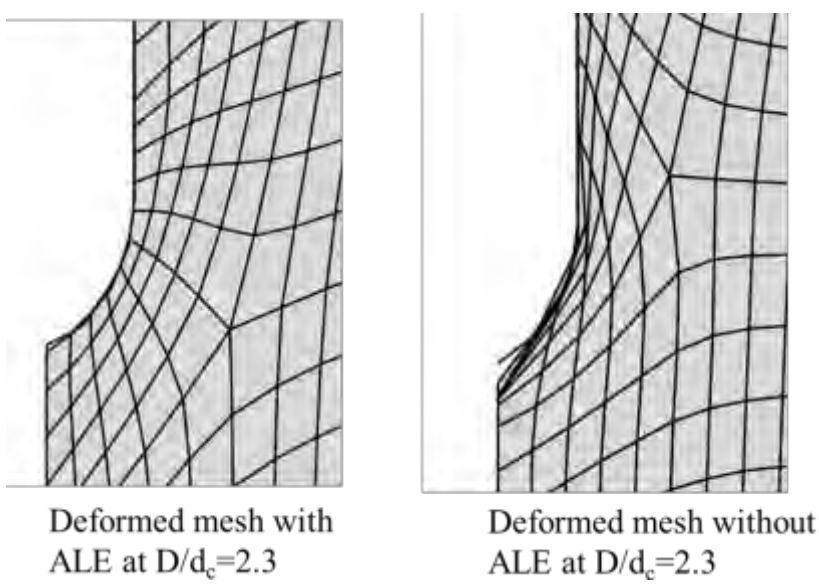

Fig. 5.27 Comparison of deformed mesh with/without ALE around cone tip

5.5.2.5. Summary

Based upon an optimization study (Appendix C) of the mesh density, the geometry around

symmetric axis, the cone discretization and the soil-cone interaction, it is determined that the analytical rigid body representing the cone penetrometer, the CAX4P elements discretizing the soil medium with R_h=0 and the coefficient of friction being tan(0.5ϕ') is implemented in the CPT simulation. The discretization of cone penetrometer and soil medium adopted for numerical analysis is shown in Fig. 5.28.

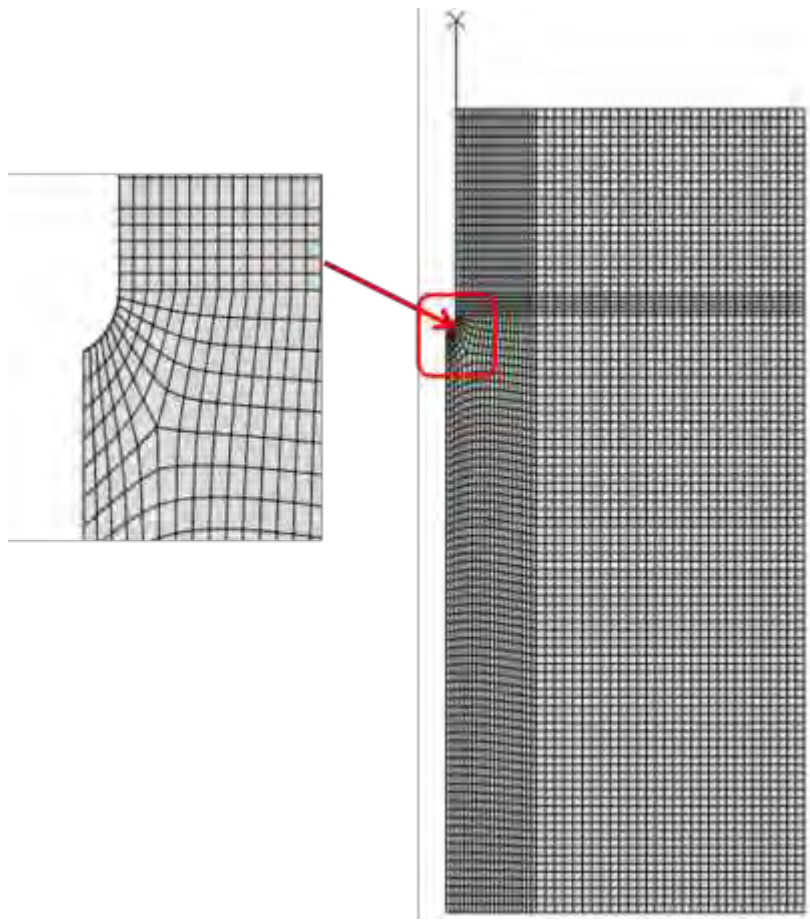

Fig. 5.28 Discretiaztion of cone and soil medium in Abaqus

5.5.3. Validation of CPT simulation

In this section, several CPT chamber tests performed in various soils are employed to investigate the effectiveness of the numerical model.

5.5.3.1. Validation with OS F55 sand-silt

The validation is done based on the CPT chamber tests using OS F55 sand-silt mixtures at different fines content from Chapter 4. The experimental cone resistance are normalized to q_{c1N} to compare with the q_{c1N} calculated from numerical simulations at σ_{vo}'=100 kPa. Soil properties are adopted from Table 5.3 except for permeability.

<u>Saturated OS F55 sand-silt mix</u>

Since the saturation status of the specimens of C_F=0% (CC-7) and 15% (CC-8) are unsured, the CPTs performed in specimens of C_F=25% are used herein. It is known that the compressibility of the soil has the effect on the cone resistance. CC-14 and 15 [$(D_{rc})_{eq}$=67/79%] and CC-20 and 21 $(D_{rc})_{eq}$=72/84%] are used to study the effect of compressibility on the cone resistance, the mechanical properties of M20 [$(D_{rc})_{eq}$=80%] and M15 [$(D_{rc})_{eq}$=67%] except Young's modulus are used in the examination.

The Young's modulus is converted from testing chamber test [CC-20(21)] at σ_{vo}'=50 kPa to σ_{vo}'=100 kPa as follows:

$m_{v\text{-recmpression}}$=6.9x10^{-5}/3.5=1.97x10^{-5} kPa^{-1} at σ_{vo}'=50 kPa, using Eq. 5.12, assuming Poisson's ratio of 0.2, the Young's modulus at σ_{vo}'=50 kPa can be estimated as

$$E_{\text{at } \sigma_{vo}'=50 \text{ kPa}} = \frac{(1+v)(1-2v)}{(1-v)m_{v-recompression}} = 45650 \text{ kPa}$$

Using Eq.5.9, the Young's modulus at σ_{vo}'=100 kPa can be estimated as

$$E_{\text{at } \sigma_{vo}'=100 \text{ kPa}} = \left(\frac{100}{50}\right)^{0.5} E_{\text{at } \sigma_{vo}'=50 \text{ kPa}} = \boxed{64560 \text{ kPa}}$$

Similarly the Young's modulus of CC-14(15) converted to σ_{vo}'=100 kPa is 46400 kPa.

The cone diameter in the simulation is 1.27 cm (the same as the experimental cone) and is placed in the pre-drilled hold with depth of 14.5 cm. The numerical penetration rates are 0.09 cm/s and 0.4 cm/s, respectively, to match the experiments. The dimension of the soil medium is 46 cm in diameter (D_L=36) and 52 cm in height. The numerical permeability is $1x10^{-7}$ m/s, nearly the same as CC-14(15) and CC-20(21). Table 5.6 compares the q_{c1N} obtained using different Young's moduli for various soils and the experiments. This table also compares the numerical q_{c1N} with experimental results. Fig. 5.29 compares the q_{c1N} between numerical results of various Young's moduli and experiments of different CPT chamber tests. For the same soil, larger Young's modulus (smaller m_v) yields larger q_{c1N} as expected. In general, q_{c1N} obtained using the Young's moduli in Table 5.3 can predict the experimental results. Hence, the Young's moduli used from Table 5.3 are used herein for OS F55 sand-silt mix in the CPT simulation.

Table 5.6 q_{c1N} between numerical results of various Young's moduli and experiments

Soil	E obtained	E_{100} kPa	q_{c1N} (v=0.09 cm/s)			q_{c1N} (v=0.4 cm/s)		
		(kPa)	Numerical	CC-14	CC-20	Numerical	CC-15	CC-21
M15 $(D_{rc})_{eq}$=67 %	CC-(14)15	46400	87	68	116	85	61	106
	CC-(20)21	64560	109			107		
	Table 5.3	55000	98			94		
M20 $(D_{rc})_{eq}$=80 %	CC-(14)15	46400	99			96		
	CC-(20)21	64560	125			119		
	Table 5.3	77500	141			135		

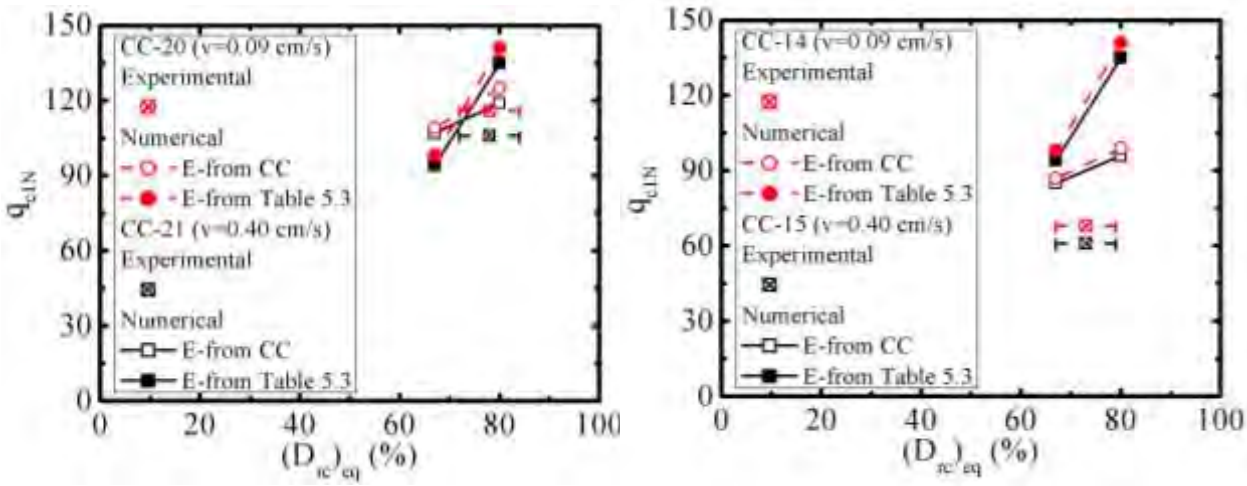

(a) CC-14 and 15 [$(D_{rc})_{eq}$=67/79%] (b) CC-20 and 21 [$(D_{rc})_{eq}$=72/84%]

Fig. 5.29 Comparison of q_{c1N} between numerical results of of various Young's moduli and experiments

Fig. 5.30 compares the q_{c1N} versus the D/d_c and the normalized excess pore water pressure ($\Delta u/\sigma_{vo}'$) at cone tip versus the z_c/d_c of OS-25 at $(D_{rc})_{eq}$=67/79% under v=0.09 cm/s between CPT chamber test (CC-14) and numerical simulation. Permeability used in the simulation is 10^{-7} m/s. It is found that reasonable agreement of q_{c1N} between experimental and numerical results is observed. However, the development of excess pore water pressure around cone tip is overestimated by the numerical model.

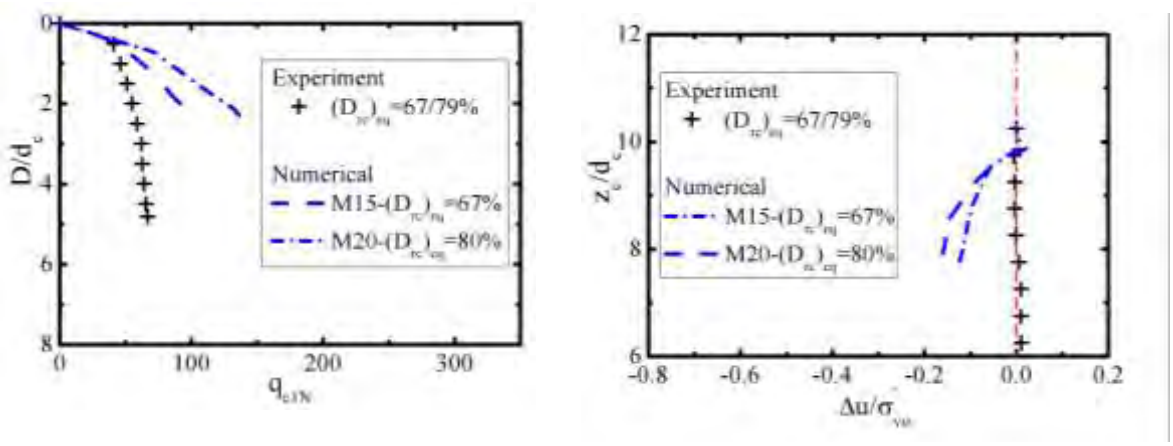

(a) q_{c1N} (b) $\Delta u/\sigma_{vo}'$ at cone tip

Fig. 5.30 Comparison of chamber test and numerical result of CC-14

Fig. 5.31 compares q_{c1N} versus D/d_c and $\Delta u/\sigma_{vo}'$ at cone tip versus z_c/d_c of OS-25 at

$(D_{rc})_{eq}$=67/79% under v=0.4 cm/s between CPT chamber test (CC-15) and numerical simulation. Reasonable agreement of either q_{c1N} or $\Delta u/\sigma_{vo}'$ between experimental and numerical results is observed.

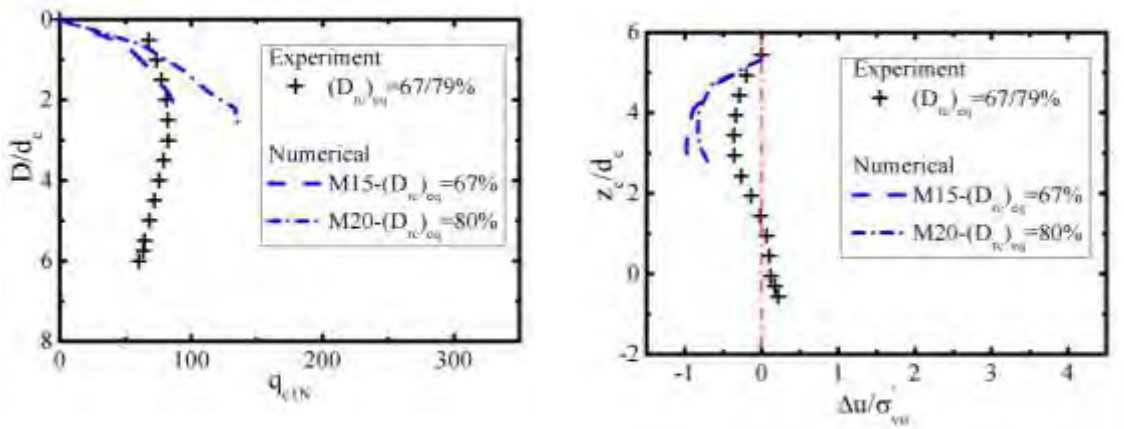

(a) q_{c1N} (b) $\Delta u/\sigma_{vo}'$ at cone tip

Fig. 5.31 Comparison of chamber test and numerical result of CC-15

Fig. 5.32 compares q_{c1N} versus D/d_c and $\Delta u/\sigma_{vo}'$ at cone tip versus z_c/d_c of OS-25 at $(D_{rc})_{eq}$=72/84% under v=0.09 cm/s between CPT chamber test (CC-20) and numerical simulation. Permeability used in the simulation is 10^{-7}m/s. Although there exists discrepancy of $\Delta u/\sigma_{vo}'$ between experimental and numerical results, reasonable agreement of steady state value for q_{c1N} between experimental and numerical result is observed. Fig. 5.33 compares q_{c1N} versus D/d_c and $\Delta u/\sigma_{vo}'$ at cone tip versus z_c/d_c of OS-25 at $(D_{rc})_{eq}$=72/84% under v=0.4 cm/s between CPT chamber test (CC-21) and numerical simulation. Reasonable agreement of either q_{c1N} or $\Delta u/\sigma_{vo}'$ between experimental and numerical results is observed.

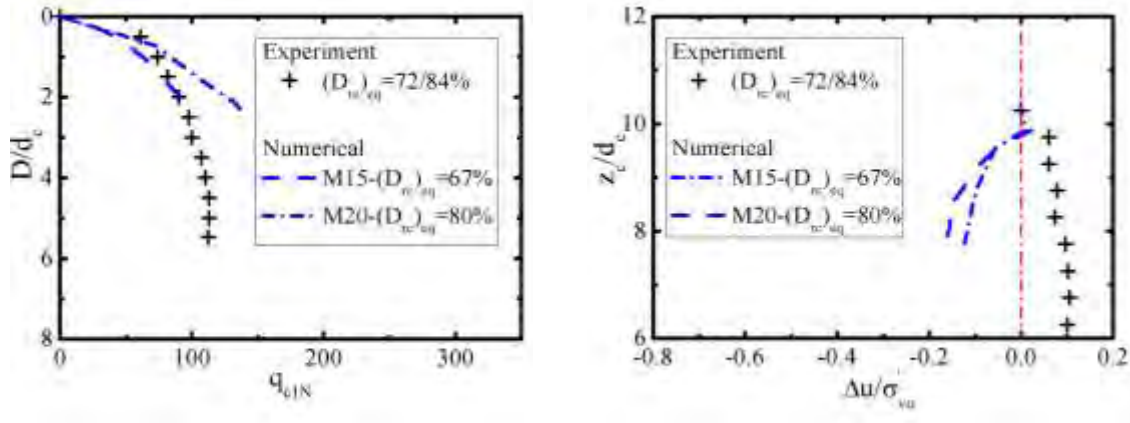

(a) q_{c1N} (b) $\Delta u/\sigma_{vo}'$ at cone tip

Fig. 5.32 Comparison of chamber test and numerical result of CC-20

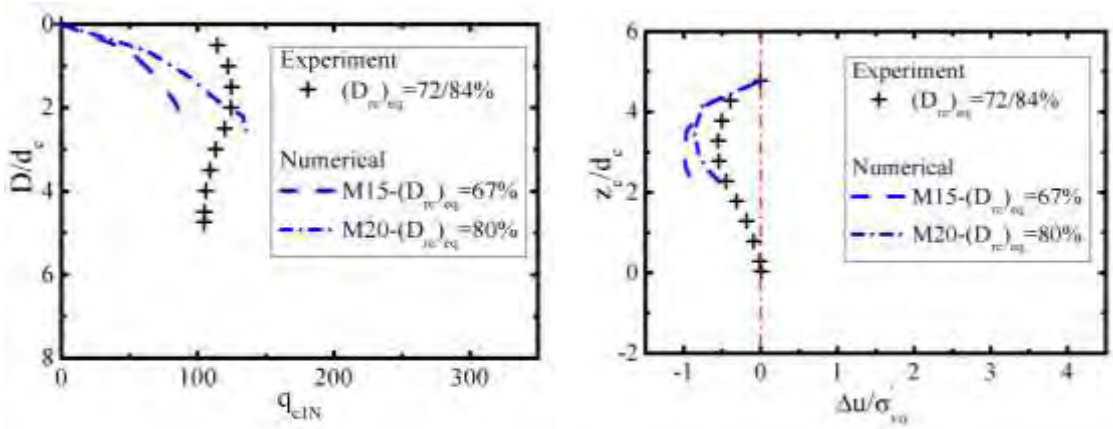

(a) q_{c1N} (b) $\Delta u/\sigma_{vo}'$ at cone tip

Fig. 5.33 Comparison of chamber test and numerical result of CC-21

<u>Dry clean sand</u>

Two cone diameters are used in the simulation, which are 1.27 cm (used in chamber tests) and 4.37 cm, respectively and the penetration rate is 0.40 cm/s. For dry clean sands, the effect of consolidation during cone penetration process is absent. As discussed in 4.3.1, there is no apparent difference of cone resistance between dry and saturated sands at the condition of d_c=1.27 cm/4.37 cm and v=0.4 cm/s since the soil is in drained condition during cone penetration. A large permeability is assigned to the soil to ensure drained condition during cone penetration (i.e. negligibly small excess pore water pressure generation).

Table 5.7 summarizes the experimental and numerical q_{c1N} for each nominal $(D_{rc})_{eq}$ as well as the soils used in the simulation. The experimental q_{c1N} of each nominal $(D_{rc})_{eq}$ is the average value of performed tests.

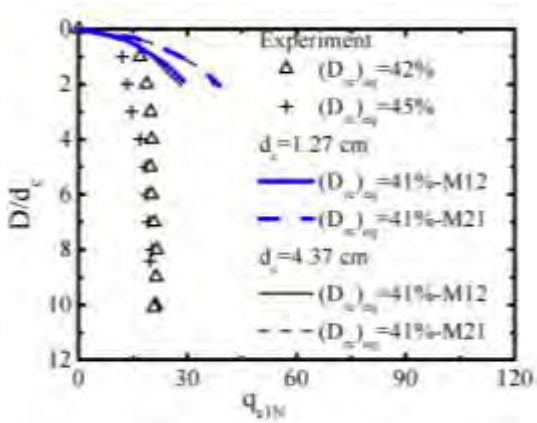

(a) Dr≈40%

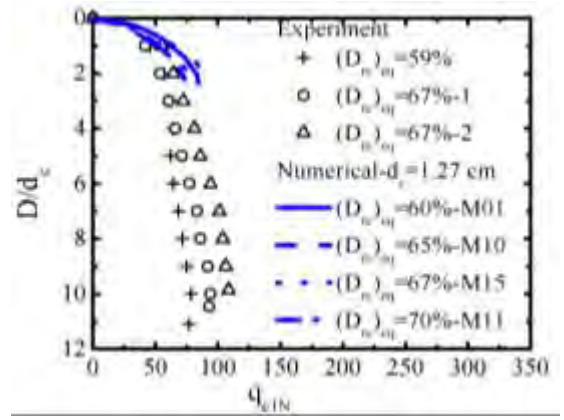

(b) Dr≈65%-1.27 cm cone

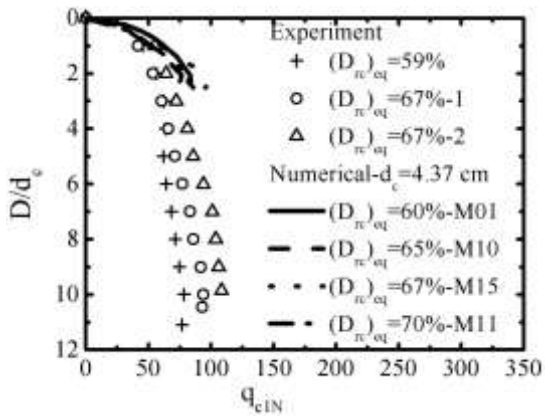

(c) Dr≈65%-4.37 cm cone

Fig. 5.34 plots experimental and numerical q_{c1N} versus D/d_c for $(D_{rc})_{eq}$≈40% and 65% using two different cone penetrometers. Reasonable agreement of measured and numerical q_{c1N} using either 1.27 cm cone or 4.37 cm is achieved at both $(D_{rc})_{eq}$≈40% and 65% for dry clean sands as can be seen in Fig. 5.35 and Table 5.7. This also indicates that the effect of cone diameter is negligible when the drainage condition is drained.

Table 5.7 Comparison of experimental and numerical results of q_{c1N} of dry clean sand

Nominal $(D_{rc})_{eq}$ (%)	$(D_{rc})_{eq}$ (%) in simulation	q_{c1N}			Soil used in the simulation
		Experimental	Predicted (d_c=1.27 cm)	Predicted (d_c=4.37 cm)	
40	41	22	39	37	M21

	41	22	29	28	M12
65	60	94	81	83	M01
	65	94	73	75	M10
	67	94	97	96	M15
	70	94	84	86	M11

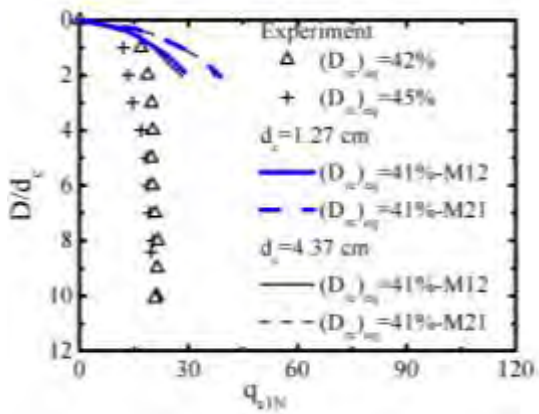

(a) D_r≈40%

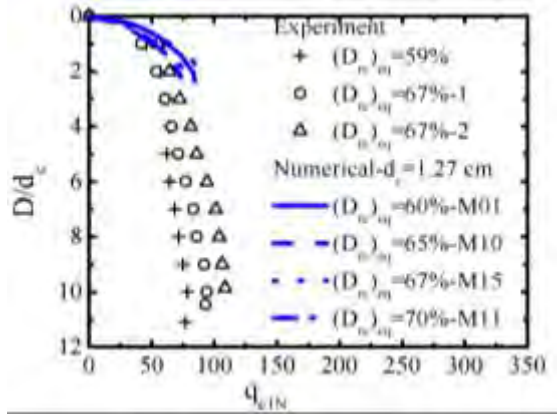

(b) D_r≈65%-1.27 cm cone

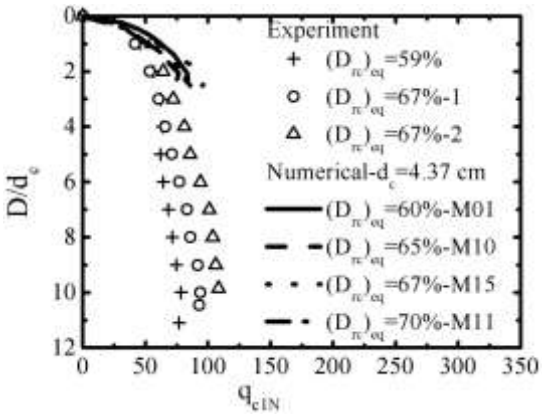

(c) D_r≈65%-4.37 cm cone

Fig. 5.34 Comparison of chamber test and numerical results using dry OS F55 sand

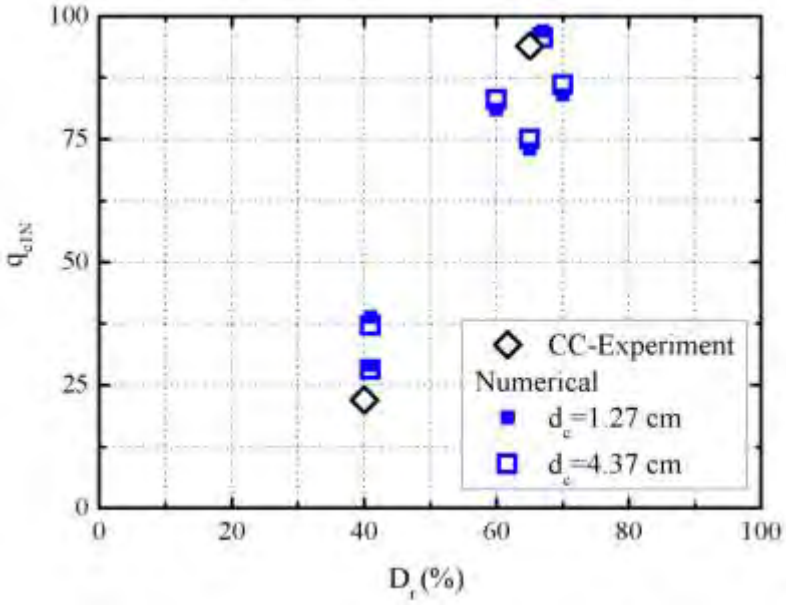

Fig. 5.35 Comparison of q_{c1N} between experiment and Abaqus using dry OS F55 sand

5.5.3.2. Validation with Monterey No 0/30 sand

The related elastic and plastic parameters of Monterey No. 0/30 sand used in the simulation are tabulated in Table 5.4. Boundary conditions of the penetration tests used in the experimental and numerical results are summarized in Table 5.8. The coefficient of friction between soil and cone is adopted as tan(0.5ϕ'), which is the same as section 5.5.3.1. The diameter of cone and penetration rate used in the experiments were 1.27 cm and 2 cm/s, respectively while the diameter of cone and penetration rate used in the simulation are 4.37 cm and 2 cm/s, respectively.

Table 5.8 Boundary conditions and results using Monterey No 0/30 sand

D_r [$(D_{rc})_{eq}$](%)	BC	σ_{vo}' (kPa)	K_0	q_c (MPa)	
				Experimental	Numerical
49	BC1	100	0.44	5.9	6.6
56	BC1	200	0.35	7.4	7.8
55	BC1	300	0.62	11.3	10.4
72	BC1	100	0.42	8.2	10.2
69	BC1	200	0.48	17.2	13.5
71	BC1	300	0.40	19.9	16.5
84	BC1	100	0.35	12.2	12.2
86	BC1	100	0.37	10.0	12.2
90	BC1	100	0.54	12.0	12.2

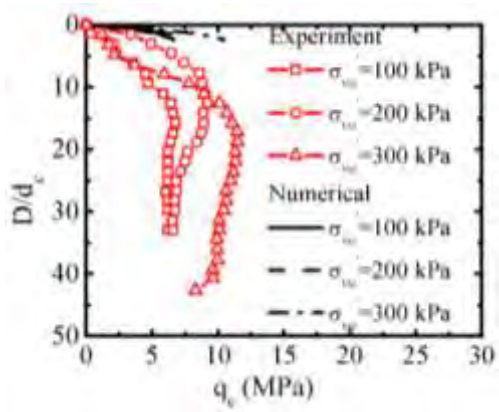

(a) D_r=45%

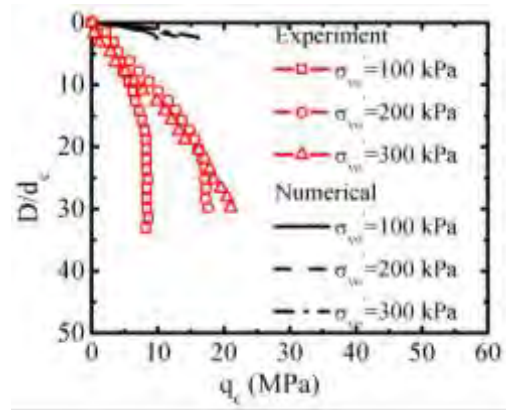

(b) D_r=65%

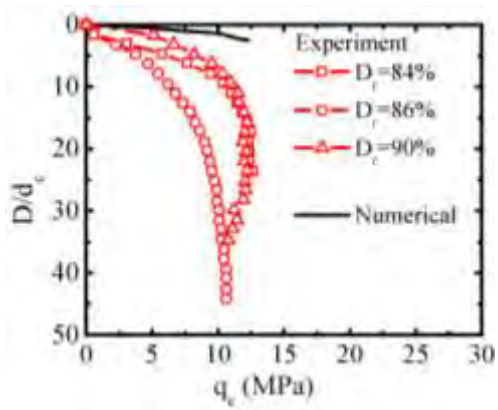

(c) D_r=85%

Fig. 5.36 Comparison of q_c versus D/d_c between calibration chamber and Abaqus using dry Monterey No. 0/30 sand

Fig. 5.36 compares the experimental and numerical q_c versus D/d_c of dry Monterey No. 0/30 sand at different D_r under various σ_{vo}'. Fig. 5.37 compares q_{c1N} obtained from experimental results and numerical analysis at different D_r. Well agreement of q_c between experimental and numerical results at all three D_r is seen. Although the CPTs performed in the calibration chamber were mainly dry sand samples, the simulated CPTs of Monterey No. 0/30 sand at different D_r under σ_{vo}'=100 kPa can still be used for the parametric study of cone resistance in silty sands by assigning different permeabilities in the numerical model.

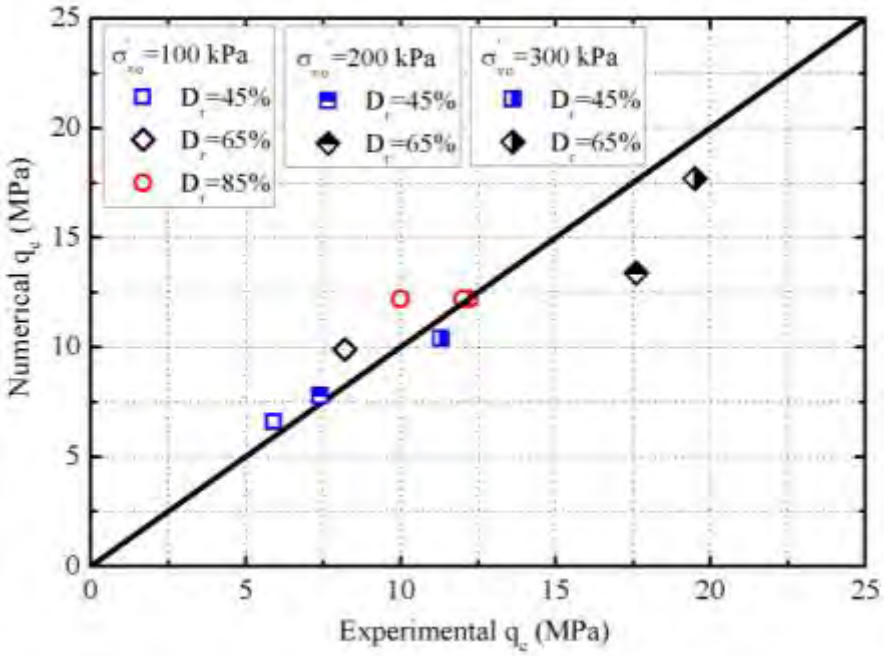

Fig. 5.37 Comparison of q_c between experimental and numerical results of dry Monterey No. 0/30 sand

5.5.3.3. Comparison with empirical equations

Soils under an initial mean effective stress of 100 kPa are used the numerical analysis. Elastic and plastic properties are adopted from Table 5.3, Table 5.4 and Table 5.5, respectively except permeability. It is found in section 6.6 that the limit value of T_o for drained is 0.04 at d_c=4.37 cm and v=2cm/s. It is also numerically shown in section 6.3 that at a given $(D_{rc})_{eq}$, the effect of permeability agrees perfectly well with the effect of penetration on the cone resistance as well as the excess pore water pressure response around cone tip when normalized into the same normalized penetration rate T_o. Hence, the permeability or penetration velocity is adjusted such at T_o<0.04 for drained condition through Eq. 2.14 in the numerical simulation. The q_{c1N} of different $(D_{rc})_{eq}$ corresponding to drained condition are compared to empirical equations proposed for sands such as Eq.5.1 and Eq.5.2.

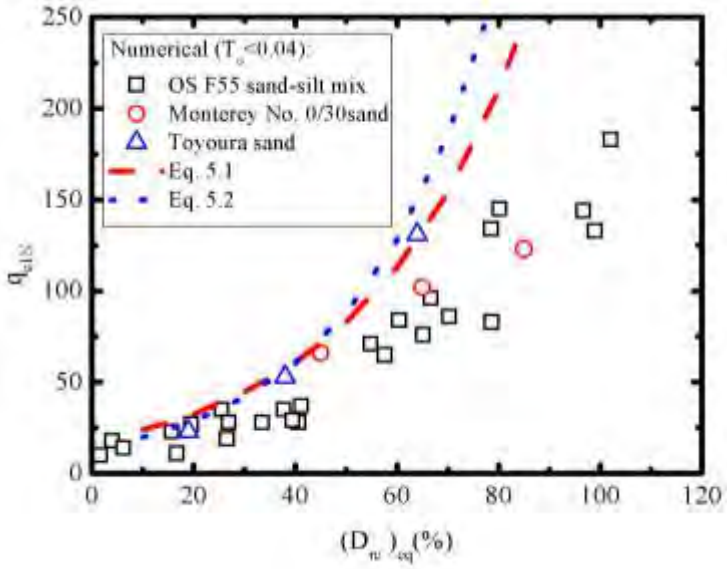

(a) Drained condition

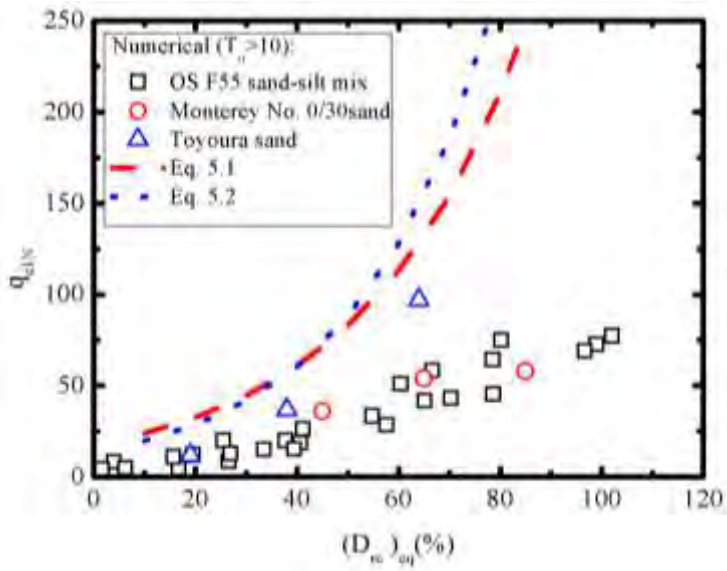

(b) Undrained condition

Fig. 5.38 Comparison of q_{c1N} obtained using abaqus and empirical equations at drained and undrained conditions

Fig. 5.38(a) presents the comparison of q_{c1N} between numerical solution at drained condition (T_o<0.04) for different soils simulated in section 5.3 and empirical equations of sand. Well agreement between numerical q_{c1N} at drained condition and empirical q_{c1N} for sands can be found in the figure.

In addition, Fig. 5.38(b) plots the numerical q_{c1N} at undrained condition (T_o>10, refer to

section 6.6). It can be seen from the figure that for a centain soil at a given $(D_{rc})_{eq}$, q_{c1N} is larger at drained condition than undrained condition.

5.5.4. Conclusion of this section

In this section, the CPT simulation using Abaqus is validated through a number of CPTs chamber tests. Although, when compared to the experiments, the numerical model overestimates the development of excess pore water pressure in saturated silty sands at some simulations, it in general captures the cone resistance profile in either dry or saturated specimens. Moreover, the prediction of q_{c1N} at drained condition using different soils is compared reasonably well with empirical equations proposed for sands.

5.6. Summary

The simulation results of monotonic undrained triaxial test using cap model in general agree well with experimental data for different types of soils although some discrepancy exists. The difference between numerical results using cap model and experiments is mainly due to that the constant instead of strain-dependent elastic modulus is used and the cap model cannot capture soils experiencing phase transformation. Because the coefficient of consolidation, as detailed in Chapter 2, plays an important role in cone resistance, the simulation of one-dimensional consolidation problem using a cap model is verified with the analytical solution.

It is determined that the analytical rigid body representing the cone penetrometer, the CAX4P elements discretizing the soil medium with R_h=0 and the coefficient of friction being tan(0.5ϕ') is implemented in the CPT simulation. Although there exists limitation on capturing the excess pore

water pressure response at cone tip, the CPT simulation using cap model provides effectiveness of the numerical model on predicting the cone resistance. In addition, the numerical model used in this study can give relatively accurate prediction of q_{c1N} at drained condition when compared to empirical equations proposed for sands.

Chapter 6. Parametric study of cone resistance: Sands and silty sands

6.1. Introduction

Based on the numerical model established in Chapter 5, this chapter performes a thorough paratmetric study using OS F55 sand-silt mix of different $(D_{rc})_{eq}$ to examine the factors affecting drainage condition of soil during cone penetration in silty sands.

Firstly, the effect of permeability on the cone resistance is thoroughly examined in different soils using standard cone (d_c=4.37 cm) at the constant penetration rate of 2 cm/s until the steady state is achieved.

Secondly, the effect of penetration rate is studied in selected soils using standard cone with diameter of 4.37 cm at $k=10^{-5}$ m/s.

Thirdly, the effect of cone diameter is investigated using two different diameter cones (d_c=1.27 and 4.37 cm) at v=2 cm/s with different permeabilities in selected soils.

Finally, the effect of these above mentioned parameters on cone resistance is quantified through the T_o. The limit value of T_o for drained and undrained conditions during cone penetration is found and compared to other investigators.

6.2. Effect of permeability on q_{c1N} and $\Delta u/\sigma_{vo}'$

In this section, several simulations are performed for soils at different $(D_{rc})_{eq}$, with a range of values for k to investigate the presence of fines on the cone resistance in silty sands. A standard cone with 4.37 cm in diameter is penetrated into the soil at a constant rate of 2 cm/s (ASTM D3441) until a steady state is reached. The effective overburden stress σ_{vo}' is 100 kPa.

6.2.1. $(D_{rc})_{eq}$=10%

Fig. 6.1 shows the meshes of the soil medium around the cone zone before and after penetration. It can be found that no heavy distortion of the elements around cone tip area is observed as the penetration depth reaches steady state.

Fig. 6.2 and Fig. 6.3 present the results of q_{c1N} and $\Delta u/\sigma_{vo}'$ at and behind the cone tip with respect to D/d_c of soil at $(D_{rc})_{eq}$=10% at different permeabilities ($k=10^{-3}$ to $k=10^{-9}$ m/s) as the steady state of penetration is achieved. It shall be noticed that, the node behind cone tip for monitoring the excess pore pressure keeps changing as the penetration is in progress. With this regard, it is necessary to locate the node behind the cone tip at each given time frame, extract and compute the corresponding $\Delta u/\sigma_{vo}'$.

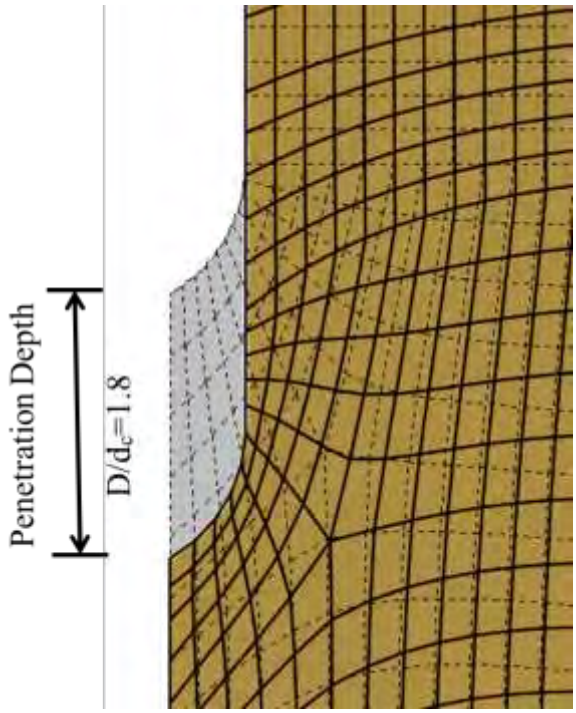

Fig. 6.1 Meshes of soil medium around the cone tip before and after penetration

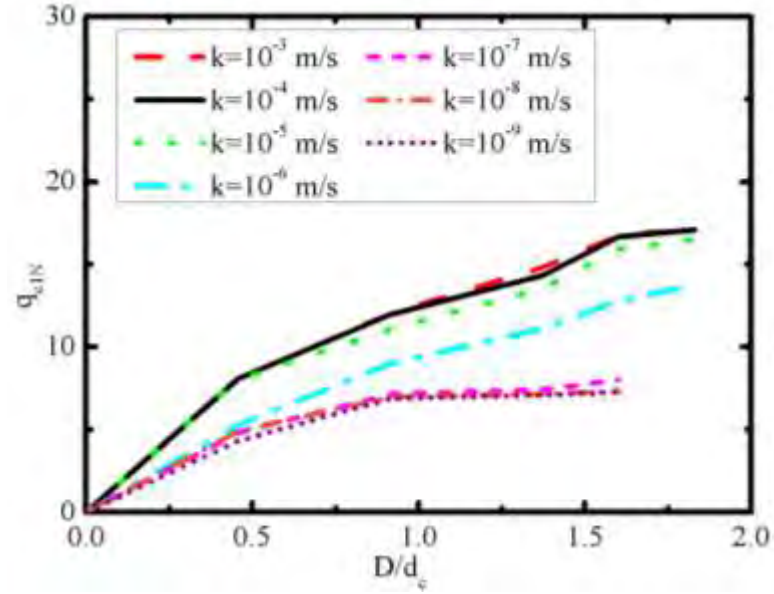

Fig. 6.2 q_{c1N} with respect to D/d_c at $(D_{rc})_{eq}$=10% with different permeabilities

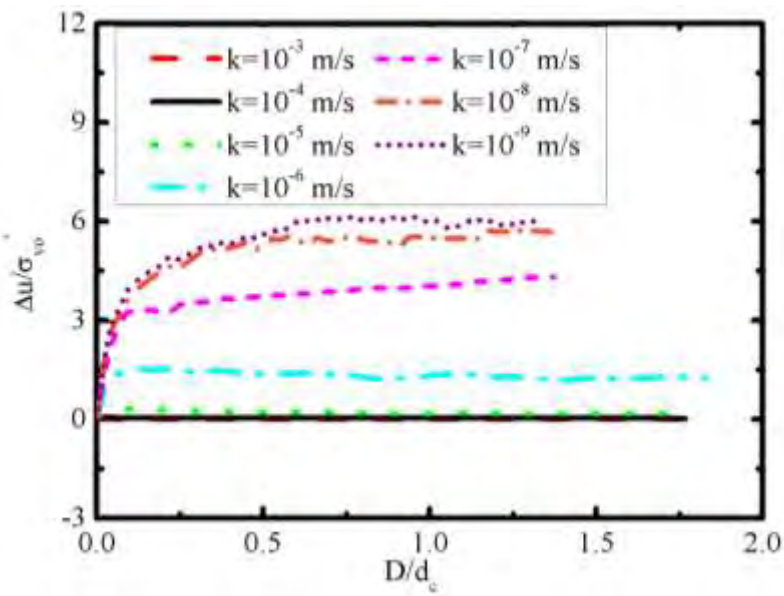

(a) At cone tip

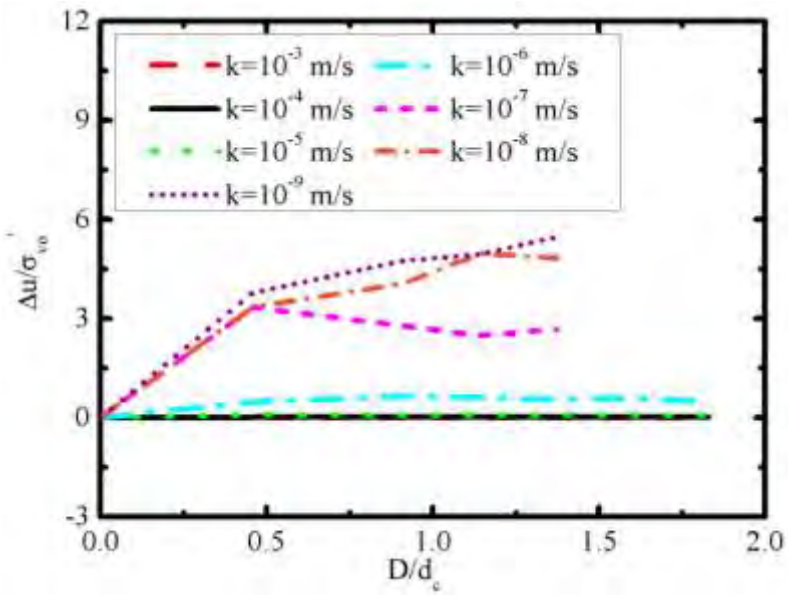

(b) Behind cone tip

Fig. 6.3 $\Delta u/\sigma_{vo}'$ with respect to D/d_c at $(D_{rc})_{eq}$=10% with different permeabilities

Fig. 6.4 presents the q_{c1N} and ($\Delta u/\sigma_{vo}'$) at/behind the cone tip with respect to k/T_o of $(D_{rc})_{eq}$=10%. The largest computed q_{c1N} (q_{c1N}=17) is associated with highest permeability $k=10^{-3}$, 10^{-4} and 10^{-5} m/s, while the lowest computed q_{c1N} is obtained at permeability $k=10^{-7}$, 10^{-8} and 10^{-9}m/s (q_{c1N}=7). q_{c1N} gradually decreases from 17 to 7 as k decreases from 10^{-5} to 10^{-7} m/s (q_{c1N}=11 at $k=10^{-6}$ m/s). The figure also shows that the highest $\Delta u/\sigma_{vo}'$ at cone tip is related to the lowest permeability of 10^{-9} m/s, and decreases as permeability increases.

As a result, the drainage condition (upper limit for q_{c1N}) occurs when permeability is larger than 10^{-5} m/s (T_o<0.03) since q_{c1N} does not deviate much and negligibly small $\Delta u/\sigma_{vo}'$ at and behind cone tip are found from $k=10^{-5}$ m/s to 10^{-4} m/s. There is no further increase on the q_{c1N} as permeability increases. On the other hand, undrained condition (lower limit for q_{c1N}) takes place as permeability is smaller than 10^{-7} m/s (T_o>3), since almost unchanged q_{c1N} is observed. Further decrease in k doesn't affect much of the q_{c1N}. Moreover, considerable positive $\Delta u/\sigma_{vo}'$ at cone tip

is spotted as permeability is smaller than 10^{-7} m/s (T_o>3). $\Delta u/\sigma_{vo}'$ at cone tip is 4.4, 5.7 and 6.3 for k=10^{-7} m/s (T_o=3.4), 10^{-8} m/s (T_o=34) and 10^{-9} m/s (T_o=334), respectively. This phenomenon is attributive to the rapid increase of normal stress when the soil is subject to penetration. The same trend of $\Delta u/\sigma_{vo}'$ behind the cone tip is also observed but with smaller amplitude when compared to $\Delta u/\sigma_{vo}'$ at the cone tip. For permeability ranged in between 10^{-5} and 10^{-7} m/s (0.03<T_o<3), partially drained condition dominates. q_{c1N} decreases from 17 to 8 (about 50% decrease in value) and $\Delta u/\sigma_{vo}'$ at cone tip increases from 0.2 to 4.4 as permeability decreases from 10^{-5} m/s to 10^{-7} m/s (0.03<T_o<3).

The EPWP contour for k ranged from 10^{-5} m/s to 10^{-8} m/s is compared in Fig. 6.5. The contours clearly imply the variation of EPWP when drained condition (k>10^{-5} m/s) transits to undrained condition (k<10^{-7} m/s).

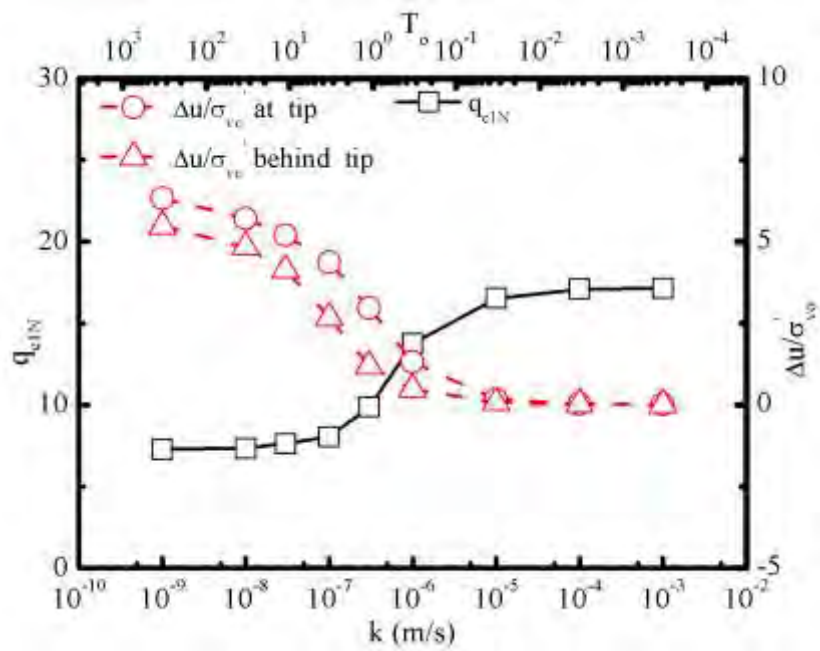

Fig. 6.4 q_{c1N} and $\Delta u/\sigma_{vo}'$ at $(D_{rc})_{eq}$=10% with different permeabilities

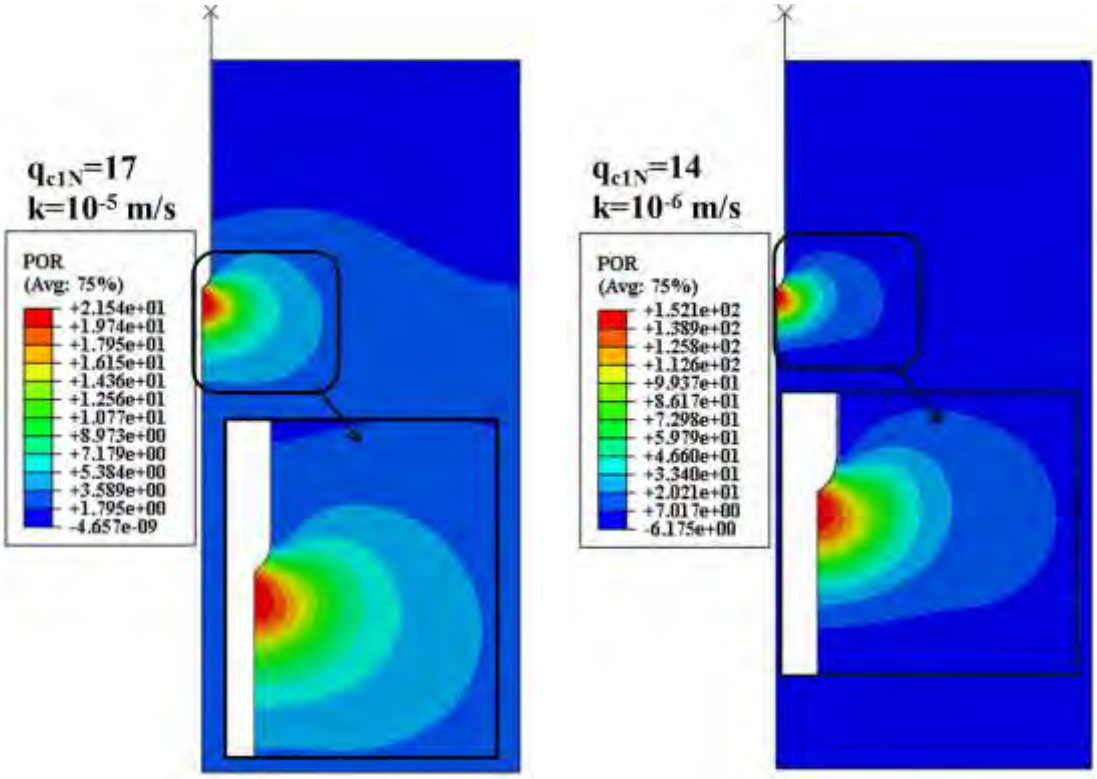

(a) T_o=0.03 (k=10^{-5} m/s)

(b) T_o=0.34 (k=10^{-6} m/s)

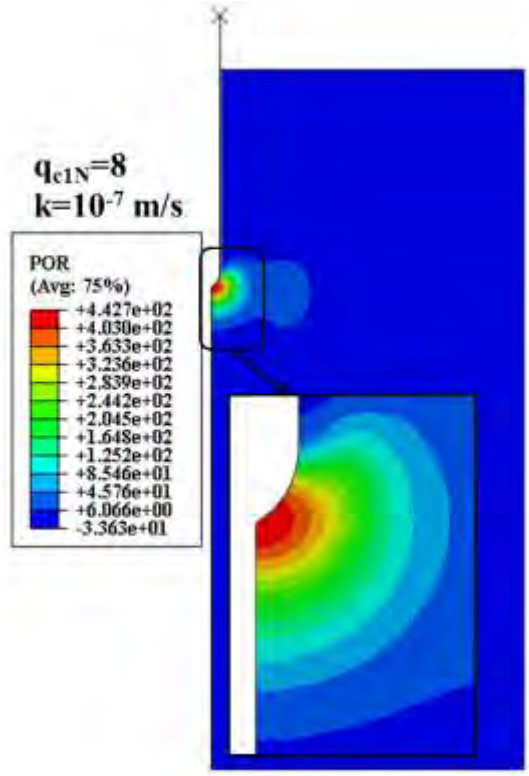

(c) T_o=3.4 (k=10^{-7} m/s)

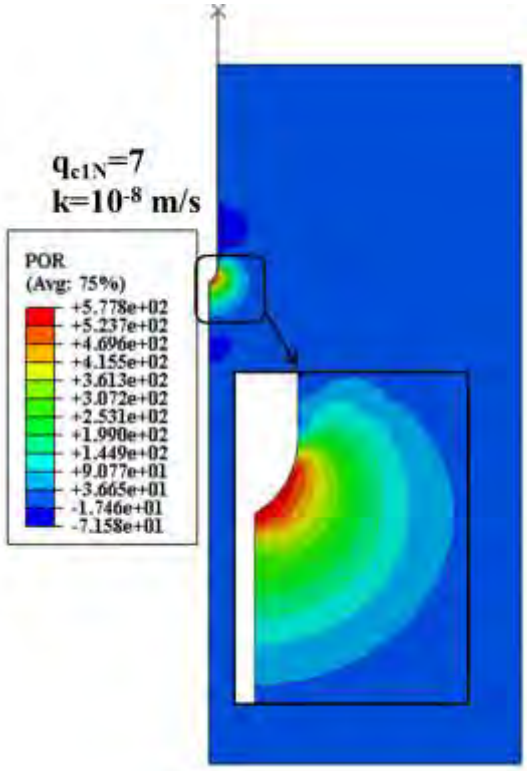

(d) T_o=34 (k=10^{-8} m/s)

Fig. 6.5 EPWP distribution at $(D_{rc})_{eq}$=10% with different permeabilities (Unit:kPa)

6.2.2. $(D_{rc})_{eq}$=41%

Fig. 6.6 presents the results of q_{c1N} with respect to D/d_c of soil at $(D_{rc})_{eq}$=41% at different permeabilities ($k=10^{-3}$ to $k=10^{-9}$ m/s). Fig. 6.7 compares the q_{c1N} and $\Delta u/\sigma_{vo}'$ at different k/T_o of soil at $(D_{rc})_{eq}$=41%. The largest computed q_{c1N} (q_{c1N}=28) is associated with highest permeability $k=10^{-3}$, 10^{-4}, 10^{-5} m/s, while the lowest computed q_{c1N} (q_{c1N}=18) is obtained at permeability $k=3x10^{-8}$, 10^{-8} and 10^{-9} m/s. This implies that the drained condition occurs when the permeability is larger than $1x10^{-5}$ m/s (T_o<0.03) and undrained condition takes places when k is less than $3x10^{-8}$ m/s (T_o>9). Partially drained condition prevails for k in the range between 10^{-5} m/s and $3x10^{-8}$ m/s (0.03<T_o<9).

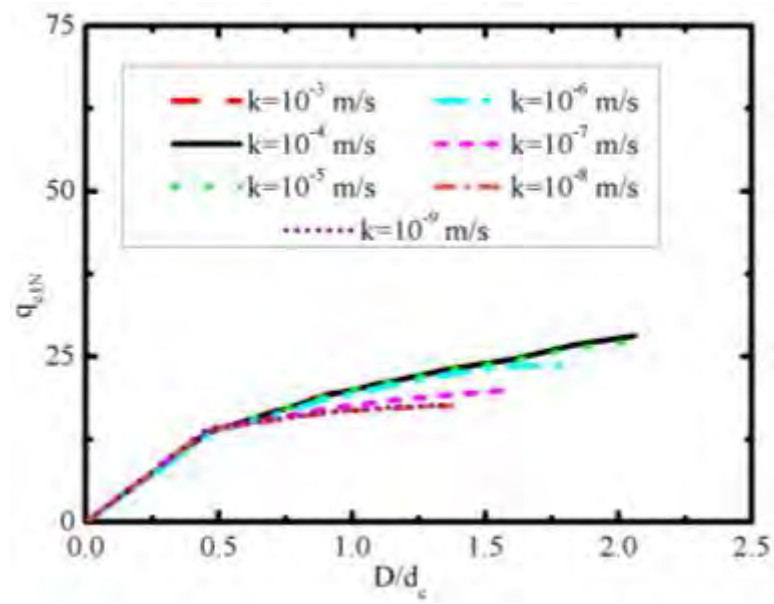

Fig. 6.6 q_{c1N} with respect to D/d_c at $(D_{rc})_{eq}$=41% with different permeabilities

High $\Delta u/\sigma_{vo}'$ ($\Delta u/\sigma_{vo}'$=13 at $k=10^{-8}$ m/s) at cone tip confirms the finding in the relationship between q_{c1N} and k. For $k<10^{-5}$ m/s (T_o<0.03), $\Delta u/\sigma_{vo}'$ at either cone tip or behind cone tip is negligibly small. However, considerable positive $\Delta u/\sigma_{vo}'$ at cone tip is spotted as permeability is smaller than $3x10^{-8}$ m/s (T_o>9). $\Delta u/\sigma_{vo}'$ are 8, 10, 13 and 13 for $k=10^{-7}$ m/s (T_o=3), $3x10^{-8}$ m/s

(T_o=9), k=10^{-8} m/s (T_o=31) and 10^{-9} m/s (T_o=308) at cone tip, respectively.

This figure also compares the q_{c1N} obtained from numerical model to that obtained from CPT chamber tests near this $(D_{rc})_{eq}$ from Chapter 4 (denoted as '-CC').

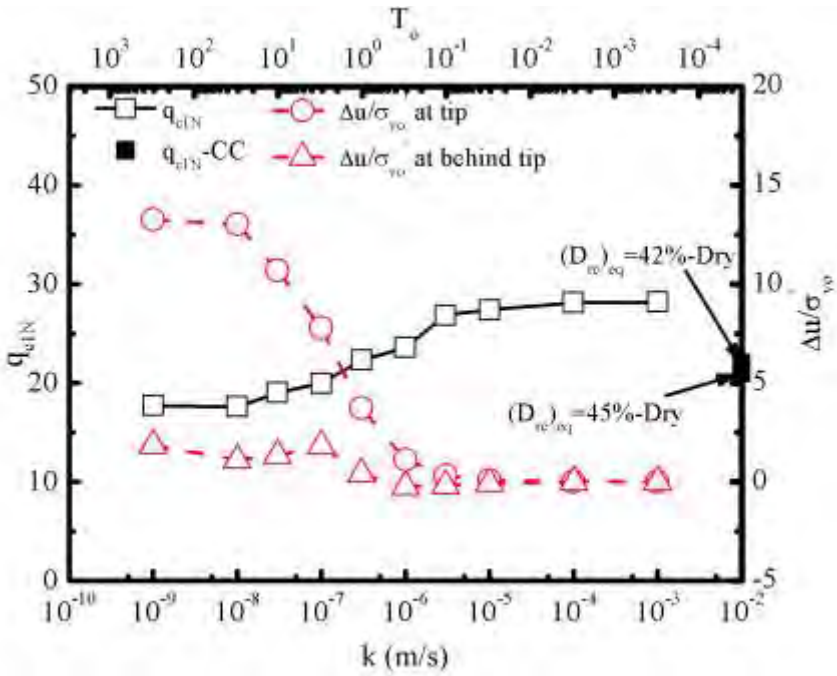

Fig. 6.7 q_{c1N} and $\Delta u/\sigma_{vo}'$ at $(D_{rc})_{eq}$=41% with different permeabilities

The EPWP contour for permeabilities ranged from 10^{-5} m/s to 10^{-8} m/s is compared in Fig. 6.8. The contours clearly imply the variation of EPWP when drained condition (k>10^{-5} m/s) transits to undrained condition (k<10^{-8} m/s).

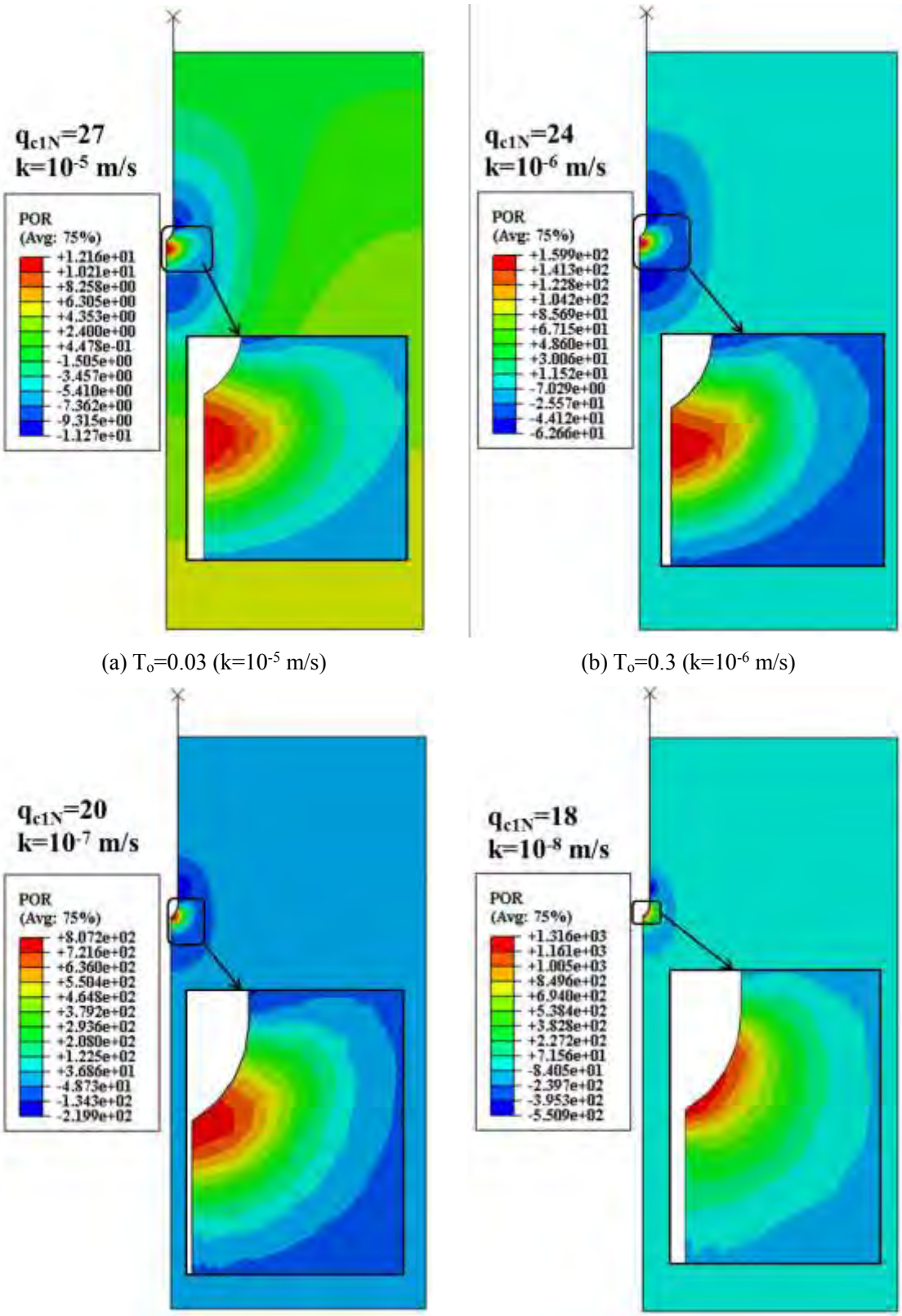

(a) T_o=0.03 (k=10^{-5} m/s)

(b) T_o=0.3 (k=10^{-6} m/s)

(c) T_o=3 (k=10^{-7} m/s)

(d) T_o=30 (k=10^{-8} m/s)

Fig. 6.8 EPWP distribution at $(D_{rc})_{eq}$=41% with different permeabilities (Unit:kPa)

6.2.3. $(D_{rc})_{eq}$=60%

Fig. 6.9 presents the results of q_{c1N} with respect to D/d_c of soil at $(D_{rc})_{eq}$=60% at different permeabilities ($k=10^{-3}$ to $k=10^{-8}$ m/s). Fig. 6.10 compares q_{c1N} and $\Delta u/\sigma_{vo}'$ behind cone tip at different k/T_o of soil at $(D_{rc})_{eq}$=60%. The changing trends of q_{c1N} and $\Delta u/\sigma_{vo}'$ are similar to $(D_{rc})_{eq}$=10% and 41%. It can be found in that the q_{c1N} doesn't decrease much and $\Delta u/\sigma_{vo}'$ is closed to zero as the permeability ranges from 10^{-3} (q_{c1N}=83) to 10^{-5} m/s (q_{c1N}=80), indicating the drained condition for permeability larger than 10^{-5} m/s (T_o<0.015). Partially drained condition prevails for k in the range between 10^{-5} m/s and $3x10^{-8}$ m/s (0.015<T_o<5). Undrained condition takes place as k is less than $3x10^{-8}$ m/s (T_o>5) since q_{c1N} stabilzes at lower limit (q_{c1N}=50) and negative $\Delta u/\sigma_{vo}'$ remains almost unchanged ($\Delta u/\sigma_{vo}'$=-2). Negative $\Delta u/\sigma_{vo}'$ ($\Delta u/\sigma_{vo}'$=-2 at $k=3x10^{-8}$ m/s) behind cone tip indicates the dilation behavior of the soil as the cone penetration progresses. Fig. 6.10 also includes CPT chamber tests near this $(D_{rc})_{eq}$ (denoted as '-CC').

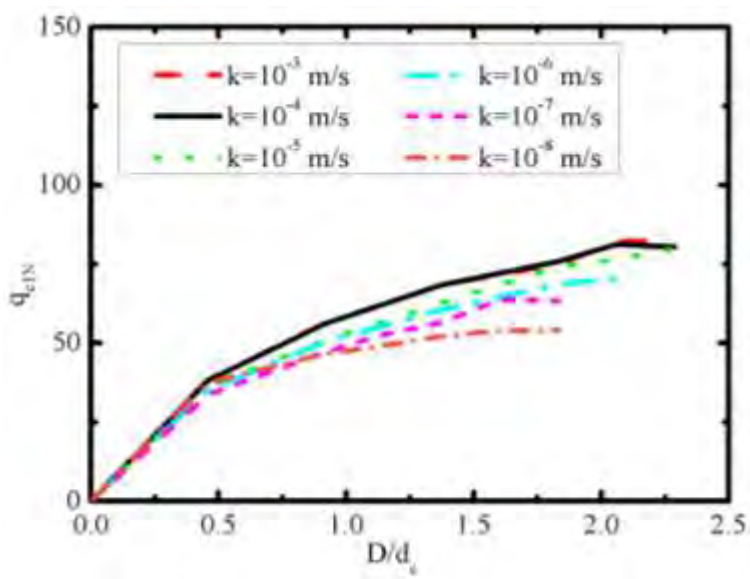

Fig. 6.9 q_{c1N} with respect to D/d_c at $(D_{rc})_{eq}$=60% with different permeabilities

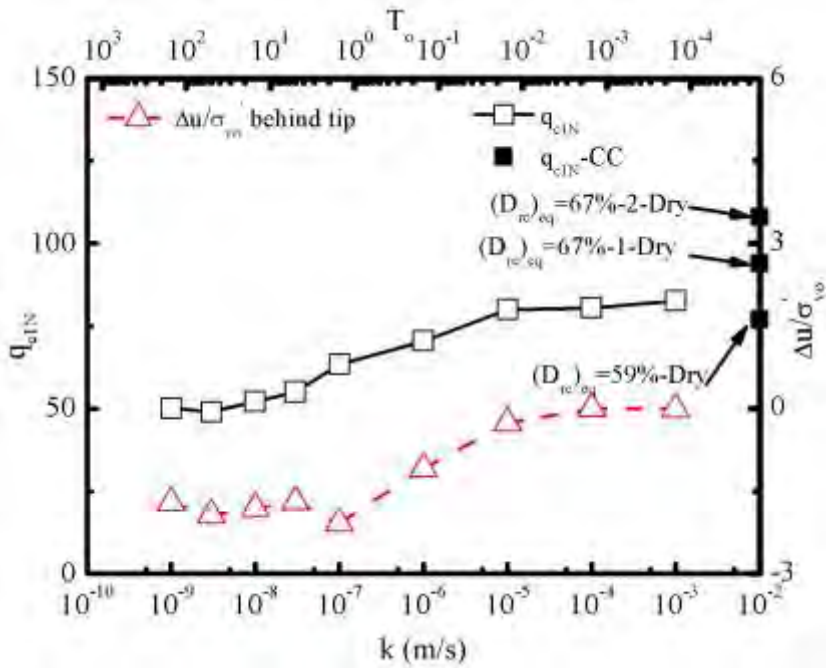

Fig. 6.10 q_{c1N} and $\Delta u/\sigma_{vo}'$ at $(D_{rc})_{eq}$=60% with different permeabilities

The EPWP contour for permeabilities ranged from 10^{-5} m/s to 10^{-8} m/s is compared in Fig. 6.11. The contour of Fig. 6.11(a) is almost identical to those obtained using permeability of 10^{-3} and 10^{-4}m/s, suggesting that drained condition dominates in these highest permeabilities. The contours clearly imply the variation of EPWP when drained condition ($k>10^{-5}$ m/s) transits to undrained condition ($k<10^{-8}$ m/s).

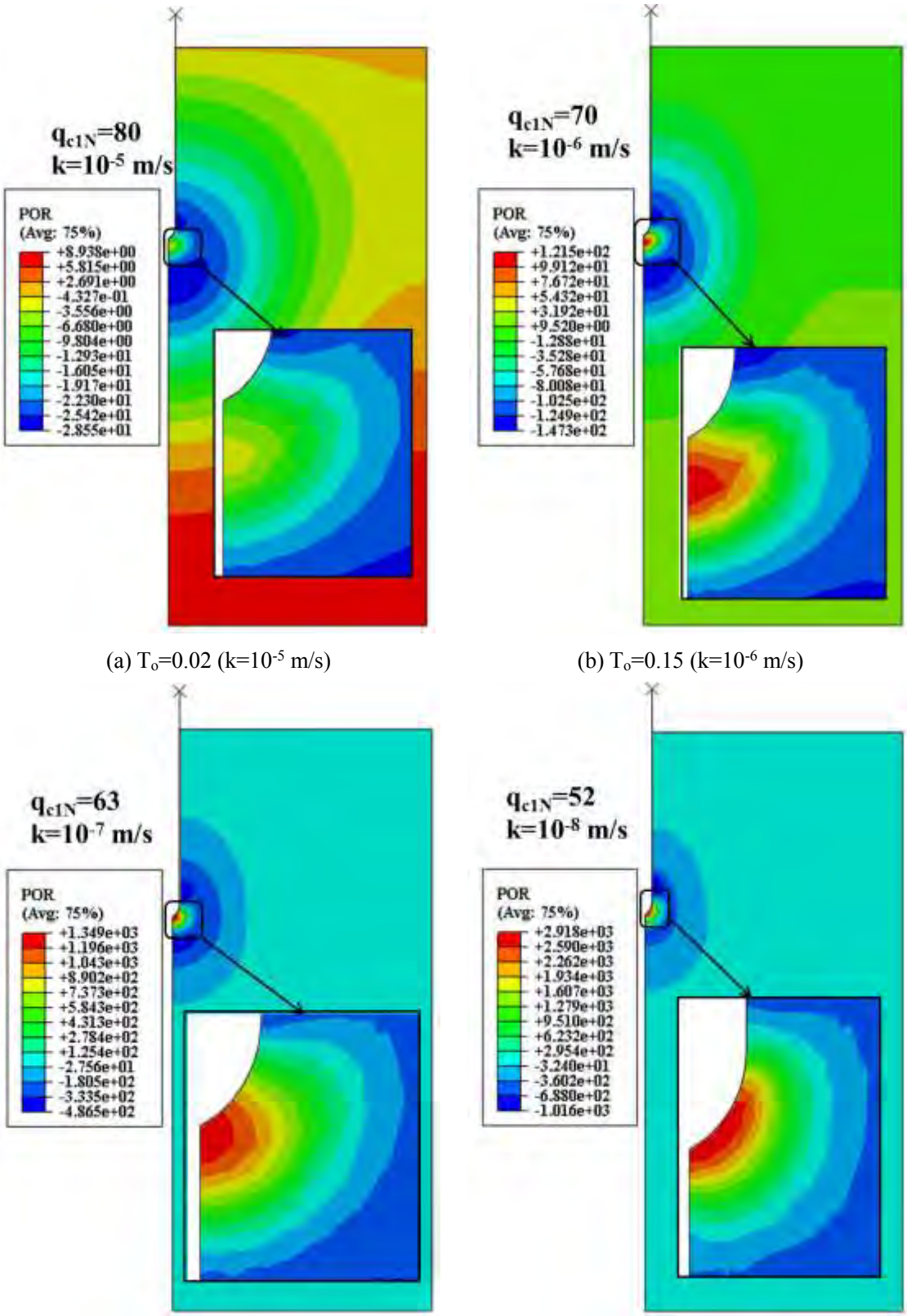

(a) T_o=0.02 (k=10^{-5} m/s) (b) T_o=0.15 (k=10^{-6} m/s)

(c) T_o=1.5 (k=10^{-7} m/s) (d) T_o=15 (k=10^{-8} m/s)

Fig. 6.11 EPWP distribution at $(D_{rc})_{eq}$=60% with different permeabilities (Unit:kPa)

6.2.4. $(D_{rc})_{eq}$=80%

Fig. 6.12 presents the results of q_{c1N} with respect to D/d_c of the soil at $(D_{rc})_{eq}$=80% at different permeabilities ($k=10^{-3}$ to $k=10^{-8}$ m/s).

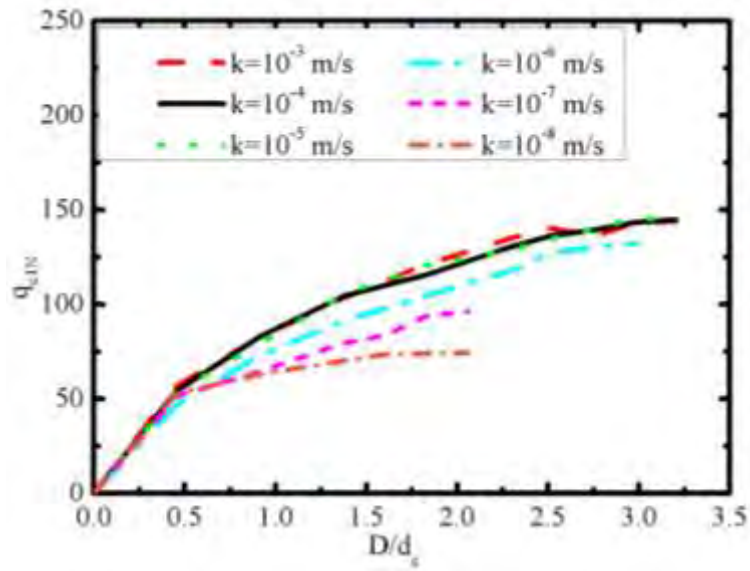

Fig. 6.12 q_{c1N} with respect to D/d_c at $(D_{rc})_{eq}$=80% with different permeabilities

Fig. 6.13 compares q_{c1N} and $\Delta u/\sigma_{vo}'$ at different k/T_o of soil at $(D_{rc})_{eq}$=80%. The drainage condition occurs when permeability is larger than 10^{-5} m/s (T_o<0.01) since the q_{c1N} does not deviate much from $k=10^{-5}$ m/s (q_{c1N}=145) to 10^{-4} m/s (q_{c1N}=144) and $\Delta u/\sigma_{vo}'$ is closed to zero. There is no further increase on the q_{c1N} as permeability increases. On the other hand, undrained condition (lower limit for q_{c1N}) takes place as permeability is smaller than 10^{-8} m/s (T_o>10), since almost unchanged q_{c1N} is observed and negative $\Delta u/\sigma_{vo}'$ remains almost unchanged ($\Delta u/\sigma_{vo}'$=-2). Nonetheless, the range of partially drained condition can be drawn for k between $k=10^{-5}$ m/s and $k=10^{-8}$ m/s (0.01<T_o<10), due to the rapid decrease in q_{c1N} (from 145 to 74) as a result of decreasing in permeability/increase in T_o.

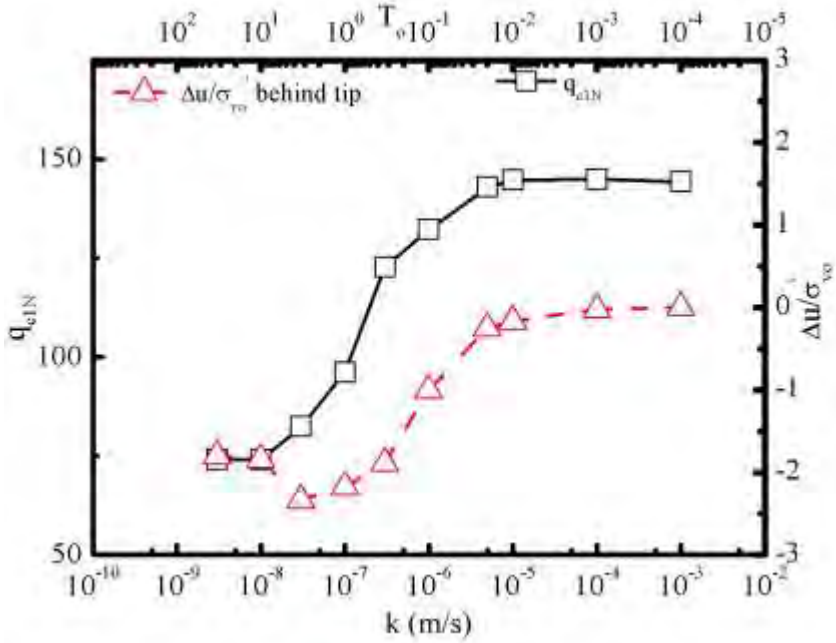

Fig. 6.13 q_{c1N} and $\Delta u/\sigma_{vo}'$ at $(D_{rc})_{eq}$=80% with different permeabilities

The EPWP contour for permeabilities ranged from 10^{-5} m/s to 10^{-8} m/s is compared in Fig. 6.14. The contour of Fig. 6.14(a) is almost identical to those obtained using permeability of 10^{-3} and 10^{-4} m/s, suggesting that drained condition dominates in these highest permeabilities. The contours clearly imply the variation of EPWP when drained condition ($k>10^{-5}$ m/s) transits to undrained condition ($k<10^{-8}$ m/s).

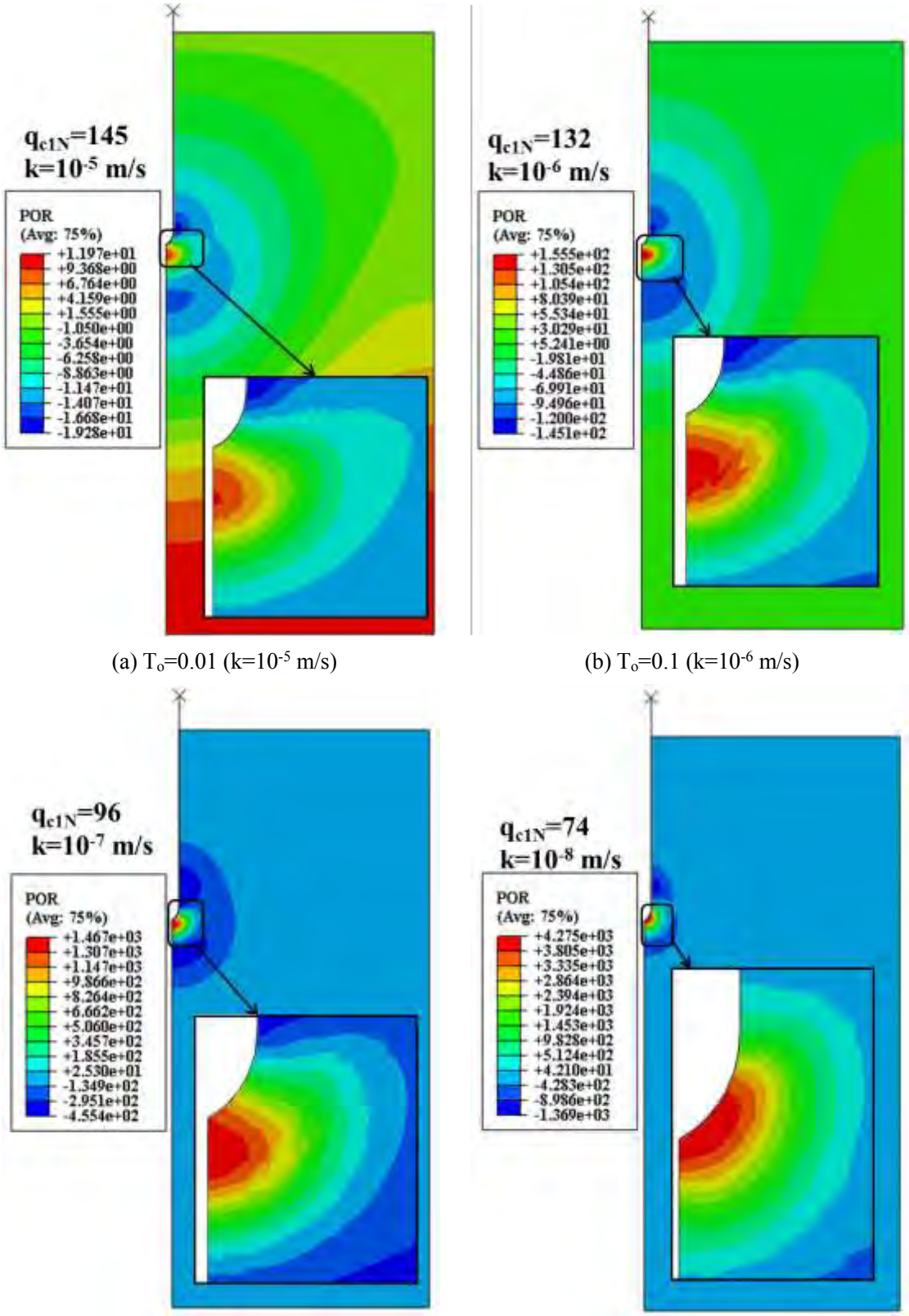

(a) T_o=0.01 (k=10^{-5} m/s) (b) T_o=0.1 (k=10^{-6} m/s)

(c) T_o=10 (k=10^{-7} m/s) (d) T_o=10 (k=10^{-8} m/s)

Fig. 6.14 EPWP distribution at $(D_{rc})_{eq}$=80% with different permeabilities (Unit:kPa)

6.3. Effect of penetration rate on q_{c1N} and $\Delta u/\sigma_{vo}'$

In this section, soils at different $(D_{rc})_{eq}$ (10%, 41% and 60%) are applied to examine the effect of penetration rate on q_{c1N} and $\Delta u/\sigma_{vo}'$ using a standard cone with 4.37 cm in diameter. The permeability is assumed to be 10^{-5} m/s with other soil properties presented in Table 5.3. The applied virtual penetration rate ranges from 0.02 cm/s to 20 cm/s.

Fig. 6.15 and Fig. 6.16 present the q_{c1N} and $\Delta u/\sigma_{vo}'$ at and behind the cone tip with respect to D/d_c of the soil at $(D_{rc})_{eq}$=10% at different penetration rates (v=0.02 cm/s to v=20 cm/s).

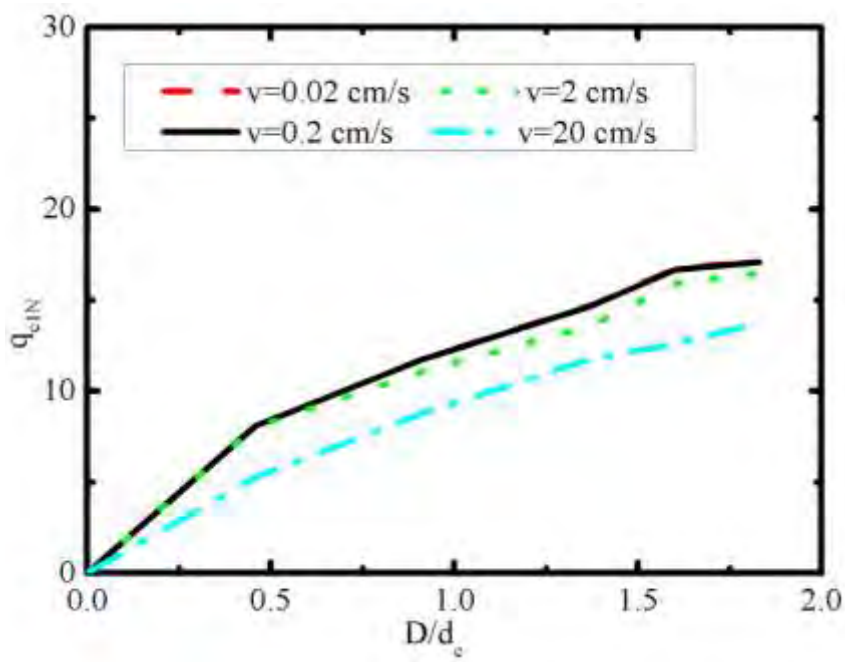

Fig. 6.15 q_{c1N} with respect to D/d_c at $(D_{rc})_{eq}$=10% with different penetration rates

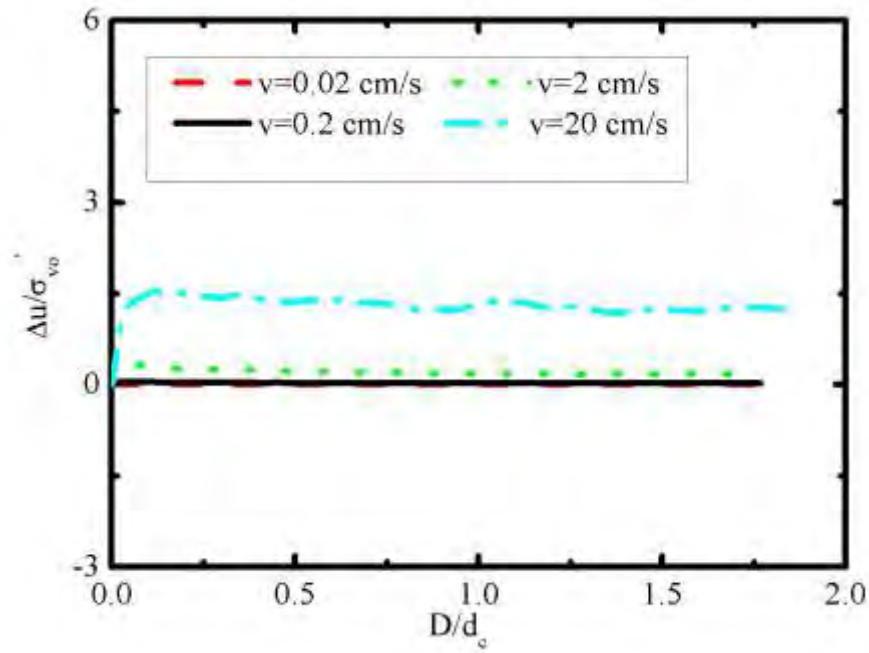

(a) At cone tip

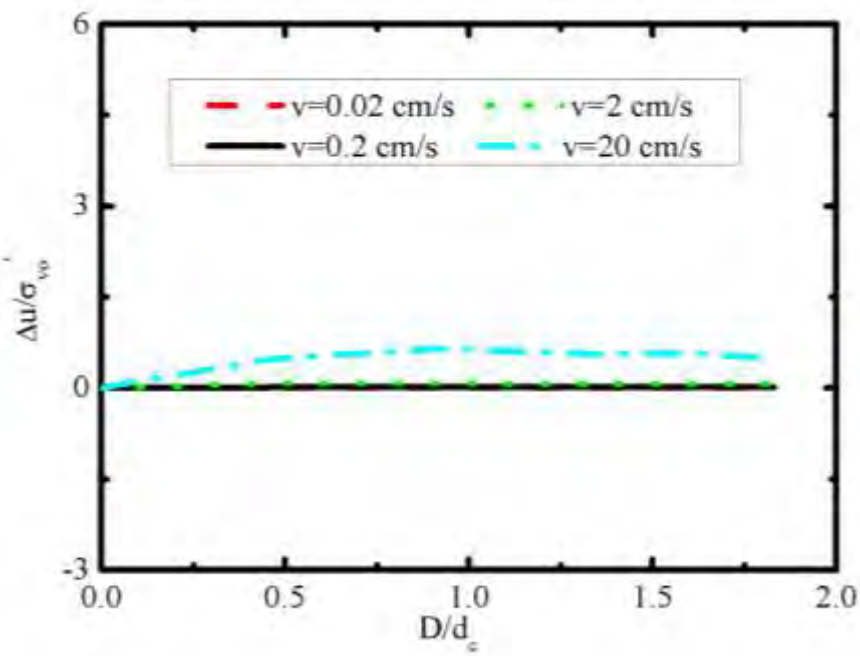

(b) Behind cone tip

Fig. 6.16 $\Delta u/\sigma_{vo}'$ with respect to D/d_c at $(D_{rc})_{eq}$=10% with different penetration rates

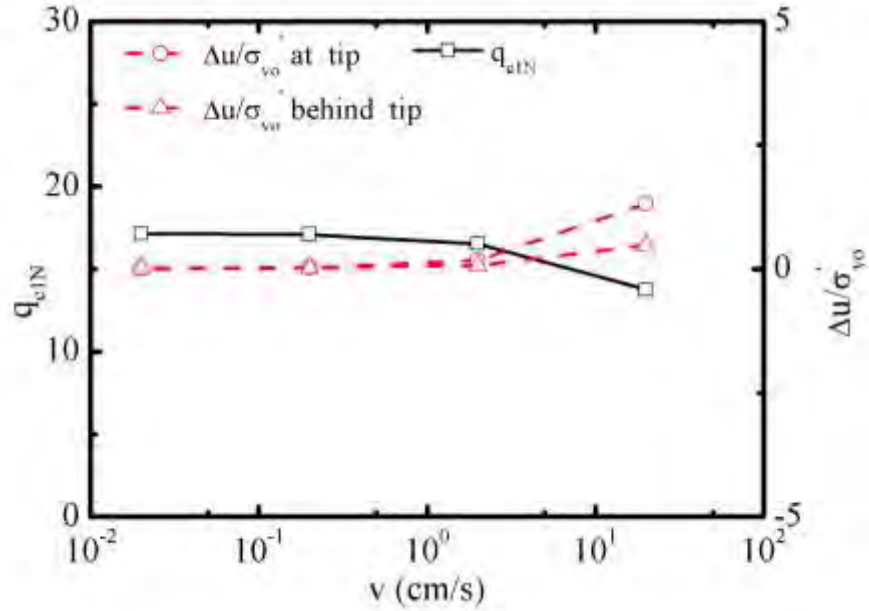

Fig. 6.17 q_{c1N} and $\Delta u/\sigma_{vo}'$ at $(D_{rc})_{eq}$=10% with different penetration rates

Fig. 6.17 shows the variation of q_{c1N} and $\Delta u/\sigma_{vo}'$ of soil at $(D_{rc})_{eq}$=10% when penetration rate changes from 0.02 cm/s to 20 cm/s. For low penetration rate, i.e., v=0.02 and 0.2 cm/s, q_{c1N} remains almost unchanged (q_{c1N}=17) and $\Delta u/\sigma_{vo}'$ is negligibly small, implying the dominance of drained condition. As the penetration rate increases from 2cm/s to 20 cm/s, q_{c1N} decreases accompanying with the increase of $\Delta u/\sigma_{vo}'$ at cone tip, indicating the transition from drained to partially drained condition.

Fig. 6.18 presents q_{c1N} and $\Delta u/\sigma_{vo}'$ with respect to T_o as permeability or penetration rate changes. The limiting value T_o of drained and undrained conditions for soil at $(D_{rc})_{eq}$=10% is 0.03 and 3, respectively. Fig. 6.18 also indicates that the effect of permeability on q_{c1N} and $\Delta u/\sigma_{vo}'$ agrees perfectly well with the effect of penetration rate after they are normalized into T_o.

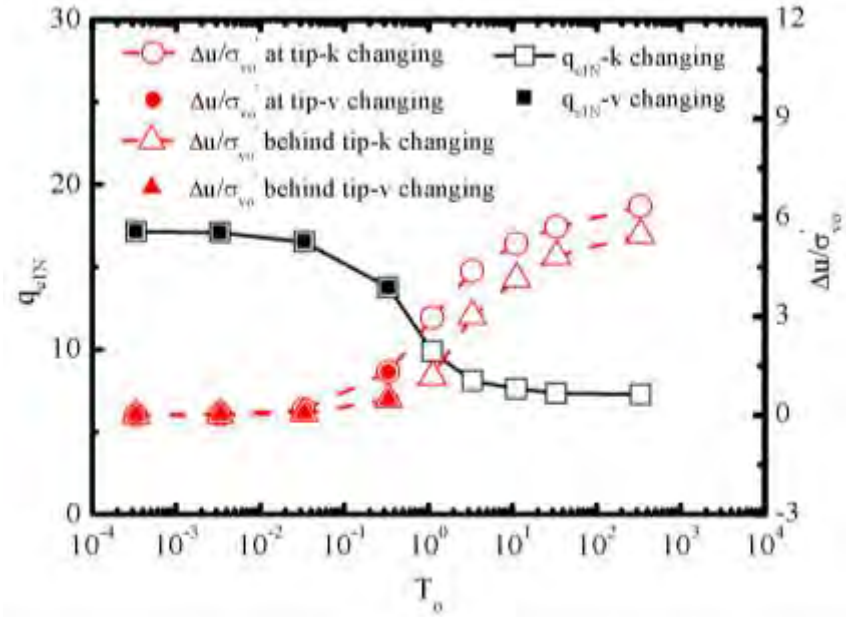

Fig. 6.18 Variation of q_{c1N} and $\Delta u/\sigma_{vo}'$ with respect to T_o at $(D_{rc})_{eq}$=10%

Fig. 6.19 plots, for a given T_o, $\Delta u/\sigma_{vo}'$ at/behind cone tip with respect to D/d_c at different combinations of permeability (k) and penetration rate (v). For example, Fig. 6.19(c) shows the $\Delta u/\sigma_{vo}'$ at cone tip and behind cone tip by two different combinations of k and v at T_o=3.4x10^{-1}. The black solid line represents the combination of permeability of 10^{-6} m/s and penetration rate of 2 cm/s at tip while the red dash line denotes the combination of permeability of 10^{-5} m/s and penetration rate of 20 cm/s at tip. Perfect agreement is found for each T_o of different combinations.

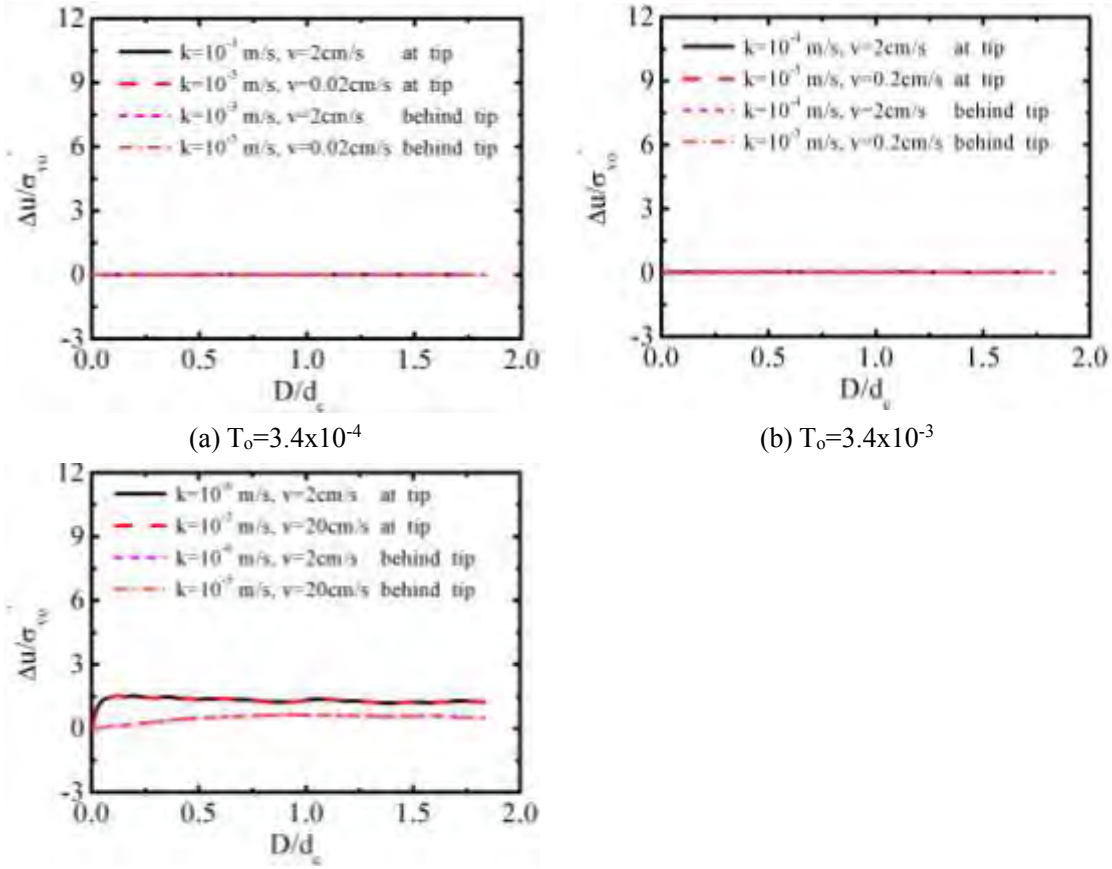

(a) T_o=3.4x10^{-4} (b) T_o=3.4x10^{-3}

(c) T_o=3.4x10^{-1}

Fig. 6.19 Comparison of changing k and v on $\Delta u/\sigma_{vo}'$ response for different T_o of soil at $(D_{rc})_{eq}$=10%

Fig. 6.20 and Fig. 6.21 present q_{c1N} and $\Delta u/\sigma_{vo}'$ with respect to T_o as permeability or penetration rate changes for $(D_{rc})_{eq}$=41% and 60%, respectively. It can be found in both figures that the effect of permeability on q_{c1N} and $\Delta u/\sigma_{vo}'$ agrees favorably well with the effect of penetration rate after they are normalized into the same T_o. These indicate that fines content C_F is not the only factor affecting cone resistance as well as excess pore water pressure response. The penetration rate as well as geometry of cone (section 6.4) shall be considered when examine the effect of fines on the cone resistance in silty sands.

The limit value of T_o for drained and undrained conditions at $(D_{rc})_{eq}$=41% are 0.03 and 10, respectively. The limit value of T_o for drained and undrained conditions at $(D_{rc})_{eq}$=61% are 0.02

and 10, respectively.

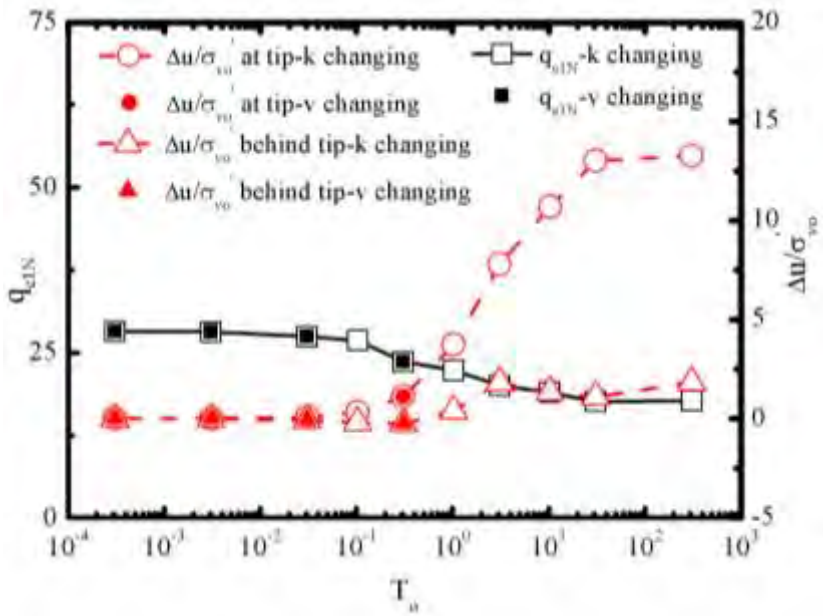

Fig. 6.20 Variation of q_{c1N} and $\Delta u/\sigma_{vo}'$ with respect to T_o at $(D_{rc})_{eq}$=41%

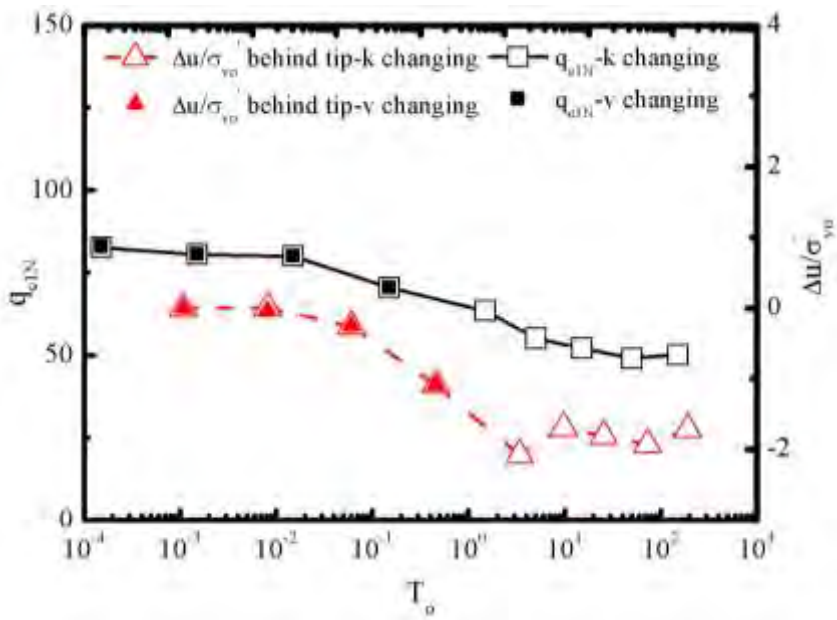

Fig. 6.21 Variation of q_{c1N} and $\Delta u/\sigma_{vo}'$ with respect to T_o at $(D_{rc})_{eq}$=60%

6.4. Effect of cone diameter on q_{c1N} and $\Delta u/\sigma_{vo}'$

In this section, the effect of cone diameter on q_{c1N} and $\Delta u/\sigma_{vo}'$ is numerically studied at three different $(D_{rc})_{eq}$ (10%, 41% and 60%). Cone diameter of 1.27 cm and 4.37 cm with penetration

rate of 2 cm/s at different permeabilities for each $(D_{rc})_{eq}$ are used. Soil properties are adopted using Table 5.3 except permeability. Four numerical permeabilities (10^{-5}, 10^{-6}, 10^{-7} and 10^{-8} m/s) are assigned for cone diameter of 1.27 cm while the numerical results using 4.37 cm diameter cone are adopted from section 6.2.

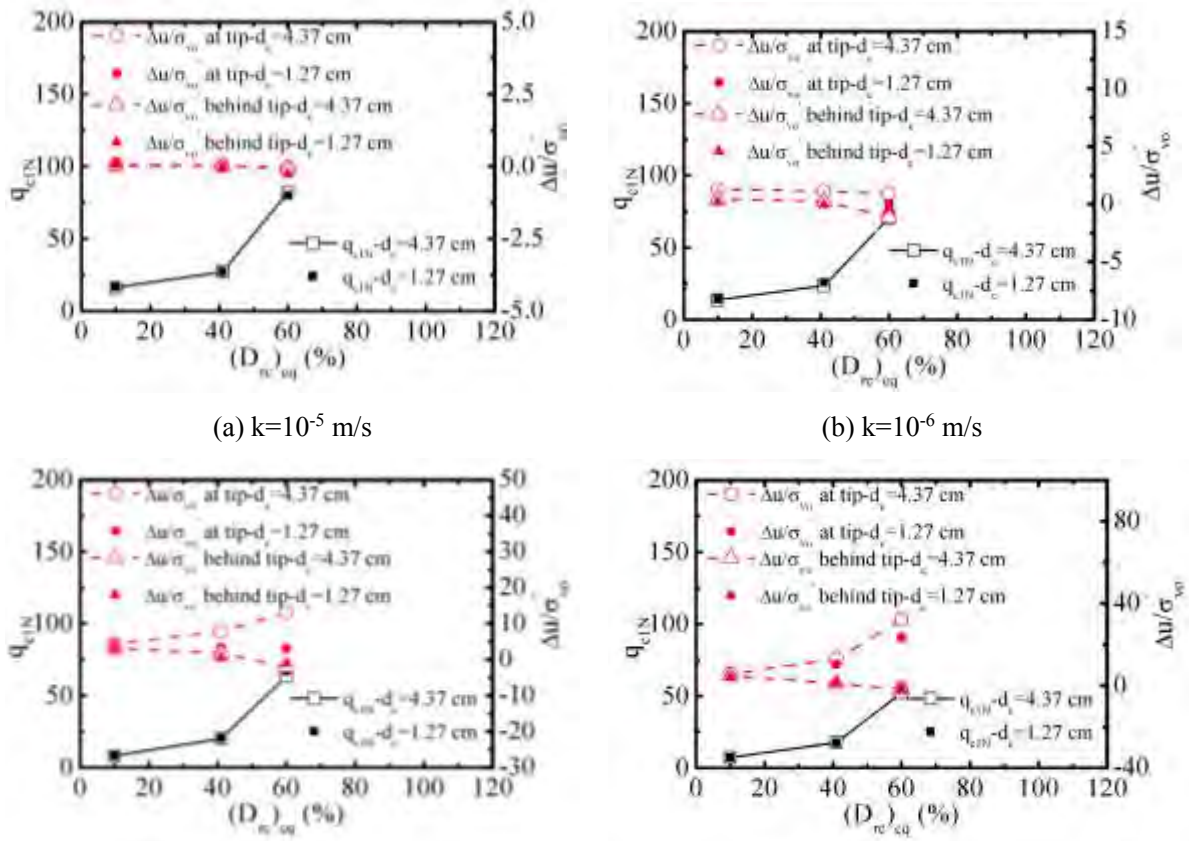

(a) k=10^{-5} m/s (b) k=10^{-6} m/s

(c) k=10^{-7} m/s (d) k=10^{-8} m/s

Fig. 6.22 Variation of q_{c1N} and $\Delta u/\sigma_{vo}'$ of different $(D_{rc})_{eq}$ at different k using two d_c

Fig. 6.22 plots q_{c1N} and $\Delta u/\sigma_{vo}'$ of different $(D_{rc})_{eq}$ at various permeabilities. When compared at the same permeability, q_{c1N} and $\Delta u/\sigma_{vo}'$ does not show significant difference between 1.27 cm and 4.37 cm diameter cone when the permeability is large [e.g. k=10^{-5} m/s, Fig. 6.22(a)] or is small [e.g. k=10^{-8} m/s, Fig. 6.22(d)]. This may be attributed to that large permeability results in drained condition while small permeability leads to undrained condition during cone penetration as

discussed previously.

However, q_{c1N} using 4.37 cm cone is smaller than that using 1.27 cm cone when $k=10^{-6}$ m/s and 10^{-7} m/s [Fig. 6.22(b) and Fig. 6.22(c)]. Meanwhile, the absolute value of $\Delta u/\sigma_{vo}'$ at or behind cone tip using 4.37 cm cone are larger than those using 1.27 cm cone. This may be due to the fact that when the drainage condition is partially drained, smaller cone would cause fast dissipation of excess pore water pressure around cone tip during penetration and consequently results in strengthening of soil.

Fig. 6.23 through Fig. 6.25 plot the q_{c1N} and $\Delta u/\sigma_{vo}'$ versus T_o using two d_c at different $(D_{rc})_{eq}$. It shall be noticed that, when compared at the same T_o, q_{c1N} and $\Delta u/\sigma_{vo}'$ obtained using d_c=4.37 cm are in good accordance with those using d_c=1.27 cm. In considering the study carried out in section 6.3 and this section, the normalized penetration rate T_o is more appropriate to quantify the effect of fines, penetration rate as well as geometry of cone on q_{c1N} and $\Delta u/\sigma_{vo}'$ in the silty sand.

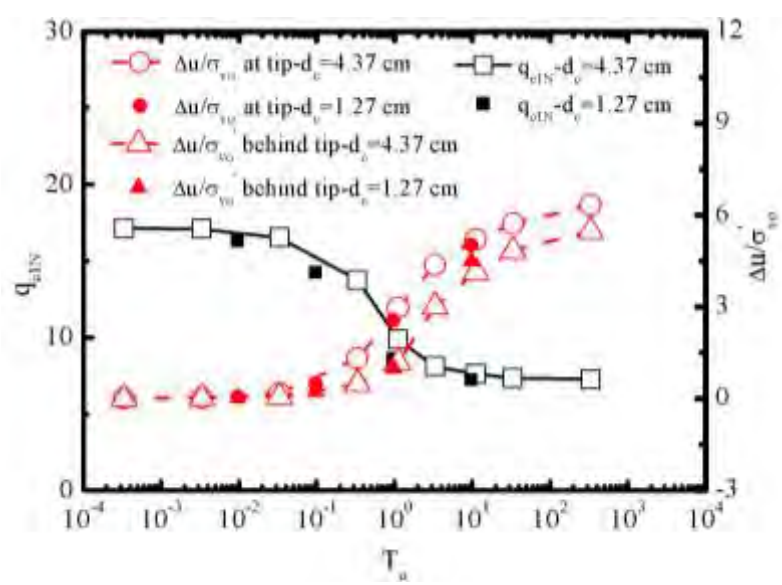

Fig. 6.23 Variation of q_{c1N} and $\Delta u/\sigma_{vo}'$ with respect to T_o at $(D_{rc})_{eq}$=10% for two d_c

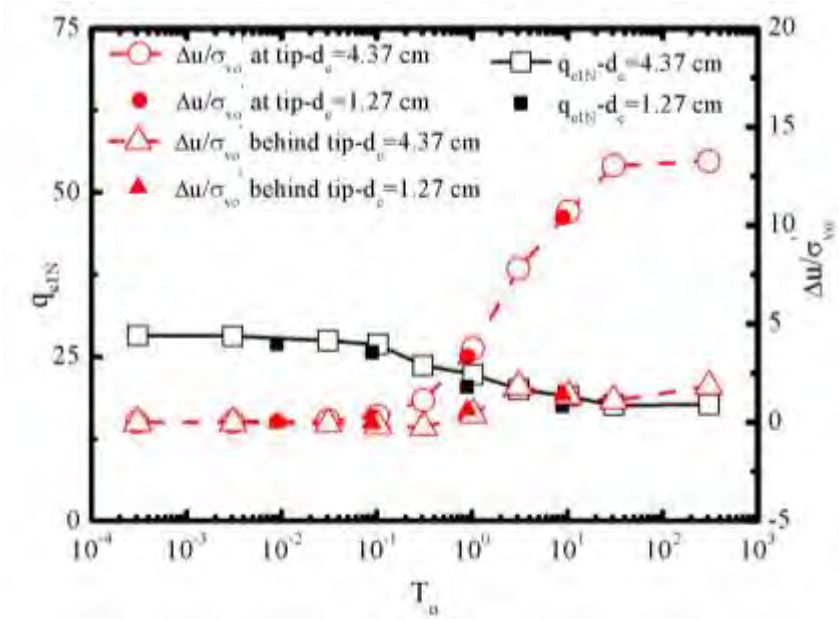

Fig. 6.24 Variation of q_{c1N} and $\Delta u/\sigma_{vo}'$ with respect to T_o at $(D_{rc})_{eq}$=41% for two d_c

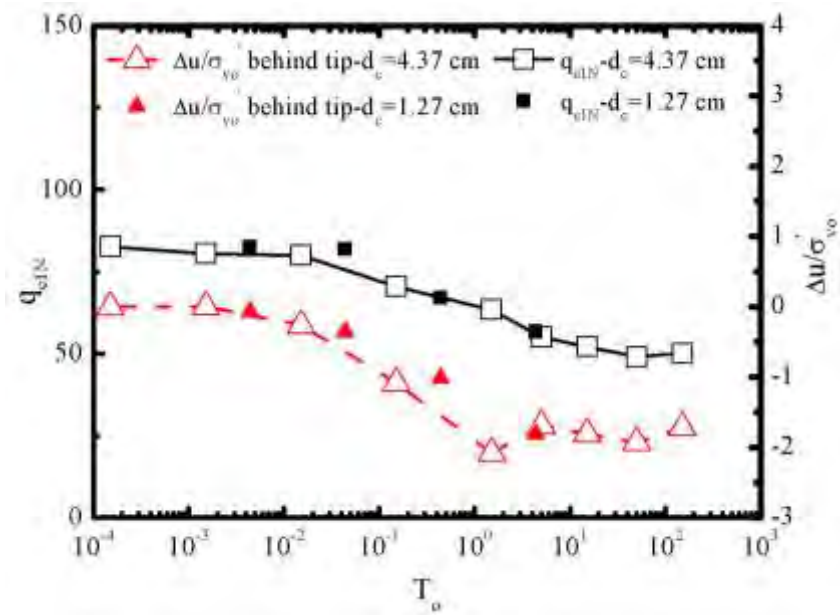

Fig. 6.25 Variation of q_{c1N} and $\Delta u/\sigma_{vo}'$ with respect to T_o at $(D_{rc})_{eq}$=60% for two d_c

The study carried out in this section, together with section 6.3. and Chapter 4, indicates that the fines content (C_F) is not the only factor affecting cone resistance as well as excess pore water pressure response around the cone tip. Hence, T_o instead of C_F shall be used to quantify the degree of consolidation during penetration in sands and silty sands.

6.5. Effect of T_o on q_{c1N} and $\Delta u/\sigma_{vo}'$

As presented in section 6.2, 6.3 and 6.4, the effect of permeability, penetration rate and diameter of cone on q_{c1N} and $\Delta u/\sigma_{vo}'$ at different $(D_{rc})_{eq}$ agree favorably well with each other after they are normalized into the same T_o. Hence, T_o is more appropriate to quantify the the degree of consolidation during penetration instead of C_F. Table 6.1 is the summary of q_{c1N}, $\Delta u_1/\sigma_{vo}'$ (at cone tip face) and $\Delta u_2/\sigma_{vo}'$ (behind cone tip) for OS F55 sand-silt mix at different $(D_{rc})_{eq}$ using d_c=4.37 cm. Numerical results obtained using 4.37 cm diameter cone with changed permeability for a given soil are for the upcoming study of the liquefaction screening in silty sands. In addition, T_o can be used to demarcate the drained, partially drained and undrained conditions during the advancement of cone penetrometer.

To demarcate the limit value of T_o for drained and undrained conditions regardless of $(D_{rc})_{eq}$, a normalized factor of $q_{c1N}/q_{c1N\text{-}ref}$ is introduced. $q_{c1N\text{-}ref}$ is the normalized cone resistance at undrained condition. Fig. 6.26 plots the relation between $q_{c1N}/q_{c1N\text{-}ref}$ and T_o for various soils at different $(D_{rc})_{eq}$. It clearly shows that the $q_{c1N}/q_{c1N\text{-}ref}$ (q_{c1N}) depends on T_o. In this figure, it may be seen that the transition from undrained to partially drained penetration occurs around $T_o \approx 10$ since $q_{c1N}/q_{c1N\text{-}ref}$ almost stabilizes at this value, and the transition from partially drained to fully drained conditions occurs around $T_o \approx 0.04$ because there is no much change of $q_{c1N}/q_{c1N\text{-}ref}$ when $T_o < 0.04$. The observed demarcation of the drainage condition is in reasonable agreement with the results reported by Ecemis (2008) (drained condition takes place at $T_o < 0.01$, undrained condition occurs at $T_o > 6$) and Yi et al. (2012) (T_o for drained and undrained conditions were 0.1 and 10, respectively). Similar experimental observation is reported in clayed soil by Kim et al. (2008), in

which the limiting valued T_o for drained and undrained conditions were 0.05 and 10, respectively.

Table 6.1 Summary of numerical CPT results using Ottawa F55 sand-silt mix

$(D_{r0})_{ac}$	v	m_v	k	c_v	T_o	Numerical Results		
(%)	(m/s)	(kPa^{-1})	(m/s)	(m^2/s)		q_{c1N}	$\Delta u_1/\sigma_{vo}'$	$\Delta u_2/\sigma_{vo}'$
10	2.0E-02	3.90E-05	1.0E-03	2.62E+00	3.34E-04	17.1	4.1E-03	1.2E-03
	2.0E-02	3.90E-05	1.0E-04	2.62E-01	3.34E-03	17.1	2.5E-02	1.5E-02
	2.0E-02	3.90E-05	1.0E-05	2.62E-02	3.34E-02	16.5	1.7E-01	6.6E-02
	2.0E-02	3.90E-05	1.0E-06	2.62E-03	3.34E-01	13.7	1.3E+00	4.8E-01
	2.0E-02	3.90E-05	3.0E-07	7.86E-04	1.11E-00	9.9	3.0E+00	1.2E+00
	2.0E-02	3.90E-05	1.0E-07	2.62E-04	3.34E-00	8.1	4.4E+00	3.0E+00
	2.0E-02	3.90E-05	3.0E-08	7.86E-05	1.11E-01	7.6	5.2E+00	4.1E+00
	2.0E-02	3.90E-05	1.0E-08	2.62E-05	3.34E-01	7.3	5.7E+00	4.8E+00
	2.0E-02	3.90E-05	1.0E-09	2.62E-06	3.34E-02	7.3	6.3E+00	5.5E+00
	2.0E-04	3.90E-05	1.0E-05	2.62E-02	3.34E-04	17.1	2.8E-03	1.6E-03
	2.0E-03	3.90E-05	1.0E-05	2.62E-02	3.34E-03	17.1	2.5E-02	1.6E-02
	2.0E-01	3.90E-05	1.0E-05	2.62E-02	3.34E-01	13.7	1.3E+00	4.8E-01
	2.0E+00	3.90E-05	1.0E-05	2.62E-02	3.34E+00	8.0	4.4E+00	3.0E+00
41	2.0E-02	3.60E-05	1.0E-03	2.83E+00	3.08E-04	28.2	1.2E-03	-2.1E-04
	2.0E-02	3.60E-05	1.0E-04	2.83E-01	3.08E-03	28.1	1.5E-02	4.3E-04
	2.0E-02	3.60E-05	1.0E-05	2.83E-02	3.08E-02	27.4	7.9E-02	-7.6E-02
	2.0E-02	3.60E-05	3.0E-06	8.50E-03	1.03E-01	26.9	3.2E-01	-1.9E-01
	2.0E-02	3.60E-05	1.0E-06	2.83E-03	3.08E-01	23.6	1.1E+00	-2.4E-01
	2.0E-02	3.60E-05	3.0E-07	8.50E-04	1.03E-00	22.3	3.7E+00	3.9E-01
	2.0E-02	3.60E-05	1.0E-07	2.83E-04	3.08E+00	20.0	7.8E+00	1.8E+00
	2.0E-02	3.60E-05	3.0E-08	8.50E-05	1.03E-01	19.0	1.1E+01	1.3E+00
	2.0E-02	3.60E-05	1.0E-08	2.83E-05	3.08E-01	17.6	1.3E+01	1.1E+00
	2.0E-02	3.60E-05	1.0E-09	2.83E-06	3.08E-02	17.7	1.3E+01	1.8E+00
	2.0E-04	3.60E-05	1.0E-05	2.83E-02	3.08E-04	28.2	1.2E-03	-2.1E-04
	2.0E-03	3.60E-05	1.0E-05	2.83E-02	3.08E-03	28.1	1.5E-02	4.3E-04
	2.0E-01	3.60E-05	1.0E-05	2.83E-02	3.08E-01	23.6	1.1E+00	-2.4E-01
	2.0E+00	3.60E-05	1.0E-05	2.83E-02	3.08E-00	20.0	7.8E+00	1.8E+00
60	2.0E-02	1.77E-05	1.0E-03	5.78E+00	1.51E-04	82.6	-2.7E-03	-4.2E-03
	2.0E-02	1.77E-05	1.0E-04	5.78E-01	1.51E-03	80.5	-1.8E-02	0.0E+00
	2.0E-02	1.77E-05	1.0E-05	5.78E-02	1.51E-02	80.0	-9.5E-02	-2.6E-01
	2.0E-02	1.77E-05	1.0E-06	5.78E-03	1.51E-01	70.5	9.4E-01	-1.1E+00
	2.0E-02	1.77E-05	1.0E-07	5.78E-04	1.51E-00	63.4	1.3E+01	-2.1E+00
	2.0E-02	1.77E-05	3.0E-08	1.73E-04	5.04E-00	55.1	2.3E+01	-1.7E+00
	2.0E-02	1.77E-05	1.0E-08	5.78E-05	1.51E-01	52.1	3.2E+01	-1.8E+00
	2.0E-02	1.77E-05	3.0E-09	1.73E-05	5.04E-01	49.0	3.4E+01	-1.9E+00
	2.0E-02	1.77E-05	1.0E-09	5.78E-06	1.51E-02	50.1	4.1E+01	-1.7E+00
	2.0E-04	1.77E-05	1.0E-05	5.78E-02	1.51E-04	82.9	-2.7E-03	-4.3E-03
	2.0E-03	1.77E-05	1.0E-05	5.78E-02	1.51E-03	80.5	-1.9E-02	-3.4E-02
	2.0E-01	1.77E-05	1.0E-05	5.78E-02	1.51E-01	70.5	9.4E-01	-1.1E+00
	2.0E+00	1.77E-05	1.0E-05	5.78E-02	1.51E-00	63.4	1.3E+01	-5.8E-01
67	2.0E-02	1.64E-05	1.0E-03	6.24E+00	1.40E-04	95.6	-9.6E-04	-2.7E-03
	2.0E-02	1.64E-05	1.0E-04	6.24E-01	1.40E-03	96.9	-1.8E-03	-2.3E-02
	2.0E-02	1.64E-05	1.0E-05	6.24E-02	1.40E-02	96.4	1.3E-02	-1.9E-01
	2.0E-02	1.64E-05	1.0E-06	6.24E-03	1.40E-01	79.0	8.0E-01	-9.3E-01
	2.0E-02	1.64E-05	1.0E-07	6.24E-04	1.40E-00	69.1	1.2E+01	-1.2E+00
	2.0E-02	1.64E-05	3.0E-08	1.87E-04	4.67E+00	61.8	2.7E+01	-1.3E+00
	2.0E-02	1.64E-05	1.0E-08	6.24E-05	1.40E-01	59.3	3.4E+01	-1.4E+00
	2.0E-02	1.64E-05	3.0E-09	1.87E-05	4.67E+01	54.9	4.3E+01	-1.4E+00
80	2.0E-02	1.16E-05	1.0E-03	8.79E+00	9.95E-05	144.2	-7.5E-06	0.0E+00
	2.0E-02	1.16E-05	1.0E-04	8.79E-01	9.95E-04	144.9	2.0E-04	-2.4E-02
	2.0E-02	1.16E-05	1.0E-05	8.79E-02	9.95E-03	144.7	2.6E-02	-1.6E-01
	2.0E-02	1.16E-05	5.0E-06	4.39E-02	1.99E-02	142.9	5.2E-02	-2.5E-01
	2.0E-02	1.16E-05	1.0E-06	8.79E-03	9.95E-02	132.2	6.5E-01	-1.0E+00
	2.0E-02	1.16E-05	3.0E-07	2.64E-03	3.32E-01	122.7	3.2E+00	-1.9E+00
	2.0E-02	1.16E-05	1.0E-07	8.79E-04	9.95E-01	96.1	1.2E+01	-2.2E+00
	2.0E-02	1.16E-05	3.0E-08	2.64E-04	3.32E-00	82.4	3.0E+01	-2.3E+00
	2.0E-02	1.16E-05	1.0E-08	8.79E-05	9.95E-00	74.0	4.1E+01	-1.8E+00
	2.0E-02	1.16E-05	3.0E-09	2.64E-05	3.32E-01	74.1	4.9E+01	-1.8E+00

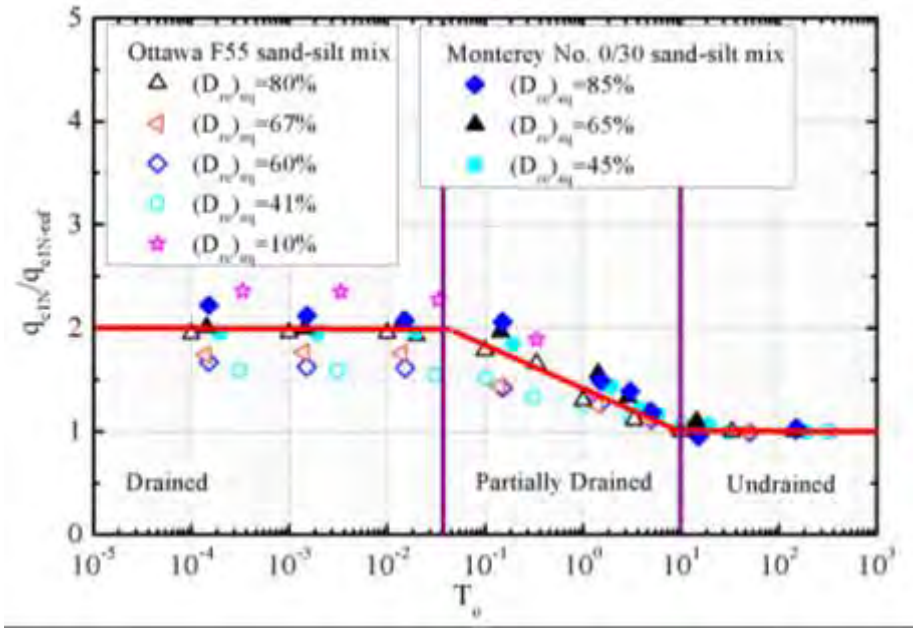

Fig. 6.26 q_{c1N}/ $q_{c1N\text{-}ref}$ versus T_o for different sand-silt mixes

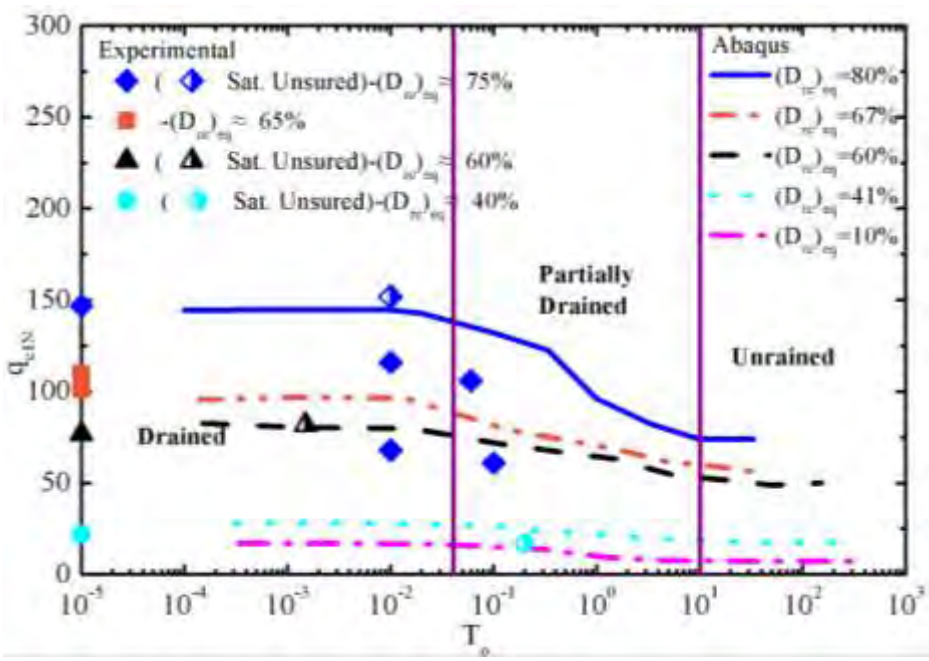

Fig. 6.27 q_{c1N} versus T_o for soils with different $(D_{rc})_{eq}$ for Ottawa F55 sand-silt mix

Fig. 6.27 plots q_{c1N} versus T_o at different $(D_{rc})_{eq}$ of OS F55 sand-silt mix and compares with performed CPTs in the testing chamber.

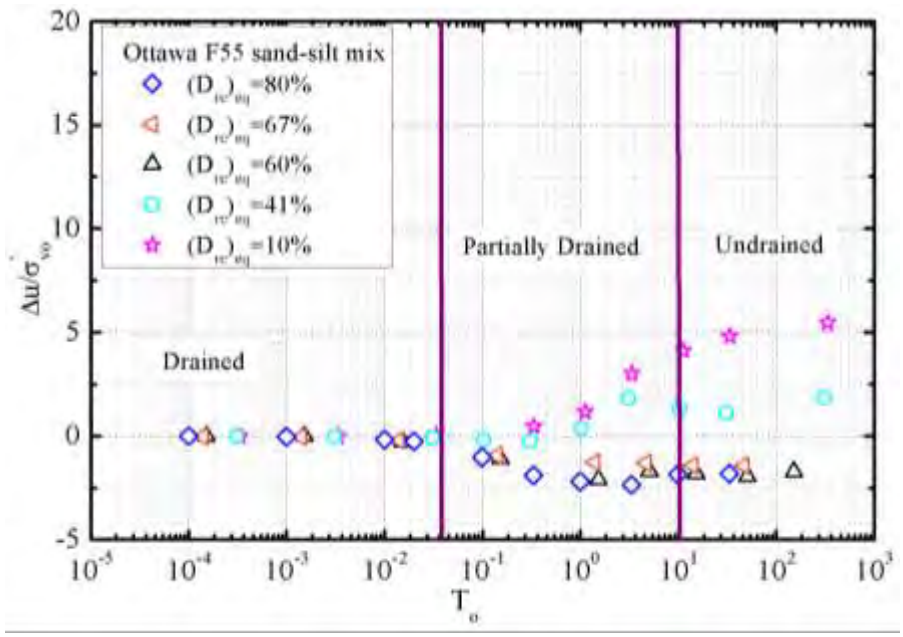

Fig. 6.28 $\Delta u/\sigma_{vo}'$ versus T_o for Ottawa F55 sand-silt mix with different $(D_{rc})_{eq}$

The effect of T_o is also reflected in the excess pore water response behind cone tip. Fig. 6.28 shows the relation between $\Delta u/\sigma_{vo}'$ behind cone tip and T_o for OS F55 sand-silt mix with different $(D_{rc})_{eq}$. The $\Delta u/\sigma_{vo}'$ remains negligibly small for all soils when $T_o<0.04$ (drained condition), which agrees well with the reported values in laminar box ($T_o=0.02$ for clean sands) in section 7.5. For dense soils, considerable amount of negative $\Delta u/\sigma_{vo}'$ develops as T_o increases from 0.04 to 10 (transition from drained to undrained condition). The negative pore pressure indicates the dilative behavior of the dense soil under penetration.

It is implied from Fig. 6.27 and Fig. 6.28 that, for a soil at a given $(D_{rc})_{eq}$ under a standard penetration rate using a standard cone, the q_{c1N} of low permeable silty sands (larger T_o) would be smaller than that of highly permeable clean sands (small T_o). This variation can be attributed to the presence of fines, leading to lower k and c_v, resulting in lower effective stress around the cone tip due to the longer dissipation time of Δu. Hence, a reduction of q_{c1N} is encountered in the silty

sand compared to the clean sand at the same $(D_{rc})_{eq.}$ In other words, the silty sand having lower k and c_v stays in undrained or partially drained conditions during cone penetration, causes a decrease in tip resistance compared to the highly permeable sand at the same $(D_{rc})_{eq}$.

6.6. Summary

Since CPT is a time dependent phenomenon, it is expected that for a soil at a given $(D_{rc})_{eq}$, q_{c1N} is dependent of T_o ($T_o=vd_c/c_v$). In this chapter, firstly the effect of fines on q_{c1N} and $\Delta u/\sigma_{vo}'$ in soils with different $(D_{rc})_{eq}$ was examined. It shows that the clean sand has a greater q_{c1N} than the silty sand when compared at the same $(D_{rc})_{eq}$ using the standard cone (d_c=4.37 cm) and penetration rate (v=2 cm/s). Because the excess pore water around cone tip develops, the drainage condition transits from drained to partially drained, or even undrained as fines content increases, which is represented by the decrease in c_v. The numerical results also point out that the penetration rate and cone diameter affect the q_{c1N} in silty sands. At a given $(D_{rc})_{eq}$, q_{c1N} decreases as v increase or d_c increase (T_o increases) in the partially drained condition. It is also suggested that the limit value of T_o for drained and undrained conditions are 0.04 and 10, respectively, which agreed favorably with other investigators.

Chapter 7. 1-g Full scale laminar box: Sand liquefaction tests

7.1. Introduction

The Structural Engineering and Earthquake Simulation Laboratory (SEESL) at the University at Buffalo (UB) hosts a 1g full-scale laminar box and shaking platform that can be used to study, identify and examine real word geotechnical-related problems. In this chapter, the new laminar box shaking system, instrumentation and sand sample preparation for the liquefaction test series at level ground (LG1) are presented.

7.2. Full scale laminar box shaking system

The full scale laminar box shaking system has the capability to test up to approximately 80 m^3 of sand simulating a soil deposit up to 6 m deep. It consists of three parts: the laminar box, the base shaker and actuator exciting system, and the bracing frame system.

7.2.1. Laminar box

Fig. 7.1(a) and (b) schematically show the inner details of the laminar box. It is a stack-ring system consisting of 40 steel rectangular-shaped laminates (rings) (L0-L39). The laminates are made of steel I-beams, typically each 0.26 m wide and 0.15 m high. The laminates are separated and supported by a number of distributed high capacity and very low friction ball bearings. The inner dimension of the box is 5.00 m (198.75 inch) in length, 2.74 m (108 inch) in width. The maximum height of the box is 6.10 m (240 inch) when all of the 40 laminates (L0-L39) are assembled. Fig. 7.1(a) shows the plan view. Fig. 7.1(b) shows the cross section of the laminar box and the cross section of the laminates. 16 ball bearing units (Fig. 7.2), each containing a number of ball bearings

(No. 41163, General Bearings Corporation), are mounted inside the top channel of the I-beam in each laminate. Table 7.1 shows the number of bearings at each location. The under side of the I-beams below the bearing support units are lined with hardened steel plates. The laminates sit on each other resting on ball bearings when they are stacked together. A small gap of typically 6.35 mm (0.25 inch) between two adjacent laminates is provided by adjusting the height of ball bearings, in order to prevent any contact interference between any adjacent laminates during horizontal sliding of the laminates. The friction coefficient between harden plate and ball bearing is around 0.6% (Appendix D). The maximum interlaminate displacement in longitudinal direction (east/west) and transverse direction (north/south) are limited to 2.86 cm (1.125 inch) and 1.59 cm (0.625 inch), respectively. This is achieved by a number of internal restraint angle pairs welded on the laminate web. Fig. 7.2 and Fig. 7.3 show the locations and the details of displacement restrainers.

The total weight of 39 laminates (L1-L39) with all the bearings and displacement restrainers is about 393 kN without soil. The ratio of the laminate weight to the saturated soil weight is about 25% (for a soil with saturated unit weight γ_{sat} of 19.2 kN/m^3).

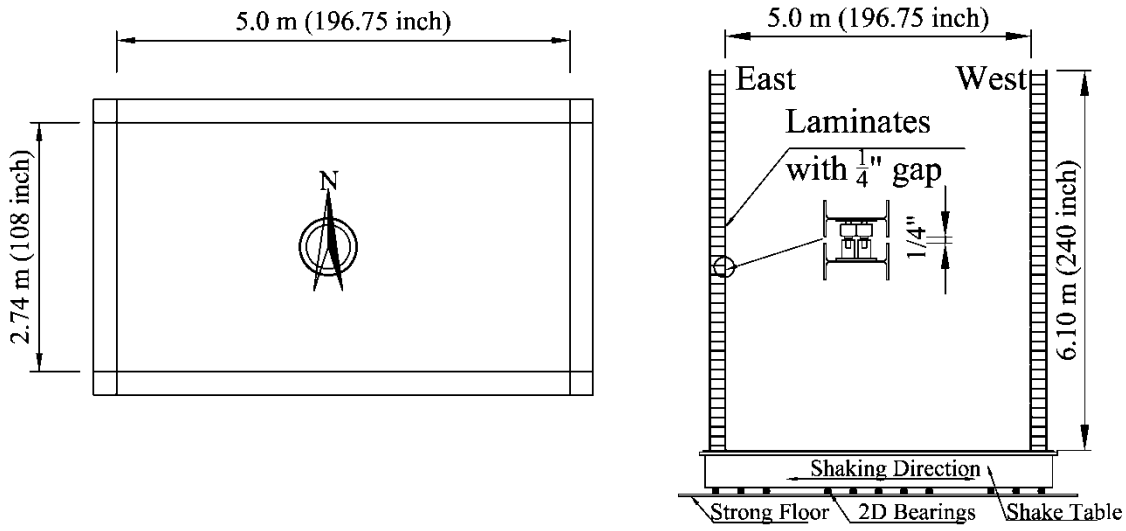

(a) Plan view (b) Cross-section

Fig. 7.1 Schematic details of laminar box

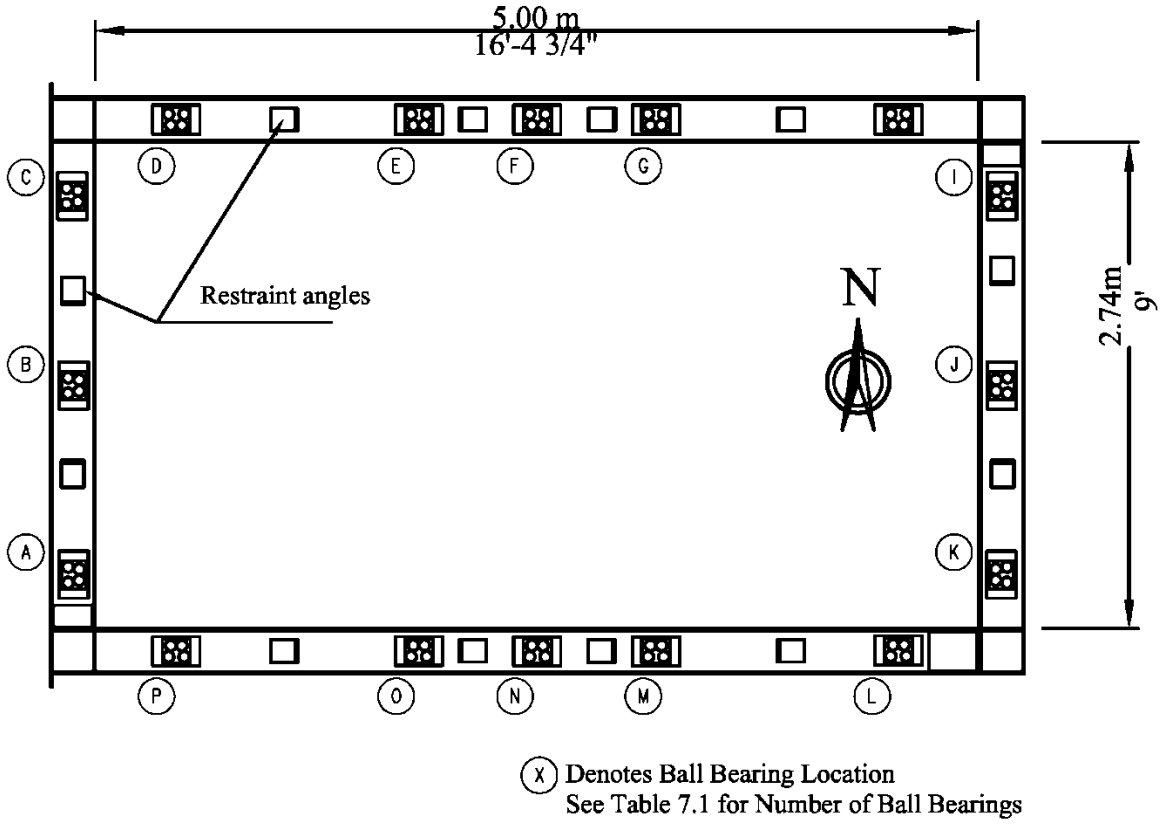

Fig. 7.2 Layout of ball bearings and internal angles distribution

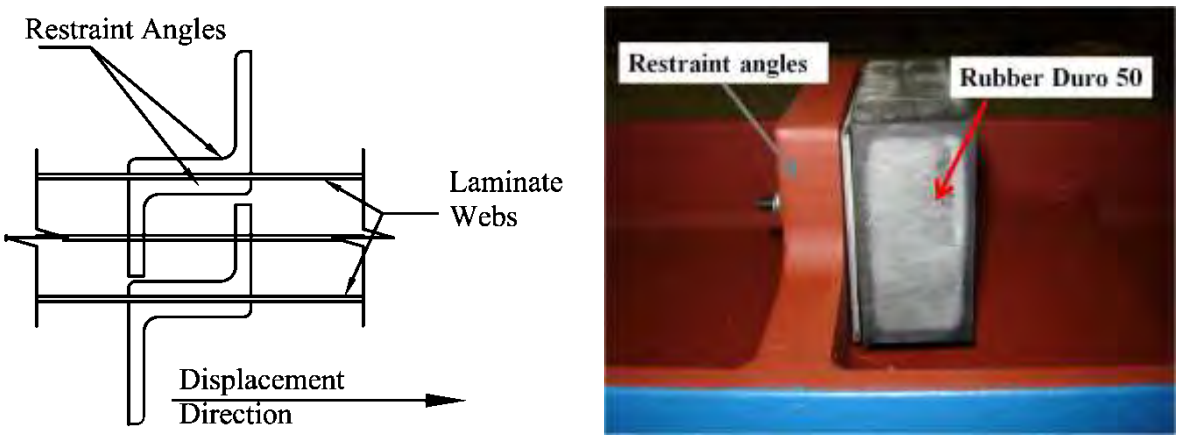

(a) A pair of Internal angles (b) Fabricated angle

Fig. 7.3 Internal restraint angles

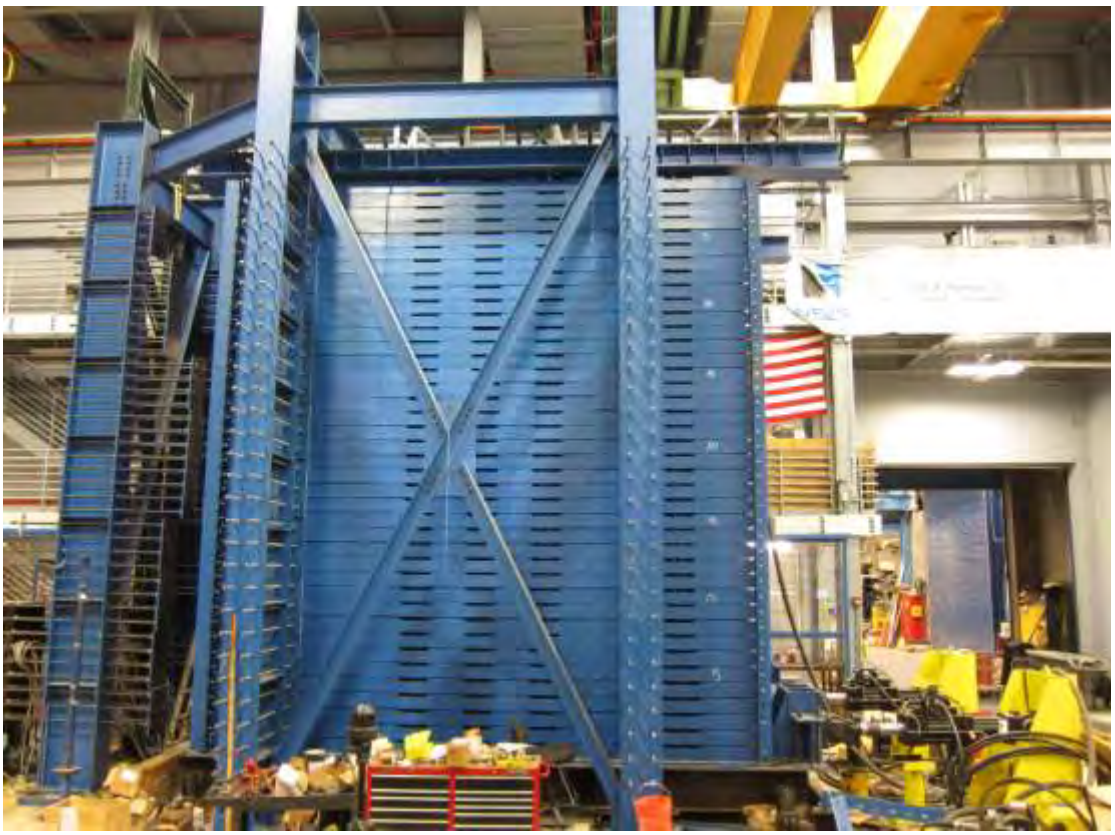

Fig. 7.4 Snapshot of laminar box

A snapshot of the final stack up of the laminar box is presented in Fig. 7.4.

Table 7.1 Number of ball bearings per location

	Location																
Laminate #	A	B	C	D	E	F	G	H	I	J	K	L	M	N	O	P	Weight (kN)
L39	1	1	1	1	1	0	1	1	1	1	1	1	1	0	1	1	9.7
L38	1	1	1	1	1	0	1	1	1	1	1	1	1	0	1	1	9.7
L37	1	1	1	1	1	0	1	1	1	1	1	1	1	0	1	1	9.7
L36	1	1	1	1	1	0	1	1	1	1	1	1	1	0	1	1	9.7
L35	1	1	1	1	1	0	1	1	1	1	1	1	1	0	1	1	9.7
L34	1	1	1	1	1	0	1	1	1	1	1	1	1	0	1	1	9.7
L33	1	1	1	1	1	0	1	1	1	1	1	1	1	0	1	1	9.7
L32	1	1	1	1	1	0	1	1	1	1	1	1	1	0	1	1	9.7
L31	1	1	1	1	1	0	1	1	1	1	1	1	1	0	1	1	9.7
L30	2	2	2	2	2	0	2	2	2	2	2	2	2	0	2	2	9.8
L29	2	2	2	2	2	0	2	2	2	2	2	2	2	0	2	2	9.8
L28	2	2	2	2	2	0	2	2	2	2	2	2	2	0	2	2	9.8
L27	2	2	2	2	2	0	2	2	2	2	2	2	2	0	2	2	9.8
L26	2	2	2	2	2	0	2	2	2	2	2	2	2	0	2	2	9.8
L25	2	2	2	2	2	0	2	2	2	2	2	2	2	0	2	2	9.8
L24	2	2	2	2	2	0	2	2	2	2	2	2	2	0	2	2	9.8
L23	2	2	2	2	2	0	2	2	2	2	2	2	2	0	2	2	9.8
L22	2	2	2	2	2	0	2	2	2	2	2	2	2	0	2	2	9.8
L21	3	3	3	3	3	0	3	3	3	3	3	3	3	0	3	3	10.0
L20	3	3	3	3	3	0	3	3	3	3	3	3	3	0	3	3	10.0
L19	3	3	3	3	3	0	3	3	3	3	3	3	3	0	3	3	10.0
L18	3	3	3	3	3	0	3	3	3	3	3	3	3	0	3	3	10.0
L17	3	3	3	3	3	0	3	3	3	3	3	3	3	0	3	3	10.0
L16	3	3	3	3	3	0	3	3	3	3	3	3	3	0	3	3	10.0
L15	3	3	3	3	3	0	3	3	3	3	3	3	3	0	3	3	10.0
L14	3	3	3	3	3	0	3	3	3	3	3	3	3	0	3	3	10.0
L13	4	4	4	4	4	0	4	4	4	4	4	4	4	0	4	4	10.2
L12	4	4	4	4	4	0	4	4	4	4	4	4	4	0	4	4	10.2
L11	4	4	4	4	4	0	4	4	4	4	4	4	4	0	4	4	10.2
L10	4	4	4	4	4	0	4	4	4	4	4	4	4	0	4	4	10.2
L9	4	4	4	4	4	0	4	4	4	4	4	4	4	0	4	4	10.2
L8	4	4	4	4	4	0	4	4	4	4	4	4	4	0	4	4	10.2
L7	4	4	4	4	4	0	4	4	4	4	4	4	4	0	4	4	10.2
L6	4	4	4	4	4	0	4	4	4	4	4	4	4	0	4	4	10.2
L5	6	6	6	6	4	0	4	6	6	6	6	6	4	0	4	6	10.4
L4	6	6	6	6	4	0	4	6	6	6	6	6	4	0	4	6	11.4
L3	6	6	6	6	4	0	4	6	6	6	6	6	4	0	4	6	11.4
L2	6	6	6	6	4	0	4	6	6	6	6	6	4	0	4	6	11.4
L1	6	6	6	6	4	0	4	6	6	6	6	6	4	0	4	6	11.4
Base(L0)	6	6	6	6	4	0	4	6	6	6	6	6	4	0	4	6	26.1

Two membrane containment bags made of 45 mil ethylene propylene diene monomer (EPDM) are placed inside the box. Prior to the placement of membrane bags, four 60 mil thick EPDM pieces are hung at the inner sides of laminate L39 and one EPDM piece is placed on top of the base shaker under the outer membrane bag to protect the membrane bags. Another protective EPDM piece is put on the bottom side of the inner membrane bag. Fig. 7.5 shows a snapshot of the protective EPDM piece and membrane bags.

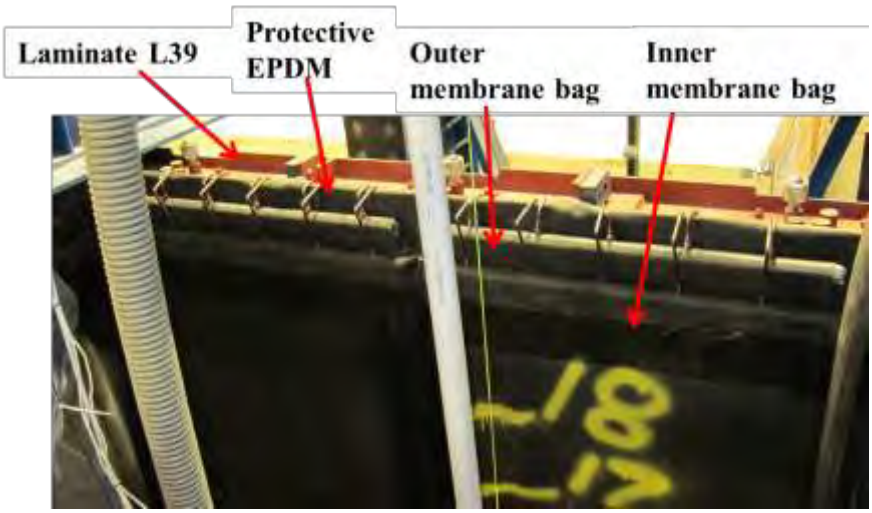

Fig. 7.5 Protective membrane and membrange bags

Fig. 7.6 shows the bottom layout of the laminar box. A perforated pipe grid is placed horizontally on the bottom of the laminar box to provide for instrumentation tie-down. A layer of 1.27cm (0.5 inch) thick plywood is laid on top of the protective EPDM piece under the pipe grid. Geotextile cloth is wrapped around the pipe grid to prevent sand depositing through holes.

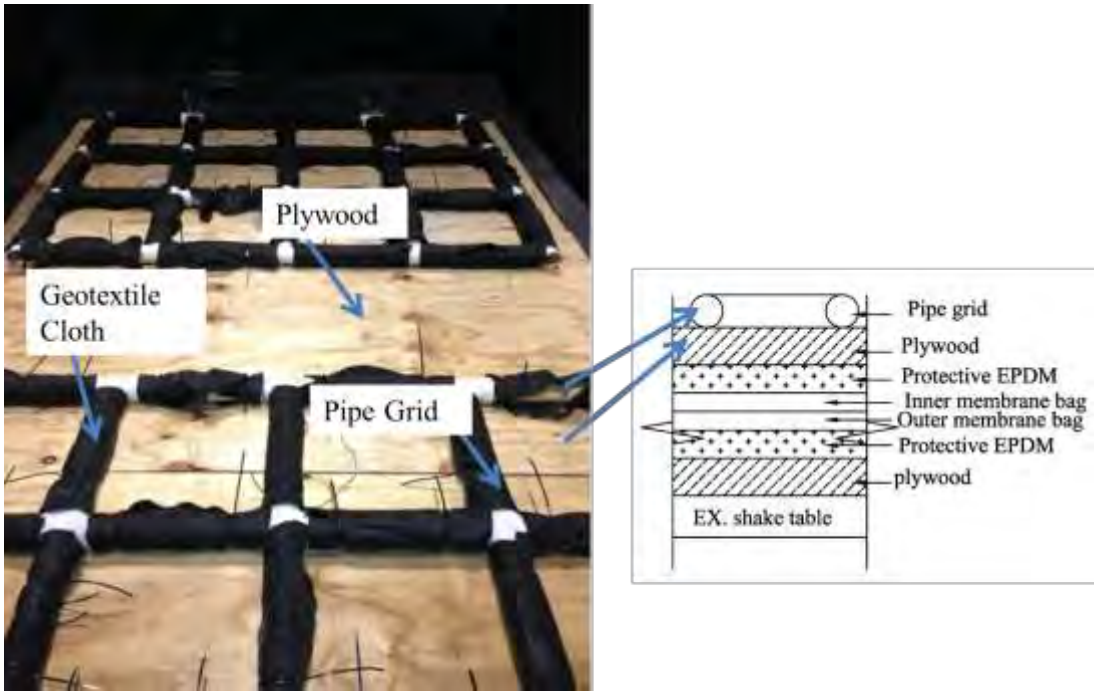

Fig. 7.6 Bottom layout of laminar box

7.2.2. Base shaker and actuators

The laminar base ring (L0) is bolted to the base shaker placed on the strong floor of SEESL. Further information of the base shaker can be referred to Bethapudi (2008) and Thevanayagam et al. (2009). Two computer-controlled MTS actuators are employed to provide shaking or seismic motion. Each actuator, mounted to the rigid reaction block and tied to the base shaker (Fig. 7.7), is capable of 900 KN, and powered by four MTS pumps each having flow capacity of 12 liters/s and working pressure of 20.7 MPa.

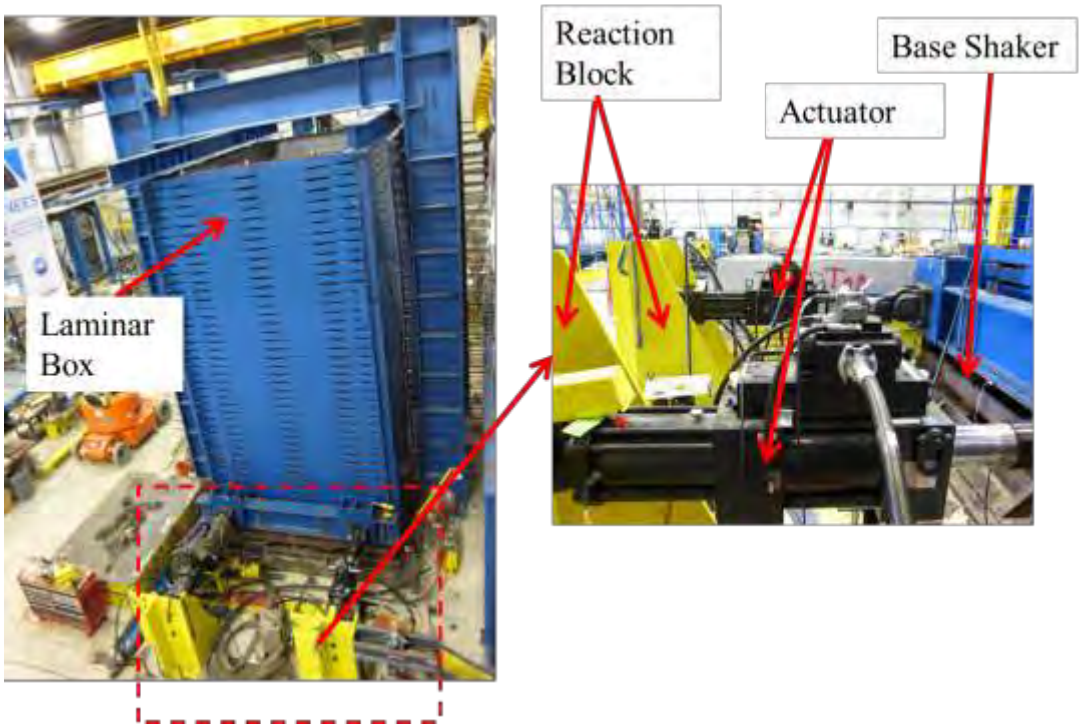

Fig. 7.7 Connection of actuators to base shaker

7.2.3. Bracing frame system

A bracing frame system attached to the strong floor is located at northern, southern and eastern side around the laminar box with restrainer beams on top of the L39.

A schematic layout of the bracing system is shown in Fig. 7.8. The bracing system is comprised of six columns (two in northern, two in southern and two in eastern direction) equipped with prestressed LEE springs (series LHL2000B) through steel rods suitable for a variety of testing configurations. A snapshot of the bracing frame system in northern direction can be seen in Fig. 7.4. Four I-beams (two transverse cross beams and two longitudinal beams) are placed on top of L39 for the anti-uplifting purpose of laminar box.

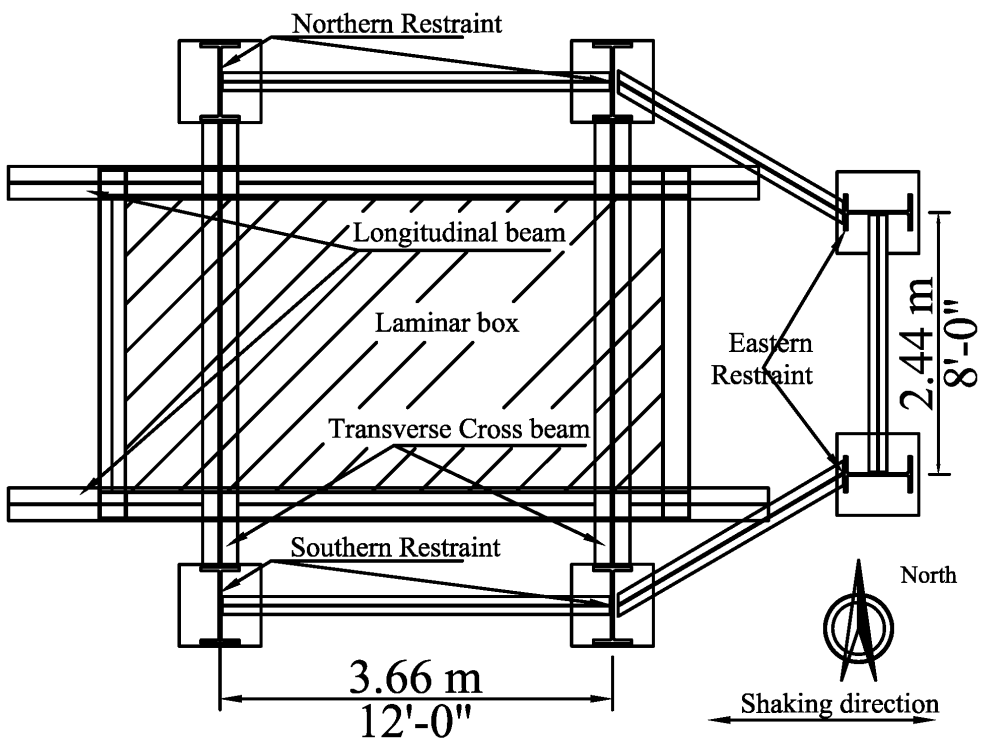

Fig. 7.8 Plan view of bracing system

7.3. Instrumentation for liquefaction test series-LG1

An instrumentation bridge is placed on top of the box, together with the pipe grid placed on the bottom of the laminar box, to provide the instrumentation positioning.

7.3.1. Instrumentation plan

Table 7.2 and Table 7.3 summarize the instrumentation sensors employed for LG1. Fig. 7.9 shows the locations and elevations of the sensors. Cartesian coordinate (0,0,0) denotes the center of box at the top of L39. x denotes the measured longitudinal distance from the center of the box (east positive) and y represents the measured transverse distance from the center of box (north positive). z indicates the measured vertical distance from the top of L39 (downwards positive) while D indicates the measure vertical distance from the top of ground surface after filling the box

with sand (downwards positive). The elevation is the measured vertical distance from the bottom of laminar box base (L0) (upward positive).

Table 7.2 Instrumentation summary

Instruments	Quantity	Model
✪ 3D-SAA (SAA)	2	Measurand Inc.
■ P-Piezometers (P)	16	GE-PDCR81 and Kulite XCL-11-250-50A
✦X-Acc (Ring and base)(AE,AW,B)	22	Honeywell Sensotec 10G
⬠Y-Acc (Ring and base) (AE,B)	9	
◄—X-Potentiometers (H)	20	MTS-Tempsonics-011004050207
⊗ Z-Potentiometers (V)	3	Space Age Control Inc.
● Settlement Plate (SP)	3	PN-62-55-7171
Cameras (CA)	4	CA2 CA3 CA4: Go Pro

A total of 16 Piezometers (P), 2 high-band width ShapeAccelArray (SAA) sensors [Fig. 7.10 (a)] are placed inside the laminar box. Three ground surface settlement plates connected to potentiometers on the instrumentation bridge (V) are placed on the top surface of the sand. A total of 25 accelerometers (AE, AW) and 19 horizontal displacement sensors (H) [Fig. 7.10 (b)] are placed on selected laminates. Six accelerometers (B) and one horizontal displacement sensor (H) are placed on the based shaker.

Table 7.3 Instrumentation locations (Cameras not included)

Laminate (Ring) #	Depth (m)	Coor.	East						North				West					South					
			Soil			Ring			Soil		Ring		soil		Ring			soil				Ring	
		x (ft)	0	5.17	3.67	8.5			-3.83	0	-8.5		-2.17	-2.5	-8.5	-8.5		-3.83	1.17	0	-3.67	8.5	
		y (ft)	-0.25	-0.25	-0.25	0			-0.25	-0.25	4.5		-0.25	-0.25	0	-4.5		-1.75	-1.8	-1.75	-1.75	-4.5	
Top		z (ft)	SAA1	Z-Pot	PPT	X-Acc	Y-Acc	X-Pot	Z-Pot	Z-Pot	X-Acc	Y-Acc	PPT	SAA2	X-Acc	X-Acc	Y-Acc	SP	SP	PPT	SP	X-Acc	Y-Acc
	-1.22	0.0																					
39	-1.07	0.5																SP2	SP1		SP3		
38	-0.91	1.0																					
37	-0.76	1.5				AE37X																	
36	-0.61	2.0																					
35	-0.46	2.5				AE35X	AE35Y								AW35X								
34	-0.30	3.0																					
33	-0.15	3.5																					
32	0.00	4.0		V3					V1	V2	Soil Surface					Soil Surface							
31	0.15	4.5						H31X												P14			
30	0.30	5.0			P7	AE30X	AE30Y								AW30X								
29	0.46	5.5						H29X												P13			
28	0.61	6.0																					
27	0.76	6.5				AE27X		H27X															
26	0.91	7.0																					
25	1.07	7.5			P6&16	AE25X		H25X							AW25X					P12&15			
24	1.22	8.0																					
23	1.37	8.5						H23X															
22	1.52	9.0																					
21	1.68	9.5			P8			H21X															
20	1.83	10.0				AE20X	AE20Y								AW20X					P11			
19	1.98	10.5						H19X															
18	2.13	11.0											P3										
17	2.29	11.5						H17X															
16	2.44	12.0																					
15	2.59	12.5			P5	AE15X		H15X												P10			
14	2.74	13.0																					
13	2.90	13.5						H13X															
12	3.05	14.0																					
11	3.20	14.5						H11X															
10	3.35	15.0				AE10X	AE10Y								AW10X								
9	3.51	15.5						H9X															
8	3.66	16.0											P2										
7	3.81	16.5						H7X															
6	3.96	17.0						H6X															
5	4.11	17.5				AE5X	AE5Y	H5X							AW5X					P9			
4	4.27	18.0						H4X															
3	4.42	18.5						H3X					P1										
2	4.57	19.0			P4	AE2X		H2X															
1	4.72	19.5				AE1X		H1X							AW1X								
0 (fixed)	4.88	20.0				AE0X	AE1Y	H0X															
Base											B2X	B2Y				B1X	B1Y					B3X	B3Y

SAA 45704

SAA 45886

Depth=measured vertical distance from top of soil surface (Downward positive)

z=Distance from top of ring/laminate 39 (Downward positive)

x=measured horizontal distance from center of soil box (East positive)

y=measured horizontal distance from center of soil box (North positive)

Positive Direction:
H0X, H17X: West
Other H(No.)X: East
B1X,B2X,AW(No.)X: West
B3X, AE(No.)X: East
B1Y,B2Y,AW(No.)Y: South
B3Y AE(No.)Y: North

X direction:
SAA-45704: East
SAA-45886: East

AE0X ADDED FROM TEST 4
H0X ADDED FROM TEST 4

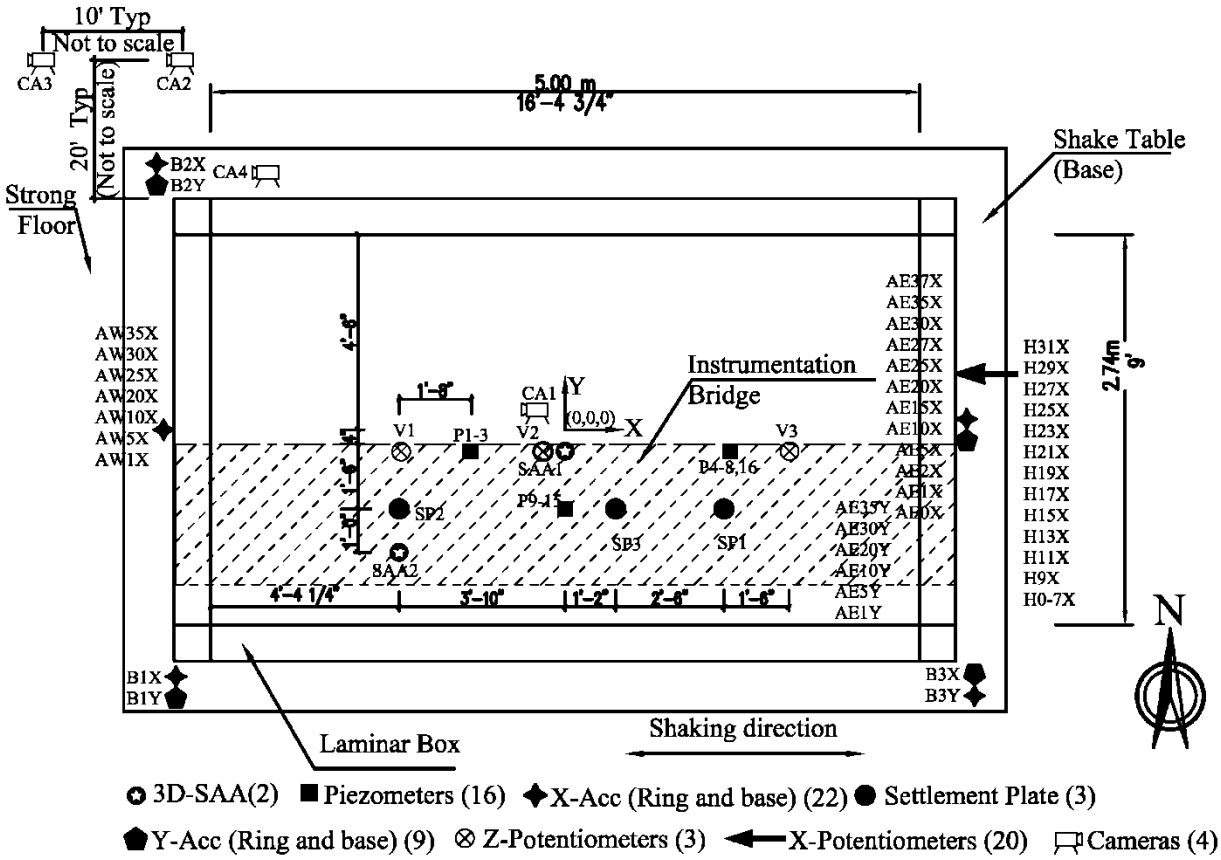

(a) Plan view

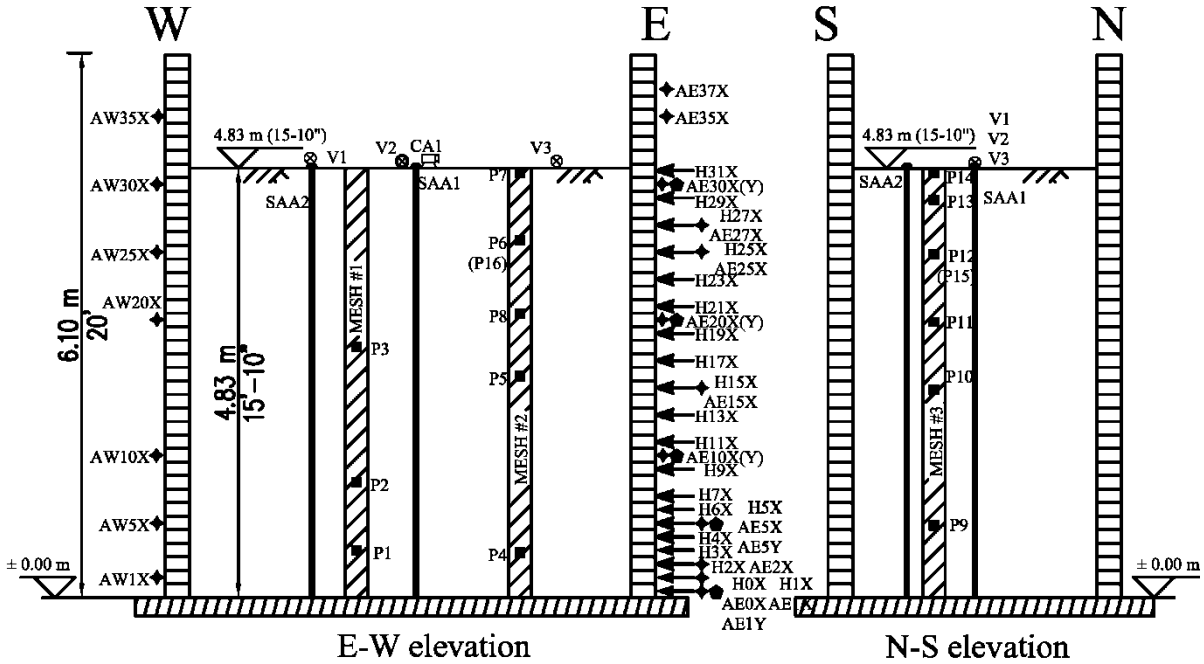

(b) Elevation view

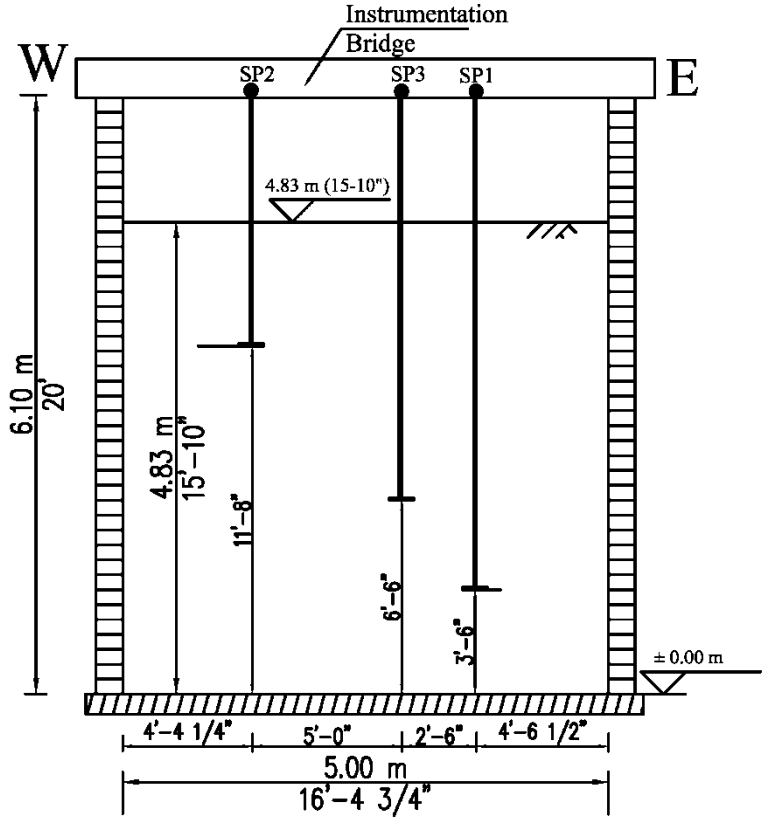

(c) Settlement plates

Fig. 7.9 Instrumentation plan

Four digital cameras are used to record the soil motion during shaking as well (see Fig. 7.9(a) for locations). Fig. 7.11 shows the captured views from four cameras used for the liquefaction experiments. CA1 [Fig. 7.11(a)] is mounted on the lab ceiling above the box to view the top sand surface. There are 40 markers, each located at center of laminate, are made prior to the liquefaction tests. CA2 [Fig. 7.11(b)] is positioned at the front of 40 markers to record the motion of each marker during shaking. The recorded video can be digitized for the horizontal displacement of soil during shaking. CA3 [Fig. 7.11(c)] is located at the north-west corner of laminar box, to monitor the motion of the entire laminar box during shaking. CA4 [Fig. 7.11(d)] is clamped on the shake table to monitor the motion of bottom laminates more closely during shaking.

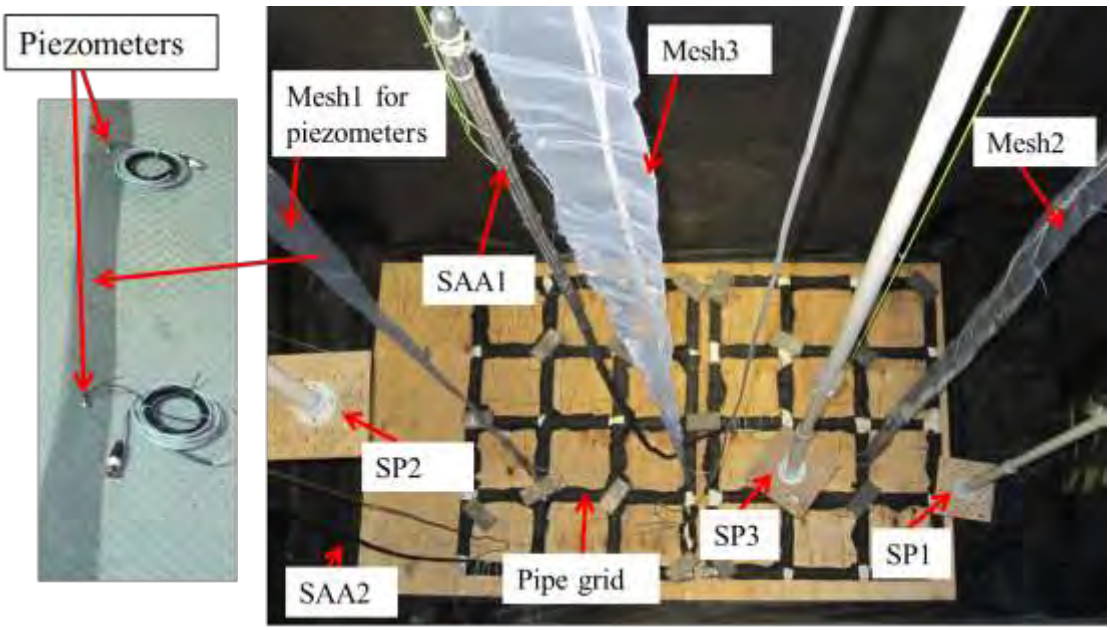

(a)

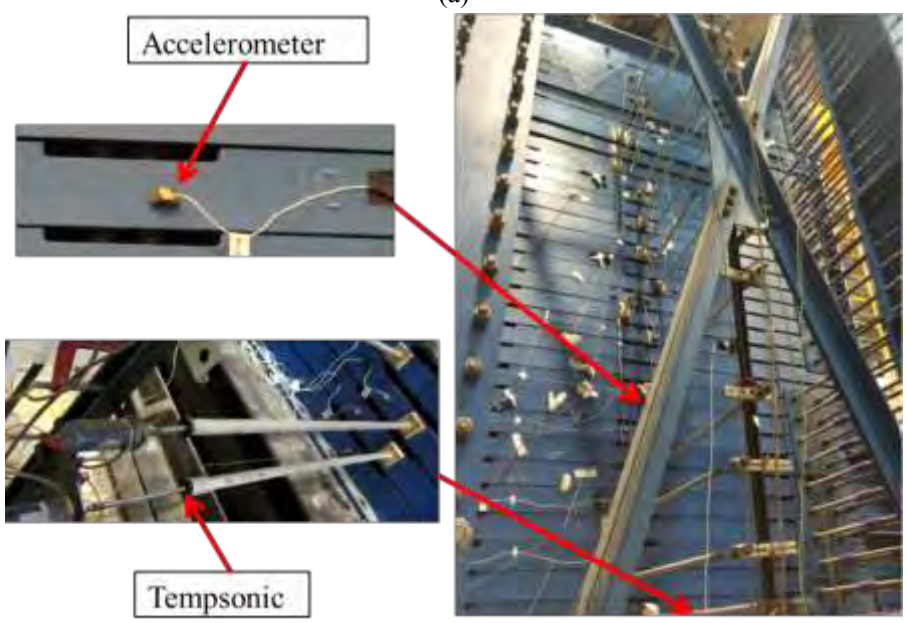

(b)

Fig. 7.10 Sensors in laminar box

(a) CA1-Ttop view

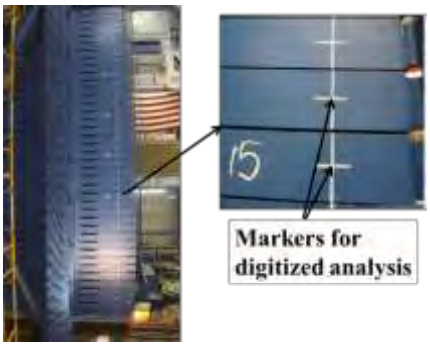

(b) CA2-Side view of markers on the laminates

(c) CA3-Side view

(d) CA4-Bottom to top upward view

Fig. 7.11 Captured views from digital cameras

A special instrument (settlement plate-SP) using potentiometer is developed to record the settlement of soil at three elevations during hydraulic filling, which is detailed in section7.4.2.

7.3.2. Summary of sensor working conditions after liquefaction experiments

This section summarizes the working conditions of sensors immediately after installation, during sand filling and prior to, during and after shaking events. The working conditions of piezometers (P) are summarized in Table 7.4. For the 16 piezometer employed in the liquefaction tests, only 4 (P1, P2, P3 and P14) survived at the end. Table 7.5 presents the working conditions of potentiometers, temposonics (V, H and SP) and SAAs. H0X was added after liquefaction test 4 (T4). H7X malfunctioned after T24 and H21X was faulty from T1. SAA1 (serial number: 45704)

was not recognized by the software after T3. Table 7.6 shows the summary of working conditions of accelerometers. CA4 was added after T3 and all of the digital cameras are working after T52.

Table 7.4 Working conditions of piezometers

Sensor Name	Sensor Type	Manufacturer	Calibration Date	Latest Check Date	Malfunction Date	Note	Working
P1	pressure-PDCR81	GE-Druck	12/1/12	10/18/13	-	Working after T 52, pwp dissipation not recorded after shaking from T1 through T3, recorded from T4 through T52	Y
P2	pressure-PDCR81	GE-Druck	12/1/12	10/18/13	-	Working after T52, pwp dissipation not recorded after shaking from T1 through T3, recorded from T4 through T52	Y
P3	pressure-PDCR81	GE-Druck	12/1/12	10/18/13	-	Working after T52, pwp dissipation not recorded after shaking from T1 through T3, recorded from T4 through T52	Y
P4	pressure-PDCR81	GE-Druck	12/1/12	10/18/13	10/9/13	Read full scale after T10 (worked unit T10), pwp dissipation not recorded after shaking from T1 through T3, recorded from T4 through T10	N
P5	pressure-PDCR81	GE-Druck	12/1/12	10/18/13	9/23/13	Read full scale on 09/23/2013	N
P6	pressure-XCL-11-250-50A	Kulite	12/1/12	10/18/13	9/19/13	Read full scale on 09/19/2013	N
P7	pressure-XCL-11-250-50A	Kulite	12/1/12	10/18/13	10/3/13	Read full scale on Test 1	N
P8	pressure-XCL-11-250-50A	Kulite	12/1/12	10/18/13	9/19/13	Read full scale on 09/19/2013	N
P9	pressure-XCL-11-250-50A	Kulite	12/1/12	10/18/13	10/3/13	Read full scale on T1	N
P10	pressure-XCL-11-250-50A	Kulite	12/1/12	10/18/13	10/3/13	Reading not changed on T2 and T3	N
P11	pressure-XCL-11-250-50A	Kulite	12/1/12	10/18/13	9/24/13	Read full scale on 09/24/2013	N
P12	pressure-XCL-11-250-50A	Kulite	12/1/12	10/18/13	9/23/13	Read full scale on 09/23/2013	N
P13	pressure-XCL-11-250-50A	Kulite	12/1/12	10/18/13	10/8/13	Read full scale after T3 (Woked unitl T3),pwp dissipation not recorded after shaking from T1 through T3	N
P14	pressure-XCL-11-250-50A	Kulite	12/1/12	10/18/13	?	Exposed in the aired after T29	?
P15	pressure-XCL-11-250-50A	Kulite	7/1/13	10/18/13	10/18/13	Not active in T1 through T3 and T32a through T38, Full scale after T50 (Worked until T50)	N
P16	pressure-XCL-11-250-50A	Kulite	7/1/13	10/18/13	10/8/13	Not active in T1 through T3, read full scale on T4	N

Table 7.5 Working conditions of potentiometers, temposonics and SAAs

Sensor Name	Sensor Type	Manufacturer	Calibration Date	Latest Check Date	Malfunction Date	Note	Working
H0X	Potentiometer-PN-62-55-7171	SpaceAge Control Inc.	10/7/13	10/18/13	-	Added after T3. working after T52	Y
H1X	Temposonics-011004050207	MTS	4/18/13	10/18/13	-	working after T52	Y
H2X	Temposonics-011004050207	MTS	4/18/13	10/18/13	-	working after T52	Y
H3X	Temposonics-011004050207	MTS	4/18/13	10/18/13	-	working after T52	Y
H4X	Temposonics-011004050207	MTS	4/18/13	10/18/13	-	working after T52	Y
H5X	Temposonics-011004050207	MTS	4/18/13	10/18/13	-	working after T52	Y
H6X	Temposonics-011004050207	MTS	4/18/13	10/18/13	-	working after T52	Y
H7X	Temposonics-011004050207	MTS	4/18/13	10/18/13	10/15/13	faulty on T25a	N
H9X	Temposonics-011004050207	MTS	4/18/13	10/18/13	-	working after T52	Y
H11X	Temposonics-011004050207	MTS	4/18/13	10/18/13	-	working after T52	Y
H13X	Temposonics-011004050207	MTS	4/18/13	10/18/13	-	working after T52	Y
H15X	Temposonics-011004050207	MTS	4/18/13	10/18/13	-	working after T52	Y
H17X	Temposonics-011004050207	MTS	4/18/13	10/18/13	-	working after T52	Y
H19X	Temposonics-011004050207	MTS	4/18/13	10/18/13	-	working after T52	Y
H21X	Temposonics-011004050207	MTS	4/18/13	10/18/13	10/3/13	faulty from T1	N
H23X	Temposonics-011004050207	MTS	4/18/13	10/18/13	-	working after T52	Y
H25X	Temposonics-011004050207	MTS	4/18/13	10/18/13	-	working after T52	Y
H27X	Temposonics-011004050207	MTS	4/18/13	10/18/13	-	working after T52	Y
H29X	Temposonics-011004050207	MTS	4/18/13	10/18/13	-	working after T52	Y
H31X	Temposonics-011004050207	MTS	4/18/13	10/18/13	-	working after T52	Y
SP1	Potentiometer-PN-62-55-7171	SpaceAge Control Inc.	12/1/12	10/18/13	-	Reading abandoned during entire shaking event	Y
SP2	Potentiometer-PN-62-55-7171	SpaceAge Control Inc.	12/1/12	10/18/13	-	Reading abandoned during entire shaking event	Y
SP3	Potentiometer-PN-62-55-7171	SpaceAge Control Inc.	12/1/12	10/18/13	-	Reading abandoned during entire shaking event	Y
V1	Potentiometer-PN-62-55-7171	SpaceAge Control Inc.	12/1/12	10/18/13	-	Replaced after T3, moved to ground surface, Removed for C50 and placed on the original location for T51 and T52	Y
V2	Potentiometer-PN-62-55-7171	SpaceAge Control Inc.	12/1/12	10/18/13	-	Buried in sand after T2	Y
V3	Potentiometer-PN-62-55-7171	SpaceAge Control Inc.	12/1/12	10/18/13	-	Replaced after T3, remained at the original position.	Y
SAA-45704	Multiple purposes measurements	Measurand	-	10/18/13	10/8/13	Not recognized by the software	N
SAA-45886	Multiple purposes measurements	Measurand	-	10/18/13	-	working after Test 52	Y

Note: Temposonic is another type of potentiometer

Table 7.6 Working conditions of accelerometers

Sensor Name	Sensor Type	Manufacturer	Calibration Date	Latest Check Date	Malfunction Date	Note	Working
B1X	Acceleration-Sensotec 10G	Honeywell	12/1/12	10/18/13	-	Working after T52	Y
B2X	Acceleration-Sensotec 10G	Honeywell	12/1/12	10/18/13	-	Working after T52	Y
B3X	Acceleration-Sensotec 10G	Honeywell	12/1/12	10/18/13	-	Working after T52	Y
B1Y	Acceleration-Sensotec 10G	Honeywell	12/1/12	10/18/13	-	Working after T52	Y
B2Y	Acceleration-Sensotec 10G	Honeywell	12/1/12	10/18/13	-	Working after T52	Y
B3Y	Acceleration-Sensotec 10G	Honeywell	12/1/12	10/18/13	-	Working after T52	Y
AE0X	Acceleration-Sensotec 10G	Honeywell	10/7/13	10/18/13	-	Added after T3, Working after T52	Y
AE1X	Acceleration-Sensotec 10G	Honeywell	12/1/12	10/18/13	-	Working after T52	Y
AE2X	Acceleration-Sensotec 10G	Honeywell	12/1/12	10/18/13	-	Working after T52	Y
AE5X	Acceleration-Sensotec 10G	Honeywell	10/7/13	10/18/13	-	Not reading in T1 through T3, checked on 2013/10/08 before T4, working from T4 through T52	Y
AE10X	Acceleration-Sensotec 10G	Honeywell	12/1/12	10/18/13	-	Working after T52	Y
AE15X	Acceleration-Sensotec 10G	Honeywell	12/1/12	10/18/13	-	Working after T52	Y
AE20X	Acceleration-Sensotec 10G	Honeywell	12/1/12	10/18/13	-	Working after T52	Y
AE25X	Acceleration-Sensotec 10G	Honeywell	12/1/12	10/18/13	-	Working after T52	Y
AE27X	Acceleration-Sensotec 10G	Honeywell	12/1/12	10/18/13	-	Working after T52	Y
AE30X	Acceleration-Sensotec 10G	Honeywell	12/1/12	10/18/13	-	Working after T52	Y
AE35X	Acceleration-Sensotec 10G	Honeywell	12/1/12	10/18/13	-	Working after T52	Y
AE37X	Acceleration-Sensotec 10G	Honeywell	N/A	10/18/13	-	Inactive in LG1	-
AW1X	Acceleration-Sensotec 10G	Honeywell	12/1/12	10/18/13	-	Working after T52	Y
AW5X	Acceleration-Sensotec 10G	Honeywell	12/1/12	10/18/13	-	Working after T52	Y
AW10X	Acceleration-Sensotec 10G	Honeywell	12/1/12	10/18/13	-	Working after T52	Y
AW20X	Acceleration-Sensotec 10G	Honeywell	12/1/12	10/18/13	-	Working after T52	Y
AW25X	Acceleration-Sensotec 10G	Honeywell	12/1/12	10/18/13	-	Working after T52	Y
AW30X	Acceleration-Sensotec 10G	Honeywell	12/1/12	10/18/13	-	Working after T52	Y
AW35X	Acceleration-Sensotec 10G	Honeywell	12/1/12	10/18/13	-	Working after T52	Y
AE1Y	Acceleration-Sensotec 10G	Honeywell	12/1/12	10/18/13	-	Moved from L1 TO L0 after T17, Working after T52	Y
AE5Y	Acceleration-Sensotec 10G	Honeywell	12/1/12	10/18/13	-	Working after T52	Y
AE10Y	Acceleration-Sensotec 10G	Honeywell	12/1/12	10/18/13	-	Working after T52	Y
AE20Y	Acceleration-Sensotec 10G	Honeywell	12/1/12	10/18/13	-	Working after T52	Y
AE30Y	Acceleration-Sensotec 10G	Honeywell	12/1/12	10/18/13	-	Working after T52	Y
AE35Y	Acceleration-Sensotec 10G	Honeywell	12/1/12	10/18/13	-	Working after T52	Y

7.4. Hydraulic filling

The soil used in the laminar box experiment is OS F55 sand. Fig. 7.12 shows the hydraulic pumping and sand placement method, which was fully described by Ecemis (2008) and Thevanayagam et al. (2009). To achieve a sand deposit of D_r≈40-50%, the water level to be maintained above sand inside the box is approximately 0.6 m and the sand diffuser pipe above water is approximately 0.3 m. Actual level readings were recorded typically every 30-45 minutes.

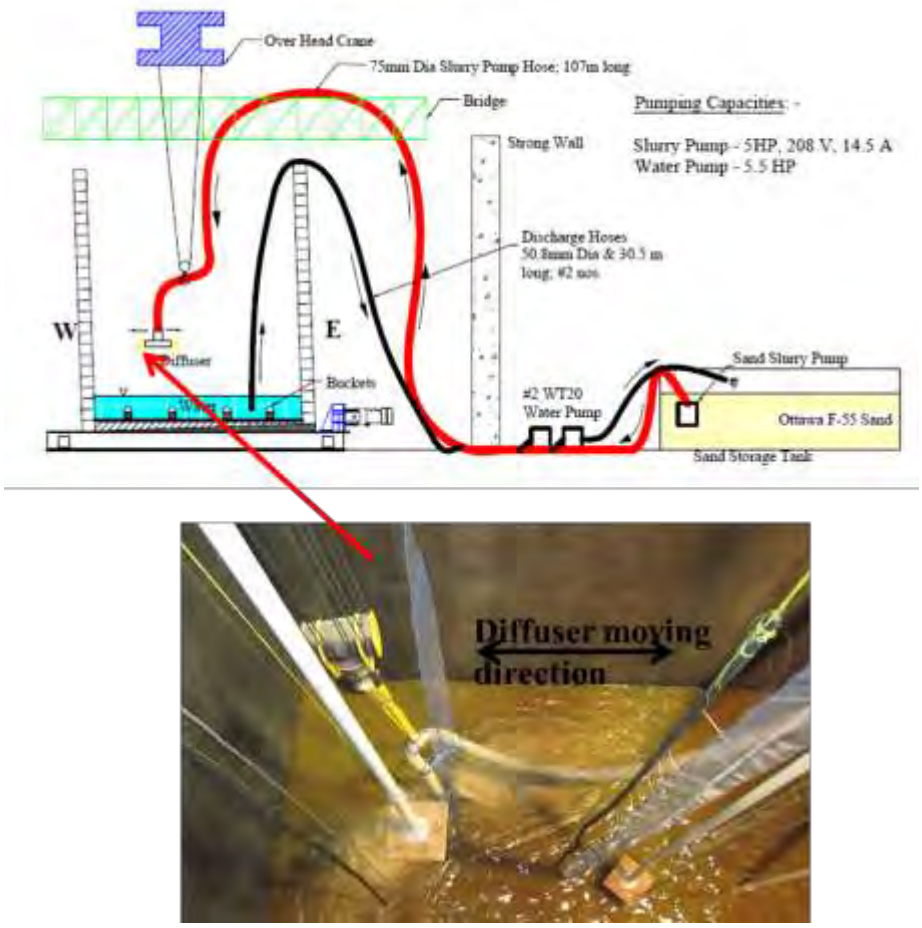

Fig. 7.12 Setup of close loop hydraulic filling

Fig. 7.13(a) shows the water level and the sand level elevations from the bottom of laminate L0. Fig. 7.13(b) compares the targeted water level as well as the actual water level maintained

above the sand level. The final sand filling height for LG1 is about 4.83m.

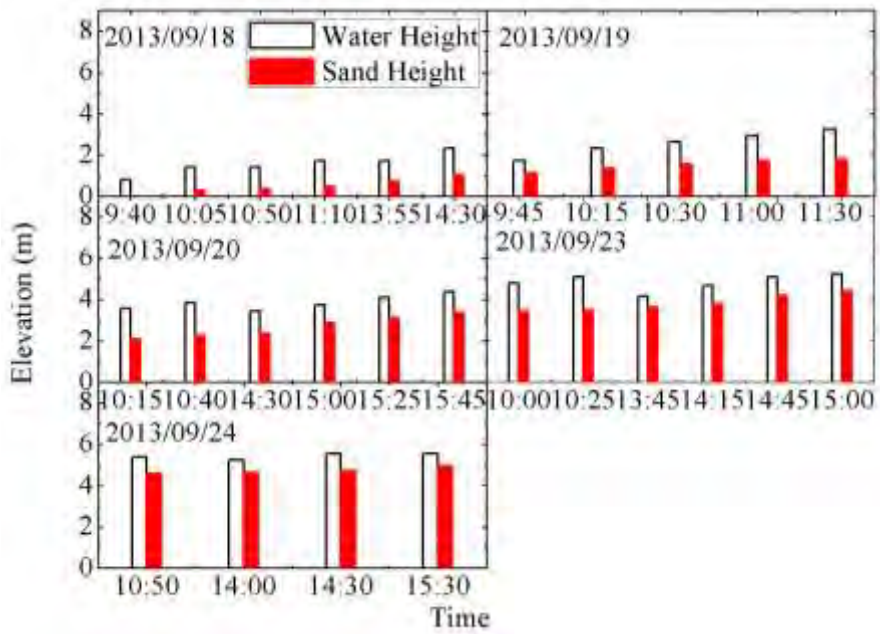

(a)

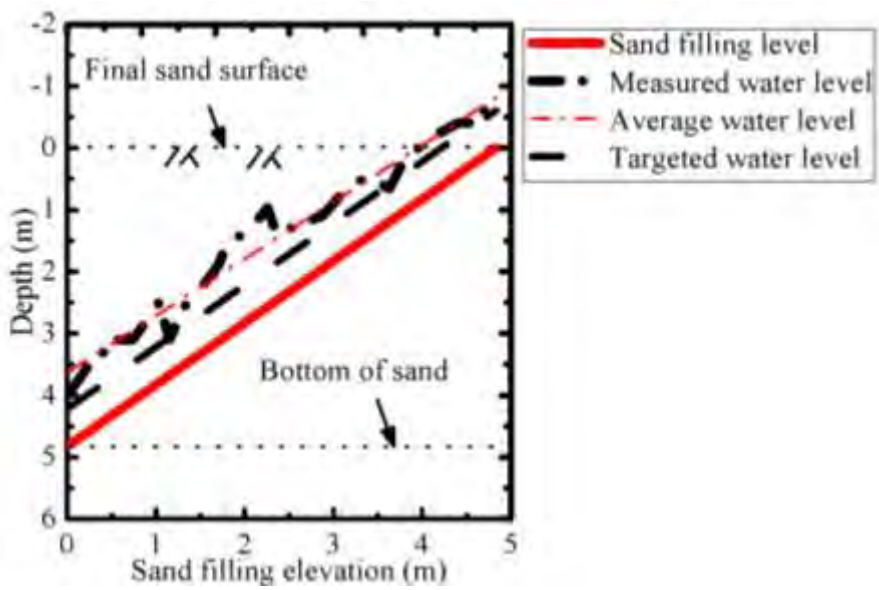

(b)

Fig. 7.13 Sand and water level during hydraulic filling

7.4.1. Bucket density tests

The in-situ relative density of sand deposit was monitored at several elevations during hydraulic placement using typically 15 cm diameter and 15 cm high metal buckets placed at the

locations shown in Fig. 7.14. The bucket density tests were only performed in the southern side of the box due to the space limitation of instrumentation beam and the operational room of hydraulic filling system. After each bucket is filled, it is slowly taken out. It is noticed that the bucket sample could easily be disturbed and densified if not retrieved from the box timely or subjected to minor vibration during the retrieval process. With this regard, the suspiciously disturbed sample is abandoned and the bucket is immediately placed into the box for the next sample collection. For this reason, the density and void ratio calculated using the bucket data should be considered approximate. Table 7.7 presents the void ratio and the corresponding relative density of the samples collected.

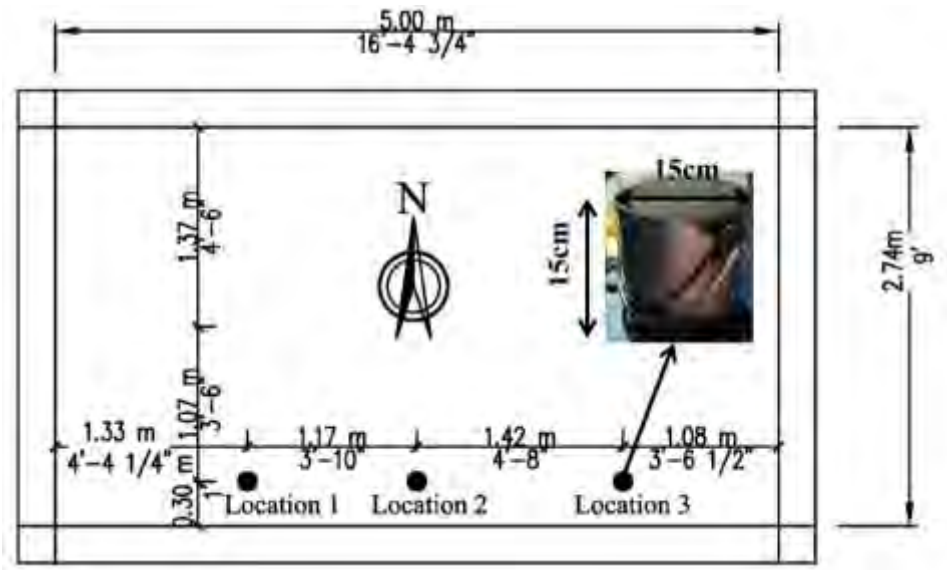

Fig. 7.14 Plan view-bucket density test locations

Table 7.7 Bucket density data

Bucket Elevation (m)	Depth (m)	Location	e	D_r (%)	Average D_r (%)
4.27	0.56	1	0.719	42	38
4.27	0.56	2	0.722	40	
4.27	0.56	3	0.739	32	
3.66	1.17	1	0.750	26	29
3.66	1.17	2	0.739	32	
3.66	1.17	3	0.745	29	
3.05	1.78	1	0.746	28	36
3.05	1.78	3	0.714	45	
2.44	2.39	1	0.719	42	39
2.44	2.39	2	0.752	25	
2.44	2.39	3	0.706	49	
1.83	3.00	1	0.716	44	39
1.83	3.00	2	0.748	27	
1.83	3.00	3	0.714	45	
0.91	3.92	1	0.746	28	28
0.91	3.92	3	0.746	28	

7.4.2. Sand settlement during filling

Three settlement plates (SPs) are used to measure the settlement of sand during hydraulic filling. The elevations and locations of settlement plate are shown in Fig. 7.9(a) and (c).

7.4.2.1. Settlement plate components

Fig. 7.15(a) to (c) show a schematic view of the settlement plate system. A short (typically 50 cm in length) supporting PVC pipe [5.0 cm inner diameter (ID)] is mounted to a perforated plywood plate at the bottom. A compressible sponge fills nearly half of the inner space of the supporting PVC pipe. A long inner PVC pipe with a smaller ID (3.81 cm) is installed freely in the inner side of the supporting pipe sitting on the sponge. The intersection of the supporting pipe (5.0 cm ID) and the inner pile (3.81 cm ID) is covered by a plastic bag to keep sand flowing into the

pipes. A string attached to the bottom plywood plate runs through the pipes to reach the top of the inner pipe and connects to a potentiometer. Fig. 7.15(a) shows the components of the settlement plate system. Fig. 7.15(b) and (c) show the bottom and the top of the system, respectively.

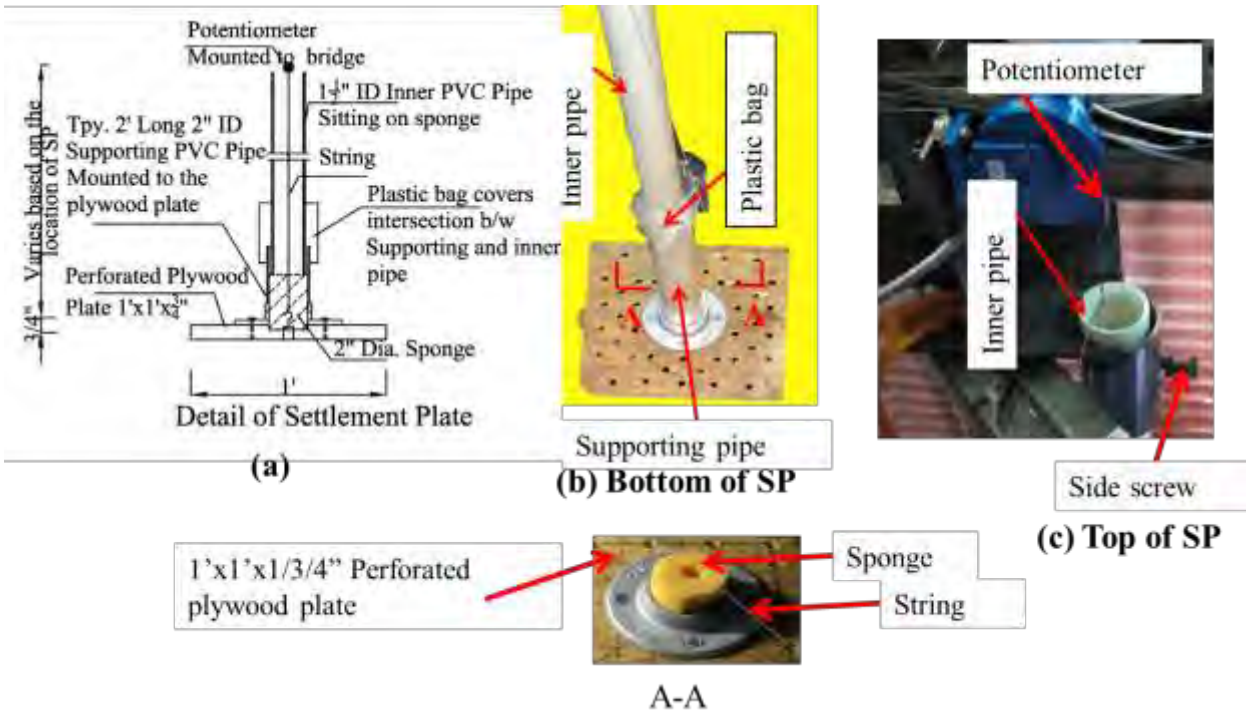

Fig. 7.15 Settlement plate components

7.4.2.2. Settlement plate activation

Fig. 7.16(a) shows the positioning of settlement plate before sand filling. Initially, the settlement plate system is hung inside the box with the bottom plate positioned at the desired elevation, tied by fish lines to the bottom pipe grid and to the top instrumentation bridge. Additionally, the top of inner pipe (3.81 cm ID) is tied to the instrumentation frame by a side screw on top of the box [Fig. 7.15(c)].

Fig. 7.16(b) shows how and when the settlement plate is activated. When the sand level reaches just above the settlement plate during filling, the fish lines connecting the bottom plate to

the instrumentation bridge are cut free and the side screw on the inner pipe is loosened and the pipe is set free. With further sand filling and the associated compression of the sand below the bottom plate level, the settlement plate moves down. The vertical displacement recorded by the potentiometer is the settlement of the sand at the plate level. The sand filling level is recorded periodically to provide the load data on the sand below the plate level as sand filling continues.

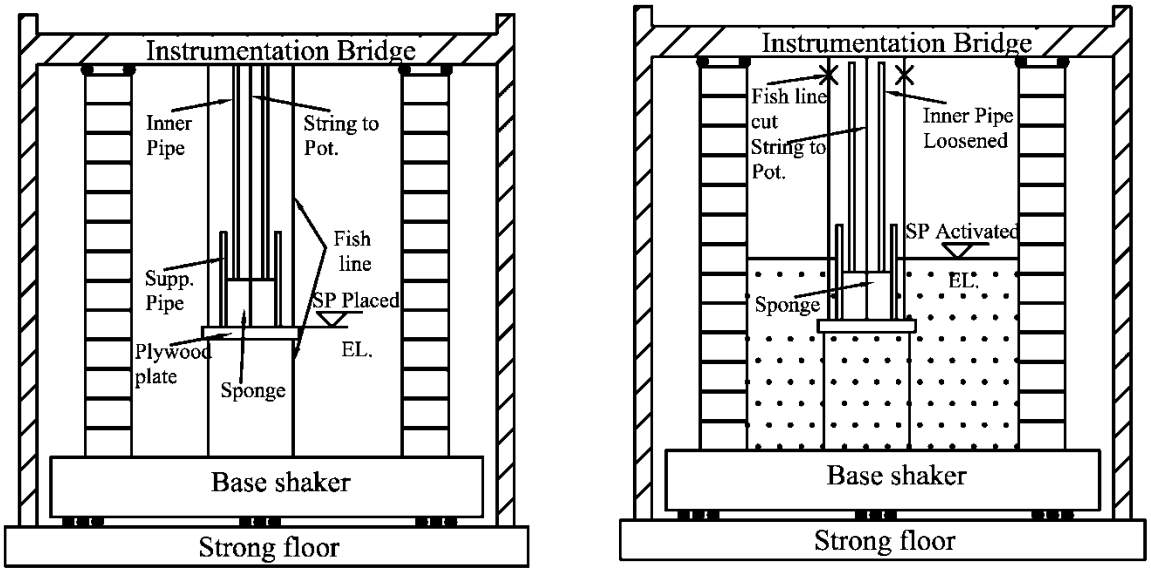

(a) SP placed in position-before filling (b) SP activated-during filling

Fig. 7.16 Activation of settlement plate

7.4.2.3. Settlement plate data

In the experiment LG1, the settlement plate SP1, SP2 and SP3 were installed at the elevation of 1.07, 3.56 and 1.98 m, repectively. The plates were activated when the corresponding sand elevation reaches 1.68, 4.17 and 3.20 m, respectively. The fish lines connected to the settlement plate were cut loose for all three settlement plates when plates were activated. However, only in one settlement plate, SP3, the inner pipe was set free.

Fig. 7.17 shows the recorded readings of the potentiometer to each settlement plate. The initial

readings of SP1, SP2 and SP3 immediately after activation are 22.6, 10.2 and 77.2 mm, respectively. However, the readings were not the actual settlement of the sand beneath the plates, but rather small gaps present between the plates and the sand beneath at the time of loosening the fish lines.

As the sand elevation builds up further the settlement plates moved vertically down representing the settlement of the sand layer beneath the plates due to the incremental loading by the weight of the sand accumulating above that layer.

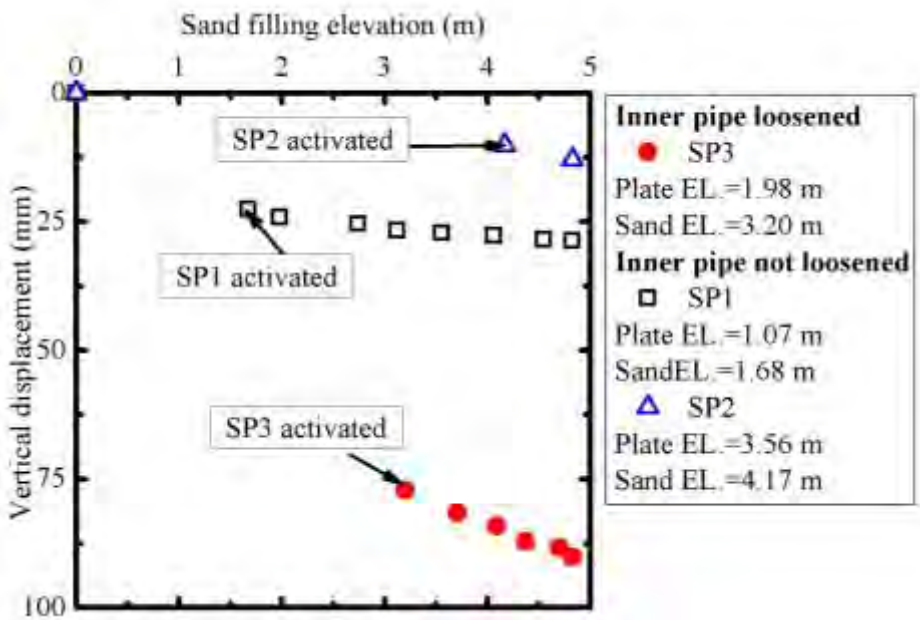

Fig. 7.17 Settlement plate data

The compressibility of sand could be estimated with the help of the vertical displacement of the settlement plate and the corresponding sand filling level after the activation of the plate. Fig. 7.18 illustrates the computation of the effective vertical stress (σ_v') at the midpoint in the soil layer below the bottom plate level. For example, if the settlement plate placed elevation is H_0 and the settlement plate activated elevation is H_1 ($H_1>H_0$),

The initial effective stress σ_{vo}' of point AA at H_0 is

$$\sigma_{v0}' = \gamma'\left(\frac{H_0}{2}\right) \qquad \text{(Eq. 7.1)}$$

Where γ' is the buoyant unit weight of sand, $\gamma'=\gamma_{sat}-\gamma_w$, γ_{sat} and γ_w are the unit weight of saturated sand and water, respectively. We assume γ_{sat}=19.1 kN/m^3 for the stress computation (e=0.748, D_r=27%, the lower bound limit of bucket density data).

The σ_v' of point AA due to the extra loading from H_0 to at H_1 is computed as:

$$\sigma_v' = \sigma_{v0}' + \gamma'(H_1 - H_0) = \gamma'\left(\frac{H_0}{2}\right) + \gamma'(H_1 - H_0) = \gamma'\left(H_1 - \frac{H_0}{2}\right) \qquad \text{(Eq. 7.2)}$$

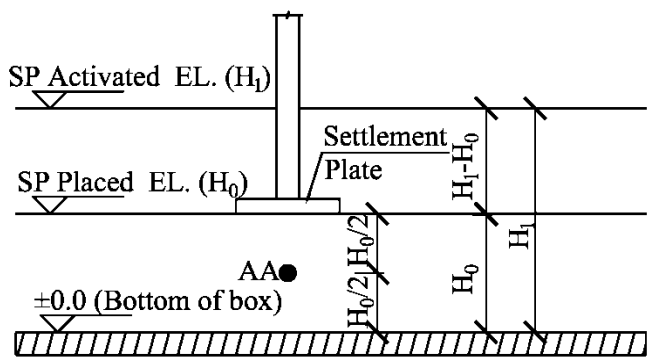

Fig. 7.18 σ_v' computation diagram

Fig. 7.19(a) plots the volumetric strain (ε_v) versus σ_v'. Based on Fig. 7.19(a), the void ratio (e) versus σ_v' of SP1 and SP3 are plotted in Fig. 7.19(b). The compression index (C_c) values for SP1 and SP3 are 0.016 and 0.046, respectively. Using these values, the void ratio obtained from bucket density tests were corrected to account for compressing the sand due to further weight of soil above it. The corrected relative density using SP1 and SP3 are plotted in Fig. 7.20(a) and (b), respectively. As discussed previously, the corrected relative density can only be an index instead of the actual value because whether the soil in the bucket is truly undisturbed during retrieval is unknown.

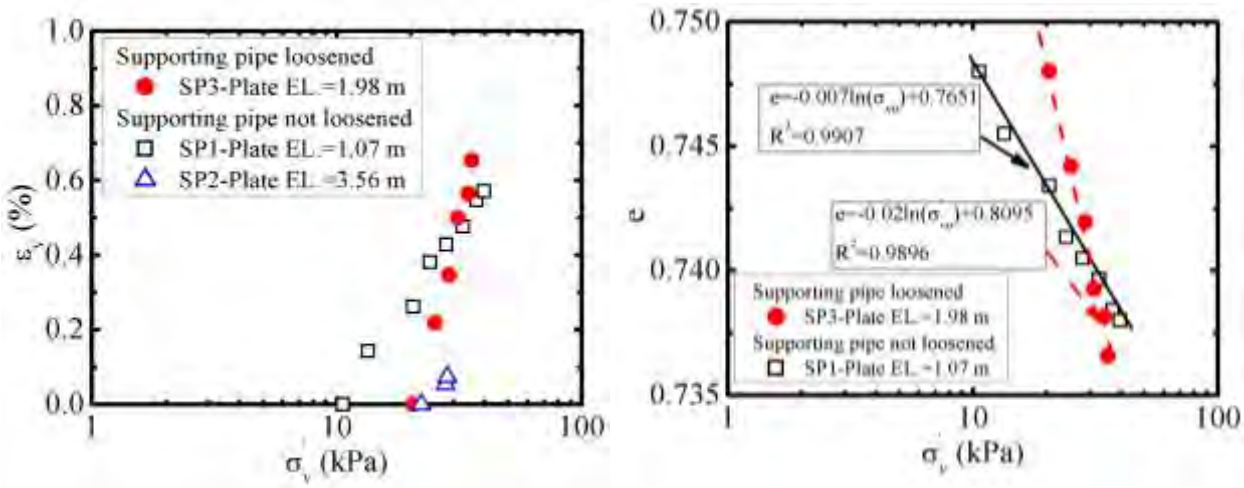

(a) ε_v versus σ_v' (b) e versus σ_v'

Fig. 7.19 ε_v and e versus σ_{vo}' of settlement plates

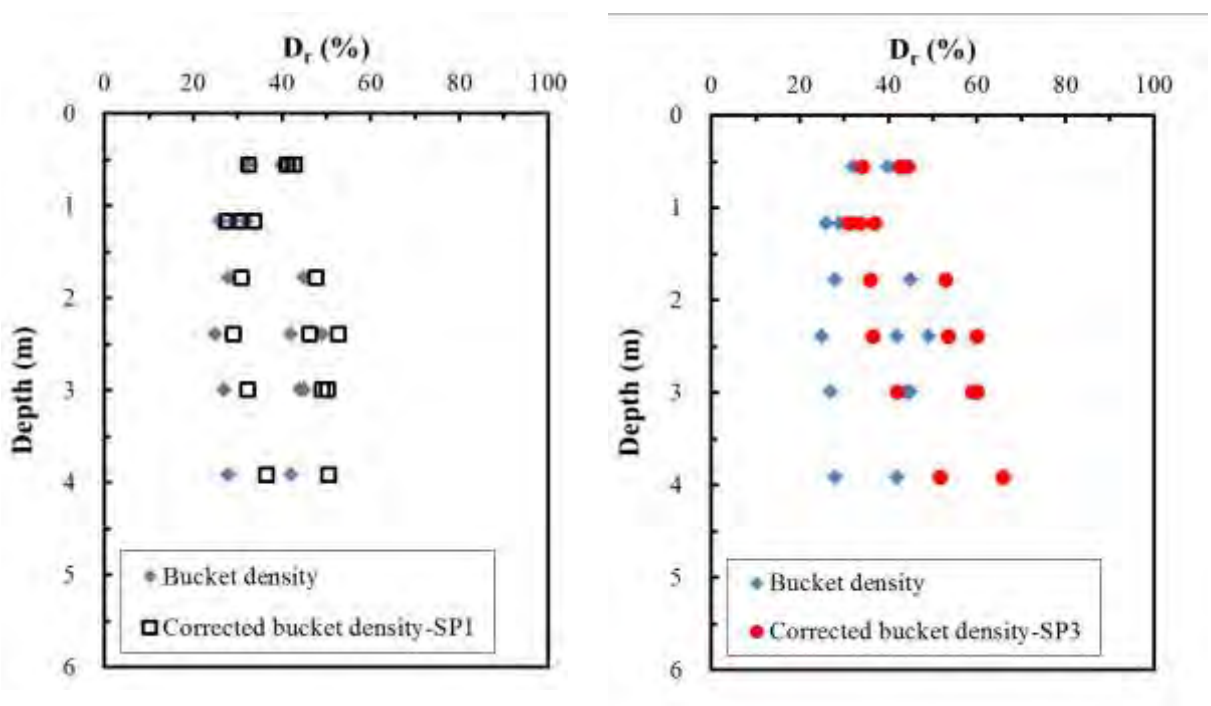

(a) SP1 data (b) SP3 data

Fig. 7.20 Corrected relative density of bucket density samples

7.5. CPTs and shear wave velocity tests

Fig. 7.21(a) shows the CPT equipment (HT-D3456, Vertek) used in the pre and post shaking CPTs and shear wave velocity tests. The projection area of cone tip is 10 cm^2 with the net area

ratio of 0.8, the sleeve area is 150 cm^2 and the piezometer is located behind the cone tip (u_2). The cone penetrometer was attached to a pulley system driven by a winch with 17.90 kN (4000 lb) lift force at the penetration rate ranged from 3.0 to 4.6 cm/s [Fig. 7.21(b)]. The penetration rate was slightly different from the ASTM standard penetration rate of 2 cm/s. A pause of few minutes was necessary for attaching a new stroke (1m in length) to the cone penetrometer or for performing shear wave velocity tests. For every CPT, the cone resistance, the pore water pressure behind cone tip, the sleeve friction and the inclination of cone with respect to depth (0.01 m interval) are recorded.

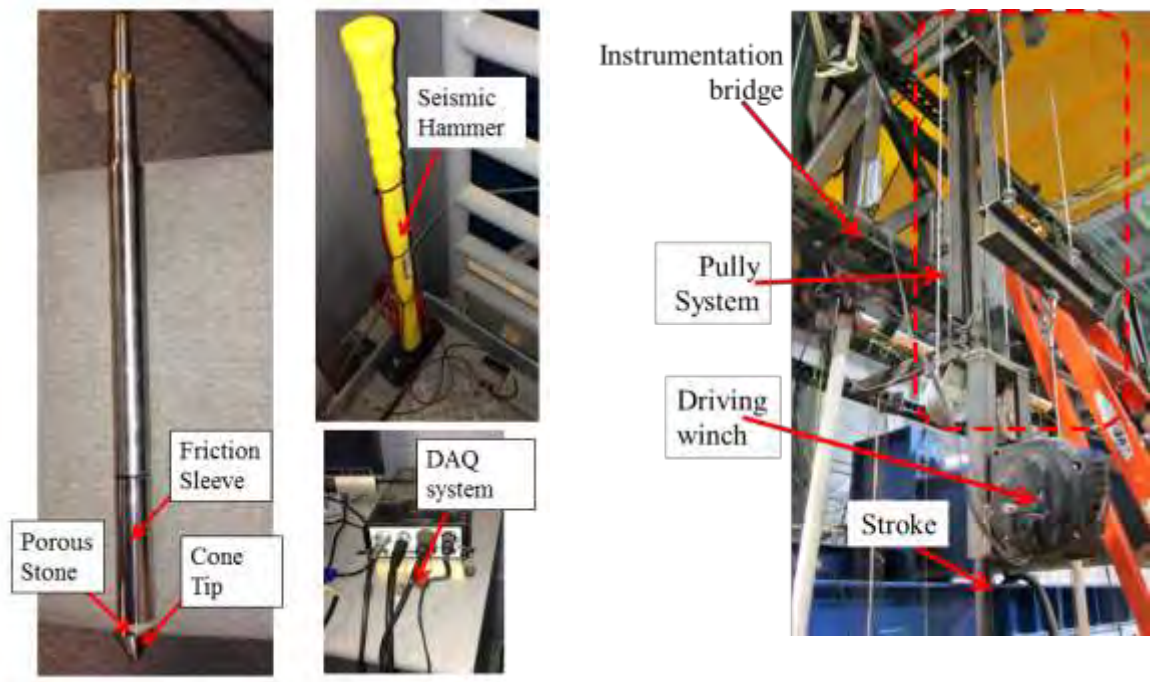

(a) CPT device (b) CPT driving system

Fig. 7.21 Device of CPT and shear wave velocity test

Shear wave velocity is measured at selected depths using a seismic hammer [Fig. 7.21(a)] along with each CPT. The shear wave is created by hitting the seismic hammer to a steel plate with the triggering device. The horizontal distance from hitting spot to cone (receiver) is 0.609 m (2 ft).

A relatively undisturbed test condition is required for the shear wave velocity test since the surrounding environments has the impact on the obtained arrival time. Several shear wave velocity tests are needed until two or three similar arrival times are recorded for each depth.

Fig. 7.22 shows the locations of performed CPTs/shear wave velocity tests. Fig. 7.23 plots the measured cone resistance (q_c), pore waer pressure behind tip (u_2), and shear wave velocity (V_s) profiles after hydraulic filling was completed and before the entire shaking event. Since the piezocone dissipation test was not conducted in the laminar box for clean Ottawa sand, a method proposed by Baligh and Levadoux (1986) is adopted to estimate the normalized penetration rate T_o (Ecemis, 2008). The reported value of 0.02 is used in this research for T_o at which v≈3.7 cm/s and d=3.56 cm.

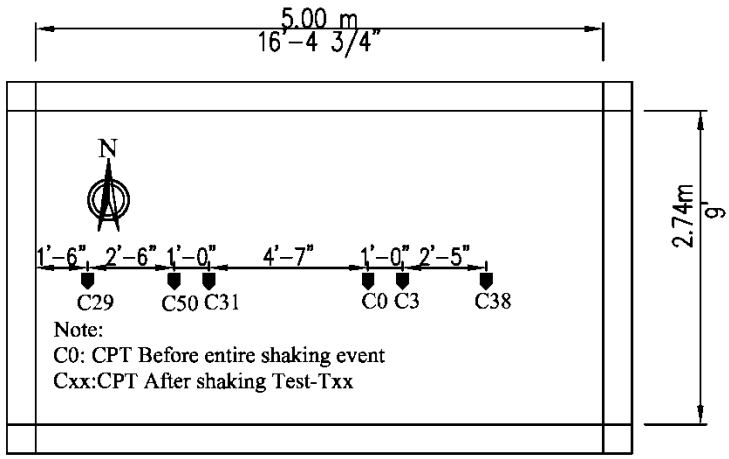

Fig. 7.22 CPT/shear wave velocity test location

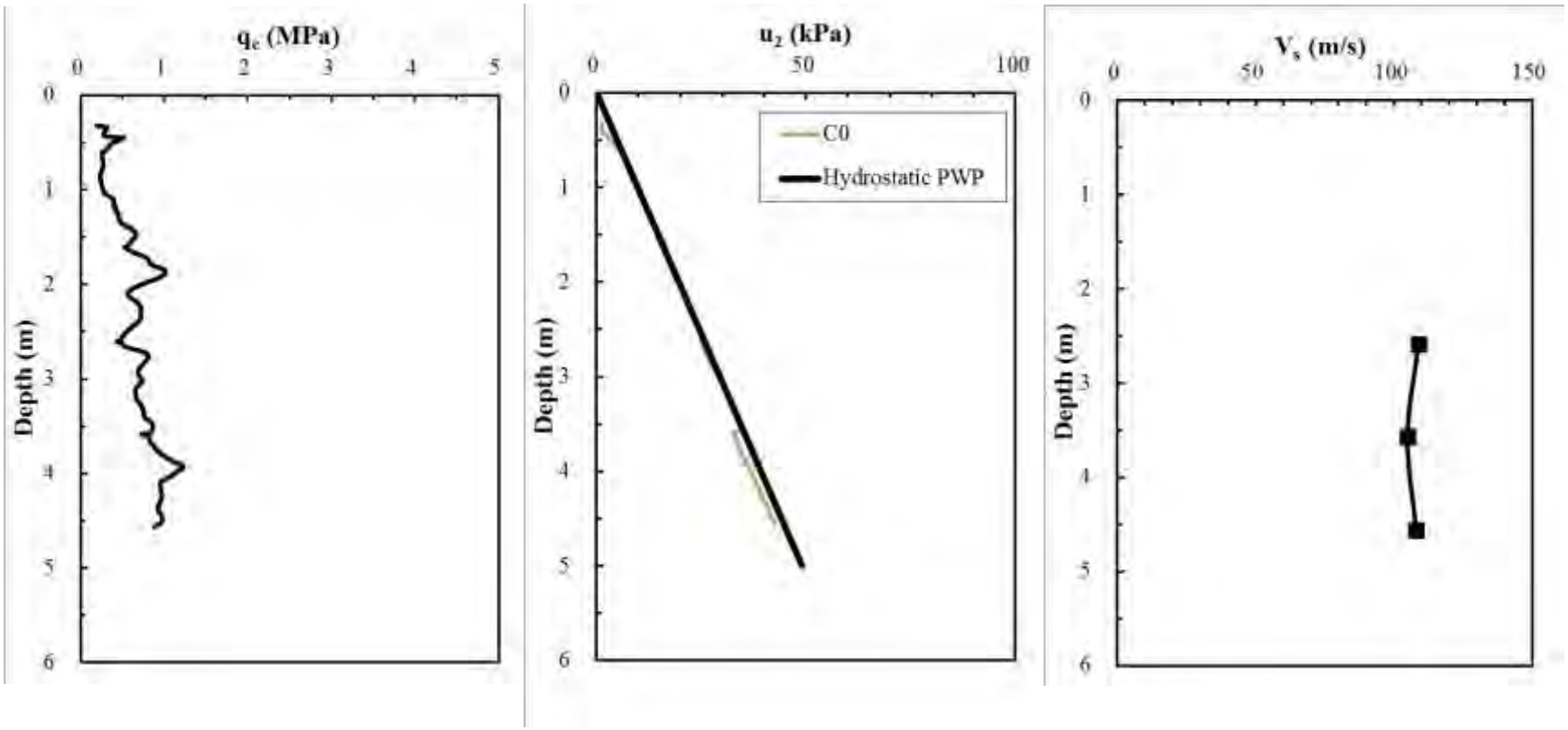

(a) q_c (b) u_2 (c) V_s

Fig. 7.23 q_c, u_2 and V_s versus depth of C0

7.6. Liquefaction experiments

Fig. 7.24 shows four planned sinusoidal input base motions (IM1 through IM4) with frequency of 2 Hz used in LG1. IM1 is the non-destructive motion with 5 cycles at a_{max}=0.015 g. The purpose of IM1 is to shake the soil at small strain levels without causing rise in pore water pressures. IM4 is the small magnitude earthquake with 5 cycles at a_{max}=0.03 g. IM3 and IM4 are large magnitude earthquakes with 15 cycles but at different peak base accelerations (a_{max}=0.03 g for IM2 and 0.10 g for IM3). It is noted that actual motions applied/measured at the base may differ slightly, as presented in the respective sections.

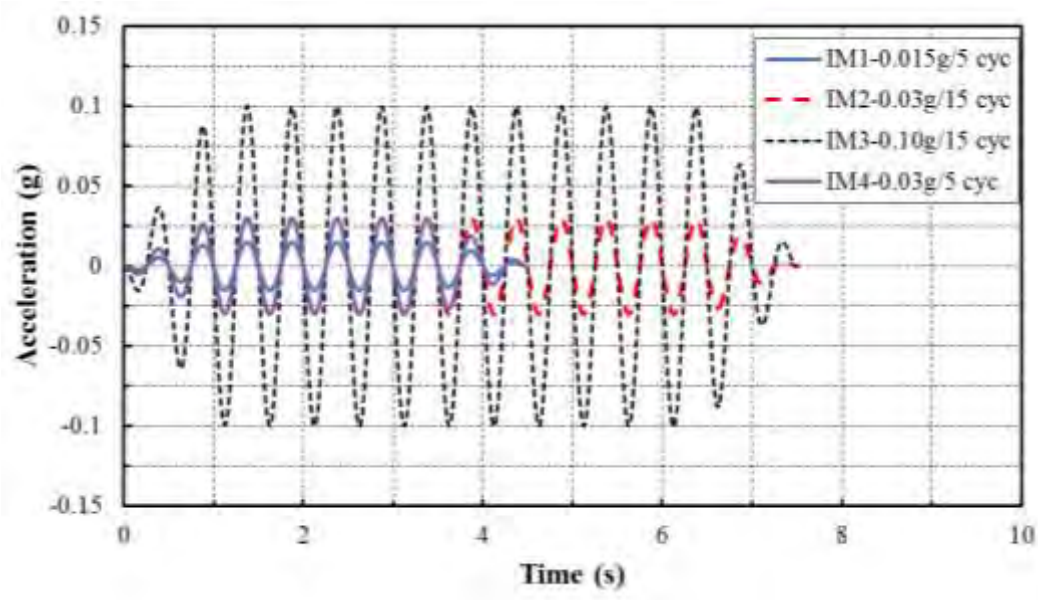

Fig. 7.24 Planned input base motions

The liquefaction tests include 8 series of shaking amounting to a total of 58 different shaking events, which can be found in Table 7.8. Shaking series 1 consists of one non-destructive motion (IM1), one large magnitude earthquake with a_{max}=0.03 g (IM2) and one large magnitude earthquake with a_{max}=0.10 g (IM3). Shaking series 2 consists of five small magnitude earthquakes

with a_{max}=0.03 g (IM4), one large magnitude of earthquake with a_{max}=0.03 g (IM2) and one large magnitude earthquake with a_{max}=0.10 g (IM3). The rest of shaking series are similar to shaking series 2 except that the non-destructive motion-IM1 is input before the five small magnitude earthquakes from shaking series 4 to 8.

A few Pre and post shaking cone penetration tests and shear wave velocity tests were also performed besides the liquefaction tests. Table 7.8 shows the timeframe of each CPT/shear wave velocity test conducted. C0 denotes the pre-shaking CPT/shear wave velocity test while Cxx represents the post-shaking CPT/shear wave velocity test performed after liquefaction test Txx.

Table 7.8 Input motion of liquefaction test in laminar box

Shaking series	Shaking event	Input Motion	a_{max} |	Cycle	Duration	Note
			g		s	
-	C0	-	-	-	-	CPT
1	T1	IM1	0.015	5	2.5	Shaking
	T2	IM2	0.030	15	7.5	Shaking
	T3	IM3	0.100	15	7.5	Shaking
-	C3	-	-	-	-	CPT
2	T4	IM4	0.030	5	2.5	Shaking
	T5	IM4	0.030	5	2.5	Shaking
	T6	IM4	0.030	5	2.5	Shaking
	T7	IM4	0.030	5	2.5	Shaking
	T8	IM4	0.030	5	2.5	Shaking
	T9	IM2	0.030	15	7.5	Shaking
	T10	IM3	0.100	15	7.5	Shaking
3	T11	IM4	0.030	5	2.5	Shaking
	T12	IM4	0.030	5	2.5	Shaking
	T13	IM4	0.030	5	2.5	Shaking
	T14	IM4	0.030	5	2.5	Shaking
	T15	IM4	0.030	5	2.5	Shaking
	T16	IM2	0.030	15	7.5	Shaking
	T17	IM3	0.100	15	7.5	Shaking
4	T18a	IM1	0.015	5	2.5	Shaking
	T18	IM4	0.030	5	2.5	Shaking
	T19	IM4	0.030	5	2.5	Shaking
	T20	IM4	0.030	5	2.5	Shaking
	T21	IM4	0.030	5	2.5	Shaking
	T22	IM4	0.030	5	2.5	Shaking
	T23	IM2	0.030	15	7.5	Shaking
	T24	IM3	0.100	15	7.5	Shaking
5	T25a	IM1	0.015	5	2.5	Shaking
	T25	IM4	0.030	5	2.5	Shaking
	T26	IM4	0.030	5	2.5	Shaking
	T27	IM4	0.030	5	2.5	Shaking
	T28	IM4	0.030	5	2.5	Shaking
	T29	IM4	0.030	5	2.5	Shaking
-	C29	-	-	-	-	CPT

(a) T1 through T29

Shaking series	Shaking event	Input Motion	a_{max} |	Cycle	Duration	Note
			g		s	
5	T30	IM2	0.03	15	7.5	Shaking
	T31	IM3	0.100	15	7.5	Shaking
-	C31	-	-	-	-	CPT
6	T32a	IM1	0.015	5	2.5	Shaking
	T32	IM4	0.03	5	2.5	Shaking
	T33	IM4	0.030	5	2.5	Shaking
	T34	IM4	0.030	5	2.5	Shaking
	T35	IM4	0.030	5	2.5	Shaking
	T36	IM4	0.030	5	2.5	Shaking
	T37	IM2	0.030	15	7.5	Shaking
	T38	IM3	0.100	15	7.5	Shaking
-	C38	-	-	-	-	CPT
7	T39a	IM1	0.015	5	2.5	Shaking
	T39	IM4	0.030	5	2.5	Shaking
	T40	IM4	0.030	5	2.5	Shaking
	T41	IM4	0.030	5	2.5	Shaking
	T42	IM4	0.030	5	2.5	Shaking
	T43	IM4	0.030	5	2.5	Shaking
	T44	IM2	0.030	15	7.5	Shaking
	T45	IM3	0.100	15	7.5	Shaking
8	T46a	IM1	0.015	5	2.5	Shaking
	T46	IM4	0.030	5	2.5	Shaking
	T47	IM4	0.030	5	2.5	Shaking
	T48	IM4	0.030	5	2.5	Shaking
	T49	IM4	0.030	5	2.5	Shaking
	T50	IM4	0.030	5	2.5	Shaking
-	C50	-	-	-	-	CPT
8	T51a	IM1	0.015	5	2.5	Shaking
	T51	IM2	0.030	15	7.5	Shaking
	T52	IM3	0.100	15	7.5	Shaking

(b) T30 through T52

7.7. Summary

The new designed full scale laminar box shaking system is covered in this chapter. Different types of instrumentation are described and the liquefaction tests and CPTs are introduced.

Chapter 8. 1-g Full scale laminar box: Sand liquefaction analysis

8.1. Introduction

This chapter presents the analysis of selected liquefaction experiments of different shaking series. Details of the analysis of acceleration, excess pore water pressure, horizontal displacement and stress-strain of soil in shaking series 1 and 2 are covered in this chapter. More experimental results are presented in Appendix E. The CPT-based and shear wave velocity based liquefaction analysis is also shown.

8.2. Liquefaction tests- Shaking series 1

This section analyzes the first shaking series, which consists of T1 (IM1), T2 (IM2) and T3 (IM3). The details of each input motion for each test can be found in section 7.6. The sample rate for this shaking series is 200 Hz. The collected data are filtered using a low-pass filter with the cutoff frequency equal to 40 Hz for T1 through T3. It shall be noticed that the data in this shaking series were not continuously recorded after shaking.

8.2.1. Base shaking

8.2.1.1. T1-IM1 (a_{max}=0.015 g/5 cyc)

Fig. 8.1(a) and (b) compare the recorded base motion at different locations in x- and y-direction of T1 (a_{max}=0.015 g/5 cyc), respectively. The ratio of the peak base acceleration in y-direction to that in x-direction at B1, B2 and B3 is 9%, 11% and 7%, respectively, indicating that the targeted one dimensional shaking is achieved.

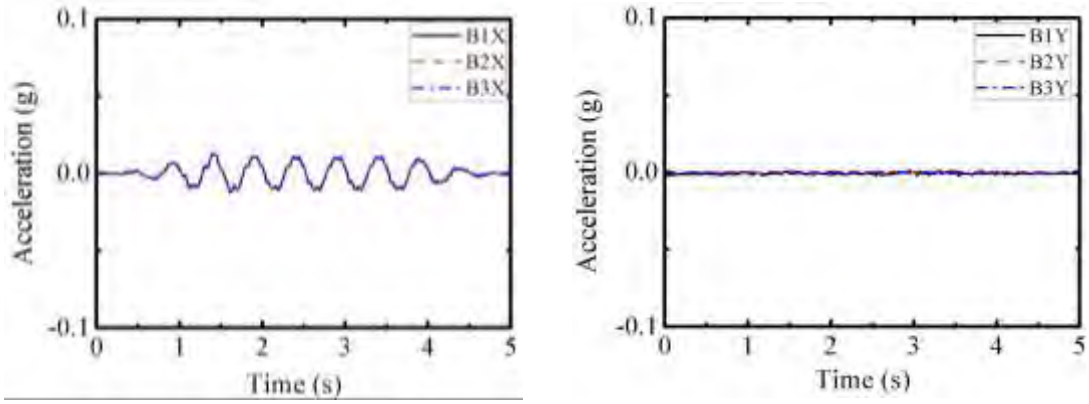

(a) x-direction (b) y-direction

Fig. 8.1 Base shaker of T1 (a_{max}=0.015 g/5 cyc)

8.2.1.2. T2-IM2 (a_{max}=0.03 g/15 cyc)

Fig. 8.2(a) and (b) compare the recorded base acceleration at different locations for both x-(shaking) and y-(non-shaking) direction of T2 (a_{max}=0.03 g/15 cyc). The ratio of the peak base acceleration in y-direction to that in x-direction at B1, B2 and B3 is 13%, 11% and 10%, respectively, indicating that the targeted one dimensional shaking is achieved.

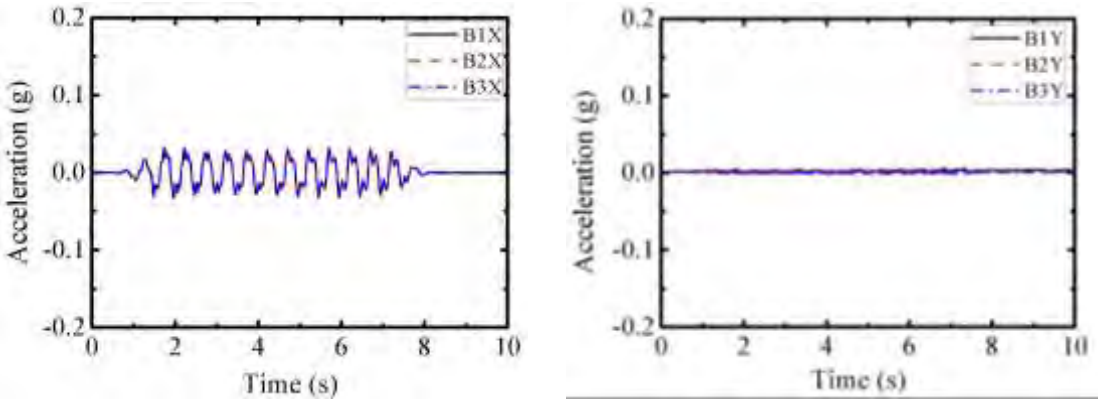

(a) x-direction (b) y-direction

Fig. 8.2 Base shaker of T2 (a_{max}=0.03 g/15 cyc)

8.2.1.3. T3-IM3 (a_{max}=0.10 g/15 cyc)

Fig. 8.3 compares the recorded base acceleration at different locations for both x-(shaking) and y-(non-shaking) direction of T3 (a_{max}=0.10 g/15 cyc). The ratio of the peak base acceleration in y-direction to that in x-direction at B1, B2 and B3 for T3 is 8%, 11% and 7%, respectively, indicating

that the targeted one dimensional shaking is achieved.

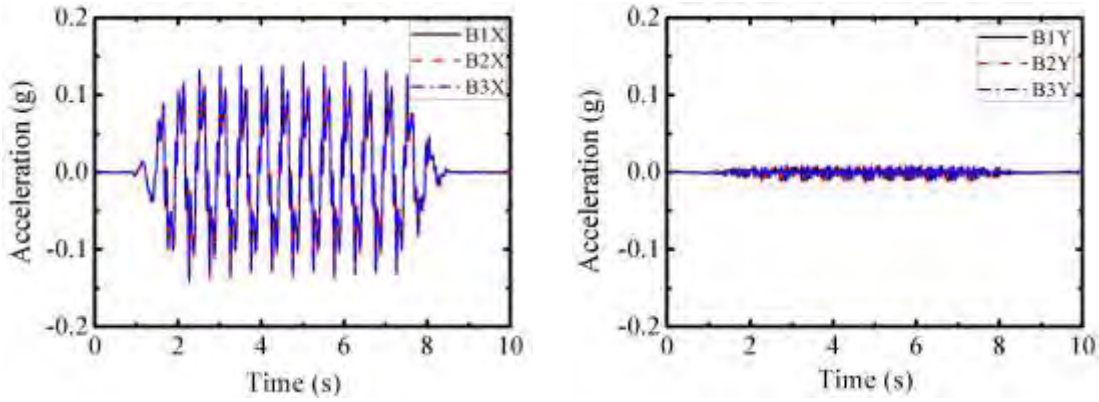

(a) x-direction (b) y-direction

Fig. 8.3 Base shaker of T3 (a_{max}=0.1 g/15 cyc)

8.2.2. Acceleration response

Due to high sampling rate and related accuracy of recordings, the acceleration recorded from the accelerometers located at various laminates is utilized to examine the soil response during shaking.

8.2.2.1. T1-IM1 (a_{max}=0.015 g/5 cyc)

Fig. 8.4 compares the acceleration time history of selected accelerometers in T1 (a_{max}=0.015 g/5 cyc). The depths of selected accelerometers are corresponding to the depths of working piezometers. The amplification factor of soil at different depths is shown in Fig. 8.5. An amplification of the acceleration of soil at all depths compared to the base is observed from the figure.

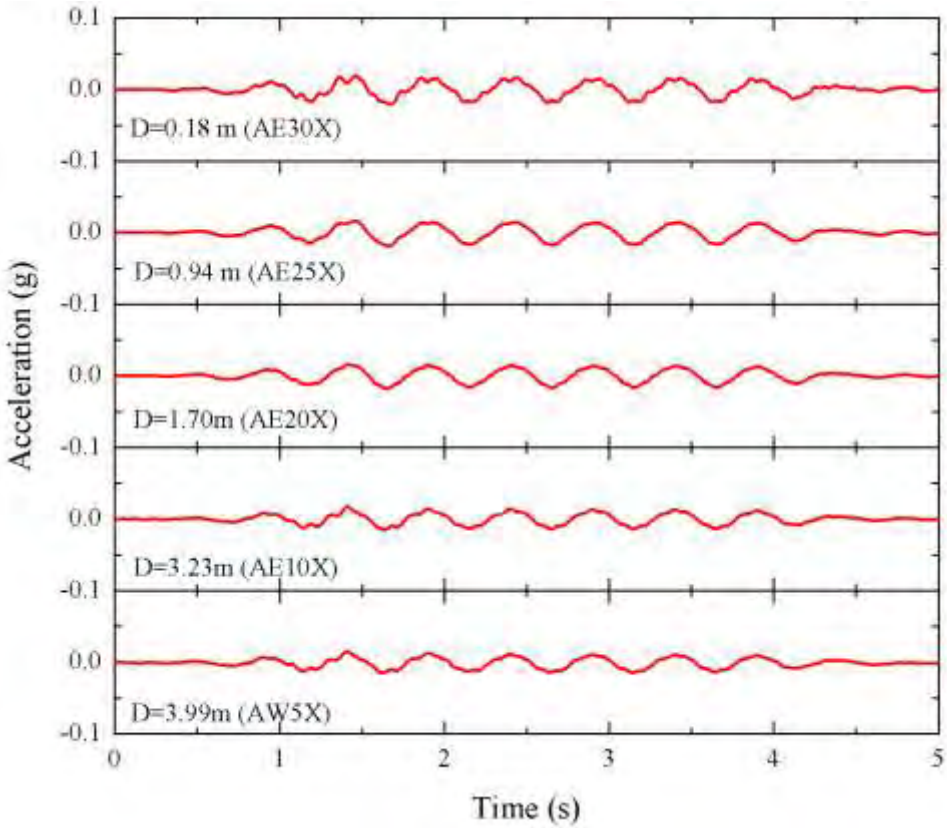

(a) Laminate acceleration

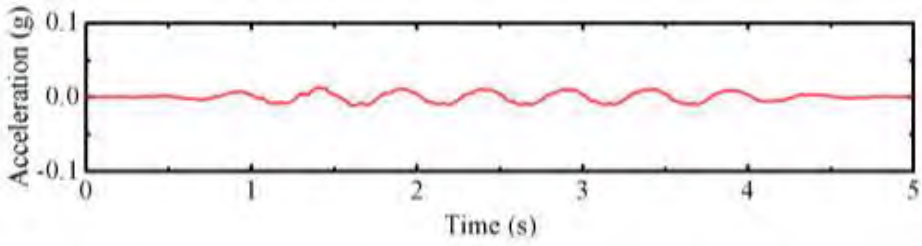

(b) B3X

Fig. 8.4 x-acceleration at different depths and base of T1 (a_{max}=0.015 g/5 cyc)

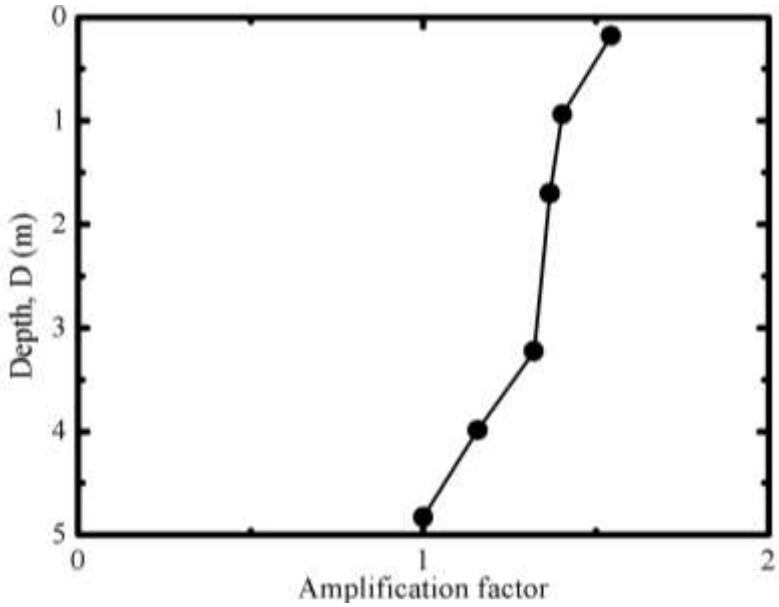

Fig. 8.5 Amplification factor profile of T1 (a_{max}=0.015 g/5 cyc)

8.2.2.2. T2-IM2 (a_{max}=0.03 g/15 cyc)

Fig. 8.6 compares the acceleration time history of selected accelerometers in T2 (a_{max}=0.03 g/15 cyc). The significant drop of acceleration between top soil surface and D=1.70 m after three shaking cycles indicates that soil in this region may liquefy. The acceleration at D=3.23 m and D=3.99 m suggests that the soil at the bottom still transmits shear stress and hence may not liquefy at the same time as the top soil stratum. Based on Fig. 8.6, the amplification factor of soil at different depths is shown in Fig. 8.7.

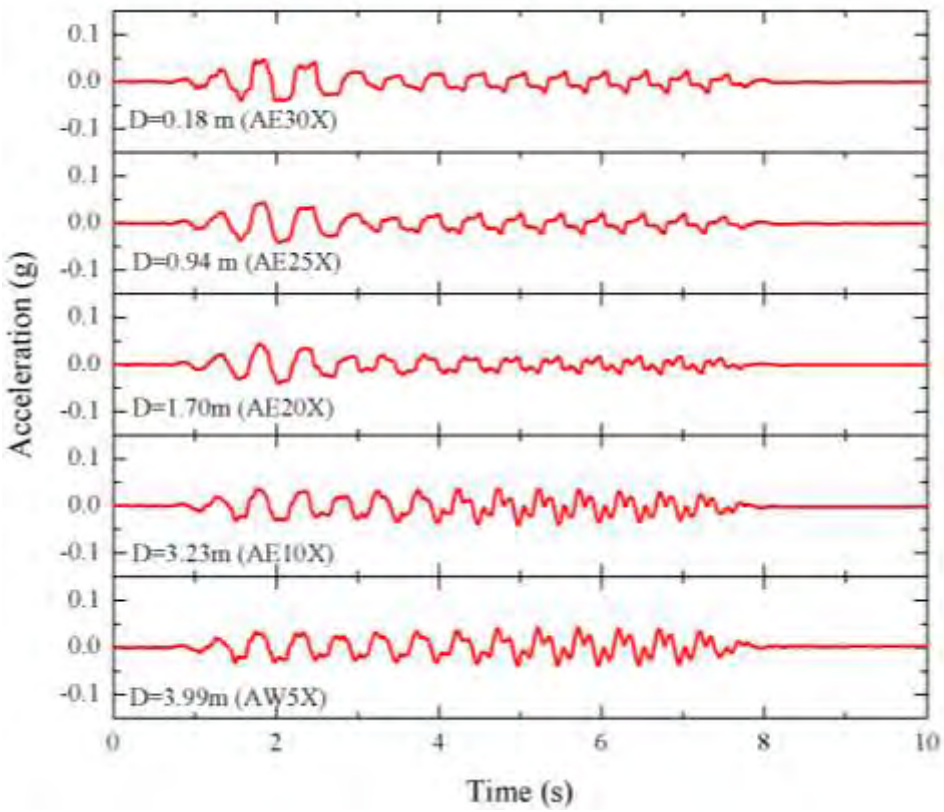

(a) Laminate acceleration

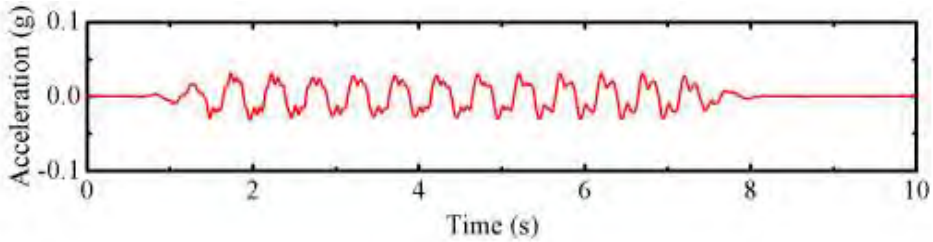

(b) B3X

Fig. 8.6 x-acceleration at different depths and base of T2 (a_{max}=0.03 g/15 cyc)

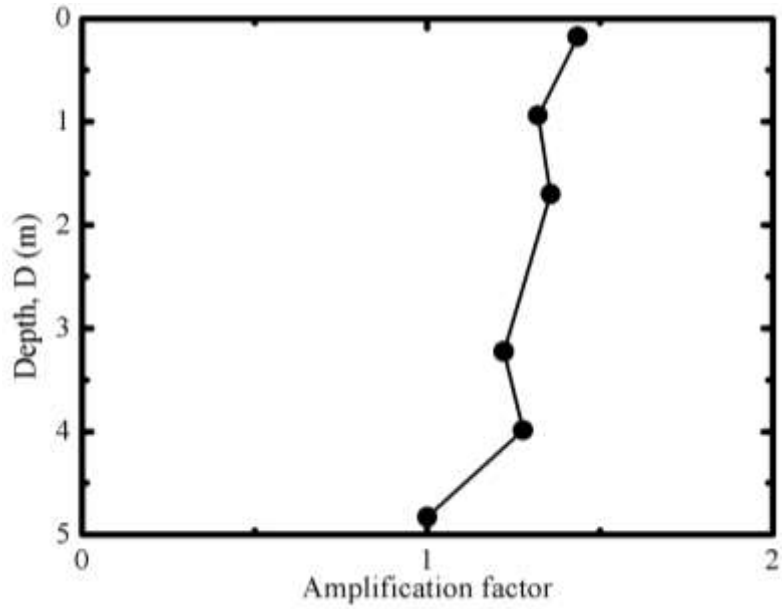

Fig. 8.7 Amplification factor profile of T2 (a_{max}=0.03 g/15 cyc)

8.2.2.3. T3-IM3 (a_{max}=0.10 g/15 cyc)

Fig. 8.8 compares the acceleration time history of selected accelerometers in T3. The significant drop of acceleration between top soil surface and D=1.70 m during the first three shaking cycles indicates that soil in this region may liquefy. However, the acceleration at D=3.23 m and 3.99 m suggests that the soil at the bottom, although gradually weaken, may still transmit shear stress and hence may not liquefy at the same time as the top soil stratum. It is noticed that the acceleration of soil at shallow depth gradually increases after three cycles. The amplification factor of soil at different depths is shown in Fig. 8.9. In this shaking event, the soil however was softened and did not transmit shaking as was the case in T1 and T2.

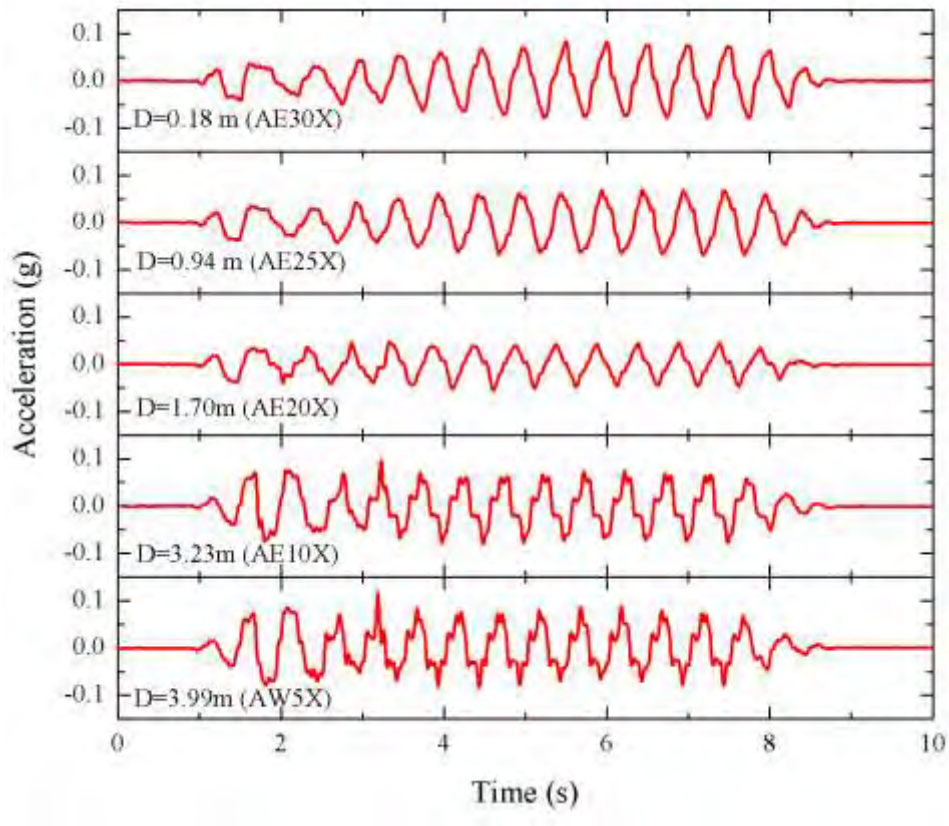

(a) Laminate acceleration

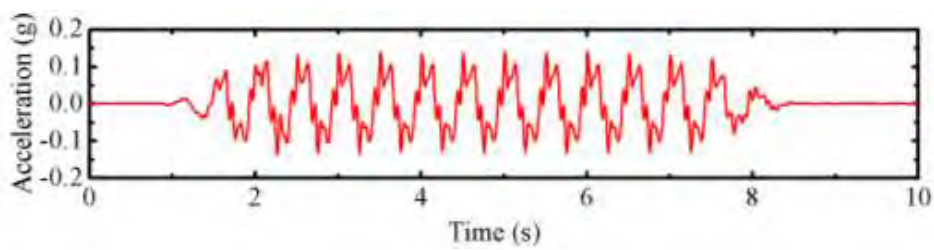

(b) B3X

Fig. 8.8 x-acceleration at different depths and base of T3 (a_{max}=0.1 g/15 cyc)

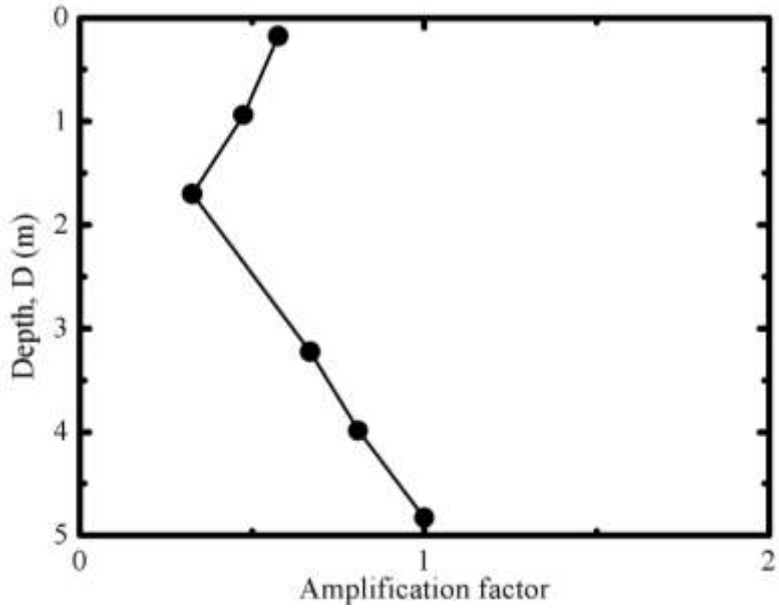

Fig. 8.9 Amplification factor profile of T3 (a_{max}=0.1 g/15 cyc)

8.2.3. Excess pore water pressure (Δu) response

As indicated previously, the dissipation of the excess pore water pressure (EPWP) Δu was not completely recorded in this shaking series.

8.2.3.1. T1-IM1 (a_{max}=0.015 g/5 cyc)

Fig. 8.10 presents the time history of normalized excess pore water pressure r_u ($\Delta u/\sigma_{vo}'$) and base acceleration of T1 (a_{max}=0.015 g/5 cyc) during shaking at different depths. There is no EPWP build up as expected, which agrees with the observation from accelerometers. Fig. 8.11 shows the time history of EPWP (Δu) of the soil profile in T1. Fig. 8.12 plots the Δu as well as r_u profile at various shaking cycle of T1.

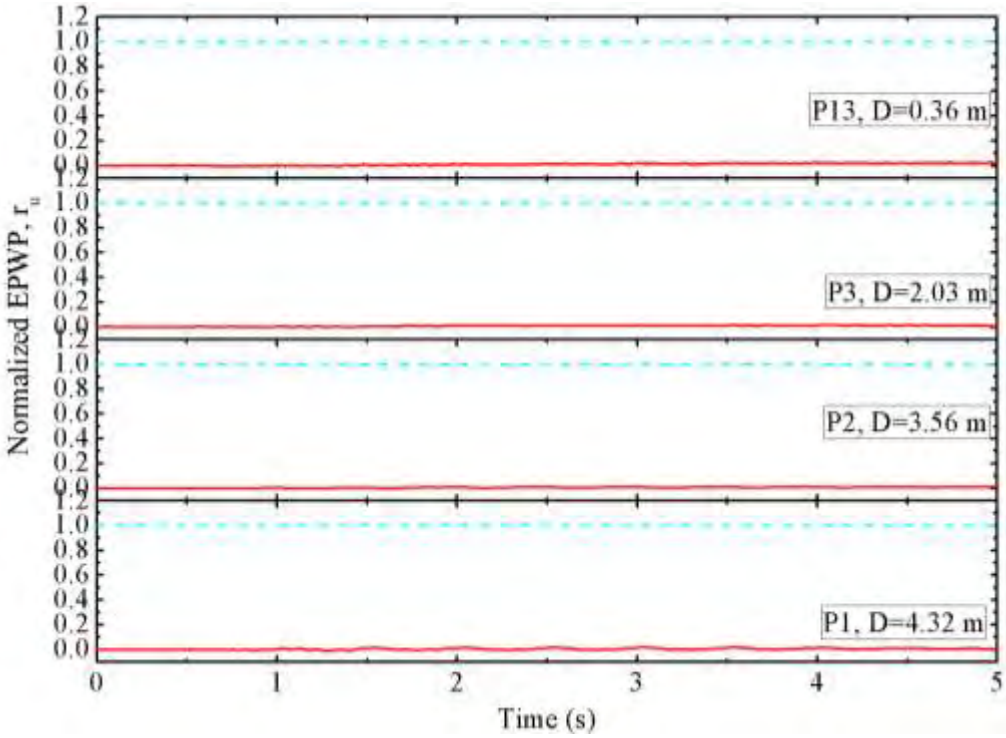

(a) r_u

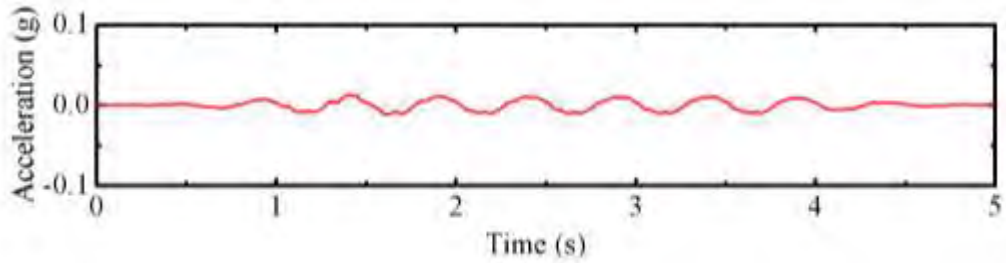

(b) B3X

Fig. 8.10 Time history of r_u and base acceleration of T1 (a_{max}=0.015 g/5 cyc)

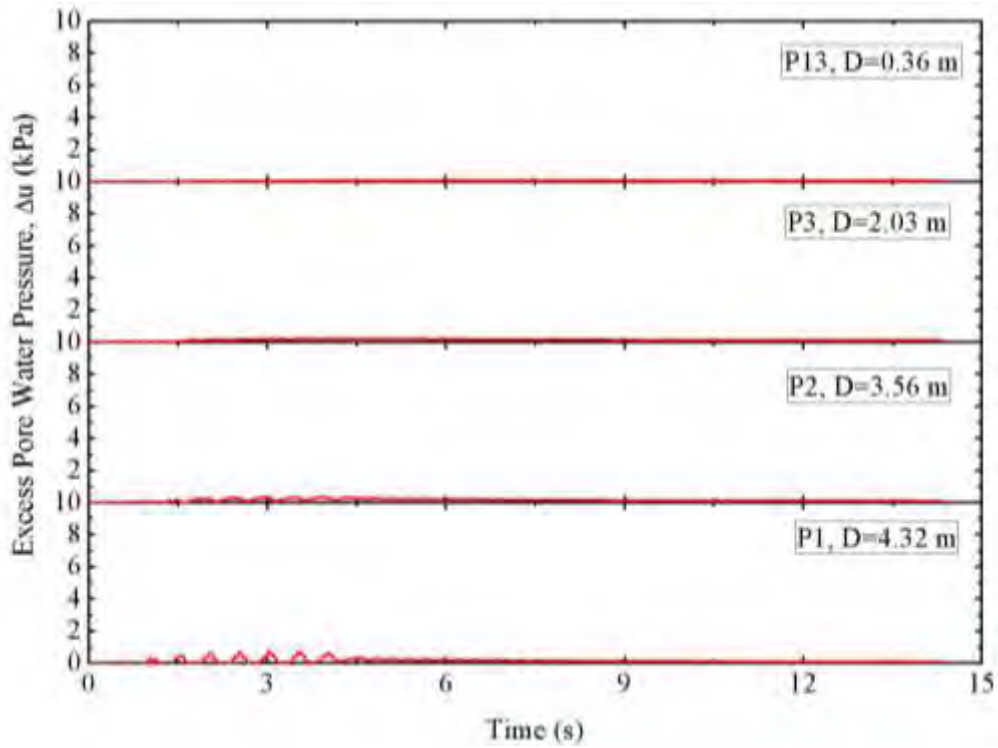

Fig. 8.11 Time history of Δu of T1 (a_{max}=0.015 g/5 cyc)

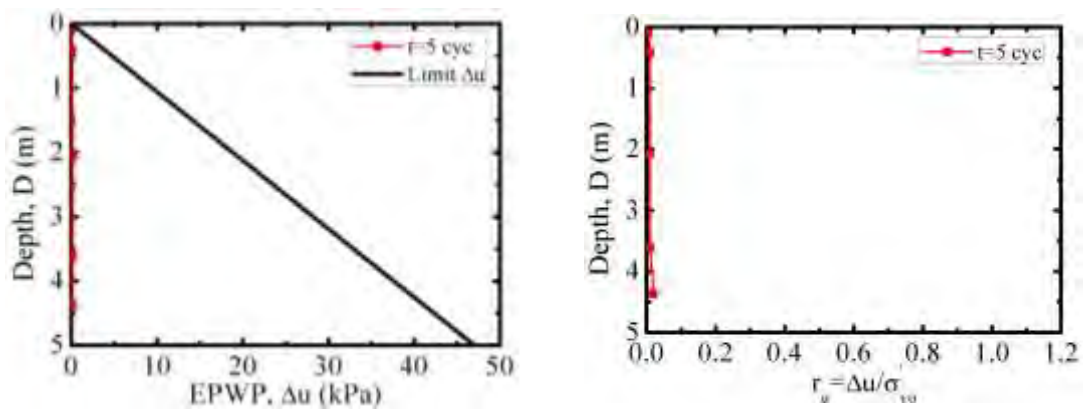

(a) Δu (b) r_u

Fig. 8.12 EPWP profiles of T1 (a_{max}=0.015 g/5 cyc)

8.2.3.2. T2-IM2 (a_{max}=0.03 g/15 cyc)

Fig. 8.13 presents the time history of normalized excess pore water pressure r_u and base acceleration of T2 (a_{max}=0.03 g/15 cyc) during shaking. Soil at shallow depth liquefies during the first three shaking cycles as r_u reaches unity while soil below 2 m remains certain strength. Soil at D=3.56 m gradually loose the strength as r_u increases to 0.94 at the end of shaking cycles. Soil at

deeper depth (D=4.32m) does not liquefy through the entire shaking (r_u=0.8). Fig. 8.14 shows the time history of excess pore water pressure (EPWP) Δu of the soil profile in T2. It is noticed that the data were not recorded during the time frame of 25s to 2695 s. Fig. 8.15 plots the Δu as well as r_u profile at various shaking cycle of T2, indicating that soil at shallow depth liquefies firstly and propagates downwards.

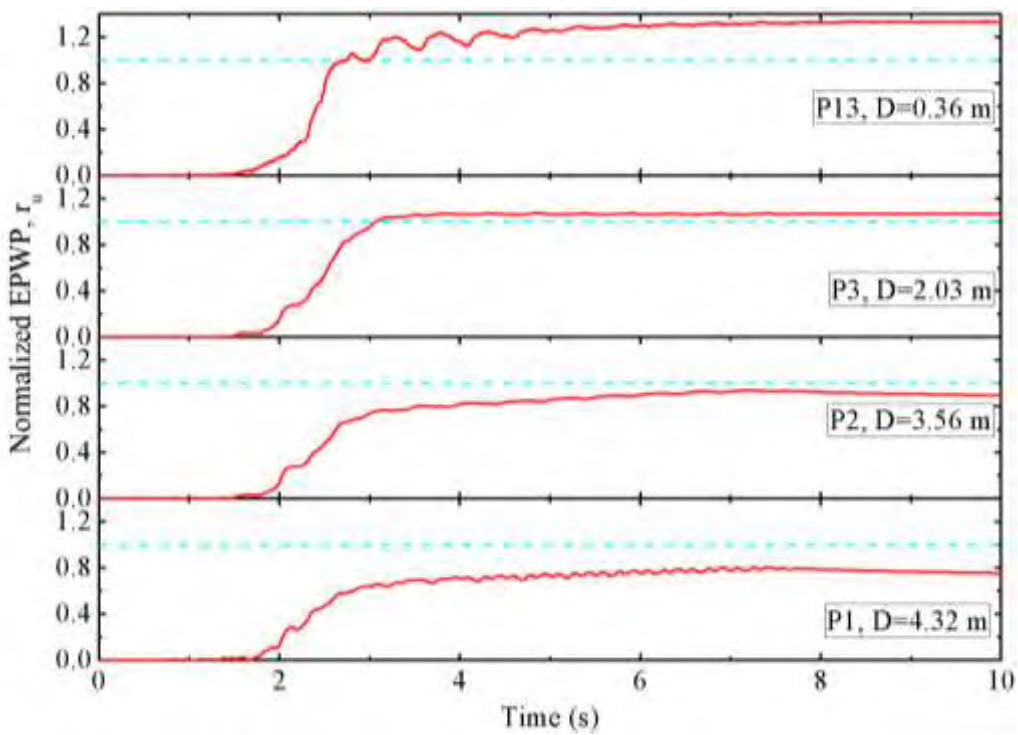

(a) r_u

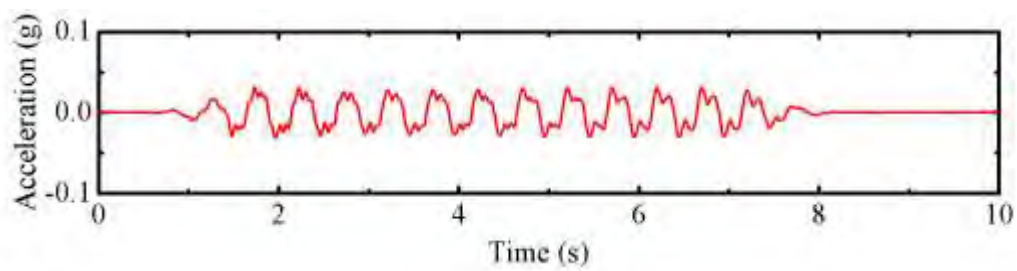

(b) B3X

Fig. 8.13 Time history of r_u and base acceleration of T2 (a_{max}=0.03 g/15 cyc)

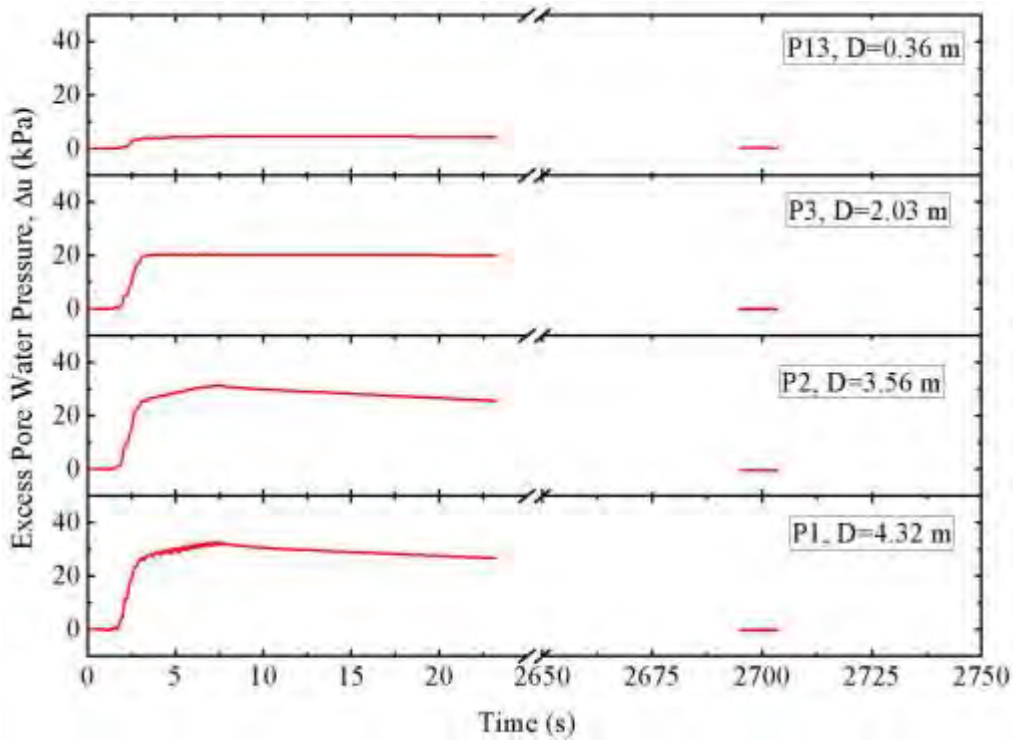

Fig. 8.14 Time history of Δu of T2 (a_{max}=0.03 g/15 cyc)

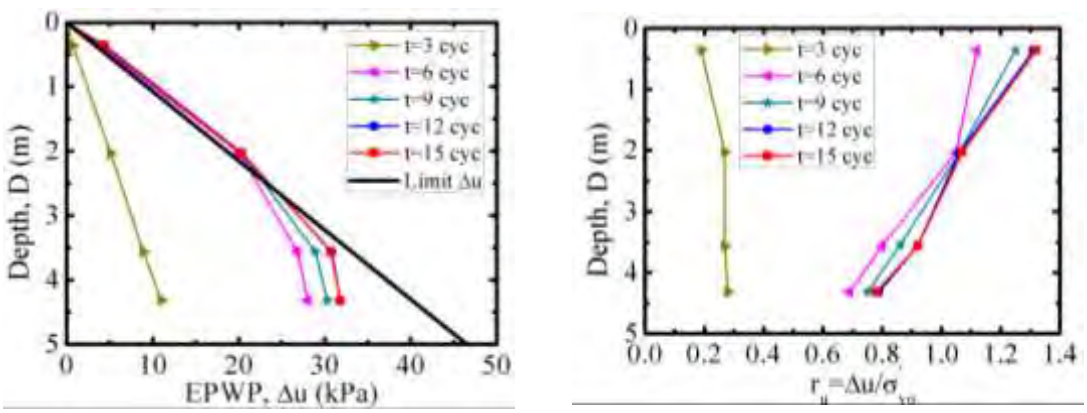

(a) Δu (b) r_u

Fig. 8.15 EPWP profiles of T2 (a_{max}=0.03 g/15 cyc)

8.2.3.3. T3-IM3 (a_{max}=0.10 g/15 cyc)

Fig. 8.16 presents the time history of normalized excess pore water pressure r_u and base acceleration of T3 (a_{max}=0.10 g/15 cyc) during shaking. The entire soil liquefies after the first three shaking cycles. Fig. 8.17 shows the time history of EPWP (Δu) of the soil profile in T3. It is noticed that the data were not recorded during the time frame of 25 to 900 s. Fig. 8.18 plots the Δu as well

as r_u profile at various shaking cycle of T3, indicating that soil liquefies at all depths in the first three shaking cycles.

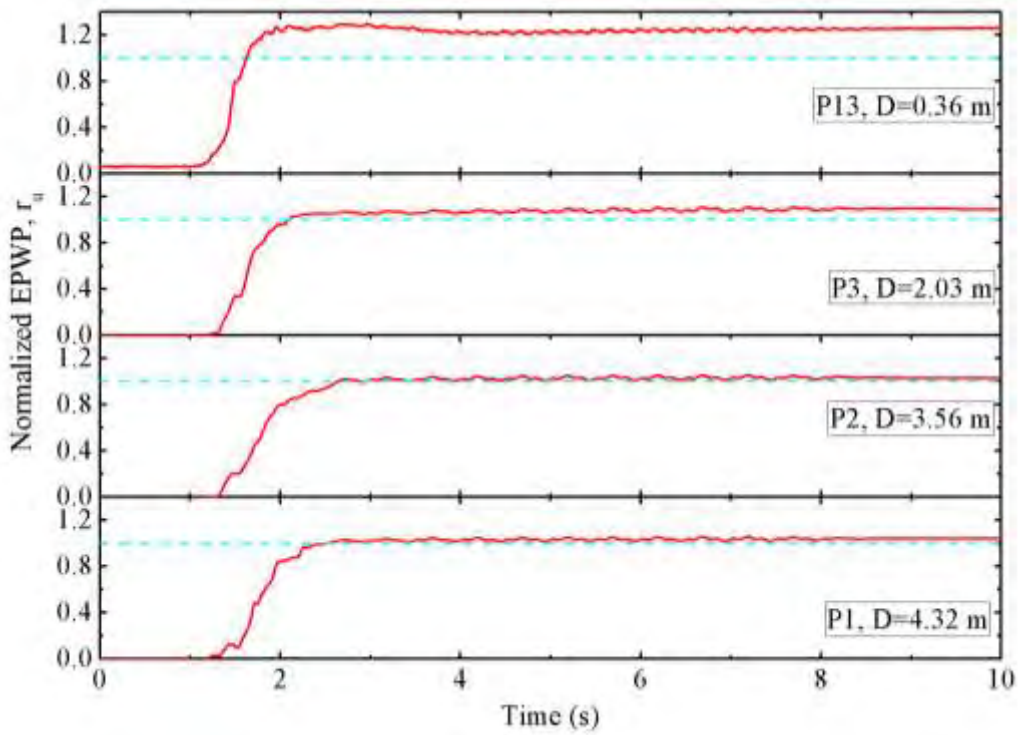

(a) r_u

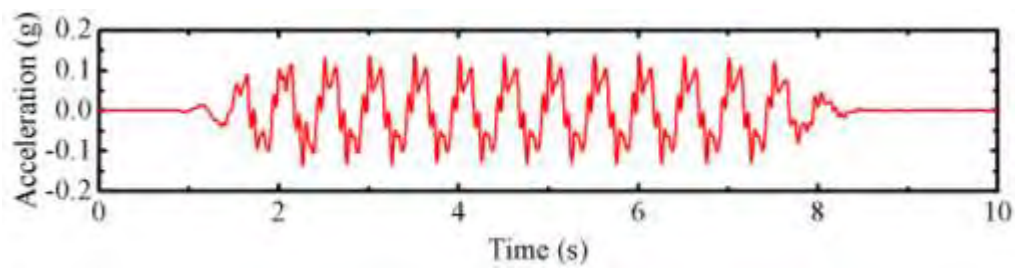

(b) B3X

Fig. 8.16 Time history of r_u and base acceleration of T3 (a_{max}=0.10 g/15 cyc)

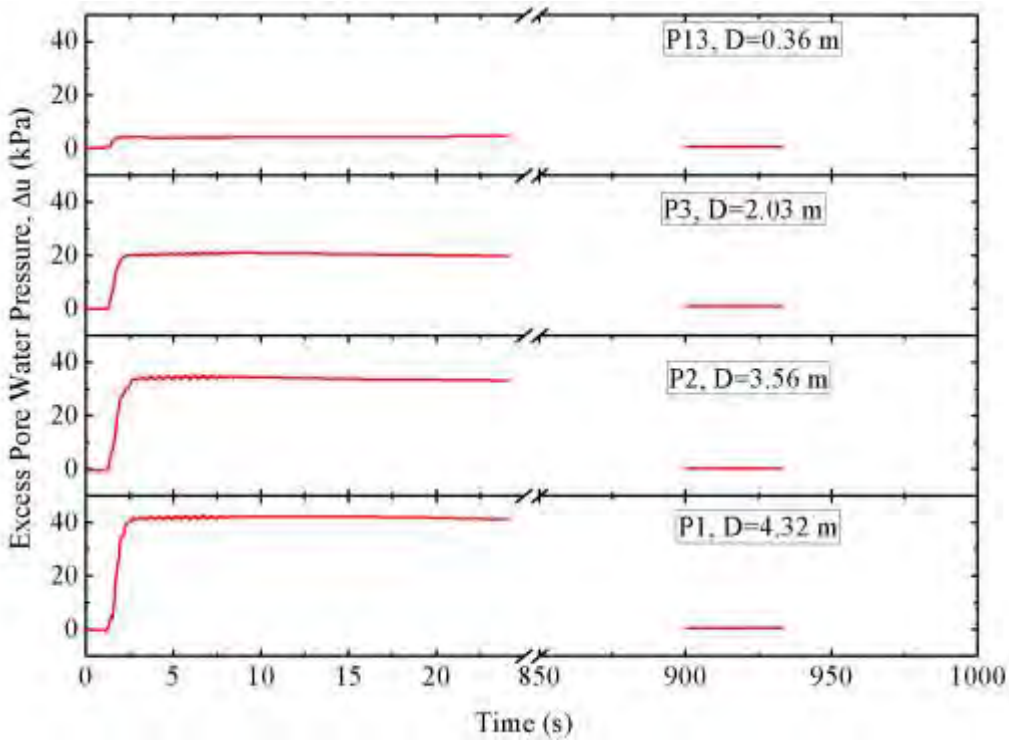

Fig. 8.17 Time history of Δu of T3 (a_{max}=0.10 g/15 cyc)

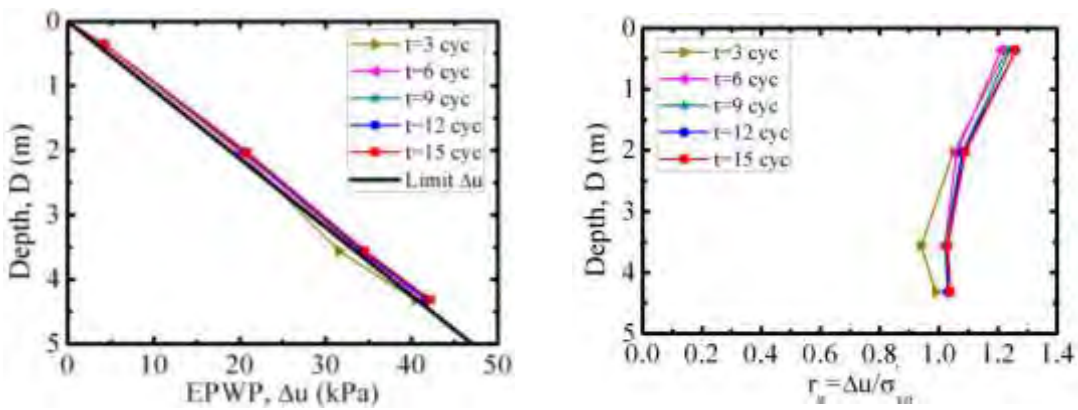

(a) Δu (b) r_u

Fig. 8.18 EPWP profiles of T3 (a_{max}=0.10 g/15 cyc)

8.2.4. Horizontal displacement response

8.2.4.1. T1-IM1 (a_{max}=0.015 g/5 cyc)

Fig. 8.19(a) plots the time history of soil horizontal displacement at selected depths in T1 (a_{max}=0.015 g/5 cyc). The variation of horizontal displacement of the soil stratum in T1 is mostly cyclic during shaking and the horizontal displacement is negligibly small after shaking. Fig. 8.19(b)

and (c) plot the time history of relative horizontal displacement of soil at selected depths in T1. The notation 'D=0.49 m (H29X-H27X)' denotes the relative displacement is taken between the horizontal displacement of laminate L29 and L27.

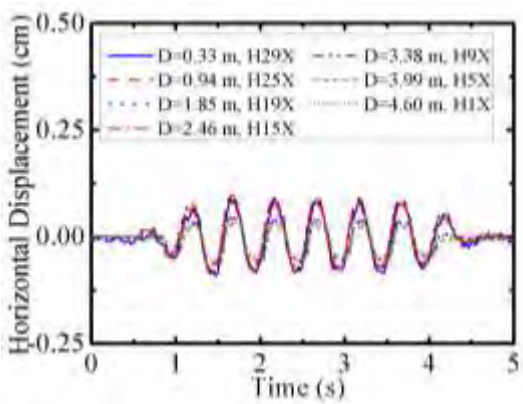

(a) Horizontal displacement

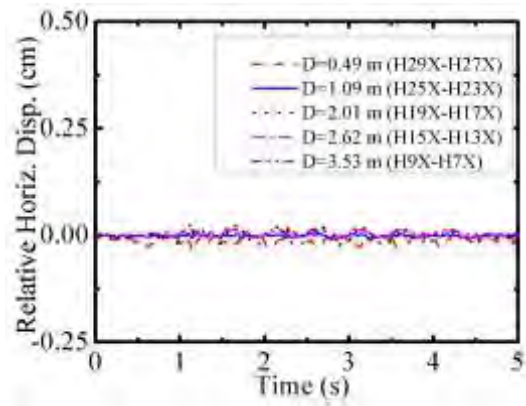

(b) Relative horiz. disp. b/w every other ring

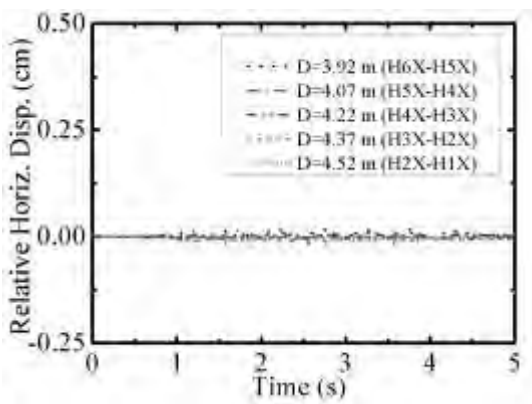

(c) Relative horiz. disp. b/w every ring

Fig. 8.19 Time history of horizontal displacement of T1 (a_{max}=0.015 g/5 cyc)

Fig. 8.20 plots the peak inter-ring drift profile of T1 in both positive and negative direction. As also shown in this figure is the peak base displacement for T1. The x-axis at top and bottom denotes the peak inter-ring drift and the peak base displacement, respectively.

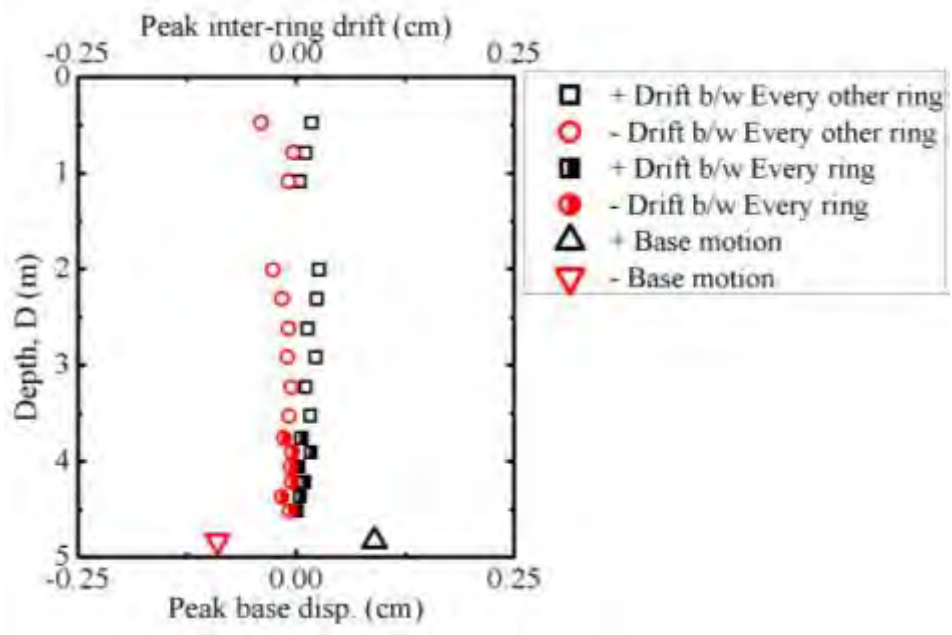

Fig. 8.20 Peak inter-ring drift profile of T1 (a_{max}=0.015 g/5 cyc)

8.2.4.2. T2-IM2 (a_{max}=0.03 g/15 cyc)

Fig. 8.21(a) plots the time history of soil horizontal displacement at selected depths in T2 (a_{max}=0.03 g/15 cyc). A sudden increase of horizontal displacement of soil at shallow and intermediate depths (D=0.33~2.46 m) at the first several shaking cycles is observed. The variation of horizontal displacement of the soil stratum is mostly cyclic during shaking and the horizontal displacement is negligibly small after shaking. Fig. 8.21(b) and (c) plot the time history of relative horizontal displacement of soil at selected depths in T2.

Fig. 8.22 plots the peak inter-ring drift profiles and the peak base displacement of T2.

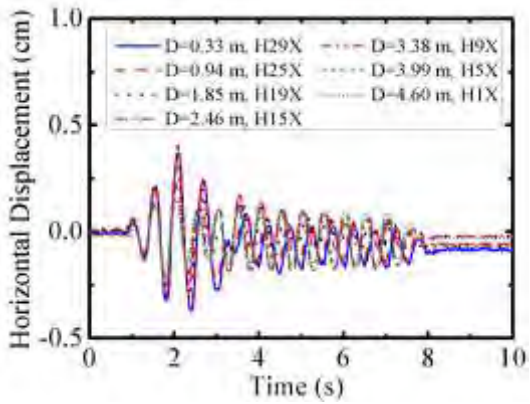

(a) Horizontal displacement

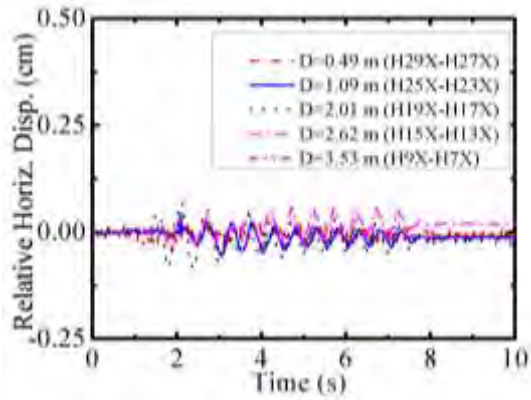

(b) Relative horiz. disp. b/w every other ring

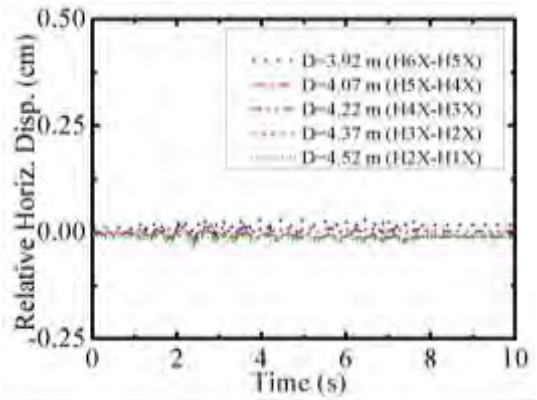

(c) Relative horiz. disp. b/w every ring

Fig. 8.21 Time history of horizontal displacement of T2 (a_{max}=0.03 g/15 cyc)

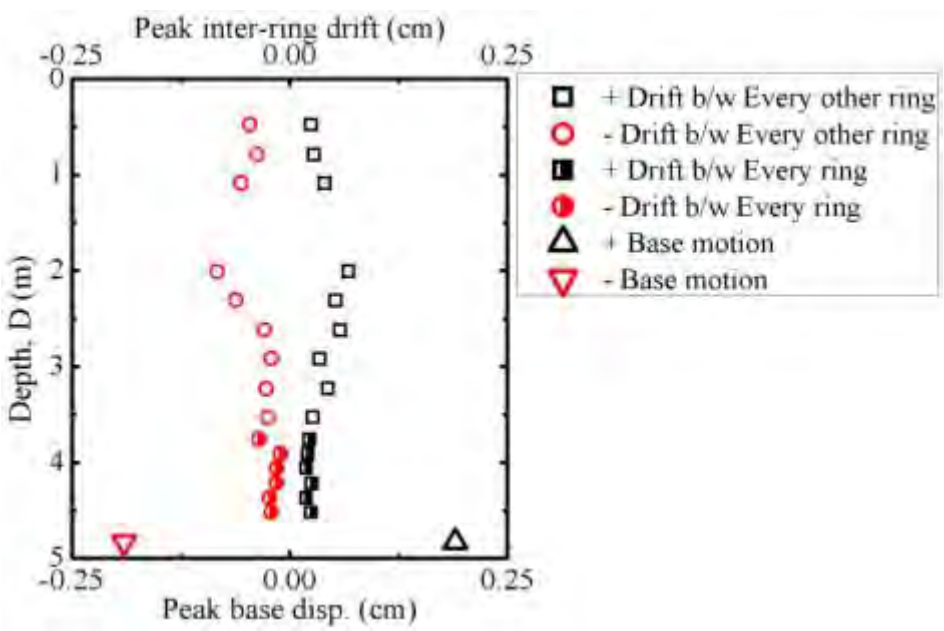

Fig. 8.22 Peak inter-ring drift profile of T2 (a_{max}=0.03 g/15 cyc)

8.2.4.3. T3-IM3 (a_{max}=0.10 g/15 cyc)

Fig. 8.23(a) plots the time history of soil horizontal displacement at selected depths in T3 (a_{max}=0.10 g/15 cyc). The sudden increase of horizontal displacement of soil at all depths at the first several shaking cycles may be associated with the initiation of liquefaction of soil at these depths. However, the variation of horizontal displacement of the soil stratum in T3 is negligibly small after shaking. Fig. 8.23 (b) and (c) plot the time history of relative horizontal displacement of the soil at selected depths in T3. Fig. 8.24 plots the peak inter-ring drift profile and the peak base displacement of T3.

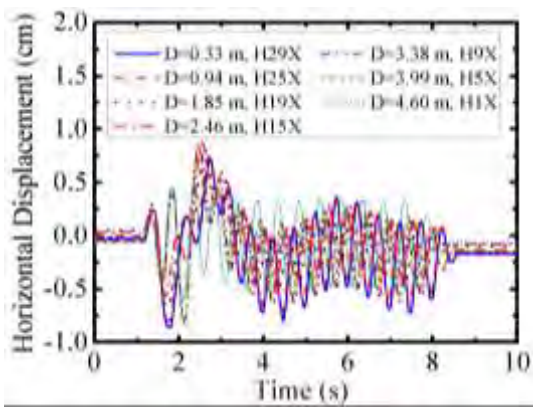

(a) Horizontal displacement

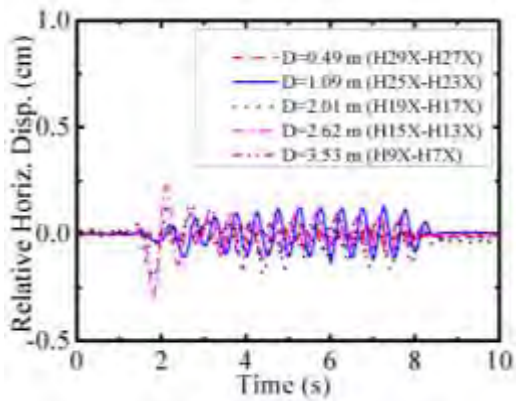

(b) Relative horiz. disp. b/w every other ring

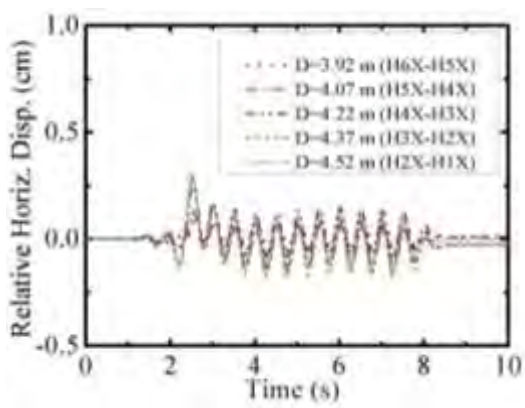

(c) Relative horiz. disp. b/w every ring

Fig. 8.23 Time history of horizontal displacement of T3 (a_{max}=0.10 g/15 cyc)

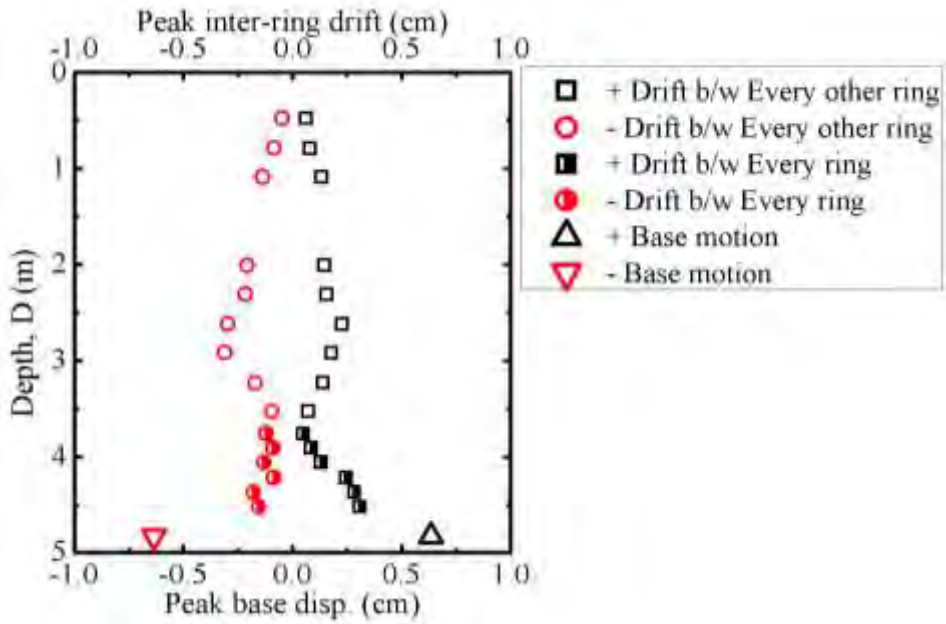

Fig. 8.24 Peak inter-ring drift profile of T3 (a_{max}=0.10 g/15 cyc)

8.2.5. Ground settlement response

The ground surface settlement plate is made in such a way that the unit weight of it is nearly same as the liquefied soil to prevent it from floating or sinking during and after shaking. Fig. 8.25 plots the time history of incremental ground settlement in shaking series 1. The data recording of T2 (a_{max}=0.03 g/15 cyc) and T3 (a_{max}=0.10 g/15 cyc) were not continuous after shaking. It was found that the ground settlement plates V1 and V3 were partially in soil after T2 and V2 was completely buried in soil after T2 (Fig. 8.26). Hence, the incremental settlement of soil in T2 and T3 can only be used as reference instead of actual value. The total settlement after T3 was obtained by subtracting the soil height before and after shaking series 1 using tape measument. Table 8.1 presents the summary of ground settlement in shaking series 1.

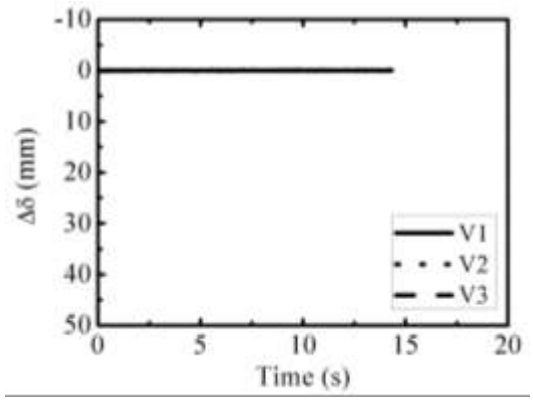

(a) T1(a_{max}=0.015 g/5 cyc)

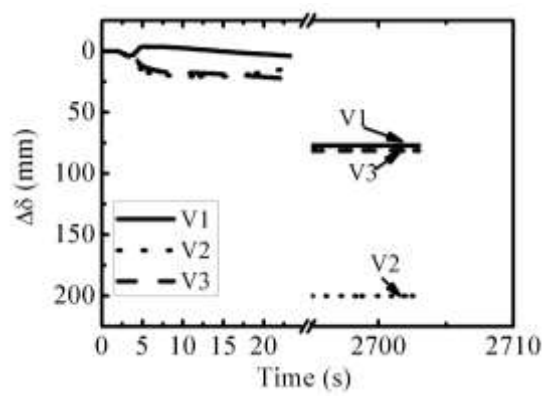

(b) T2(a_{max}=0.03 g/15 cyc)

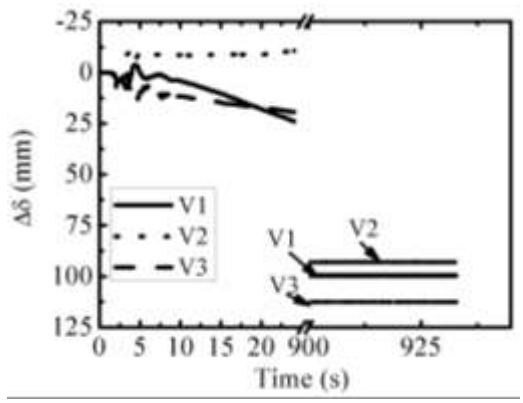

(c) T3(a_{max}=0.10 g/5 cyc)

Fig. 8.25 Time history of incremental ground settlement in shaking series 1

Table 8.1 Ground settlement of shaking series 1

Shaking series	Shaking Event	Input Motion	V1	V2	V3	Tape Measurement	Δδ for each shaking test	Cumulative Settlement δ
			(mm)	(mm)	(mm)	(mm)	mm	mm
1	T1	IM1 (a_{max}=0.015 g/5 cyc)	0	0	0	-	0	0
	T2	IM2 (a_{max}=0.03 g/15 cyc)	77	200	81	-	-	-
	T3	IM3 (a_{max}=0.10 g/15 cyc)	177	293	194	129	-	129

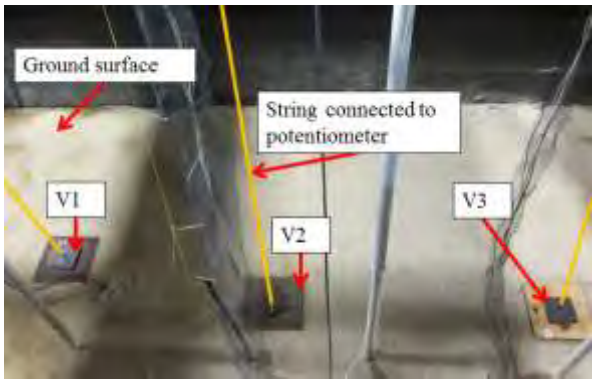

(a) Before Shaking

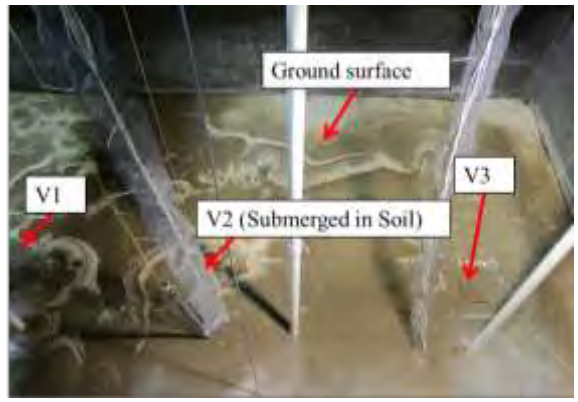

(b) After shaking (T2)

(c) After shaking (T3)

Fig. 8.26 Conditions of V1,V2 and V3 before and after shaking series 1

8.2.6. Stress-strain response

The acceleration recorded from the laminates as mentioned previously is used to study the stress-strain response of soil during shaking. Since the soil stratum in the laminar box performs in the one-dimensional shear beam pattern, the average shear stress and shear strain of soil can be evaluated using System Identification techniques (Zeghal and Elgamal, 1994). Fig. 8.27 schematically illustrates the approach and locations at which the shear stress-strain relationship is estimated. Two consecutive potentiometers or accelerometers located on the laminates are employed to evaluate the average shear stress or strain of soil at the midpoint depth of these two sensors.

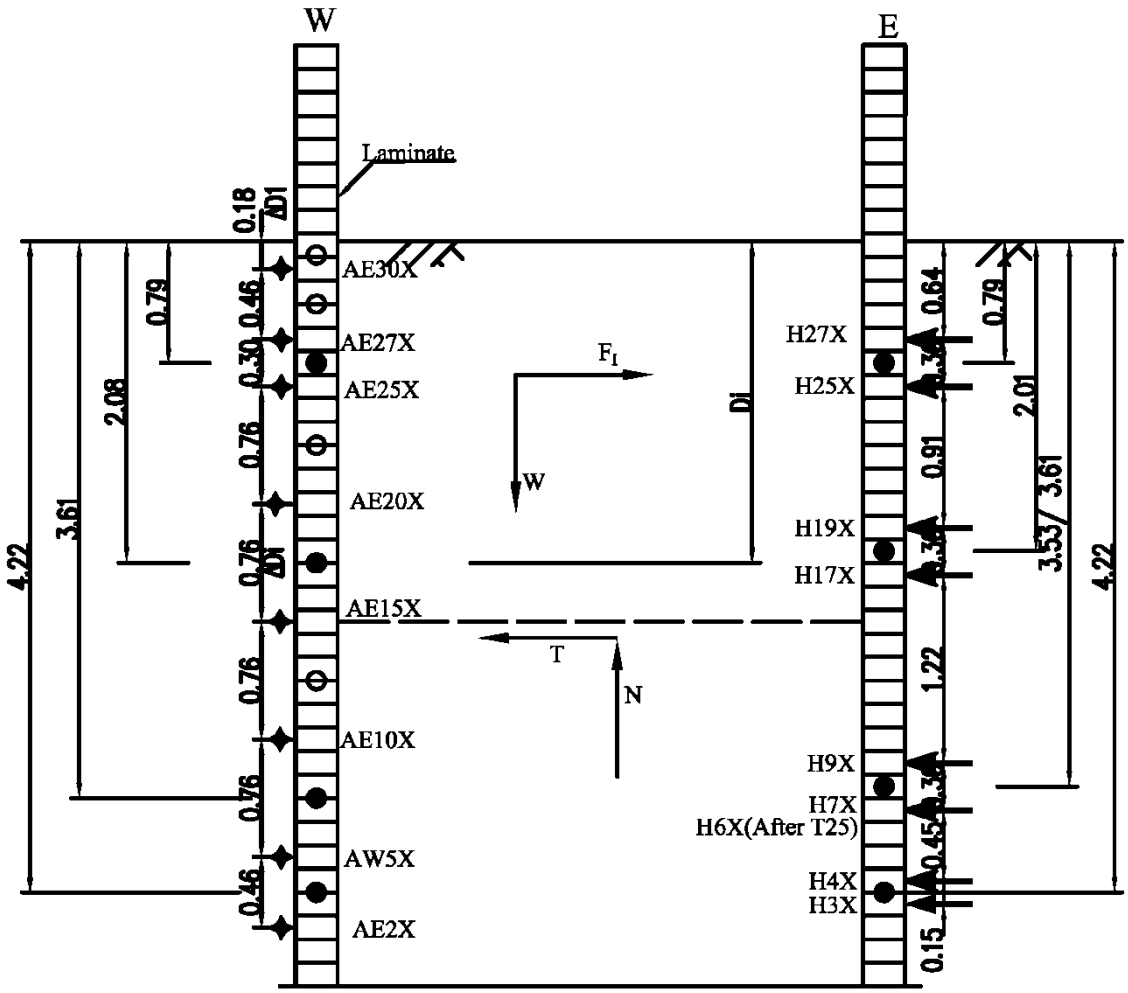

Note:
1. The accelerometers and temposonics/potentiometers are plotted in different sides for clarity.
2. Unit:m

Fig. 8.27 Locations and free body diagram of shear stress-shear strain estimation

The shear strain at a certain depth (Fig. 8.27) is computed as

$$\gamma_i = \frac{u_{i-1} - u_i}{\Delta D_i} \times 100\% \qquad \text{(Eq. 8.1)}$$

Where

u_{i-1} and u_i are the horizontal displacements recorded from two consecutive potentiometers of the ith layer of soil stratum, respectively.

ΔD_i is the thickness of the ith layer of soil stratum between two adjacent sensors.

For the estimation of shear stress at D_i, the equation from the free body diagram is determined as follows:

$$F_I - T = 0$$
$$W - N = 0 \qquad \text{(Eq. 8.2)}$$
$$\tau = \frac{T}{A}$$

Where A is the area of laminar box (A=13.70 m^2)

F_I is the total inertial force, $F_I = \sum_{j=1}^{i} M_j a_j$

M_j is the total mass of the soil plus laminates containing the soil in sublayer j,

a_j is the average acceleration between two adjacent accelerometers in sublayer j.

T is the tangential force exerted on the soil body

W is the total weight of the soil plus the laminates containing the soil

$W = \sum_{j=1}^{i} (\gamma_{sat} \Delta D_j A + m_j g)$, m_j is the subtotal of mass of laminates in the sublayer j.

N is the normal force acting on the soil body

The estimated shear stress and strain amplitudes accuracy (Eq. 8.1 and 8.2) is the function of (1) instrument spacing configuration, and (2) recorded acceleration wave lengths $\lambda=(V_s/f)$ where V_s is shear wave velocity and f is frequency. It shall be noticed that at some locations the two adjacent accelerometers are several laminates away from each other (e.g. AE20X and AE25X), which may introduce errors in calculating the shear stress. Also there are several free rings above soil surface (rings not containing soil). Moreover, the inertia effect of these free rings is not considered in the stress computation.

8.2.6.1. T1-IM1 (a_{max}=0.015 g/5 cyc)

The time history of shear stress and shear strain at different depths in T1 (a_{max}=0.015 g/5 cyc) are plotted in Fig. 8.28 and Fig. 8.29, respectively. Fig. 8.30 plots the shear stress-strain response at different depths in T1, which indicates that there is no stiffness degradation observed during the entire shaking.

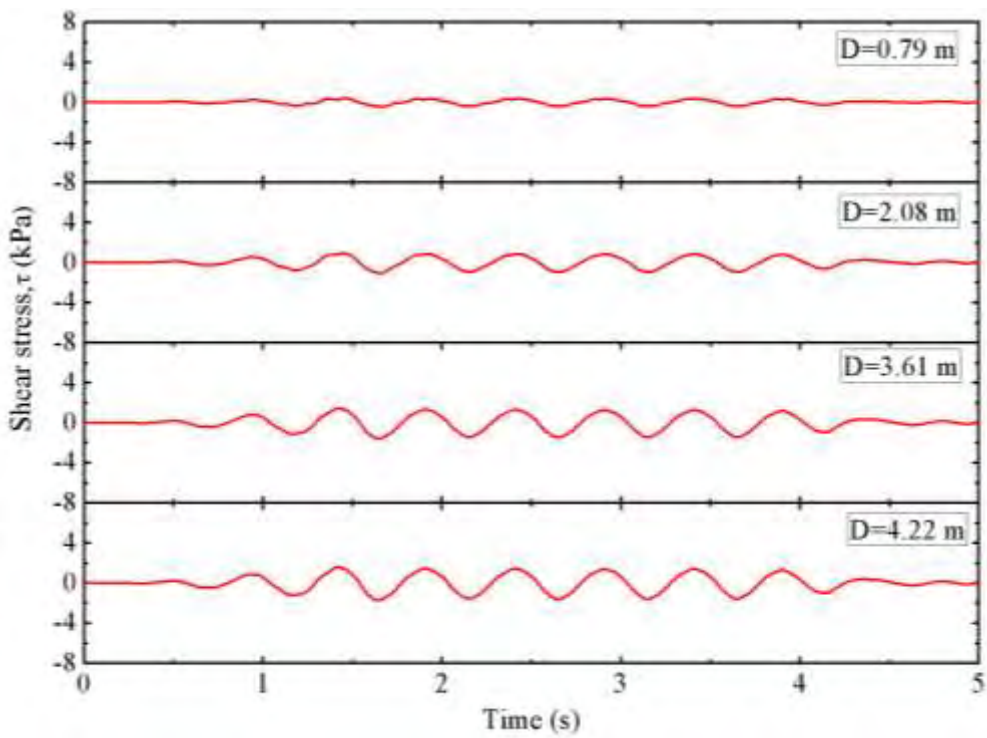

(a) Shear stress

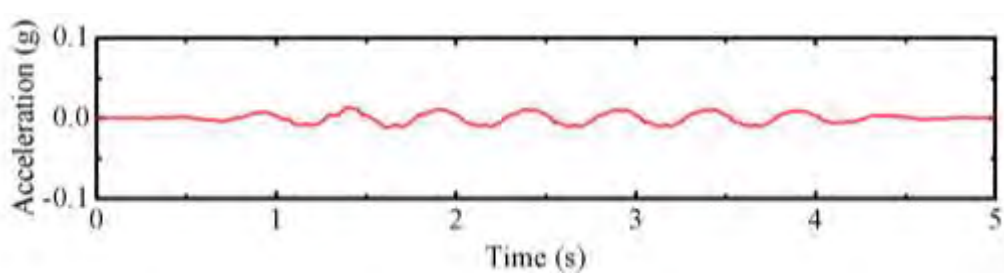

(b) B3X

Fig. 8.28 Time history of shear stress of T1 (a_{max}=0.015 g/5 cyc)

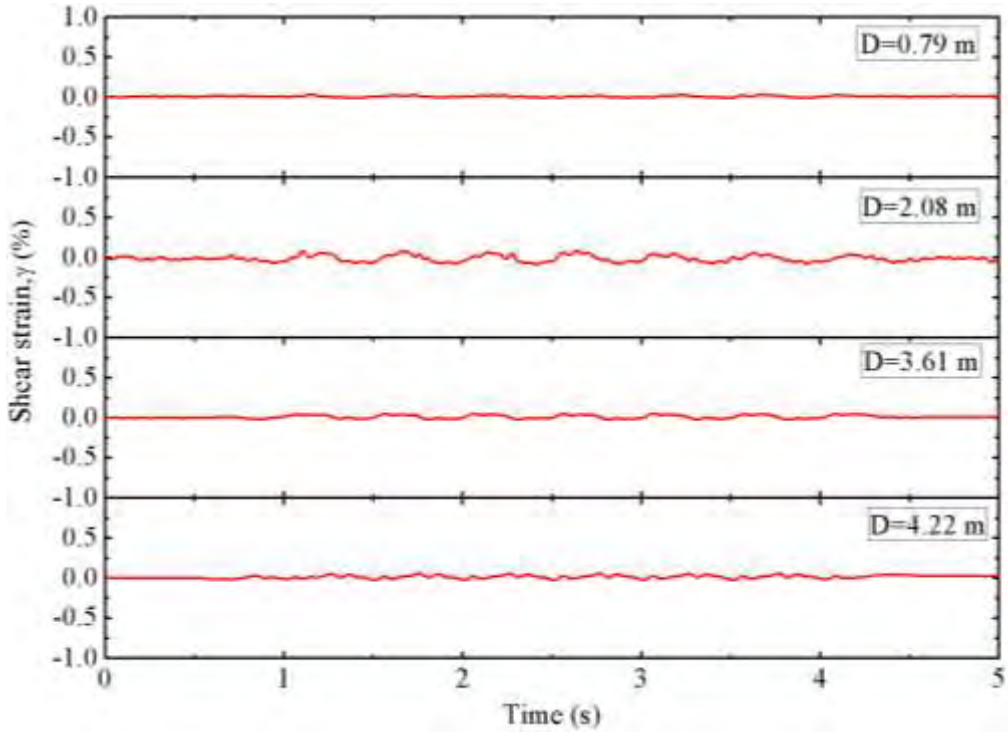

(a) Shear strain

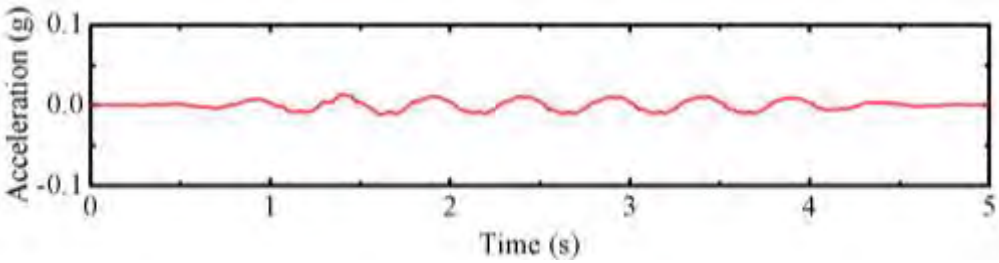

(b) B3X

Fig. 8.29 Time history of shear strain of T1 (a_{max}=0.015 g/5 cyc)

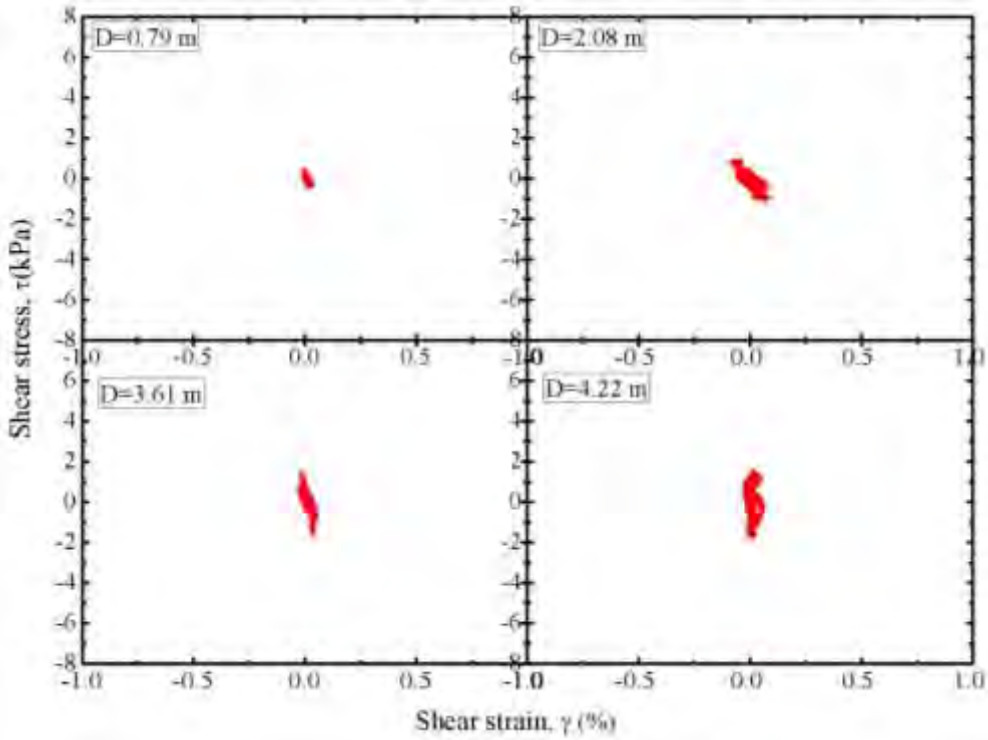

Fig. 8.30 Shear stress- strain loop of T1 (a_{max}=0.015 g/5 cyc)

8.2.6.2. T2-IM2 (a_{max}=0.03 g/15 cyc)

The time history of shear stress and shear strain at different depths in T2 (a_{max}=0.03 g/15 cyc) are plotted in Fig. 8.31 and Fig. 8.32, respectively. Fig. 8.31 shows that the shear stress of soil at all depths increases at the first three shaking cycles and decreases afterwards as the excess pore water pressure builds up. Also from this figure, it is observed that the shear stress increases as depth increases at the first three shaking cycles. Fig. 8.33 plots the shear stress-strain response of soil at different depths at two time frames (0-3 cyc and 4-15 cyc) in T2. The stress-strain response exhibits a low-strain stiffness increasing with depth as expected in the first time frame. Shear stress degradation and shear strain development (stiffness degradation) are observed at shallow and intermediate depth (D=0.79 m and D=2.08 m) after three shaking cycles as the excess pore water pressure builds up. There is apparent shear stress degradation but no apparent shear strain

development observed at deep depth (D=3.61 m and D=4.22 m) when compared at these two time frames.

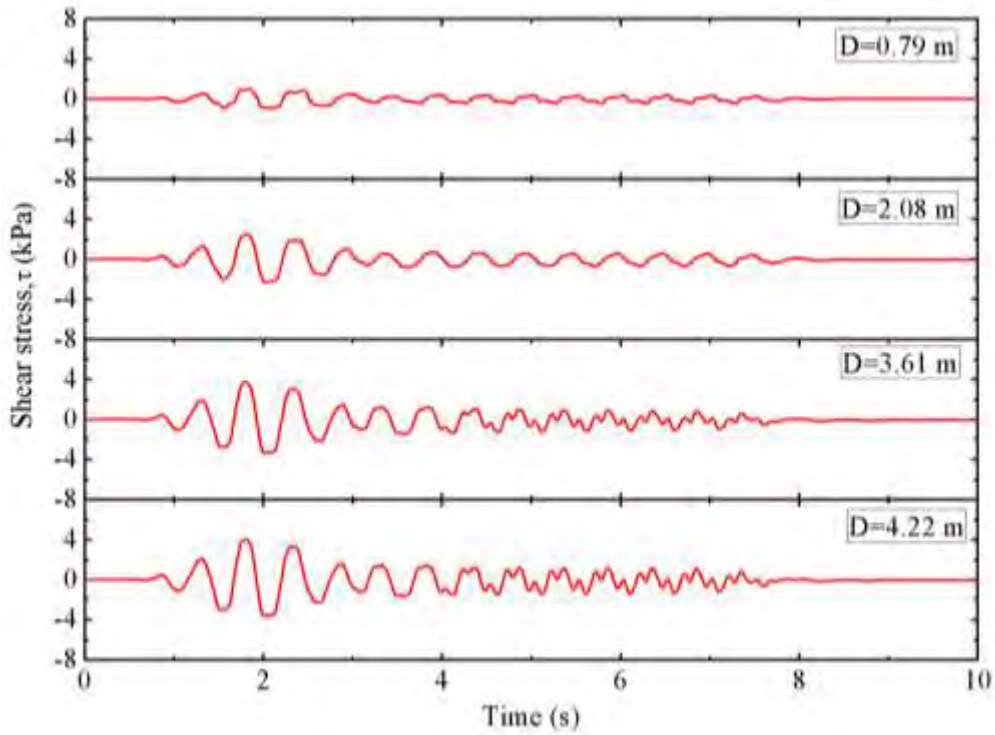

(a) Shear stress

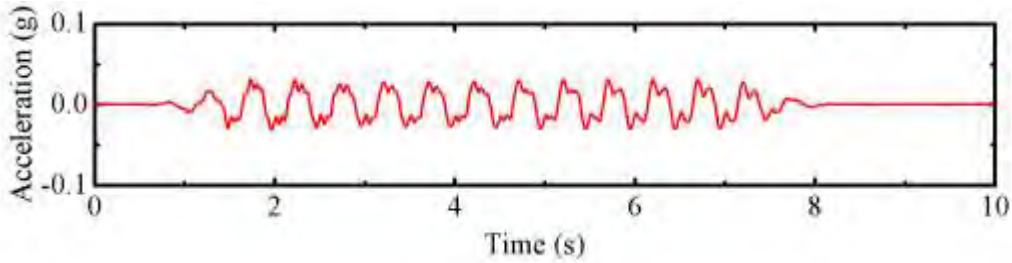

(b) B3X

Fig. 8.31 Time history of shear stress of T2 (a_{max}=0.03 g/15 cyc)

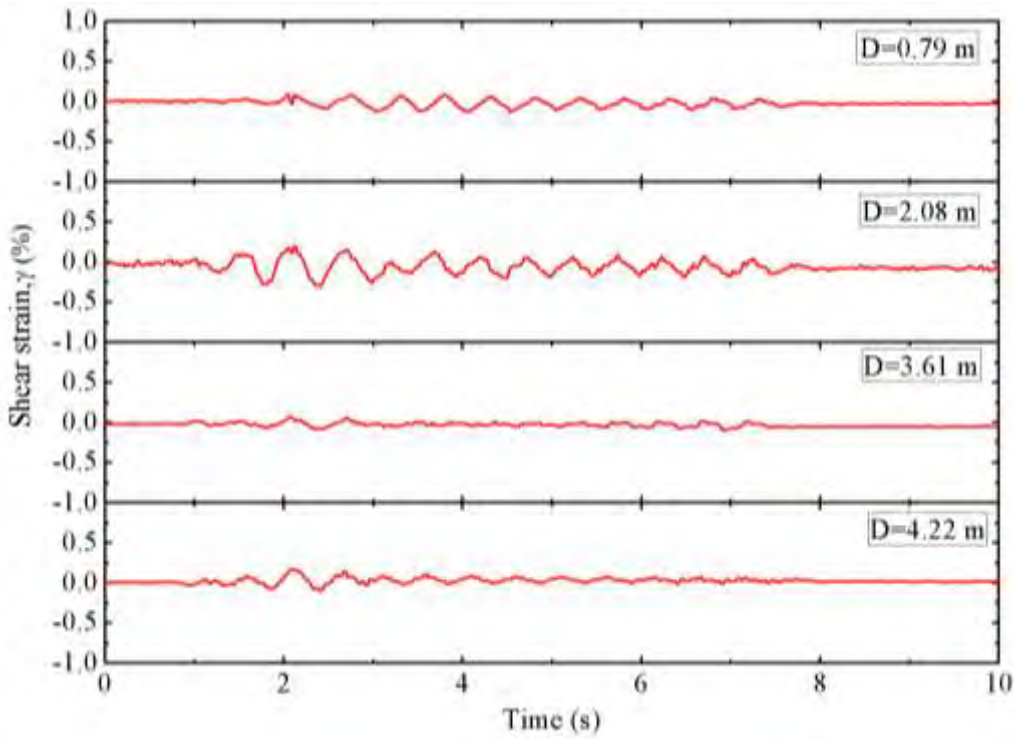

(a) Shear strain

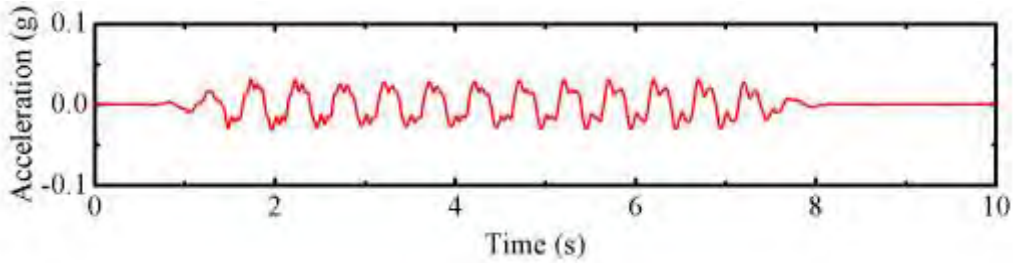

(b) B3X

Fig. 8.32 Time history of shear strain of T2 (a_{max}=0.03 g/15 cyc)

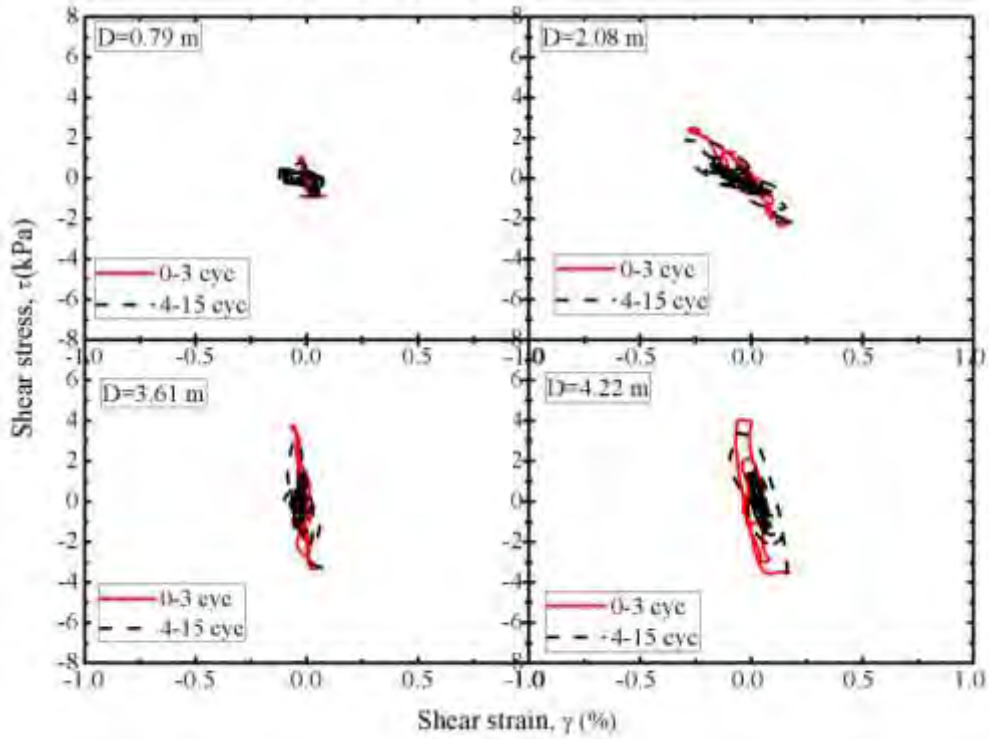

Fig. 8.33 Shear stress- strain loop of T2 (a_{max}=0.03 g/15 cyc)

8.2.6.3. T3-IM3 (a_{max}=0.10 g/15 cyc)

The time history of shear stress at different depths in T3 (a_{max}=0.10 g/15 cyc) is plotted in Fig. 8.34. It shows that at shallow and intermediate depth (D=0.79 m and D=2.08 m), there is no much shear stress development at the first three shaking cycles. However, it gradually increases afterwards as the shaking continues. However, the shear stress of soil at deep depth (D=3.61 m and D=4.22 m) increases at the first three shaking cycles and decreases afterwards as the shaking continues. Also from this figure, it is observed that the shear stress increases as depth increases at the first three shaking cycles. Fig. 8.35 shows the time history of shear strain at different depths in T3. It is noticed that the shear strain of soil develops at all depths during shaking. Fig. 8.36 plots the shear stress-strain response at different depths at the two time frames in T3. For soil at shallow and intermediate depth (D=0.79 m and D=2.08 m), there is no apparent stiffness degradation

observed between the two time frames. For soil at deep depth (D=0.3.61 m and D=4.22 m), the degradation of soil stiffness between these two time frames is clearly found.

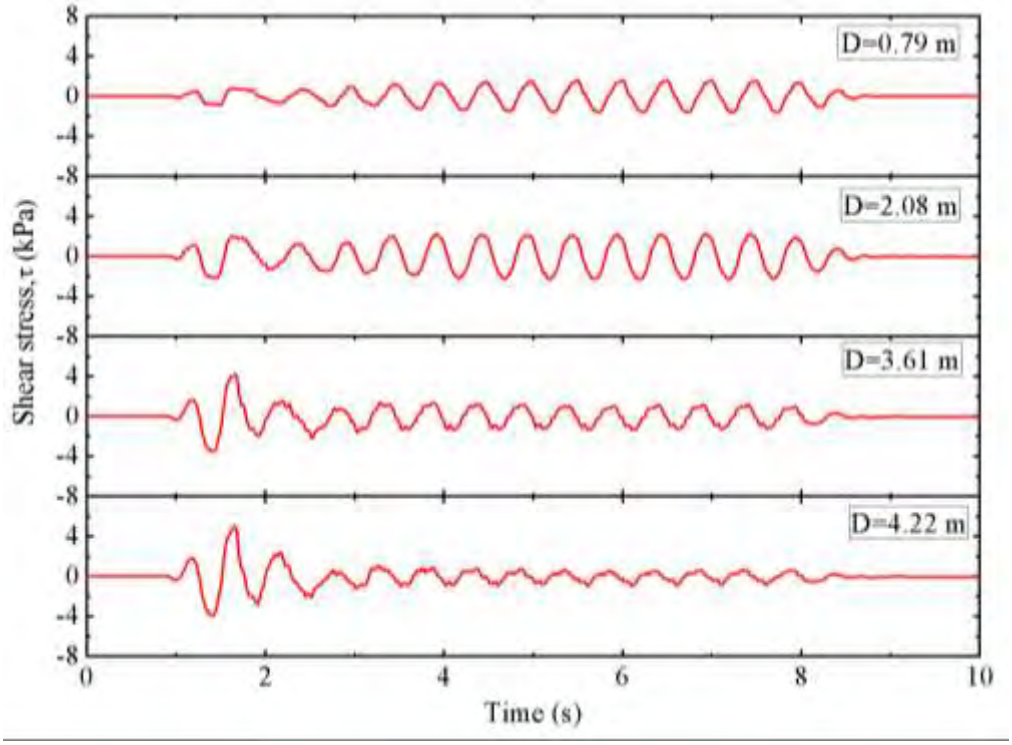

(a) Shear stress

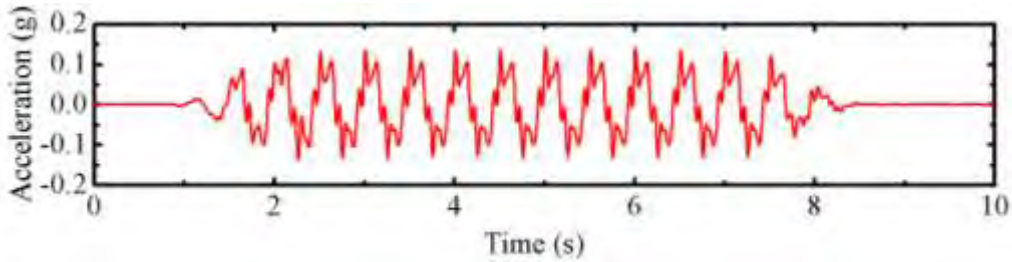

(b) B3X

Fig. 8.34 Time history of shear stress of T3 (a_{max}=0.10 g/15 cyc)

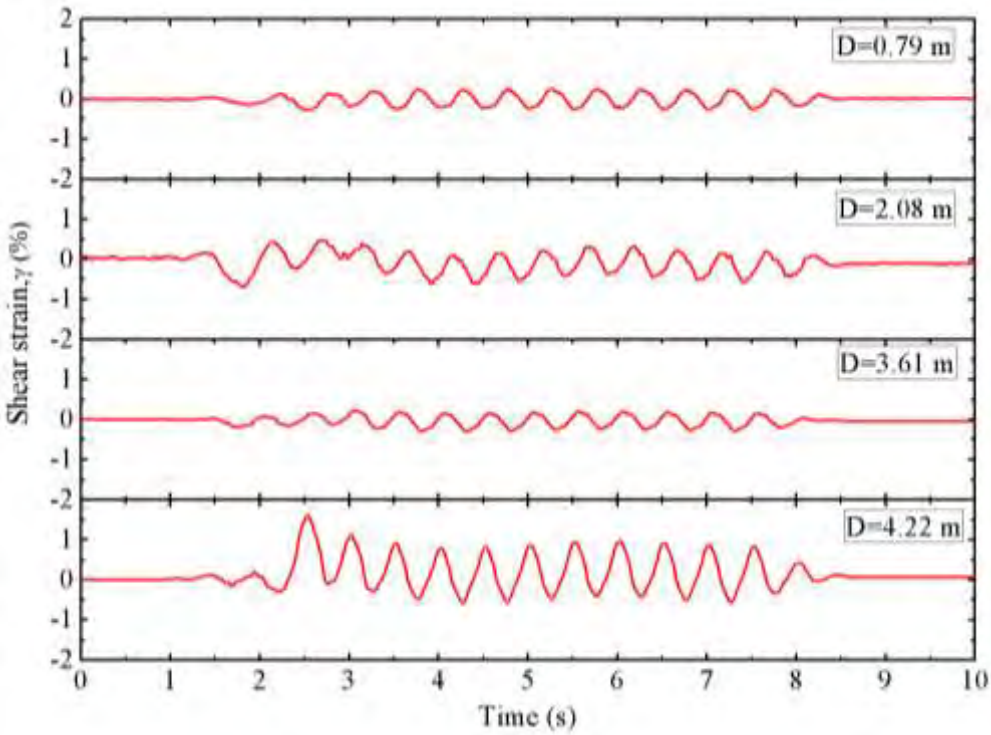

(a) Shear strain

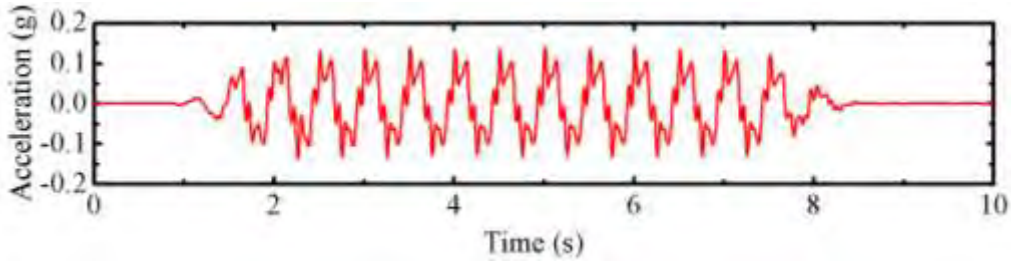

(b) B3X

Fig. 8.35 Time history of shear strain of T3 (a_{max}=0.10 g/15 cyc)

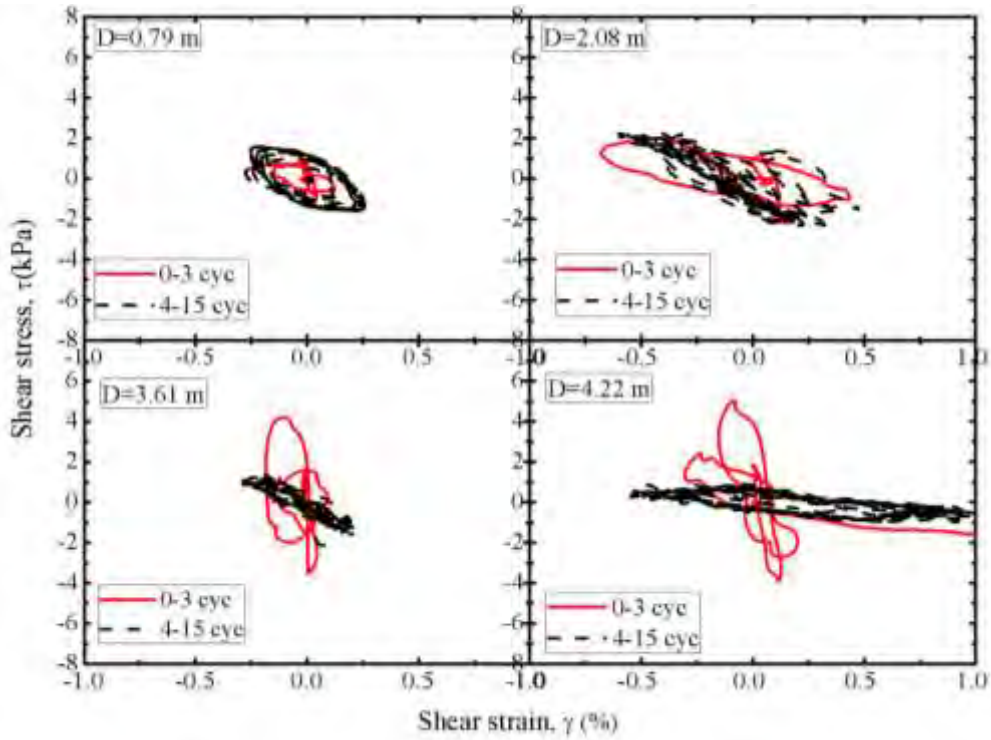

Fig. 8.36 Shear stress- strain loop of at different depths of T3 (a_{max}=0.10 g/15 cyc)

8.2.7. Cone resistance, shear wave velocity and liquefaction resistance

Fig. 8.37 plots the semi-empirical correlation between CRR-q_{c1N} proposed by Robertson and Wride (1998). Besides cone resistance, shear wave velocity (V_s) has been employed as a useful tool to evaluate the liquefaction potential since both shear wave velocity and liquefaction resistance are similarly influenced by many of the same factors such as void ratio, state of stress, stress history and geologic age (Andrus and Stokoe, 2000).

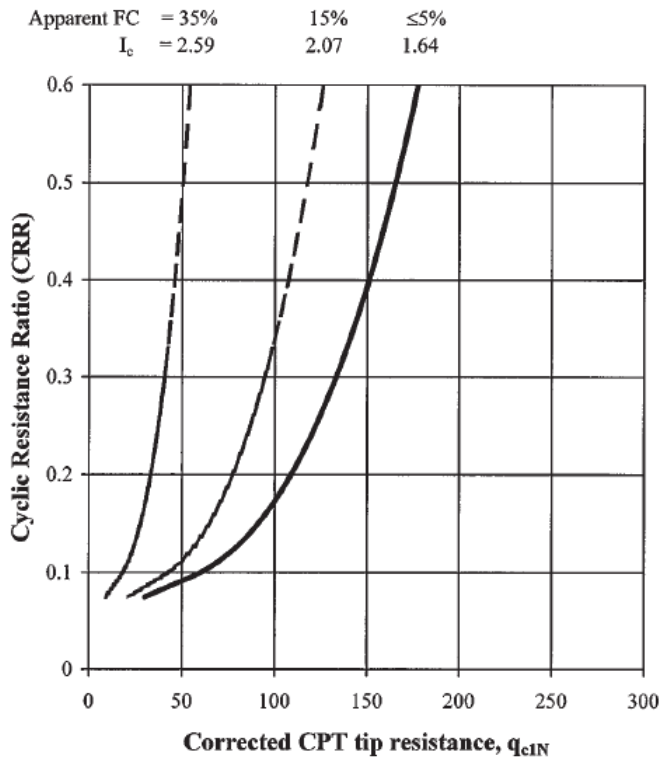

Fig. 8.37 Field based liquefaction screening chart using cone resistance (Robertson and Wride, 1998)

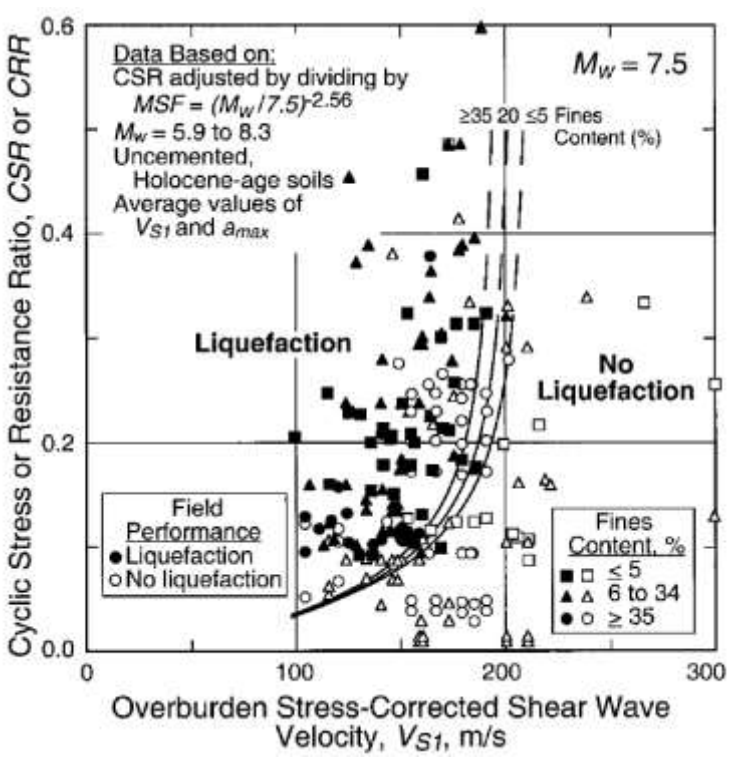

Fig. 8.38 Field based liquefaction screening chart using shear wave velocity (Andrus and Stokoe, 2000)

The overburden stress corrected shear wave velocity V_{s1} is defined by (Sykora 1987; Robertson et al., 1992) as:

$$V_{s1} = V_s \left(\frac{P_{at}}{\sigma'_{vo}} \right)^{0.25} \qquad \text{(Eq. 8.3)}$$

Where P_{at} is the atmospheric pressure, σ_{vo}' is the initial effective overburden stress in the same unit as P_{at} and V_s is the measured shear wave velocity.

As can be observed from Fig. 8.38, the CSR/CRR for a given V_{s1} is dependent on the silt content (C_F) of silty sand, which is similar to the CPT based liquefaction assessment (Fig. 8.37). Generally, the silty sand with higher silt content yields higher CSR/CRR with the same V_{s1}, but the CSR/CRR remains unchanged when C_F>35%. It shall be noticed that application of liquefaction assessment to other sites using Fig. 8.38 requires verification and necessary modification because this V_{s1} based liquefaction triggering chart is limited to uncemented, Holocene-aged soils.

8.2.8. Liquefaction analysis

In this section, the estimation of q_{c1N}, V_{s1} and CSR for T2 and T3 is described. In T2 (a_{max}=0.03 g/15 cyc), the q_{c1N} and V_{s1} of soil at different depths (corresponding to working piezometer depths) obtained from C0 are used because T1 is only for the system identification purpose. It is found that the relative density of soil increases as liquefaction tests continue and it is known that the q_{c1N} and V_{s1} are related to the relative density. Hence, the q_{c1N} and V_s of soil at various depths used in T3 (a_{max}=0.10 g/15 cyc) are linearly interpolated between C0 and C3 in terms of test number. It shall be noticed that the used linear interpolation method relating the q_{c1N}

and V_{s1} linearly to the test number would introduce errors in obtaining the actual values of q_{c1N} and V_{s1}. Three methods are resorted to estimate the CSR in the liquefaction test. The ratio of the total weigh of saturated soil and laminates over the weight of saturated soil is applied to correct the estimated average shear stress (laminate factor). Table 8.3 provides the q_{c1N}, V_{s1} and CSR of soil at different depths and number of cycles for r_u to reach unity in T2 and T3.

Below shows an example of how the q_{c1N} and V_{s1} is estimated and CSR is calculated in T3.

Sample calculation:

A constant unit weight of saturated sand (γ_{sat}=19.2 kN/m^3) is assumed in the interpolation, corresponding to D_r=42% and ϕ'=31 deg. [Fig. 5.9(c)]. The coefficient of lateral earth pressure at rest is K_0=1-sin(ϕ')=0.485

<u>@D=2.03 m</u>

<u>Estimating q_{c1N}:</u>

q_c=0.67 MPa for C0, using Eq. 2.7

$$C_q = \min(1.7, \left(\frac{P_{at}}{\sigma'_{vo}}\right)^{0.5}) = \min(1.7, \left(\frac{101.325}{(19.2-9.8)(2.03)}\right)^{0.5}) = \min(1.7, 2.28) = 1.7$$

$$q_{c1N} = C_q \frac{q_c}{P_{at}} = 1.7\left(\frac{0.67\times10^3}{101.325}\right) = 11$$

q_c=1.23 MPa for C3

$$q_{c1N} = C_q \frac{q_c}{P_{at}} = 1.7\left(\frac{1.23\times10^3}{101.325}\right) = 21$$

Since C0 corresponds to liquefaction test 2 and C3 corresponds to the liquefaction test 4 or we can say liquefaction test 2 corresponds to C1 and liquefaction test 3 corresponds to C2. We

assume that the q_{c1N} linearly increases with test number. Hence, q_{c1N} of T3 at D=2.03 m can be estimated from:

$$q_{c1N} \text{ at T3} = 11 + \frac{(21-11)}{(3-1)}(2-1) = \boxed{16}$$

Estimating CSR:

As introduced previously, the laminate factor shall be applied to correct the effect of laminate weight on the $a_{max\text{-}ground}$. The total weight of laminates is 393 kN (L1-L39). Given that the dimension of laminar box is 5 m in length, 2.74 m in width and 5.95 m in height (L1-L39), the soil weight is 1565 kN. Hence the laminate factor is (1565+393)/1605=1.25. There are three methods to estimate the CSR of the soil at a given depth.

Method I, using Eq. 2.5

The maximum ground acceleration $a_{max\text{-}ground}$=0.049 g from AE30X. For D=2.03 m, the reduction factor r_d=0.990 according to Fig. 2.2. Applying Eq. 2.5. the CSR at D=2.03 m from laminar box can be estimated as follows:

$$(CSR)_{LB} = L_F 0.65 \frac{a_{\max-ground}}{g} \sigma_v r_d / \sigma_{vo}^{'} = 1.25(0.65)\left(\frac{0.049g}{g}\right)\frac{(19.2)(0.990)}{(19.2-9.8)} = \boxed{0.081}$$

Since the liquefaction test performed in laminar box is a one-dimensional shaking, the CSR shall be corrected for multi-shaking direction by Castro (1975) and Seed et al. (1978):

$$CSR = 0.9\frac{2(1+2K_0)}{3\sqrt{3}}\left(CSR\right)_{LB} = 0.9\frac{2(1+2\times 0.485)}{3\sqrt{3}}(0.081) = \boxed{0.055}$$

Method II, using shear stress estimated from section 8.2.6

τ_{max} @D=2.03m=2.3 kPa, σ_{vo}'=(19.2-9.8)(2.03)=19.1 kPa

$$(CSR)_{LB} = \frac{\tau_{\max}}{\sigma'_{vo}} = \frac{2.3}{19.1} = 0.121$$

Corrected for multi-shaking direction

$$CSR = 0.9\frac{2(1+2K_0)}{3\sqrt{3}}\left(CSR\right)_{LB} = 0.9\frac{2(1+2\times 0.485)}{3\sqrt{3}}(0.121) = \boxed{0.082}$$

<u>Method III, using amplification factor from the non-destructive motion and a_{max} from base-shaker</u>

The amplification factor from non-destructive motion T1 (IM1) is 1.5 and the a_{max} at base shaker is 0.144 g, using Eq. 2.9. so the $a_{max\text{-}ground}$=1.5(0.144)=0.216 g

$$(CSR)_{LB} = L_F\, 0.65\frac{a_{\max-ground}}{g}\sigma_v r_d / \sigma'_{vo} = 1.25(0.65)\left(\frac{0.216g}{g}\right)\frac{(19.2)(0.990)}{(19.2-9.8)} = \boxed{0.354}$$

Corrected for multi-shaking direction

$$CSR = 0.9\frac{2(1+2K_0)}{3\sqrt{3}}\left(CSR\right)_{LB} = 0.9\frac{2(1+2\times 0.485)}{3\sqrt{3}}(0.354) = \boxed{0.241}$$

Table 8.2 summarizes the estimated $(CSR)_{LB}$ and CSR of soil at D=2.03 m using different methods.

Table 8.2 Estimated $(CSR)_{LB}$ and CSR at D=2.03 m of T3 using different methods

Method type	Method I	Method II	Method III
$(CSR)_{LB}$	0.081	0.121	0.354
CSR	0.055	0.082	0.242

<u>@D=2.47 m</u>

It shall be noted that the depth at which V_s is used for interpolation for each CPT is not exactly the same, but it is within acceptable range. For instance, the depth for interpolation of C0 is 2.59 m while it is 2.35 m of C3. Hence the average depth of 2.47 m is used for representation.

<u>Estimating V_{s1}:</u>

V_s=106 m/s of C0, using Eq. 9.3

$$V_{s1} = V_s \left(\frac{P_{at}}{\sigma'_{vo}} \right)^{0.25} = 106 \left(\frac{101.325}{(9.4)(2.59)} \right)^{0.25} = 151 m/s$$

V_s=89 m/s of C3, using Eq. 9.3

$$V_{s1} = V_s \left(\frac{P_{at}}{\sigma'_{vo}} \right)^{0.25} = 89 \left(\frac{101.325}{(9.4)(2.35)} \right)^{0.25} = 130 m/s$$

$$V_{s1} \text{ at T3} = 151 + \frac{(130-151)}{(3-1)}(2-1) = \boxed{140 m/s}$$

Similarly, the interpolation method is used to approximate the cone resistance and shear wave velocity of the soil stratum before each liquefaction test of large magnitude earthquakes (IM2 and IM3) when there is no direct CPT or shear wave velocity test performed (Table 7.8).

The correlation between q_{c1N} and CSR as well as the correlation between V_{s1} and CSR determined from liquefaction tests T2 and T3 are plotted in Fig. 8.39(a) and (b), respectively. The notation 'T2-0.03-C0-NL' in the figure denotes the liquefaction test T2 at a_{max} =0.03 g (0.03) using direct CPT C0 data (C0) and the soil does not liquefy (NL) while the notation 'T3-0.10-CX-L' represents the liquefaction test T3 at a_{max} =0.1 g (0.10) using CPT interpolation data (CX) and the soil liquefies (L). "R-W(1998)" represents the correlation of CRR-q_{c1N} established by Robertson and Wride (1998) in Fig. 8.39(a). "A-S(1998)" denotes the correlation of CRR-V_{s1} proposed by Andrus and Stokoe (2000) in Fig. 8.39(b). More data points of CSR-q_{c1N} and CSR-V_{s1} for other liquefaction tests can be referred to section 8.5.

Table 8.3 q_{c1N} V_{s1} and CSR/CSR for T2 and T3

T2-IM2(0.03 g/15 cyc)						
Depth	q_{c1N}	V_{s1}	CSR			r_u(cycles to unity)
(m)		(cm/s)	Method I	Method II	Method III	
0.97	4	-	0.053	0.075	0.056	1.0(N/A)
2.03	11	-	0.052	0.086	0.055	1.0(6)
2.47	-	151	0.052	0.082	0.055	-
3.05	-	136	0.052	0.078	0.055	-
3.56	14	-	0.051	0.075	0.054	0.94
4.32	18	132	0.051	0.067	0.054	0.78
T3-IM3(0.10 g/15 cyc)						
Depth	q_{c1N}	V_{s1}	CSR			r_u(cycles to unity)
(m)		(cm/s)	Method I	Method II	Method III	
0.97	5	-	0.055	0.120	0.243	1.0(N/A)
2.03	16	-	0.055	0.082	0.242	1.0(2)
2.47	-	141	0.055	0.083	0.241	-
3.05	-	137	0.054	0.085	0.240	-
3.56	21	-	0.054	0.086	0.238	1.0(3)
4.32	-	-	0.054	0.084	0.237	1.0(3)

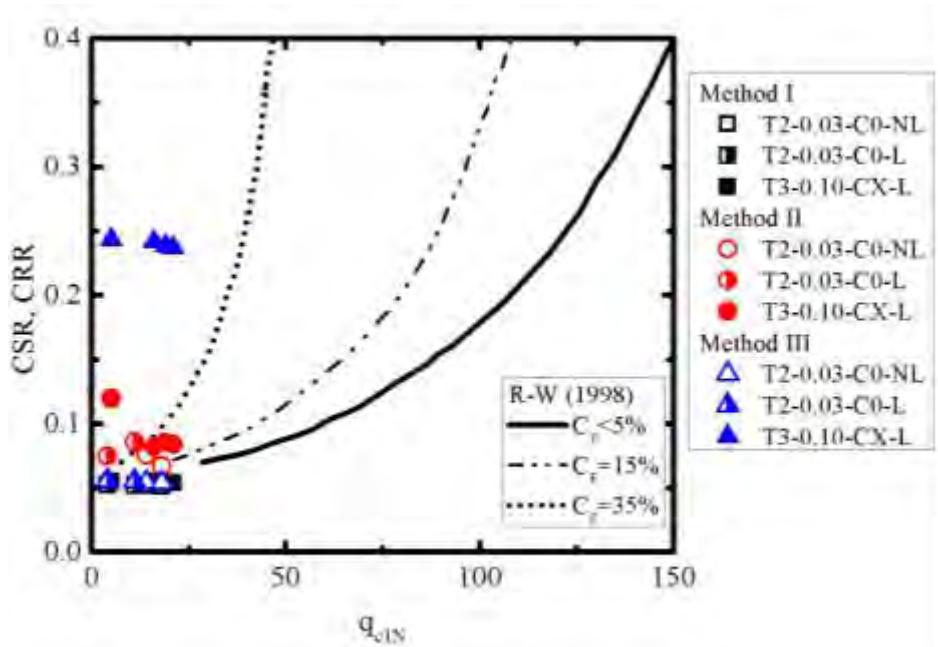

(a) CSR/CRR vs q_{c1N}

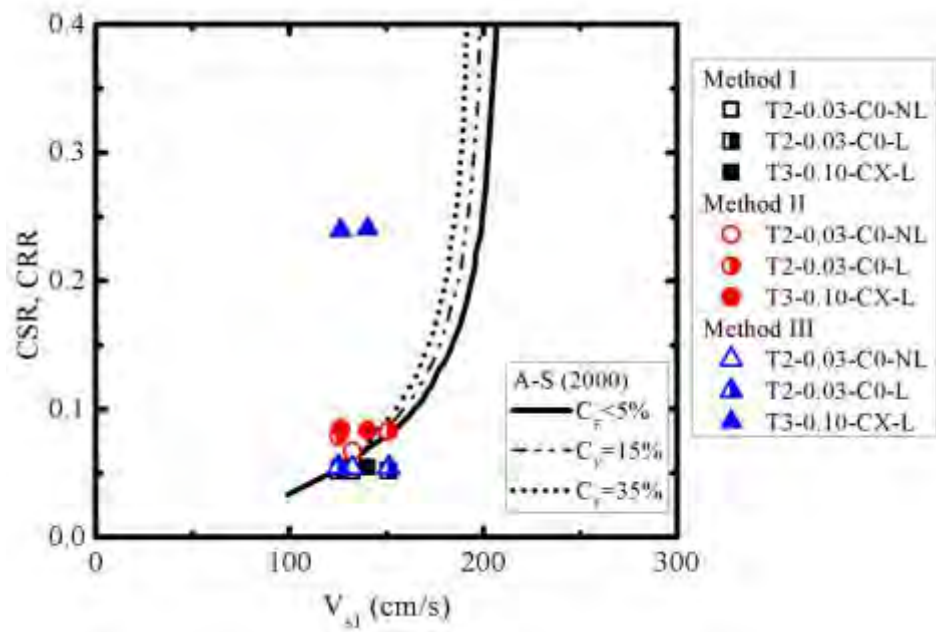

(b) CSR/CRR vs V_{s1}

Fig. 8.39 Correlation between q_{c1N} and CSR/CRR, Vs1 and CSR/CRR for T2 and T3

8.3. Liquefaction tests- Shaking series 2

This section analyzes the second shaking series, which consists of T4 through T8 (IM4), T9 (IM2) and T10 (IM3). The purpose of liquefaction tests-T4 through T8 (IM4) is to study the soil

response under several small magnitude earthquakes before experiencing large magnitude earthquakes [T9 (IM2) and T10 (IM3)]. The analyses of T4, T8, T9 and T10 are presented. The sample rate for this shaking series and shaking series afterwards are 256 Hz. The collected data are filtered using a low-pass filter with the cutoff frequency equal to 50 Hz.

8.3.1. Base shaking

8.3.1.1. T4 and T8-IM4 (a_{max}=0.03 g/5 cyc)

Fig. 8.40 and Fig. 8.41 compare the recorded base motion at different locations in x- and y-direction of T4 and T8 (a_{max}=0.03 g/5 cyc), respectively. The ratio of the peak base acceleration in y-direction to that in x-direction at B1, B2 and B3 for T4 is 11%, 12% and 8%, respectively while it is 13%, 10% and 7%, respectively for T8.

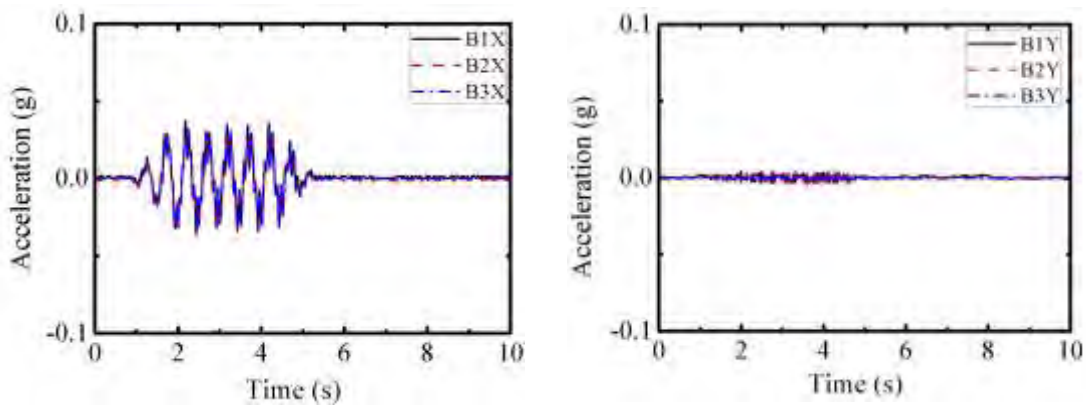

(a) x-direction (b) y-direction

Fig. 8.40 Base shaker of T4 (a_{max}=0.03 g/5 cyc)

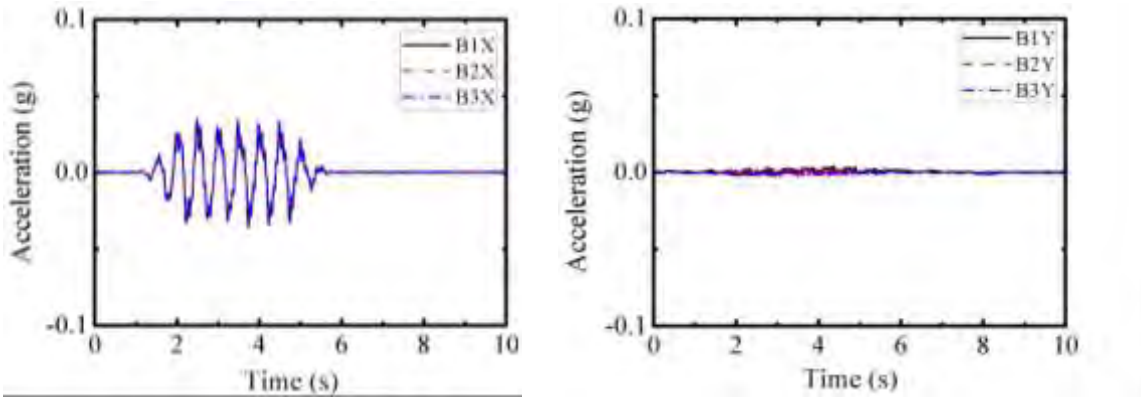

(a) x-direction (b) y-direction

Fig. 8.41 Base shaker of T8 (a_{max}=0.03 g/5 cyc)

8.3.1.2. T9-IM2 (a_{max}=0.03 g/15 cyc)

Fig. 8.42(a) and (b) compare the recorded base motion at different locations for both x-(shaking) and y-(non-shaking) direction of T9 (a_{max}=0.03 g/15 cyc). The ratio of the peak base acceleration in y-direction to that in x-direction at B1, B2 and B3 for T9 is 10%, 12% and 9%, respectively.

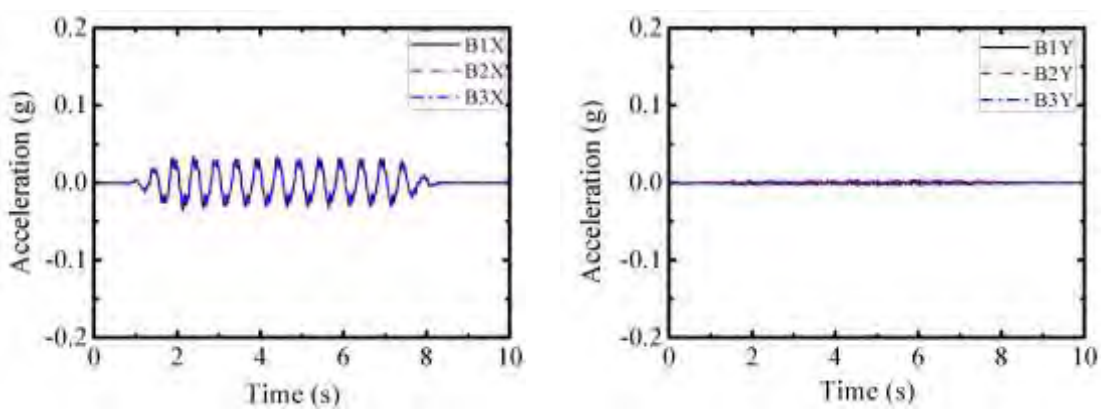

(a) x-direction (b) y-direction

Fig. 8.42 Base shaker of T9 (a_{max}=0.03 g/15 cyc)

8.3.1.3. T10-IM3 (a_{max}=0.10 g/15 cyc)

Fig. 8.43(a) and (b) compares the recorded base acceleration at different locations for both x-(shaking) and y-(non-shaking) direction of T10 (a_{max}=0.10 g/15 cyc), respectively. The ratio of the peak base acceleration in y-direction to that in x-direction at B1, B2 and B3 are 8%, 9% and 5%,

respectively.

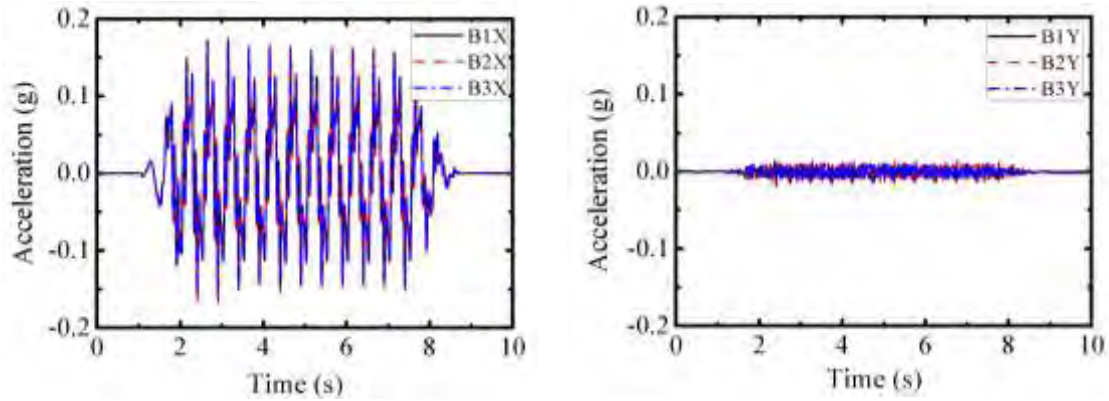

(a) x-direction (b) y-direction

Fig. 8.43 Base shaker of T10 (a_{max}=0.10 g/15 cyc)

8.3.2. Acceleration response

8.3.2.1. T4 and T8-IM4 (a_{max}=0.03 g/5 cyc)

Fig. 8.44 compares the acceleration of soil at selected depths of T4 and T8 (a_{max}=0.03 g/5 cyc). For T4, The significant drop of acceleration between top soil surface and D=3.23 m after three shaking cycles indicates that soil in this region may liquefy while the acceleration at D=3.99 m suggests that the soil at the bottom, although gradually weaken, may still transmit shear stress and hence may not liquefy at the same time as the top soil stratum.

For T8, although the drop of acceleration of soil at shallow depth (D=0.18 to 1.70 m) after three shaking cycles is observed, there is no attenuation of acceleration of soil at deep depths (D=3.23 and 3.99 m) during the entire shaking. This indicates that the liquefaction of soil at deep depth may not occur during the entire shaking. Compare the acceleration response of soil in T8 to T4 at the same depth, it can be implied that the soil densifies due to repetitive shaking from T4 to T8. The amplification factor of soil at different depths of T4 and T8 is shown in Fig. 8.45.

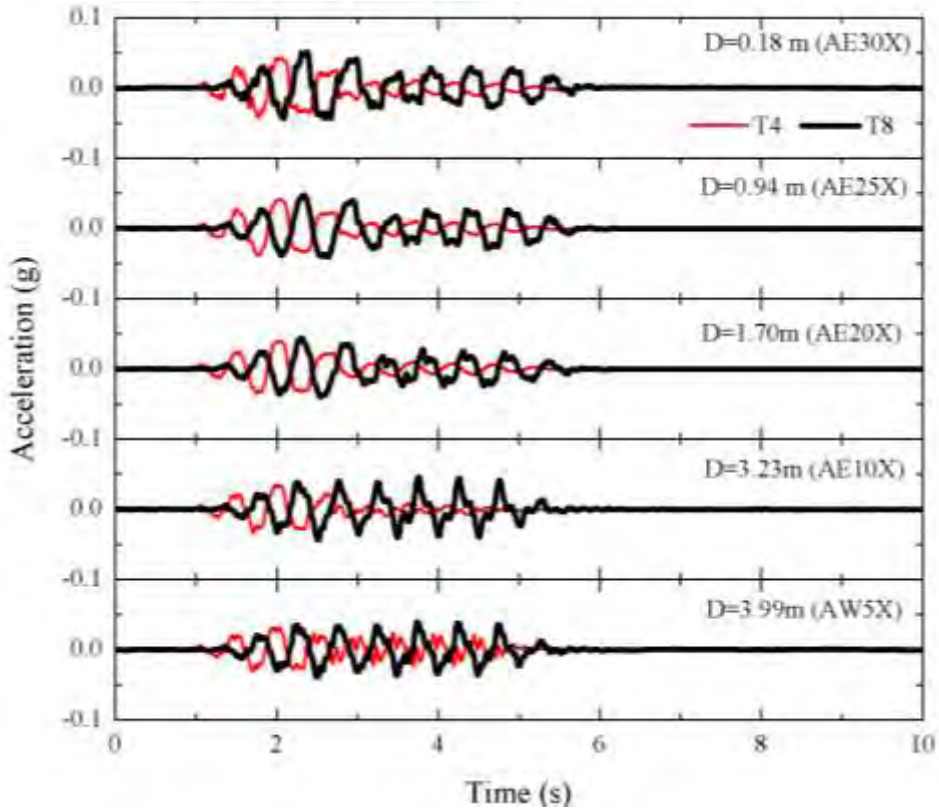

(a) Laminate acceleration

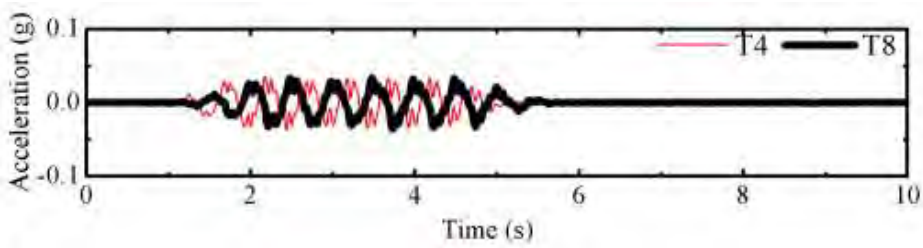

(b) B3X

Fig. 8.44 x-acceleration at different depths and base of T4 and T8 (a_{max}=0.03g/5 cyc)

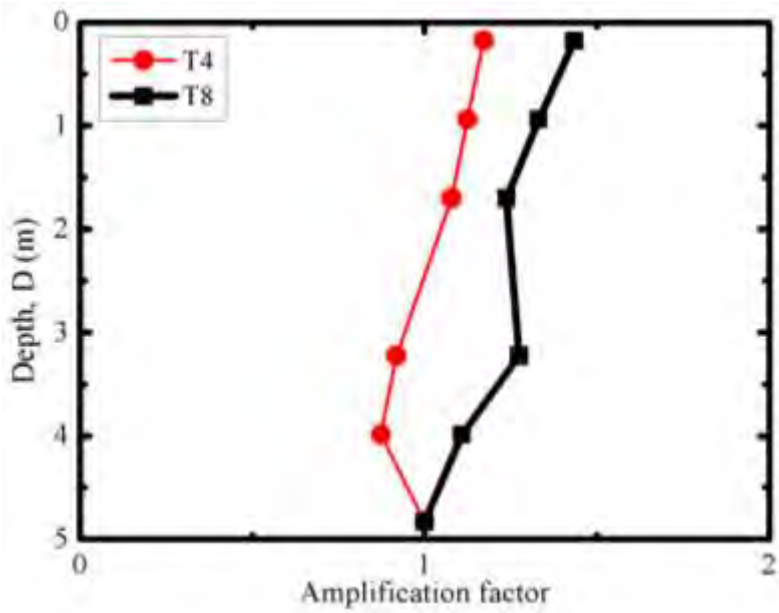

Fig. 8.45 Amplification factor profiles of T4 and T8 (a_{max}=0.03 g/5 cyc)

8.3.2.2. T9-IM2 (a_{max}=0.03 g/15 cyc)

Fig. 8.46 compares the acceleration of soil at selected depths of T9 (a_{max}=0.03 g/15 cyc). An amplification of acceleration at ground surface compared to the base is encountered in T9, unlike T2 (a_{max}=0.03 g/15 cyc) in which the attenuation of the acceleration at ground surface is spotted. This is indicative of the densification of soil during repetitive shakings. The amplification factor of soil at different depths is shown in Fig. 8.47.

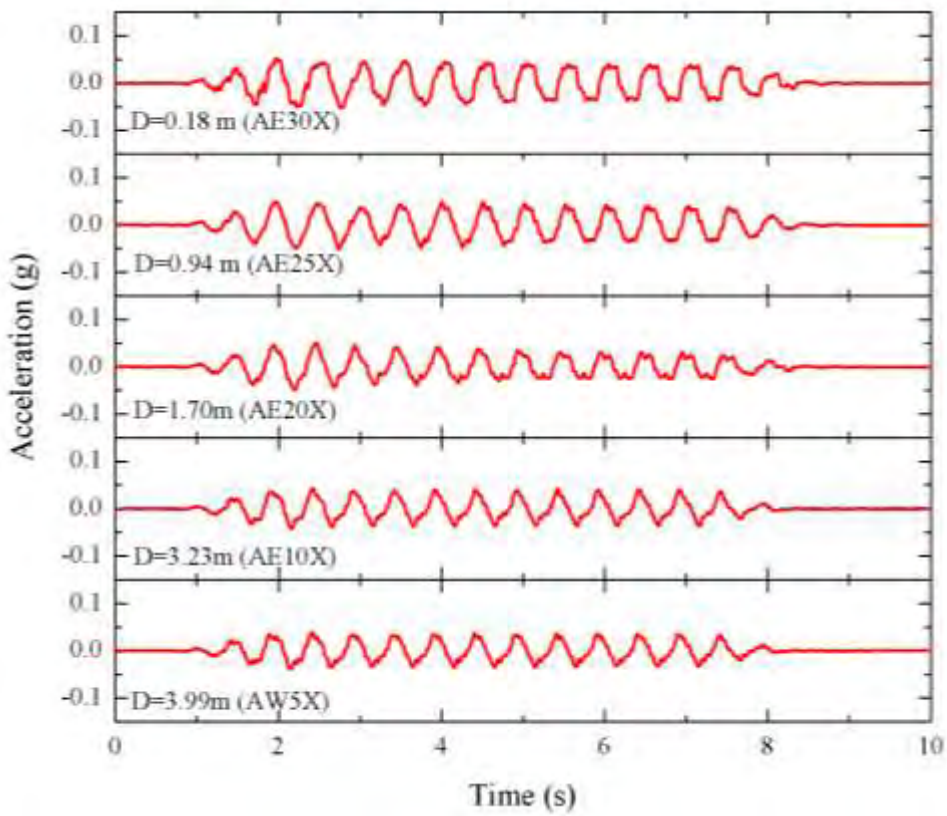

(a) Laminate acceleration

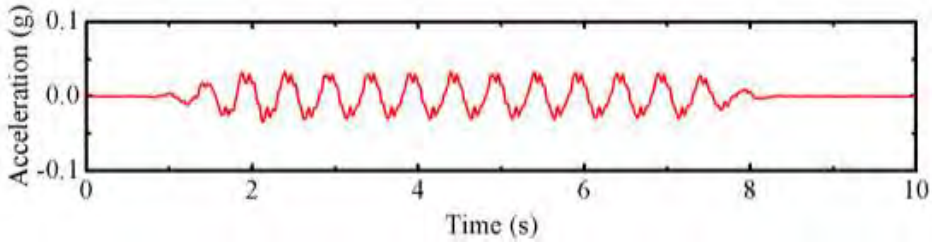

(b) B3X

Fig. 8.46 x-acceleration at different depths and base of T9 (a_{max}=0.03 g/15 cyc)

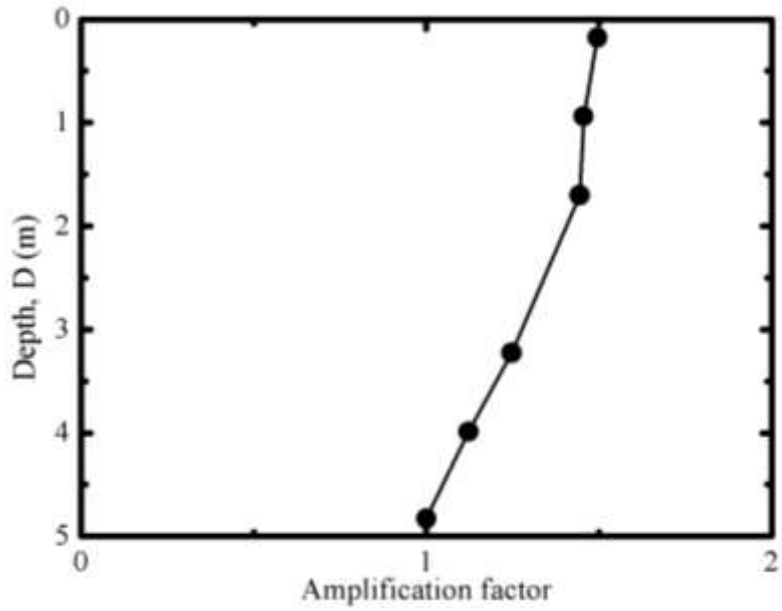

Fig. 8.47 Amplification factor profile of T9 (a_{max}=0.03 g/15 cyc)

8.3.2.3. T10-IM3 (a_{max}=0.10 g/15 cyc)

Fig. 8.48 compares the acceleration of soil at selected depths of T10 (a_{max}=0.10 g/15 cyc). The significant drop of acceleration between top soil surface and D=3.23 m indicates that soil in this region may liquefy. The acceleration at D=3.99 m suggests that the soil at the bottom, although gradually weaken, may still transmit shear stress and hence may not liquefy at the same time as the top soil stratum. It is noticed that a gradual increase of acceleration at all depths is observed after six shaking cycles. The amplification factor of soil at different depths is shown in Fig. 8.49.

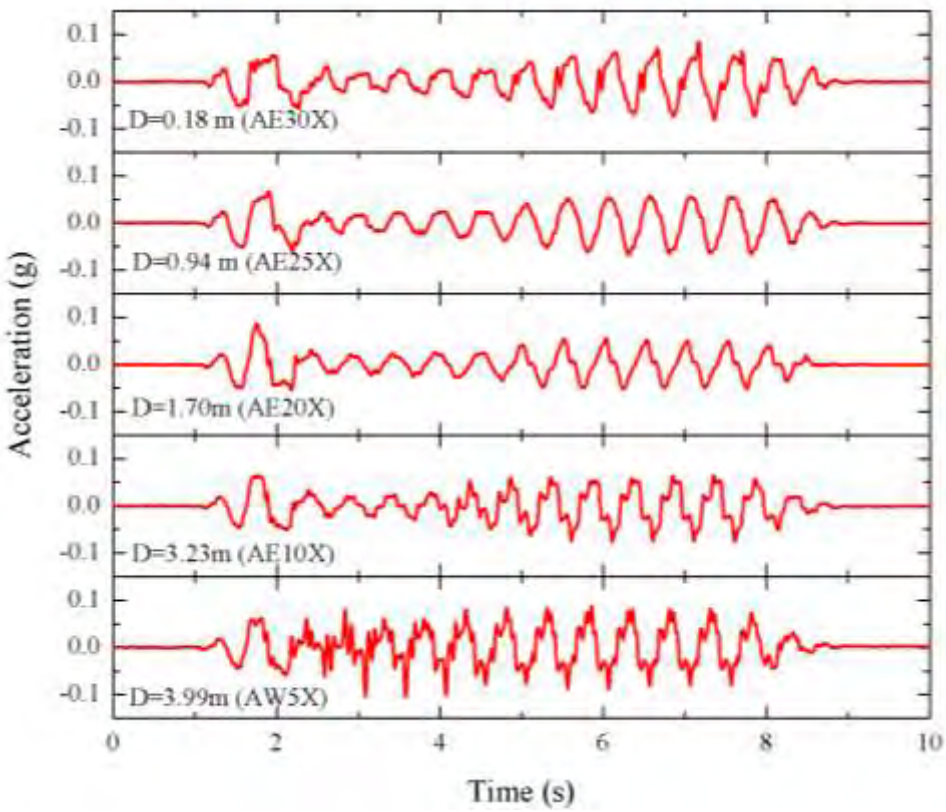

(a) Laminate acceleration

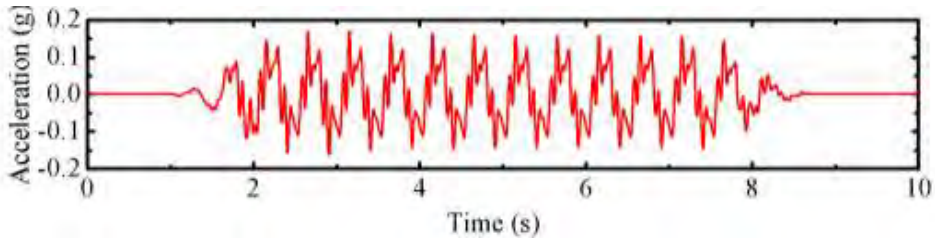

(b) B3X

Fig. 8.48 x-acceleration at different depths and base of T10 (a_{max}=0.10 g/15 cyc)

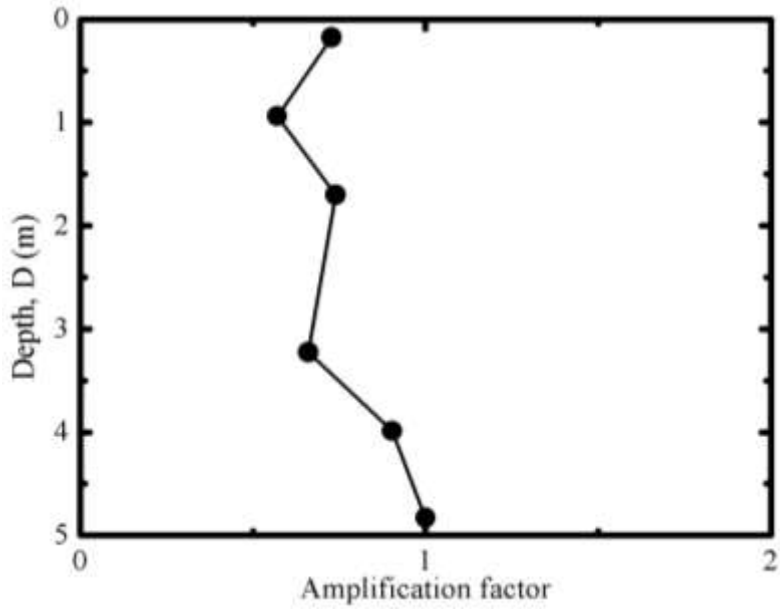

Fig. 8.49 Amplification factor profile of T10 (a_{max}=0.10 g/15 cyc)

8.3.3. Excess pore water pressure (Δu) response

8.3.3.1. T4 and T8-IM4 (a_{max}=0.03 g/5 cyc)

Fig. 8.50 presents the time history of normalized excess pore water pressure r_u and base acceleration during shaking of T4 and T8 (a_{max}=0.03 g/5 cyc). For T4, r_u builds up rapidly. For T8, r_u increases fast at shallow and intermediate depth (D=0.97 and 2.08 m), which is similar to T4. However, r_u decreases as depth increases at deep depth (D=3.56 and 4.32 m).

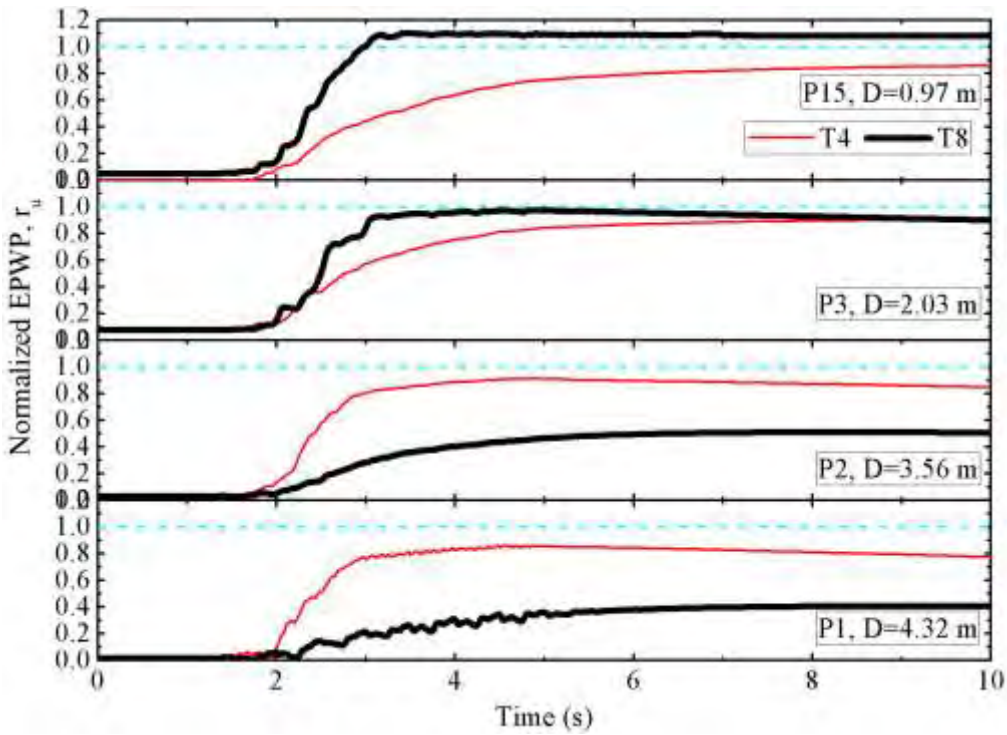

(a) r_u

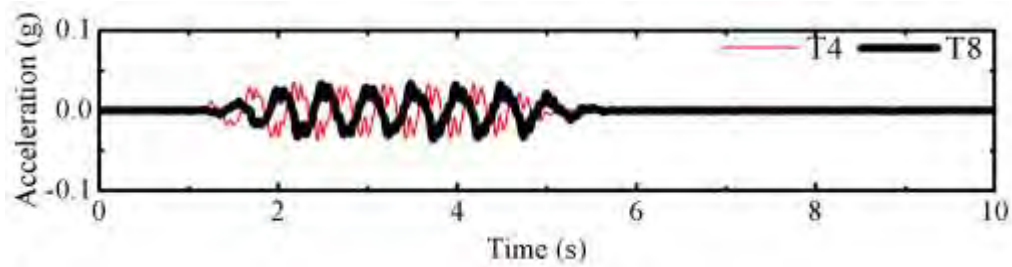

(b) B3X

Fig. 8.50 Time history of r_u and base acceleration of T4 and T8 (a_{max}=0.03 g/5 cyc)

Fig. 8.51 and Fig. 8.52 show the time history of EPWP (Δu) of T4 and T8. The decrease of plateau of Δu as depth increases of both tests indicates the upward migration of Δu.

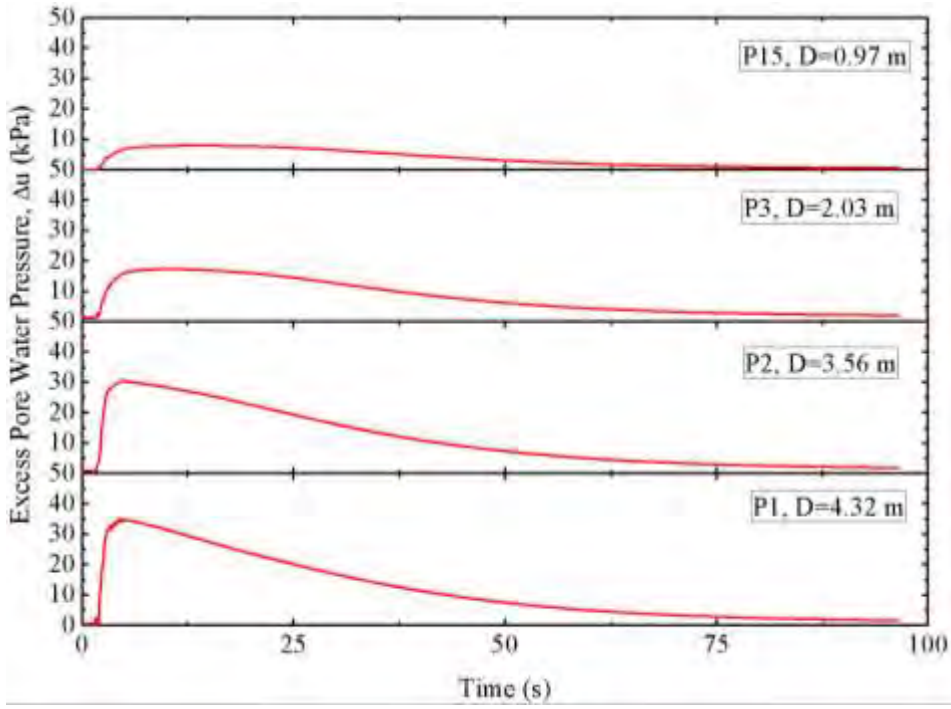

Fig. 8.51 Time history of Δu of T4 (a_{max}=0.03 g/5 cyc)

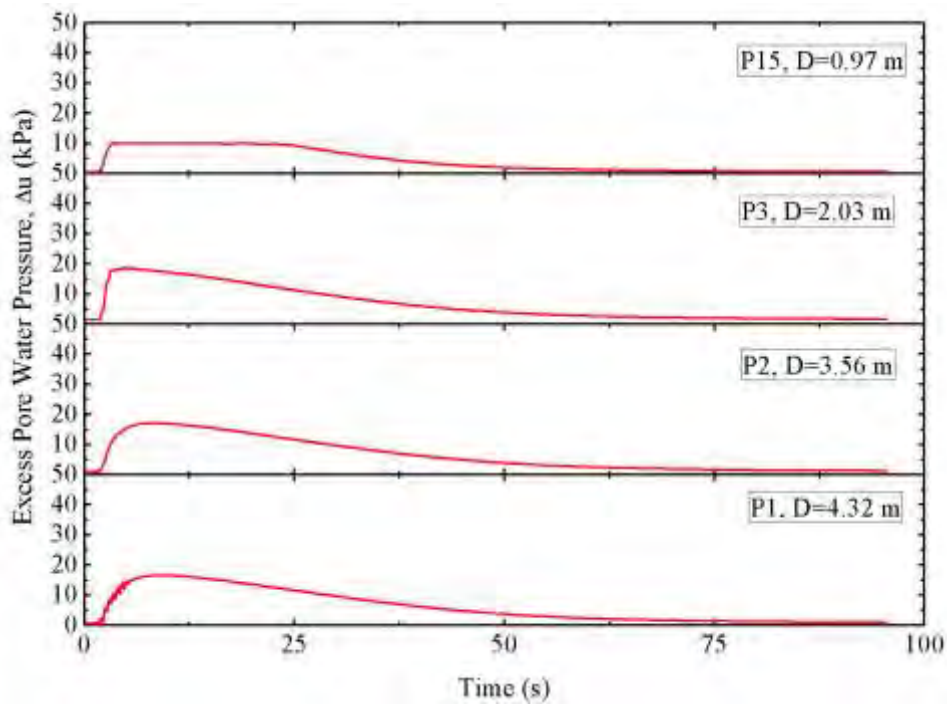

Fig. 8.52 Time history of Δu of T8 (a_{max}=0.03 g/5 cyc)

Fig. 8.53 and Fig. 8.54 plot the Δu as well as r_u with respect to depth at various shaking cycle for T4 and T8.

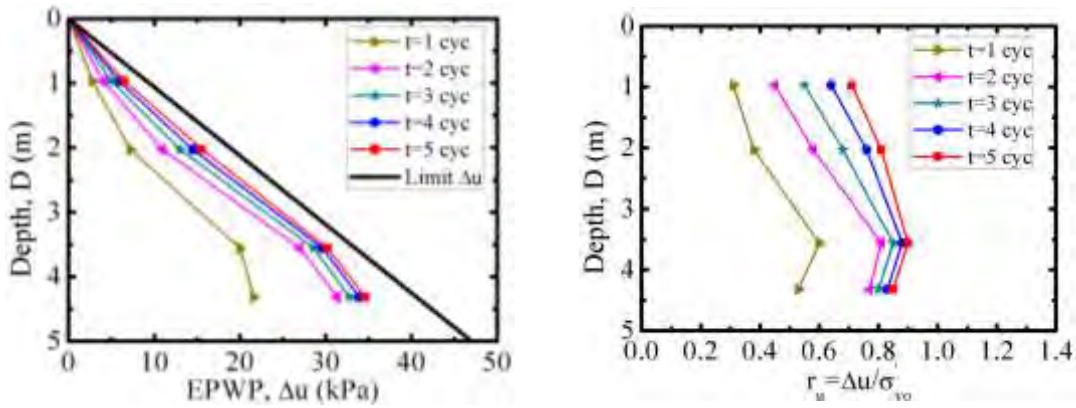

(a) Δu (b) r_u

Fig. 8.53 EPWP profiles of T4 (a_{max}=0.03 g/5 cyc)

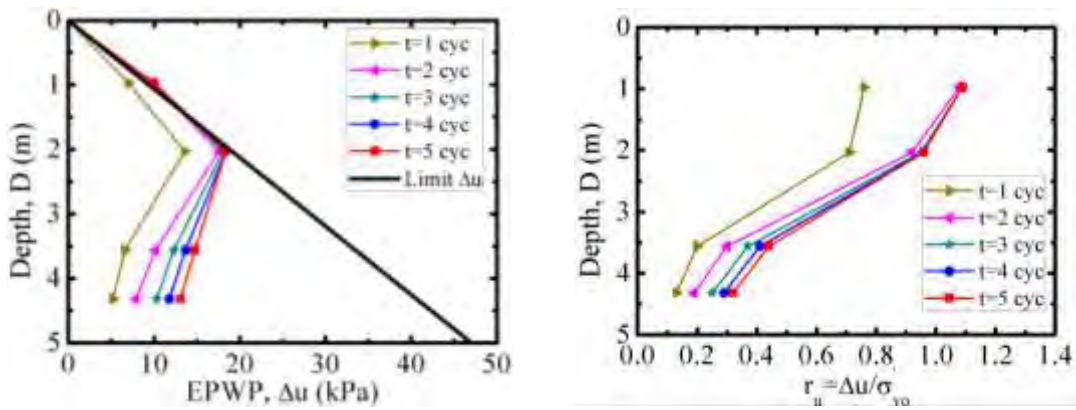

(a) Δu (b) r_u

Fig. 8.54 EPWP profiles of T8 (a_{max}=0.03 g/5 cyc)

8.3.3.2. T9-IM2 (a_{max}=0.03 g/15 cyc)

Fig. 8.55 presents the time history of normalized excess pore water pressure r_u and base acceleration during shaking of T9 (a_{max}=0.03 g/15 cyc). r_u near soil surface (D=0.97 m) reached unity after three shaking cycles, indicative of the liquefaction initiation of the soil at this depth. However, r_u decreases below unity as depth increases, indicating that soil may not liquefy as depth increases.

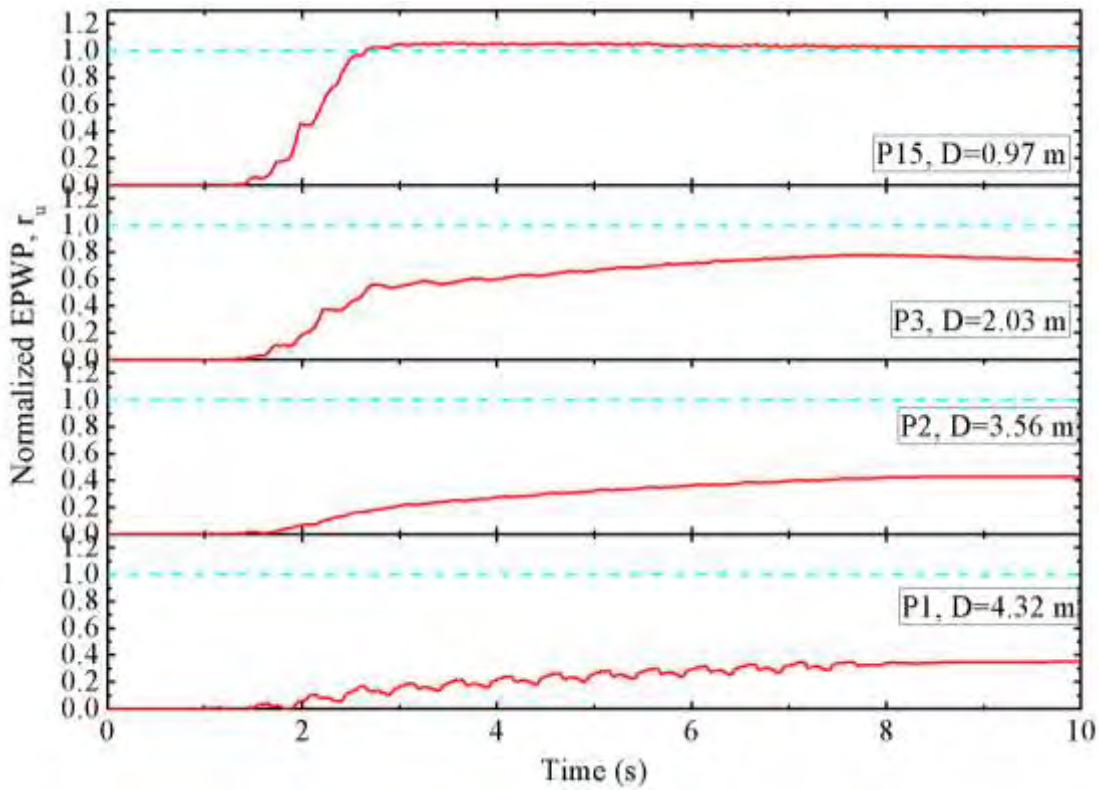

(a) r_u

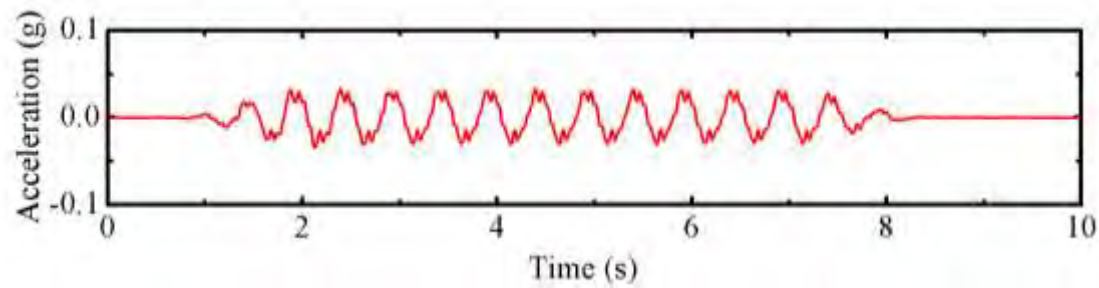

(b) B3X

Fig. 8.55 Time history of r_u and base acceleration of T9 (a_{max}=0.03 g/15 cyc)

Fig. 8.56 shows the time history of EPWP (Δu) of the soil profile in T9. The decrease of plateau of Δu as depth increases indicates the upward migration of Δu. Fig. 8.57 plots the Δu as well as r_u with respect to depth of T9 at various shaking cycle. r_u of soil at shallow depth (D=0.97 m) reaches unity quickly after the first three shaking cycles. Although r_u (D=2.03 m) of soil at intermediate depth does not reaches unity substantial r_u development is observed as shaking goes on. r_u of soil at deep depth (D=3.56 m to 4.32 m) remains at low value after shaking, showing that

the soil at this depth does not liquefy. Similar to the comparison of laminate accelerations between T2 and T9, the EPWP profile comparison between T2 (Fig. 8.15) and T9 suggests a strengthening trend of soil as shaking continues.

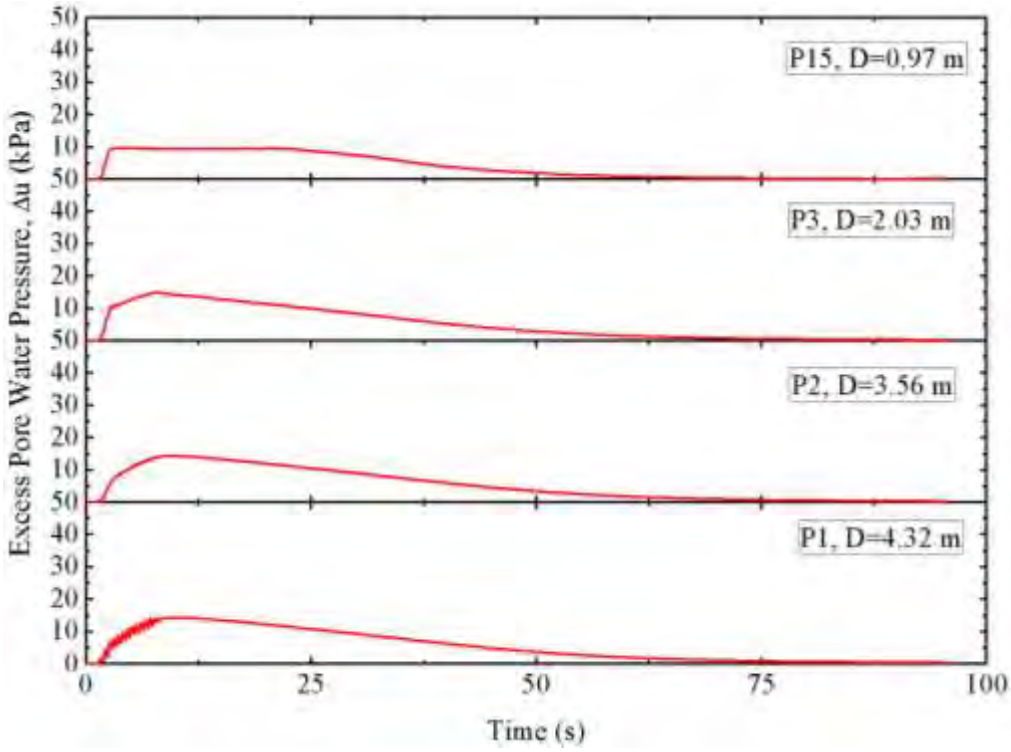

Fig. 8.56 Time history of Δu of T9 (a_{max}=0.03 g/15 cyc)

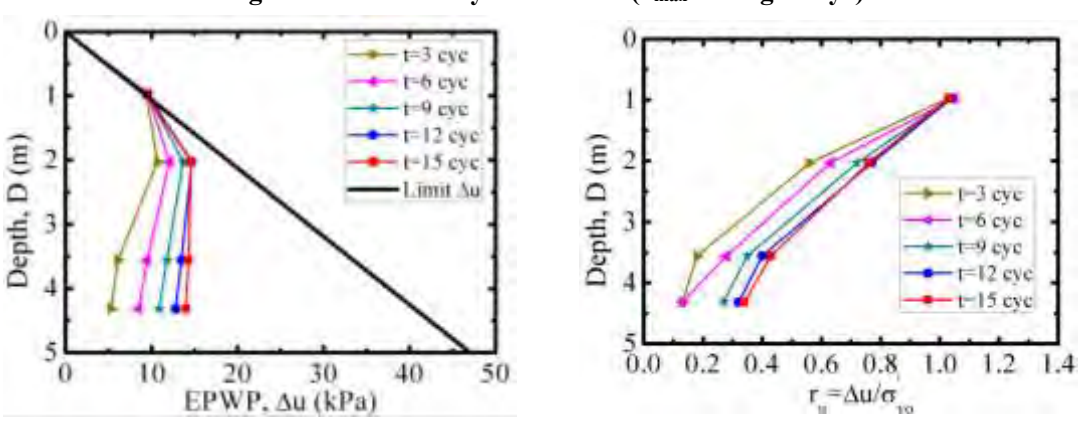

(a) Δu (b) r_u

Fig. 8.57 EPWP profiles of T9 (a_{max}=0.03 g/15 cyc)

8.3.3.3. T10-IM3 (a_{max}=0.10 g/15 cyc)

Fig. 8.58 presents the time history of normalized excess pore water pressure r_u and base

acceleration during shaking of T10 (a_{max}=0.10 g/15 cyc). It can be seen from Fig. 8.58 that soil at shallow depth liquefies at the first two cycles while the soil below 2 m remains certain strength. However, the entire soil stratum liquefies after nine shaking cycles.

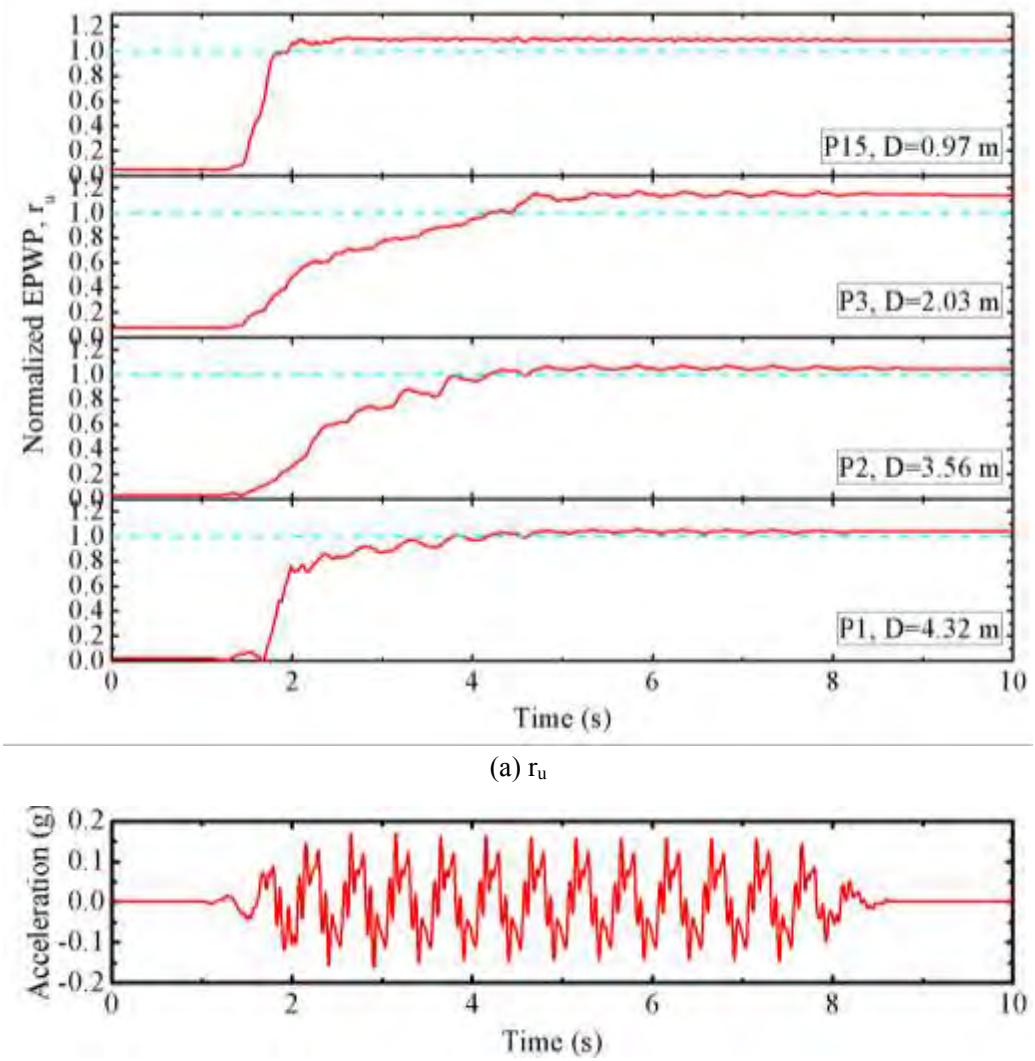

(a) r_u

(b) B3X

Fig. 8.58 Time history of r_u and base acceleration of T10 (a_{max}=0.10 g/15 cyc)

Fig. 8.59 shows the time history of EPWP (Δu) of the soil profile of T10. The decrease of plateau of Δu as depth increases indicates the upward migration of Δu. Fig. 8.60 plots the Δu as well as r_u with respect to depth at various shaking cycle of T10, indicating that soil at shallow depth liquefies firstly and propagates downwards.

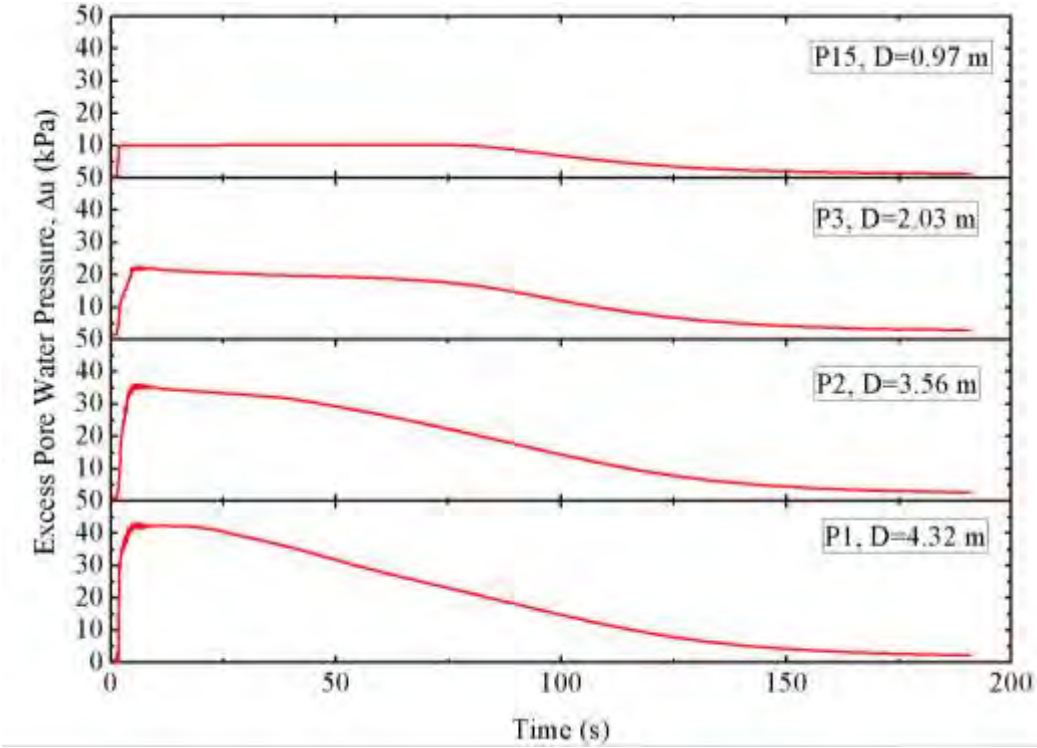

Fig. 8.59 Time history of Δu of T10 (a_{max}=0.10 g/15 cyc)

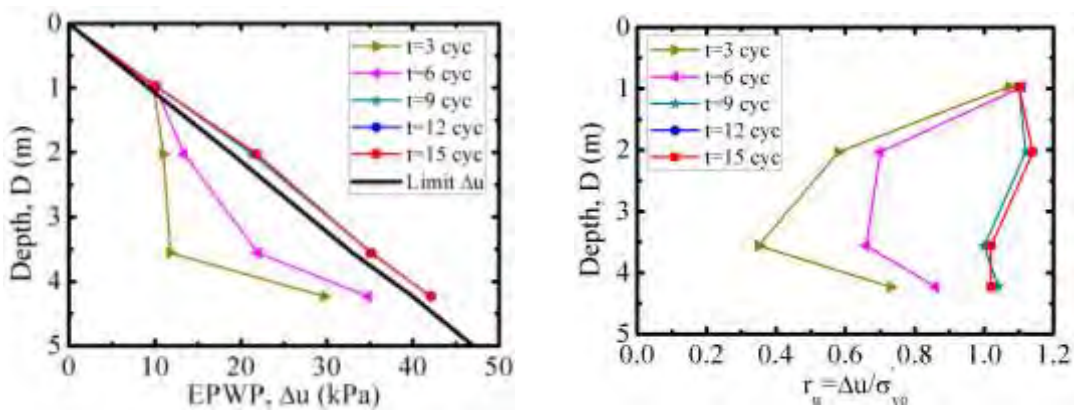

(a) Δu (b) r_u

Fig. 8.60 EPWP profiles of T10 (a_{max}=0.10 g/15 cyc)

8.3.4. Horizontal displacement response

8.3.4.1. T4 and T8-IM4 (a_{max}=0.03 g/5 cyc)

Fig. 8.61(a) and Fig. 8.62(a) plot the time history of horizontal displacement of the soil at selected depths in T4 and T8 (a_{max}=0.03 g/5 cyc). The peak horizontal displacement of soil gradually increases as depth decreases for both tests at the first several shaking cycles. The

variation of horizontal displacement of the soil stratum in both T4 and T8 is mostly cyclic during shaking and the horizontal displacement is negligibly small after shaking. Fig. 8.61(b) and (c) and Fig. 8.62(b) and (c) plot the time history of relative horizontal displacement of the soil at selected depths in T4 and T8.

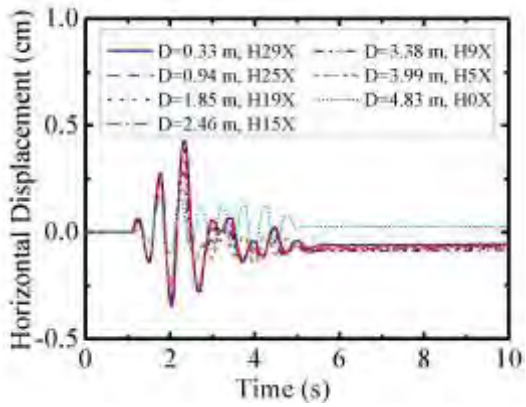

(a) Horizontal displacement

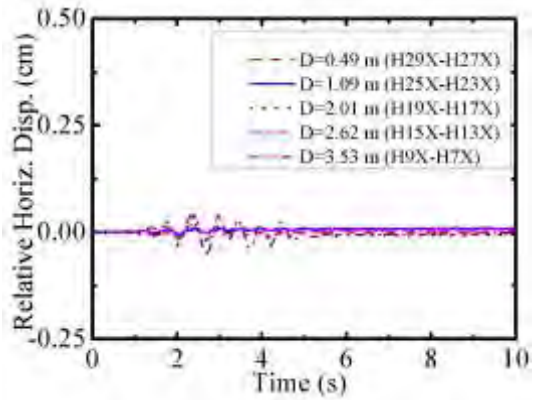

(b) Relative horiz. disp. b/w every other ring

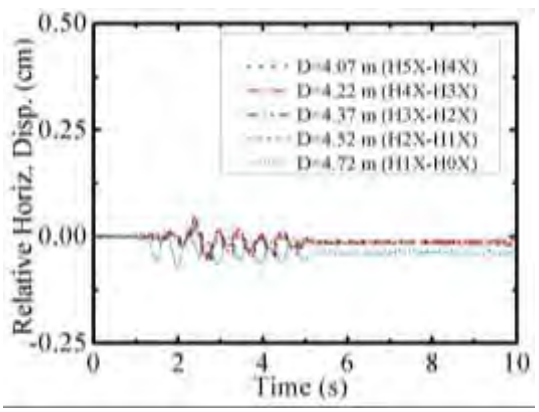

(c) Relative horiz. disp. b/w every ring

Fig. 8.61 Time history of horizontal displacement of T4 (a_{max}=0.03 g/5 cyc)

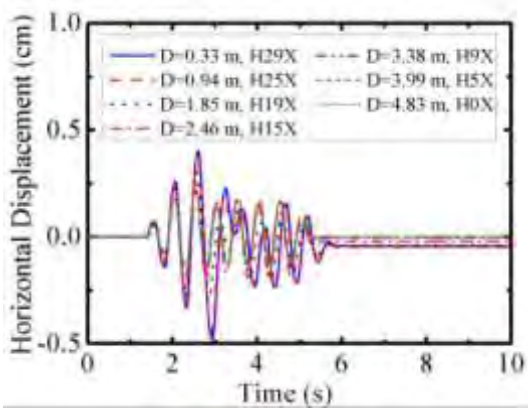

(a) Horizontal displacement

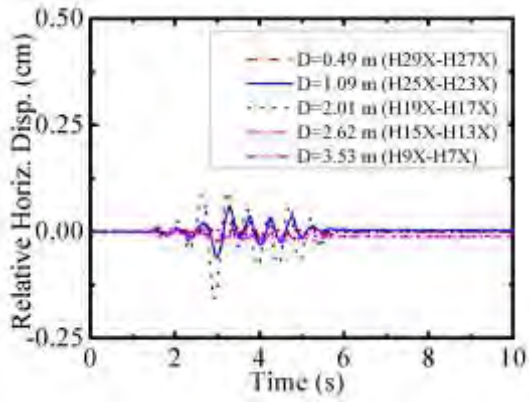

(b) Relative horiz. disp. b/w every other ring

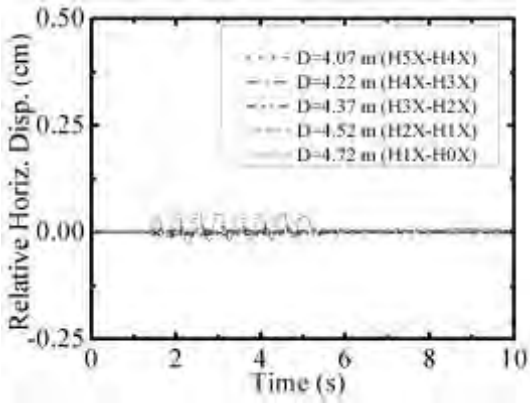

(c) Relative horiz. disp. b/w every ring

Fig. 8.62 Time history of horizontal displacement of T8 (a_{max}=0.03 g/5 cyc)

Fig. 8.63 and Fig. 8.64 plot the peak inter-ring drift profiles of T4 and T8, respectively.The peak base displacement of T4 and T8 are also shown in these two figures.

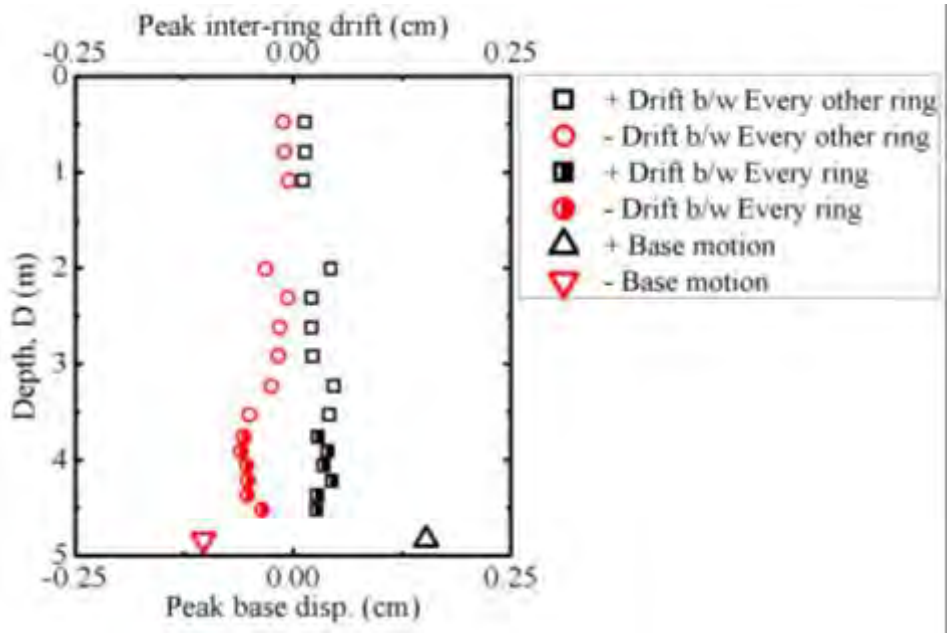

Fig. 8.63 Peak inter-ring drift profile of T4 (a_{max}=0.03 g/5 cyc)

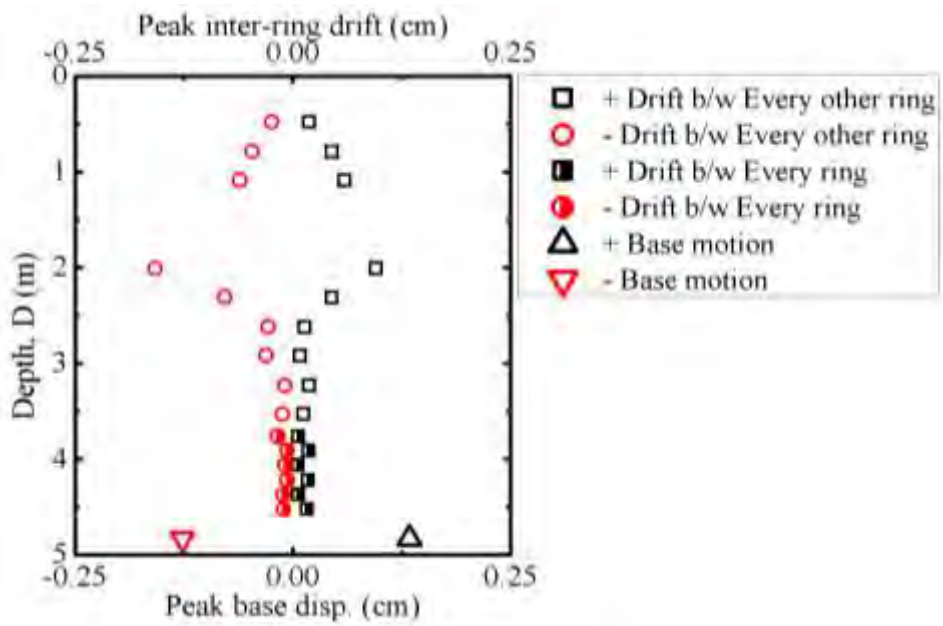

Fig. 8.64 Peak inter-ring drift profile of T8 (a_{max}=0.03 g/5 cyc)

8.3.4.2. T9-IM2 (a_{max}=0.03 g/15 cyc)

Fig. 8.65(a) plots the time history of horizontal displacement of the soil at selected depths in T9 (a_{max}=0.03 g/15 cyc). The variation of horizontal displacement of the soil is mostly cyclic during shaking and the horizontal displacement is negligibly small after shaking. Fig. 8.65(b) and

(c) plot the time history of relative horizontal displacement of the soil at selected depths in T9. Fig. 8.66 plots the peak inter-ring drift profile and the peak base displacement of T9.

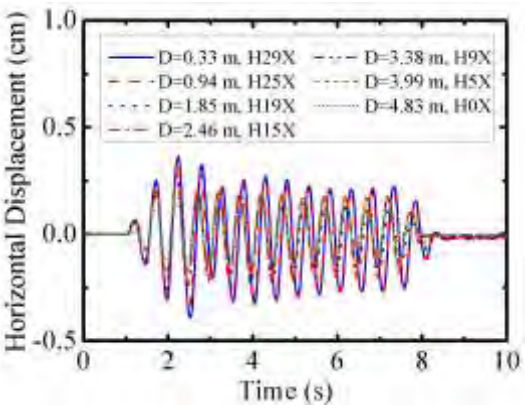

(a) Horizontal displacement

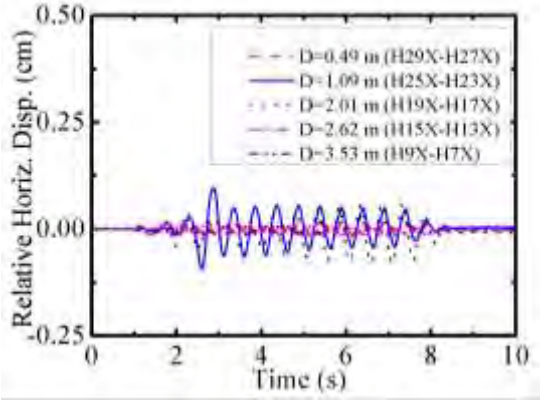

(b) Relative horiz. disp. b/w every other ring

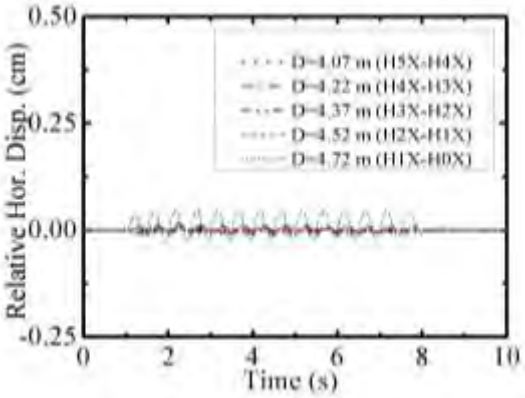

(c) Relative horiz. disp. b/w every ring

Fig. 8.65 Time history of horizontal displacement of T9 (a_{max}=0.03 g/15 cyc)

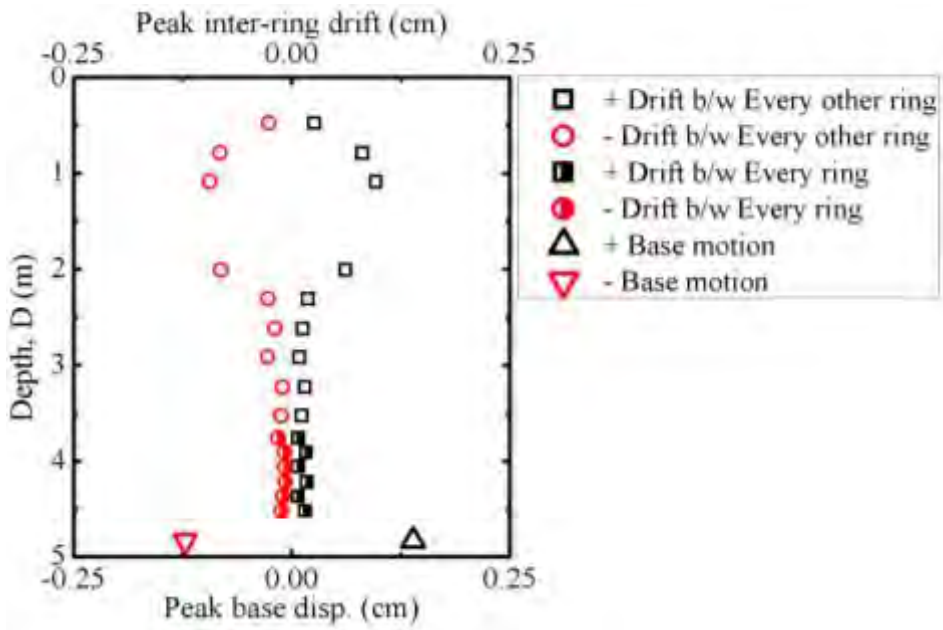

Fig. 8.66 Peak inter-ring drift profile of T9 (a_{max}=0.03 g/15 cyc)

8.3.4.3. T10-IM3 (a_{max}=0.10 g/15 cyc)

Fig. 8.67(a) plots the time history of horizontal displacement of the soil at selected depths in T10 (a_{max}=0.10 g/15 cyc). The sudden increase of horizontal displacement of soil at all depths at the first several shaking cycles is observed. However the variation of horizontal displacement of the soil stratum in T10 is mostly cyclic during shaking and the horizontal displacement is negligibly small after shaking. Fig. 8.67(b) and (c) plot the time history of relative horizontal displacement of the soil at selected depths in T10.

Fig. 8.68 plots the peak inter-ring drift profile and the peak base displacement of T10.

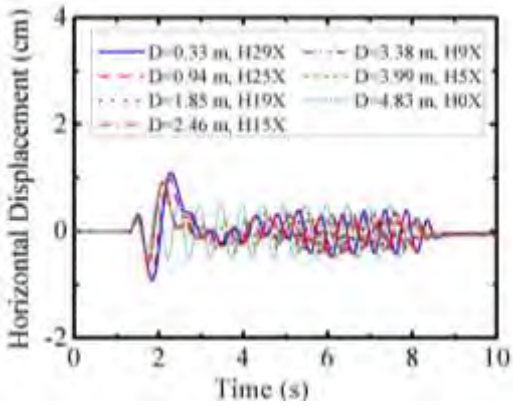

(a) Horizontal displacement

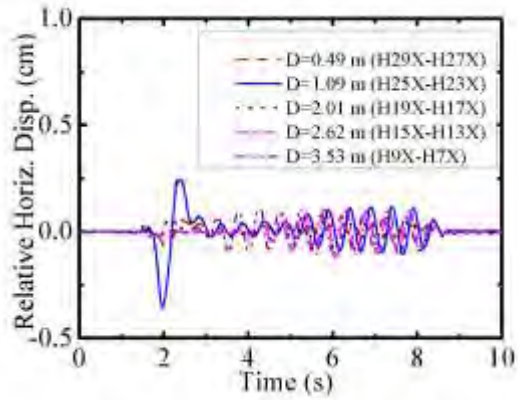

(b) Relative horiz. disp. b/w every other ring

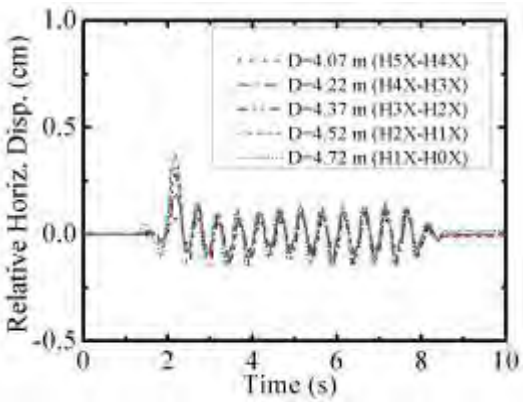

(c) Relative horiz. disp. b/w every ring

Fig. 8.67 Time history of horizontal displacement of T10 (a_{max}=0.10g/15cyc)

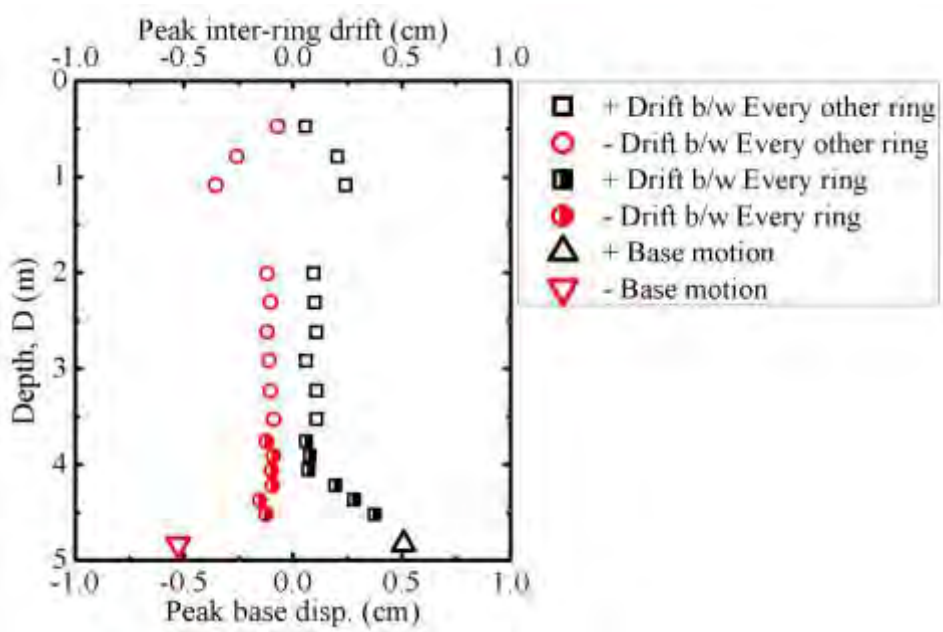

Fig. 8.68 Peak inter-ring drift profile of T10 (a_{max}=0.10 g/15 cyc)

8.3.5. Ground settlement response

As discussed in section 8.2.5, V1 and V3 were partially buried in the soil. Hence, they were taken out to the ground surface before T4 (Fig. 8.69). Fig. 8.70 plots the time history of incremental ground settlement in shaking series 2. Table 8.4 summarizes the incremental and total ground settlement of liquefaction tests in shaking series 2. The average incremental settlement of each liquefaction test is based on the incremental settlement of V1 and V3 because V2 was buried in the soil after T2.

(a) Before T4 (a_{max}=0.03 g/5 cyc) (b) After T10 (a_{max}=0.10 g/15 cyc)

Fig. 8.69 Conditions of V1,V2 and V3 before and after shaking series 2

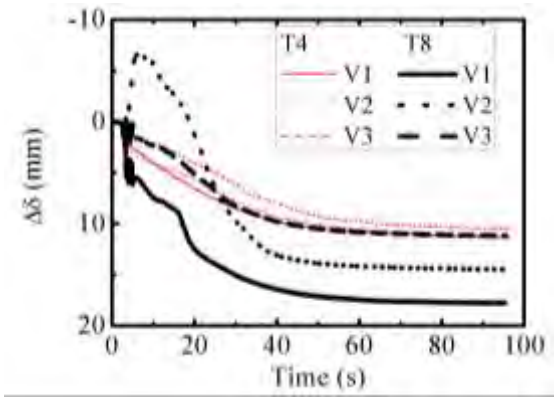

(a) T4 and T8 (a_{max}=0.03 g/5 cyc)

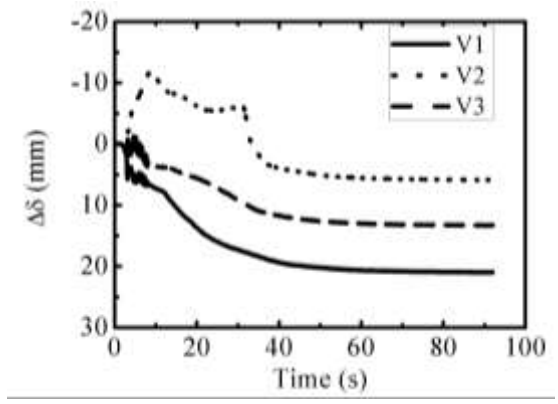

(b) T9 (a_{max}=0.03 g/15 cyc)

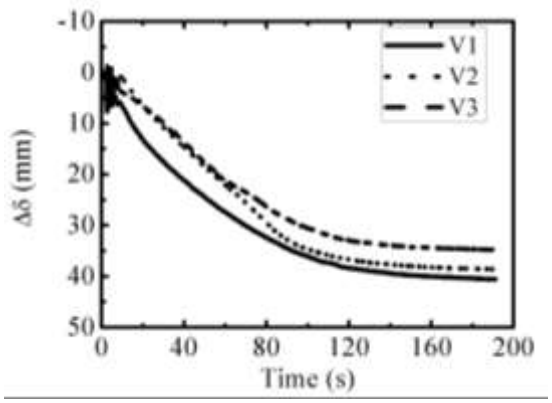

(c) T10 (a_{max}=0.10 g/15 cyc)

Fig. 8.70 Time history of incremental ground settlement in shaking series 2

Table 8.4 Ground settlement of liquefaction tests-shaking series 2

Shaking series	Shaking event	Input Motion	Δδ for each shaking test			$\Delta\delta_{ave.}$	Cumulative Settlement δ
			V1	V2	V3		
			(mm)	(mm)	(mm)	(mm)	(mm)
2	T4	IM4 (a_{max}=0.03 g/5 cyc)	11	11	11	11	140
	T5	IM4 (a_{max}=0.03 g/5 cyc)	10	11	10	10	150
	T6	IM4 (a_{max}=0.03 g/5 cyc)	9	10	9	9	160
	T7	IM4 (a_{max}=0.03 g/5 cyc)	20	24	12	19	178
	T8	IM4 (a_{max}=0.03 g/5 cyc)	18	15	11	15	193
	T9	IM2 (a_{max}=0.03 g/15 cyc)	21	6	14	14	207
	T10	IM3 (a_{max}=0.10 g/15 cyc)	41	39	35	38	245

8.3.6. Stress-strain response

8.3.6.1. T4 and T8-IM4 (a_{max}=0.03 g/5 cyc)

The time history of shear stress at different depths at two time frames in T4 and T8 (a_{max}=0.03

g/5 cyc) is plotted in Fig. 8.71. For T4, the shear stress of soil at all depths increases at the first two shaking cycles and decreases afterwards as shaking continues. For T8, the trend of shear stress development is similar to T4 but with larger peak value. Fig. 8.72 shows the time history of shear strain at different depths in T4 and T8. For T4, shear strain development is observed at deep depth (D=3.61 m and D=4.22 m). For T8, shear strain development is observed at shallow and intermediate depth (D=0.79 m and D=2.08 m).

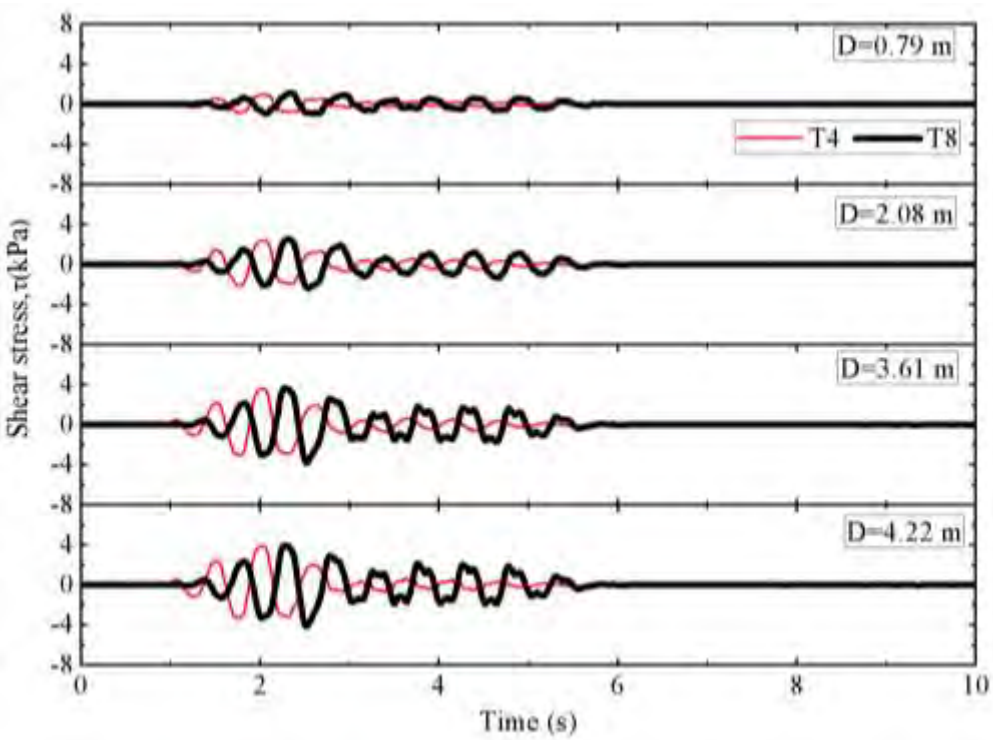

(a) Shear stress

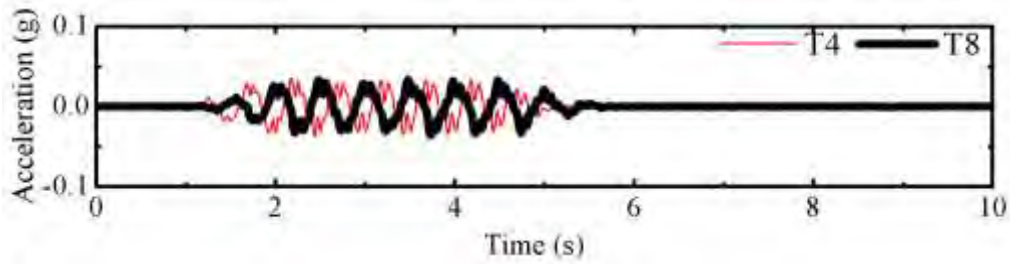

(b) B3X

Fig. 8.71 Time history of shear stress of T4 and T8 (a_{max}=0.03 g/5 cyc)

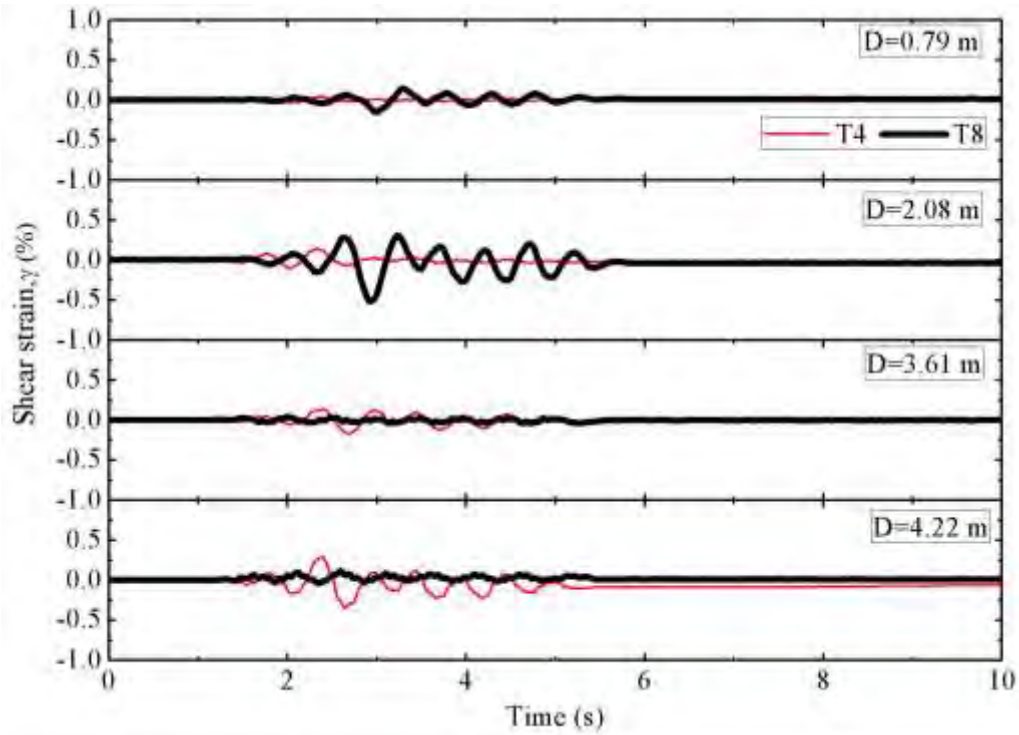

(a) Shear strain

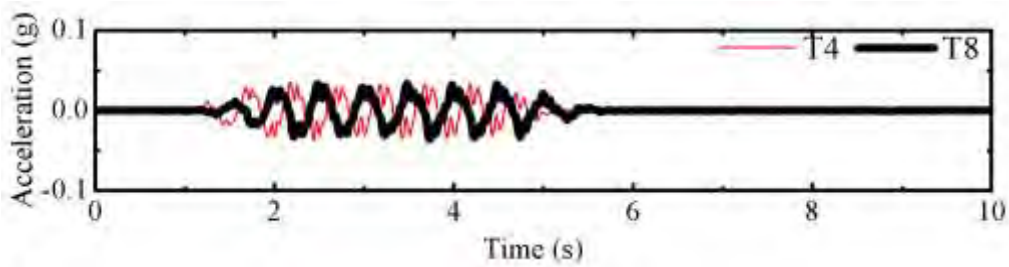

(b) B3X

Fig. 8.72 Time history of shear strain of T4 and T8 (a_{max}=0.03 g/5 cyc)

The shear stress-strain response at different depths in T4 and T8 are plotted in Fig. 8.73 and Fig. 8.74, respectively. For T4, shear stress degradation and shear strain development at all depths are spotted. For T8, shear stress degradation and shear strain development are observed at shallow and intermediate depth (D=0.79 m and D=2.08 m) after two cycles as the EPWP builds up. There is apparent shear stress degradation but no apparent shear strain development at deep depth (D=3.61 m and D=4.22 m) when compared at the two time frames.

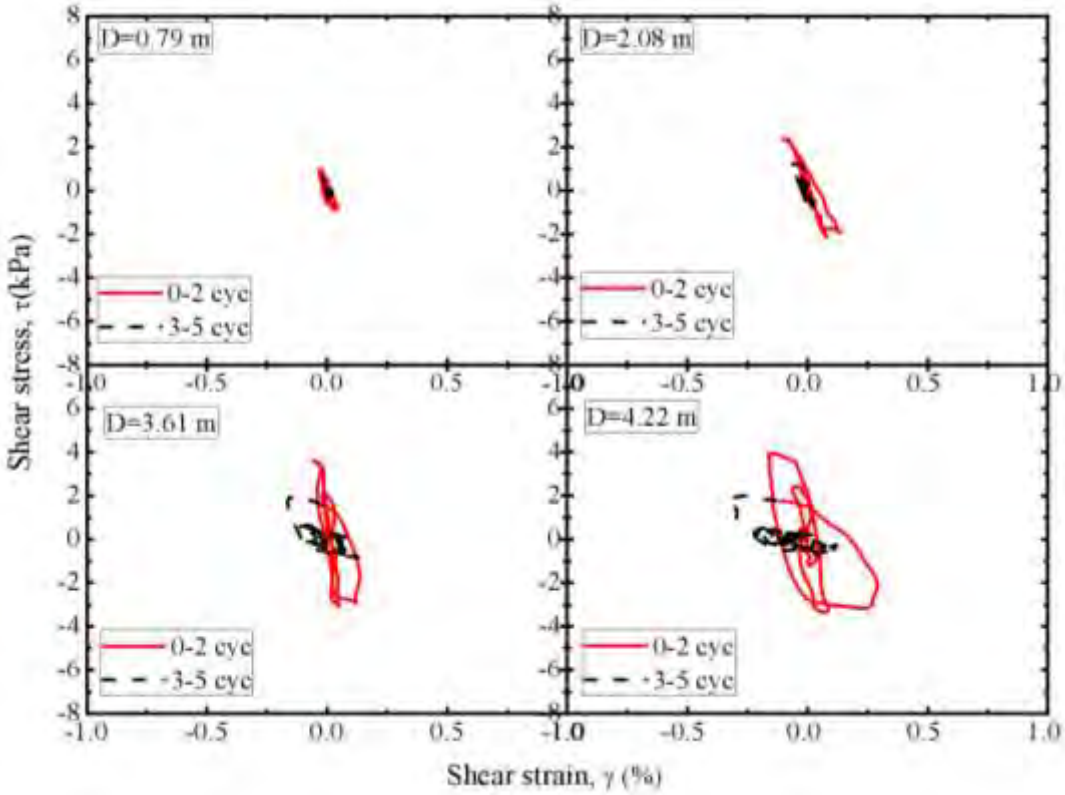

Fig. 8.73 Shear stress- strain loop of T4 (a_{max}=0.03 g/5 cyc)

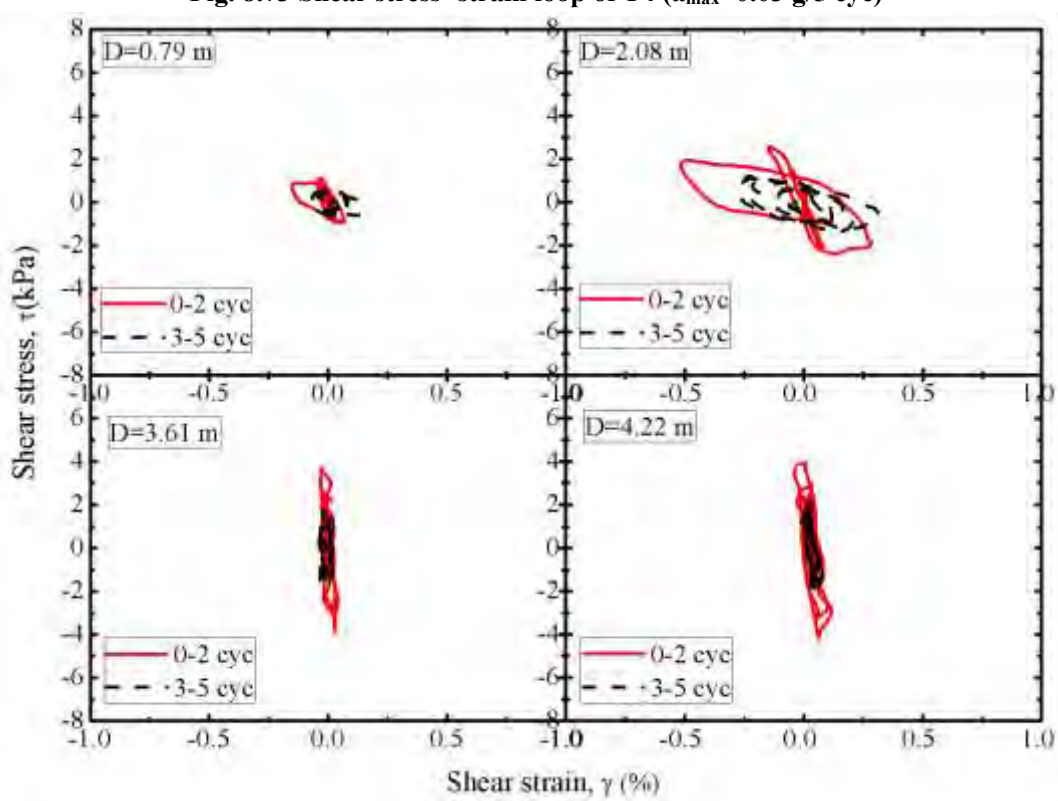

Fig. 8.74 Shear stress- strain loop of T8 (a_{max}=0.03 g/5 cyc)

8.3.6.2. T9-IM2 (a_{max}=0.03 g/15 cyc)

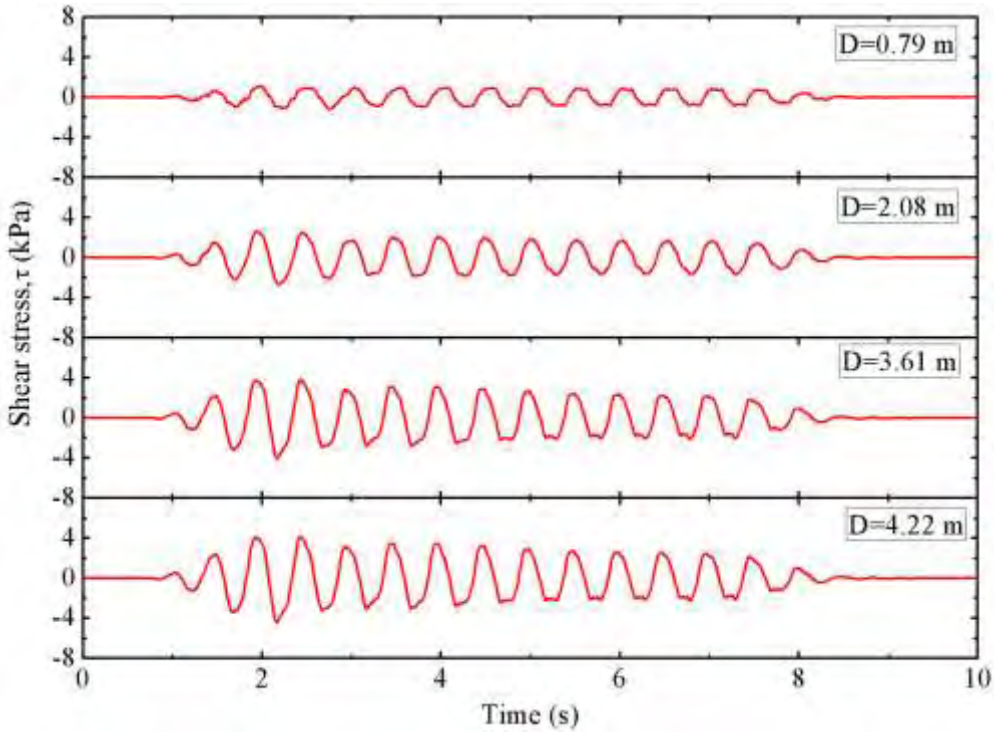

(a) Shear stress

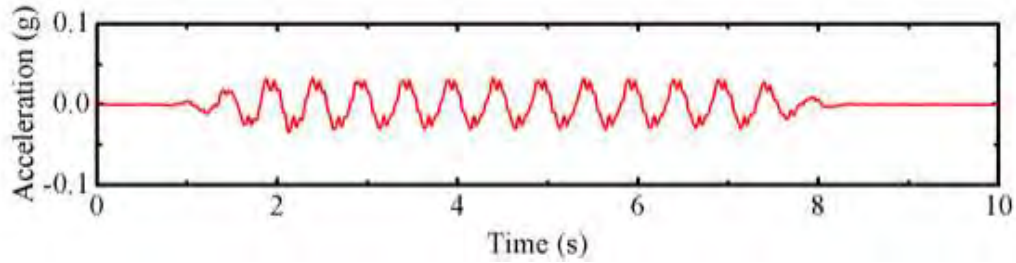

(b) B3X

Fig. 8.75 Time history of shear stress of T9 (a_{max}=0.03 g/15 cyc)

The time history of shear stress at different depths in T9 (a_{max}=0.03 g/15 cyc) is plotted in Fig. 8.75. There is no apparent shear stress degradation observed of soil at all depths. The time history of shear strain at different depths in T9 is plotted in Fig. 8.76. There is apparent development shear strain observed at shallow and intermediated depth (D=0.79 m and D=2.08 m) while there is no apparent shear strain development observed at deep depth (D=3.61 m and D=4.22 m).The shear stress-strain response at different depths at two time frames in T9 is plotted in Fig. 8.77.

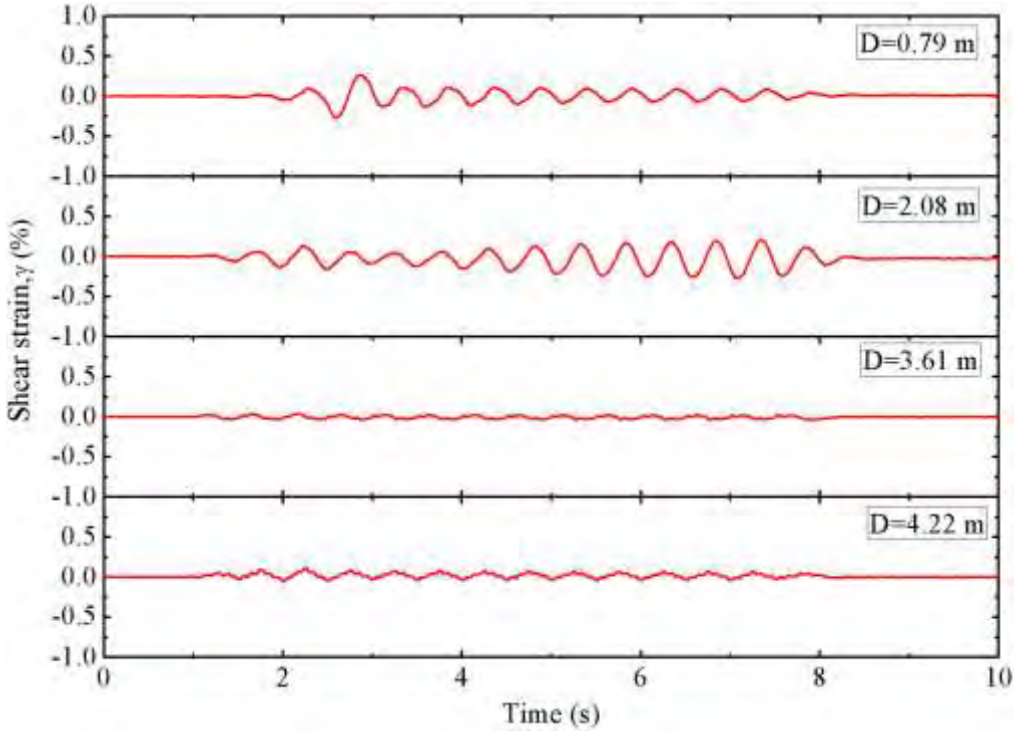

(a) Shear strain

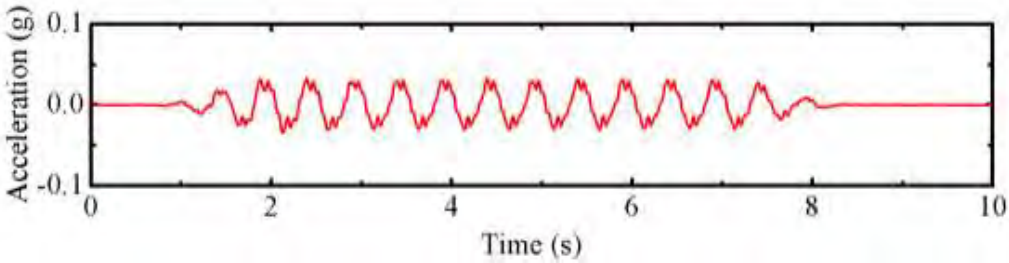

(b) B3X

Fig. 8.76 Time history of shear strain of T9 (a_{max}=0.03 g/15 cyc)

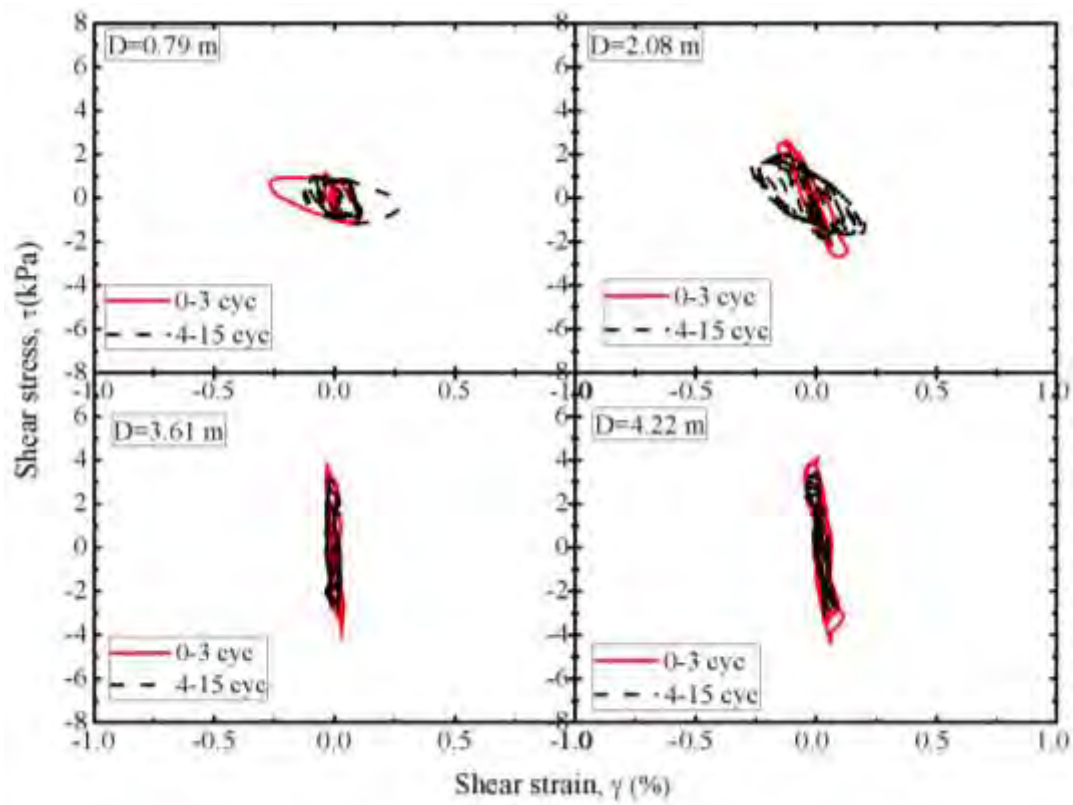

Fig. 8.77 Shear stress- strain loop of T9 (a_{max}=0.03 g/15 cyc)

8.3.6.3. T10-IM3 (a_{max}=0.10 g/15 cyc)

The time history of shear stress at different depths in T10 (a_{max}=0.10 g/15 cyc) is plotted in Fig. 8.78. It shows that at shallow and intermediate depth (D=0.79 m and D=2.08 m), shear stress develops at the first three shaking cycles and decreases between shaking cycle 4 to 6. However, it gradually increases afterwards and remains cyclic as the shaking continues. Nonetheless, the shear stress of soil at deep depth (D=3.61 m and D=4.22 m) increases at the first three shaking cycles and decreases afterwards as the shaking continues. Also from this figure, it is observed that the shear stress increases as the depth increases at the first three cycles. The time history of shear strain at different depths in T10 (a_{max}=0.10 g/15 cyc) is plotted in Fig. 8.79. It is noticed that there is considerable amount of shear strain development of soil at all depths. Fig. 8.80 plots the shear

stress-strain response of soil at different depths at two time frames in T10. Stiffness degradation is observed at all depths between the two time frames.

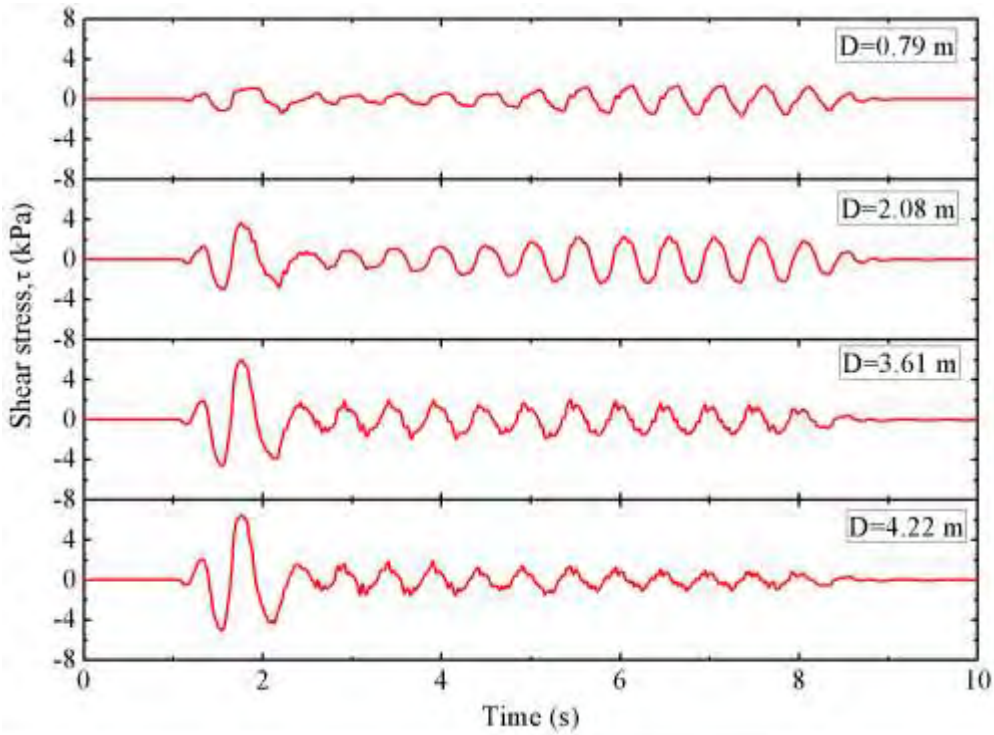

(a) Shear stress

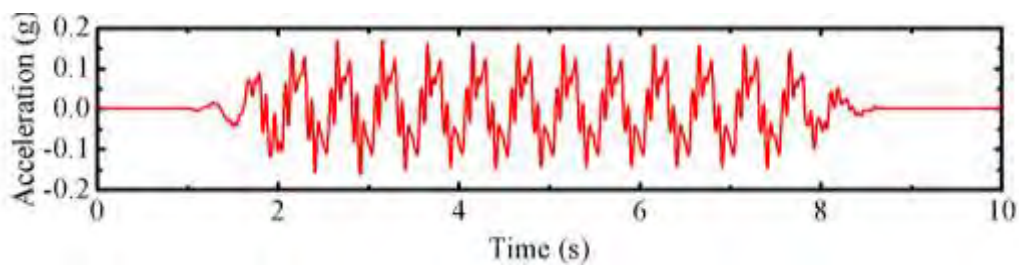

(b) B3X

Fig. 8.78 Time history of shear stress of T10 (a_{max}=0.10 g/15 cyc)

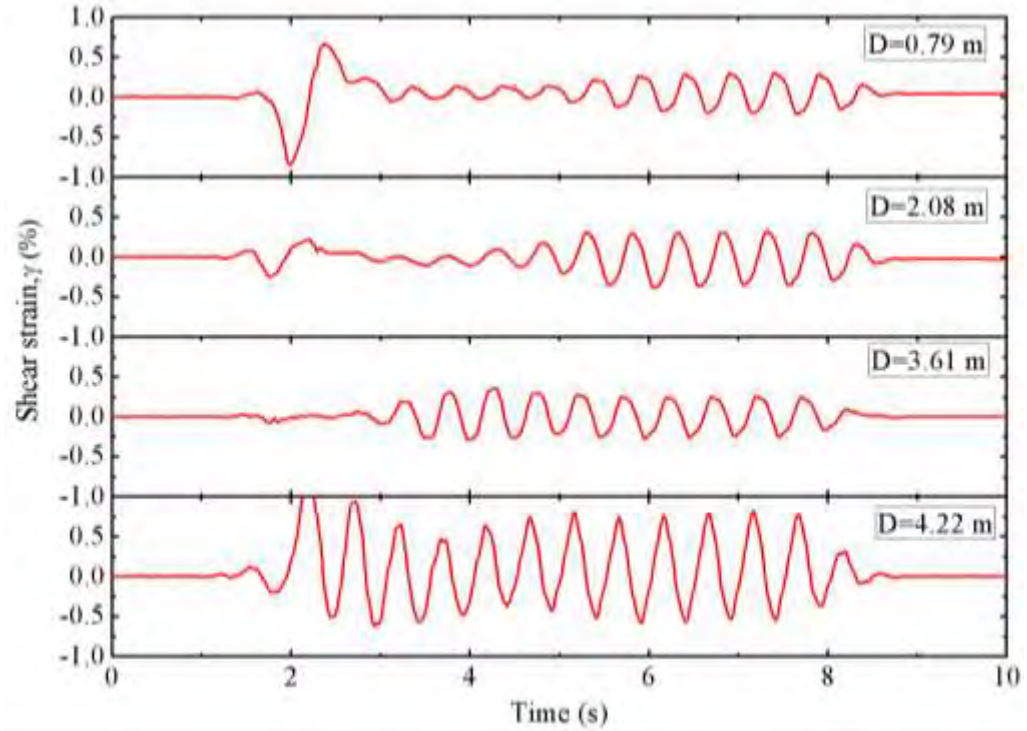

(a) Shear strain

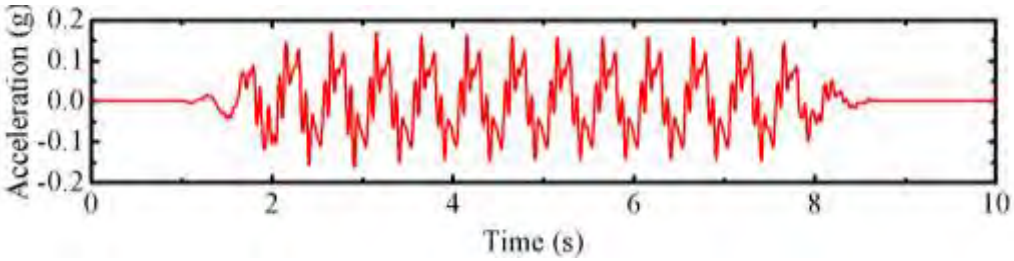

(b) B3X

Fig. 8.79 Time history of shear strain of T10 (a_{max}=0.10 g/15 cyc)

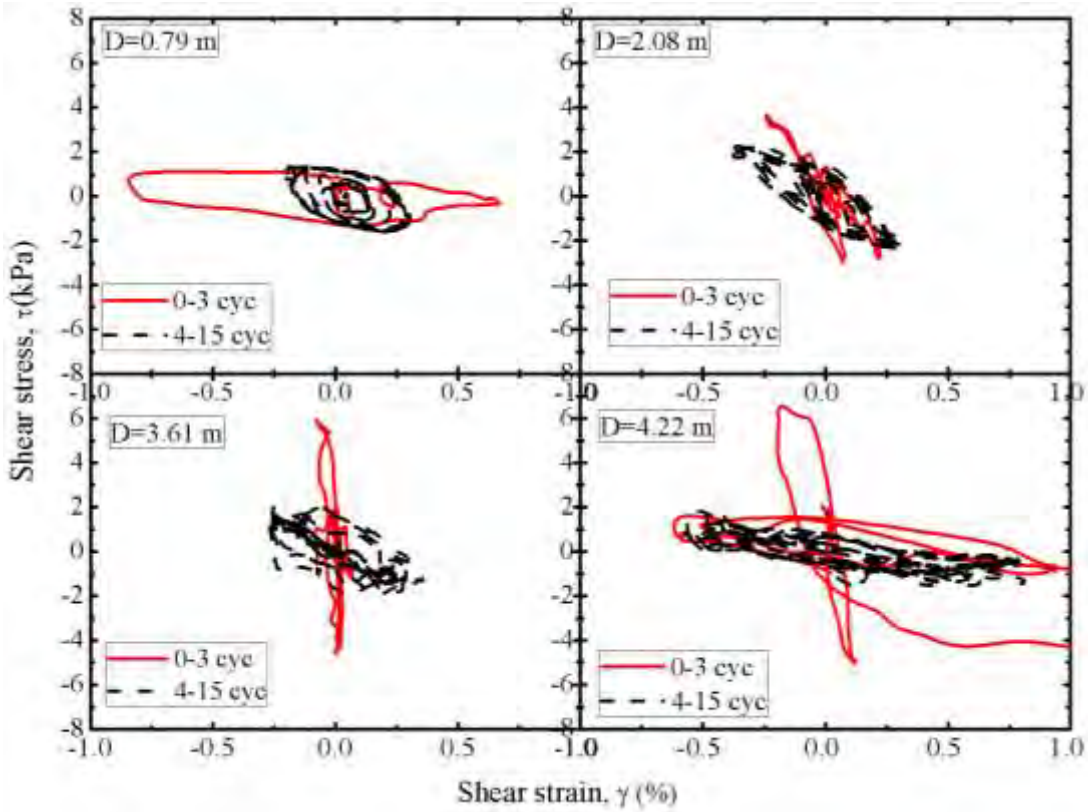

Fig. 8.80 Shear stress- strain loop of T10 (a_{max}=0.10 g/15 cyc)

8.4. CPT and shear wave velocity results

Fig. 8.81(a)-(c) present the profiles of the measured cone resistance (q_c), the pore water pressure behind cone tip (u_2) and the shear wave velocities (V_s) for different CPTs. Fig. 8.82(a)-(c) plot the profiles of the normalized cone resistance q_{c1N}, the normalized pore water pressure behind cone tip ($\Delta u/\sigma_{vo}'$) and the normalized shear wave velocities (V_{s1}) for different CPTs. It can be seen that the increasing trend of both q_{c1N} and V_{s1} indicates the densification of sand deposit due to repetitive shakings. The negligible $\Delta u/\sigma_{vo}'$ at each CPT implies the drained condition of soil during the cone advancement.

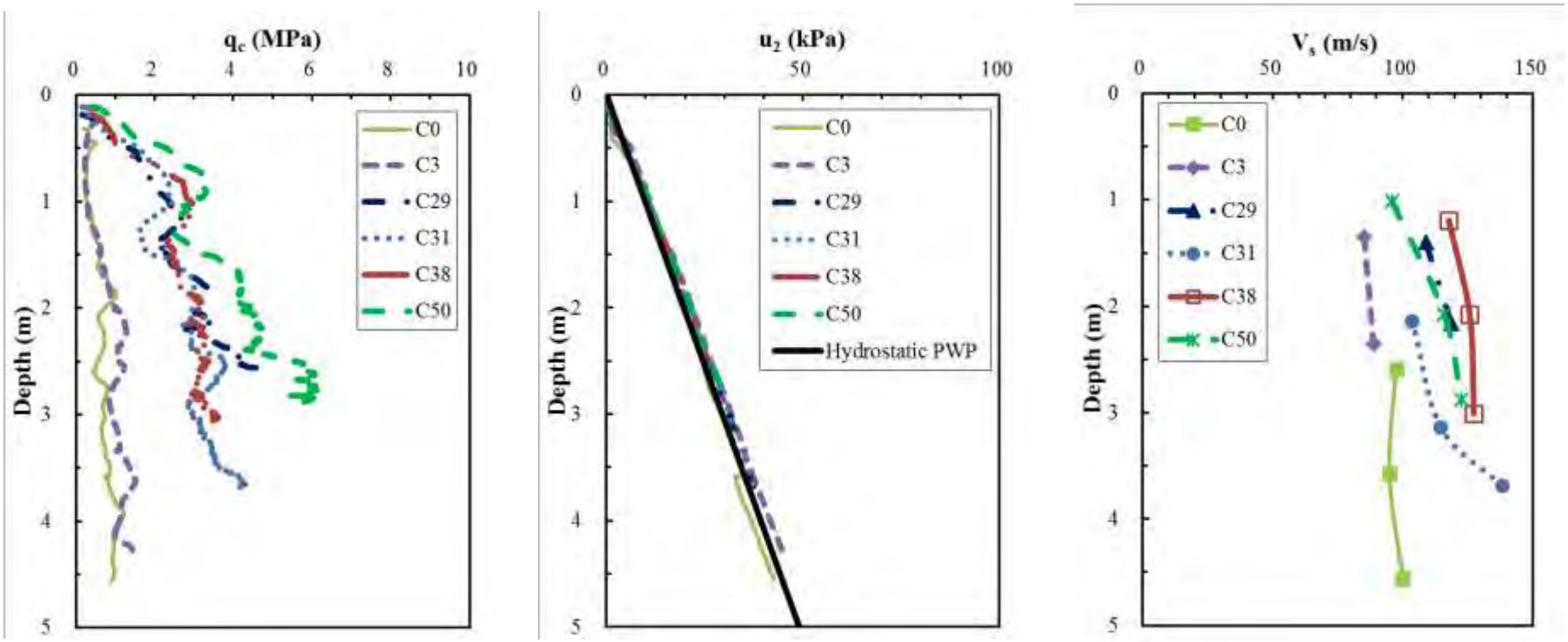

(a) q_c (b) u_2 (c) V_s

Fig. 8.81 Profiles of q_c, u_2 and V_s of different CPTs

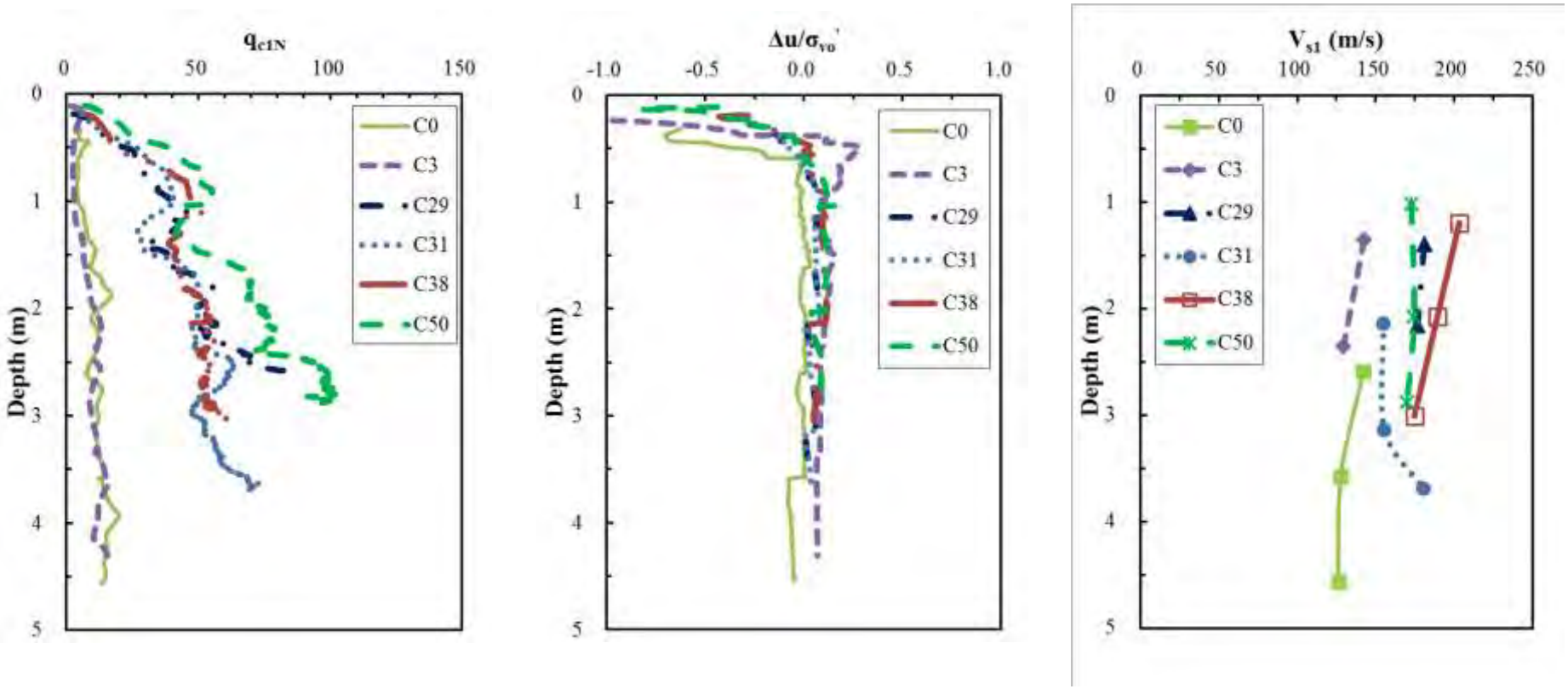

(a) q_{c1N} (b) $\Delta u/\sigma_{vo}'$ (c) V_{s1}

Fig. 8.82 Profiles of q_{c1N}, $\Delta u_2/\sigma_{vo}'$ and V_{s1} of different CPTs

Fig. 8.83(a) and (b) shows the q_{c1N} and the V_{s1}versus the performed CPT test number at selected depths (corresponding to the working piezometer depths), respectively. The interpolation method used in section 8.2.8 is employed to approximate the q_{c1N} and V_{s1} of soil stratum before each large magnitude earthquake (liquefaction tests performed in IM2 and IM3) when there is no direct CPT performed.

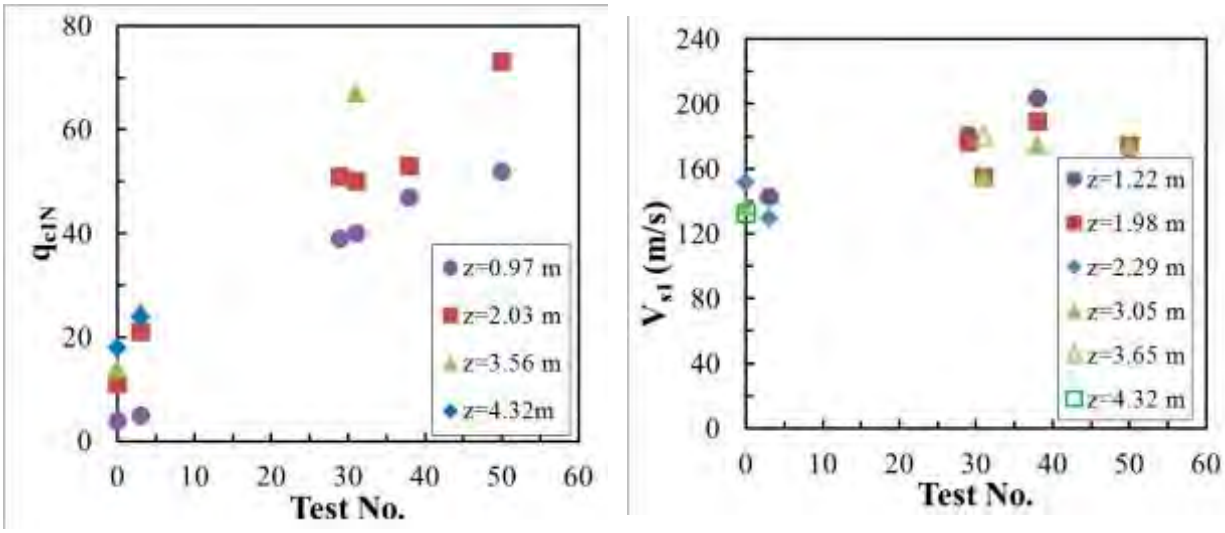

(a) q_{c1N} (b)V_{s1}

Fig. 8.83 q_{c1N} and V_{s1} versus CPT test number at selected depths

8.5. CPT-based and V_s-based liquefaction analysis

Table 8.5 summarizes the $q_{c1N,}$ V_{s1} and CSR at selected depths of each liquefaction test for IM2 and IM3. Fig. 8.84(a), Fig. 8.85(a) and Fig. 8.86(a) plot the correlation between q_{c1N} and CSR using three estimation methods introduced in section 8.2.8. as well as the field based CRR-q_{c1N} relationship. Fig. 8.84, Fig. 8.85 and Fig. 8.86(b) show the correlation between V_{s1} and CSR using three estimation methods and the field based CRR-V_{s1} relationship. The notations are explained in section 8.2.8.

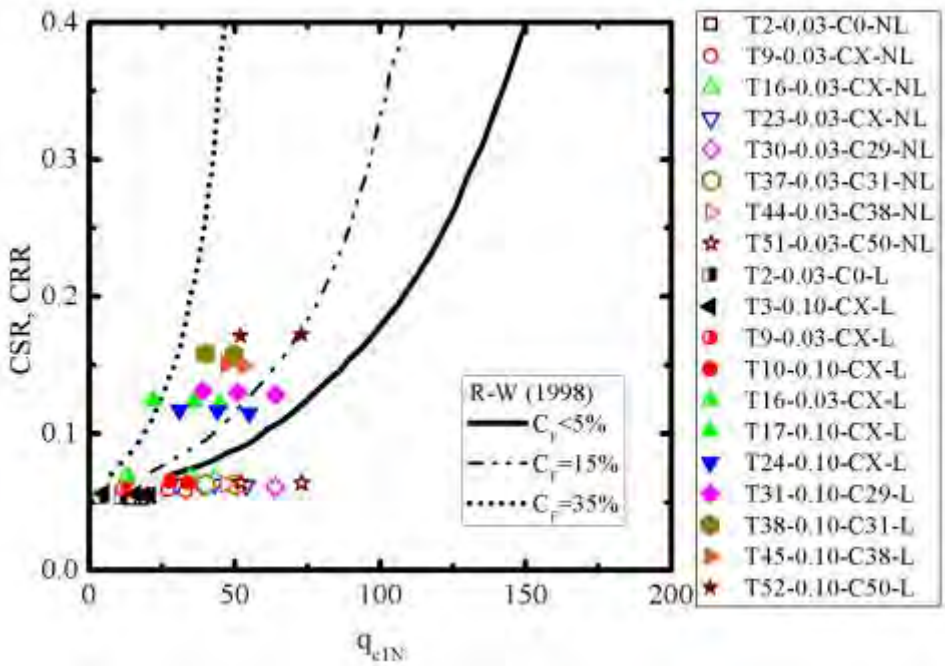

(a) CSR/CRR vs q_{c1N}

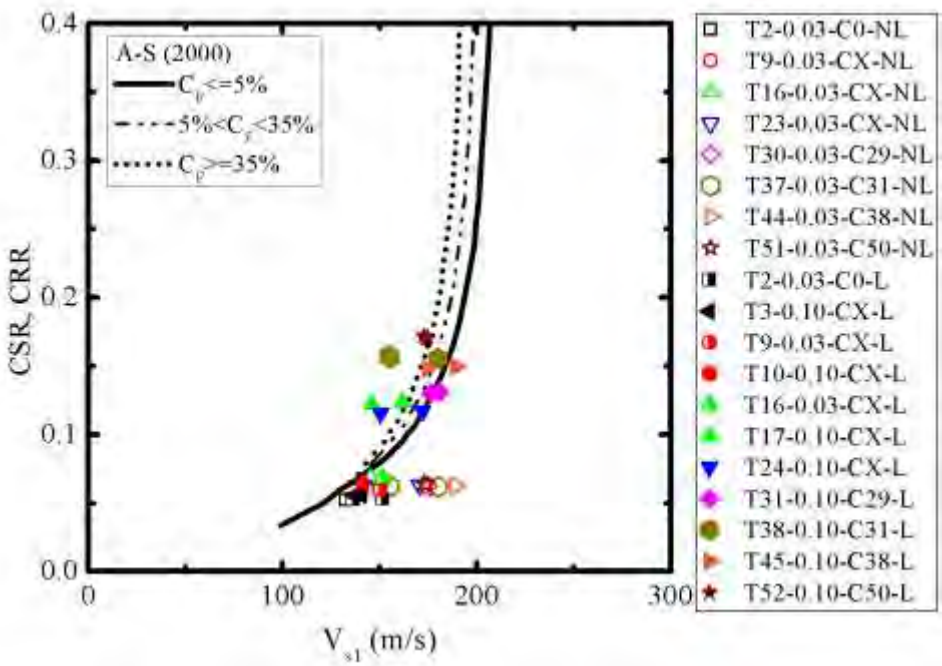

(b) CSR/CRR vs V_{s1}

Fig. 8.84 Correlation between q_{c1N} and CSR, V_{s1} and CSR in LG1-Method I

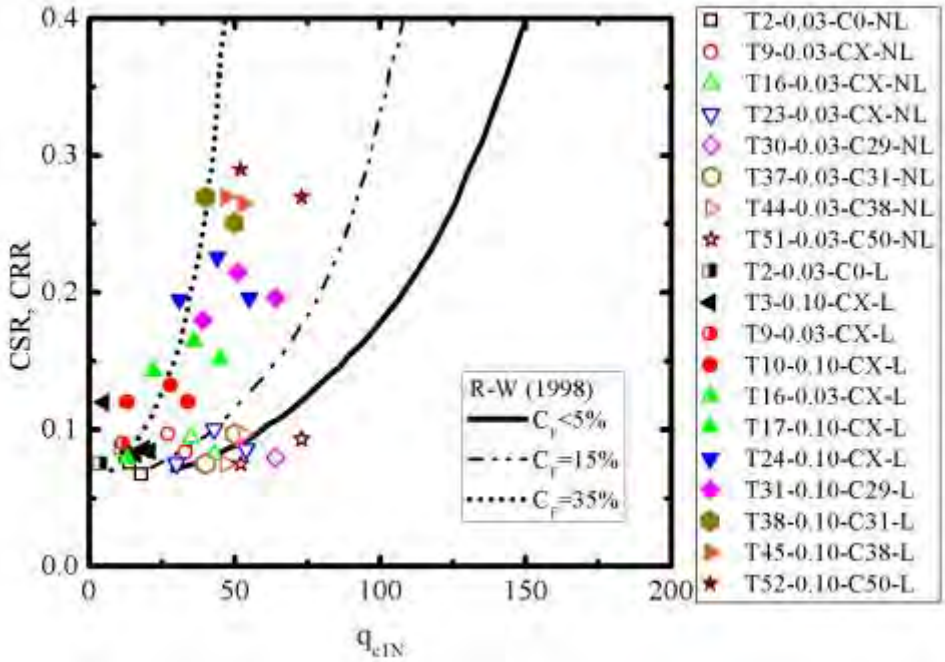

(a) CSR/CRR vs q_{c1N}

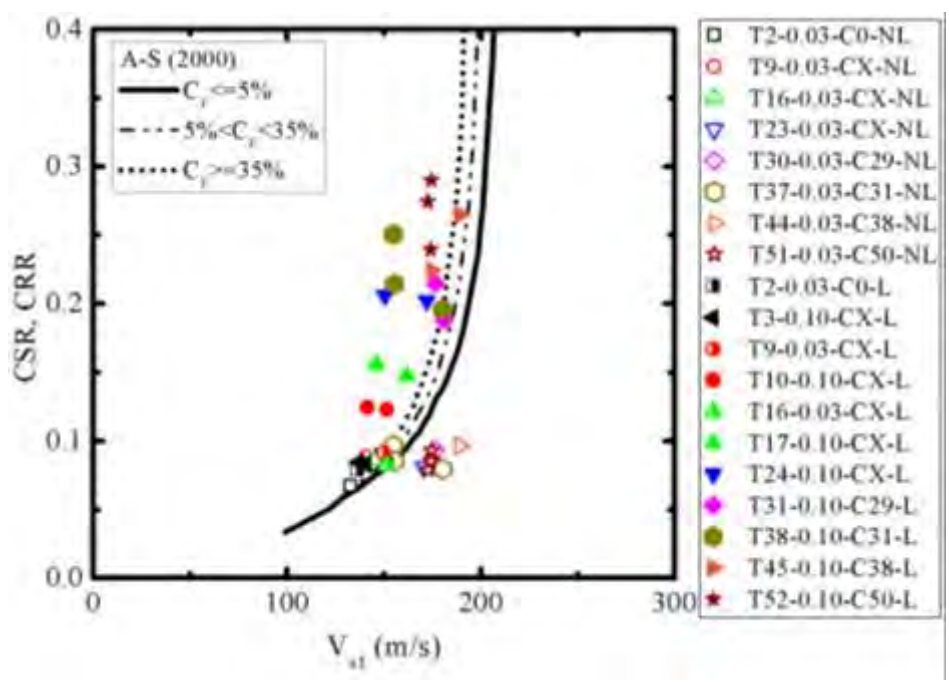

(b) CSR/CRR vs V_{s1}

Fig. 8.85 Correlation between q_{c1N} and CSR, V_{s1} and CSR in LG1-Method II

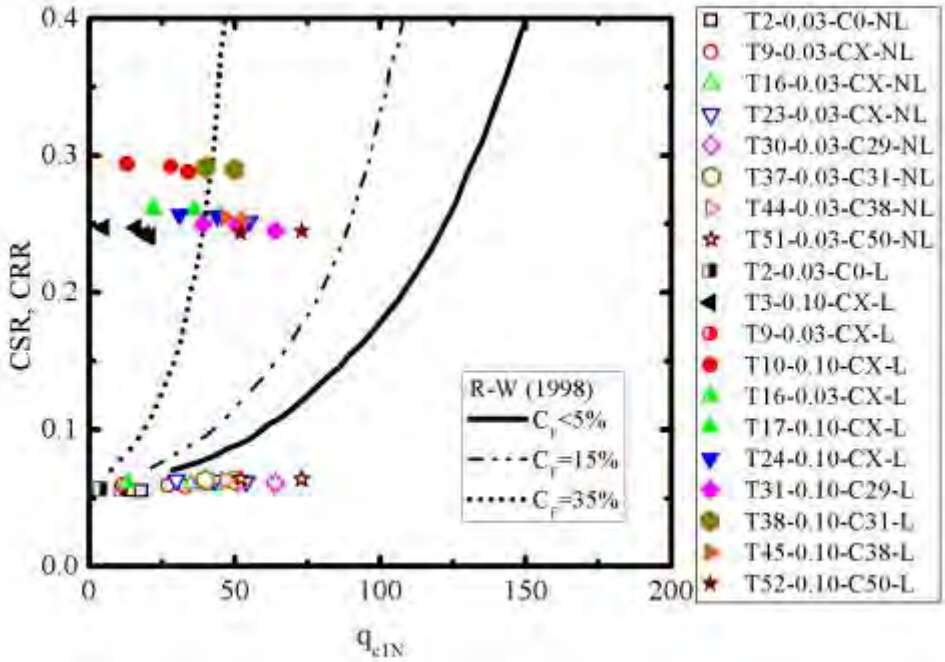

(a) CSR/CRR vs q_{c1N}

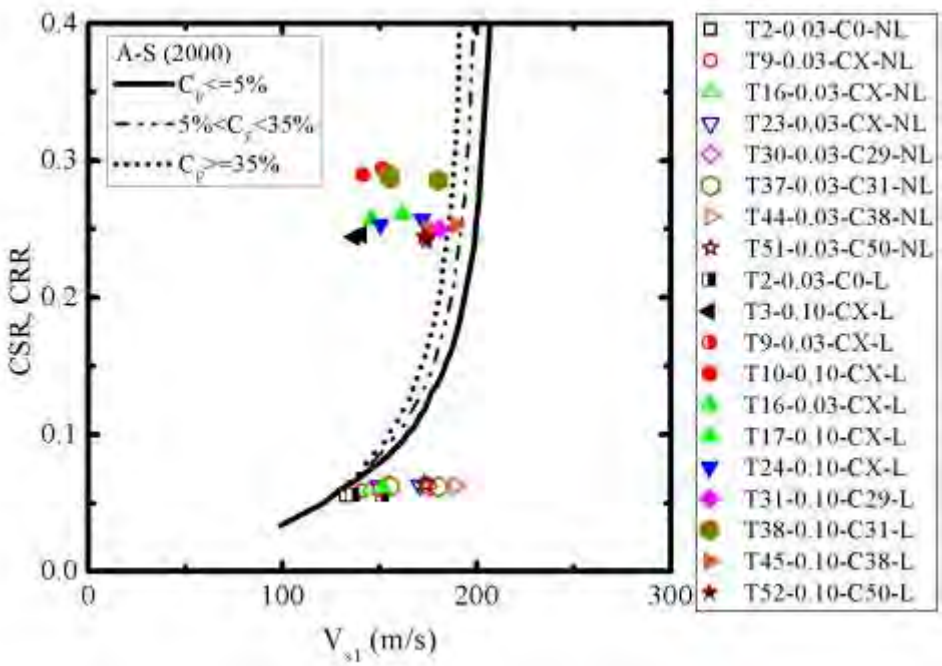

(b) CSR/CRR vs V_{s1}

Fig. 8.86 Correlation between q_{c1N} and CSR, V_{s1} and CSR in LG1-Method III

Table 8.5 Summary of q_{c1N}, V_{s1} and CSR for IM2 and IM3

Test No.	Input Motion	D=0.97m					D=1.22 m			
		r_u-P15	q_{c1N}	CSR			V_{s1} (cm/s)	CSR		
				Method I	Method II	Method III		Method I	Method II	Method III
T2	IM2	-	4	0.053	0.075	0.056	-	0.052	0.077	0.056
T3	IM3	-	5	0.055	0.120	0.243	-	0.055	0.111	0.243
T9	IM2	1.0 (4)	12	0.059	0.090	0.059	152	0.059	0.091	0.059
T10	IM3	1.0 (2)	13	0.064	0.120	0.289	154	0.064	0.123	0.289
T16	IM2	1.0 (4)	21	0.068	0.079	0.060	162	0.067	0.082	0.060
T17	IM3	1.0 (3)	22	0.122	0.142	0.257	163	0.122	0.147	0.257
T23	IM2	0.12	30	0.062	0.075	0.062	171	0.062	0.081	0.062
T24	IM3	1.0 (3)	31	0.115	0.195	0.253	173	0.115	0.202	0.253
T30	IM2	0.09	39	0.061	0.075	0.061	181	0.061	0.079	0.061
T31	IM3	1.0 (6)	39	0.129	0.180	0.246	181	0.129	0.188	0.246
T37	IM2	-	45	0.062	0.075	0.062	-	0.062	0.080	0.062
T38	IM3	-	46	0.156	0.269	0.286	-	0.156	0.265	0.286
T44	IM2	0.08	47	0.062	0.075	0.062	-	0.062	0.080	0.062
T45	IM3	1.0 (3)	47	0.148	0.269	0.250	-	0.148	0.268	0.250
T51	IM2	-	52	0.063	0.075	0.063	173	0.063	0.079	0.063
T52	IM3	-	52	0.169	0.269	0.241	173	0.169	0.274	0.241

Note:

The value in parentheses in the r_u column indicates the number of cycles to cause the initiation of liquefaction.

Test No.	Input Motion	D=2.03m						D=2.47 m			
		r_u-P3	q_{c1N}	V_{s1} (cm/s)	CSR			V_{s1} (cm/s)	CSR		
					Method I	Method II	Method III		Method I	Method II	Method III
T2	IM2	1.0 (6)	11	-	0.052	0.086	0.055	151	0.052	0.083	0.055
T3	IM3	1.0 (2)	16	-	0.055	0.082	0.242	140	0.055	0.083	0.241
T9	IM2	0.6	27	-	0.058	0.097	0.058	-	0.058	0.093	0.058
T10	IM3	1.0 (6)	28	-	0.064	0.132	0.287	-	0.064	0.129	0.286
T16	IM2	0.5	35	-	0.067	0.094	0.059	-	0.067	0.090	0.059
T17	IM3	1.0 (8)	36	-	0.121	0.165	0.255	-	0.121	0.161	0.254
T23	IM2	0.1	43	-	0.062	0.100	0.062	-	0.061	0.096	0.061
T24	IM3	1.0 (3)	44	-	0.114	0.225	0.251	-	0.114	0.217	0.250
T30	IM2	0.09	51	177	0.061	0.093	0.061	-	0.060	0.089	0.060
T31	IM3	1.0 (6)	51	177	0.128	0.215	0.244	-	0.127	0.209	0.243
T37	IM2	0.1	52	155	0.062	0.097	0.062	-	0.061	0.092	0.061
T38	IM3	1.0 (3)	53	155	0.155	0.250	0.285	-	0.154	0.235	0.284
T44	IM2	0.07	53	188	0.062	0.097	0.062	-	0.061	0.092	0.061
T45	IM3	1.0 (3)	53	188	0.147	0.265	0.249		0.146	0.247	0.248
T51	IM2	0.07	73	173	0.063	0.093	0.063	-	0.063	0.090	0.063
T52	IM3	1.0 (4)	73	173	0.168	0.290	0.239	-	0.168	0.268	0.238

Note:

The value in parentheses in the r_u column indicates the number of cycles to cause the initiation of liquefaction.

Test No.	Input Motion	D=3.05 m				D=3.56m				
		V_{s1} (cm/s)	CSR			r_u-P2	q_{c1N}	CSR		
			Method I	Method II	Method III			Method I	Method II	Method III
T2	IM2	125	0.052	0.079	0.055	0.92	14	0.051	0.075	0.054
T3	IM3	126	0.054	0.085	0.240	1.0 (3)	21	0.054	0.086	0.238
T9	IM2	133	0.058	0.088	0.058	0.5	33	0.057	0.084	0.057
T10	IM3	134	0.063	0.124	0.284	1.0 (6)	34	0.063	0.120	0.283
T16	IM2	141	0.066	0.086	0.059	0.6	43	0.066	0.082	0.059
T17	IM3	143	0.120	0.155	0.253	1.0 (8)	45	0.120	0.151	0.252
T23	IM2	149	0.061	0.090	0.061	0.1	54	0.061	0.086	0.061
T24	IM3	151	0.113	0.206	0.249	1.0(4)	55	0.113	0.196	0.248
T30	IM2	-	0.060	0.084	0.060	0.08	-	0.060	0.080	0.060
T31	IM3	-	0.127	0.202	0.242	1.0 (6)	-	0.126	0.196	0.241
T37	IM2	160	0.061	0.085	0.061	0.1	-	0.061	0.080	0.061
T38	IM3	160	0.153	0.214	0.282	1.0 (4)	-	0.153	0.196	0.281
T44	IM2	175	0.061	0.087	0.061	0.06	-	0.061	0.082	0.061
T45	IM3	175	0.146	0.224	0.247	1.0 (3)	-	0.145	0.204	0.245
T51	IM2	171	0.062	0.085	0.062	0.05	-	0.062	0.082	0.062
T52	IM3	171	0.167	0.239	0.237	1.0 (6)	-	0.166	0.214	0.236

Note:

The value in parentheses in the r_u column indicates the number of cycles to cause the initiation of liquefaction.

Test No.	Input Motion	D=4.32 m					
		r_u-P1	q_{c1N}	V_{s1} (cm/s)	CSR		
					Method I	Method II	Method III
T2	IM2	0.78	18	132	0.051	0.067	0.054
T3	IM3	1.0 (3)	-	-	0.054	0.084	0.237
T9	IM2	0.3	-	-	0.057	0.074	0.057
T10	IM3	1.0 (6)	-	-	0.063	0.109	0.281
T16	IM2	0.26	-	-	0.066	0.072	0.058
T17	IM3	1.0 (8)	-	-	0.119	0.141	0.250
T23	IM2	0.03	-	-	0.060	0.076	0.060
T24	IM3	1.0 (6)	-	-	0.112	0.180	0.246
T30	IM2	0.07	-	-	0.059	0.072	0.059
T31	IM3	1.0 (6)	-	-	0.125	0.176	0.239
T37	IM2	0.05	-	-	0.060	0.072	0.060
T38	IM3	0.94	-	-	0.152	0.176	0.279
T44	IM2	0.05	-	-	0.060	0.074	0.060
T45	IM3	0.9	-	-	0.144	0.183	0.244
T51	IM2	0.05	-	-	0.062	0.074	0.062
T52	IM3	0.8	-	-	0.165	0.195	0.235

Note:

The value in parentheses in the r_u column indicates the number of cycles to cause the initiation of liquefaction.

8.6. Summary

A series of large scale liquefaction tests along with CPTs and shear wave velocity tests using clean sand are performed in the laminar box to provide part of the validation for the T_o dependent CRR-q_{c1N} relationship proposed in section 9.3. Nonetheless, additional experiments performed in silty sands at different fines contents are needed to further enrich the data set.

Chapter 9. CPT-based liquefaction screening of sands and silty sands

9.1. Introduction

As discussed in Chapter 4 and Chapter 6, the fines content (C_F) is not the only factor influencing the cone penetration resistance in sands and silyt sand. Hence, in this chapter, a liquefaction screen chart based on the correlation between $(CRR)_{filed}$ and q_{c1N} obtained from Chapter 6 at different narrow ranges of T_o is proposed.

Firstly, the $(CRR)_{tx}$ is based on the undrained cyclic triaxial test data reported by Thevanayagam et al. (2003). It is then corrected for multi-directional shaking and used to obtain $(CRR)_{field}$ corresponding to 15 cycles of shaking for sands and silty sands. A unique relationship is obtained between $(CRR)_{tx}/(CRR)_{field}$ and $(D_{rc})_{eq}$ for sands and silty sands prepared by different soil mixtures under $C_F<C_{Fth}$.

Secondly, the relationship between q_{c1N} and $(D_{rc})_{eq}$ of different narrow ranges of T_o from Chapter 6 is replotted. Based on these two relationships, a T_o dependent CRR-q_{c1N} liquefaction screening chart is proposed.

Finally the proposed correlation between $(CRR)_{field}$ versus q_{c1N} is compared to the experiments presented in Chapter 4, Chapter 8 and previous liquefaction experiments (Ecemis, 2008) and the current field based correlations.

9.2. $(CRR)_{field}$ and q_{c1N} versus $(D_{rc})_{eq}$

Based on the proposed framework (Thevanayagam, 2007a and b) and the collected relevant papers, a unique correlation between $(CRR)_{tx}$ required to cause liquefaction in 15 cycles after the

specimen was isotropically consolidated to 100 kPa and $(D_{rc})_{eq}$ for $C_F<C_{Fth}$ is established in Fig. 9.1.

In contrast to unidrection shaking in cyclic triaixial tests, earthquakes produce shear stress in different directions. It is been shown that multidirectional shaking would cause pore water pressure build up more rapidly than does unidirectional shaking. A reduction factor of 0.9 shall be applied to the $(CRR)_{tr}$ when corrected to $(CRR)_{field}$, giving the relationship between $(CRR)_{field}$ and $(CRR)_{tr}$ as follows by Castro (1975) and Seed et al. (1978):

$$(CRR)_{field} = 0.9\frac{2(1+2K_0)}{3\sqrt{3}}(CRR)_{tx} \qquad \text{(Eq. 9.1)}$$

where K_0 is the coefficient of lateral earth pressure at rest.

The correlation between $(CRR)_{field}$ and $(D_{rc})_{eq}$ for $C_F<C_{Fth}$ can be obtained based upon the above equation in Fig. 9.2.

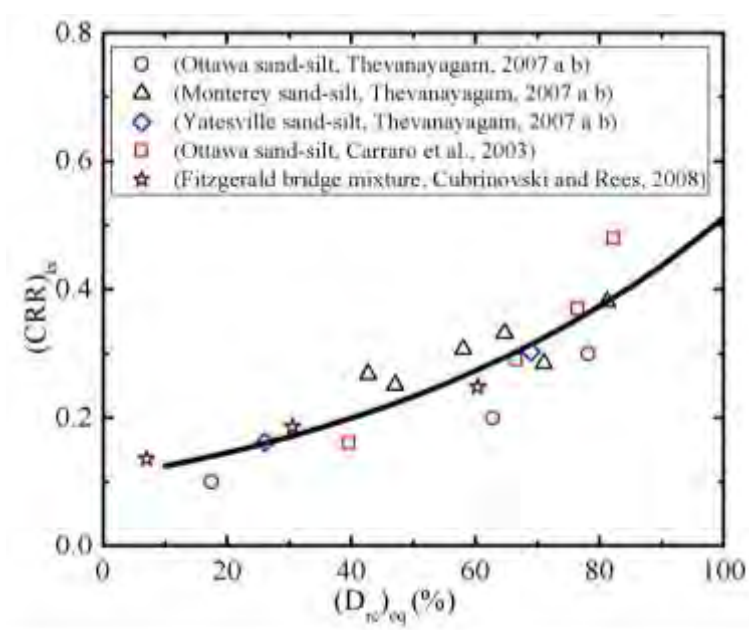

Fig. 9.1 $(CRR)_{tx}$ versus $(D_{rc})_{eq}$ at $C_F<C_{Fth}$

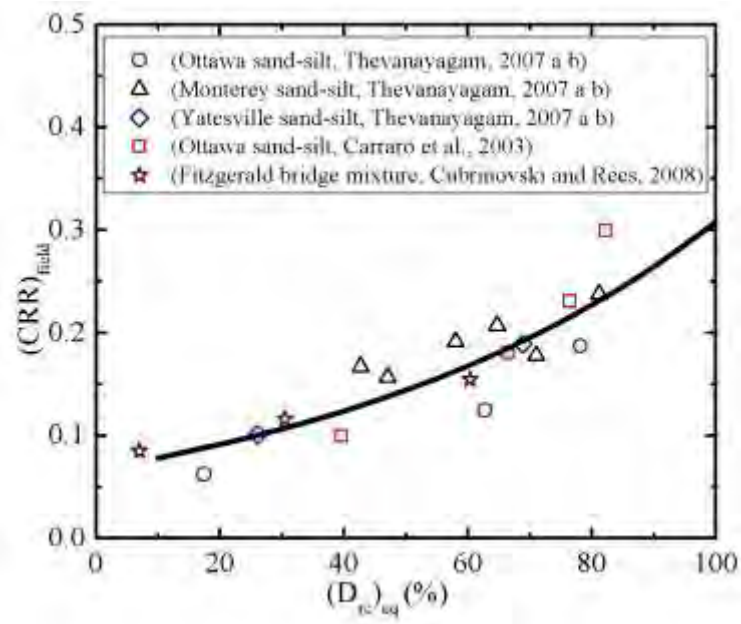

Fig. 9.2 $(CRR)_{field}$ versus $(D_{rc})_{eq}$ at $C_F<C_{Fth}$

The $(CRR)_{tx}$ required to cause liquefaction at 15 cycles in cyclic undrained triaxial test and the corresponding corrected $(CRR)_{field}$ for OS F55 sand-silt with various $(D_{rc})_{eq}$ used in the numerical simulation are tabulated in Table 9.1.

Table 9.1 $(D_{rc})_{eq}$ versus $(CRR)_{tx}$ and $(CRR)_{field}$ used in CPT simulation

Soil	$(D_{rc})_{eq}$	$(CRR)_{tx}$	$(CRR)_{field}$
M20	80	0.475	0.300
M05	79	0.346	0.229
M11	70	0.287	0.187
M15	67	0.264	0.172
M10	65	0.255	0.172
M01	60	0.230	0.154
M21	41	0.149	0.103
M12	41	0.147	0.104
M07	27	0.107	0.078
M17	26	0.105	0.071
M09	17	0.086	0.064
M28	81	0.475	0.305
M23	60	0.229	0.149
M26	40	0.146	0.098
M22	22	0.097	0.063
M24	18	0.089	0.060
M36	45	0.164	0.112
M32	40	0.144	0.100
M31	10	0.074	0.052
M34	8	0.071	0.053
M48	66	0.259	0.169
M47	38	0.139	0.091
M45	18	0.088	0.064

Fig. 9.3 compares q_{c1N} computed from numerical analysis versus $(D_{rc})_{eq}$ at different T_o and experimental data. Each curve is replotted from Fig. 6.27.The q_{c1N}-$(D_{rc})_{eq}$ data points show a down shifting trend as T_o increases from 0.04 to 10 (drained condition to undrained condition).

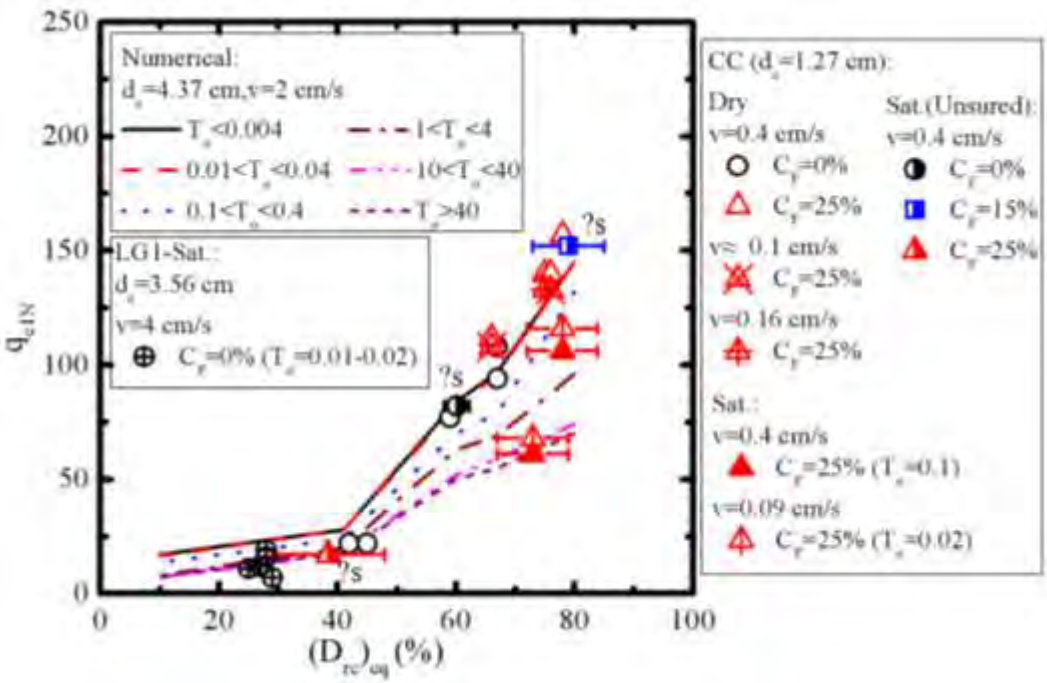

Fig. 9.3 q_{c1N} versus $(D_{rc})_{eq}$ at different T_o of Ottawa F55 sand-silt mix

9.3. $(CRR)_{field}$ versus q_{c1N}

Fig. 9.4 plots the proposed T_o dependent $(CRR)_{field}$ versus q_{c1N}. Each curve corresponding to a narrow range of T_o. The CRR-q_{c1N} curve shifts to left as T_o increase from the 0.04 to 10. However, further increase or decrease of T_o does not affect much of the CRR-q_{c1N} curve.

This figure also compares the proposed curves with numerical results denoted by 'numerical' from a set of soils simulated in the monotonic undrained triaxial tests reported by Thevanayagam et al. (2003). Each soil is assigned to two different permeabilities to ensure the drained and undrained condition. The q_{c1N} related to drained and undrained condition of each soil is obtained from the numerical model and the corresponding $(CRR)_{field}$ of that soil is estimated from Fig. 9.2.

In addition, this figure compares the proposed curves with experiments conducted at UB [Chapter 4, Chapter 7 and previous liquefaction tests using laminar box (LG0-Ecemis,2008)]. 'CC-

L' denotes experiments performed in the testing chamber. 'LG1-L/LG1-NL' represents liquefaction tests performed in the laminar box in which liquefaction/no-liquefaction is spotted using CSR computation method I. It is implied in this figure that, at a given q_{c1N}, the CRR required to cause liquefaction is to increase with an increase of T_o up to the undrained limit value (increase of fines content up to C_{Fth}) or is to decrease with a decrease of T_o until the drained limit value. On the other hand, at a given CRR, the q_{c1N} required to resist liquefaction is to decrease with an increase of T_o up to the undrained limit value (increase of fines content up to C_{Fth}), or is to increase with an decrease of T_o until the drained limit value.

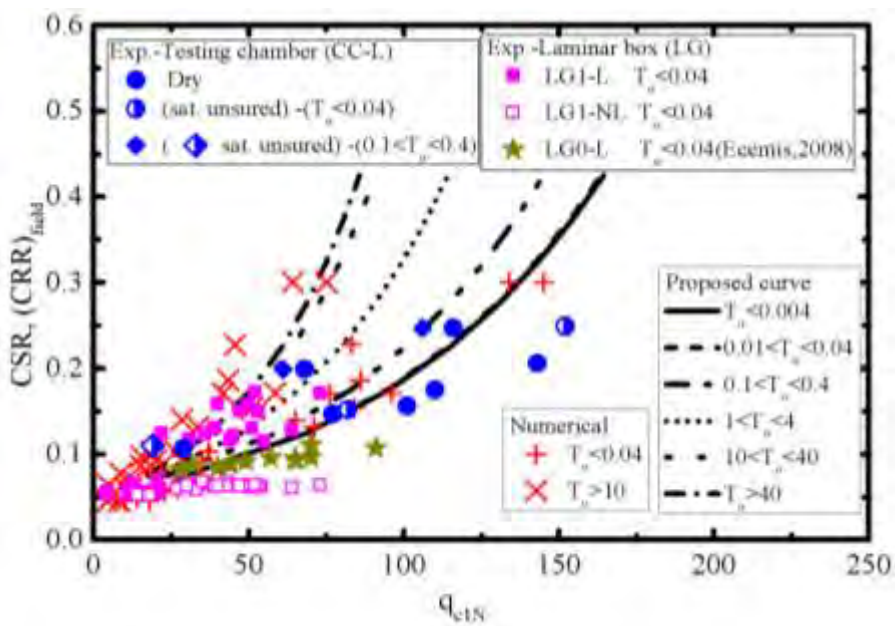

Fig. 9.4 Comparison between proposed T_o dependent $(CRR)_{field}$–q_{c1N} and numerical and laboratory data

Fig. 9.5 compares the proposed $(CRR)_{field}$-q_{c1N} correlation to the existing field based correlations. The notation "I-B(2008)" indicates the CRR-q_{c1N} correlation proposed by Idriss and Boulanger (2008) while "R-W(1998)" represents the correlation established by Robertson and Wride (1998). It can be seen that the proposed $(CRR)_{field}$-q_{c1N} for T_o< 0.01 and 0.01<T_o<0.04

correspond to the clean sand curve, $0.1<T_o<0.4$ and $1<T_o<4$ correspond to the 10% and 15% silt content curve and $10<T_o<40$ and $T_o>40$ correspond to the 35% or larger silt content curve.

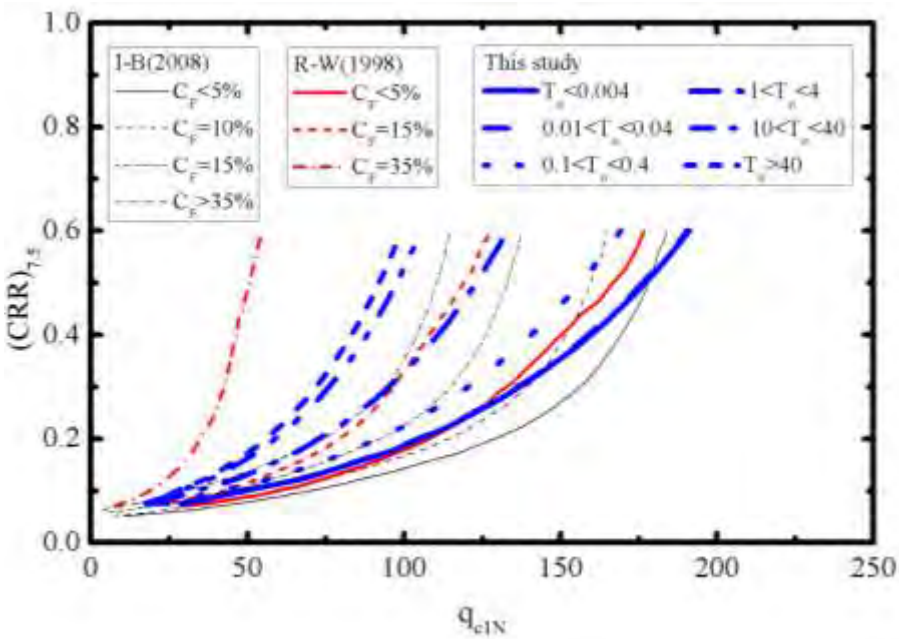

Fig. 9.5 Comparison between proposed T_o dependent $(CRR)_{field}$–q_{c1N} and field based correlation

9.4. Summary

In this chapter, a liquefaction screen chart based on the correlation between measured $(CRR)_{filed}$ and q_{c1N} at different narraw ranges of T_o obtained from numerical analyses is proposed. The proposed $(CRR)_{field}$ versus q_{c1N} for clean sand agrees reasonably well with the counterpart of experimental results from testing chamber and laminar box. Moreover, the proposed liquefaction screen chart is in good agreement with the in-situ based correlations at different fines contents. The effect of fines on the cone resistance is reflected in the left shifting of the curve as T_o increases. However, further research is needed to further evaluate and validate such a procedure using field data and physical model tests.

Chapter 10. Conclusion and future work

The objective of this study is to experimentally and numerically examine the effect of non-plastic fines on the cone resistance in silty sands. The major conclusions and recommendations for further work obtained from this research are presented in the following paragraphs.

10.1. Conclusion and findings

A number of CPT chamber tests were carried out using a newly-developed rigid wall testing chamber at different penetration rates in specimens with vaired fines contents (0, 15 and 25%). In addition, a numerical model incorporated the Arbitrary Lagrangian Eulerian (ALE) mesh technique into cap plasticity model to perform the parametric study of permeability, penetration rate and cone diameter on cone resistance. The adopted ALE mesh technique alleviates the heavy distortion of elements around the cone tip area during the cone advancement and provides high quality mesh in the large strain analysis. Based upon the experimental and numerical results:

1) In both experimental and numerical studies for saturated sands and silty sands, the normalized cone resistance (q_{c1N}) decreased with an increase in silt content, at the same [$(D_{rc})_{eq}$], from 0 to 25%. However this influence of silt content on penetration resistance was absent for dry sands and silty sands at the same [$(D_{rc})_{eq}$]. The difference of penetration resistance in saturated sands and silty sands, is thought to be due to partial drainage occurring in saturated silty sands whereas the penetration process is thought to be nearly drained in saturated sands. In the case of dry soils, this pore pressure influence is absent and hence the same penetration resistance is observed in sands and silty sands.

2) Both experimental data and numerical results point that as T_o increases, which indicataes the increase in silt content (decrease in c_v), q_{c1N} decreases, for the soil at the same $(D_{rc})_{eq}$. It is because that the excess pore water pressure around cone tip develops, resulting in penetration process transiting from drained to partially drained or even undrained condition as T_o increases. In addition, the numerical analysis shows that v and d_c also influence q_{c1N} in silty sands. At a given $(D_{rc})_{eq}$, q_{c1N} decreases as T_o increases (v increase or d_c increase) in the partially drained condition.

Since fines content is not the only factor affecting the cone resistance a T_o dependent CRR-q_{c1N} was proposed. A series of liquefaction tests along with cone penetration tests using clean sand performed in a full scale laminar box, together with the CPT chamber tests using sands containing different amount of silt contents, were used to to support the relationship. The proposed curve corresponding to clean sand agrees well with the counterpart of experimental data from laminar box and testing chamber. The effect of fines on the cone resistance is reflected in the left shifting of the CRR-q_{c1N} relationship as T_o increases, which agrees with the field based correlations.

10.2. Suggestions for future research

Experimentally, the maximum penetration rate used in this research was 0.4 cm/s, which is one fifth of the standard penetration rate and the cone diameter was 1.27 cm, which is about one third of the standard cone. This means that the T_o of CPT performed in the current system would be about 1/15 of that conducted in the field for the same soil using Eq. 2.14. In addition, Ottawa

F55 sand-silt mix was the only soil sample used in the experiment. Hence:

1) More model cone penetrometer experiements performed under higher penetration rates (e.g. 2 cm/s or higher) at different fines contents using different soil mixtures are needed to further validate the effect of fines on cone resistance in silty sands.
2) More CPTs at faster penetration rates (e.g 2 cm/s or higher) are required to further examine the effect of penetration rate on cone resistance in silty sands.
3) The effect of cone diameter on cone resistance in silty sands needs to be experimentally examined.

In addition, the liquefaction tests along with CPTs performed using laminar were merely in sands, more laboratory tests conducted in silty sands at different fines contents are needed to validate the proposed T_o dependent CRR-q_{c1N} relationship.

Numerically, although the constitutive model-cap plasticity model used in this study shows reasonable results compared to the experimental data in either undrained triaxial tests or CPTs performed in testing chamber for different soils, soils with phase transformation cannot be captured correctly. A user developed material is needed for this type of soil, for example, the phase transformation point could be considered as an additional parameter.

Reference

Abaqus 6.10, 2010. *User's manual*, Hibbitt, Karlsson and Sorensen, Inc. (HKS), Fremont, CA.

Andrus, R. D. and Stokoe, K. H. ,2000. "Liquefaction resistance of soils from shearwave velocity", *J. Geotech. and Geoenv. Eng.*, ASCE, Vol. 126(11), 1015-1025

Aubeny, C. P., 1992. "Rational interpretation of in situ tests in cohesive soils", *PhD Dissertation*, MIT, Cambridge, MA.

Baligh, M. M. and Levadoux, J. ,1986a. "Consolidation after Undrained Piezocone Penetration I: Prediction", *Journal of Geotechnical Eng.*, Vol. 112(7), 707-725

Baligh, M. M. and Levadoux, J., 1986b. "Consolidation after undrained piezocone penetration II: Interpretation", *Journal of Geotechnical Eng*., Vol. 112(7), 727-745

Been, K., Crooks, J. H. A., and Rothenburg, L., 1988. "A critical appraisal of CPT calibration chamber tests", *Proceedings of the First International Symposium on Penetration Testing (ISOPT-1)*, Orlando, FL, U.S.A.

Been, K., Jefferies, M. G. and Hachey, J., 1991a. "The critical state of sands", *Geotechnique* 41(3), 365–381.

Been, K. and Kosar, K. M., 1991b." Hydraulic fracture simulations in a calibration chamber", *Proceedings of the First International Symposium on Calibration Chamber Testing*, Potsdam, NY, U.S.A

Bethapudi, R., 2008. "Liquefaction induced lateral spreading in large-scale shake testing", *Master thesis*, State University of New York at Buffalo, Amherst, NY, USA.

Borden, R. H., 1991. "Boundary displacement induced by DMT penetration", *Proceedings of the First International Symposium on Calibration Chamber Tests*, Potsdam, NY, U.S.A.

Campanella, R.G., Gillespie, D. and Robertson, P.K., 1982. "Pore pressures during cone penetration testing", *2ND European Symposium on Penetration Testing,* Amsterdam, The Netherlands.

Campanella, R.G., Robertson, P.K. and Gillespie, D. 1986. "Factors affecting the pore water pressure and its measurement around a penetration cone", *Proceeding of 39th Canadian Geotechnical Conference*, Ottawa, Canada.

Castro, G. ,1975. "Liquefaction and cyclic mobility of saturated sands", *Journal of Geotechnical Engineering Division*, ASCE, 101(6), 551–569.

Carreara, A., COOP, M., and Lancellotta, R., 2011. "Influence of grading on the mechanical behaviour of Stava tailings", *Geotechnique*, 61(11),935-946

Carraro, J.A.H., Bandini, P., and Salgado, R., 2003. "Liquefaction resistance of clean and nonplastic silty sands based on cone penetration resistance", *Journal of Geotechnical and Geoenvironmental Engineering*, 129(11), 965-976.

Chang, N.-Y. ,1987. "Liquefaction susceptibility of fine-grained soils. Preliminary study report", *Contract No. DACW39-84-M-4230*, U.S. Army Corps of Engineers, Waterways Experimental Station, Vicksburg, MO.

Chen, W.F., and Baladi, G.Y., 1985. "Soil plasticity theory and implementation", *Publisher:*

Elsevier.

Chien, L., Oh, Y. ,and Chang C., 2002. "Effects of fines content on liquefaction strength and dynamic settlement of reclaimed soil", *Canadian Geotechnical Journal*, 39,254-265.

Chung, S., Randolph, M.F., Schneider., J.A., 2006. "Effect of penetration rate on penetrometer resistance in clay", *Journal of Geotechnical and Geoenvironmental Engineering*, 132(9), 1188-1196.

Coduto, D.P., 2001. "Foundation design principle and practices", *Publisher: Prentice Hall*, Upper Saddle River, NJ, USA.

Cubrinovski, M., and Rees, S., 2008. "Effects of fines on undrained behavior of sands", *University of Canterbury Research Repository*.

Durgunoglu and Mitchell, J.K, 1975 a and b. "Static penetration resistance of soils, I-Analysis; II-Evaulation of theory and implications for practice", ASCE Special conference on In-situ Measurements of Soil Properties, Raleigh, NC, I, 151-189.

De Borst, R. and Vermeer, P. A.,1984. "Possibilities and limitations of finite element for limit analysis", *Geotechnique*, 34(2), 199-210.

Ecemis, N., 2008. "Effects of permeability and compressibility on liquefaction screening using cone penetration resistance", *Ph.D dissertation*, State University of New York at Buffalo, Amherst, NY, USA.

Finnie, I. M. S., and Randolph, M. F., 1994. "Punch-through and liquefaction induced failure of

shallow foundations on calcareous sediments", *Proc. 17th Int. Conf. on the Behavior of Offshore Structures*, Vol. 1, Massachusetts Institute of Technology, Boston, 217-230.

Fu, X.J., 2006. "Test study on characteristic of strain softening of saturated silty sand", *Master Thesis*, Hohai University, Nanjing, P.R. of China. (In Chinese)

Gadala, .M.S, and Wang, J., 1998. "ALE formulation and its application in solid mechanics", Comput. Methods Appl. Mech. Engrg., 167, 33-55.

Garizio, G. M., 1997. "Determinazione dei parametric geotecnici e in particolare di K0 da prove penetrometriche," M.Sc. Department of Structural Engineering, Politecnico di Toriono.

Griffiths, D. V., 1982. "Elasto-plastic analysis of deep foundations in cohesive soils", *Int.J. Numer. and Analytical Methods in Geomech.*, Vol. 6, 211-218.

Gui M.W., Bolton, M.D., Garnier, J.G., Corte, J.F., Bagge, G., Laue, J., Renzi, R., 1998. "Guidelines for cone penetration tests in sand", *Centrifuge 98*, Editor: Kimura, Kusakabe and Takemura, Balkema, Rotterdam, ISBN 90 54109866.

Hardin, B.O. and Drnevich, V.P., 1972. "Shear modulus and damping in soils: measurement and parameter effect", Journal of the soil mechanics and foundations Division, ASCE, 98(6), 603-624.

Hazirbaba, K, and Rathje, E. M., 2009. "Pore pressure generation of silty sands due to induced shear strains", *Journal of Geotechnical and Geoenvironmental Engineering*, 135(12),1892-1905.

House, A. R., Oliveira, J. R.M.S., and Randolph, M. F., 2001. "Evaluating the coefficient of consolidation using penetration tests", *Inte Journal of Physical Modelling n Geotechnics*, 1(3),

17–25.

Houlsby, G. T., and Hitchman, R., 1988. "Calibration chamber tests of a cone penetrometer in sand", *Geotechnique*, 38(1), 39-44.

Huang, A.B., Holtz, R.D., and Chameau, J.L., 1988. "A calibration chamber for cohesive soils", *Geotechnical Testing Journal*, 11(1), 30-35.

Huang, A. B., Holtz, R. D., and Chameau, J. L., 1991. "A laboratory study of pressuremeter tests in clays", Journal of Geotechnical Engineering, 117,1549-1567.

Huang, W., Sheng, D., Sloan, S.W. and Yu, H.S., 2004. "Finite element analysis of cone penetration in cohesionless soil", Computer and Geotechnics 2004(31), 517-528.

Hsu, H., Huang, A., 1999. "Calibration of Cone Penetration Test in Sand", *Proc. Natl. Sci. Counc. ROC(A)*, 23(5), 579-590.

Ishihara, K. , 1985. "Stability of natural deposits during earthquakes", *Proc., XI Int. Conf. on Soil Mechanics*, 321–376.

Idriss, I. M. and Boulanger, R. W., 2008. "Soil liquefaction during earthquakes", Monograph MNO-12, Earthquake Engineering Research Institute, Oakland, CA, 261 pp.

Jaeger, R. A., DeJong, J.T., Boulanger, R. W., Low, H. E., and Randolph, M. F., 2010. "Variable penetration rate CPT in an intermediate soil", *Proc. 2nd Int. Symp. onCone Penetration Testing*.

Jamiolkowski, M., Lo Presti, D. C. F. and Manassero, M., 2001. "Evaluation of relative density and shear strength of sands from CPT and DMT", *Soil Behavior and Soft Ground Construction*, ASCE, Geotechnical special publication No. 119, 201-238.

Kim, K., Prezzi, M., Salgado, R., and Lee, W., 2008. "Effect of penetration rate on cone penetration resistance in saturated clayey soils", *Journal of Geotechnical and Geoenvironmental Engineering*, 134(8), 1142-1153.

Kiousis, P.D., and Voyiadjis, G.Z., 1985. "Lagrangean continuum theory for saturated porous media", *Journal of Engineering Mechanics*, 111(10), 1277-1288.

Kiousis PD, Voyiadjis G.Z., Tumay M.T., 1988. "A large strain theory and its application in the analysis of the cone penetration mechanism", *International Journal for Numerical and Analytical Methods in Geomechanics*,12,45-60.

Kokusho, T., Ito, F., Nagao, Y., Green, A.R., 2012. "Influence of Non/low-plastic fines and associated aging effects on liquefactioin resistance", *Journal of Geotechnical and Geoenvironmental Engineering*, 138(6), 747-755.

Kramer, S., 1996. "Geotechnical earthquake engineering", Prentice Hall, Upper Saddle River, NJ, *ISBN:0-13-374943-6*.

Kulhawy, F.H. and Mayne, P.W., 1990. "Manual on estimating soil properties for foundation design", EL-6800 research project 1493-6.
http://www.geoplanning.it/test/wp-content/uploads/2012/02/manual-on-estimating-soil-properties-for-foundation-design.pdf

Kumar, J., Baju, K.V.S.B., 2009. "Penetration rate effect on Miniature Cone tip resistance for different cohesionless material", *Geotechnical Testing Journal*, 32(4), 1-10.

Kulhawy, F. H. ,1991. "Fifteen+ years of model foundation testing in large chambers", *Proceedings of the First International Symposium on Calibration Chamber Tests*, Potsdam, NY, U. S.A.

Lancellotta, R. ,1983. "Analisi di affidabilita in ingegneria geotecnica", *Atti dell'Istituto di Scienza delle Costruzioni*, No 625, Politecnico di Torino.

Lu, Q., Randolph, M. F., Hu, Y. & Bugarski, I. C. ,2004. "Anumerical study of cone penetration in clay", *Geotechnique* 54(4), 257–267

Mahutka, K. P., Konig, F., and Grabe, J. , 2006. "Numerical modelling of pile jacking, driving and vibratory driving", *In Numerical modelling of construction processes in geotechnical engineering for urban environment* (ed. Th. Triantafylidis), pp. 235–246. London, UK: Taylor & Francis.

Markauskas, D., Kacianaukas, R., and Katzenbach, R., 2005. "Simulation of piezocone penetration in saturated porous medium using the FE remeshing technique", *Foundations of civil and Environmental Engineering*, 6, 103-116.

Mayne, P.W., and Kulhawy, F.H., 1991. "Calibration chamber database and boundary effects correction for CPT data", *Proceedings of the First International Symposium on Calibration Chamber Tests*, Potsdam, NY, U.S.A, 257-264.

Miller, G.A., Muraleetharan, K.K., Tan, N.K., and Lauder, D.R., 2002. "A calibration chamber for unsaturated soil testing.", *Proceedings of the 3rd International Conference on Unsaturated soils*, UNSAT 2002, Recife, Brazil, 10-13 March, 2002. Balkema, Lisse, the Nerthelands, Vol. 2, 453-

457.

Mitchell, J. K., and Tseng, D. J. ,1990. "Assessment of liquefaction potential by cone penetration resistance", *Proc., H. Bolton Seed Memorial Symp.*, J. M. Duncan, edited, 335–350.

Mitchell J.K., 1993. "Fundamentals of Soil Behavior", Second ed. Wiley Interscience Published.

Murthy, T.G., Loukidis, D., Carraro, A.H., Prezzi, M., and Salgado, R., 2007. "Undrained monotonic response of clean and silty sands", *Geotechnique*, 57(3), 273-288.

Naeini, S.A., and Baziar, M.H., 2004. "Effect of fines content on steady-state strength of mixed and layered samples of a sand", *Soil Dynamic and Earthquake Engineering*, 24,181-187.

Ni, Q., Tan, T.S., Dasari, G.R. and Hight D.W., 2004. "Contribution of fines to the compressive strength of mixed soils", *Geotechnique* , 54(9), 561-569.

Oliveira, J.R.M.S., Almeida, M.S.S., Motta, H.P.G., Almeida, M.C.F., 2011. "Influence of Penetration Rate on Penetrometer Resistance", *Journal of Geotechnical and Geoenvironmental Engineering*, 137(7), 695-703.

O'Neill, M. W. ,1991. "Houston's calibration chamber: case history", *Proceedings of the First International Symposium on Calibration Chamber Tests*, Potsdam, NY, U.S.A.

Papadopoulou, A., and Tika, T., 2008. "The effect of fines on critical state and liquefaction resistance and characteristics of non-plastic silty sands", *Soil and Foundations*,48(5), 713-725.

Parkin, A. K., 1988. "The calibration of cone penetrometers", *Proceedings of the First*

International Symposium on Penetration Testing (ISOPT-1), Orlando, FL, U.S.A.

Polito, C.P., and Martin II, J.R., 2001. "Effect of nonplastic fines on the liquefaction resistance of sands", *Journal of Geotechnical and Geoenvironmental Engineering*, 127(5), 408-415.

Poulos, S. J. ,1981. "The Steady state of deformation", *Journal of Geotechnical Engineering*, 107 (GT5): 553–562.

Pournaghiazar, M., Russell, A. R., Khalili, N., 2011. "Development of a new calibration chamber for conducting cone penetration tests in unsaturated soils", *Canadian Geotechnical Journal*, 48,314-321.

Puppala, A.J., 1993. "Effect of cementation on the cone resistance in sands: A calibration chamber study", *Ph.D dissertation*, Louisiana State University, LA, USA.

Rahman, M.M., Lo, S.R., and Gnanendran, C.T., 2008. "On equivalent granular void ratio and steady state behaviour of loose sand with fines", *Canadian Geotechnical Journal*, 45,1439-1456.

Randolph, M. F. and Hope, S., 2004. "Effect of cone velocity on the cone resistance and excess pore pressures", *IS Osaka - Engineering Practice and Performance of Soft Deposits*, Osaka, Japan, 147-152.

Robertson, P.K., and Campanella, R.G., 1985. "Liquefaction potential of sands using CPT", *Journal of Geotechnical Engineering*, 111(3), 384-403.

Robertson, P.K., Campanella, R.G., Gillespie, D. and Greig, J., 1986. "Use of piezometer cone data", *ASCE specialty conference, proceedings of In Situ '86*, Blacksburg, Virginia, USA.

Robertson, P. K., Woeller, D. J., and Finn, W. D. L. (1992). ‘‘Seismic cone penetration test for evaluating liquefaction potential under cyclic loading", *Can. Geotech. J.*, Ottawa, 29, 686–695

Robertson, P. K., and Wride (Fear), C. E.,1998. "Evaluating cyclic liquefaction potential using the cone penetration test", *Canadian Geotechnical Journal*, 35, 442–459.

Roscoe, K., Schofield, A. N. and Wroth, C. P. ,1958. "On the yielding of soils", *Geotechnique* 8(1), 22–53.

Salgado, R., Bandini, P., and Karim, A., 2000. "Shear strength and stiffness of silty sand", *Journal of Geotechnical and Geoenvironmental Engineering*, 126(5), 451–462.

Salgado, R., Boulanger, R.W., and Mitchell, J.K., 1997a. "Lateral stress effects on CPT liquefaction resistance correlations", *Journal of Geotechnical and Geoenvironmental Engineering*, 123(8), 726-735.

Salgado, R., Mitchell, J.K., and Jamiolkowski, M, 1997b. "Cavity expansion and penetration resistance in sand", *Journal of Geotechnical and Geoenvironmental Engineering*, 123(4), 344-354.

Salgodo, R., Mitchell, J.K., Jamiolkowski, M., 1998. "Calibration chamber size effects on penetration resistance in sand", *Journal of Geotechnical and Geoenvironmental Engineering*, 124(9), 878-888.

Schmertmann, J. H. ,1976. "An updated correlation between relative density D_r and Fugro type electric cone bearing, q_c", *Contract Report DACW 39-76 M 6646 WES*, Vicksburg, Miss.

Schneider, J. A., Lehane, B. M., and Schnaid F. ,2007. "Velocity effects on piezocone tests in normally and overconsolidated clays", *Int. J. of Physical Modelling in Geotechnics*, 7(2): 23–34.

Seed, H. B., and De Alba, P. ,1986. "Use of SPT and CPT tests for evaluating the liquefaction resistance of sands." *Proceeding, Speciality Conference on Use of In-Situ Testing in Geotechnical Engineering*, INSITU'86, Geotechnical Special Publication No. 6, ASCE, New York,281–302.

Seed, H.B., and Idriss, I.M., 1967. "Analysis of soil liquefaction: Niigata earthquake", *Journal of the Soil Mechanics and Foundations Division*, ASCE, 93(SM3): 83–108.

Seed, H. B., Martin, G. R., and Pyke, R. M. 1978. "Effects of multidirectional shaking on pore pressure development in sands". *Journal of Geotechnical Engineering Division*, ASCE, 104(1), 27–44.

Seed, H.B. 1979. "Soil liquefaction and cyclic mobility evaluation for level ground during earthquakes", *Journal of the Geotechnical Engineering Division*, ASCE, 105(GT2): 201–255.

Sharp, M.K., Dobry, R. and Phillips, R., 2010. "CPT-Based Evaluation of Liquefaction and Lateral Spreading in Centrifuge", *Journal of Geotechnical and Geoenvironmental Engineering*, 136(10), 1334-1346.

Shenthan, T. ,2001. "Factors affecting liquefaction mitigation in silty soils using stone columns", *M.S. Thesis*, State University of New York at Buffalo, NY.

Shibata, T. and Teparaska, W., 1988. "Evaluation of liquefaction potentials of soils using cone penetration tests", *Soils and Foundations*, 28(2), 49-60.

Singh, S., 1996. "Liquefaction Characteristics of Silts", *Geotechnical and Geological Engineering*, 14,1-19.

Stamatopoulos, C.A., 2010. "An experimental study of the liquefaction strength of silty sand in terms of state parameter", *Soil Dynamics and Earthquake Engineering*, 30, 662-678.

Stark, T. D., and Olson, S. M., 1995. "Liquefaction resistance using CPT and field case histories.'' *Journal of Geotechnical Engineering*, 121(12), 856–869.

Stokoe, K. H., II, Lee, S. H. H., and Knox, D. P. ,1985. "Shear moduli measurements under true triaxial stresses", *Advances in the art of testing under cyclic conditions*, ASCE, New York, 166–185.

Susila, E., Hryciw, R.D., 2003. "Large displacement FEM modelling of the cone penetration test (CPT) in normally consolidated sand", *Int. J. Numer. Anal. Meth. Geomech.*, 27,585 – 602.

Sykora, D. W. ,1987. "Creation of a data base of seismic shear wave velocities for correlation analysis", *Geotech. Lab. Miscellaneous Paper GL-87-26, U.S. Army Engineer Waterways Experiment Station*, Vicksburg, Miss.

Tan, N.K., 2005. "Pressuremeter and cone penetrometer testingin a calibration chamber with unsaturated minco silt", *Ph.D dissertation*, the University of Oklahoma, Norman, OK,USA

Timoshenko, S., and Woinowsky-Krieger., 1959. "Theory of plates and shells", Mcgraw-Hill Book Company, ISBN-0-07-064779-8.

Teh, C. I. and Houlsby, G. T., 1991, "An Analytical Study of the Cone Penetration Test in Clay", *Geotechnique*, 41(1), 17–34.

Thevanayagam, S., 1998. "Effects of fines and confining stress on undrained shear strength of silty

sands", *Journal of Geotechnical and Geoenvironmetal Engineering*, 124(6), 479-491.

Thevanayagam, S. and Martin, G. R. 2002. "Liquefaction in silty soils – screening and remediation issues ", *Soil Dynamics and Earthquake Engineering*, Vol. 22, 1035-1042.

Thevanayagam, S., Shenthan, T., Mohan, S., and Liang, J., 2002. "Undrained fragility of clean sands, silty sands and sandy silts", *Journal of Geotechnical and Geoenvironmental Engineering*, 128(10),849-859.

Thevanayagam, S., Shenthan, T., and Kanagalingam, T., 2003. "Role of intergranular contacts on mechanisms causing liquefaction and slope Failures in silty sands", *Research Report No. 240.6 T338r 2003*, U.S. Geological Survey, Department of Interior, https://igsrglib03.er.usgs.gov/ipac20/ipac.jsp?session=1248XI66G5396.4212&menu=search&aspect=subtab13&npp=15&ipp=20&spp=20&profile=r&ri=&term=thevanayagam&index=.AW&aspect=subtab13&term=&index=JTK&term=&index=.SW&term=&index=.TW&term=&index=.GW&x=15&y=12#focus.

Thevanayagam, S., 2007a. "Intergrain contact density indices for granular mixes-I: framework", *Earthquake Engineering & Engineering Vibration*, 6(2), 123-134.

Thevanayagam, S., 2007b. "Intergrain contact density indices for granualar mixes-II: liquefaction resistance", *Earthquake Engineering & Engineering Vibration*, 6(2), 135-146.

Thevanayagam, S., Ecemis, N., 2008. "Effects of permeability on liquefaction resistance and cone Resistance", Geotechnical Earthquake Engineering and Soil Dynamics IV,1-11.

Thevanayagam, S., Kanagalingam, T., Reinhorn, A., Tharmendhira, R., Dobry, R., Pitman, M., Abdoun, T., Elgamal, A., Zeghal, M., Ecemis, N., and El Shamy, U., 2009. "Laminar Box System for 1-g Physical Modeling of Liquefaction and Lateral Spreading", *ASTM*, 32(5), 1-12.

Tolooiyan, A., and Gavin, K., 2011. "Modelling the cone penetration test in sand using cavity expansion and arbitrary lagrangian eulerian finite element methods", *Computers and Geotechnics*, 38(4), 482-490.

Troncoso, J. H., and Verdugo, R. ,1985. "Silt content and dynamic behavior of tailing sands", *Proc., XI Int. Conf. on Soil Mechanics and Foundation Engineering*, 1311–1314.

Tumay, M.T., Acar, Y.B., Cekirge, M., and Ramesh, N., 1985. "Flow field around cones in steady penetration", *Journal of the Geotechnical engineering*, 111, 193-204

Van den Berg, V. ,1994. "Analysis of soil penetration", *Ph.D. dissertation*, Delft University, Delft, The Netherlands.

Verdugo, R., and Ishihara, K., 1996. "The steady state of sandy soils", *Soils and Foundations* ,36(2), 81–91.

Voyiadjis G.Z., and Abu-Farsakh Y.M., 1997. "Coupled theory of mixtures for clayey soils", *Computers and Geotechnics*, 20(3 – 4), 195 – 222.

Xenaki, V.C., and Athanasopoulos, G.A., 2003. "Liquefaction resistance of sand-silt mixture: an experimental investigation of the effect of fines", *Soil Dynamic and Earthquake Engineering*, 23,183-194.

Wei, L., 2004. " Numerical simulation and field verification of inclined piezocone penetration test in cohesive soils", *Ph.D dissertation*, Louisiana State University, Baton Rouge , LA, USA.

Yang S.L., Sandven, R., and Grande, L., 2006."Steady-state lines of sand-silt mixture", *Canadian Geotechnical Journal*, 43, 1213-1219.

Yi, J.T., Goh, S.H., LEE, F.H., and Randolph, M.F., 2012. "A numerical study of cone penetration in fine-grained soils allowing for consolidation effects ", *Geotechnique*, 62(8), 707-719.

Youd, T.L., and Idriss, I.,M., 2001. "Liquefaction resistance of soils: summary report from 1996 NCEER and 1998 NCEER/NSF workshops on evaluation of liquefaction resistance of soils", *Journal of Geotechnical and Geoenvironmental Engineering*, 127(4), 297-313.

Yu, H. S., Herrmann, L. R. & Boulanger, R. W. (2000). "Analysis of steady cone penetration in clay", *Journal of Geotechnical and Geoenvironmental Engineering*, 126(7), 594–605.

Zeghal M. and A-W. M. Elgamal, 1994. "Analysis of Wildlife Site Using Earthquake Records", *Journal of Geotechnical Engineering*, ASCE. 120(6), pp. 996-1017.

Appendix A CPT simulation using FLAC

This appendix presents a preliminary study of CPT simulation using FLAC. Mohr-Coulomb model is used as the constitutive model. All the parameters are adopted from Ecemis (2008). Only three soils are used in the preliminary study.

Table A. 1 Soil parameters used in the FLAC (After Ecemis, 2008)

Soil type	Void Ratio	Equivalent inter-granular Void Ratio	Relative Density	Equivalent inter-granular relative density	Permeability.	Elastic Modulus	Poisson Ratio	Friction Angle	Dilation angle
	e	$(e_c)_{eq}$	D_r	$(D_{rc})_{eq}$	k	E	υ	ϕ	ψ
			(%)	(%)	m/s	(kPa)		(Deg.)	(Deg.)
M31	0.580	0.780	53	10	2.97E-06	29107	0.2	29	2
M47	0.403	0.727	83	38	8.10E-07	18791	0.2	34	8
M08	0.684	0.684	98	98	1.06E-05	68100	0.2	36	35

A.1 Undrained triaxial test simulation

The dimension of the numerical model is 1 m in diameter and 1 m in height and a velocity of $1x10^{-6}$ m/step is applied at the top of the model. The comparisons of simulation using FLAC and experiment are shown in Fig.A. 1 through Fig.A. 3. It is noticed that the excessive plastic dilation is encountered in the simulation for dilative soil.

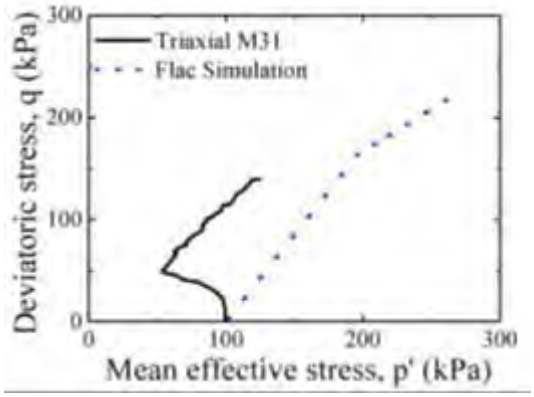

(a) q-p' plot

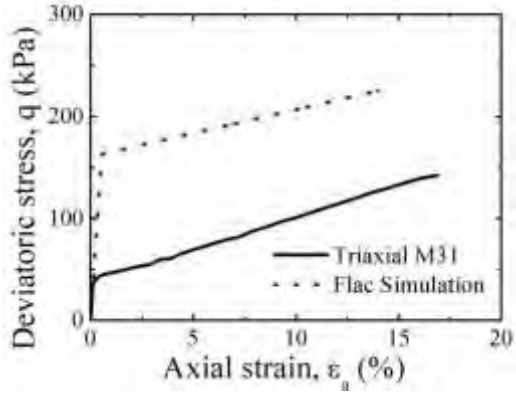

(b) q-ε_a plot

Fig.A. 1 Simulation of M31 using FLAC

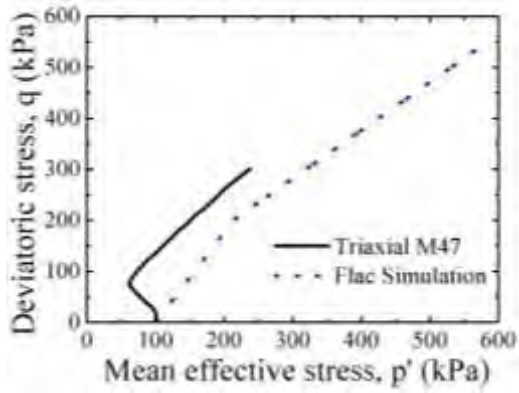

(a) q-p' plot

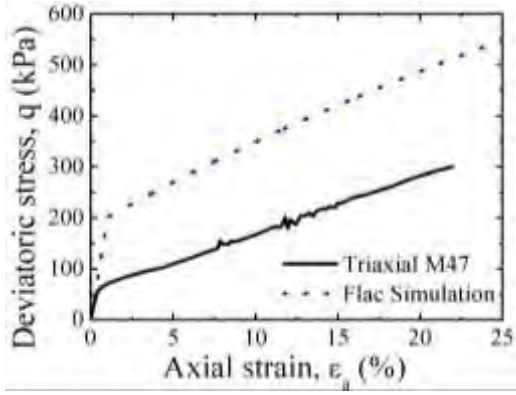

(b) q-ε_a plot

Fig.A. 2 Simulation of M47 using FLAC

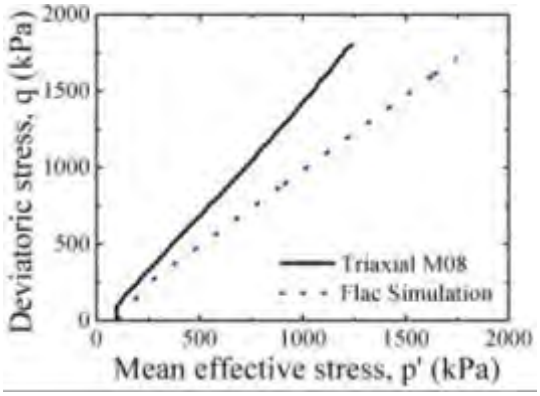

(a) q-p' plot

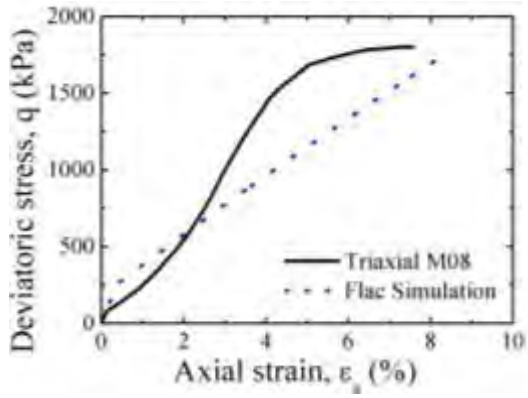

(b) q-ε_a plot

Fig.A. 3 Simulation of M08 using FLAC

A.2 One dimensional consolidation simulation

Fig.A. 4 (a) shows the model setup of one dimensional consolidation simulation using FLAC.

A cylindrical soil column with 0.05 m in radius and 1 m in height is used to perform the one dimensional consolidation simulation with one way drainage at top. The instant load charge is 100 kPa. Fig.A. 4 (b) compares the numerical results at different permeabilities with Terzaghi solution. Well agreement is achieved between numerical simulation and analytical solution at all permeabilities.

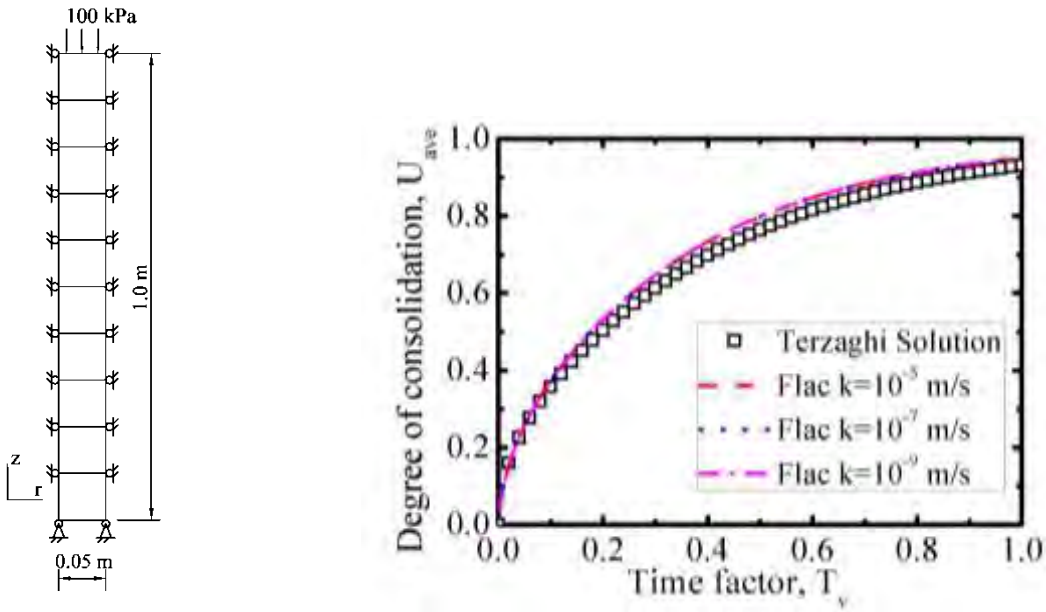

(a) Model (b) Comparison between numerical and analytical solutions

Fig.A. 4 Simulation of one dimensional consolidation using FLAC

A.3 CPT simulation

Two steps comprise the simulation, the geostatic step and the 'penetration' step.

In the geostatic step, the gradient of vertical stress of soil is considered, which limits the constitutive models to elastic and Mohr-Coulomb material.

In the penetration step, there was problem when we tried to model the interface between soil and cone and drove the cone into the soil medium at a designated penetration rate. As a result, an alternative was made to simulate the penetration process with the absence of the interface between

the cone and the soil. We applied the designated vertical penetration rate to soil nodes along the cone path. It shall be noticed that the horizontal displacement of soil around the cone tip due to penetration is ignored in this simulation.

A.3.1 Model setup

Fig.A. 5 shows the numerical model setup and boundary conditions using FLAC. An axisymmetric model to simulate the CPT. Since the cone is not modelled, the dimension of the soil medium is 0.8 m in radius and 1.8 m in height, the same as the model used in Abaqus. A cavity of R_h=0.013 cm around the symmetric axis is introduced. The 'cone' diameter is 4.37 cm.

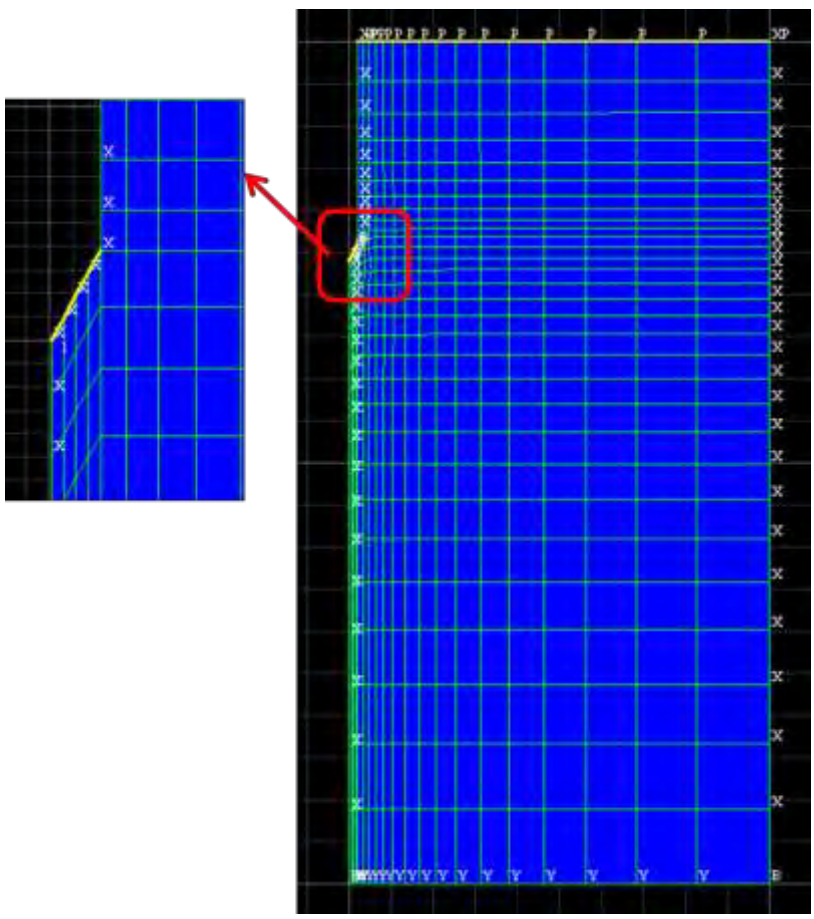

Fig.A. 5 Model setup and boundary conditions in FLAC

For the displacement field of soil medium, the displacement in z direction is constrained at

bottom end and only displacement in r direction at left and right end is restrained in geostatic and penetration step. For the flow fluid field/pore pressure of soil medium, all of boundaries are considered as undrained except the top side boundary.

A.3.2 Results

The designated penetration rate applied on the soil nodes along the cone tip path is 2 cm/s, which is the ASTM standard penetration rate. The penetration is stopped after 1 second. The parametric study of q_{c1N} and $\Delta u/\sigma_{vo}'$ for $(D_{rc})_{eq}$ =10% and 98 % are presented in Fig.A. 6 and Fig.A. 7. For both $(D_{rc})_{eq}$=10 and 98%, the q_{c1N} firstly increases as k increases from 10^{-9} to 10^{-6} m/s. However, it decreases as further increase of k. The considerable negative $\Delta u/\sigma_{vo}'$ at tip is observed for $(D_{rc})_{eq}$=10% at low permeability (e.g. $k<10^{-7}$ m/s), which contracts with field observation. It is may be attributive to excessive amount of plastic dilation at yielding due to the normality rule used.

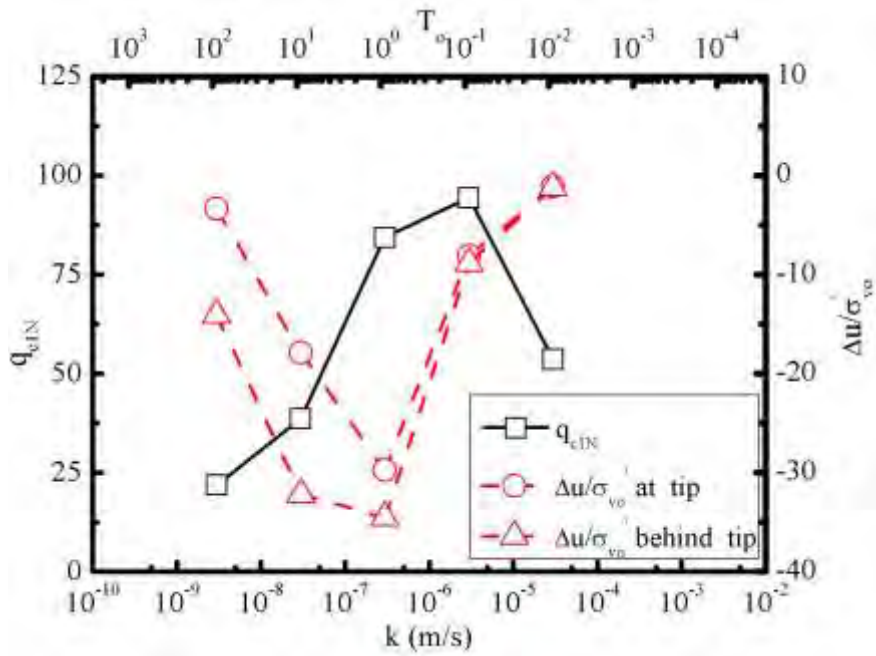

Fig.A. 6 q_{c1N} and $\Delta u/\sigma_{vo}'$ at different permeabilities of soil at $(D_{rc})_{eq}$=10% using FLAC

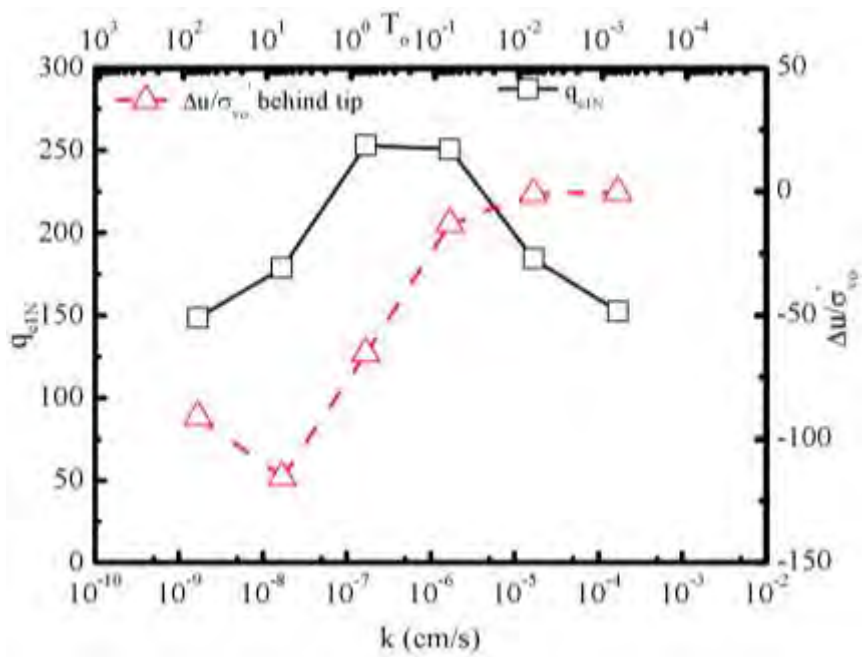

Fig.A. 7 q_{c1N} and $\Delta u/\sigma_{vo}'$ at different permeabilities of soil at $(D_{rc})_{eq}$=98% using FLAC

A.4 Recommended Further study

Similar stress-balance technique used in the first step of Abaqus could possibly solve the

problem that FLAC does not support materials other than elastic and Mohr-Coulomb material. This method assumes that the vertical effective stress in the soil medium is 100 kPa everywhere since the main interest is the development of stress and excess pore pressure of soil around the cone tip area and the gradient of vertical stress of soil is of secondary consideration. Other constitutive models may be able to be implemented into the CPT simulation after the stress-balance issue is solved.

The horizontal displacement of soil around the cone tip shall be considered when under penetration. A more appropriate way of applying the motion on the soil nodes along the cone path needs to be developed.

Appendix B Parametric study of cap model and monotonic triaxial simulation using Abaqus

In this appendix, firstly a parametric study on key parameters of cap plasticity model is performed using $(D_{rc})_{eq}$=80% soil. And more monotonic undrained triaxial tests are simulated using Abaqus.

B.1 Parametric study

In this section, parameters of cap model affecting the stress path as well as stress-strain relationship are studied using undrained monotonic triaxial test M20 [equivalent relative density $(D_{rc})_{eq}$ =80%], to better understand the importance of each cap plasticity parameter.

B.1.1 Elastic modulus (E) study

Fig.B. 1 compares the experiment data with numerical results using various elastic moduli with other parameters remaining identical. It is found that larger elastic modulus leads soil to reaching steady state faster in terms of axial strain. It is also observed that the material has the elastic perfectly plastic behavior when $(K_b)(\varepsilon_{vol}{}^{pl}|_0)>p_f'$. The influence of Young's modulus only affect the rate of soil reaching steady state if $\varepsilon_{vol}{}^{pl}|_0=0$.

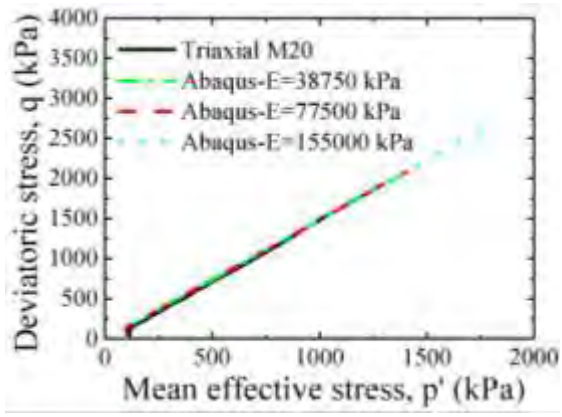

(a) p'-q plot

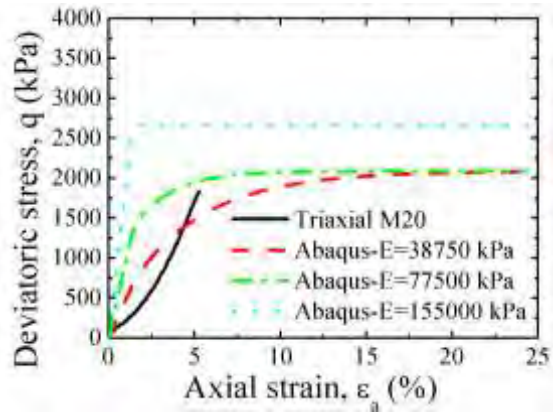

(b) q-ε_a plot

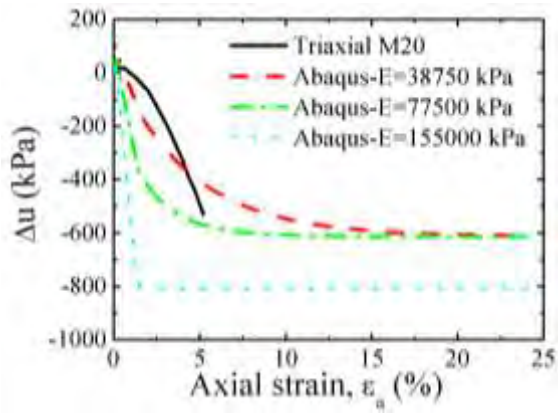

(c) Δu-ε_a plot

Fig.B. 1 Stress path and stress- and pore pressure-strain curve of M20 with E changing

B.1.2 Eccentricity parameter (R) study

The eccentricity parameter-R, determining the shape of strain-hardening yield surface, is studied by assigning various values, R=0.1,1 and 10, respectively. As can be shown in Fig.B. 2, the smaller the R value is, the more dilation the soil would exhibit.

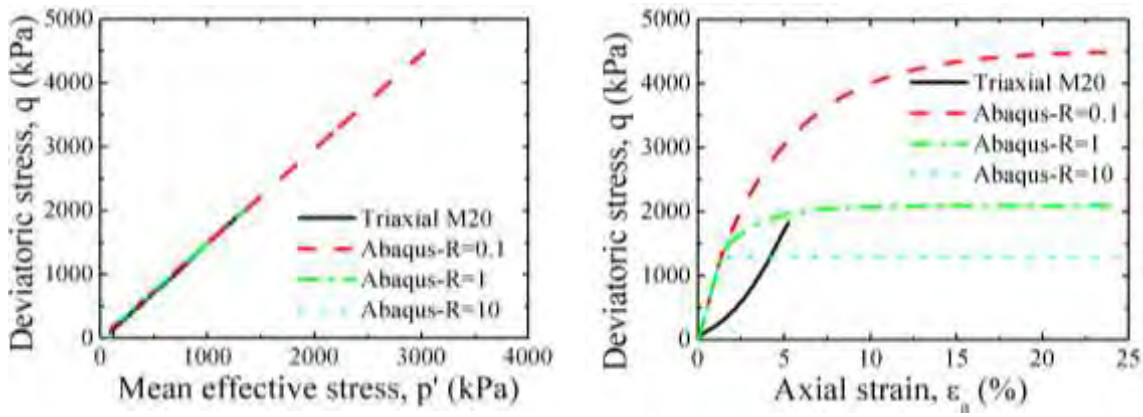

(a) p'-q plot (b) q-ε_a plot

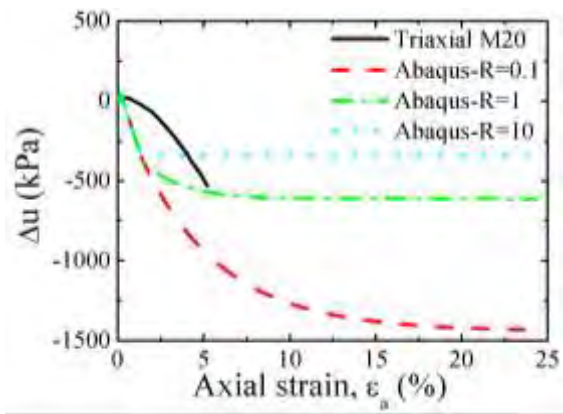

(c) Δu-ε_a plot

Fig.B. 2 Stress path and stress- and pore pressure-strain curve of M20 with R changing

B.1.3 Initial cap yield surface position ($\varepsilon_{vol}^{pl}|_0$) study

The initial cap yield surface defines the initial position of cap on the hardening curve and measures the initial consolidation position of the specimen. Three small values of $\varepsilon_{vol}^{pl}|_0$-0.00, 0.02 and 0.03 have been studied, and the results from Fig.B. 3 show that when $\varepsilon_{vol}^{pl}|_0$ is within [0, p_f'/K_b], it only affects the stress-strain response but not the stress path. However, larger value of $\varepsilon_{vol}^{pl}|_0$ (e.g. $\varepsilon_{vol}^{pl}|_0 > p_f'/K_b$) influences not only the stress-strain relationship but also the stress path.

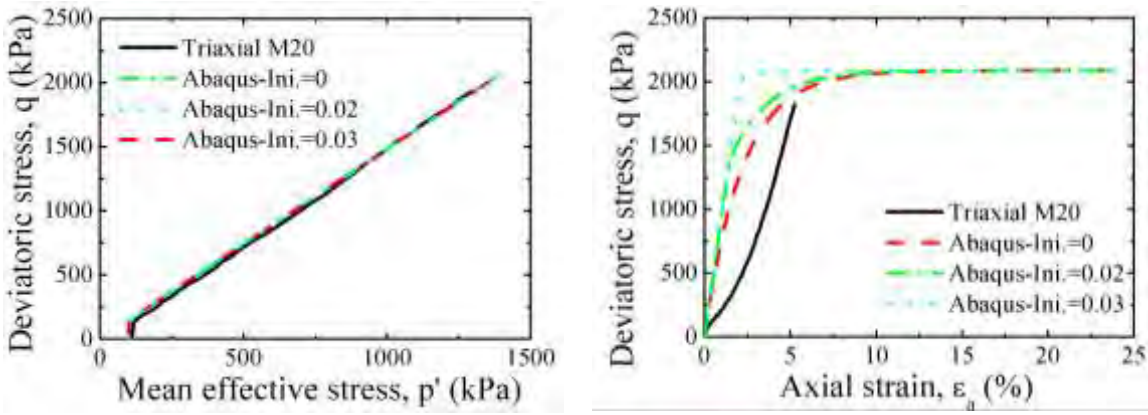

(a) p'-q plot (b) q-ε_a plot

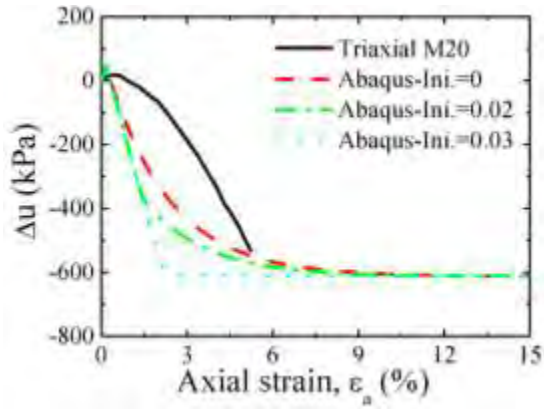

(c) Δu-ε_a plot

Fig.B. 3 Stress path and stress- and pore pressure-strain curve of M20 with $\varepsilon_{vol}{}^{pl}|_0$ changing

B.1.4 Transition parameter (α) study

Three different values of α are examined in this section, which are 0.0, 0.01 and 0.05, respectively. It is seen in Fig.B. 4 that the variation of α does not significantly affect the stress path as well as stress-strain relationship.

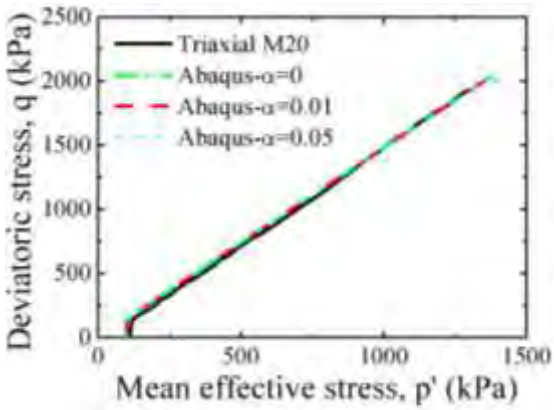

(a) p'-q plot

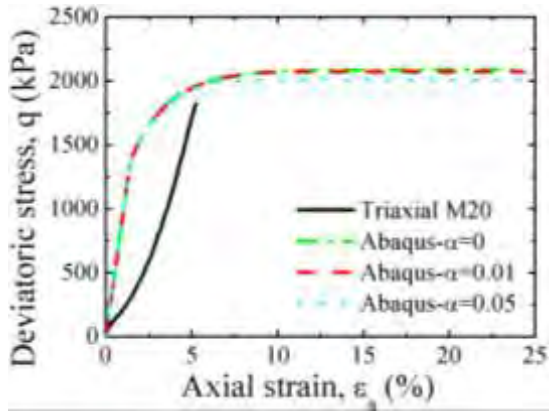

(b) q-ε_a plot

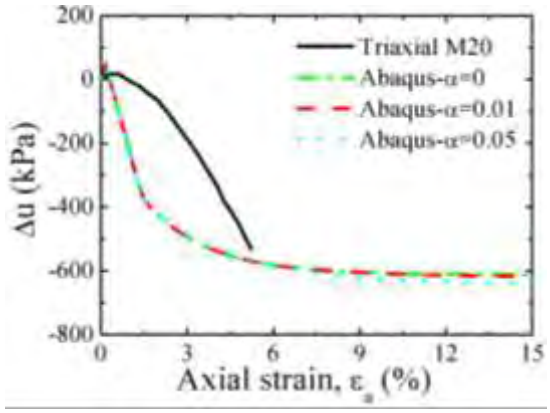

(c) Δu-ε_a plot

Fig.B. 4 Stress path and stress- and pore pressure-strain curve of M20 with α changing

B.2 Simulation of OS F55 sand-silt mix

In this section, more monotonic undrained triaxial tests reported by Thevanayagam et al. (2003) are employed to examine the effectiveness of the cap plasticity model.

B.2.1 C_F=0%

B.2.1.1 M08[$(D_{rc})_{eq}$=102%]

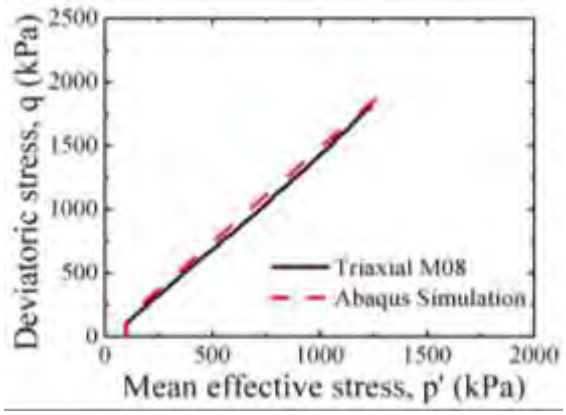

(a)q-p' plot

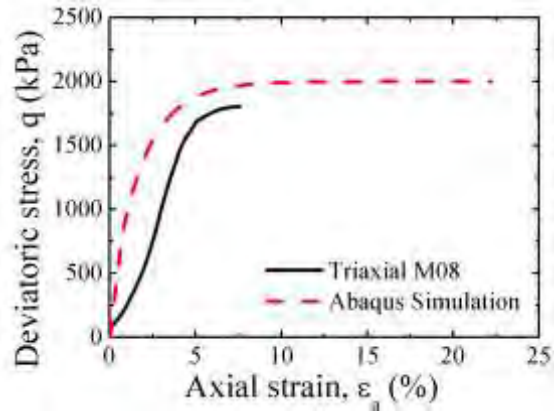

(b) q-ε_a plot

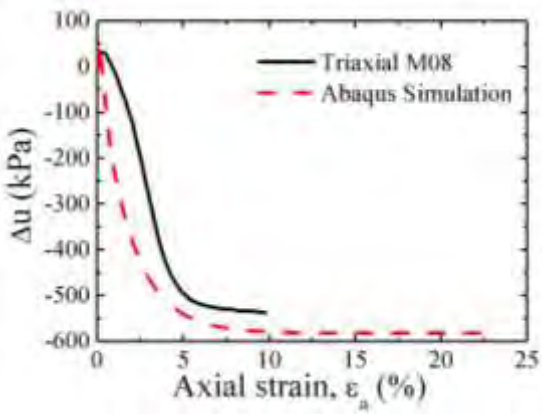

(c) Δu-ε_a plot

Fig.B. 5 Simulation of M08 [$(D_{rc})_{eq}$=102%]

B.2.1.2 M14[$(D_{rc})_{eq}$=99%]

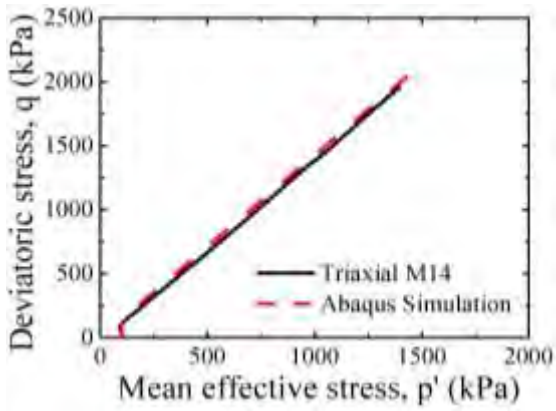

(a)q-p' plot

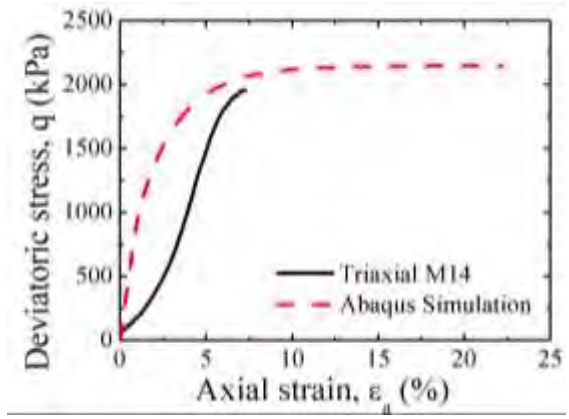

(b) q-ε_a plot

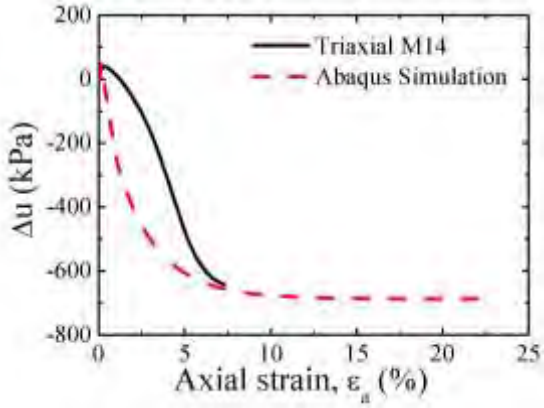

(c) Δu-ε_a plot

Fig.B. 6 Simulation of M14 [$(D_{rc})_{eq}$=99%]

B.2.1.3 M20[$(D_{rc})_{eq}$=80%]

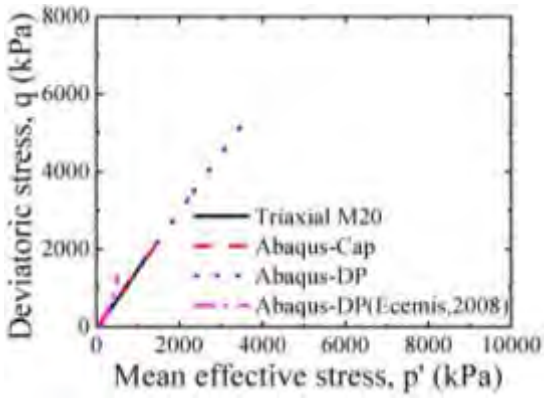

(a)q-p' plot

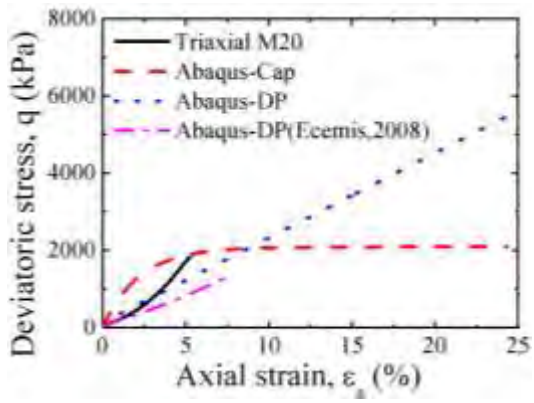

(b) q-ε_a plot

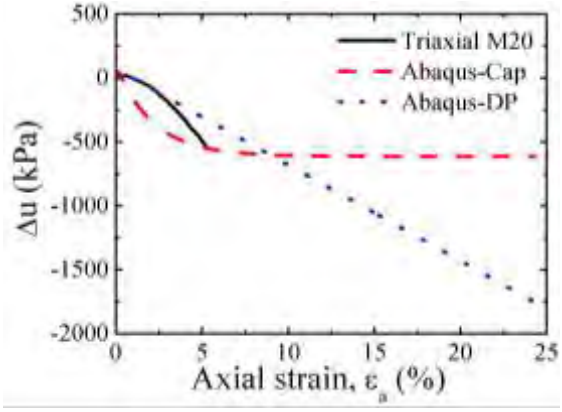

(c) Δu-ε_a plot

Fig.B. 7 Simulation of M20 [$(D_{rc})_{eq}$=80%]

B.2.1.4 M05[$(D_{rc})_{eq}$=79%]

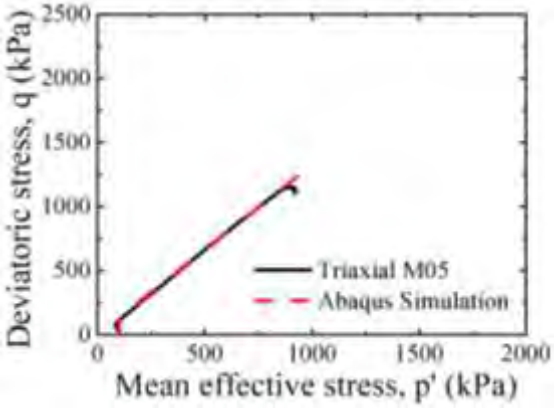

(a)q-p' plot

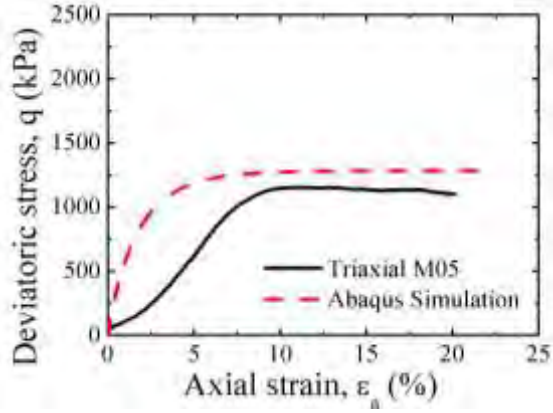

(b) q-ε_a plot

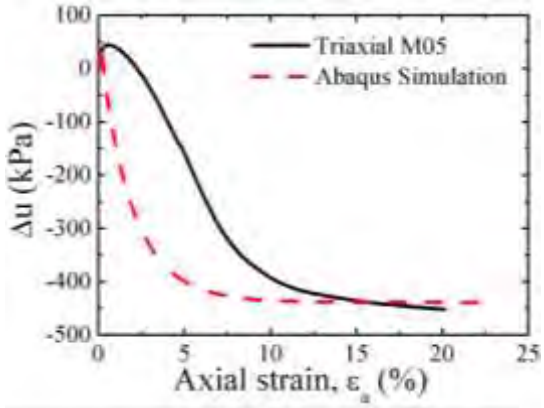

(c) Δu-ε_a plot

Fig.B. 8 Simulation of M05 [$(D_{rc})_{eq}$=79%]

B.2.1.5 M11[$(D_{rc})_{eq}$=70%]

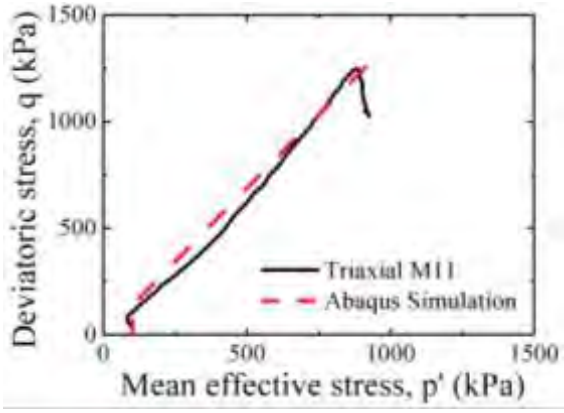

(a)q-p' plot

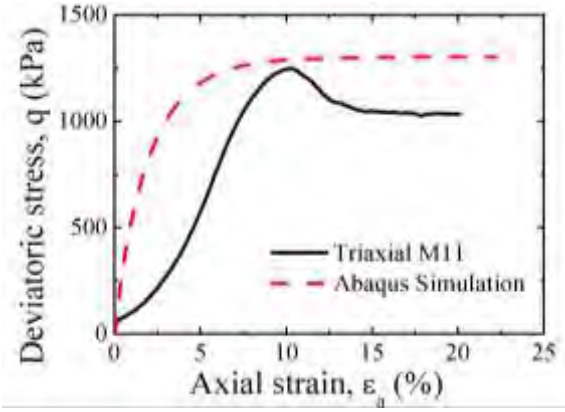

(b) q-ε_a plot

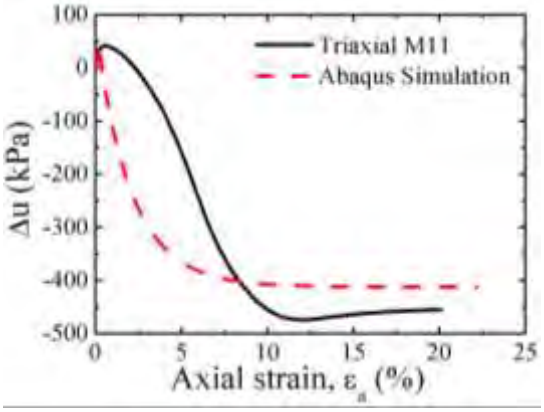

(c) Δu-ε_a plot

Fig.B. 9 Simulation of M11 [$(D_{rc})_{eq}$=70%]

B.2.1.6 M15[$(D_{rc})_{eq}$=67%]

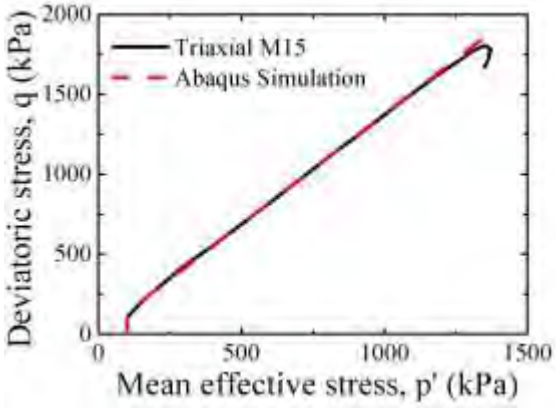

(a)q-p' plot

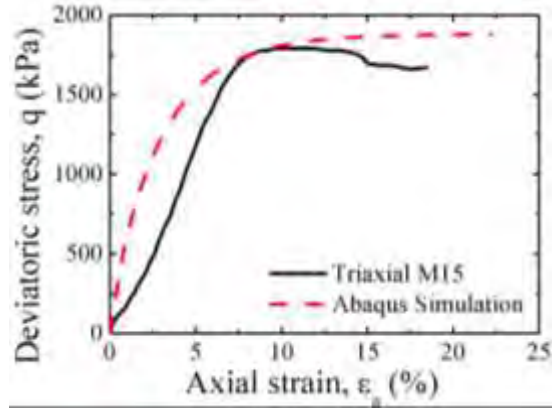

(b) q-ε_a plot

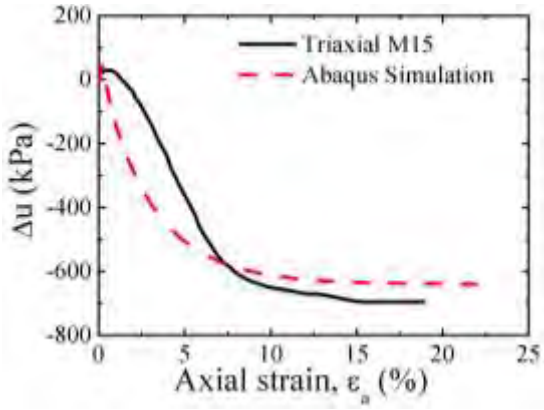

(c) Δu-ε_a plot

Fig.B. 10 Simulation of M15 [$(D_{rc})_{eq}$=67%]

B.2.1.7 M10[$(D_{rc})_{eq}$=65%]

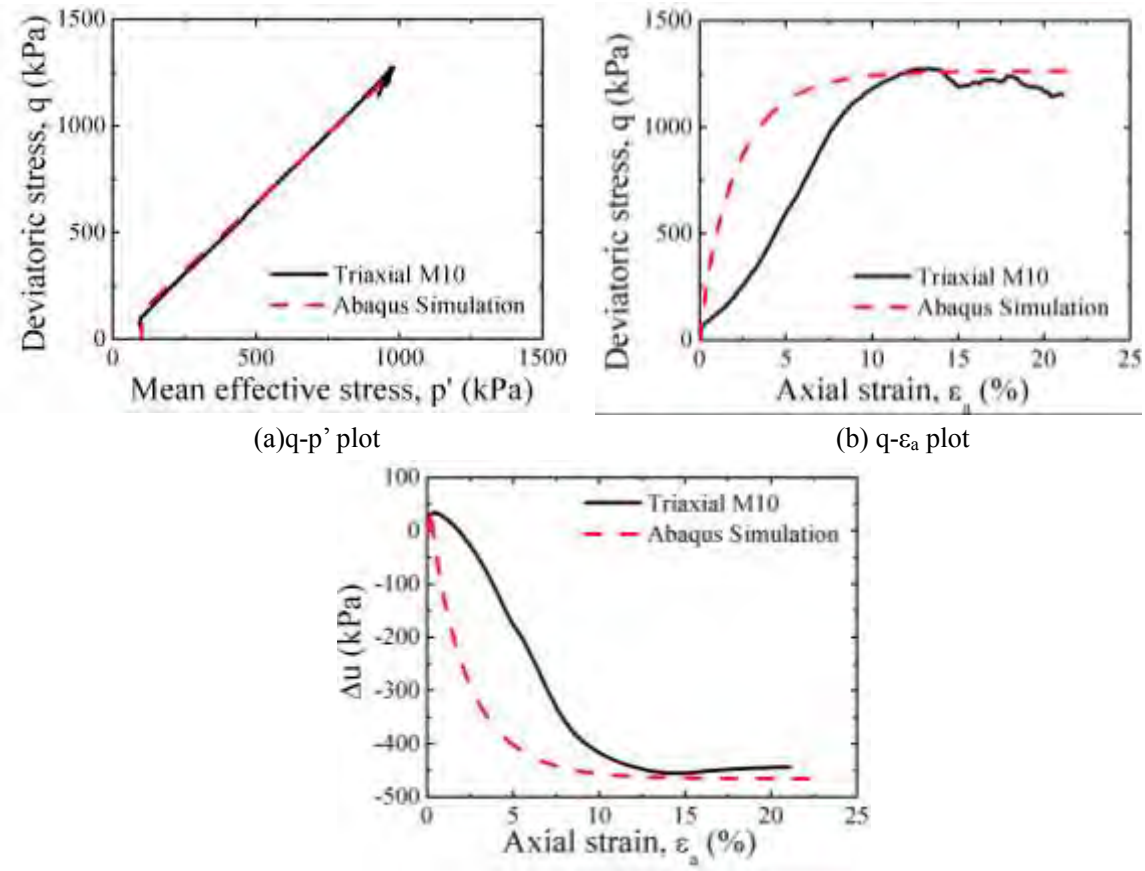

(a)q-p' plot (b) q-ε_a plot

(c) Δu-ε_a plot

Fig.B. 11 Simulation of M10 [$(D_{rc})_{eq}$=65%]

B.2.1.8 M01[$(D_{rc})_{eq}$=60%]

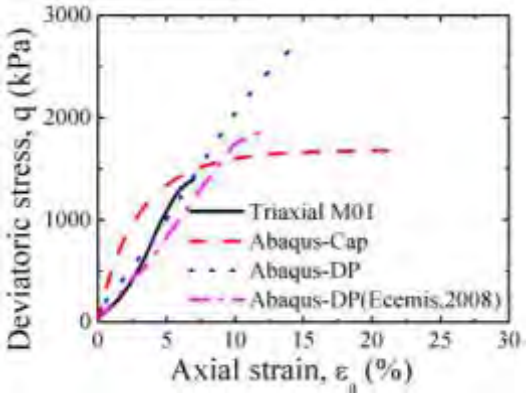

(a)q-p' plot

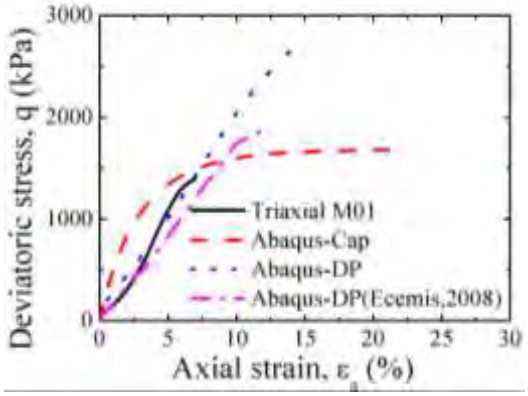

(b) q-ε_a plot

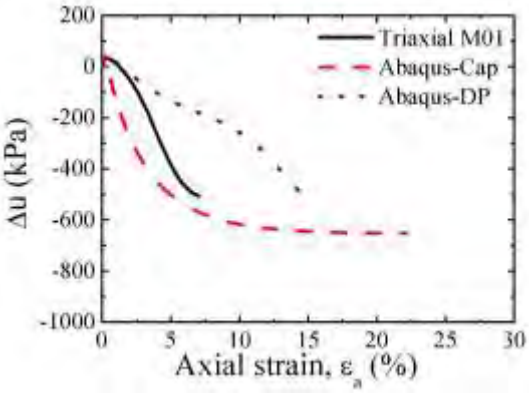

(c) Δu-ε_a plot

Fig.B. 12 Simulation of M01 [$(D_{rc})_{eq}$=60%]

B.2.1.9 M21[$(D_{rc})_{eq}$=41%]

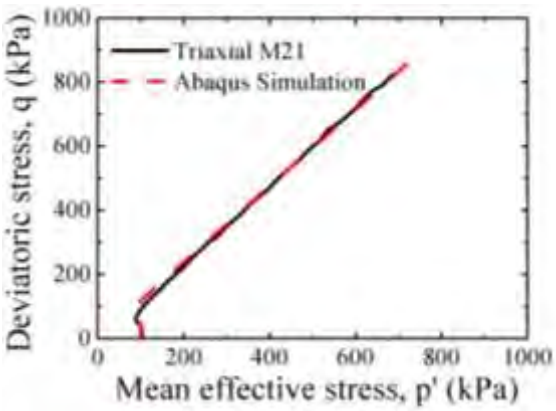

(a)q-p' plot

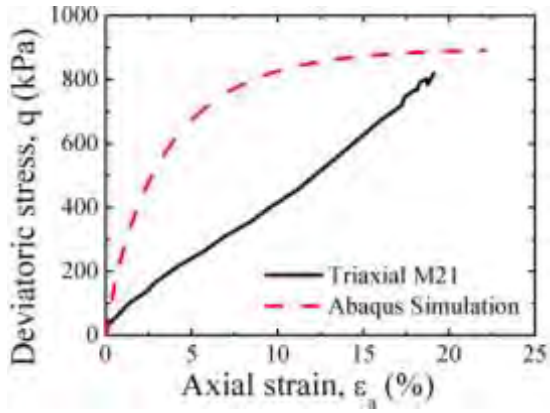

(b) q-ε_a plot

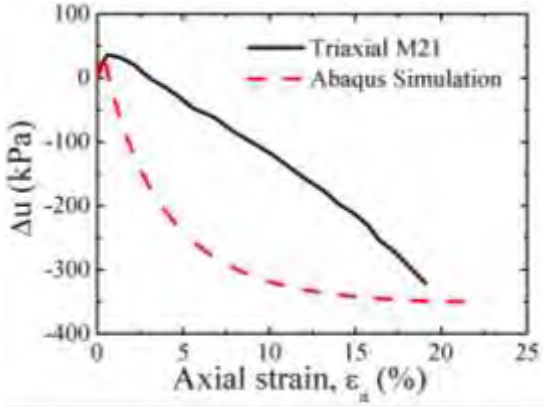

(c) Δu-ε_a plot

Fig.B. 13 Simulation of M21 [$(D_{rc})_{eq}$=41%]

B.2.1.10 M12[$(D_{rc})_{eq}$=41%]

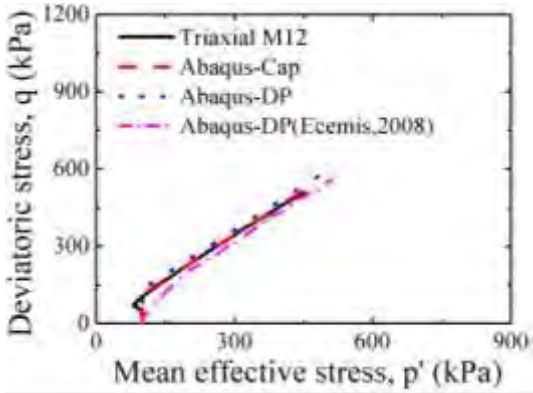

(a)q-p' plot

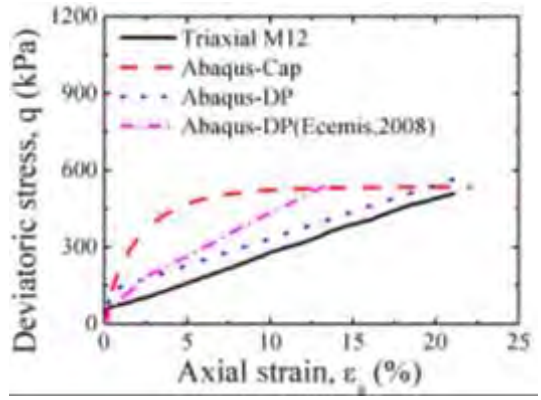

(b) q-ε_a plot

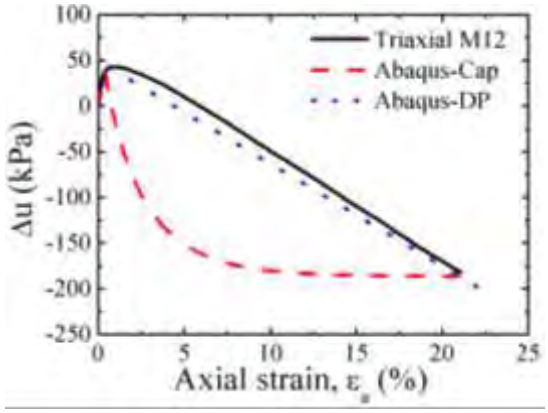

(c) Δu-ε_a plot

Fig.B. 14 Simulation of M12 [$(D_{rc})_{eq}$=41%]

B.2.1.11 M07[$(D_{rc})_{eq}$=27%]

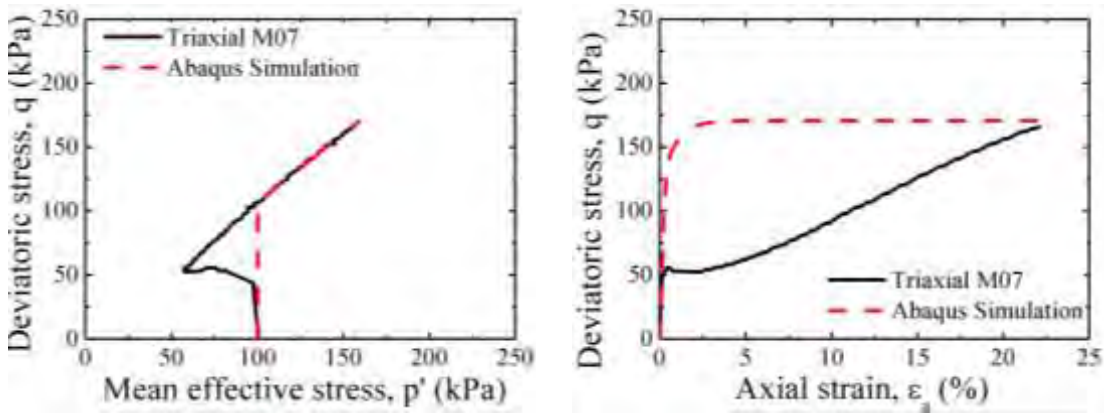

(a)q-p' plot (b) q-ε_a plot

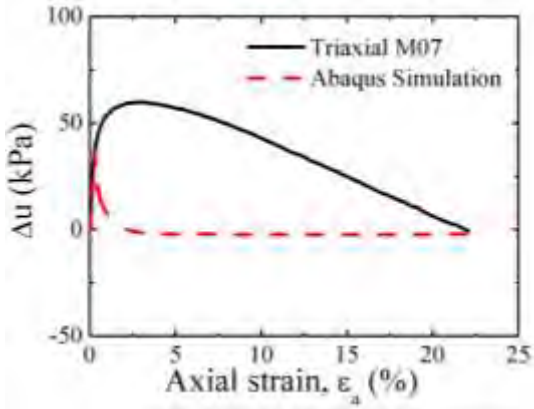

(c) Δu-ε_a plot

Fig.B. 15 Simulation of M07 [$(D_{rc})_{eq}$=27%]

B.2.1.12 M17[$(D_{rc})_{eq}$=26%]

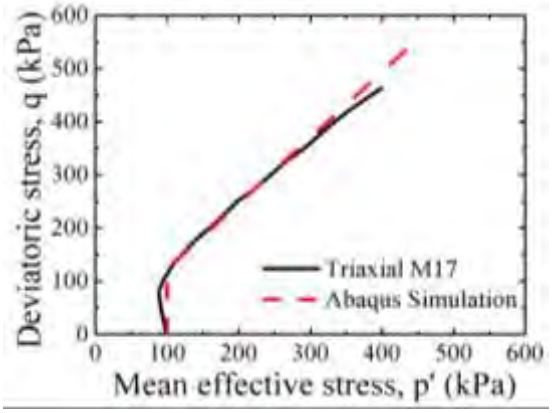

(a)q-p' plot

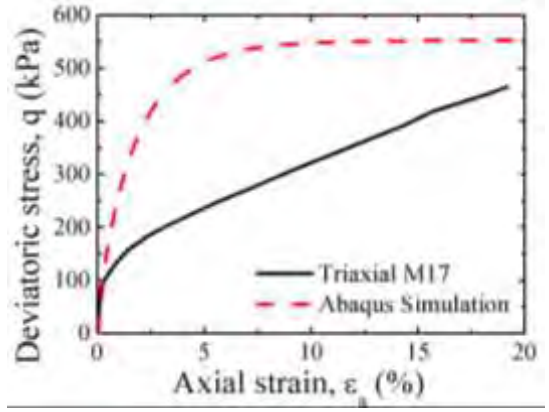

(b) q-ε_a plot

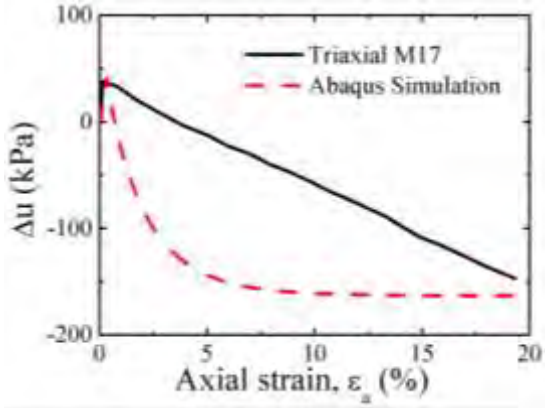

(c) Δu-ε_a plot

Fig.B. 16 Simulation of M17 [$(D_{rc})_{eq}$=26%]

B.2.1.13 M09[$(D_{rc})_{eq}$=17%]

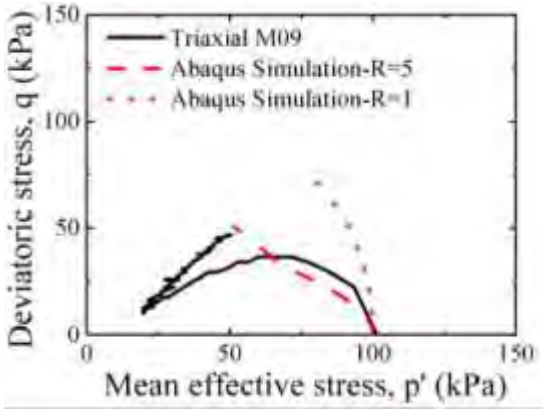

(a)q-p' plot

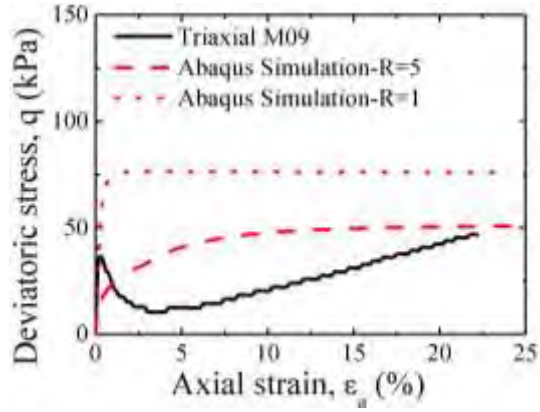

(b) q-ε_a plot

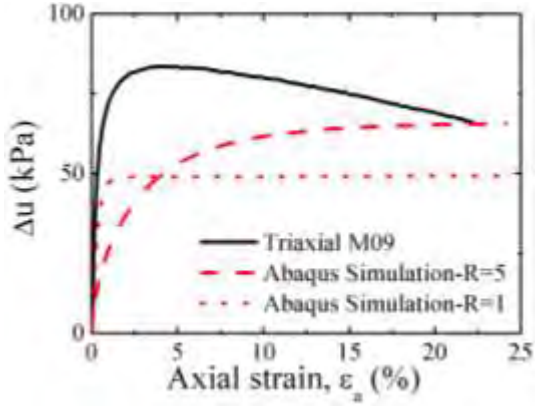

(c) Δu-ε_a plot

Fig.B. 17 Simulation of M09 [$(D_{rc})_{eq}$=17%]

B.2.2 C_F=7%

B.2.2.1 M28[$(D_{rc})_{eq}$=81%]

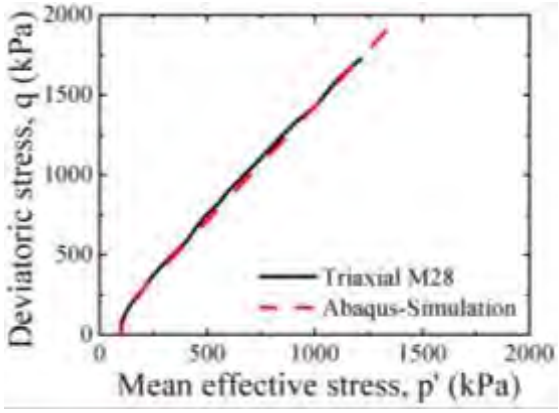

(a)q-p' plot

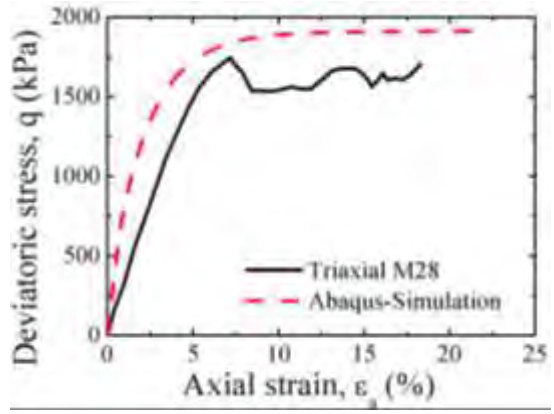

(b) q-ε_a plot

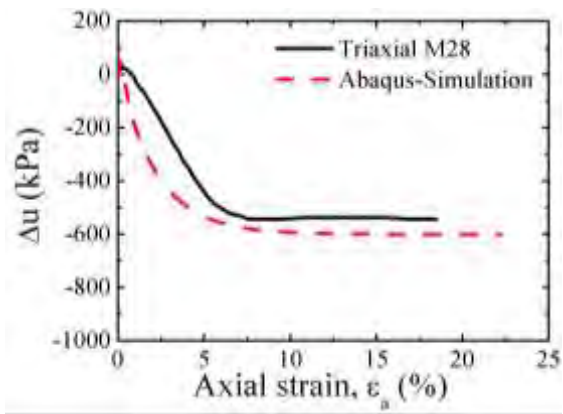

(c) Δu-ε_a plot

Fig.B. 18 Simulation of M28 [$(D_{rc})_{eq}$=81%]

B.2.2.2 M23[$(D_{rc})_{eq}$=60%]

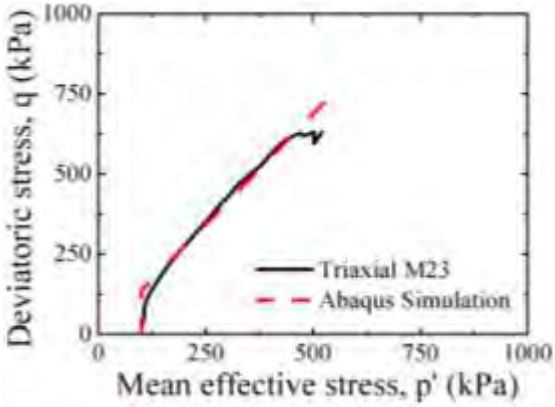

(a)q-p' plot

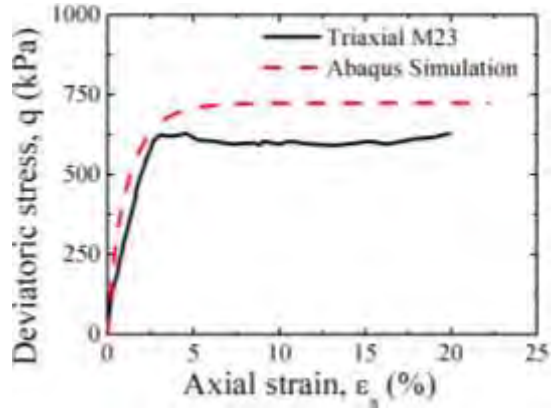

(b) q-ε_a plot

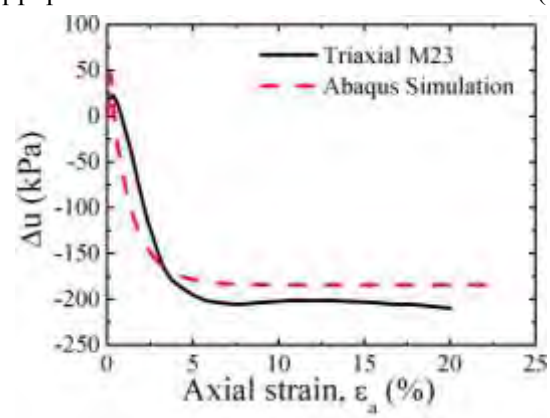

(c) Δu-ε_a plot

Fig.B. 19 Simulation of M23 [$(D_{rc})_{eq}$=60%]

B.2.2.3 M26[$(D_{rc})_{eq}$=40%]

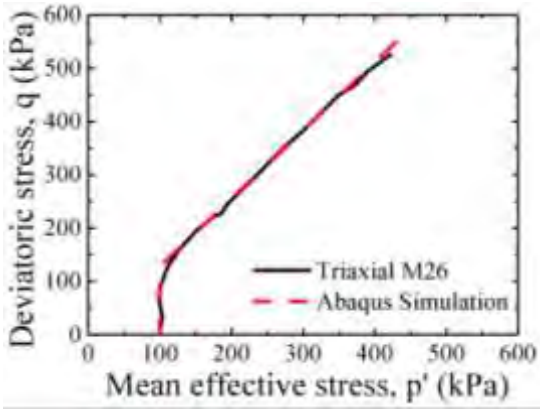

(a)q-p' plot

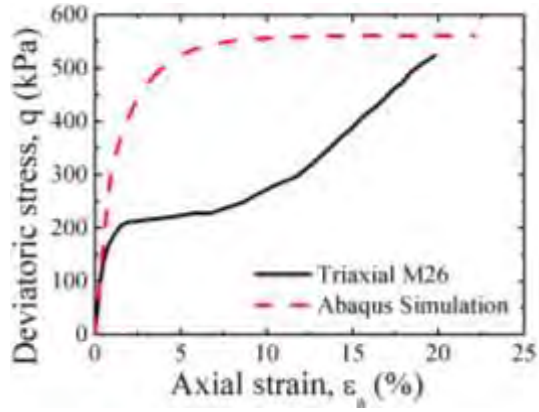

(b) q-ε_a plot

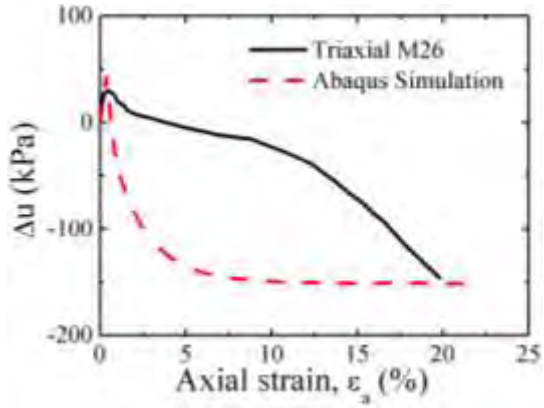

(c) Δu-ε_a plot

Fig.B. 20 Simulation of M26[$(D_{rc})_{eq}$=40%]

B.2.2.4 M22[$(D_{rc})_{eq}$=22%]

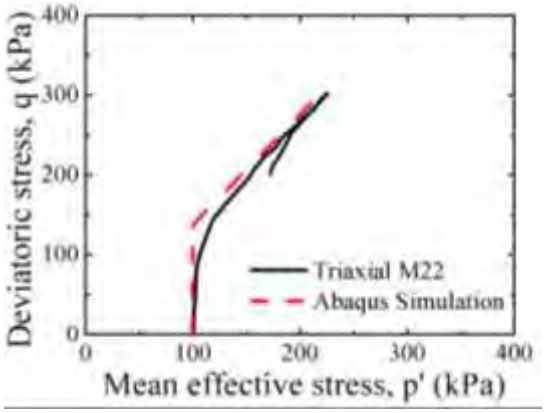

(a)q-p' plot

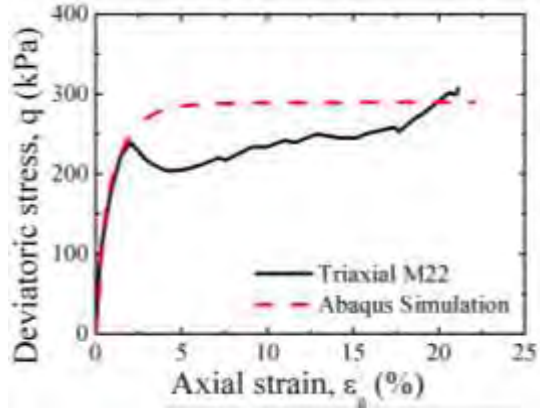

(b) q-ε_a plot

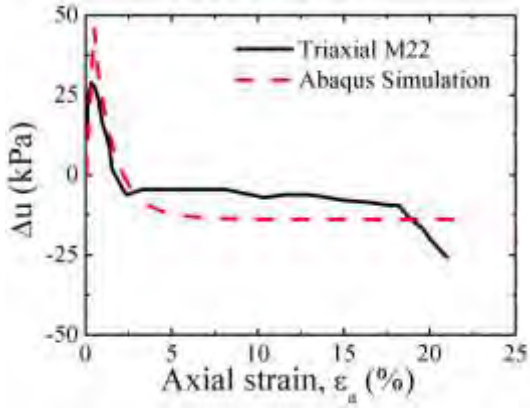

(c) Δu-ε_a plot

Fig.B. 21 Simulation of M22[$(D_{rc})_{eq}$=22%]

B.2.2.5 M24[$(D_{rc})_{eq}$=18%]

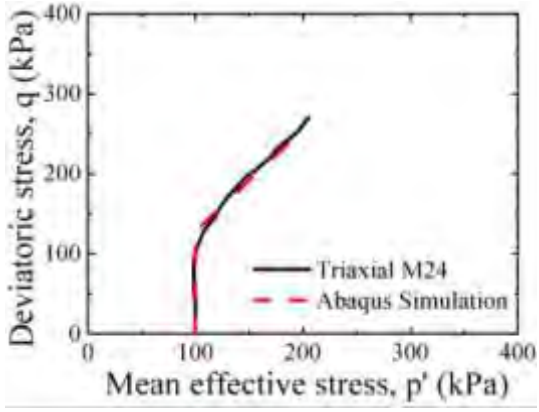

(a)q-p' plot

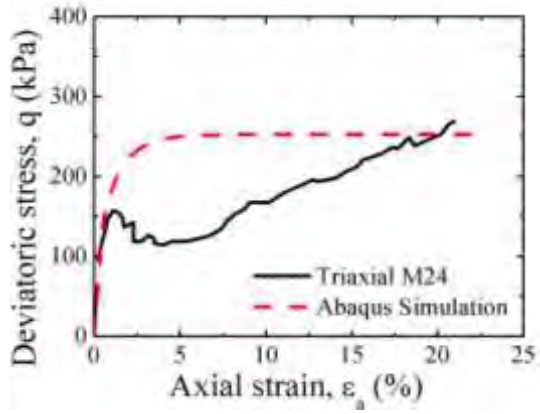

(b) q-ε_a plot

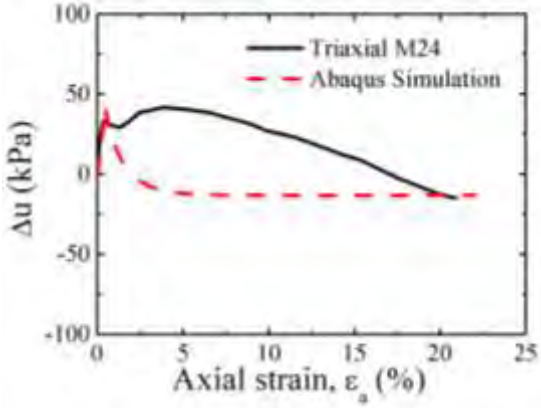

(c) Δu-ε_a plot

Fig.B. 22 Simulation of M24[$(D_{rc})_{eq}$=18%]

B.2.3 C_F=15%

B.2.3.1 M37[$(D_{rc})_{eq}$=102%]

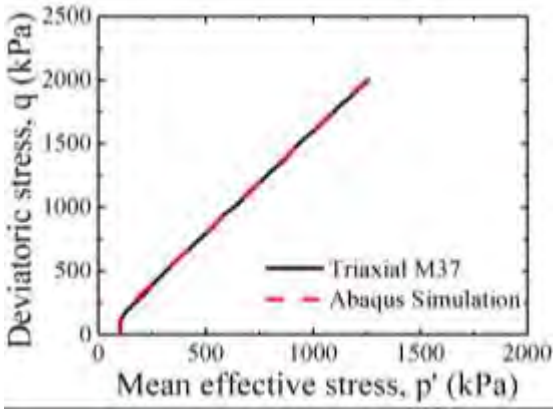

(a)q-p' plot

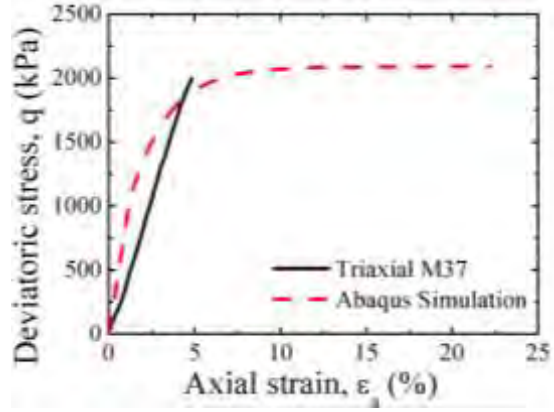

(b) q-ε_a plot

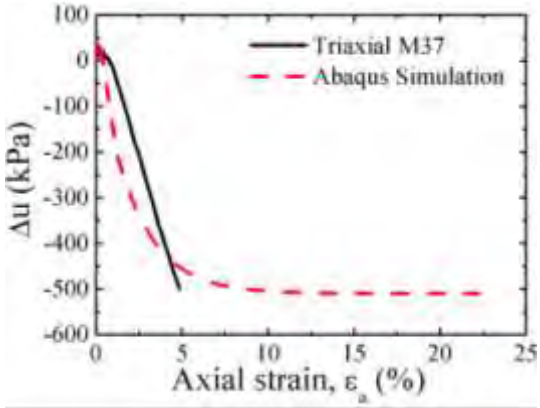

(c) Δu-ε_a plot

Fig.B. 23 Simulation of M37[$(D_{rc})_{eq}$=102%]

B.2.3.2 M36[$(D_{rc})_{eq}$=45%]

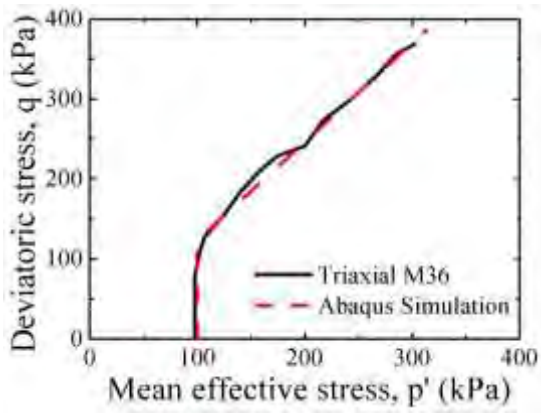

(a)q-p' plot

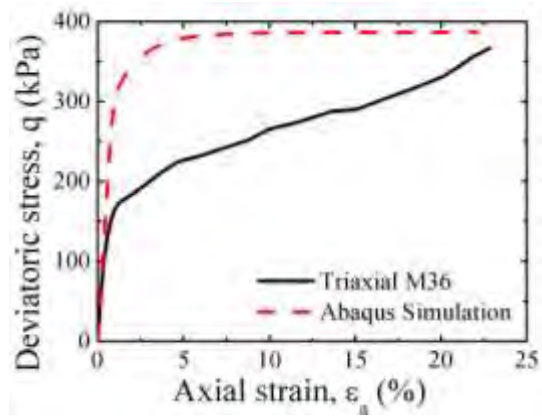

(b) q-ε_a plot

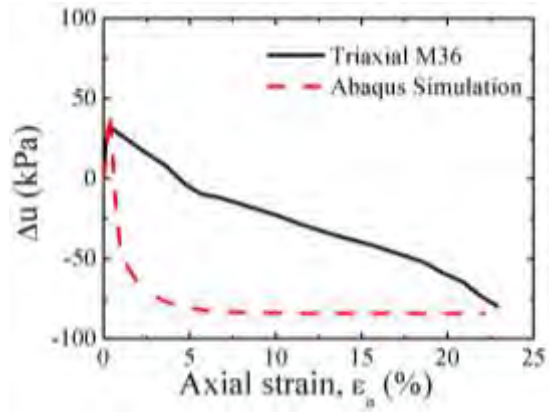

(c) Δu-ε_a plot

Fig.B. 24 Simulation of M36[$(D_{rc})_{eq}$=45%]

B.2.3.3 M32[$(D_{rc})_{eq}$=40%]

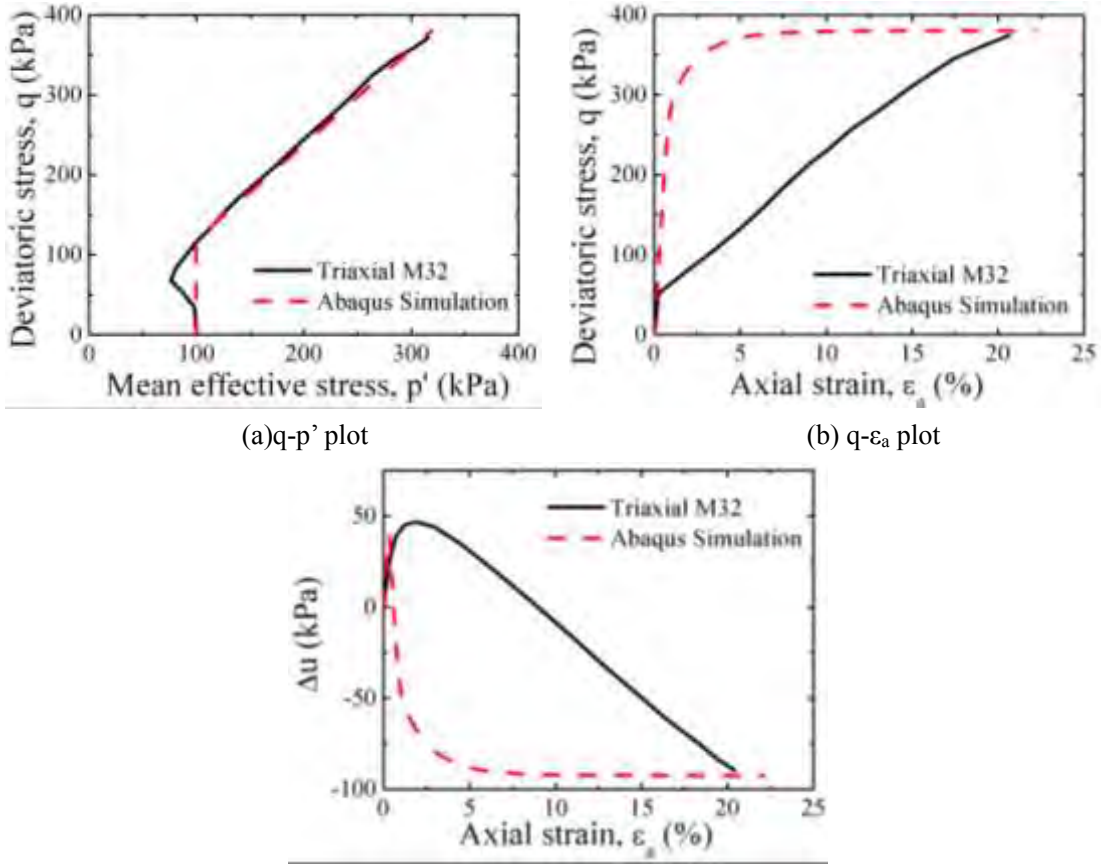

(a)q-p' plot (b) q-ε_a plot

(c) Δu-ε_a plot

Fig.B. 25 Simulation of M32[$(D_{rc})_{eq}$=40%]

B.2.3.4 M31[$(D_{rc})_{eq}$=10%]

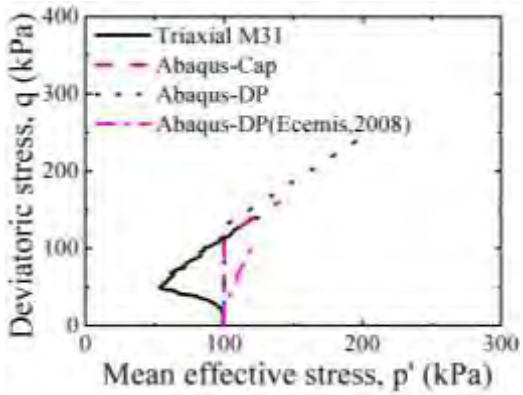

(a)q-p' plot

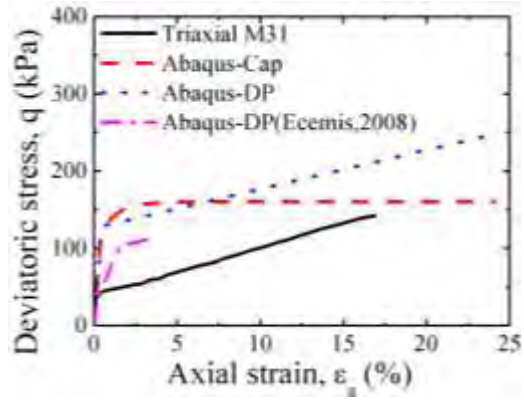

(b) q-ε_a plot

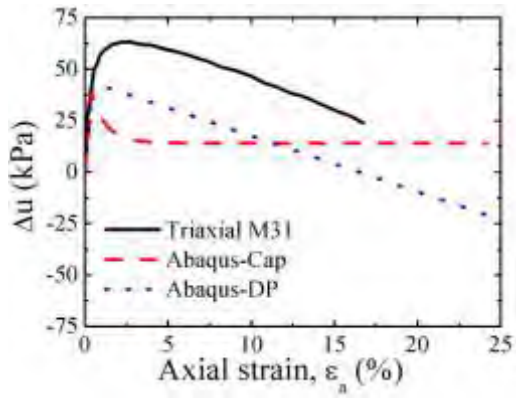

(c) Δu-ε_a plot

Fig.B. 26 Simulation of M31[$(D_{rc})_{eq}$=10%]

B.2.3.5 M34[$(D_{rc})_{eq}$=8%]

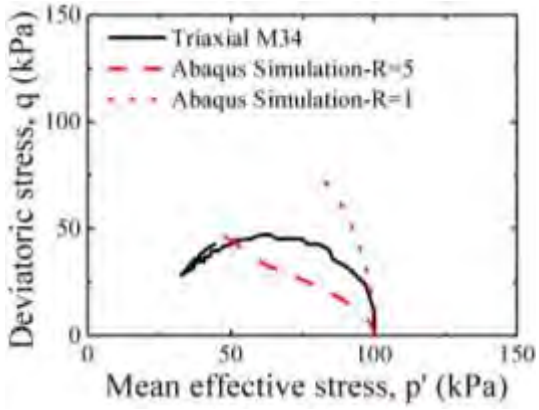

(a)q-p' plot

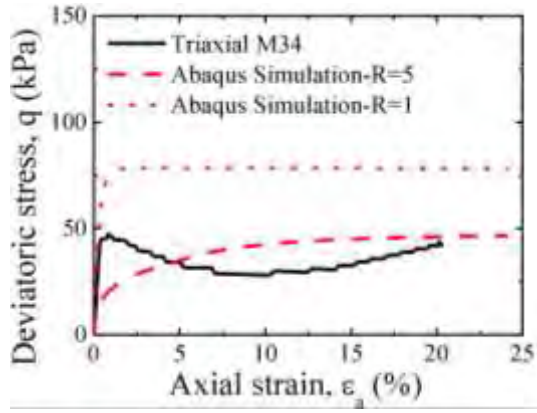

(b) q-ε_a plot

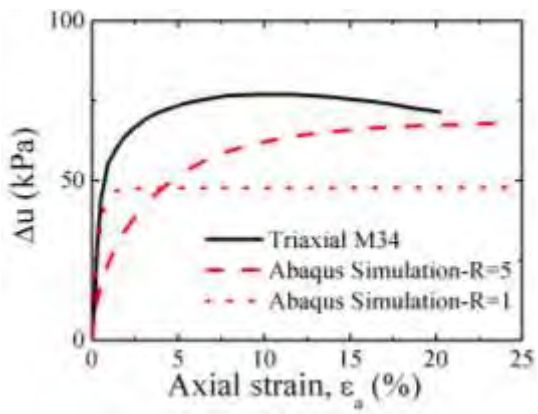

(c) Δu-ε_a plot

Fig.B. 27 Simulation of M34[$(D_{rc})_{eq}$=8%]

B.2.4 C_F=25%

B.2.4.1 M48[$(D_{rc})_{eq}$=66%]

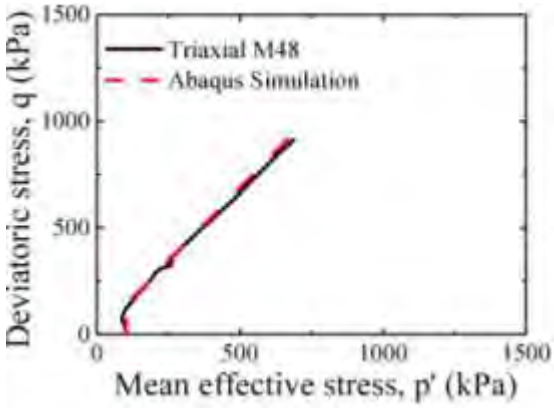

(a)q-p' plot

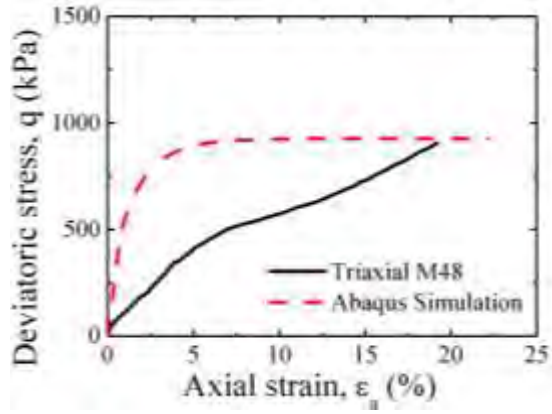

(b) q-ε_a plot

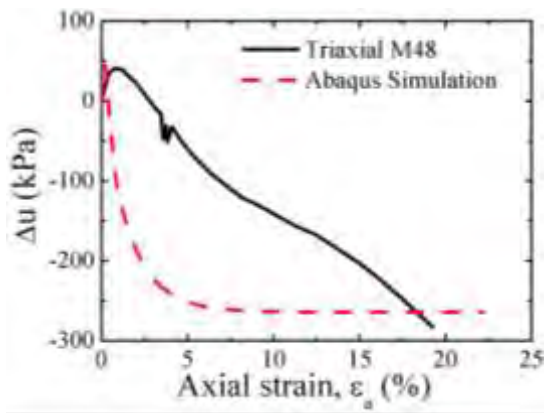

(c) Δu-ε_a plot

Fig.B. 28 Simulation of M48[$(D_{rc})_{eq}$=66%]

B.2.4.2 M47[$(D_{rc})_{eq}$=38%]

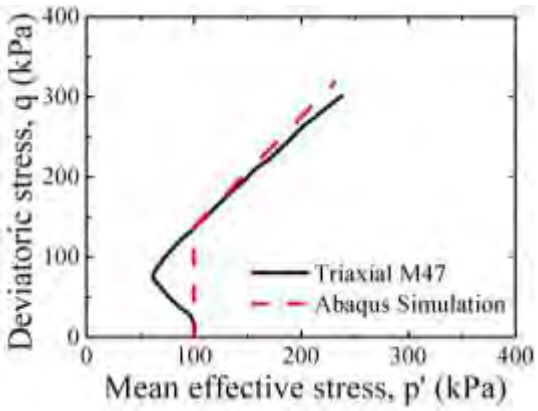

(a)q-p' plot

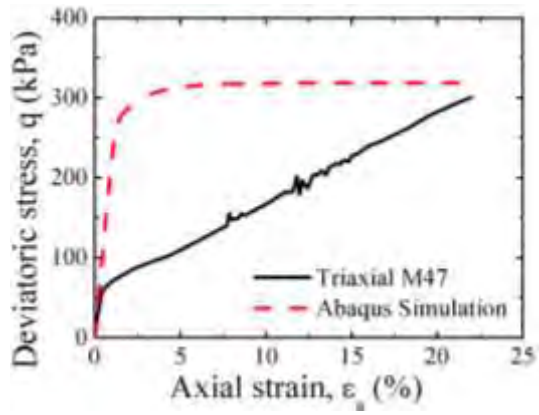

(b) q-ε_a plot

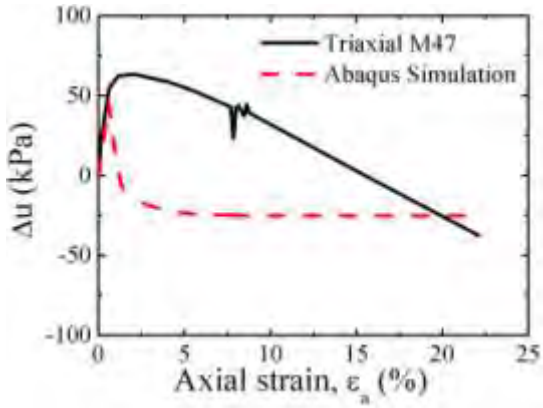

(c) Δu-ε_a plot

Fig.B. 29 Simulation of M47[$(D_{rc})_{eq}$=38%]

B.2.4.3 M45[$(D_{rc})_{eq}$=18%]

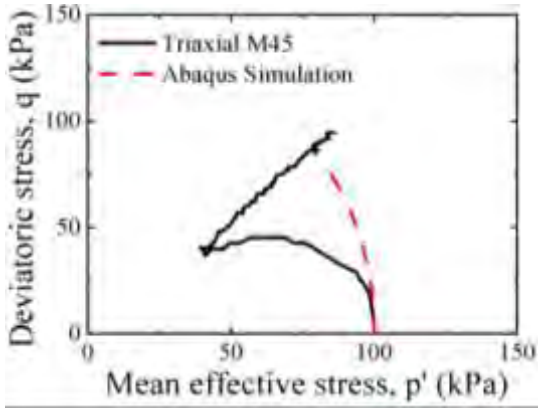

(a)q-p' plot

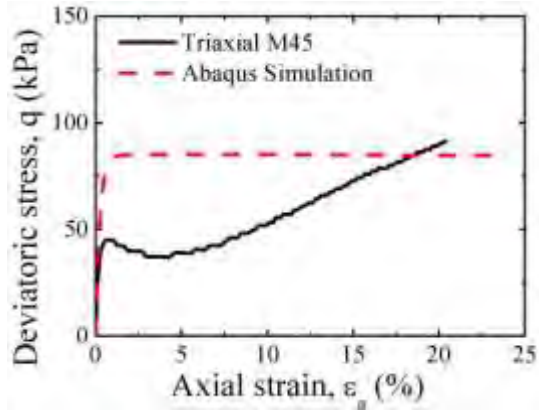

(b) q-ε_a plot

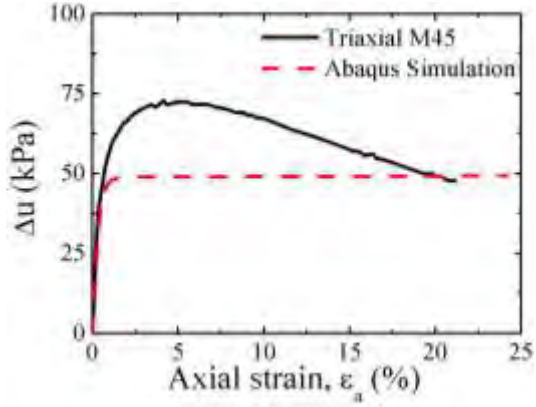

(c) Δu-ε_a plot

Fig.B. 30 Simulation of M45[$(D_{rc})_{eq}$=18%]

Appendix C Optimization of CPT simulation and effect of k on q_{c1N} using Drucker-Prager Model in Abaqus

Soil M31 [$(D_{rc})_{eq}$ =10%], M12 [$(D_{rc})_{eq}$ =41%] and M01 [$(D_{rc})_{eq}$=60%] are utilized to conduct the parametric study of CPT in Abaqus, in order to optimize the numerical model. The properties of these three soils can be found in Table 5.2 and Table 5.3 in Chapter 6.

C.1 Study on convergence

In this convergence study, R_h=0.13 cm for soil medium is selected while the CAX4R element is chosen to discretize the cone penetrometer. The coefficient of friction between cone and soil is termed as tanϕ'. Two meshes (fine and coarse) shown in Fig.C. 1 are set up for the numerical analysis, which are fine mesh (177 CAX4R elements for cone and 10725 CAX4P elements for soil stratum) and coarse mesh (50 CAX4R elements for cone and 4825 CAX4P elements), respectively.

Fig.C. 2 presents the comparison of q_{c1N} of different soils between two meshes. There are no distinct differences of the numerical results between two meshes for the soils simulated in the convergence study, indicating that the coarse mesh for soil medium and cone penetrometer adopted in the numerical analysis can be set as the primary discretization for the entire research.

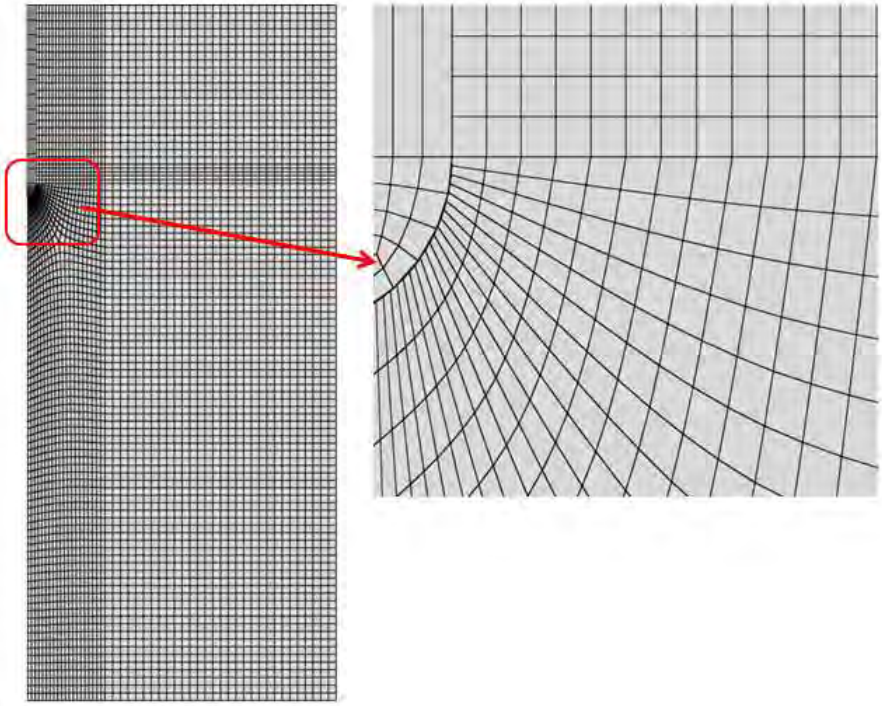

(a) coarse mesh

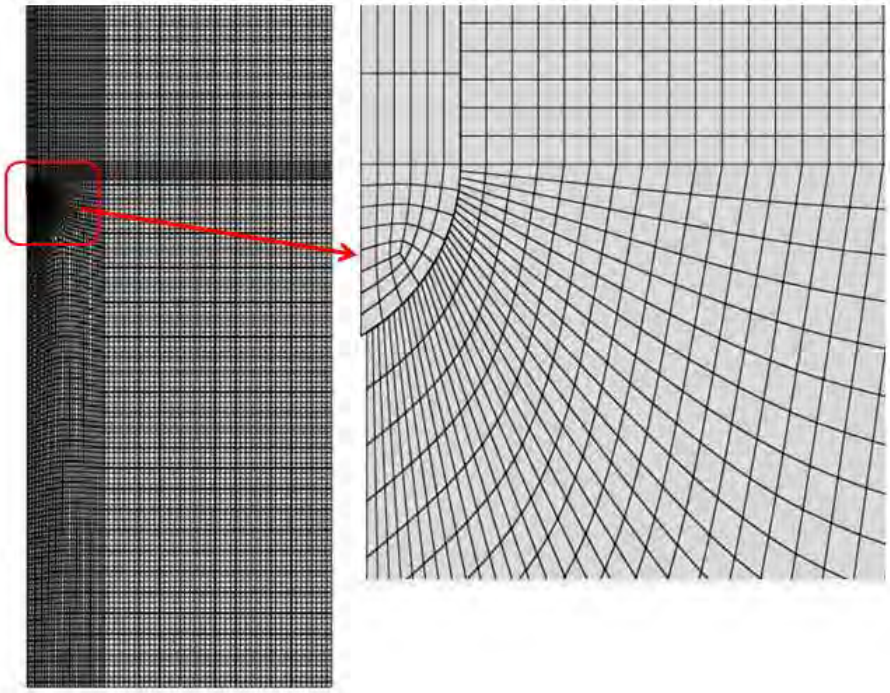

(b) fine mesh

Fig.C. 1 Two FEM meshes used in CPT simulation

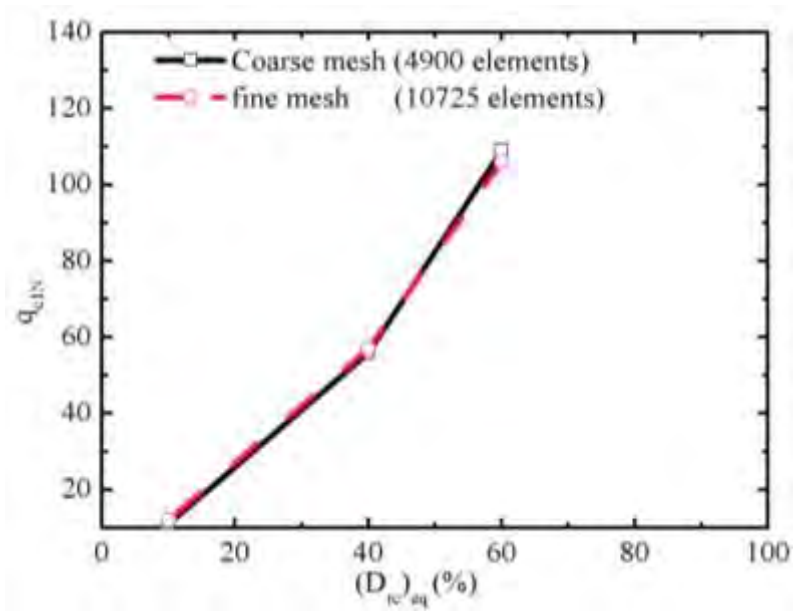

Fig.C. 2 Comparison of q_{c1n} of different soils between two meshes

C.2 Study on discretization types of cone penetrometer

In this section, numerical results from different soils using two types of cone penetrometer as shown in Fig.C. 3 are compared and summarized. Geometry of R_h=0 is employed as stated in section C.3 and the coefficient of friction between soil and cone is assumed to be 0.1.

(a) Non rigid cone discretization (b) Rigid cone discretization

Fig.C. 3 Cone penetrometer represented by different discretizations

Fig.C. 3(a) presents the cone penetrometer discretized by CAX4R element (a 4-node bilinear axisymmetric quadrilateral, reduced integration, hourglass control element). The properties of steel

are assigned to the discretized elements. On the other hand, since the cone penetrometer is much stiffer than the soil medium, an analytical rigid body can be employed to model the cone [Fig.C. 3(b)].

q_{c1N} versus $(D_{rc})_{eq}$ using two different cone discretizations is plotted in Fig.C. 4. As can be seen in the figure, well agreement between these two discretization methods is achieved. One distinct advantage of the analytical rigid body discretization over the non-rigid cone discretization lies in that Abaqus is not performing computation on this part and hence it is cost effective in terms of computation time. Thus the analytical rigid cone representation (rigid cone) is adopted hereafter.

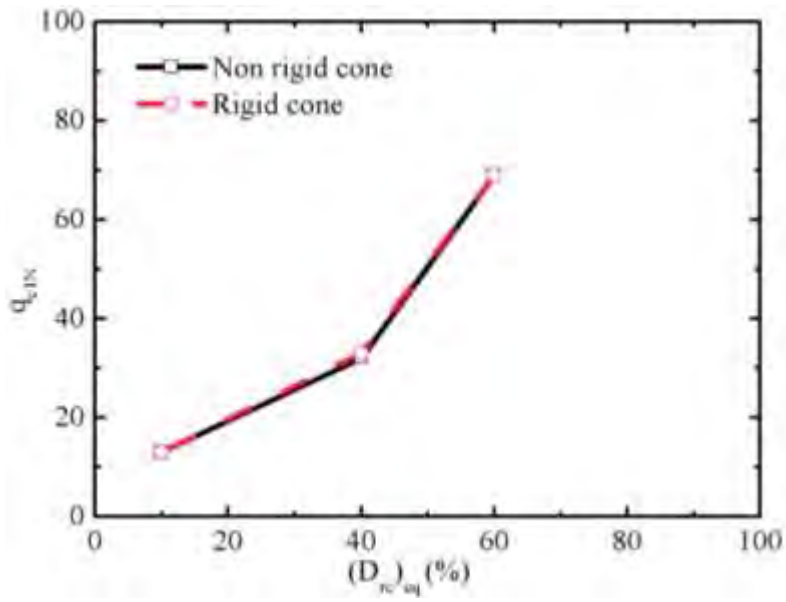

Fig.C. 4 Comparison of q_{c1N} of different soils between two different discretizations on cone

C.3 Study on geometric variation of soil medium in the symmetric axis

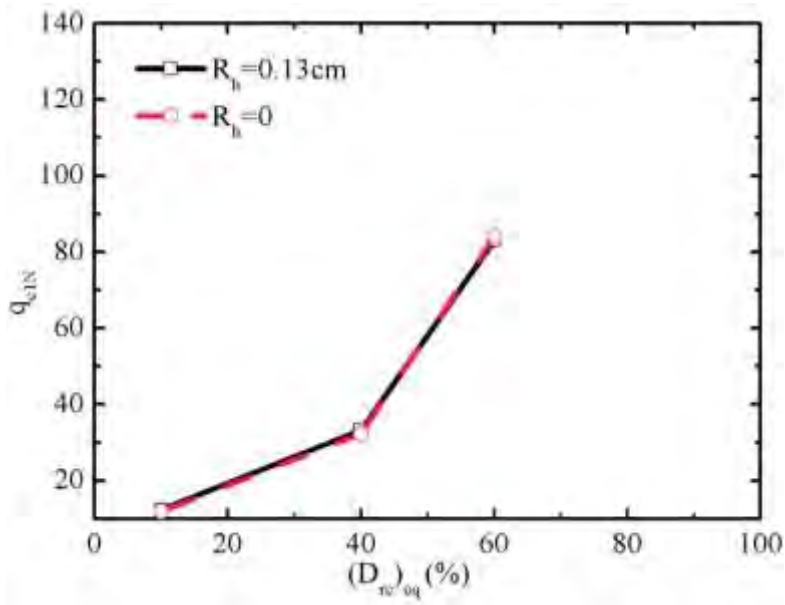

Fig.C. 5 Comparison of q_{c1N} of different soils between R_h=0 and R_h=0.13cm

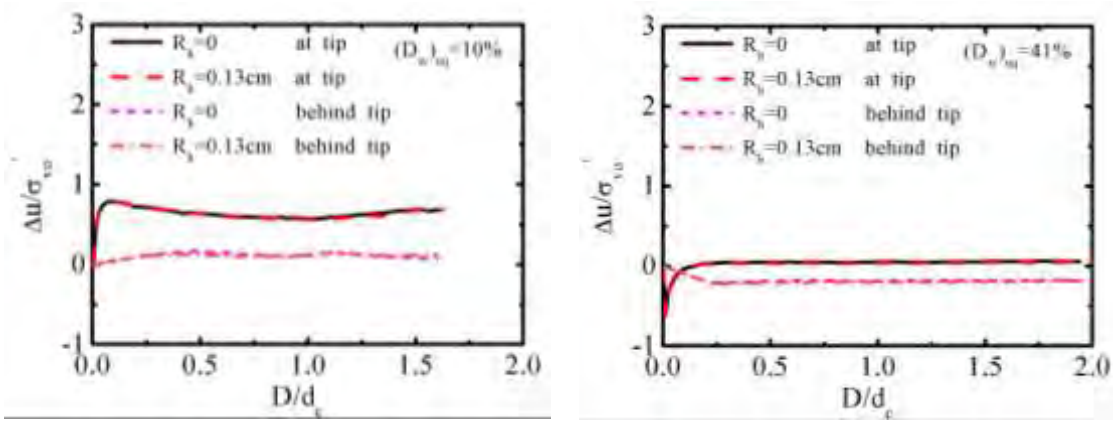

(a) $(D_{rc})_{eq}$=10% (a) $(D_{rc})_{eq}$=41%

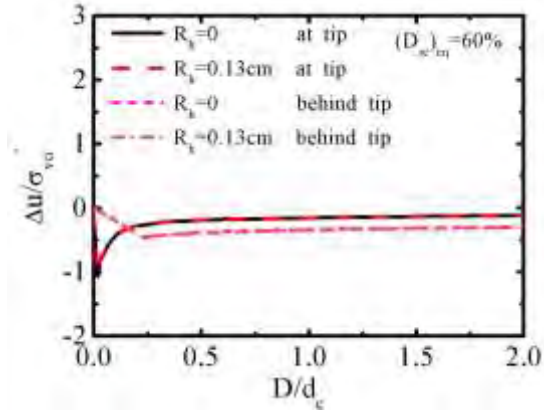

(c) $(D_{rc})_{eq}$=60%

Fig.C. 6 Comparison of $\Delta u/\sigma_{vo}'$ of different soils between R_h=0 and R_h=0.13cm

Two types of geometries at the left bottom side of soil medium as mentioned previously (Fig.

5.24) are examined in this section, namely R_h=0 and 0.13cm. The cone penetrometer is modelled using analytical rigid body. The coefficient of friction between soil and cone is termed as tan(0.5ϕ'). The numerical results of q_{c1N} at different $(D_{rc})_{eq}$ using these two geometries well agree with each other (Fig.C. 5). Moreover, the $\Delta u/\sigma_{vo}'$ at and behind cone tip for these two geometries are compared well in Fig.C. 6. The geometry with R_h=0 cm is hereafter adopted for examining the effect of fines content on the cone resistance in silty sands since it denotes the real in-situ boundary conditions.

C.4 Study on friction between soil and cone

Coulomb friction is assumed for the soil-cone friction analysis. The coefficients of friction between soil and cone being zero, tan(0.5ϕ') and tan(ϕ') are examined in this section. Coarse mesh with R_h=0 representing soil and analytical rigid cone are adopted in this sensitivity study.

Fig.C. 7 shows the variation of q_{c1N} with respect to $(D_{rc})_{eq}$ computed at coefficient of friction equal to zero, tan(0.5ϕ') and tan(ϕ'). The increases of q_{c1N} are about 100% at all three $(D_{rc})_{eq}$ when coefficient of friction increases from 0 to tan(0.5ϕ') while q_{c1N} increases about 10-30% depending on the $(D_{rc})_{eq}$ when coefficient of friction increases from tan(0.5ϕ') to tan(ϕ'). The large divergence in q_{c1N} between two soil-cone interface conditions affirms the previous investigations that the friction between soil and cone plays important role affecting the cone resistance (Voyiadjis and Abu-Farsakh, 1997).

In this study, it is noticed that the friction coefficient being tan(0.5ϕ') would yield relatively reasonable numerical results in terms of q_{c1N} as well as $\Delta u/\sigma_{vo}'$ in both clean sands and silty sands

when compared to experimental data. The selected friction of tan(0.5ϕ') between cone and soil medium is also adopted by other researchers in numerical study of CPT in sands (Susila and Hryciw, 2003; Tolooiyan and Gavin, 2011).

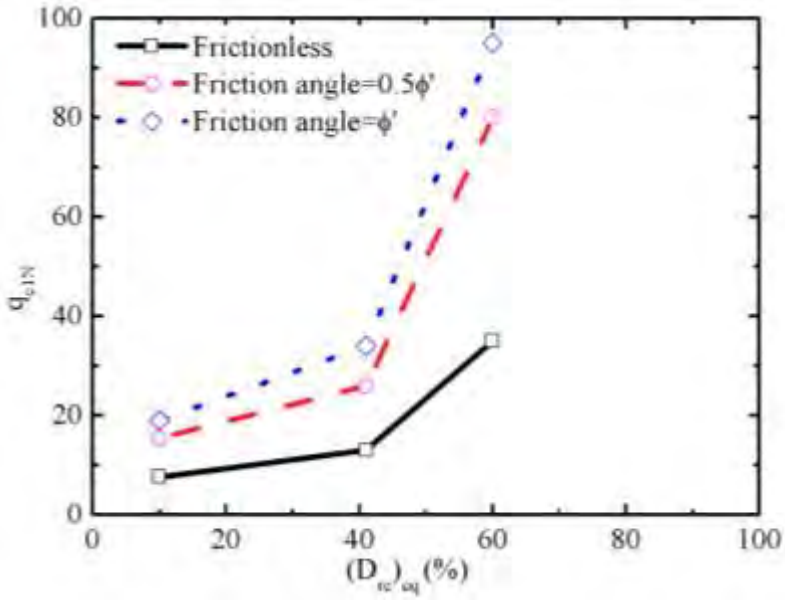

Fig.C. 7 Comparison of q_{c1N} of different soils between different interface friction angles

C.5 Study on effect of k on q_{c1N} using Drucker-Prager (DP) model

This section summarizes numerical results obtained using linear Drucker-Prager model for three different $(D_{rc})_{eq}$- 10%, 41% and 60%.

Table C. 1 Summary of numerical results using Drucker Prager

$(D_{rc})_{eq}$	d_c	v	E	m_v	k	c_v	T_0	Drucker-Prager		
(%)	(m)	(m/s)	(kPa)	(kPa^{-1})	(m/s)	(m^2/s)		q_{c1N}	$\Delta u_1/\sigma_{vo}'$	$\Delta u_2/\sigma_{vo}'$
10	0.0437	0.02	23100	3.90E-05	1.0E-03	2.62E+00	3.34E-04	-	-	-
		0.02	23100	3.90E-05	1.0E-04	2.62E-01	3.34E-03	12.7	3.0E-03	-5.7E-03
		0.02	23100	3.90E-05	1.0E-05	2.62E-02	3.34E-02	12.1	7.7E-03	-5.0E-02
		0.02	23100	3.90E-05	1.0E-06	2.62E-03	3.34E-01	10.3	-2.2E-01	-5.8E-01
		0.02	23100	3.90E-05	1.0E-07	2.62E-04	3.34E+00	6.7	-2.1E+00	-2.9E+00
		0.02	23100	3.90E-05	3.0E-08	7.86E-05	1.11E+01	-	-	-
		0.02	23100	3.90E-05	1.0E-08	2.62E-05	3.34E+01	5.6	-5.3E+00	-6.8E+00
		0.02	23100	3.90E-05	1.0E-09	2.62E-06	3.34E+02	5.7	-8.4E+00	-1.4E+01
41	0.0437	0.02	25000	3.60E-05	1.0E-03	2.83E+00	3.08E-04	-	-	-
		0.02	25000	3.60E-05	1.0E-04	2.83E-01	3.08E-03	34.0	-9.4E-03	-1.3E-02
		0.02	25000	3.60E-05	1.0E-05	2.83E-02	3.08E-02	33.0	-1.8E-01	-2.2E-01
		0.02	25000	3.60E-05	5.0E-06	1.42E-02	6.17E-02	-	-	-
		0.02	25000	3.60E-05	1.0E-06	2.83E-03	3.08E-01	33.3	-1.5E+00	-1.8E+00
		0.02	25000	3.60E-05	3.0E-07	8.50E-04	1.03E+00	-	-	-
		0.02	25000	3.60E-05	1.0E-07	2.83E-04	3.08E+00	31.9	-7.1E+00	-9.4E+00
		0.02	25000	3.60E-05	3.0E-08	8.50E-05	1.03E+01	-	-	-
		0.02	25000	3.60E-05	1.0E-08	2.83E-05	3.08E+01	27.4	-1.8E+01	-2.8E+01
		0.02	25000	3.60E-05	1.0E-09	2.83E-06	3.08E+02	19.7	-2.8E+01	-4.3E+01
60	0.0437	0.02	50958	1.77E-05	1.0E-03	5.78E+00	1.51E-04	-	-	-
		0.02	50958	1.77E-05	1.0E-04	5.78E-01	1.51E-03	104.4	-1.6E-01	0.0E+00
		0.02	50958	1.77E-05	1.0E-05	5.78E-02	1.51E-02	110.0	-1.5E+00	-1.2E+00
		0.02	50958	1.77E-05	1.0E-06	5.78E-03	1.51E-01	124.5	-1.1E+01	-9.1E+00
		0.02	50958	1.77E-05	1.0E-07	5.78E-04	1.51E+00	129.6	-5.1E+01	-4.1E+01
		0.02	50958	1.77E-05	3.0E-08	1.73E-04	5.04E+00	-	-	-
		0.02	50958	1.77E-05	1.0E-08	5.78E-05	1.51E+01	115.4	-1.0E+02	-1.2E+02
		0.02	50958	1.77E-05	1.0E-09	5.78E-06	1.51E+02	77.4	-9.9E+01	-1.8E+02

C.5.1 $(D_{rc})_{eq}$=10%

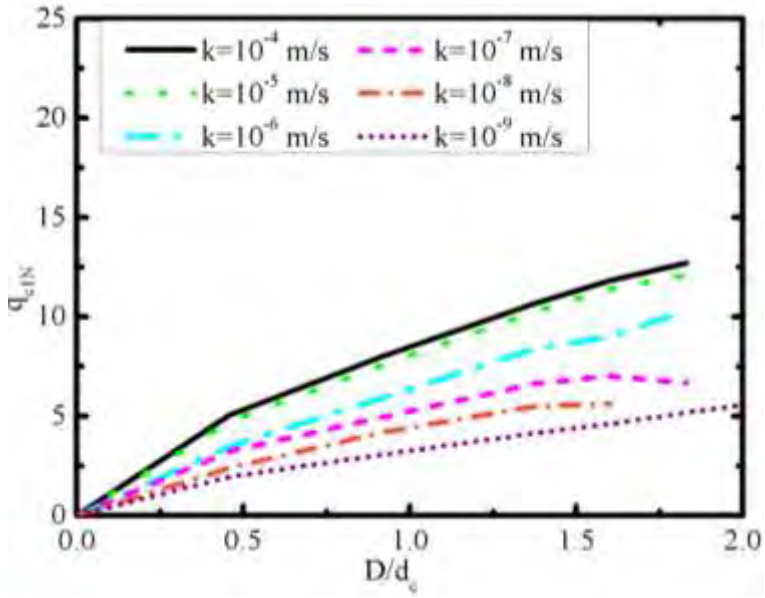

Fig.C. 8 q_{c1N} with respect to D/d_c for different permeabilities at $(D_{rc})_{eq}$=10% using DP

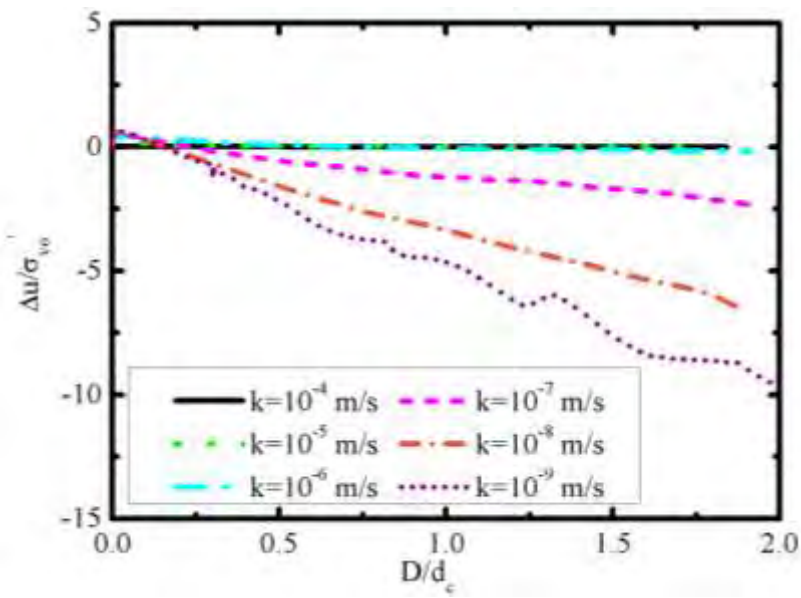

(a) at tip

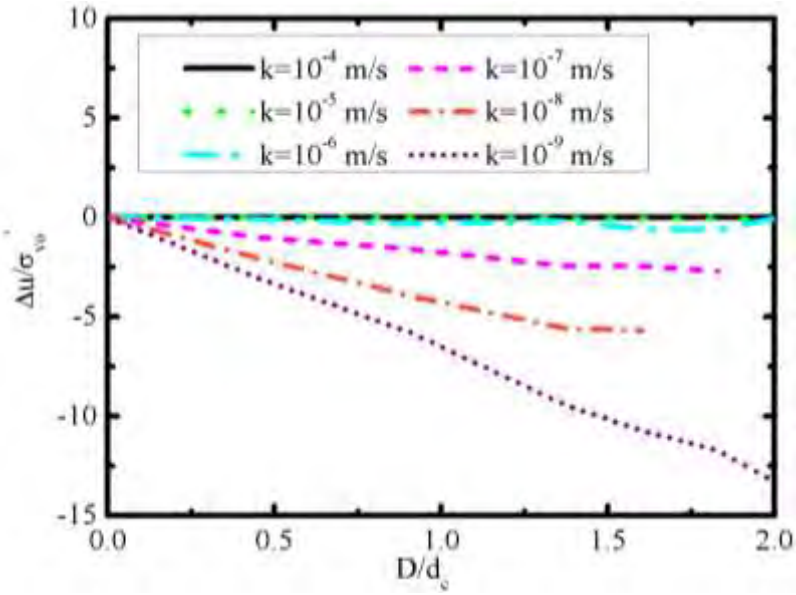

(a) behind tip

Fig.C. 9 $\Delta u/\sigma_{vo}'$ with respect to D/d_c for different permeabilities at $(D_{rc})_{eq}$=10% using DP

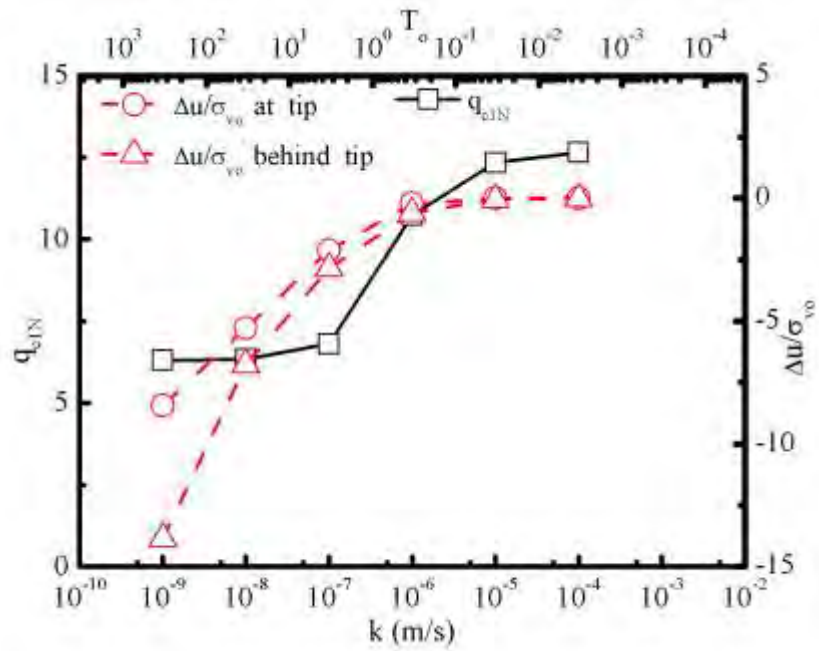

Fig.C. 10 q_{c1N} and $\Delta u/\sigma_{vo}'$ at different permeabilities of soil at $(D_{rc})_{eq}$=10% using DP

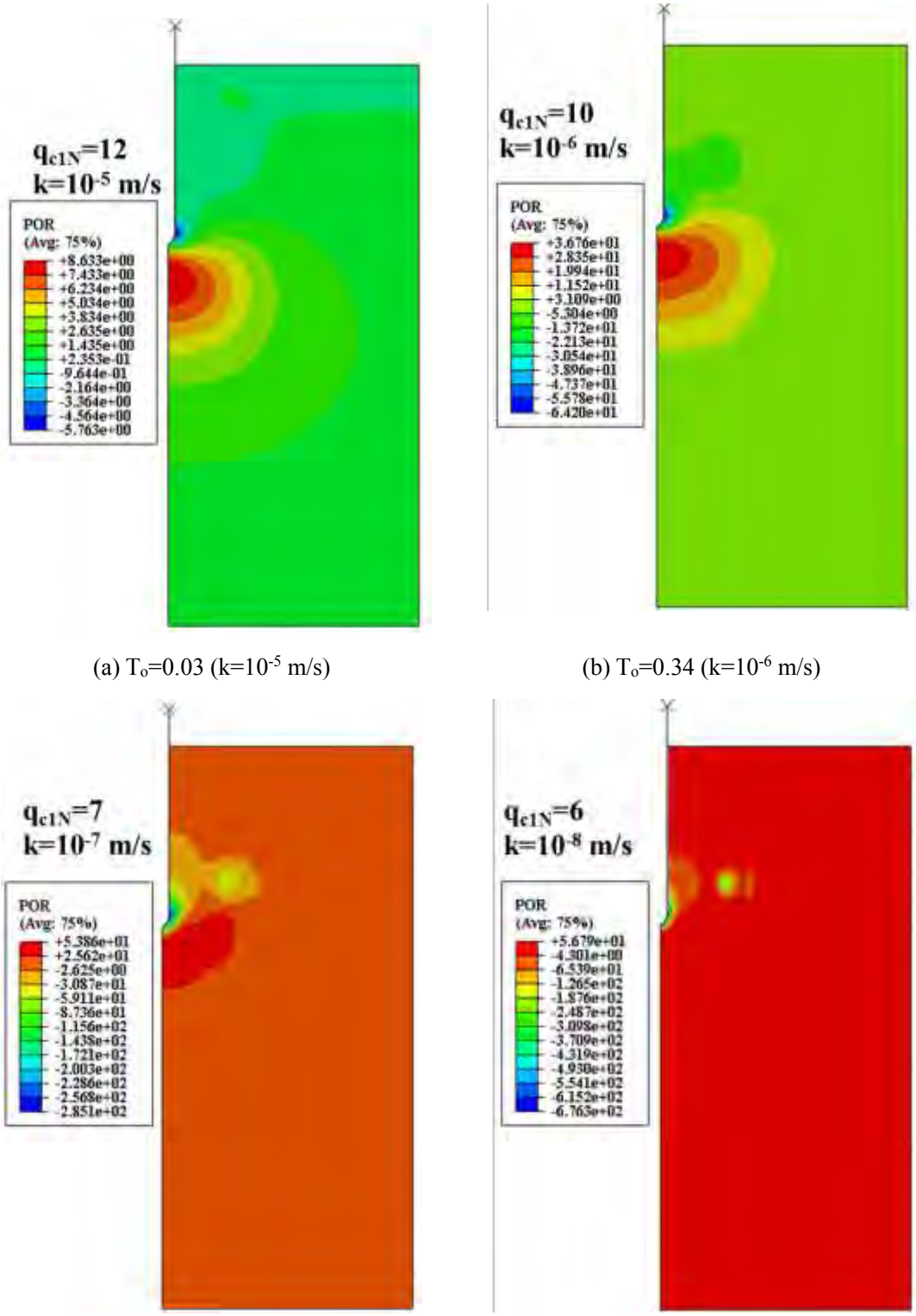

(a) T_o=0.03 (k=10^{-5} m/s)

(b) T_o=0.34 (k=10^{-6} m/s)

(c) T_o<3.4 (k=10^{-7} m/s)

(d) T_o=34 (k=10^{-8} m/s)

Fig.C. 11 EPWP distribution of Soil at $(D_{rc})_{eq}$=40% with different permeabilities using DP (Unit:kPa)

C.5.2 $(D_{rc})_{eq}$=41%

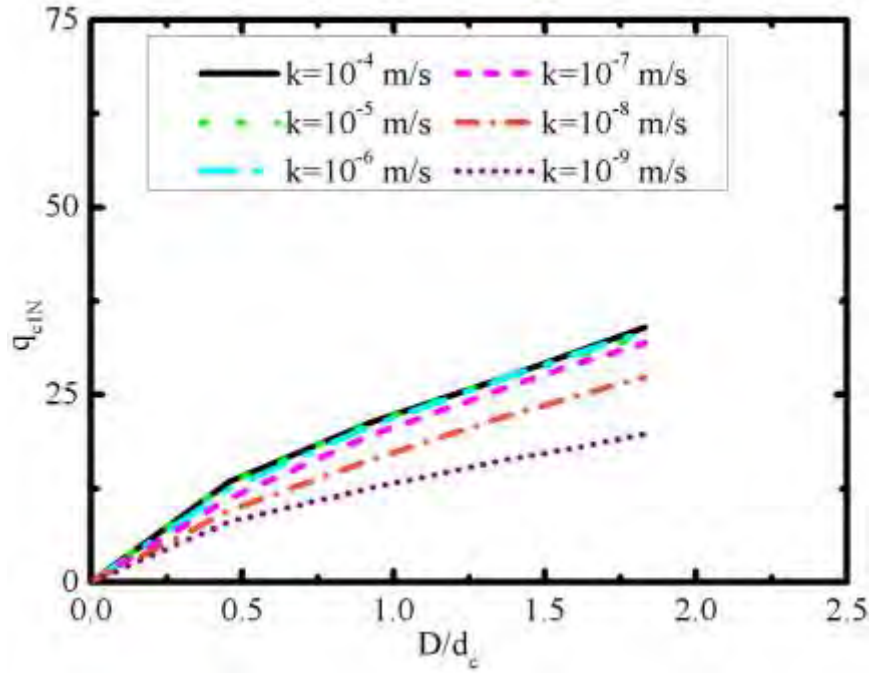

Fig.C. 12 q_{c1N} with respect to D/d_c for different permeabilities at $(D_{rc})_{eq}$=41% using DP

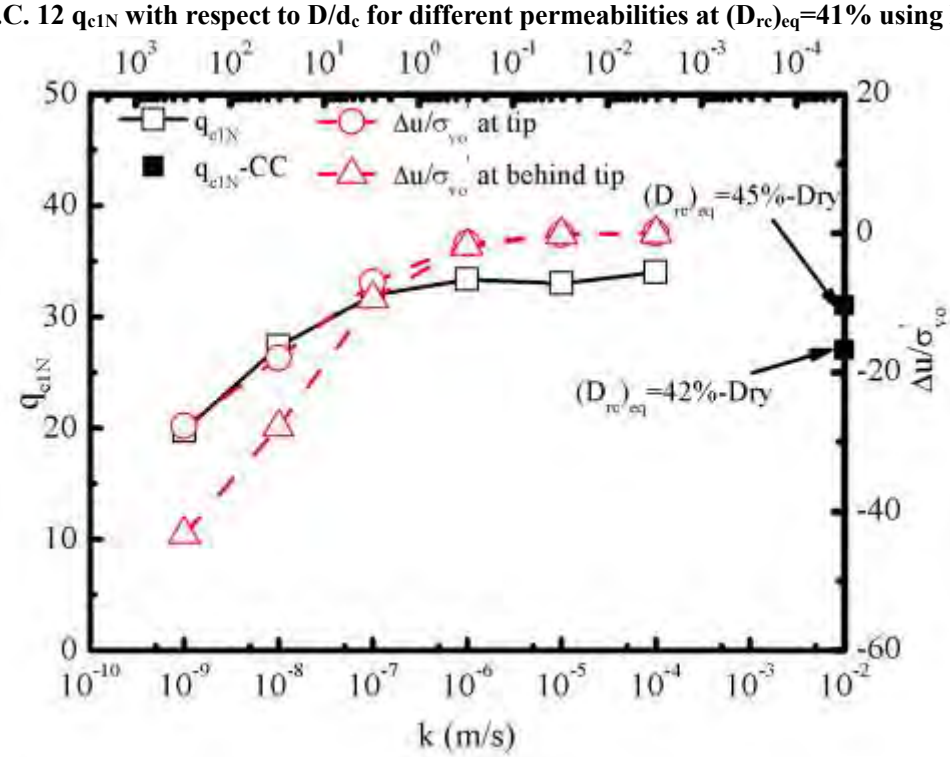

Fig.C. 13 q_{c1N} and $\Delta u/\sigma_{vo}'$ at different permeabilities of soil at $(D_{rc})_{eq}$=41% using DP

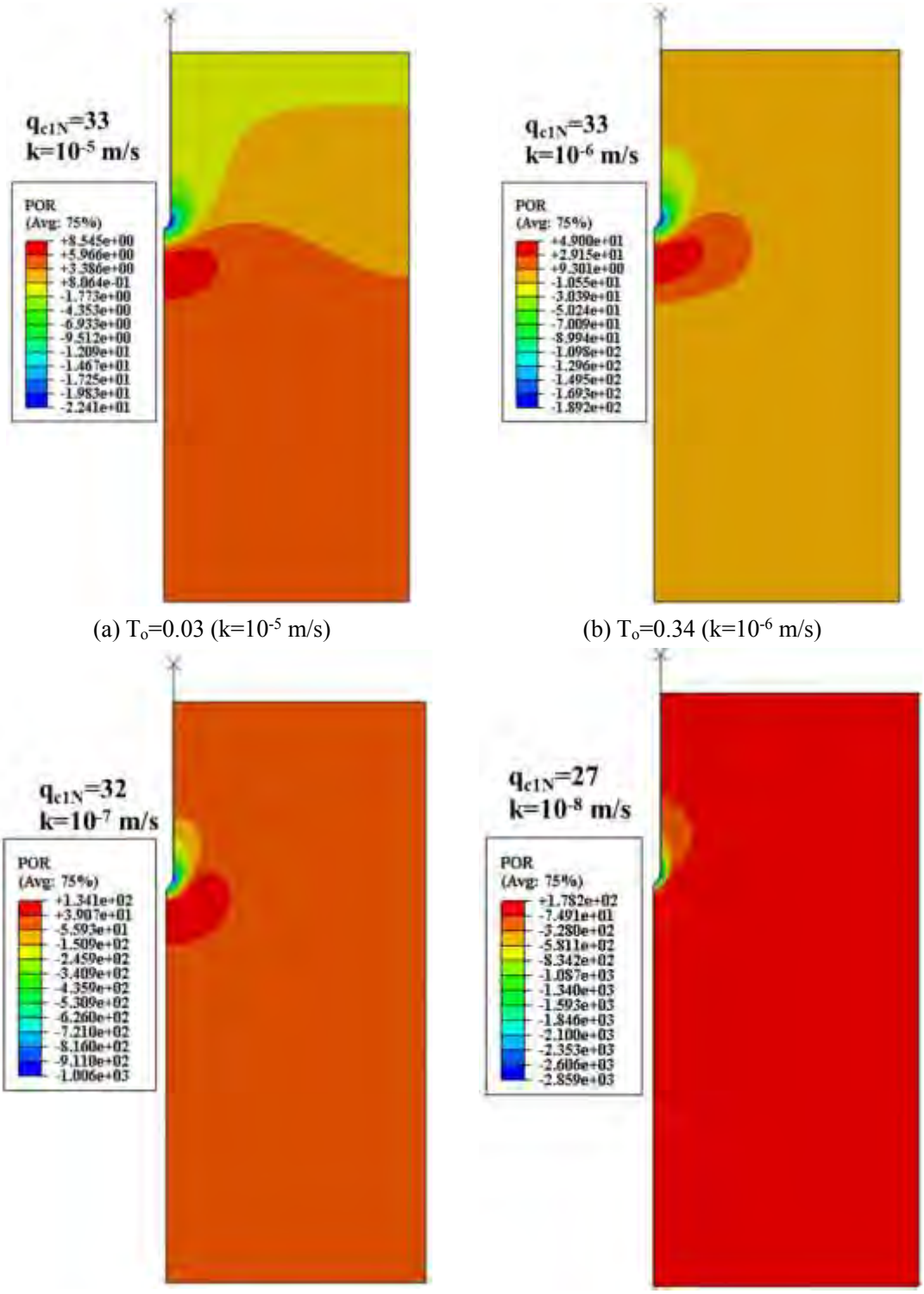

(a) T_o=0.03 (k=10^{-5} m/s) (b) T_o=0.34 (k=10^{-6} m/s)

(c) T_o<3.4 (k=10^{-7} m/s) (d) T_o=34 (k=10^{-8} m/s)

Fig.C. 14 EPWP distribution of Soil at $(D_{rc})_{eq}$=41% with different permeabilities using DP (Unit:kPa)

C.5.2 $(D_{rc})_{eq}$=60%

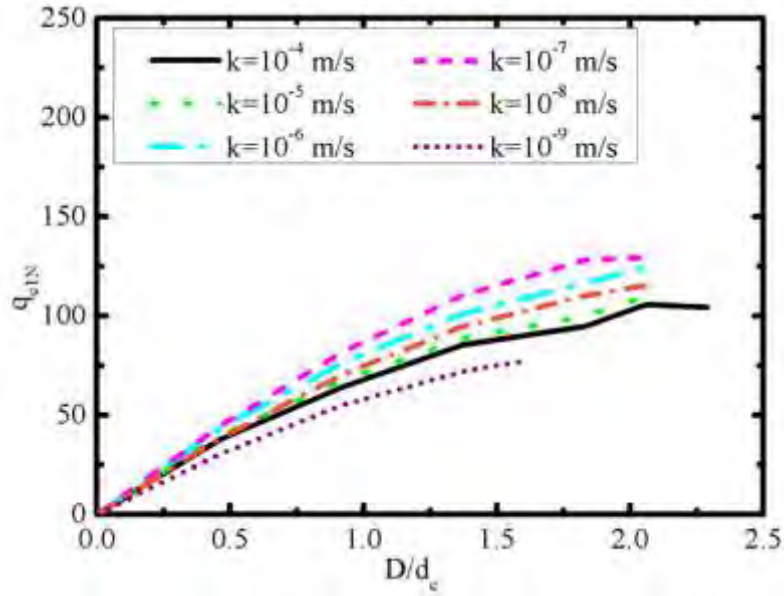

Fig.C. 15 q_{c1N} with respect to D/d_c for different permeabilities at $(D_{rc})_{eq}$=60% using DP

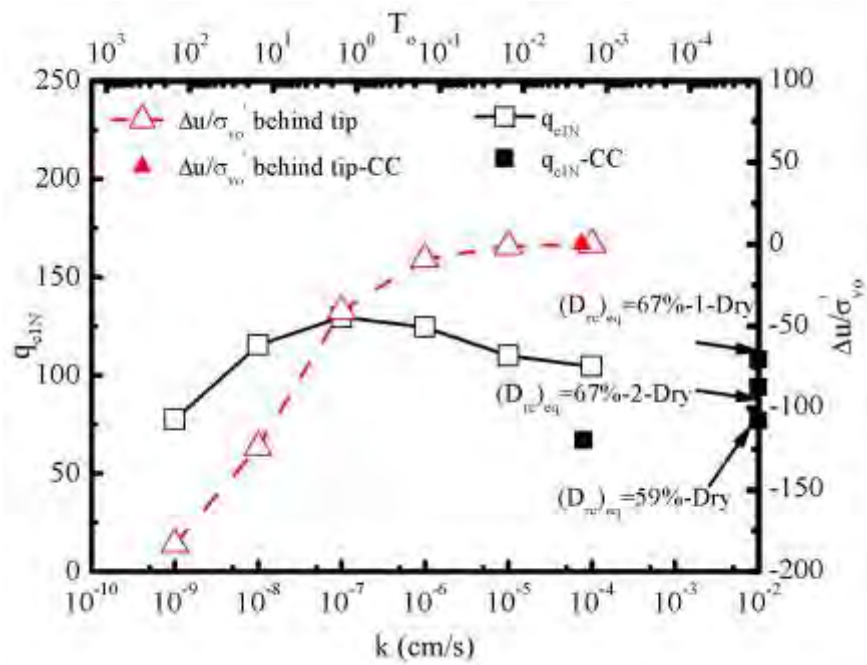

Fig.C. 16 q_{c1N} and $\Delta u/\sigma_{vo}'$ at different permeabilities of soil at $(D_{rc})_{eq}$=60% using DP

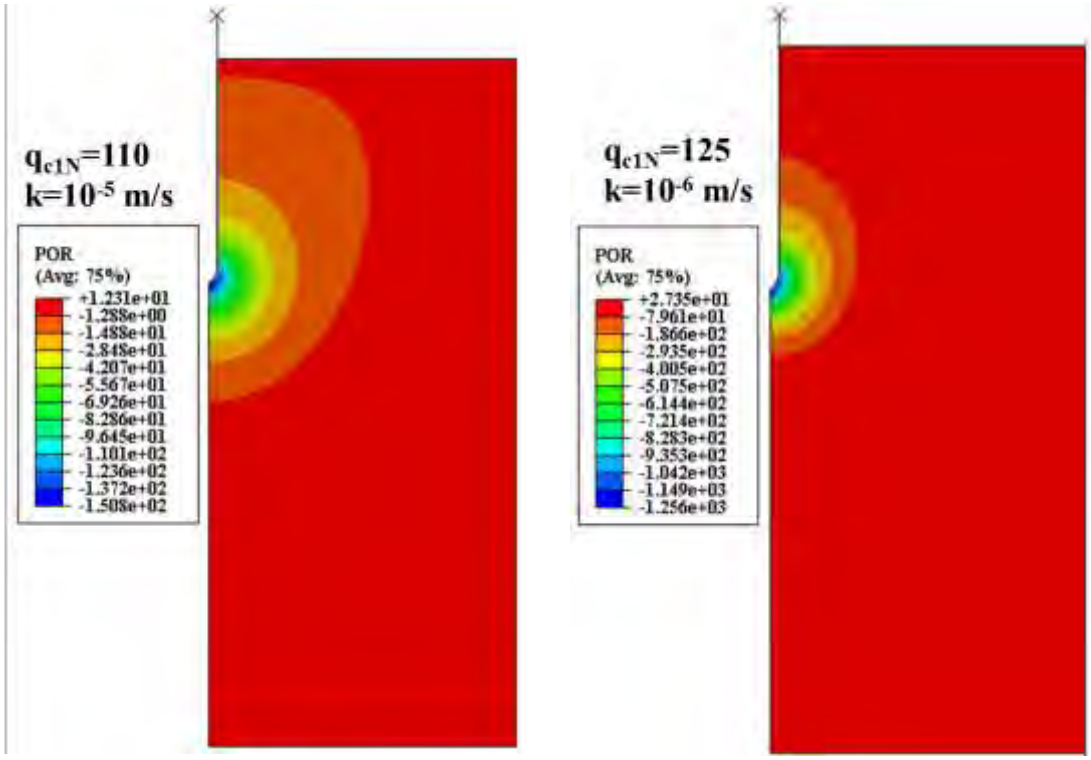

(a) T_o=0.03 (k=10^{-5} m/s) (b) T_o=0.34 (k=10^{-6} m/s)

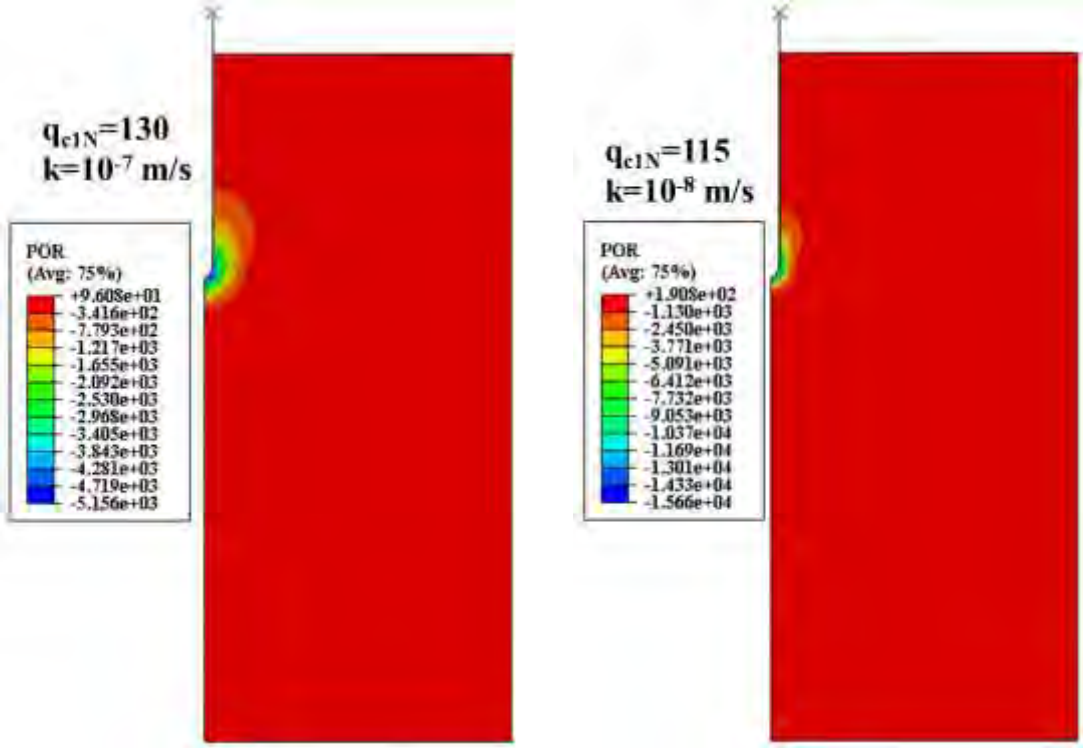

(c) T_o<3.4 (k=10^{-7} m/s) (d) T_o=34 (k=10^{-8} m/s)

Fig.C. 17 EPWP distribution of Soil at $(D_{rc})_{eq}$=60% with different permeabilities using DP (Unit:kPa)

Appendix D Determination of friction coefficient of ball bearings

D.1 Introduction

This appendix presents determinatioin of the friction coefficient of ball bearings

A force sensor connected to data acquisition system is attached to the laminate to which the force is applied. The force is applied manually until the laminate slides with respect to the laminate underneath it. The entire process is recorded and the greatest force recorded is determined as the sliding force, i.e. the friction force.

Two sets of tests are conducted to evaluate the friction efficient of ball bearings. The first set of test (test D.1 (T-D.1) and test D.2 (T-D.2)) is managed such that there is no laminate on the top of laminate to which the force sensor is attached (Fig. D.1 (a)), i.e. only one laminate is used to determine the coefficient while the second set of test (test D.3 (T-D.3) and test D.4(T-D.4)) is done such that there are four laminates on the top of laminate to which the force sensor is attached (Fig. D.1 (b)), i.e. there are total of five laminate used to define the coefficient of friction.

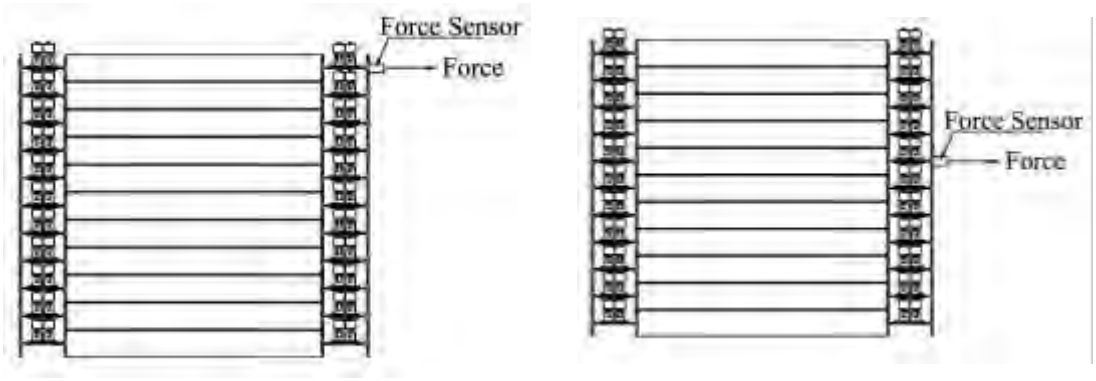

(a) 1 laminate (ring) (b) 5 laminates (rings)

Fig.D. 1 Number of laminates used to define the friction coefficient

D.2 Test results

Fig. D.2 and Table D.1 summarize test results of these two sets. Fig. D.2 presents the force versus time as the manual force is applied to the laminate(s) of the four tests. Table D.1 shows the sliding/friction force of each test as well as the corresponding friction coefficient, from which the 0.6% friction efficient is determined based on test D.3 and test D.4.

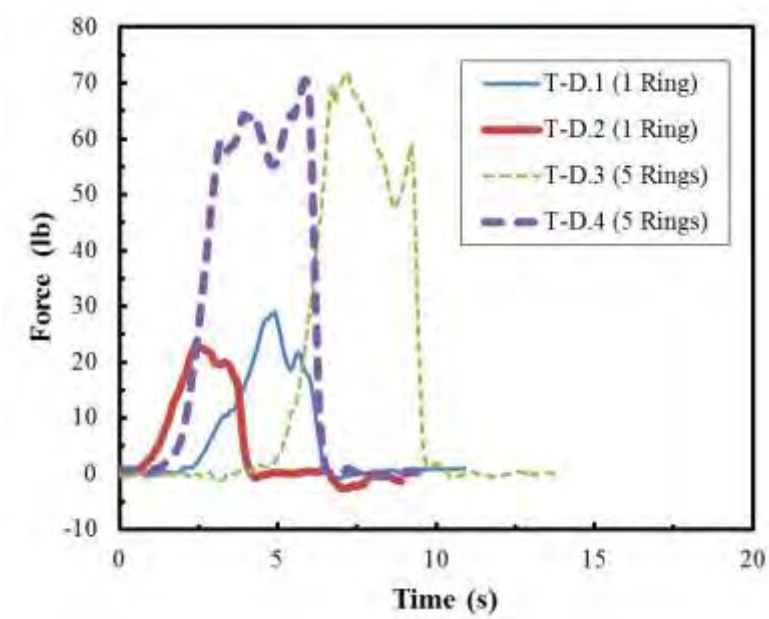

Fig.D. 2 Force versus time during the manual pulling process

Table D. 1 Summary of friction coefficient of each test

Test Name	Number of laminates	Total Friction Force	F per Laminate	Wt. Per Laminate	Friction Coefficient
		(lb)	(lb)	(lb)	
Test D.1	1	29	29	2300	1.3%
Test D.2	1	23	23	2300	1.0%
Test D.3	5	72	14	2300	0.6%
Test D.4	5	70	14	2300	0.6%

Appendix E Liquefaction experiments of LG1

This appendix summarizes some of the liquefaction experiments subject to different shaking series as introduced in Chapter 7. Only liquefaction tests of IM2 (a_{max}=0.03 g/15 cyc) and IM3 (a_{max}=0.10 g/15 cyc) are presented after shaking series 3. The sample rate from shaking series 3 to 8 is 256 Hz. This appendix also includes raw data for each shear wave velocity performed.

E.1 Liquefaction tests-shaking series 3

This shaking series consists of T11 through T15 (IM4), T16 (IM2) and T17 (IM3)-refer to Fig. 7.24 and Table 7.8 for details. Only T11, T15, T16 and T17 are presented in this section.

E.1.1 Base shaker

E.1.1.1 T11 and T15-IM4 (a_{max}=0.03 g/5 cyc)

Fig.E. 1 and Fig.E. 2 compare the recorded base acceleration at different locations for both x-(shaking) and y-(non-shaking) direction of T11 and T15 (a_{max}=0.03 g/5 cyc), respectively.

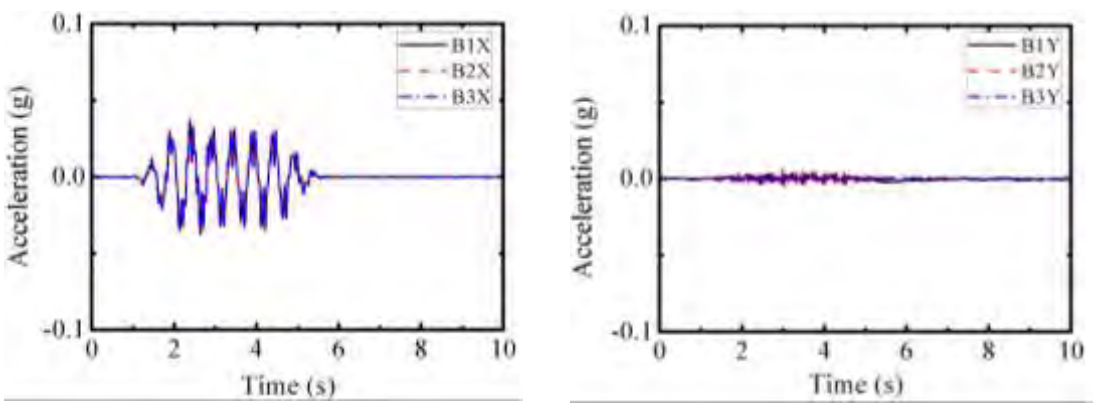

(a) x-direction (b) y-direction

Fig.E. 1 Base shaker of T11 (a_{max}=0.03 g/5 cyc)

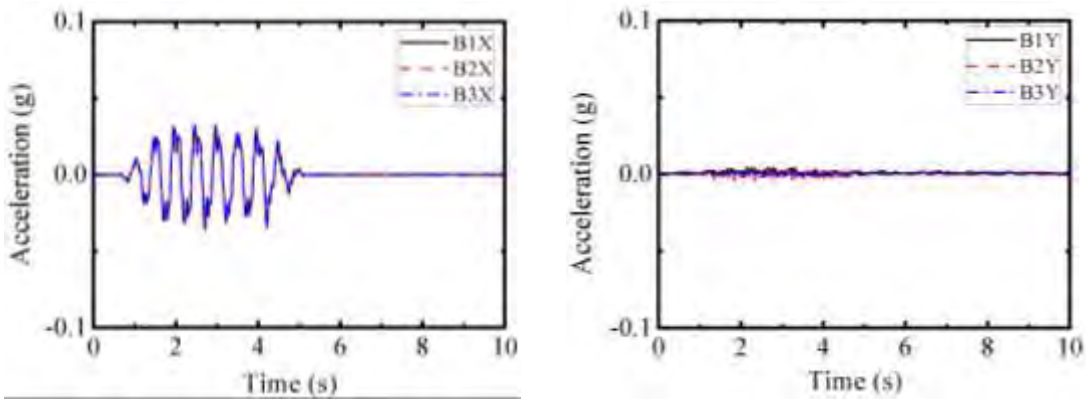

(a) x-direction (b) y-direction

Fig.E. 2 Base shaker of T15 (a_{max}=0.03 g/5 cyc)

E.1.1.2 T16-IM2 (a_{max}=0.03 g/15 cyc)

Fig.E. 3 compares the recorded base acceleration at different locations for both x-(shaking) and y-(non-shaking) direction of T16 (a_{max}=0.03 g/15 cyc).

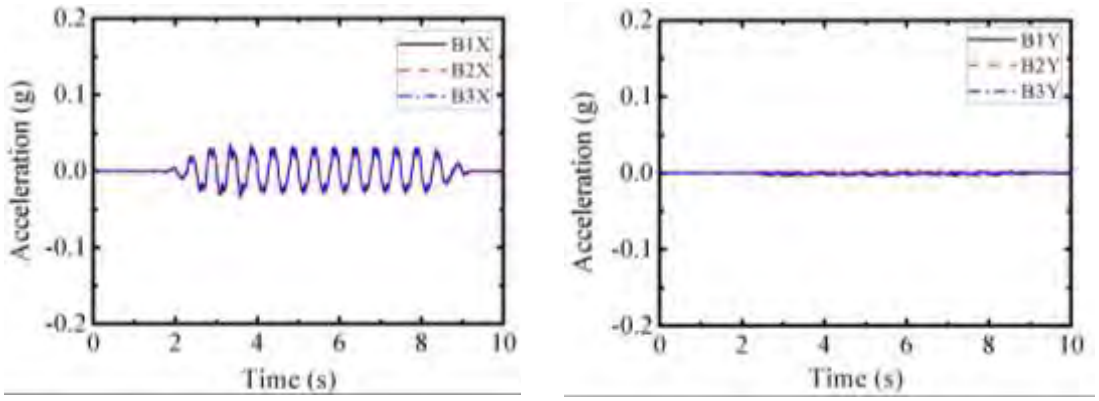

(a) x-direction (b) y-direction

Fig.E. 3 Base shaker of T16 (a_{max}=0.03 g/15 cyc)

E.1.1.3 T17-IM3 (a_{max}=0.10 g/15 cyc)

Fig.E. 4 compares the recorded base acceleration at different locations for both x-(shaking) and y-(non-shaking) direction of T17 (a_{max}=0.10 g/15 cyc).

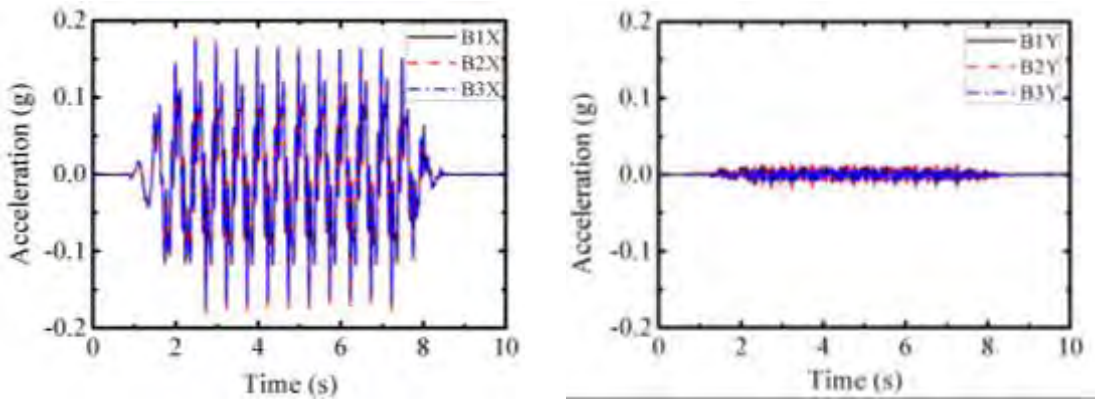

(a) x-direction (b) y-direction

Fig.E. 4 Base shaker of T17 (a_{max}=0.10 g/15 cyc)

E.1.2 Acceleration response

E.1.2.1 T11 and T15-IM4 (a_{max}=0.03 g/5 cyc)

Fig.E. 5 compares the acceleration from selected accelerometers as the base motion of T11and T15 (a_{max}=0.03 g/5 cyc) are input. It is noticed that the accelerometer located at laminate 27 instead of laminate 30 is extracted to be the surface acceleration recorder because of post liquefaction densification of soil after series of shaking. Based on Fig.E. 5, the amplification factor of soil at different depths is shown in Fig.E. 6.

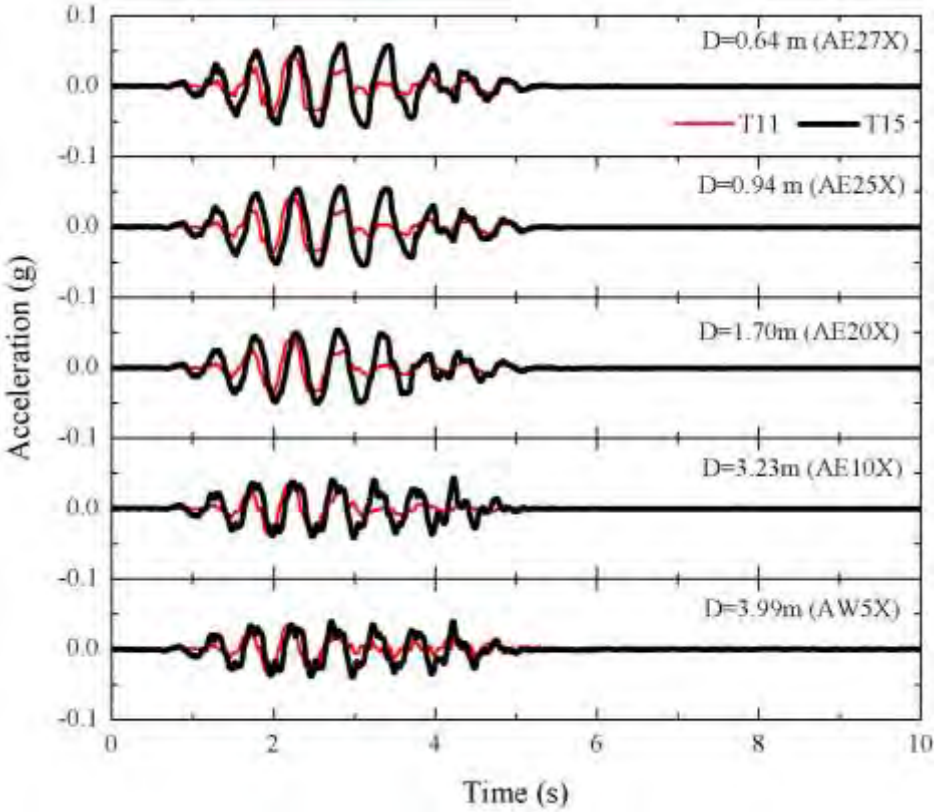

(a) Laminate acceleration

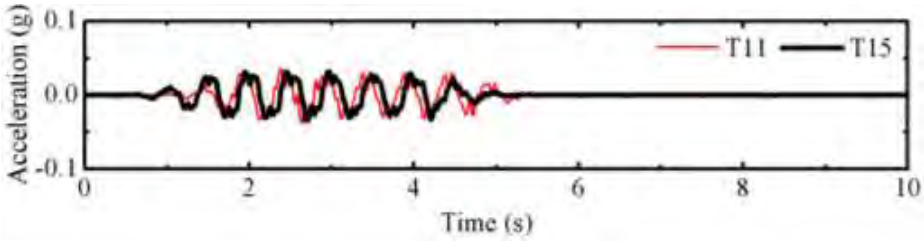

(b) B3X

Fig.E. 5 x-acceleration at different depths and base of T11 and T15 (a_{max}=0.03g/5 cyc)

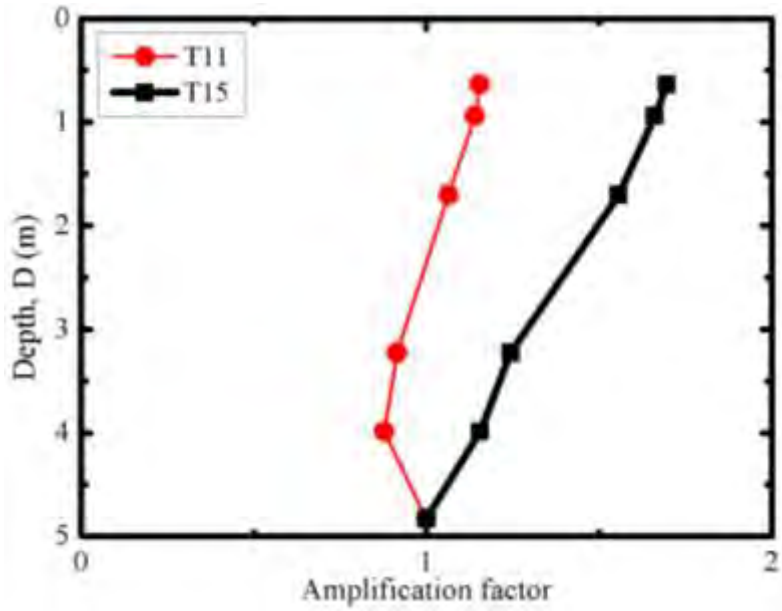

Fig.E. 6 Amplification factor profiles of T11 and T15 (a_{max}=0.03 g/5 cyc)

E.1.2.2 T16-IM2 (a_{max}=0.03 g/15 cyc)

Fig.E. 7 compares the acceleration from selected accelerometers as the base motion of T16 (a_{max}=0.03 g/15 cyc) is input. It is noticed that the accelerometer located at laminate 27 instead of laminate 30 is extracted to be the surface acceleration recorder because of post liquefaction densification of soil after series of shaking. Based on Fig.E. 7, the amplification factor of soil at different depths is shown in Fig.E. 8.

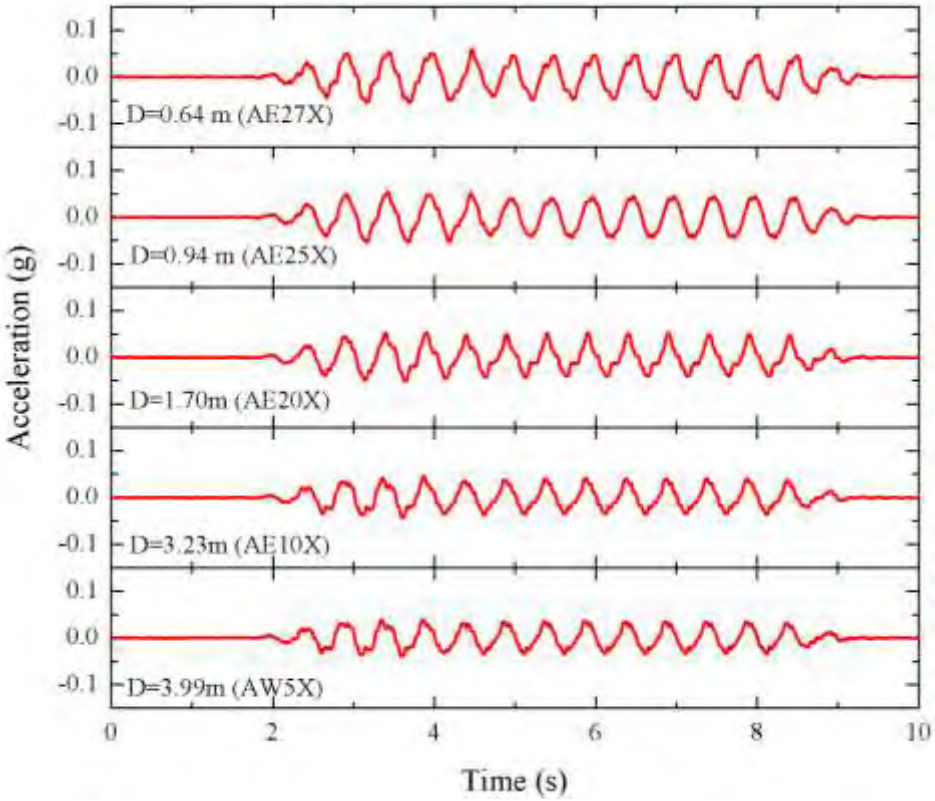

(a) Laminate acceleration

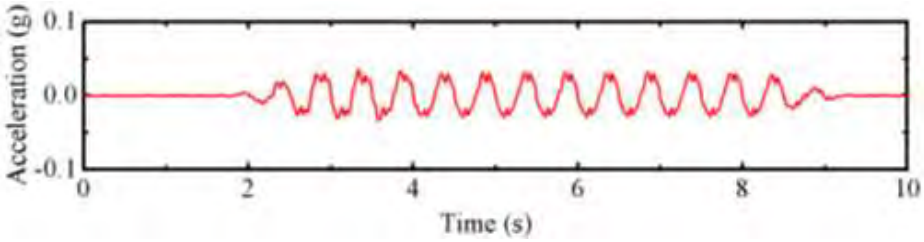

(b) B3X

Fig.E. 7 x-acceleration at different depths and base of T16 (a_{max}=0.03g/15 cyc)

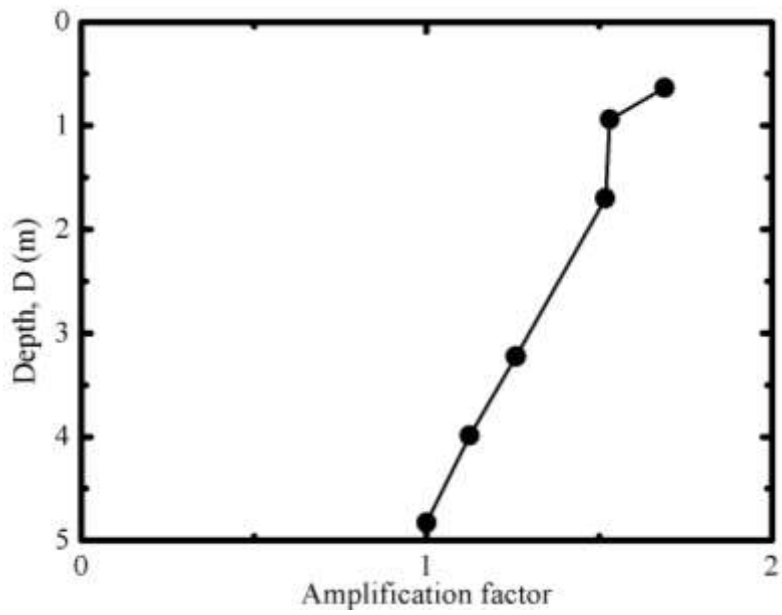

Fig.E. 8 Amplification factor profile of T16 (a_{max}=0.03 g/15 cyc)

E.1.2.3 T17-IM3 (a_{max}=0.10 g/15 cyc)

Fig.E. 9 compares the acceleration from selected accelerometers as the base motion of T17 (a_{max}=0.10 g/15 cyc) is input. It is noticed that the accelerometer located at laminate 27 instead of laminate 30 is extracted to be the surface acceleration recorder because of post liquefaction densification of soil after series of shaking. Based on Fig.E. 9, the amplification factor of soil at different depths is shown in Fig.E. 10.

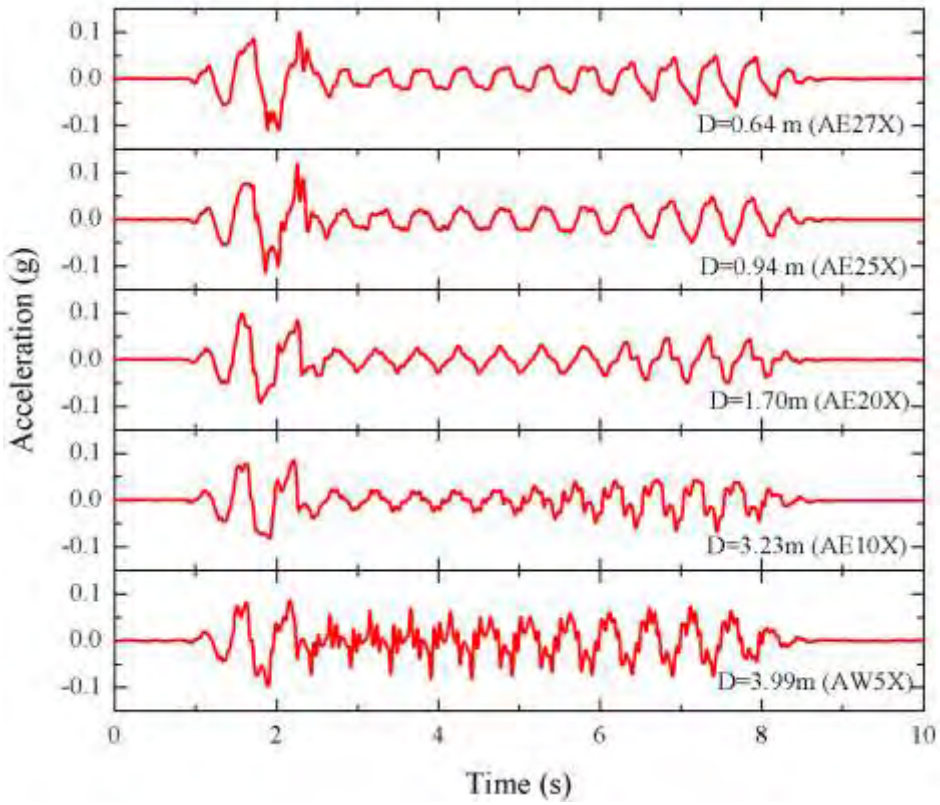

(a) Laminate acceleration

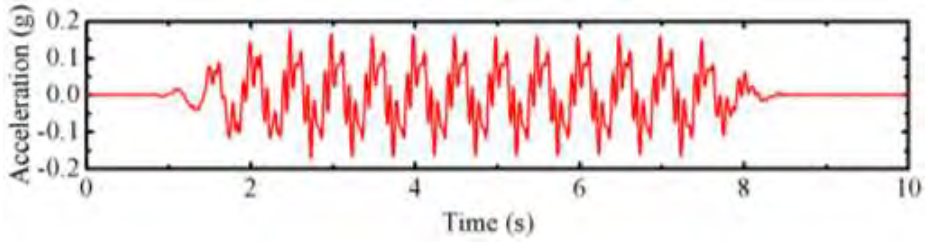

(b) B3X

Fig.E. 9 x-acceleration at different depths and base of T17 (a_{max}=0.10 g/15 cyc)

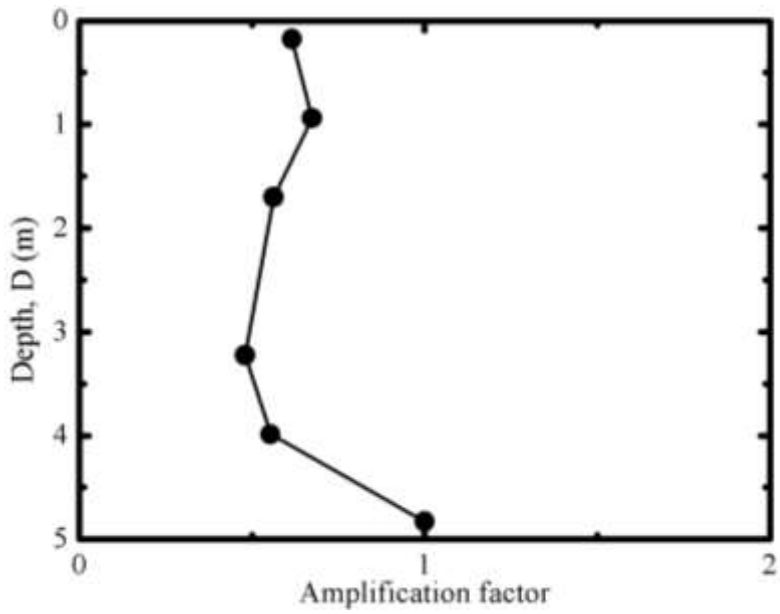

Fig.E. 10 Amplification factor profile of T17 (a_{max}=0.10 g/15 cyc)

E.1.3 Excess pore water pressure (Δu) response

E.1.3.1 T11 and T15-IM4 (a_{max}=0.03 g/5 cyc)

Fig.E. 11 presents the time history of normalized excess pore water pressure r_u and base acceleration during shaking of T11 and T15 (a_{max}=0.03 g/5 cyc), to better observe whether and when liquefaction occurs (i.e., r_u reaches unity) at different soil depths. Fig.E. 12 and Fig.E. 13 show the time history of excess pore water pressure (EPWP) Δu of the soil profile recorded by piezometers of T11 and T15. Fig.E. 14 and Fig.E. 15 plot the Δu as well as r_u with respect to depth at various shaking cycle for T11 and T15.

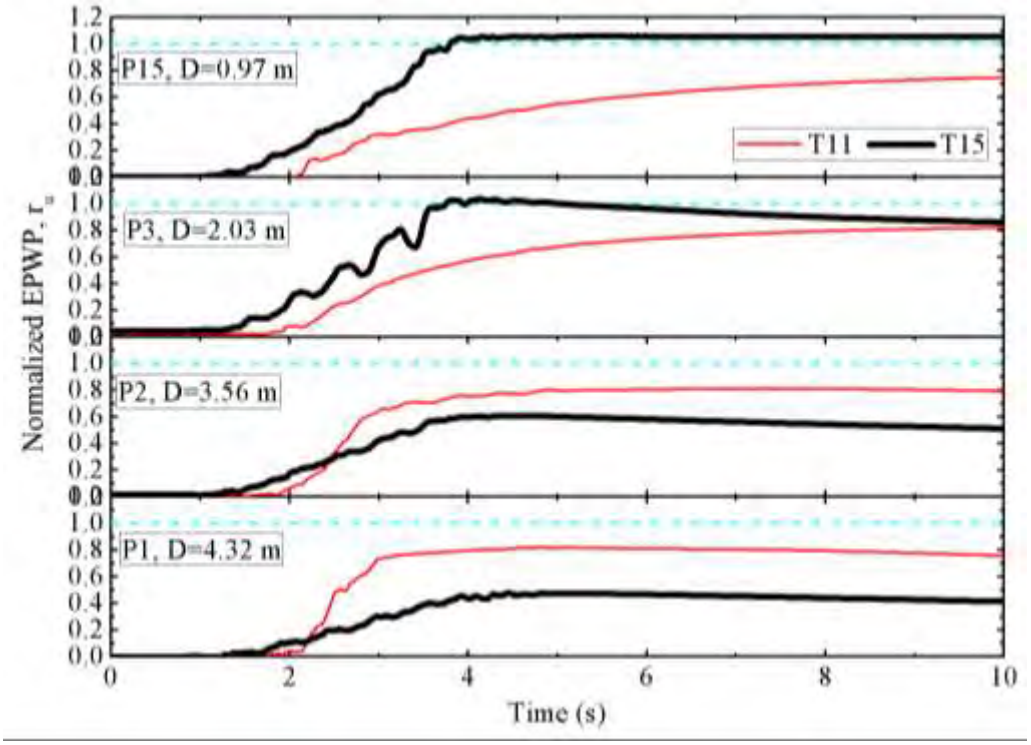

(a) r_u

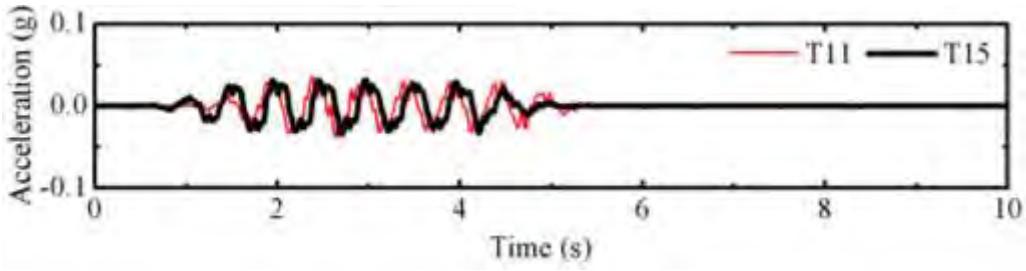

(b) B3X

Fig.E. 11 Time history of r_u and base acceleration of T11 and T15 (a_{max}=0.03 g/5 cyc)

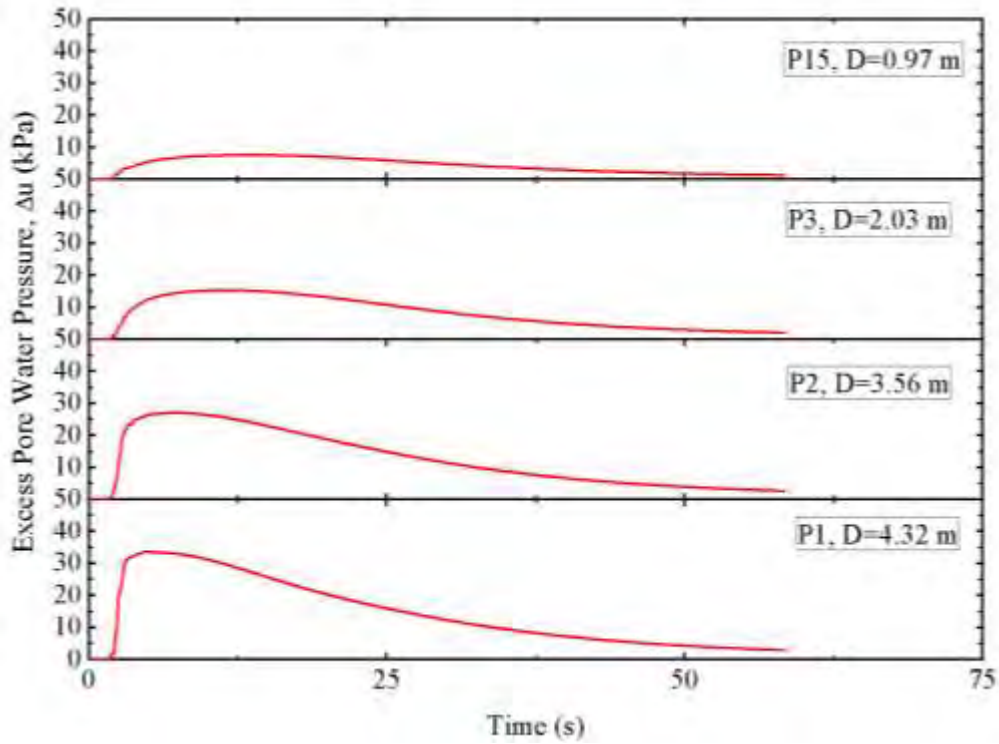

Fig.E. 12 Time history of Δu of T11 (a_{max}=0.03 g/5 cyc)

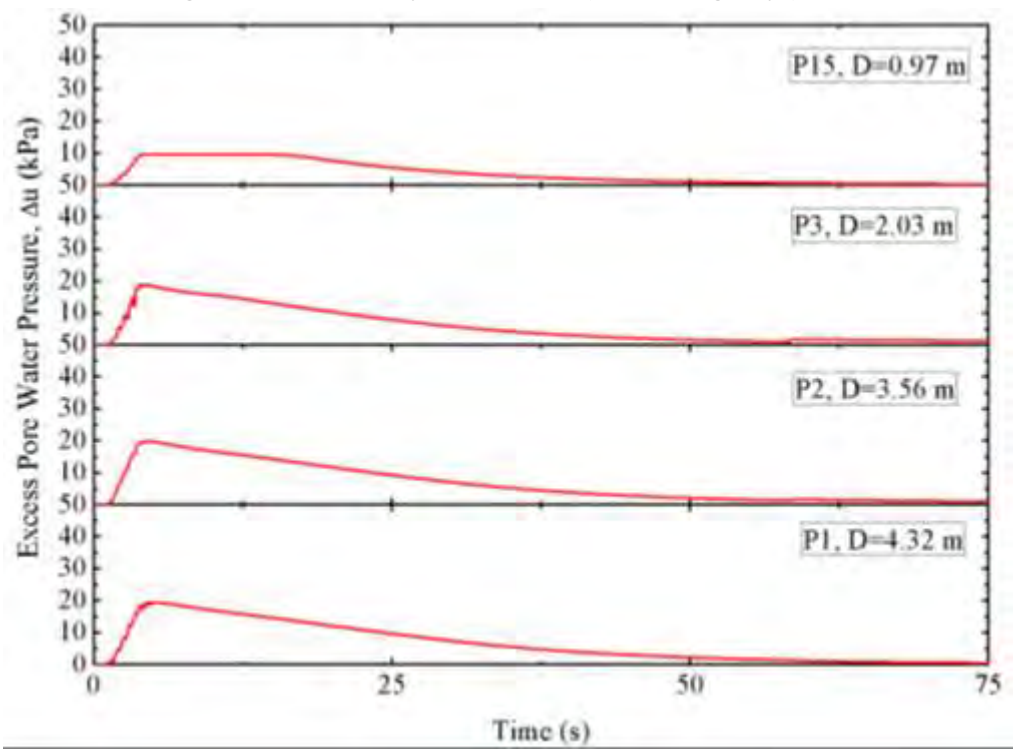

Fig.E. 13 Time history of Δu of T15 (a_{max}=0.03 g/5 cyc)

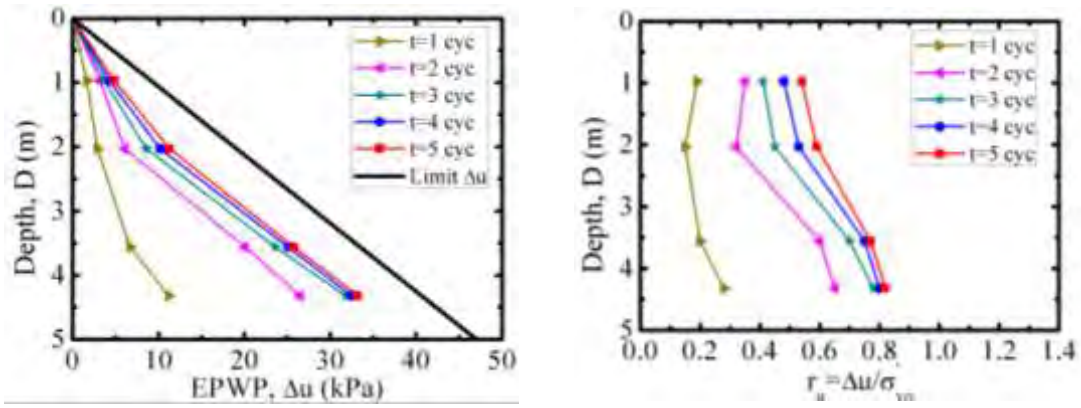

(a) Δu vs D (b) r_u vs D

Fig.E. 14 EPWP profiles of T11 (a_{max}=0.03 g/5 cyc)

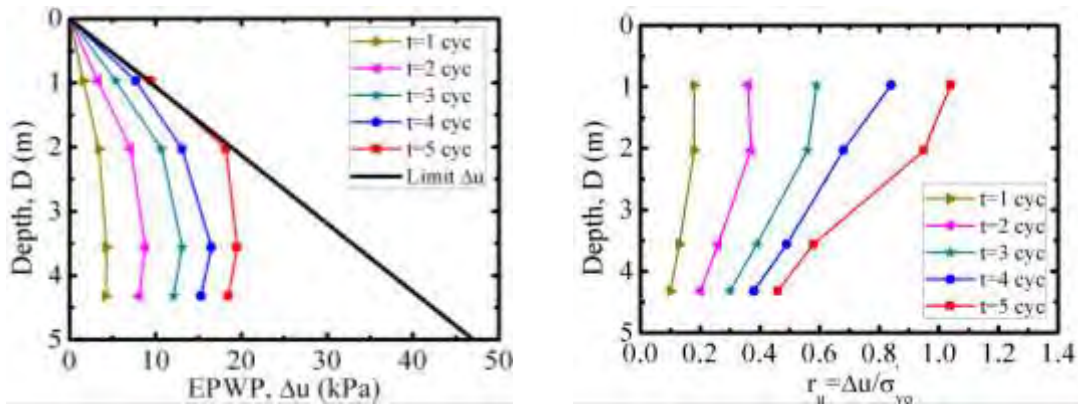

(a) Δu vs D (b) r_u vs D

Fig.E. 15 EPWP profiles of T15 (a_{max}=0.03 g/5 cyc)

E.1.3.2 T16-IM2 (a_{max}=0.03 g/15 cyc)

Fig.E. 16 presents the time history of normalized excess pore water pressure r_u and base acceleration during shaking of T16 (a_{max}=0.03 g/15 cyc), to better observe whether and when liquefaction occurs (i.e., r_u reaches unity) at different soil depths. Fig.E. 17 shows the time history of excess pore water pressure (EPWP) Δu of the soil profile recorded by piezometers of T16. Fig.E. 18 plots the Δu as well as r_u with respect to depth at various shaking cycle for T16.

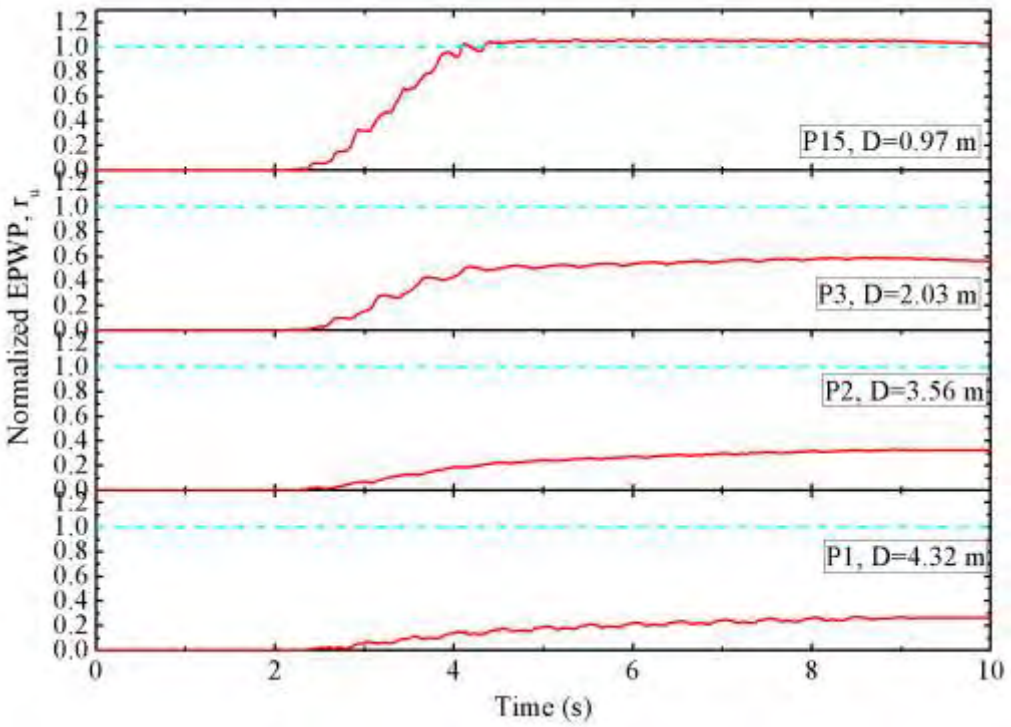

(a) r_u

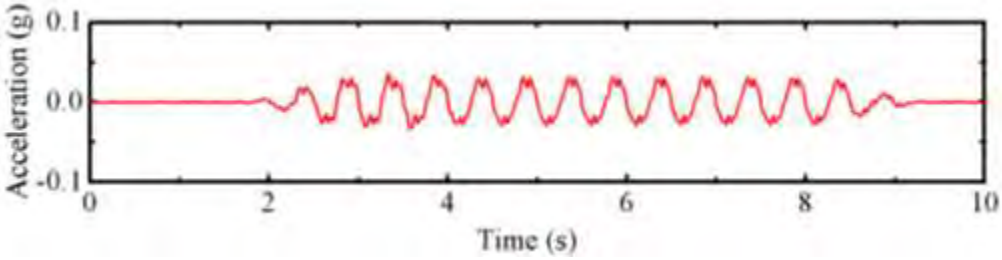

(b) B3X

Fig.E. 16 Time history of r_u and base acceleration of T16 (a_{max}=0.03 g/15 cyc)

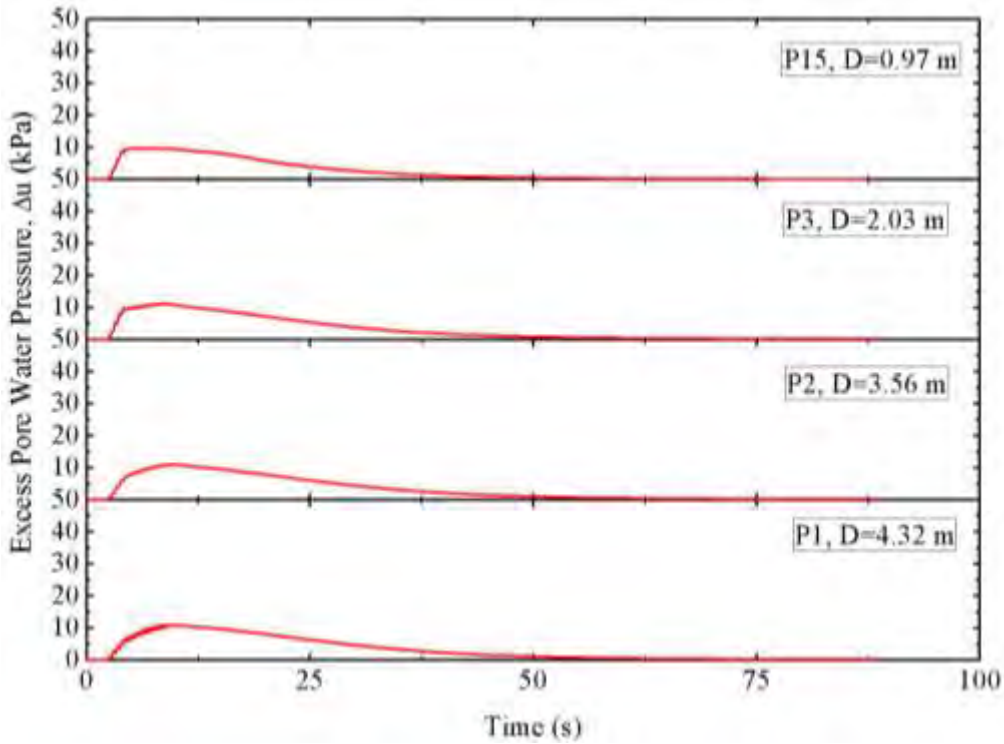

Fig.E. 17 Time history of Δu of T16 (a_{max}=0.03 g/15 cyc)

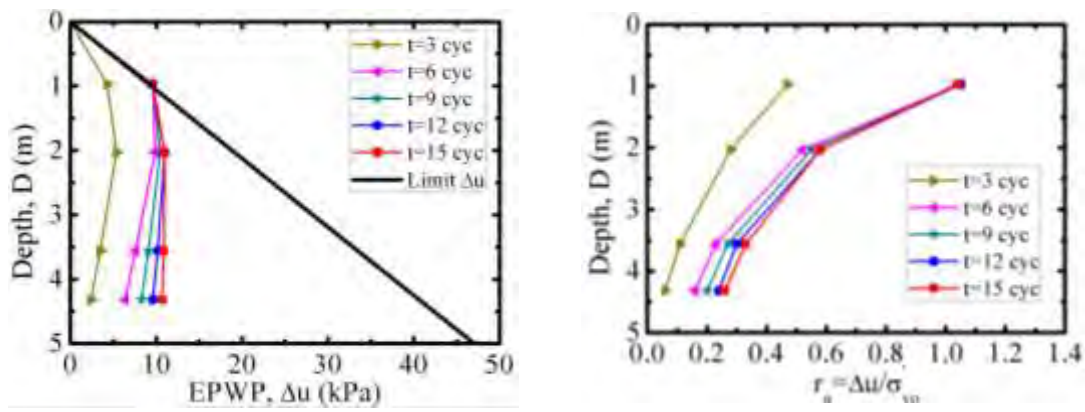

(a) Δu vs D (b) r_u vs D

Fig.E. 18 EPWP profiles of T16 (a_{max}=0.03 g/15 cyc)

E.1.3.3 T17-IM3 (a_{max}=0.10 g/15 cyc)

Fig.E. 19 presents the time history of normalized excess pore water pressure r_u and base acceleration during shaking of T17 (a_{max}=0.10 g/15 cyc), to better observe whether and when liquefaction occurs (i.e., r_u reaches unity) at different soil depths. Fig.E. 20 shows the time history of excess pore water pressure (EPWP) Δu of the soil profile recorded by piezometers of T17. Fig.E.

21 plots the Δu as well as r_u with respect to depth at various shaking cycle for T17.

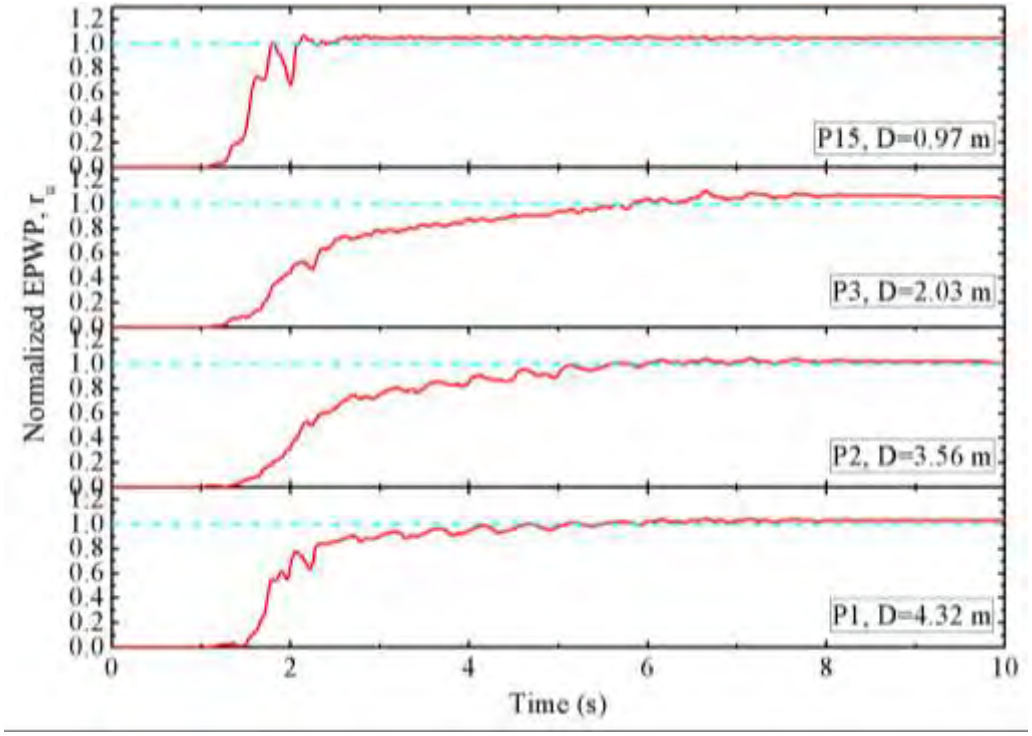

(a) r_u

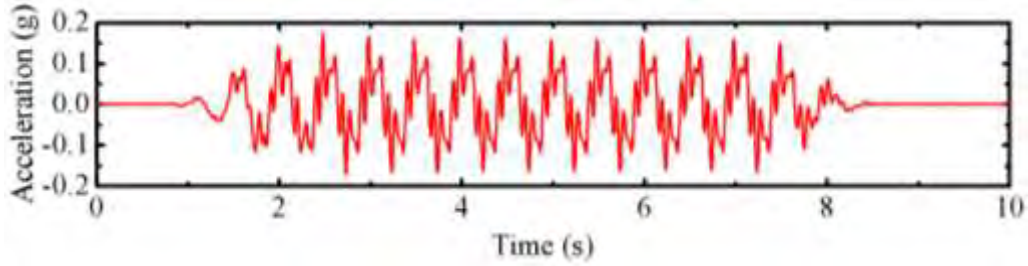

(b) B3X

Fig.E. 19 Time history of r_u and base acceleration of T17 (a_{max}=0.10 g/15 cyc)

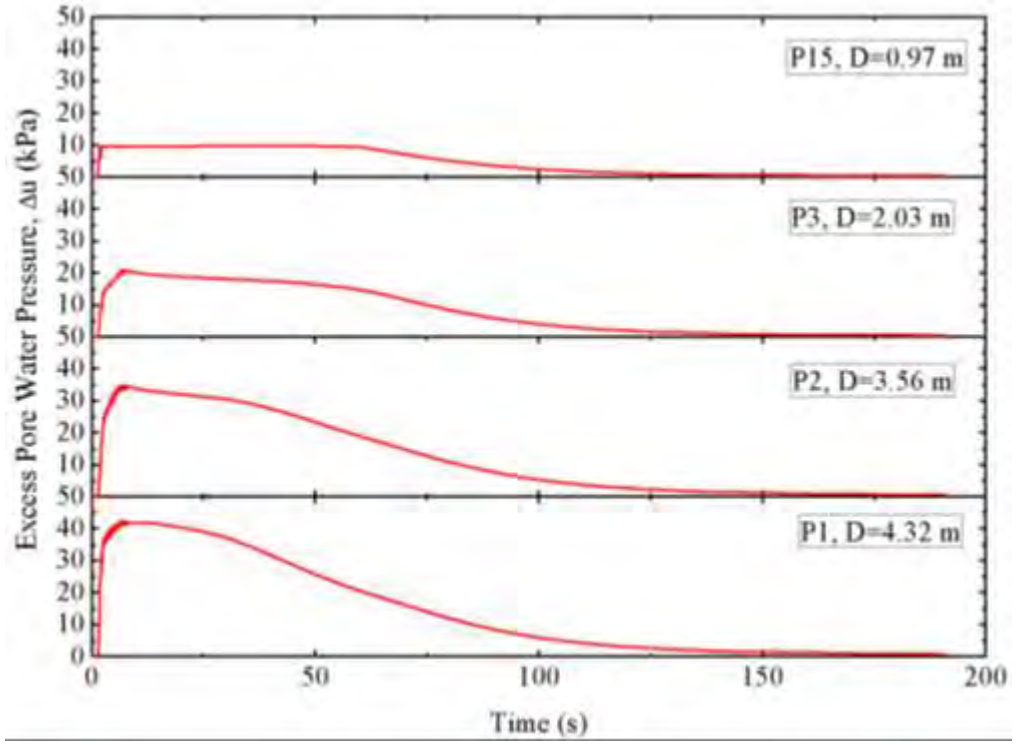

Fig.E. 20 Time history of Δu of T17 (a_{max}=0.10 g/15 cyc)

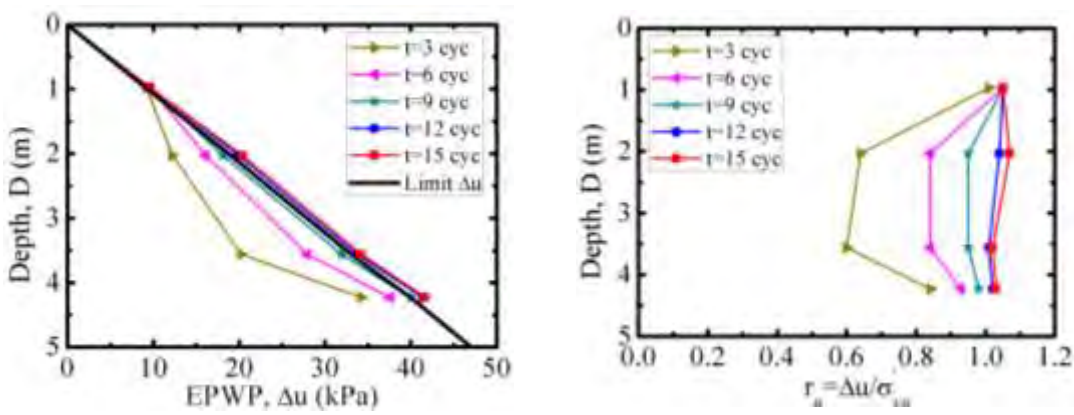

(a) Δu vs D (b) r_u vs D

Fig.E. 21 EPWP profiles of T17 (a_{max}=0.10 g/15 cyc)

E.1.4 Horizontal displacement response

E.1.4.1 T11 and T15-IM4 (a_{max}=0.03 g/5 cyc)

Fig.E. 22(a) and Fig.E. 23(a) plot the time history of horizontal displacement of the soil at selected depths in T11 and T15 (a_{max}=0.03 g/5 cyc). Fig.E. 22(b) and (c) and Fig.E. 23(b) and (c) plot the time history of relative horizontal displacement of the soil at selected depths in T11 and

T15.

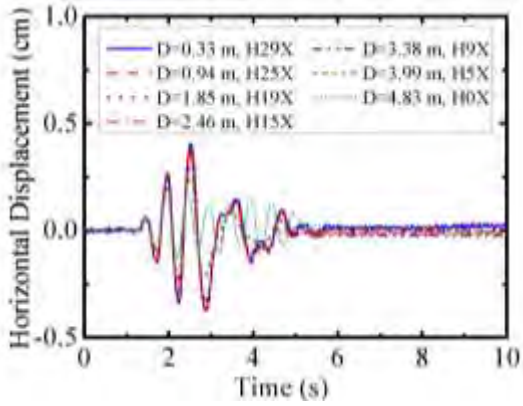

(a) Horizontal displacement

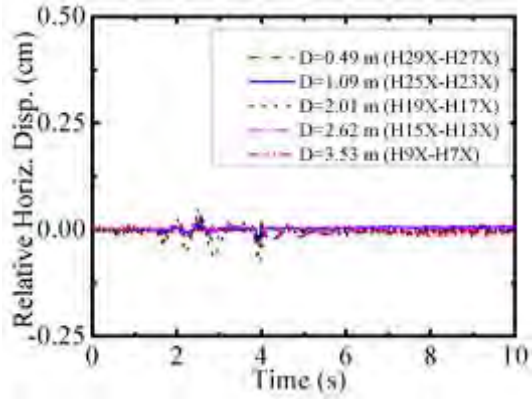

(b) Relative horiz. disp. b/w every other ring

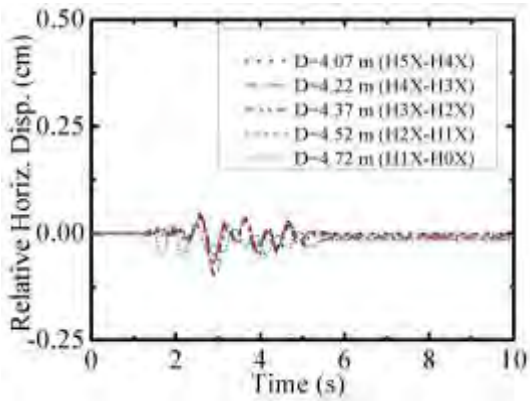

(c) Relative horiz. disp. b/w every ring

Fig.E. 22 Time history of horizontal displacement of T11 (a_{max}=0.03 g/5 cyc)

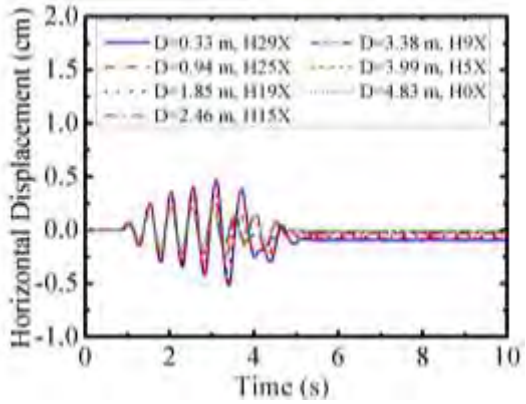

(a) Horizontal displacement

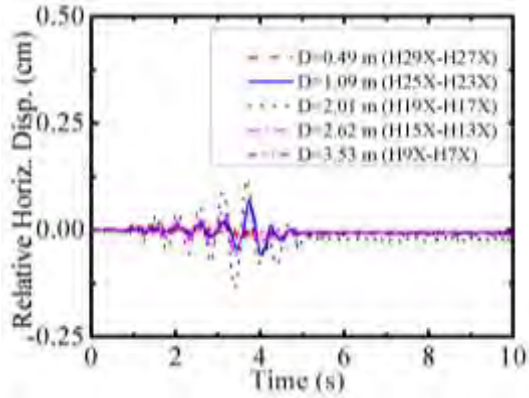

(b) Relative horiz. disp. b/w every other ring

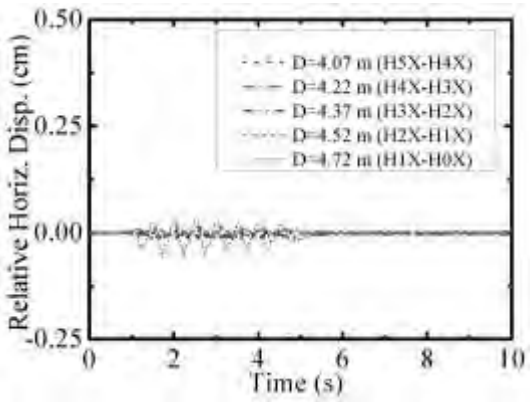

(c) Relative horiz. disp. b/w every ring

Fig.E. 23 Time history of horizontal displacement of T15 (a_{max}=0.03 g/5 cyc)

E.1.4.2 T16-IM2 (a_{max}=0.03 g/15 cyc)

Fig.E. 24(a) plots the time history of horizontal displacement of the soil at selected depths in T16 (a_{max}=0.03 g/15 cyc). Fig.E. 24(b) and (c) plot the time history of relative horizontal displacement of the soil at selected depths in T16.

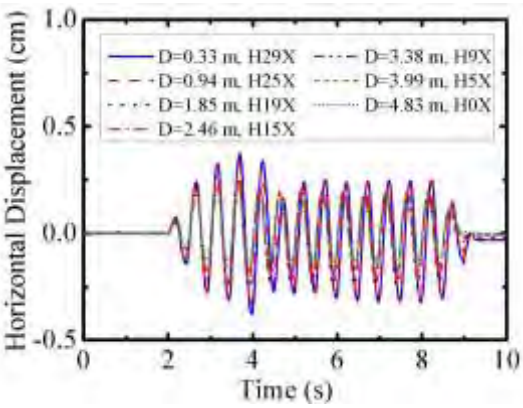

(a) Horizontal displacement

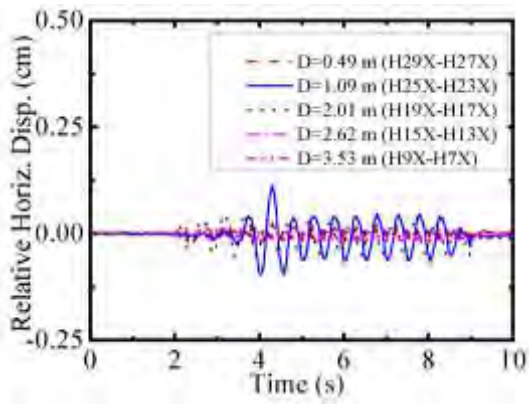

(b) Relative horiz. disp. b/w every other ring

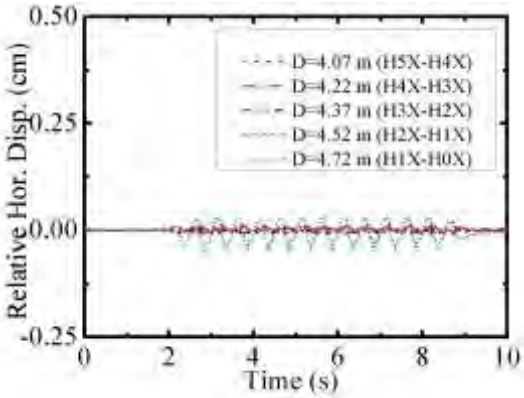

(c) Relative horiz. disp. b/w every ring

Fig.E. 24 Time history of horizontal displacement of T16 (a_{max}=0.03 g/15 cyc)

E.1.4.3 T17-IM3 (a_{max}=0.10 g/15 cyc)

Fig.E. 25(a) plots the time history of horizontal displacement of the soil at selected depths in T17 (a_{max}=0.10 g/15 cyc). Fig.E. 25(b) and (c) plot the time history of relative horizontal displacement of the soil at selected depths in T17.

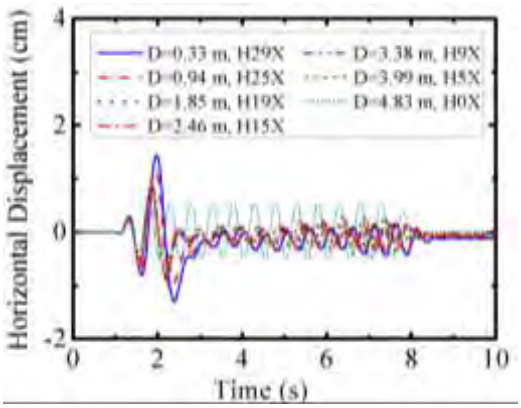

(a) Horizontal displacement

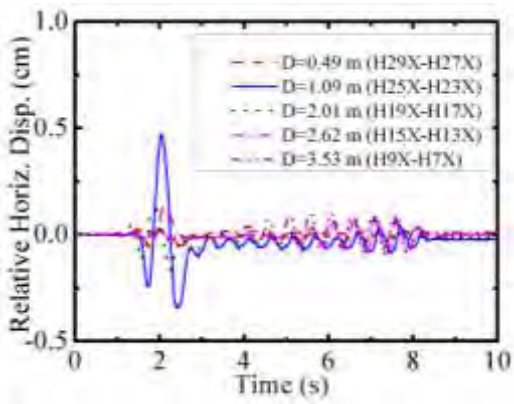

(b) Relative horiz. disp. b/w every other ring

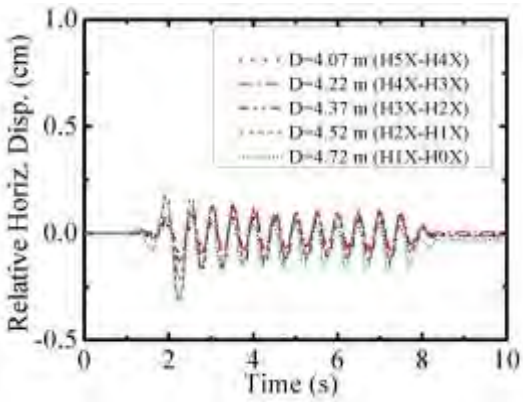

(c) Relative horiz. disp. b/w every ring

Fig.E. 25 Time history of horizontal displacement of T17 (a_{max}=0.10 g/15 cyc)

E.1.5 Ground settlement response

Fig.E. 26 plots the time history of incremental ground settlement in shaking series 3 while Table E. 1 summarizes the incremental and total ground settlement of liquefaction tests in shaking series 3. The average incremental settlement of each liquefaction test is based on the incremental settlement of V1 and V3 because V2 was buried in the soil after T2.

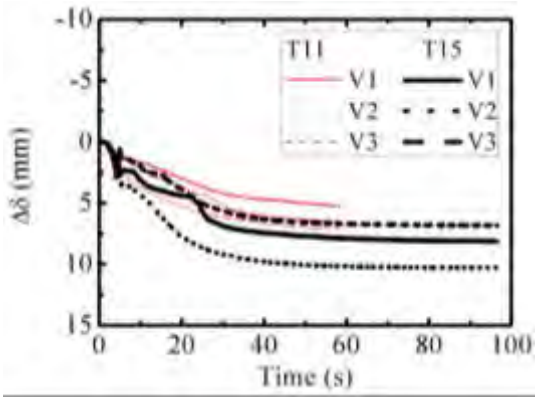

(a) T11 and T15 (a_{max}=0.03 g/5 cyc)

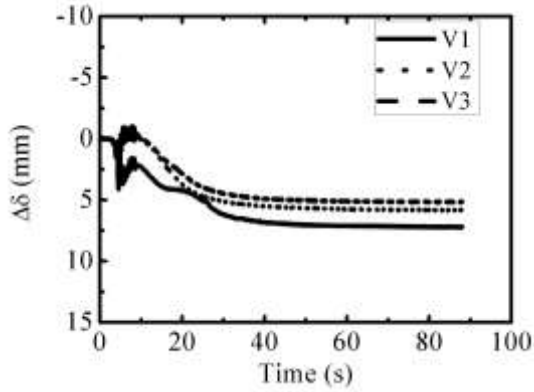

(b) T16 (a_{max}=0.03 g/15 cyc)

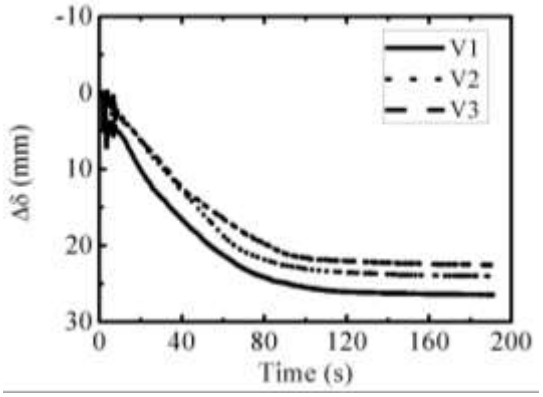

(c) T17 (a_{max}=0.10 g/15 cyc)

Fig.E. 26 Time history of incremental ground settlement in shaking series 3

Table E. 1 Ground settlement of liquefaction tests-shaking series 3

Shaking series	Shaking event	Input Motion	Δδ for each shaking test			$\Delta\delta_{ave.}$	Cumulative Settlement δ
			V1	V2	V3		
			(mm)	(mm)	(mm)	(mm)	(mm)
3	T11	IM4 (a_{max}=0.03 g/5 cyc)	5	7	7	6	251
	T12	IM4 (a_{max}=0.03 g/5 cyc)	5	5	5	5	256
	T13	IM4 (a_{max}=0.03 g/5 cyc)	5	5	5	5	261
	T14	IM4 (a_{max}=0.03 g/5 cyc)	5	5	4	5	265
	T15	IM4 (a_{max}=0.03 g/5 cyc)	8	10	7	8	273
	T16	IM2 (a_{max}=0.03 g/15 cyc)	7	6	5	6	279
	T17	IM3 (a_{max}=0.10 g/15 cyc)	27	24	23	25	304

E.1.6 Stress-strain response

E.1.6.2 T11 and T15-IM4 (a_{max}=0.03 g/5 cyc)

The time history of shear stress of the soil at different depths in T11 and T15 (a_{max}=0.03 g/5 cyc) is plotted in Fig.E. 27. Fig.E. 28 shows the time history of shear strain of the soil at different depths in T11 and T15.

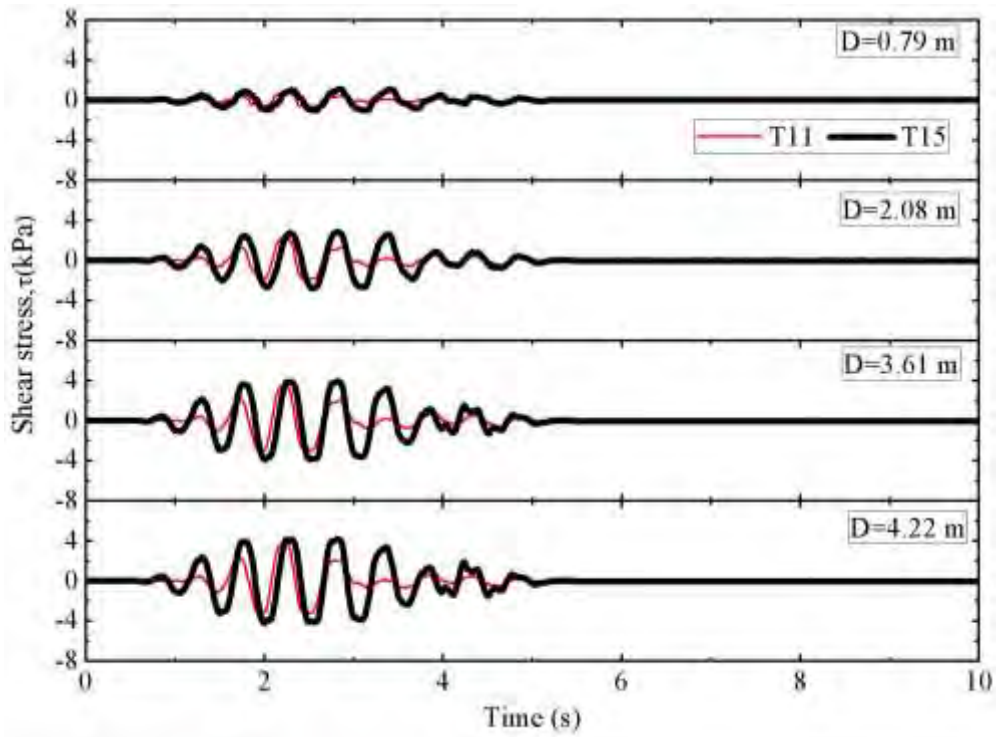

(a) Shear stress

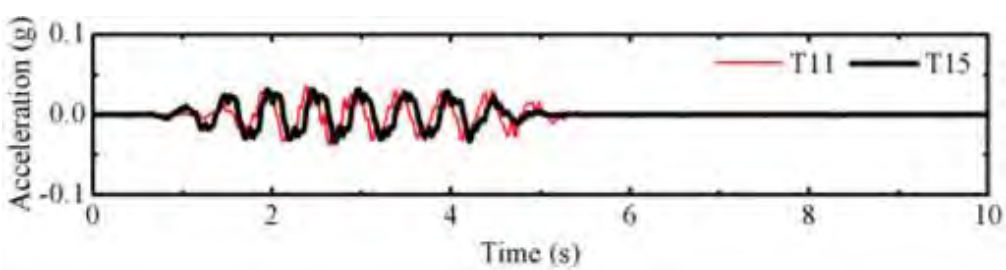

(b) B3X

Fig.E. 27 Time history of shear stress of T11 and T15 (a_{max}=0.03 g/5 cyc)

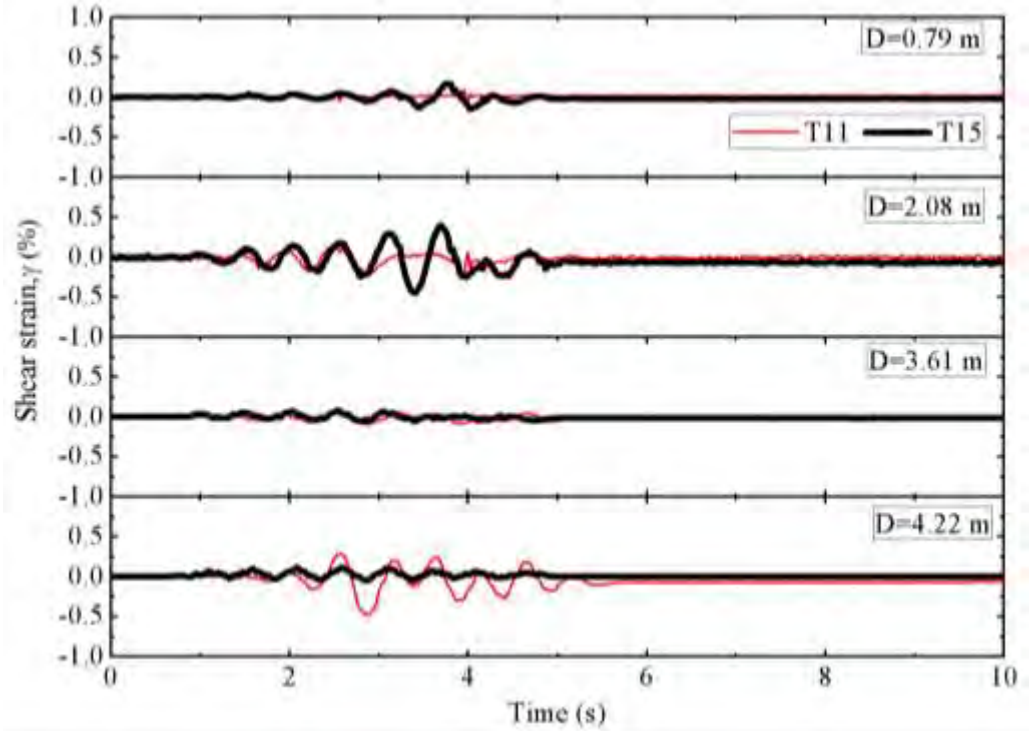

(a) Shear strain

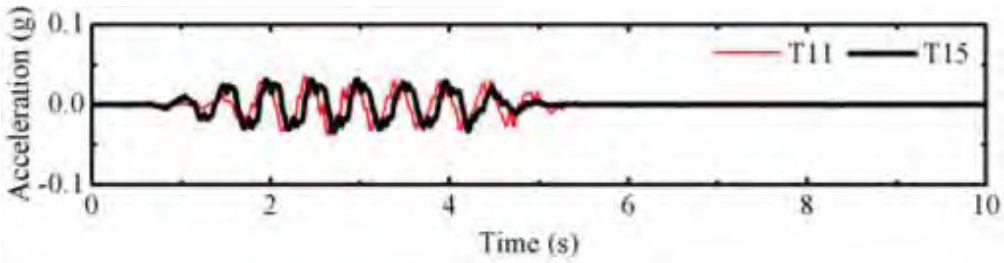

(b) B3X

Fig.E. 28 Time history of shear strain of T11 and T15 (a_{max}=0.03 g/5 cyc)

Based on Fig.E. 27 and Fig.E. 28, the shear stress-strain response of soil at different depths in T11 and T15 are plotted in Fig.E. 29 and Fig.E. 30, respectively.

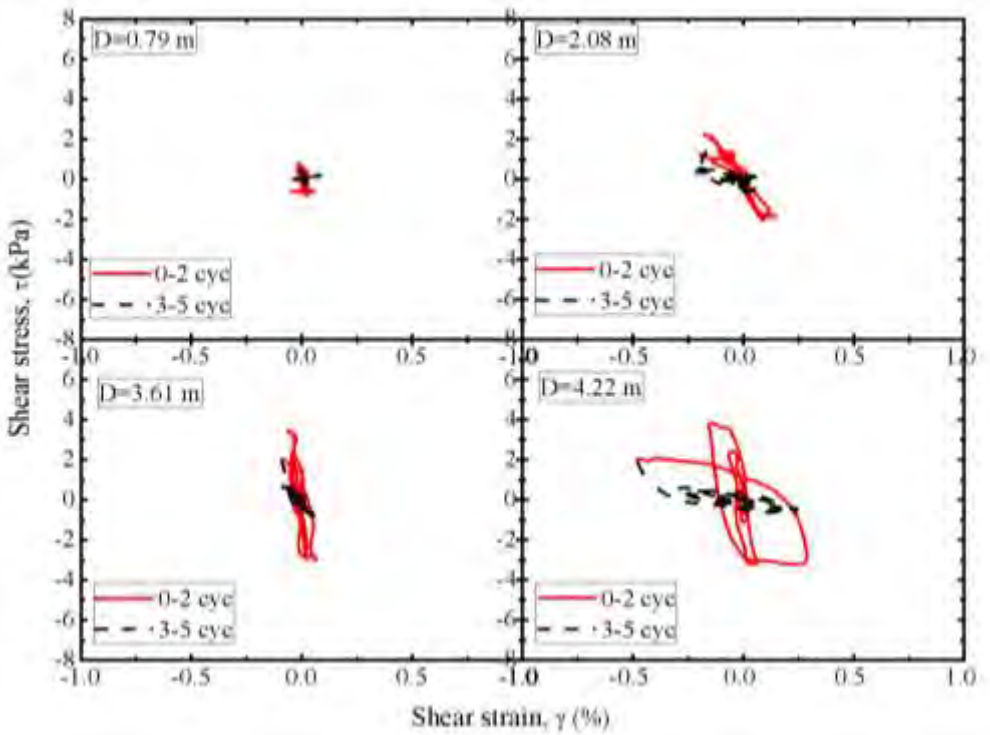

Fig.E. 29 Shear stress- strain loop of T11 (a_{max}=0.03 g/5 cyc)

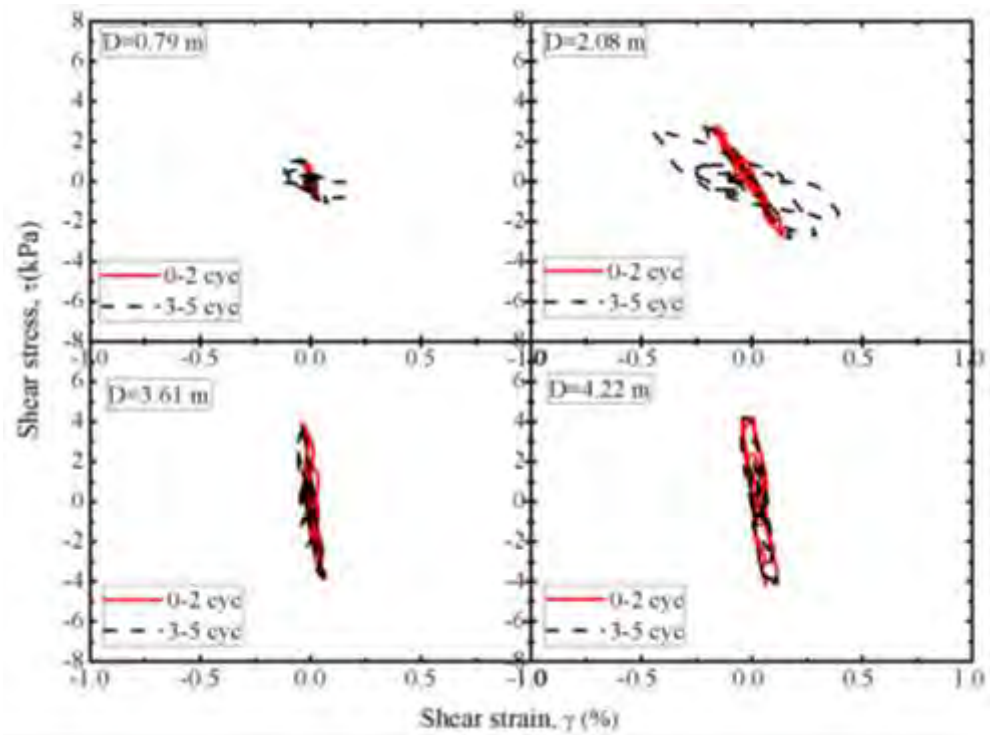

Fig.E. 30 Shear stress- strain loop of T15 (a_{max}=0.03 g/5 cyc)

E.1.6.2 T16-IM2 (a_{max}=0.03 g/15 cyc)

The time history of shear stress of the soil at different depths in T16 (a_{max}=0.03 g/15 cyc) is

plotted in Fig.E. 31. Fig.E. 32 shows the time history of shear strain of the soil at different depths in T16. Based on Fig.E. 31 and Fig.E. 32, the shear stress-strain response of the soil at different depths in T16 is plotted in Fig.E. 33.

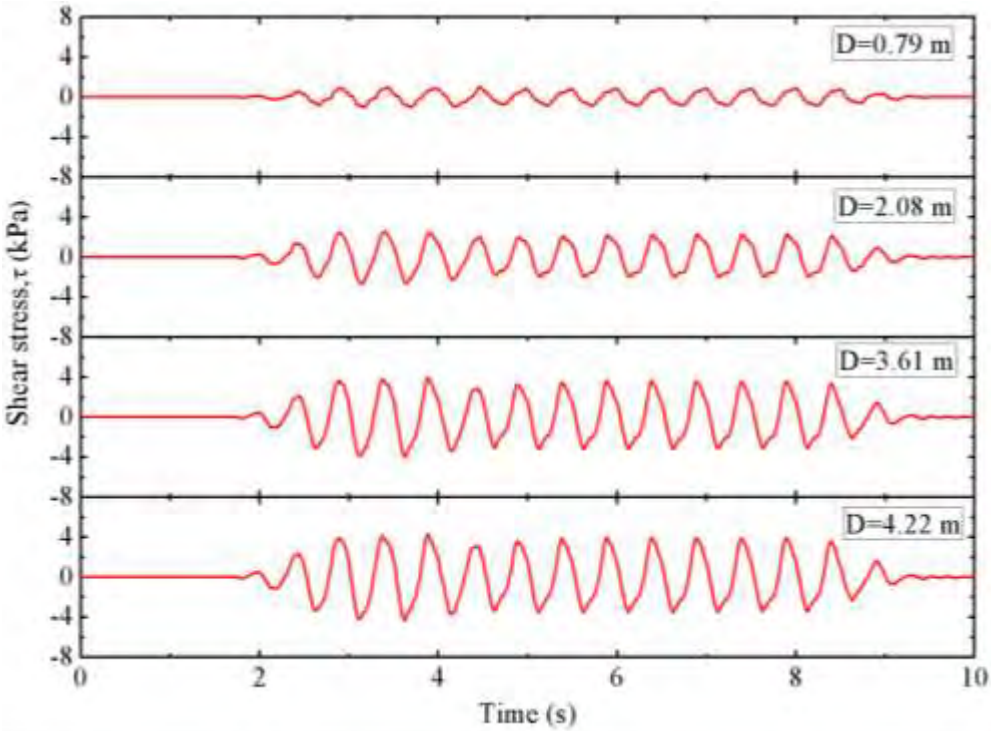

(a) Shear stress

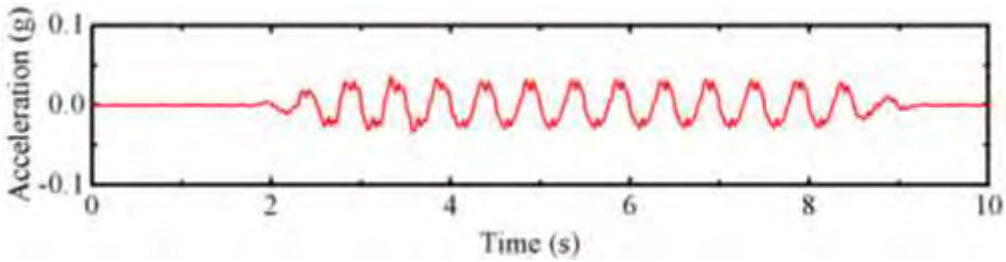

(b) B3X

Fig.E. 31 Time history of shear stress of T16 (a_{max}=0.03 g/15 cyc)

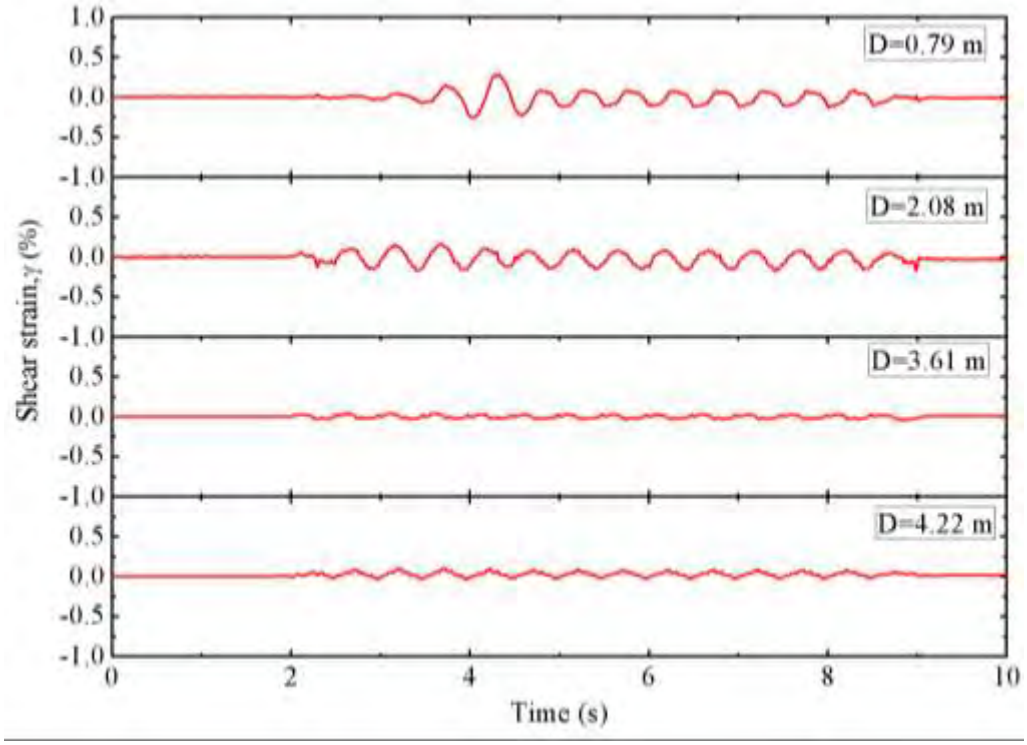

(a) Shear strain

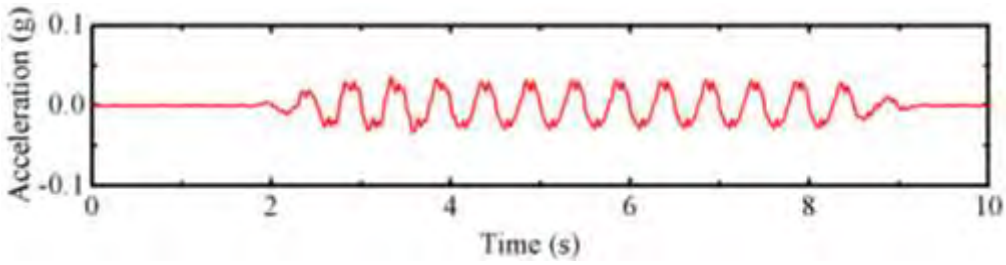

(b) B3X

Fig.E. 32 Time history of shear strain of T16 (a_{max}=0.03 g/15 cyc)

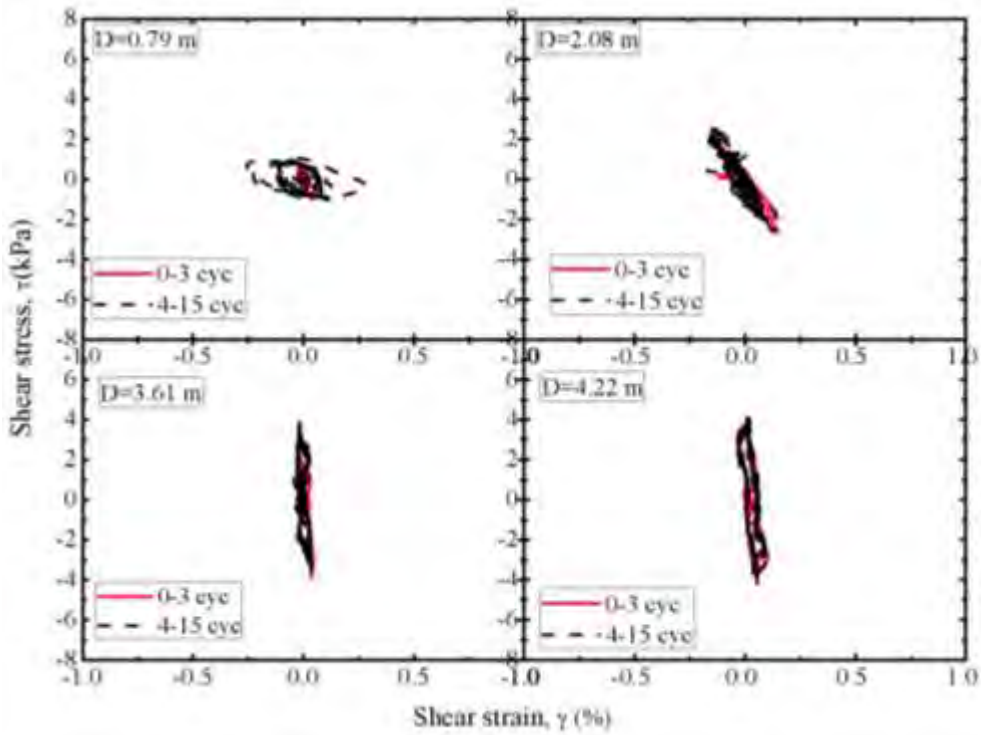

Fig.E. 33 Shear stress- strain loop of T16 (a_{max}=0.03 g/15 cyc)

E.1.6.3 T17-IM3 (a_{max}=0.10 g/15 cyc)

The time history of shear stress of the soil at different depths in T17 (a_{max}=0.10 g/15 cyc) is plotted in Fig.E. 34. Fig.E. 35 shows the time history of shear strain of the soil at different depths in T17. Based on Fig.E. 34 and Fig.E. 35, the shear stress-strain response of the soil at different depths in T17 is plotted in Fig.E. 36.

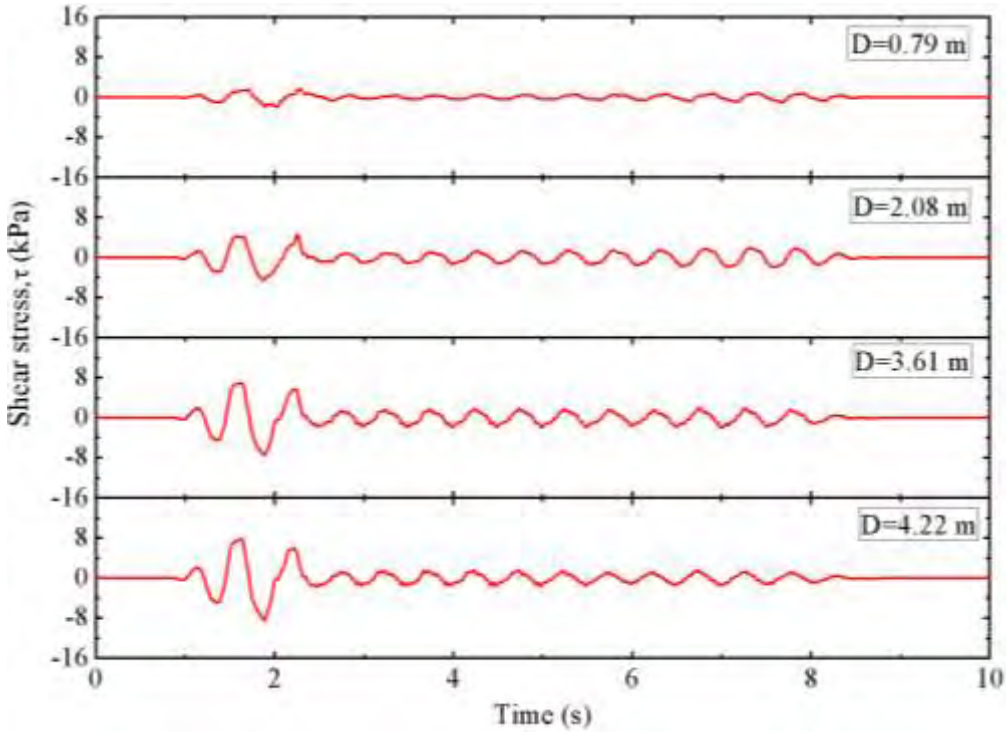

(a) Shear stress

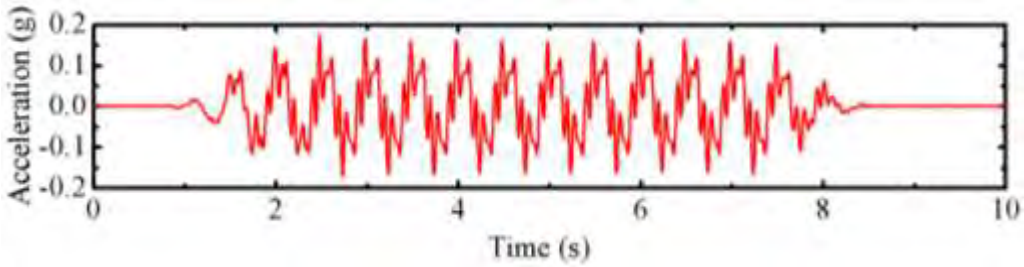

(b) B3X

Fig.E. 34 Time history of shear stress of T17 (a_{max}=0.10 g/15 cyc)

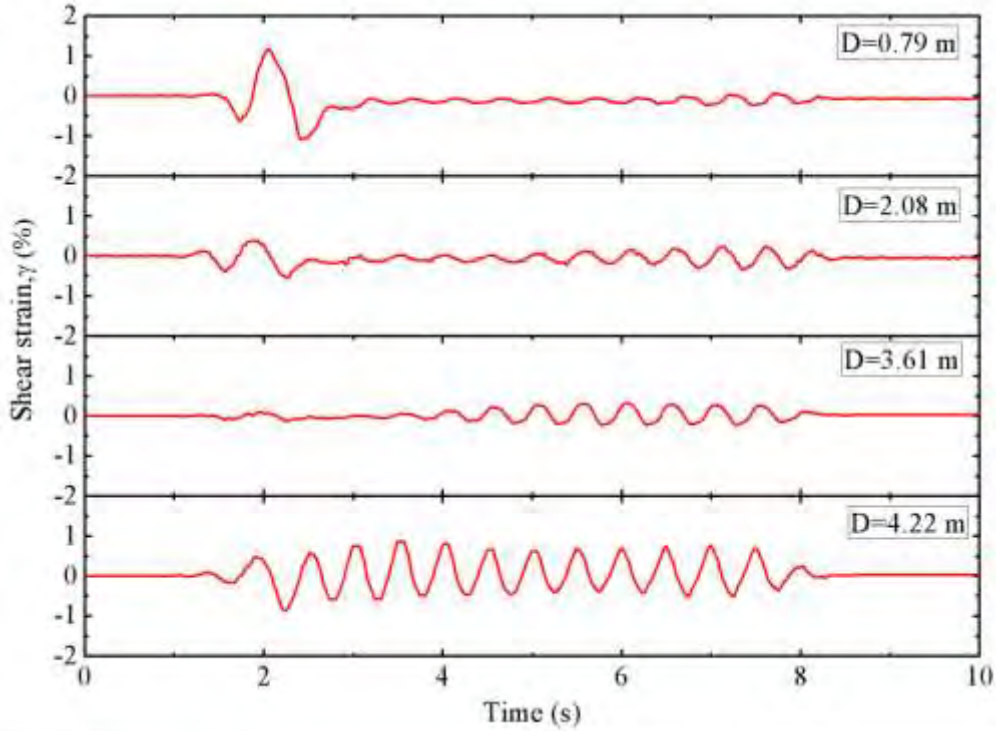

(a) Shear strain

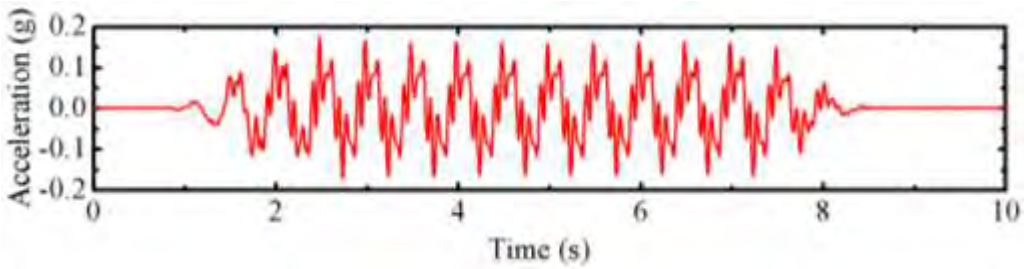

(b) B3X

Fig.E. 35 Time history of shear strain of T17 (a_{max}=0.10 g/15 cyc)

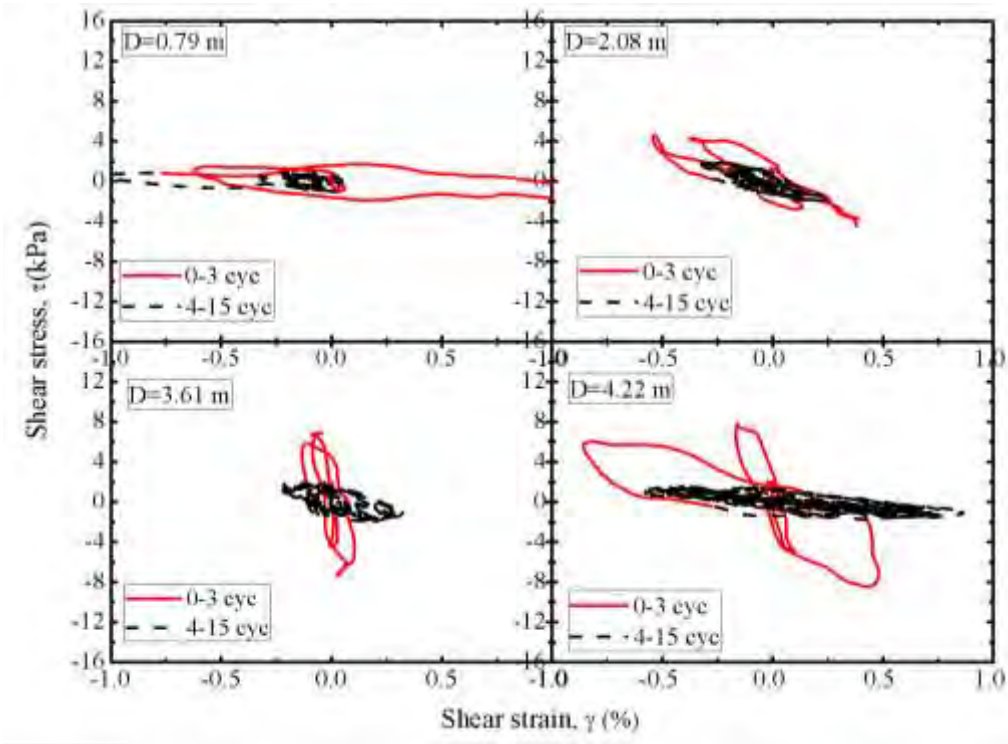

Fig.E. 36 Shear stress- strain loop of T17 (a_{max}=0.10 g/15 cyc)

E.2 Liquefaction tests-shaking series 4

This shaking series consists of T18a (IM1), T18 through T22 (IM4), T23 (IM2) and T24 (IM3)-refer to Fig. 7.24 and Table 7.8 for details. Only T23 and T24 are presented in this section.

E.2.1 Base shaker

E.2.1.1 T23-IM2 (a_{max}=0.03 g/15 cyc)

Fig.E. 37 compares the recorded base acceleration at different locations for both x-(shaking) and y-(non-shaking) direction of T23 (a_{max}=0.03 g/15 cyc).

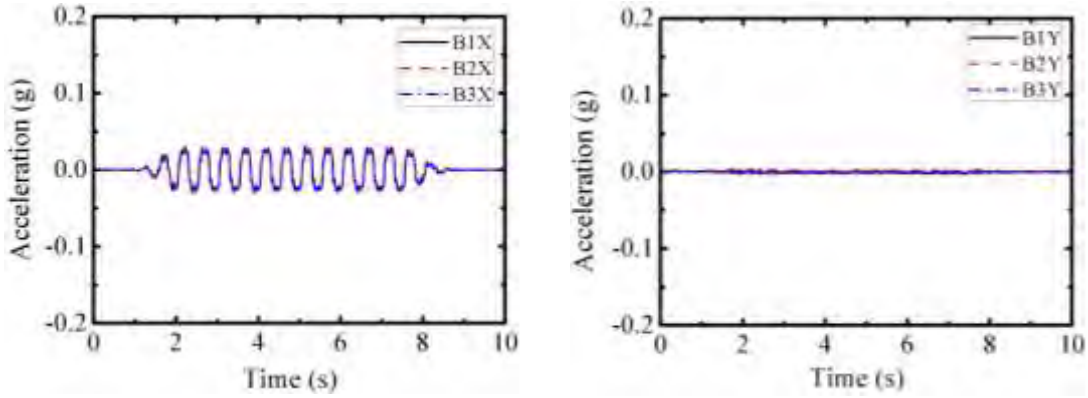

(a) x-direction (b) y-direction

Fig.E. 37 Base shaker of T23 (a_{max}=0.03 g/15 cyc)

E.2.1.2 T24-IM3 (a_{max}=0.10 g/15 cyc)

Fig.E. 38 compares the recorded base acceleration at different locations for both x-(shaking) and y-(non-shaking) direction of T24 (a_{max}=0.10 g/15 cyc).

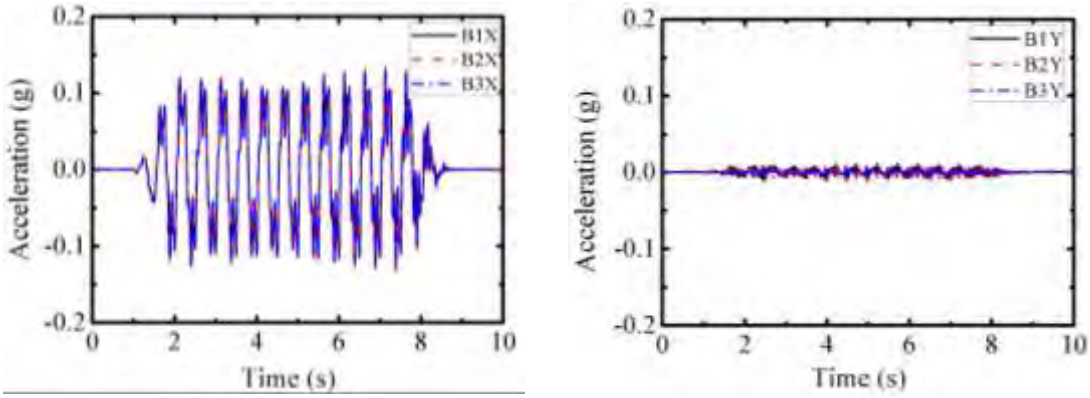

(a) x-direction (b) y-direction

Fig.E. 38 Base shaker of T24 (a_{max}=0.10 g/15 cyc)

E.2.2 Acceleration response

E.2.2.1 T23-IM2 (a_{max}=0.03 g/15 cyc)

Fig.E. 39 compares the acceleration from selected accelerometers as the base motion of T23 (a_{max}=0.03 g/15 cyc) is input. It is noticed that the accelerometer located at laminate 27 instead of laminate 30 is extracted to be the surface acceleration recorder because of post liquefaction densification of soil after series of shaking. The amplification factor of soil at different depths is

shown in Fig.E. 40.

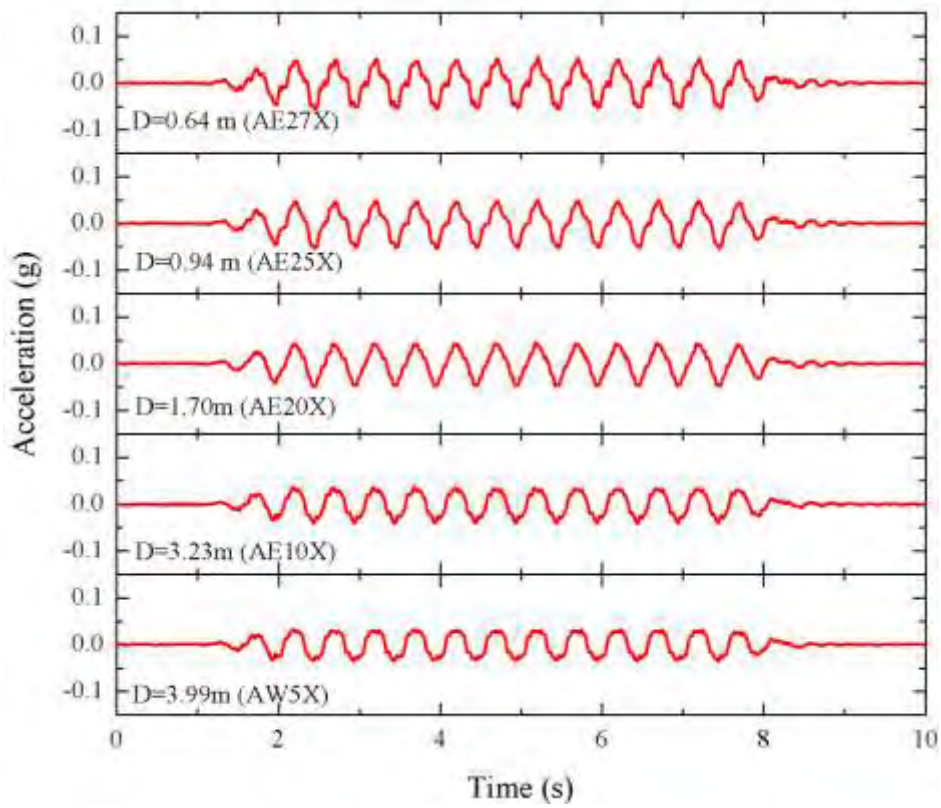

(a) Laminate acceleration

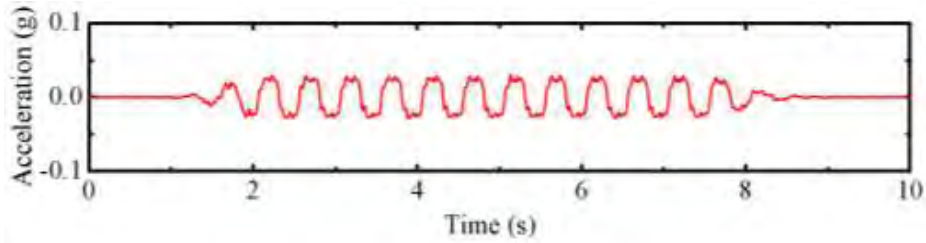

(b) B3X

Fig.E. 39 x-acceleration at different depths and base of T23 (a_{max}=0.03g/15 cyc)

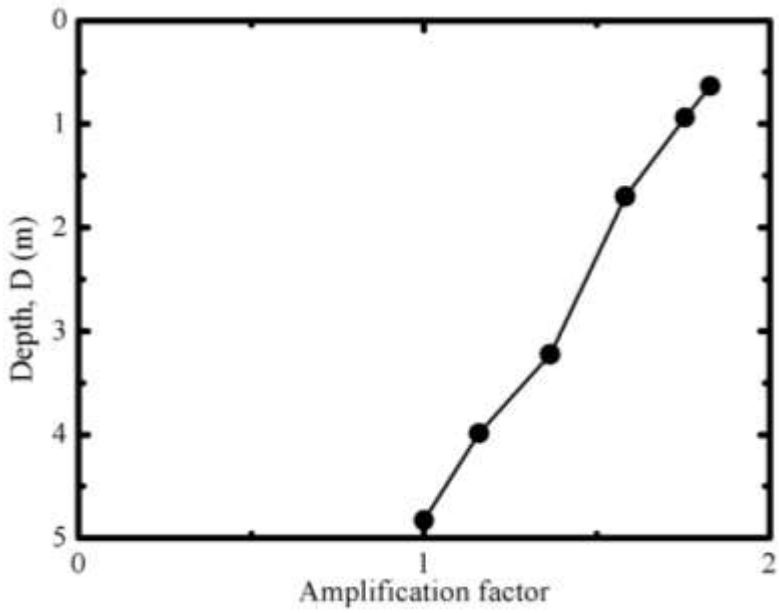

Fig.E. 40 Amplification factor profile of T23 (a_{max}=0.03 g/15 cyc)

E.2.2.2 T24-IM3 (a_{max}=0.10 g/15 cyc)

Fig.E. 41compares the acceleration from selected accelerometers as the base motion of T24 (a_{max}=0.10 g/15 cyc) is input. It is noticed that the accelerometer located at laminate 27 instead of laminate 30 is extracted to be the surface acceleration recorder because of post liquefaction densification of soil after series of shaking. The amplification factor of soil at different depths is shown in Fig.E. 42.

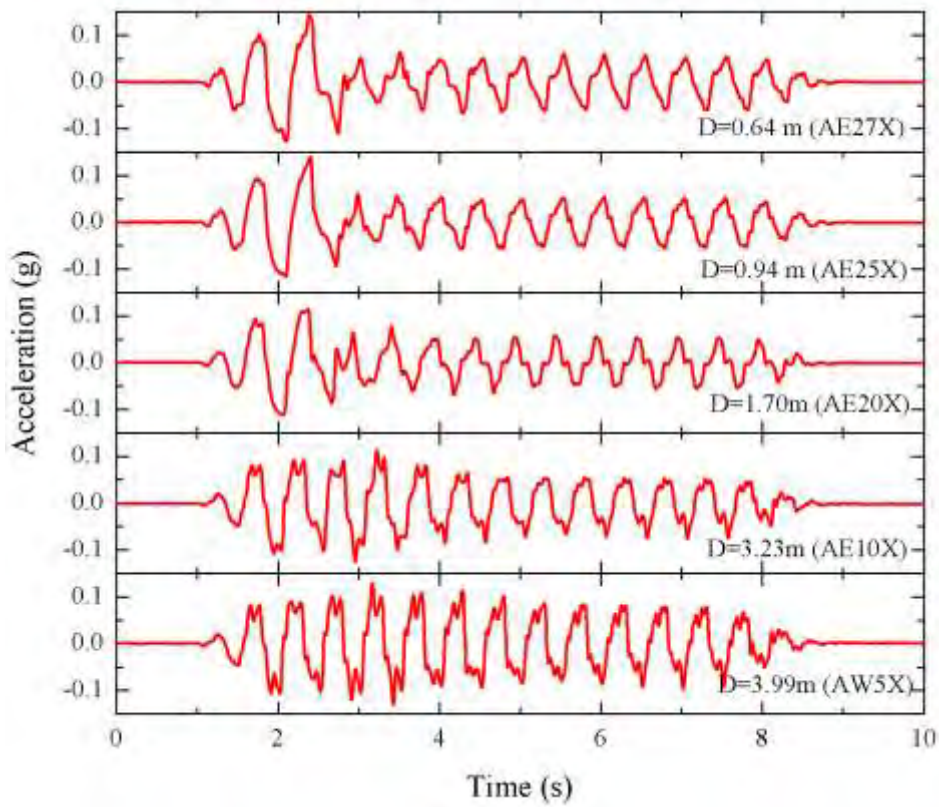

(a) Laminate acceleration

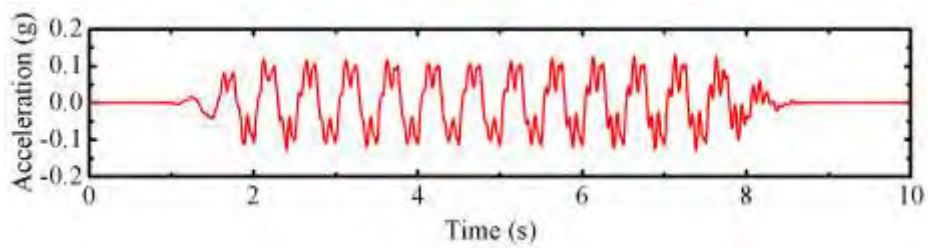

(b) B3X

Fig.E. 41 x-acceleration at different depths and base of T24 (a_{max}=0.10 g/15 cyc)

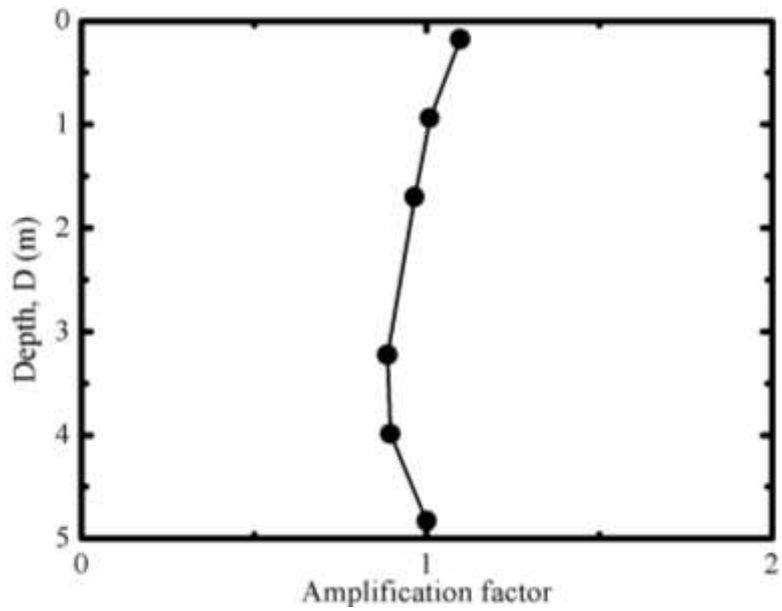

Fig.E. 42 Amplification factor profile of T24 (a_{max}=0.10 g/15 cyc)

E.2.3 Excess pore water pressure (Δu) response

E.2.3.1 T23-IM2 (a_{max}=0.03 g/15 cyc)

Fig.E. 43 presents the time history of normalized excess pore water pressure r_u and base acceleration during shaking of T23 (a_{max}=0.03 g/15 cyc), to better observe whether and when liquefaction occurs (i.e., r_u reaches unity) at different soil depths. Fig.E. 44 shows the time history of the excess pore water pressure (EPWP) Δu of the soil profile recorded by piezometers of T23. Fig.E. 45 plots the Δu as well as r_u with respect to depth at various shaking cycle for T23.

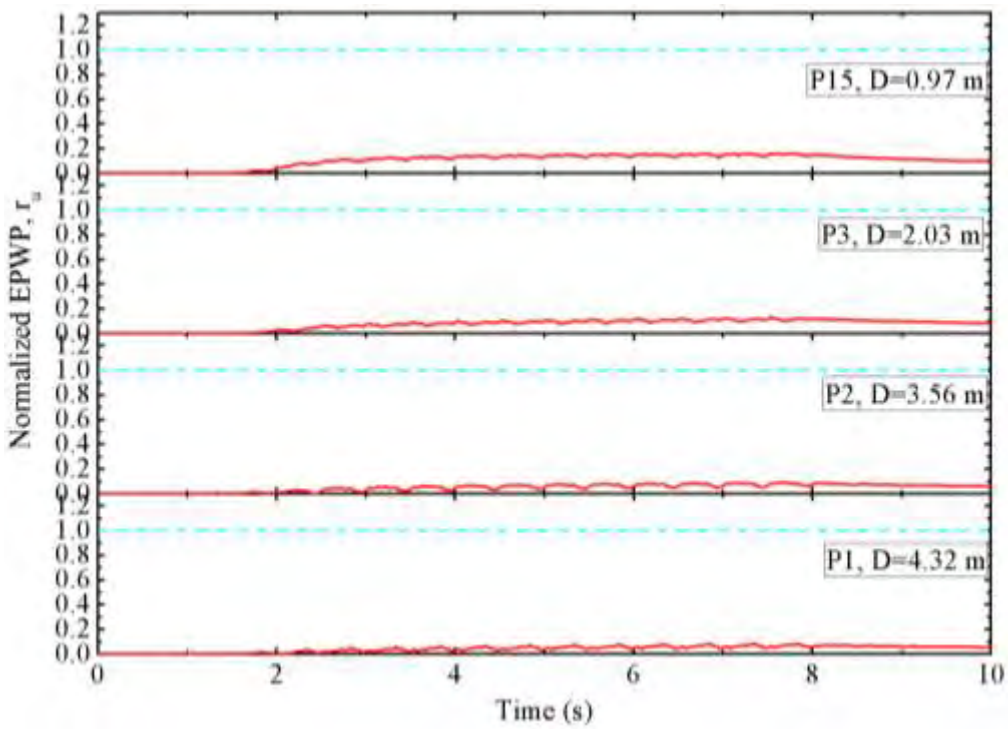

(a) r_u

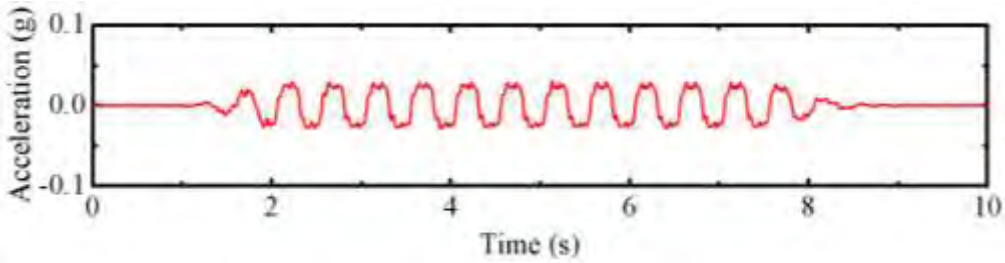

(b) B3X

Fig.E. 43 Time history of r_u and base acceleration of T23 (a_{max}=0.03 g/15 cyc)

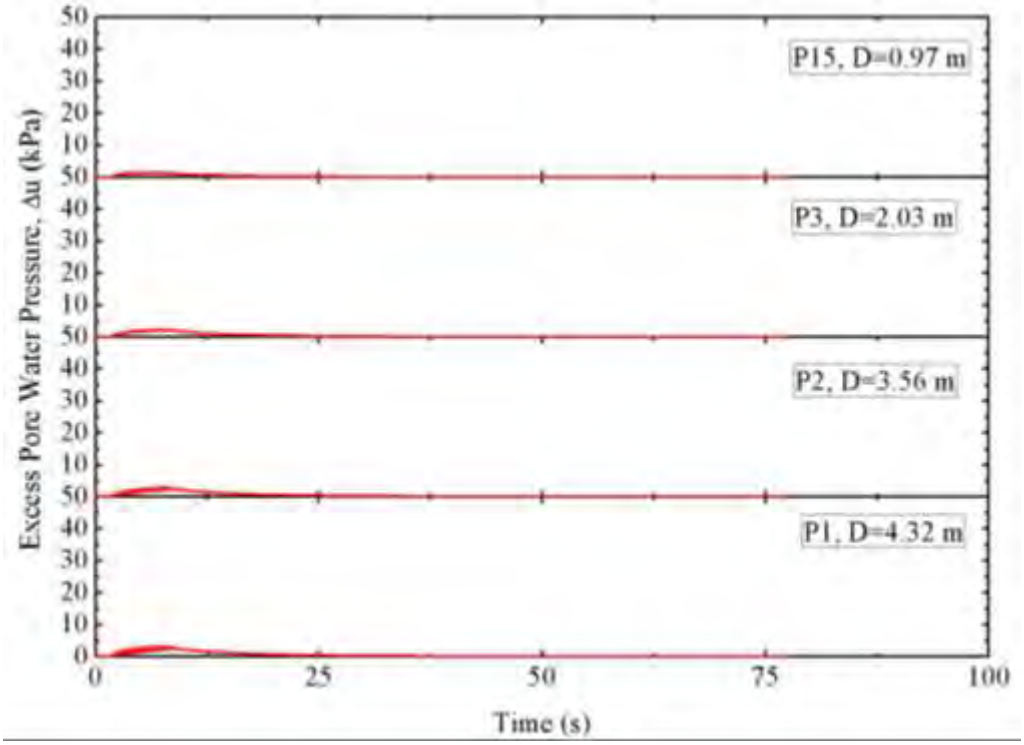

Fig.E. 44 Time history of Δu of T23 (a_{max}=0.03 g/15 cyc)

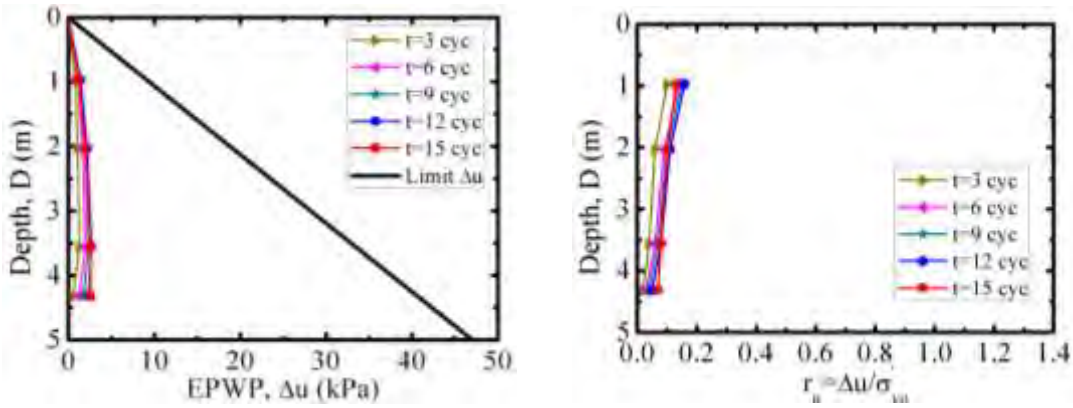

(a) Δu vs D (b) r_u vs D

Fig.E. 45 EPWP profiles of T23 (a_{max}=0.03 g/15 cyc)

E.2.3.2 T24-IM3 (a_{max}=0.10 g/15 cyc)

Fig.E. 46 presents the time history of normalized excess pore water pressure r_u and base acceleration during shaking of T24 (a_{max}=0.10 g/15 cyc), to better observe whether and when liquefaction occurs (i.e., r_u reaches unity) at different soil depths. Fig.E. 47 shows the time history of the excess pore water pressure (EPWP) Δu of the soil profile recorded by piezometers of T24.

Fig.E. 48 plots the Δu as well as r_u with respect to depth at various shaking cycle for T24.

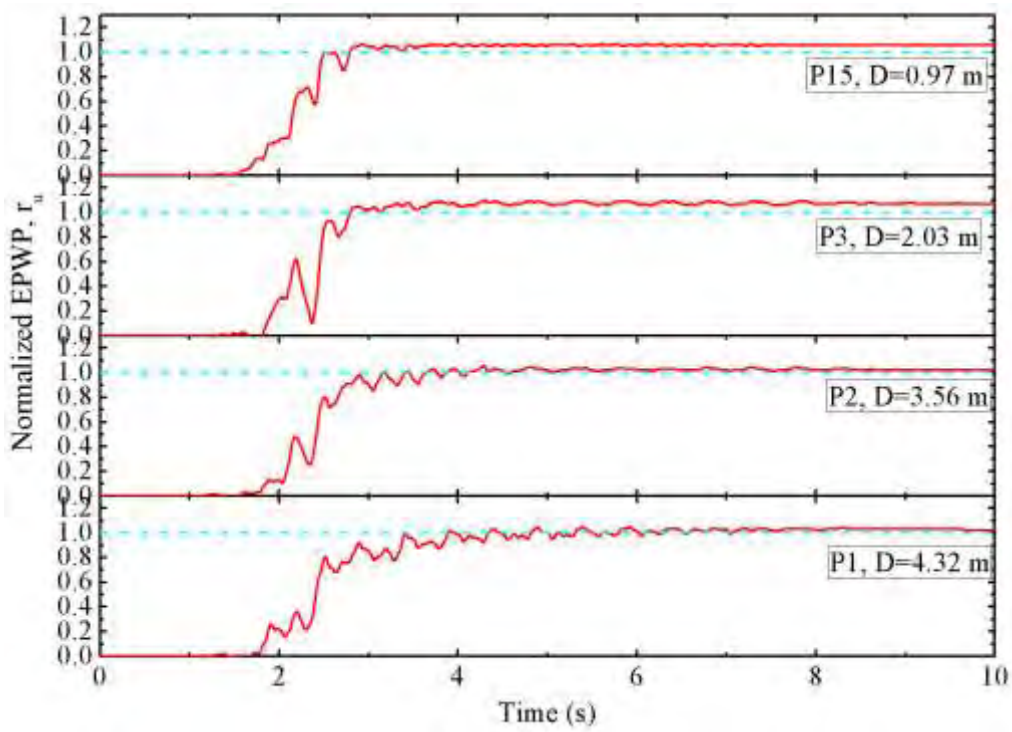

(a) r_u

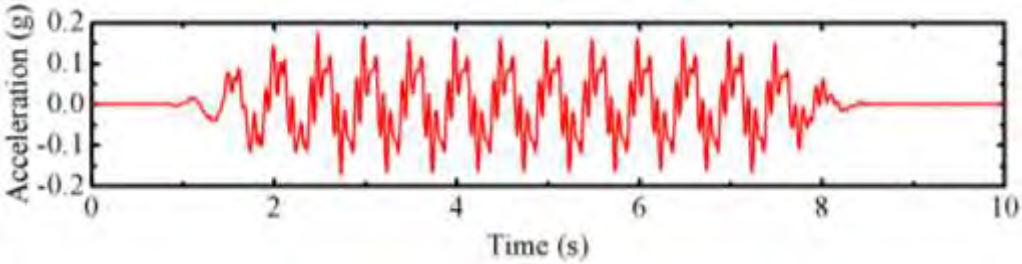

(b) B3X

Fig.E. 46 Time history of r_u and base acceleration of T24 (a_{max}=0.10 g/15 cyc)

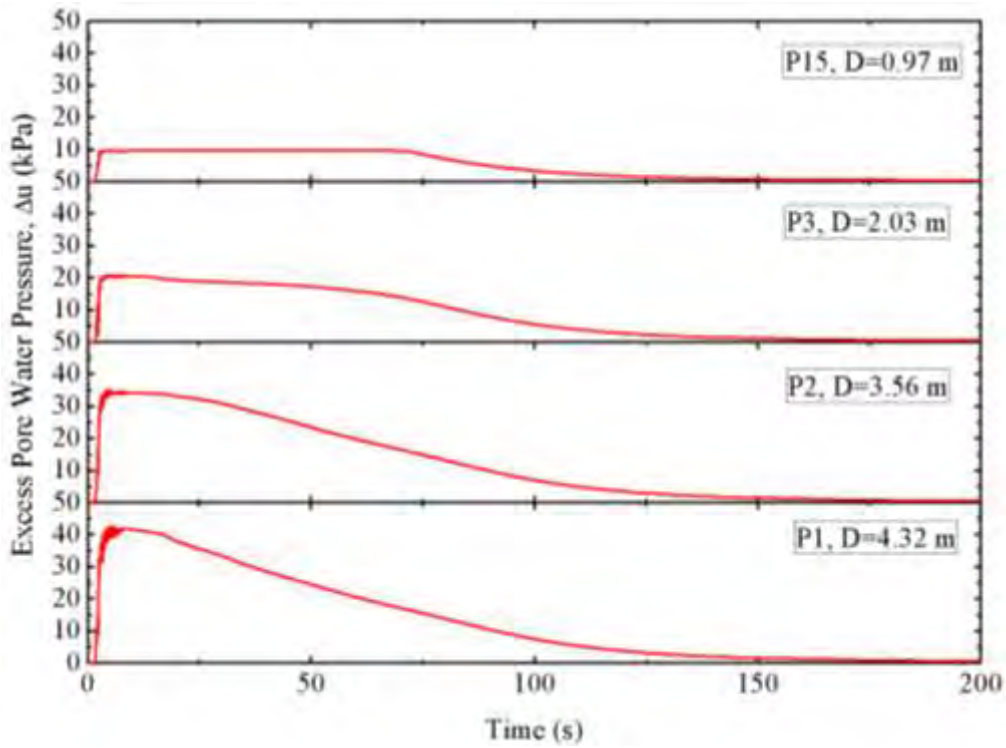

Fig.E. 47 Time history of Δu of T24 (a_{max}=0.10 g/15 cyc)

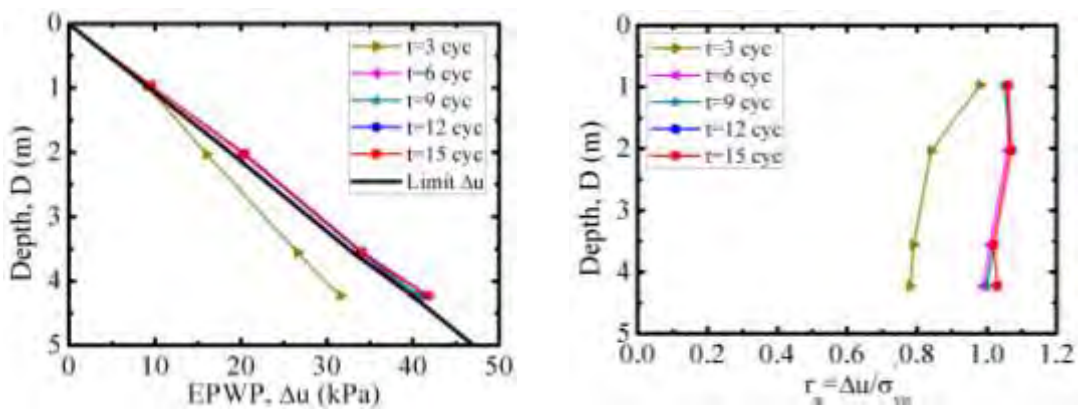

(a) Δu vs D (b) r_u vs D

Fig.E. 48 EPWP profiles of T24 (a_{max}=0.10 g/15 cyc)

E.2.4 Horizontal displacement

E.2.4.1 T23-IM2 (a_{max}=0.03 g/15 cyc)

Fig.E. 49(a) plots the time history of horizontal displacement of the soil at selected depths in T23 (a_{max}=0.03 g/15 cyc). Fig.E. 49(b) and (c) plot the time history of relative horizontal displacement of the soil at selected depths in T23.

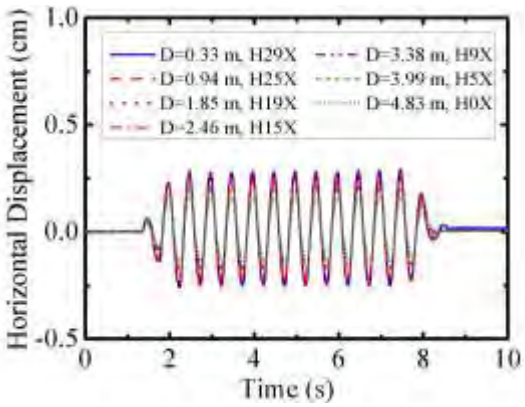

(a) Horizontal displacement

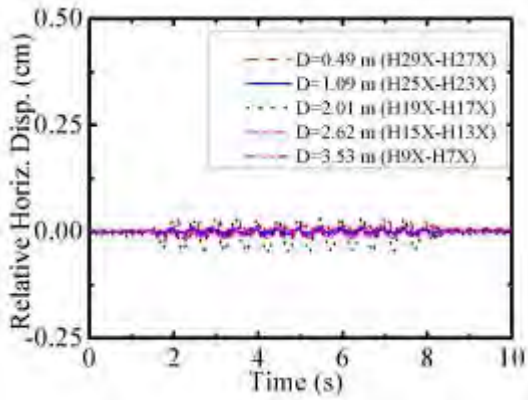

(b) Relative horiz. disp. b/w every other ring

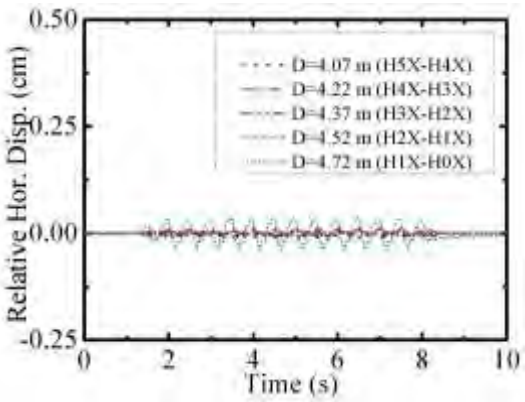

(c) Relative horiz. disp. b/w every ring

Fig.E. 49 Time history of horizontal displacement of T23 (a_{max}=0.03 g/15 cyc)

E.2.4.2 T24-IM3 (a_{max}=0.10 g/15 cyc)

Fig.E. 50(a) plots the time history of horizontal displacement of the soil at selected depths in T24 (a_{max}=0.10 g/15 cyc). Fig.E. 50(b) and (c) plot the time history of relative horizontal displacement of the soil at selected depths in T24.

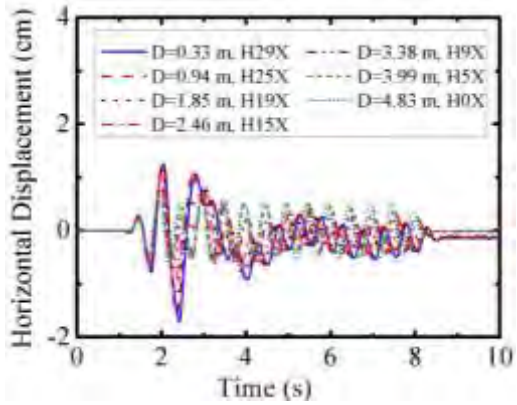

(a) Horizontal displacement

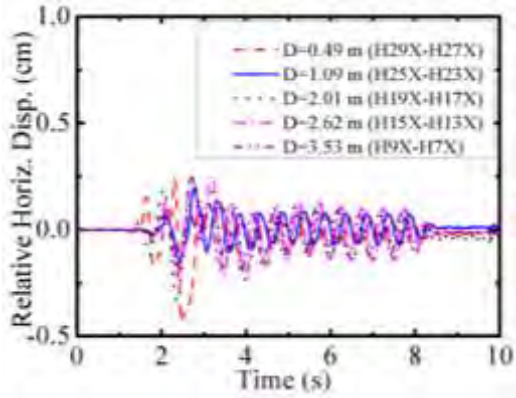

(b) Relative horiz. disp. b/w every other ring

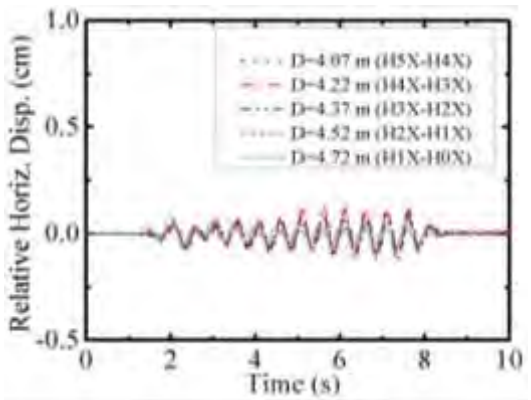

(c) Relative horiz. disp. b/w every ring

Fig.E. 50 Time history of horizontal displacement of T24 (a_{max}=0.10 g/15 cyc)

E.2.5 Ground settlement

Fig.E. 51 plots the time history of incremental ground settlement in shaking series 4 while Table E. 2 summarizes the incremental and total ground settlement of liquefaction tests in shaking series 4. The average incremental settlement of each liquefaction test is based on the incremental settlement of V1 and V3 because V2 was buried in the soil after T2.

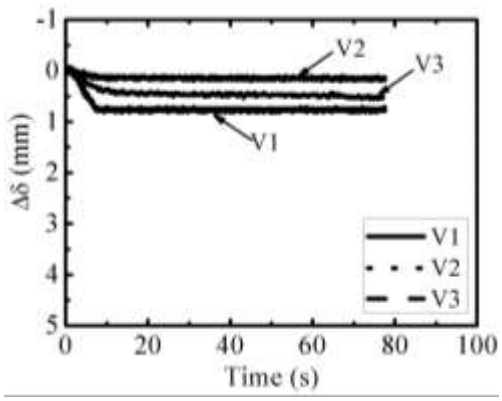

(a) T23 (a_{max}=0.03 g/15 cyc)

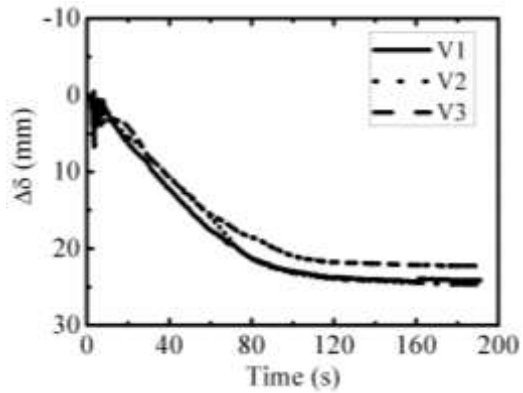

(c) T24 (a_{max}=0.10 g/15 cyc)

Fig.E. 51 Time history of incremental ground settlement in shaking series 4

Table E. 2 Ground settlement of liquefaction tests-shaking series 4

Shaking series	Shaking event	Input Motion	Δδ for each shaking test			$\Delta\delta_{ave.}$	Cumulative Settlement δ
			V1	V2	V3		
			(mm)	(mm)	(mm)	(mm)	(mm)
4	T18a	IM1 (a_{max}=0.015 g/5 cyc)	0	0	0	0	304
	T18	IM4 (a_{max}=0.03 g/5 cyc)	4	4	4	4	308
	T19	IM4 (a_{max}=0.03 g/5 cyc)	4	4	4	4	312
	T20	IM4 (a_{max}=0.03 g/5 cyc)	4	4	4	4	316
	T21	IM4 (a_{max}=0.03 g/5 cyc)	4	4	2	3	319
	T22	IM4 (a_{max}=0.03 g/5 cyc)	1	1	1	1	320
	T23	IM2 (a_{max}=0.03 g/15 cyc)	1	0	1	1	321
	T24	IM3 (a_{max}=0.10 g/15 cyc)	24	25	22	23	344

E.2.6 Stress-strain response

E.2.6.1 T23-IM2 (a_{max}=0.03 g/15 cyc)

The time history of shear stress of the soil at different depths in T23 (a_{max}=0.03 g/15 cyc) is plotted in Fig.E. 52. Fig.E. 53 shows the time history of shear strain of the soil at different depths in T23. The shear stress-strain response of the soil at different depths in T23 is plotted in Fig.E. 54.

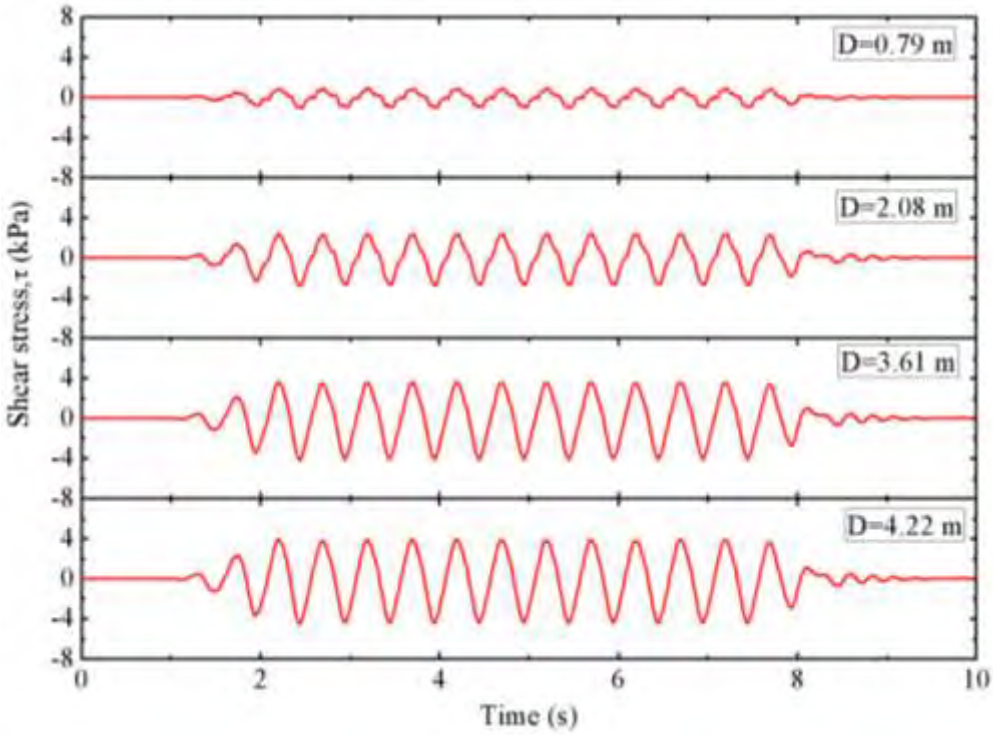

(a) Shear stress

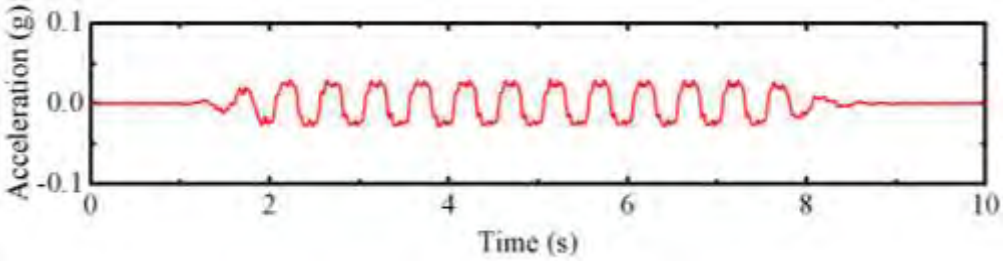

(b) B3X

Fig.E. 52 Time history of shear stress of T23 (a_{max}=0.03 g/15 cyc)

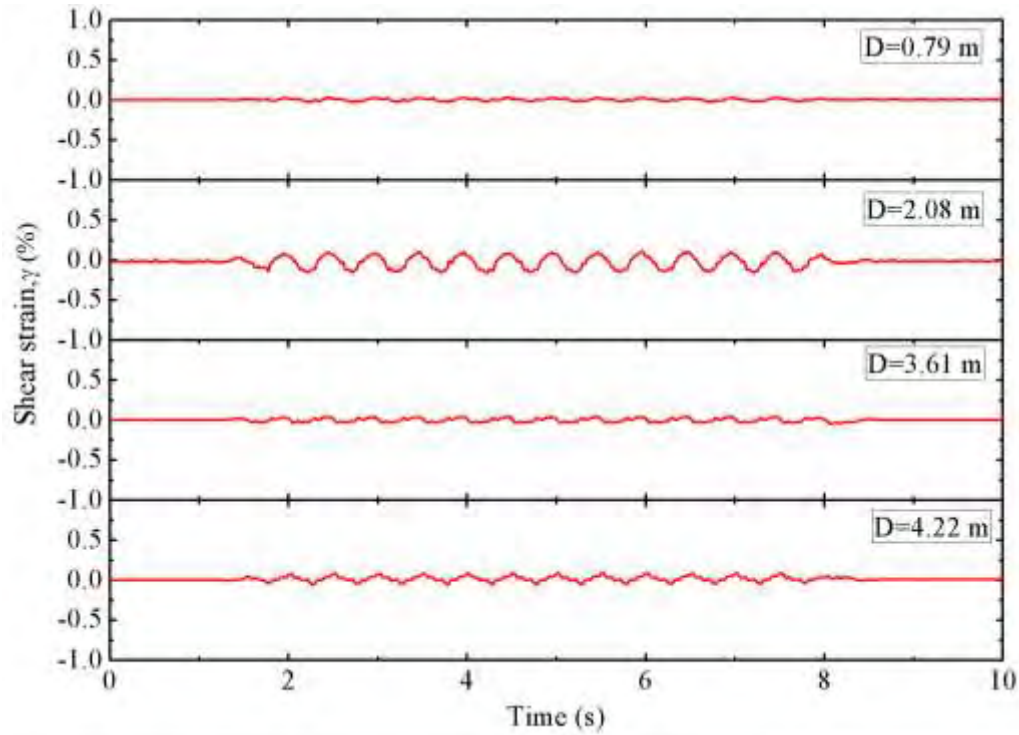

(a) Shear strain

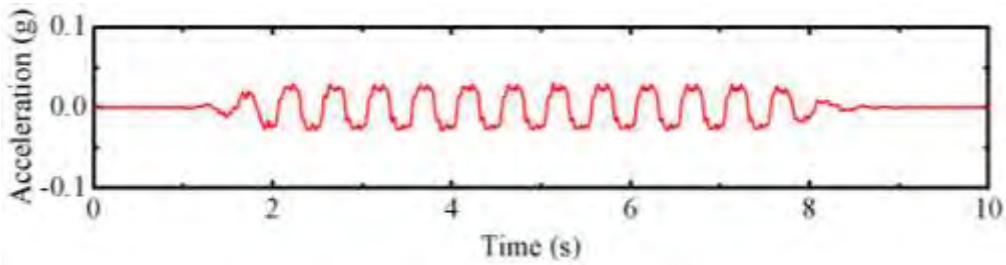

(b) B3X

Fig.E. 53 Time history of shear strain of T23 (a_{max}=0.03 g/15 cyc)

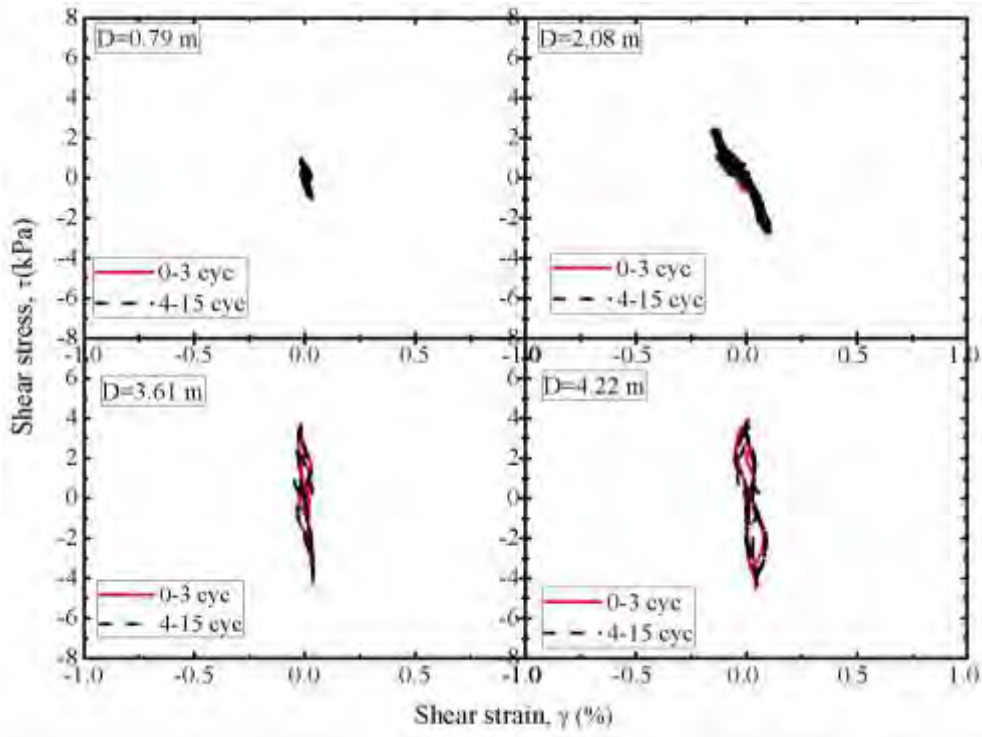

Fig.E. 54 Shear stress- strain loop of T23 (a_{max}=0.03 g/15 cyc)

E.2.6.2 T24-IM3 (a_{max}=0.10 g/15 cyc)

The time history of shear stress of the soil at different depths in T24 (a_{max}=0.10 g/15 cyc) is plotted in Fig.E. 55. Fig.E. 56 shows the time history of shear strain of the soil at different depths in T24. The shear stress-strain response of the soil at different depths in T24 is plotted in Fig.E. 57.

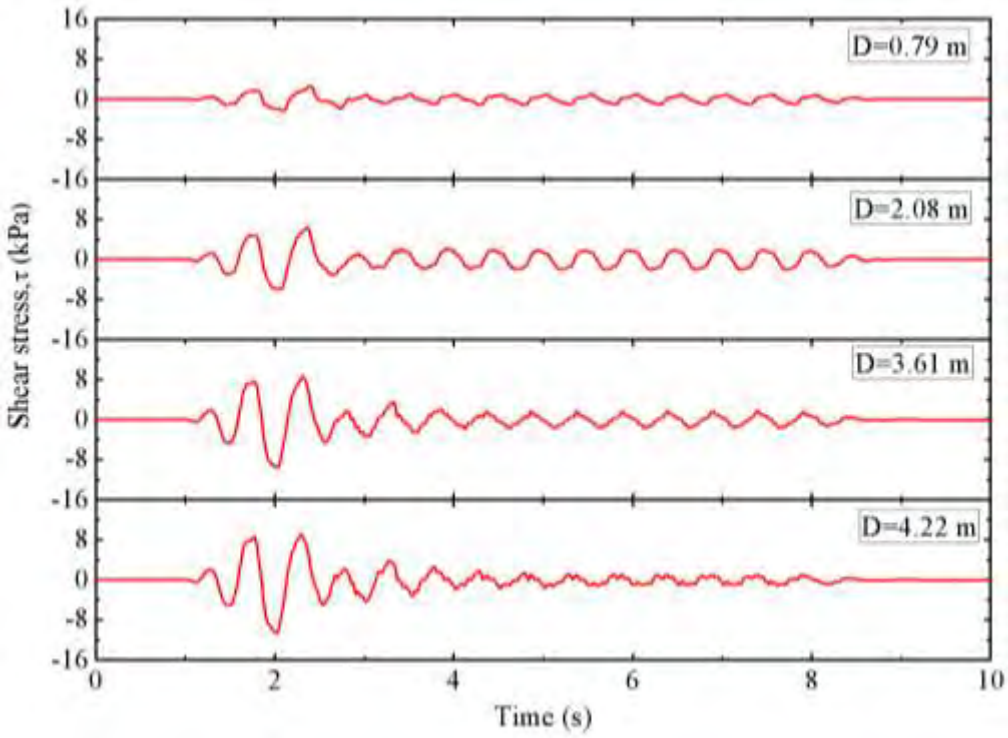

(a) Shear stress

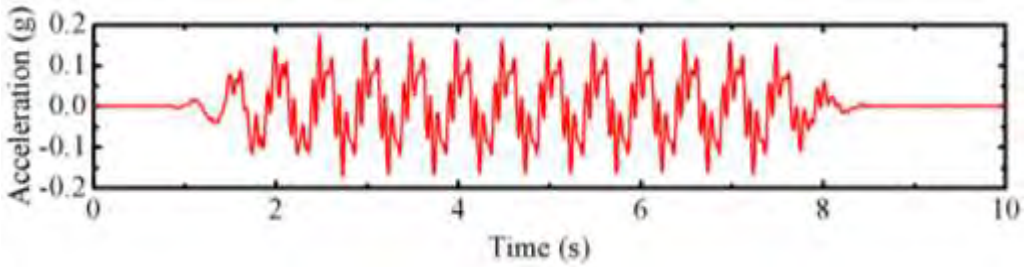

(b) B3X

Fig.E. 55 Time history of shear stress of T24 (a_{max}=0.10 g/15 cyc)

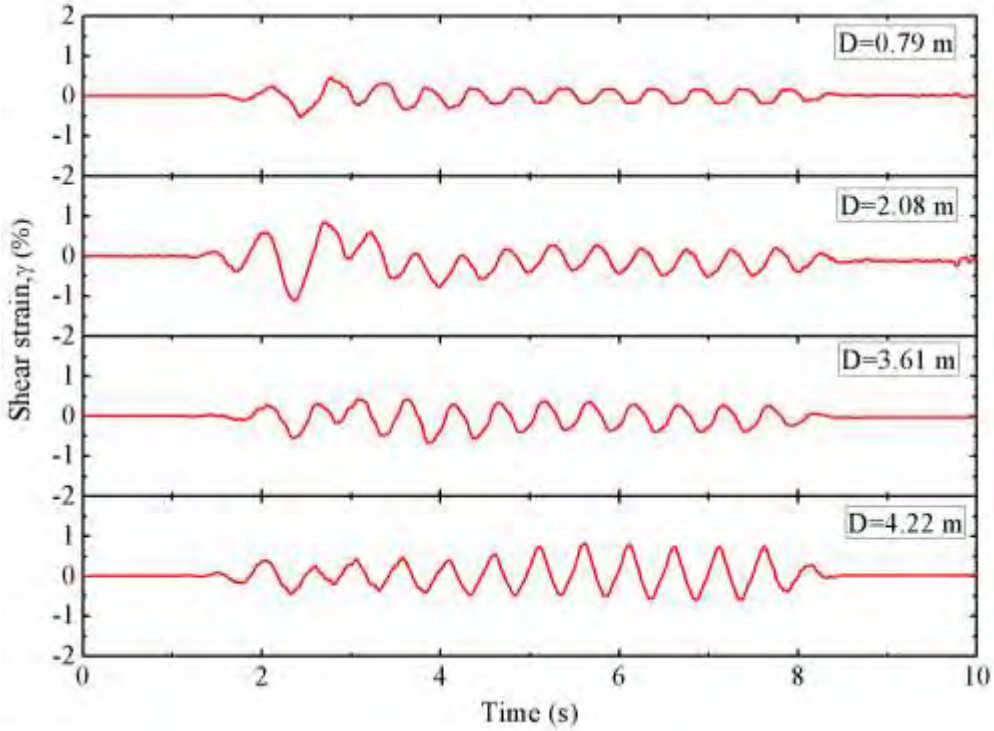

(a) Shear strain

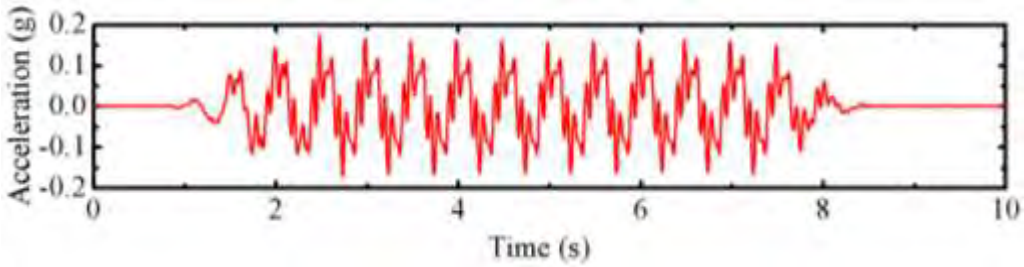

(b) B3X

Fig.E. 56 Time history of shear strain of T24 (a_{max}=0.10 g/15 cyc)

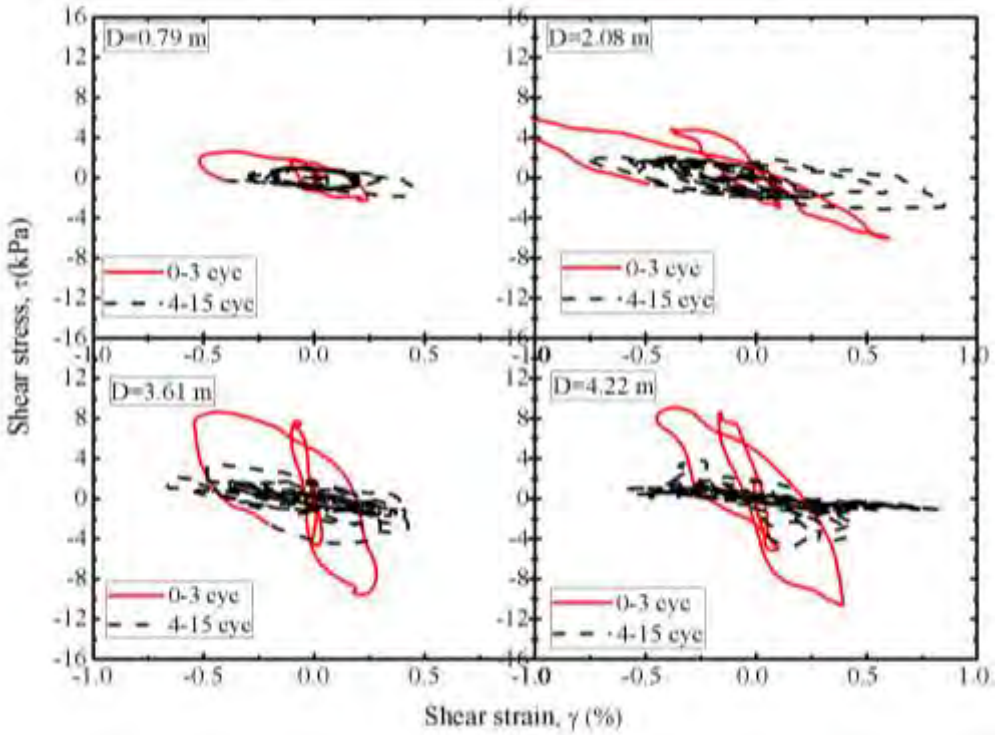

Fig.E. 57 Shear stress- strain loop of T24 (a_{max}=0.10 g/15 cyc)

E.3 Liquefaction tests-shaking series 5

This shaking series consists of T25a (IM1), T25 through T29 (IM4), T30 (IM2) and T31 (IM3)-refer to Fig. 7.24 and Table 7.8 for details. Only T30 and T31 are presented in this section.

E.3.1 Base shaker

E.3.1.1 T30-IM2 (a_{max}=0.03 g/15 cyc)

Fig.E. 58 compares the recorded base acceleration at different locations for both x-(shaking) and y-(non-shaking) direction of T30 (a_{max}=0.03 g/15 cyc).

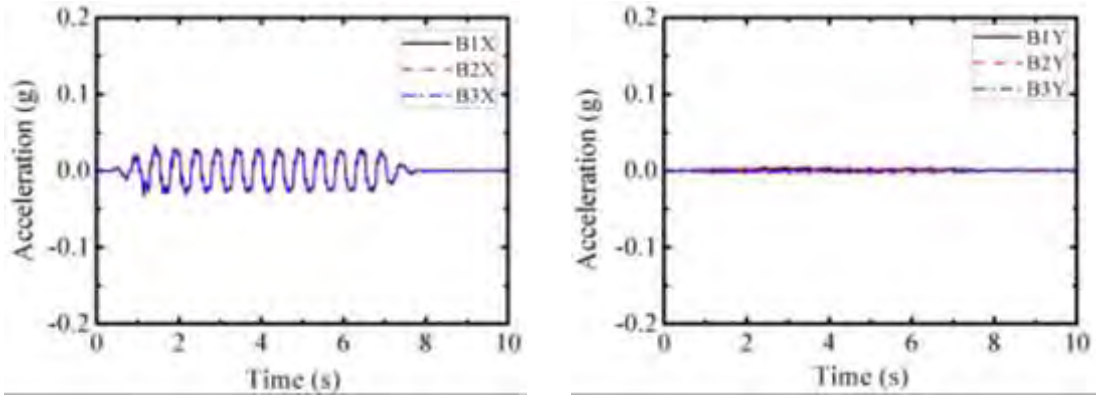

(a) x-direction (b) y-direction

Fig.E. 58 Base shaker of T30 (a_{max}=0.03 g/15 cyc)

E.3.1.2 T31-IM3 (a_{max}=0.10 g/15 cyc)

Fig.E. 59 compares the recorded base acceleration at different locations for both x-(shaking) and y-(non-shaking) direction of T31 (a_{max}=0.10 g/15 cyc).

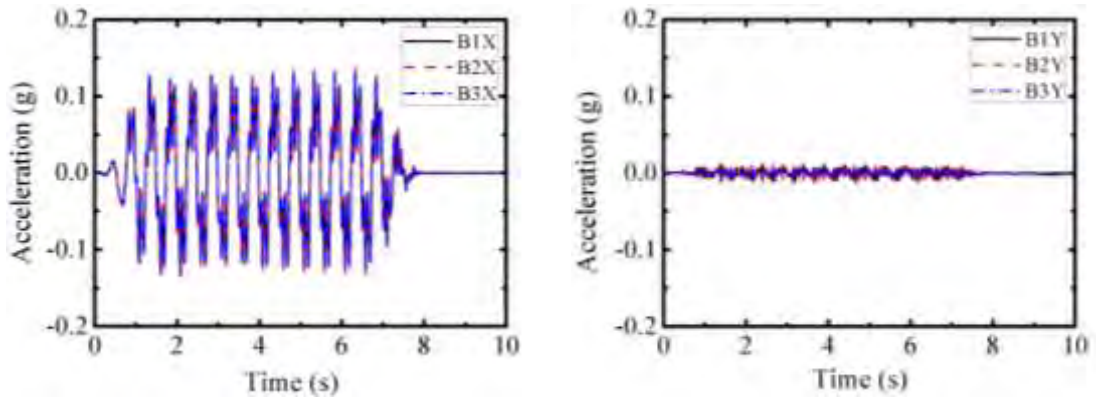

(a) x-direction (b) y-direction

Fig.E. 59 Base shaker of T31 (a_{max}=0.10 g/15 cyc)

E.3.2 Acceleration response

E.3.2.1 T30-IM2 (a_{max}=0.03 g/15 cyc)

Fig.E. 60 compares the acceleration from selected accelerometers as the base motion of T30 (a_{max}=0.03 g/15 cyc) is input. It is noticed that the accelerometer located at laminate 27 instead of laminate 30 is extracted to be the surface acceleration recorder because of post liquefaction densification of soil after series of shaking. The amplification factor of soil at different depths is

shown in Fig.E. 61.

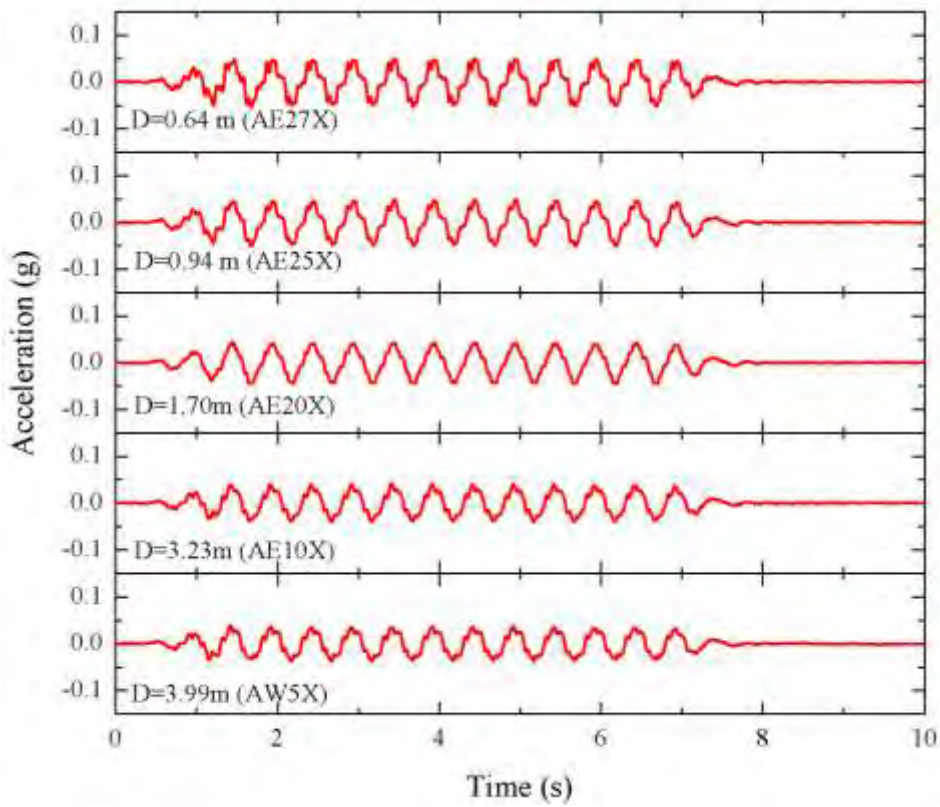

(a) Laminate acceleration

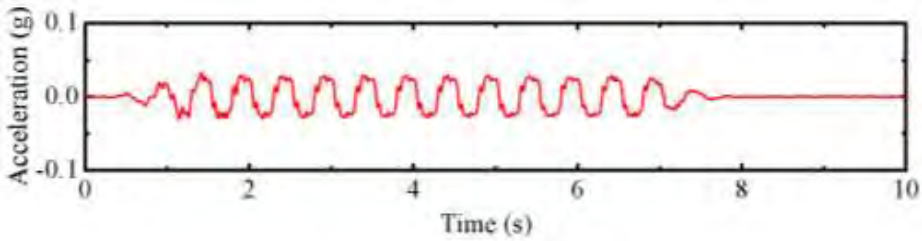

(b) B3X

Fig.E. 60 x-acceleration at different depths and base of T30 (a_{max}=0.03g/15 cyc)

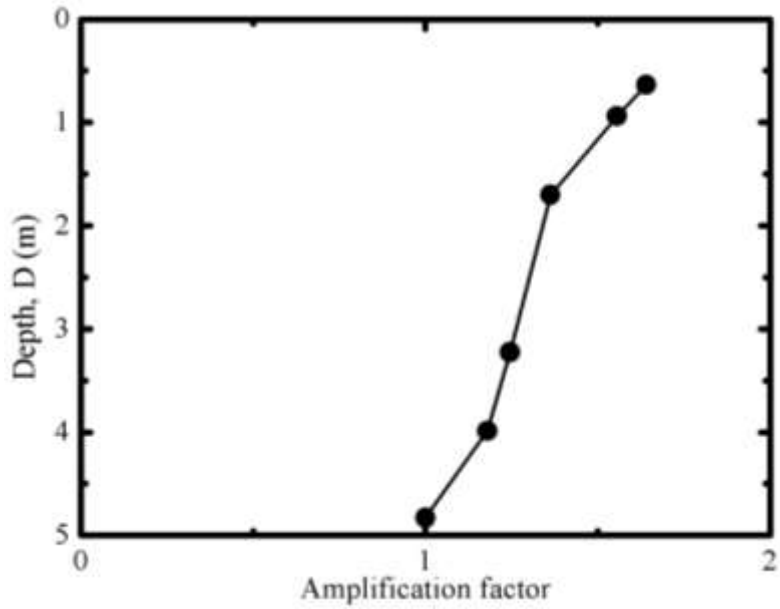

Fig.E. 61 Amplification factor profile of T30 (a_{max}=0.03 g/15 cyc)

E.3.2.2 T31-IM3 (a_{max}=0.10 g/15 cyc)

Fig.E. 62 compares the acceleration from selected accelerometers as the base motion of T31 (a_{max}=0.10 g/15 cyc) is input. It is noticed that the accelerometer located at laminate 27 instead of laminate 30 is extracted to be the surface acceleration recorder because of post liquefaction densification of soil after series of shaking. The amplification factor of soil at different depths is shown in Fig.E. 63.

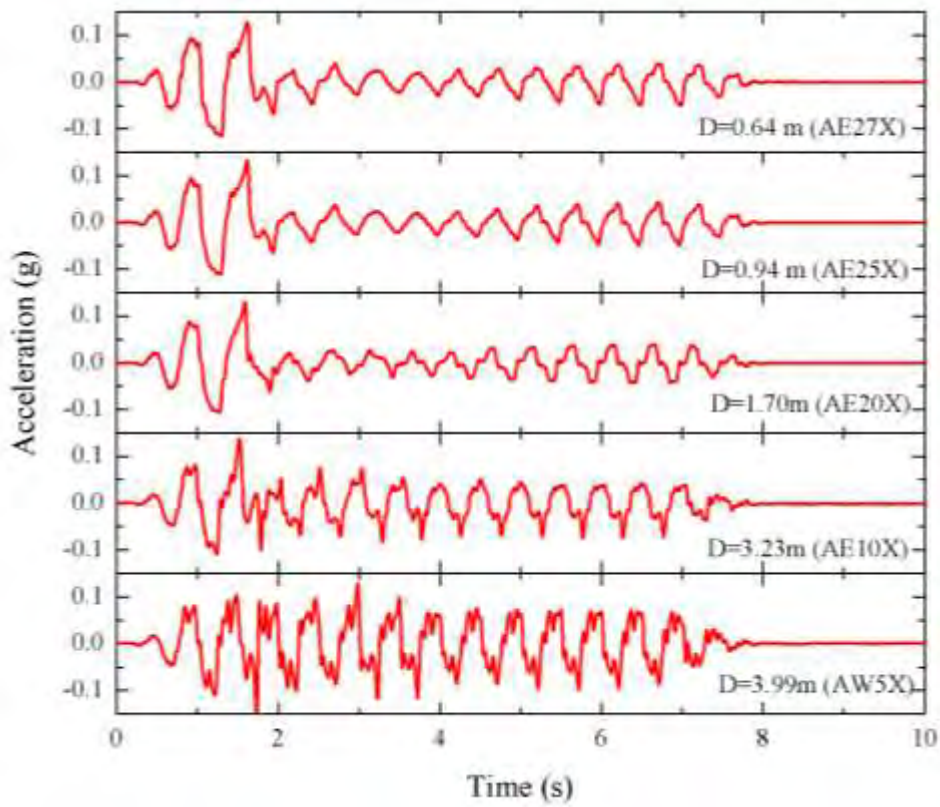

(a) Laminate acceleration

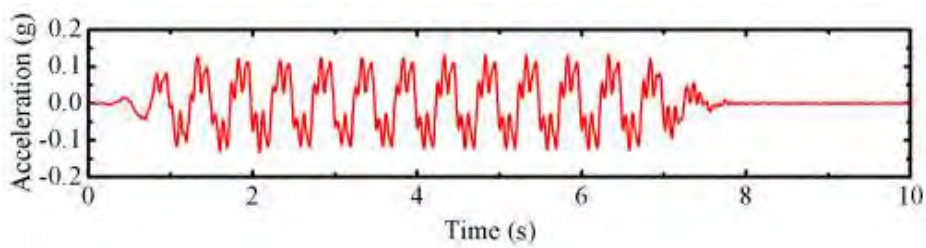

(b) B3X

Fig.E. 62 x-acceleration at different depths and base of T31 (a_{max}=0.10 g/15 cyc)

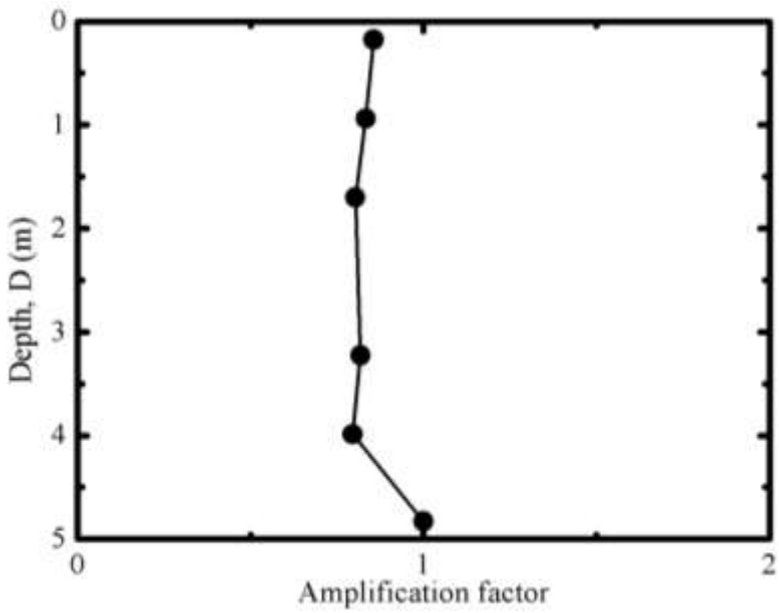

Fig.E. 63 Amplification factor profile of T31 (a_{max}=0.10 g/15 cyc)

E.3.3 Excess pore water pressure (Δu) response

E.3.3.1 T30-IM2 (a_{max}=0.03 g/15 cyc)

Fig.E. 64 presents the time history of normalized excess pore water pressure r_u and base acceleration during shaking of T30 (a_{max}=0.03 g/15 cyc), to better observe whether and when liquefaction occurs (i.e., r_u reaches unity) at different soil depths. Fig.E. 65 shows the time history of the excess pore water pressure (EPWP) Δu of the soil profile recorded by piezometers of T30. Fig.E. 66 plots the Δu as well as r_u with respect to depth at various shaking cycle for T30.

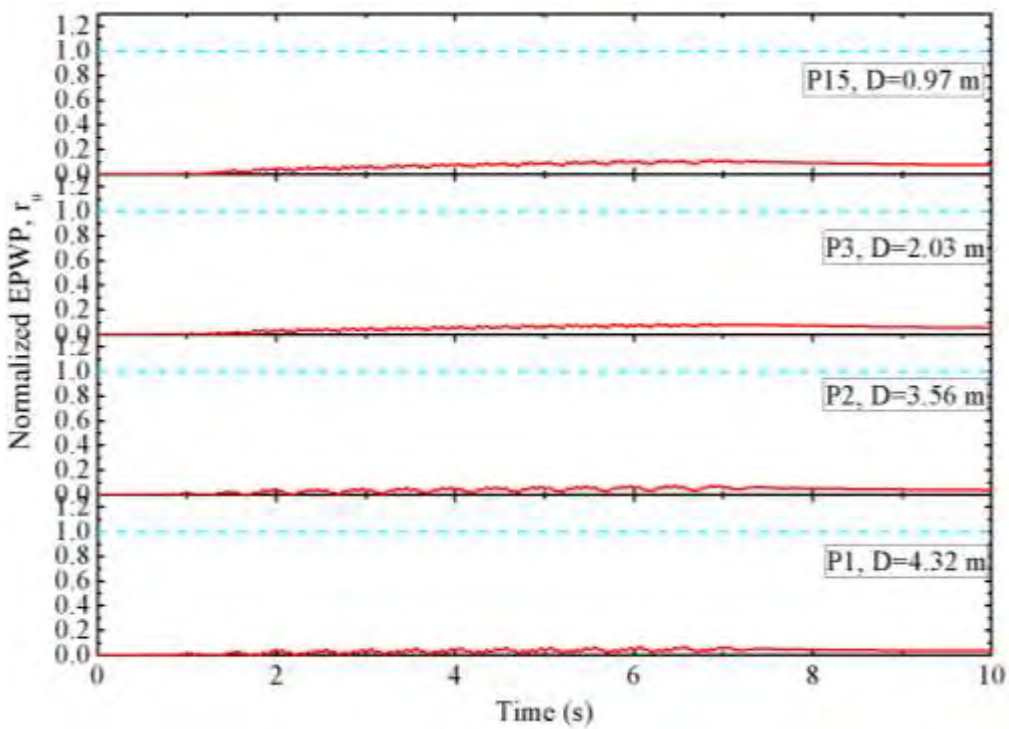

(a) r_u

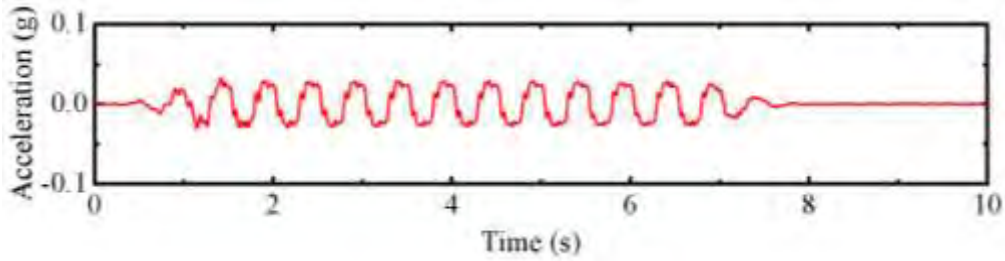

(b) B3X

Fig.E. 64 Time history of r_u and base acceleration of T30 (a_{max}=0.03 g/15 cyc)

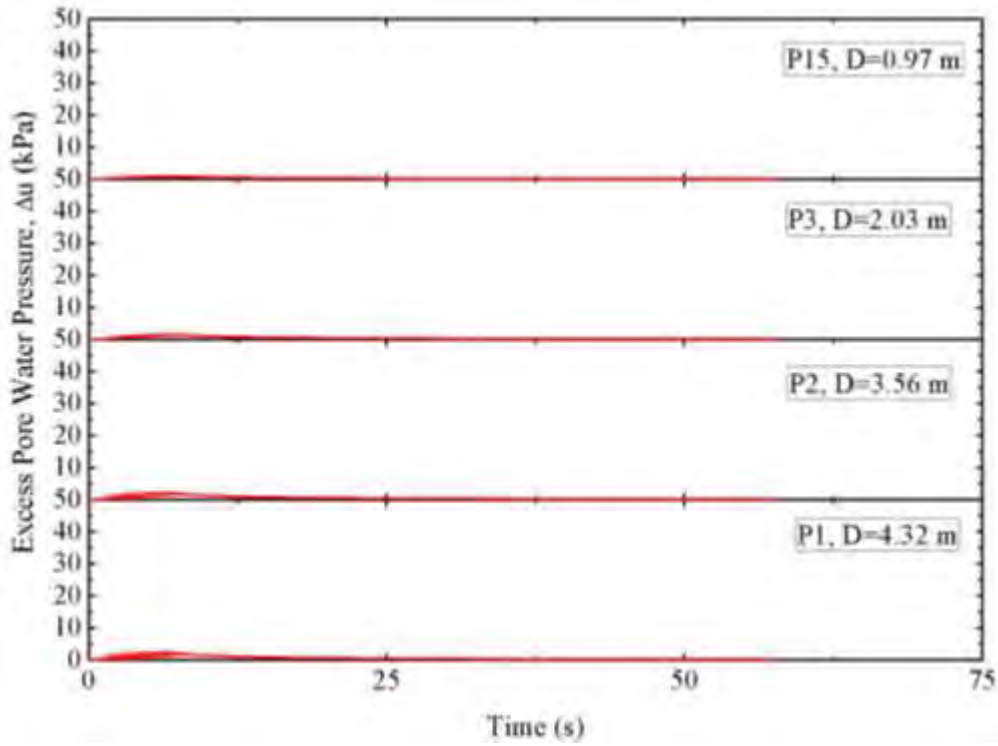

Fig.E. 65 Time history of Δu of T30 (a_{max}=0.03 g/15 cyc)

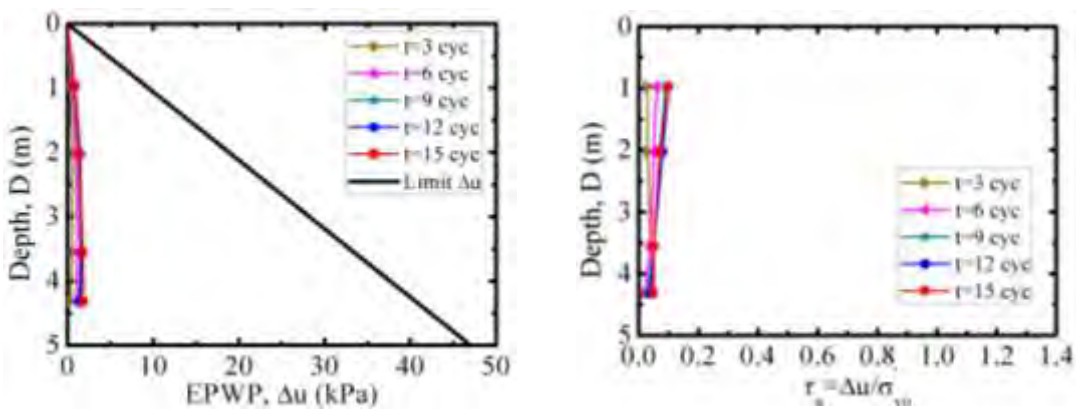

(a) Δu vs D (b) r_u vs D

Fig.E. 66 EPWP profiles of T30 (a_{max}=0.03 g/15 cyc)

E.3.3.2 T31-IM3 (a_{max}=0.10 g/15 cyc)

Fig.E. 67 presents the time history of normalized excess pore water pressure r_u and base acceleration during shaking of T31 (a_{max}=0.10 g/15 cyc), to better observe whether and when liquefaction occurs (i.e., r_u reaches unity) at different soil depths. Fig.E. 68 shows the time history of the excess pore water pressure (EPWP) Δu of the soil profile recorded by piezometers of T31.

Fig.E. 69 plots the Δu as well as r_u with respect to depth at various shaking cycle for T31.

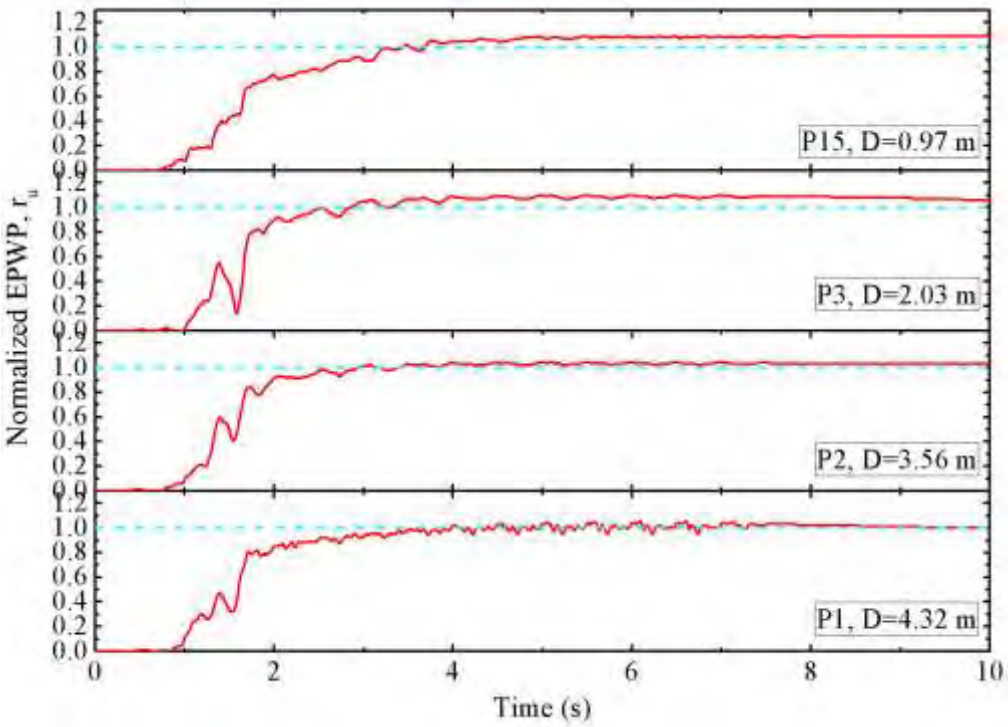

(a) r_u

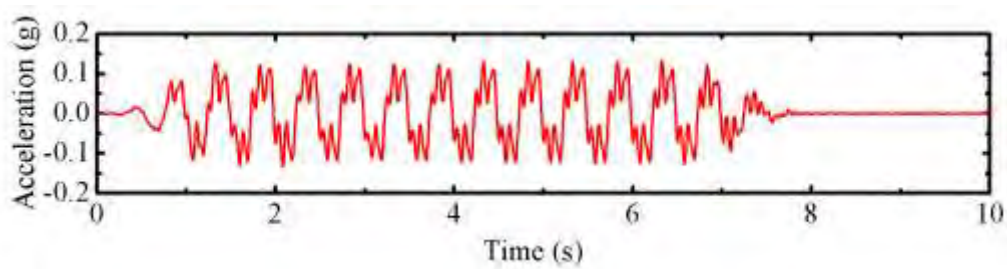

(b) B3X

Fig.E. 67 Time history of r_u and base acceleration of T31 (a_{max}=0.10 g/15 cyc)

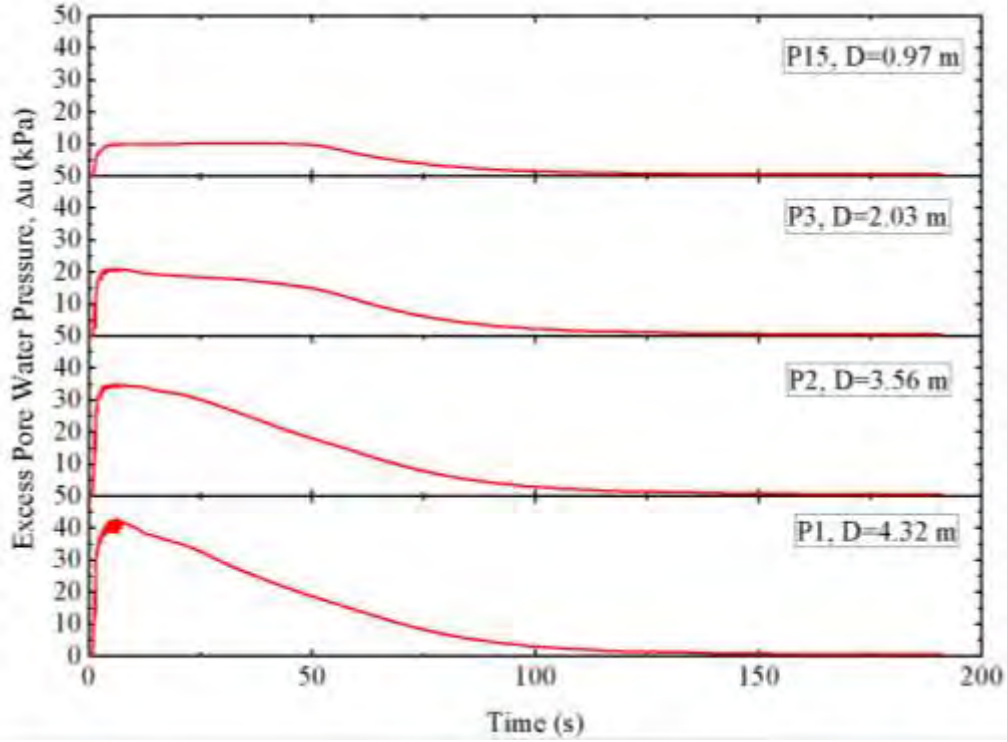

Fig.E. 68 Time history of Δu of T31 (a_{max}=0.10 g/15 cyc)

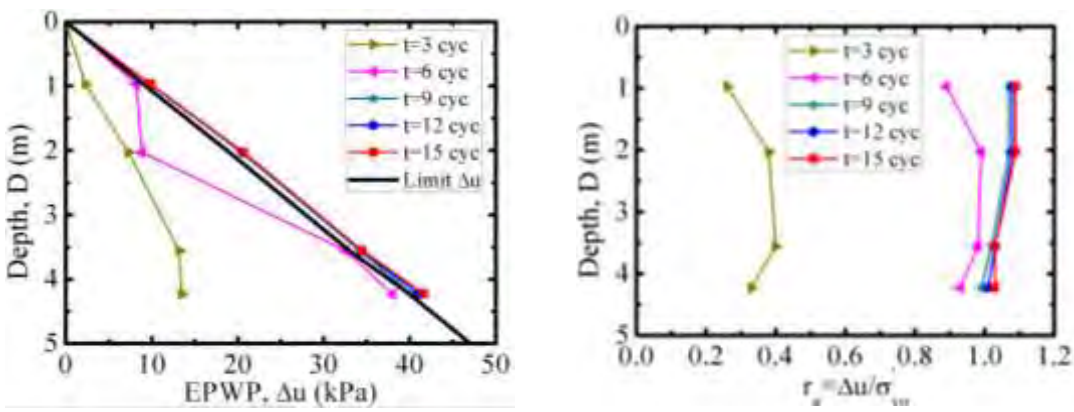

(a) Δu vs D (b) r_u vs D

Fig.E. 69 EPWP profiles of T31 (a_{max}=0.10 g/15 cyc)

E.3.4 Horizontal displacement

E.3.4.1 T30-IM2 (a_{max}=0.03 g/15 cyc)

Fig.E. 70(a) plots the time history of horizontal displacement of the soil at selected depths in T30 (a_{max}=0.03 g/15 cyc). Fig.E. 70(b) and (c) plot the time history of relative horizontal displacement of the soil at selected depths in T30.

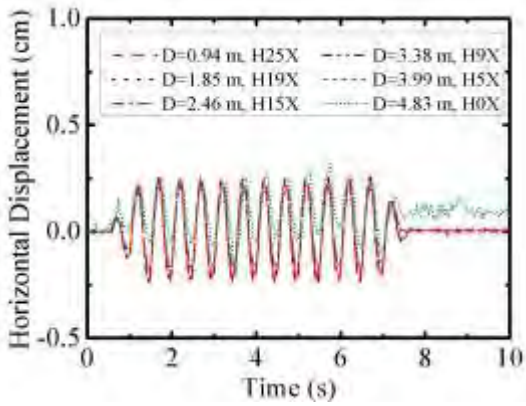

(a) Horizontal displacement

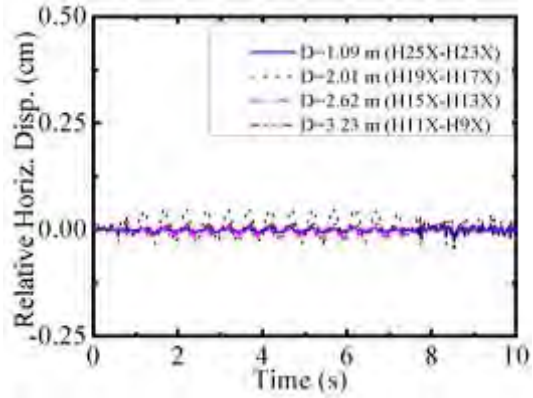

(b) Relative horiz. disp. b/w every other ring

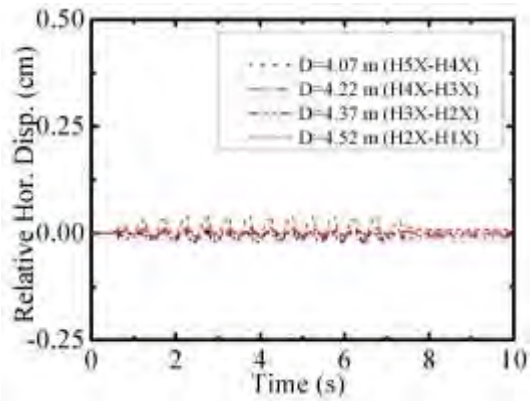

(c) Relative horiz. disp. b/w every ring

Fig.E. 70 Time history of horizontal displacement of T30 (a_{max}=0.03 g/15 cyc)

E.3.4.2 T31-IM3 (a_{max}=0.10 g/15 cyc)

Fig.E. 71(a) plots the time history of horizontal displacement of the soil at selected depths in T31 (a_{max}=0.10 g/15 cyc). Fig.E. 71(b) and (c) plot the time history of relative horizontal displacement of the soil at selected depths in T31.

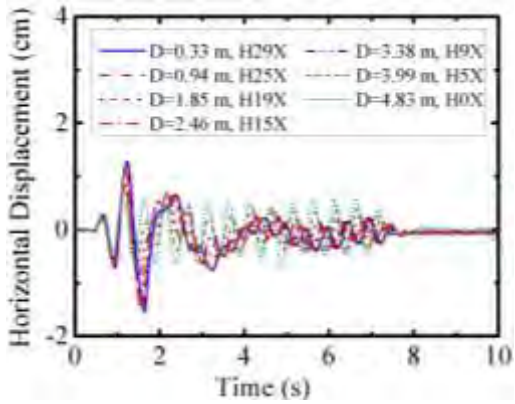

(a) Horizontal displacement

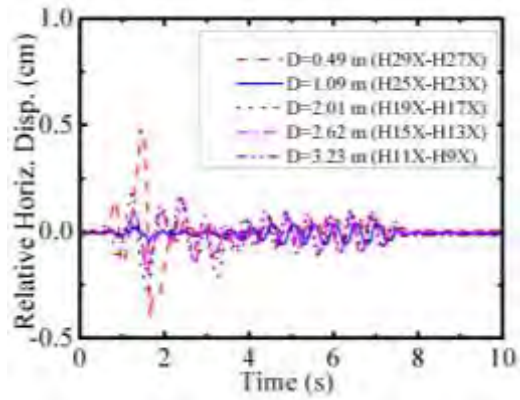

(b) Relative horiz. disp. b/w every other ring

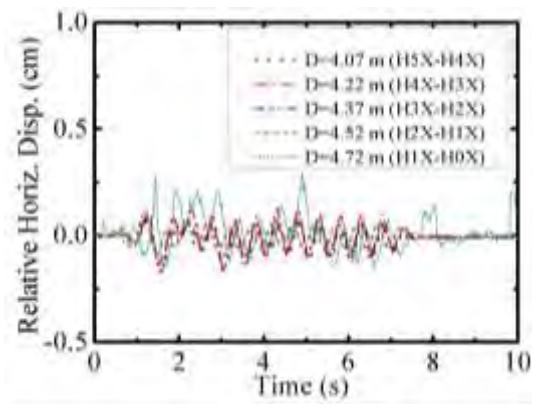

(c) Relative horiz. disp. b/w every ring

Fig.E. 71 Time history of horizontal displacement of T31 (a_{max}=0.10 g/15 cyc)

E.3.5 Ground settlement

Fig.E. 72 plots the time history of incremental ground settlement in shaking series 5 while Table E. 3 summarizes the incremental and total ground settlement of liquefaction tests in shaking series 4. The average incremental settlement of each liquefaction test is based on the incremental settlement of V1 and V3 because V2 was buried in the soil after T2.

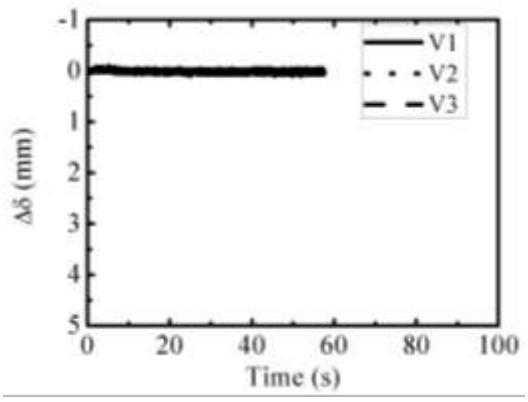

(a) T30 (a_{max}=0.03 g/15 cyc)

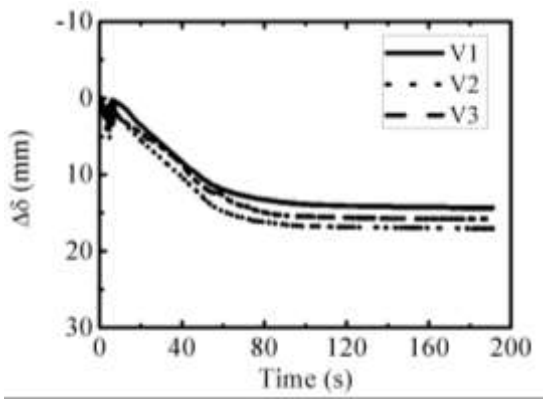

(c) T31 (a_{max}=0.10 g/15 cyc)

Fig.E. 72 Time history of incremental ground settlement in shaking series 5

Table E. 3 Ground settlement of liquefaction tests-shaking series 5

Shaking series	Shaking event	Input Motion	Δδ for each shaking test			$\Delta\delta_{ave.}$	Cumulative Settlement δ
			V1	V2	V3		
			(mm)	(mm)	(mm)	(mm)	(mm)
5	T25a	IM1 (a_{max}=0.015 g/5 cyc)	0	0	0	0	344
	T25	IM4 (a_{max}=0.03 g/5 cyc)	6	6	5	6	349
	T26	IM4 (a_{max}=0.03 g/5 cyc)	5	6	4	5	354
	T27	IM4 (a_{max}=0.03 g/5 cyc)	5	6	4	5	358
	T28	IM4 (a_{max}=0.03 g/5 cyc)	2	1	1	2	360
	T29	IM4 (a_{max}=0.03 g/5 cyc)	0	0	0	0	360
	T30	IM2 (a_{max}=0.03 g/15 cyc)	0	0	0	0	360
	T31	IM3 (a_{max}=0.10 g/15 cyc)	14	17	16	15	375

E.3.6 Stress-strain response

E.3.6.1 T30-IM2 (a_{max}=0.03 g/15 cyc)

The time history of shear stress of the soil at different depths in T30 (a_{max}=0.03 g/15 cyc) is plotted in Fig.E. 73. Fig.E. 74 shows the time history of shear strain of the soil at different depths in T30. The shear stress-strain response of the soil at different depths in T30 is plotted in Fig.E. 75.

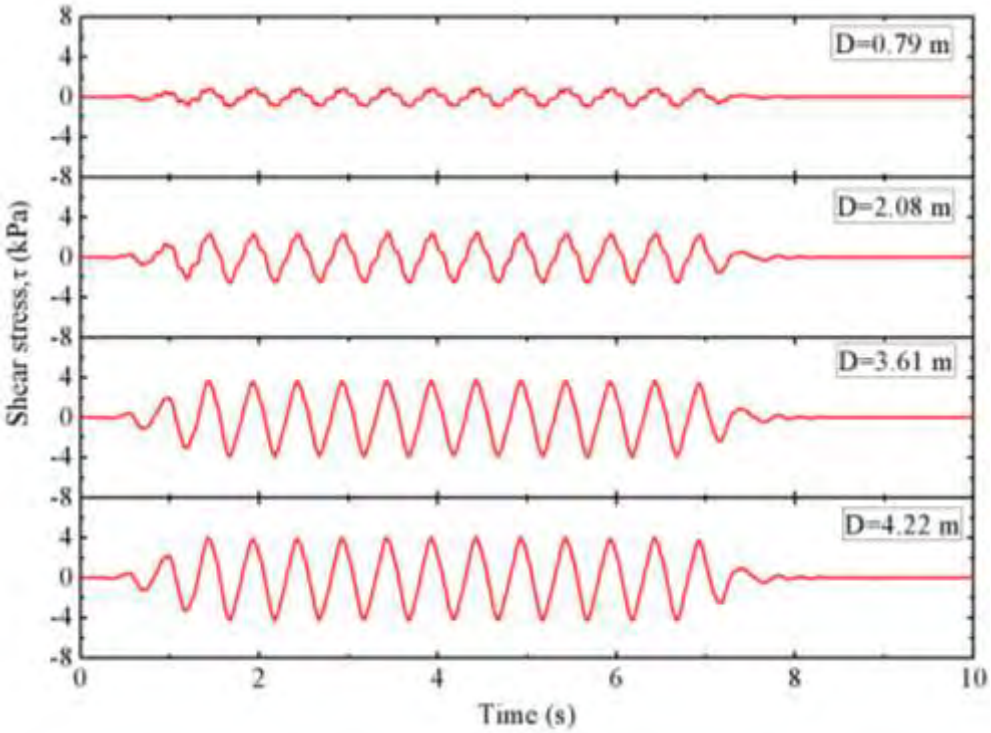

(a) Shear stress

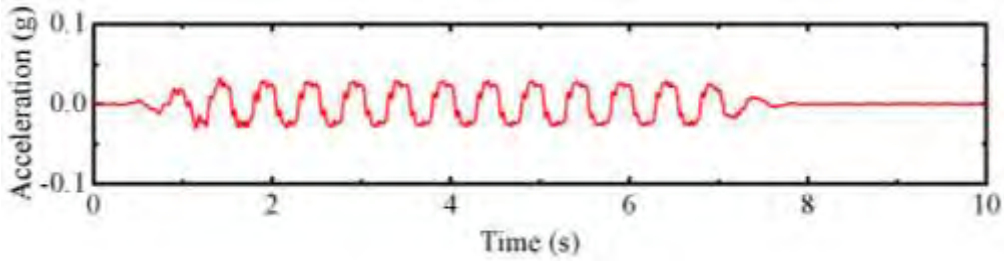

(b) B3X

Fig.E. 73 Time history of shear stress of T30 (a_{max}=0.03 g/15 cyc)

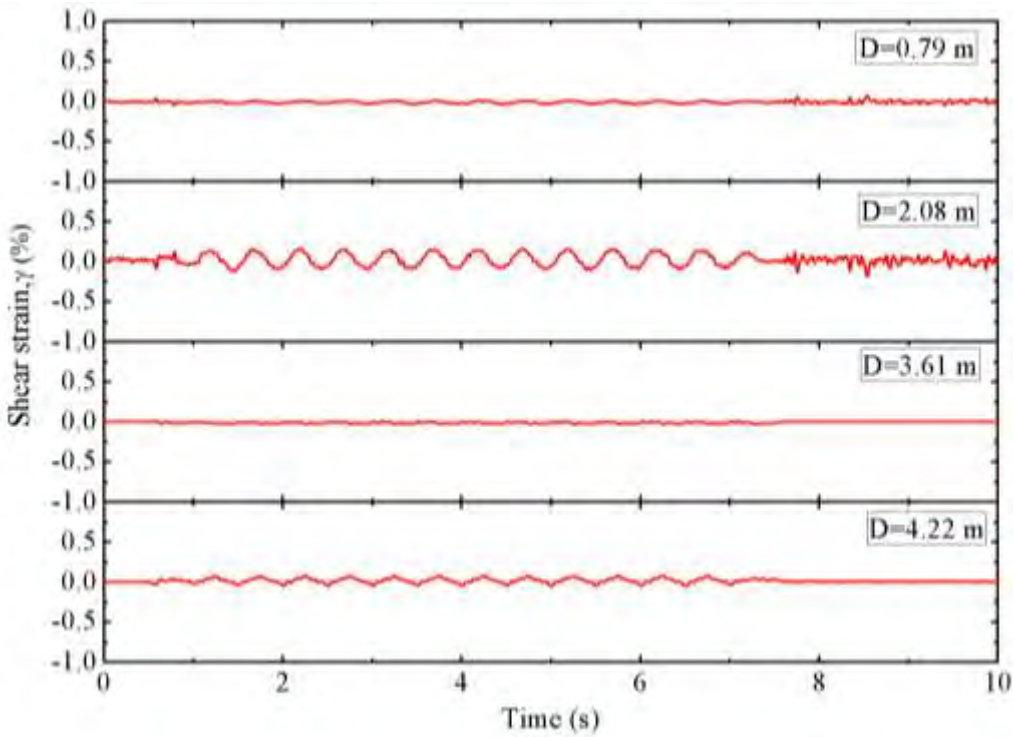

(a) Shear strain

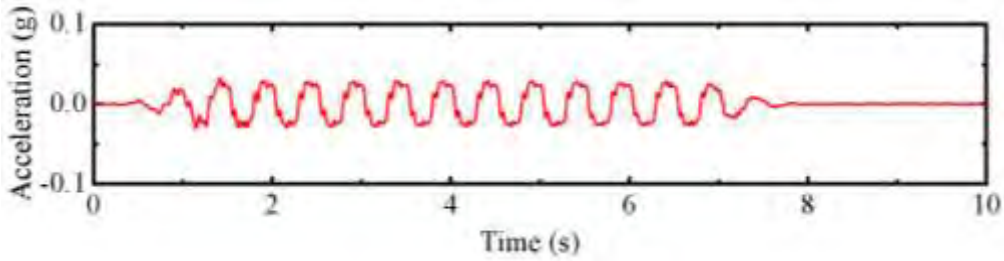

(b) B3X

Fig.E. 74 Time history of shear strain of T30 (a_{max}=0.03 g/15 cyc)

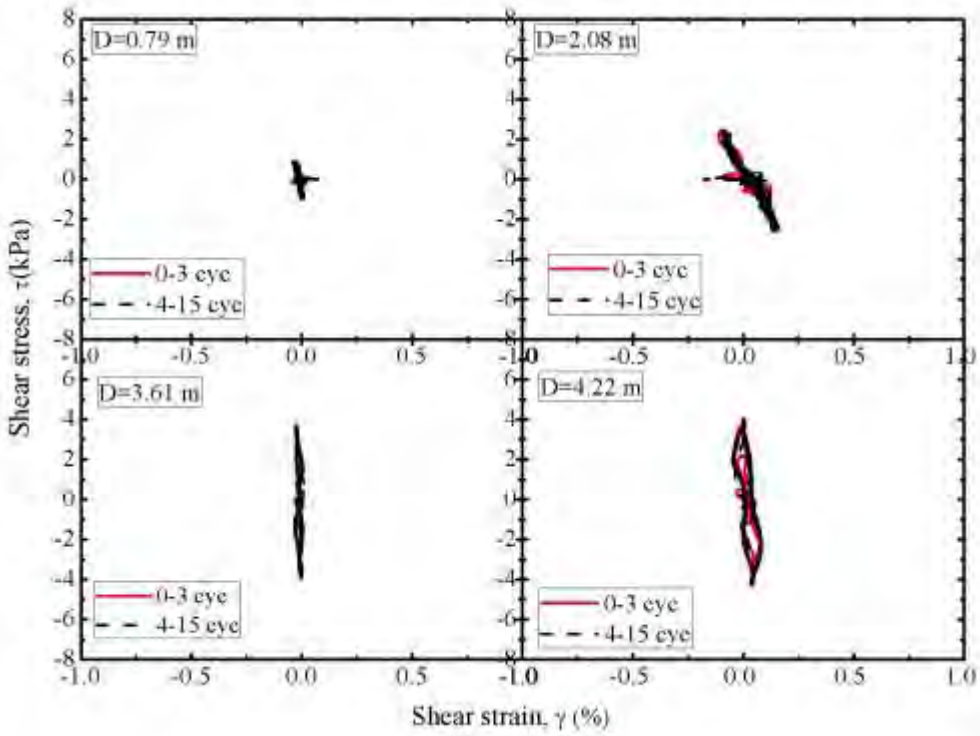

Fig.E. 75 Shear stress- strain loop of T30 (a_{max}=0.03 g/15 cyc)

E.3.6.2 T31-IM3 (a_{max}=0.10 g/15 cyc)

The time history of shear stress of the soil at different depths in T31 (a_{max}=0.10 g/15 cyc) is plotted in Fig.E. 76. Fig.E. 77 shows the time history of shear strain of the soil at different depths in T31. The shear stress-strain response of the soil at different depths in T31 is plotted in Fig.E. 78.

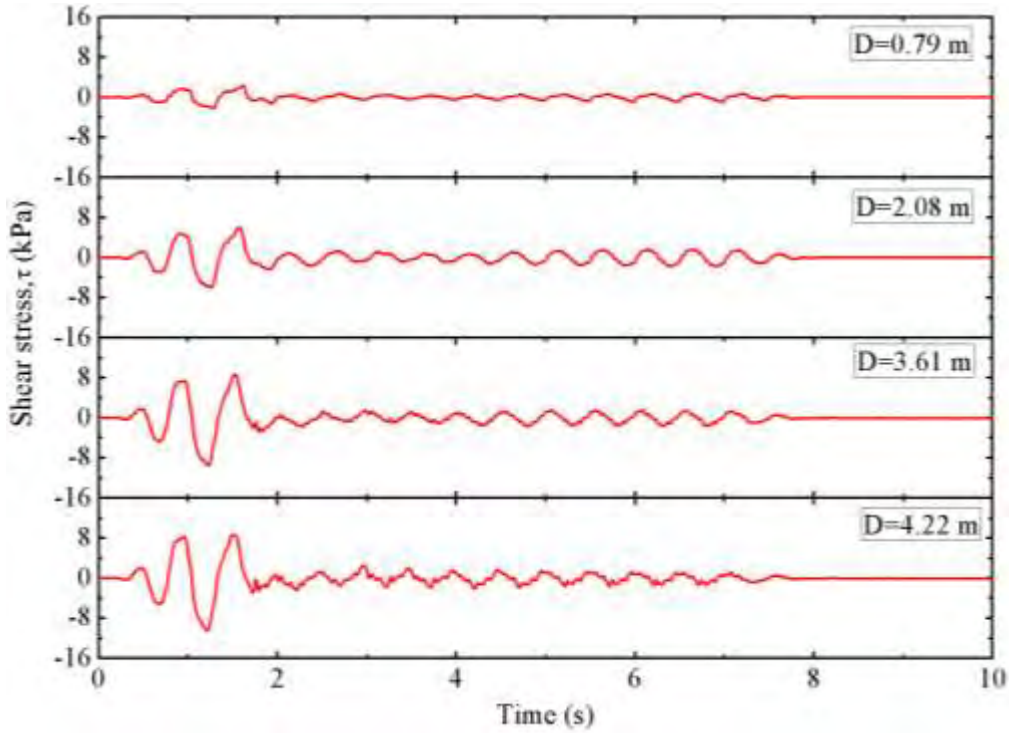

(a) Shear stress

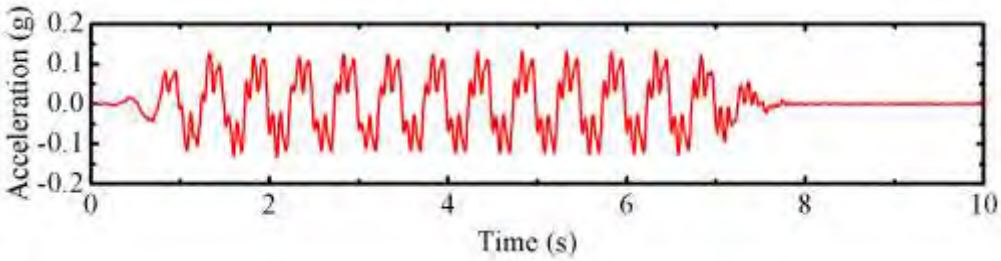

(b) B3X

Fig.E. 76 Time history of shear stress of T31 (a_{max}=0.10 g/15 cyc)

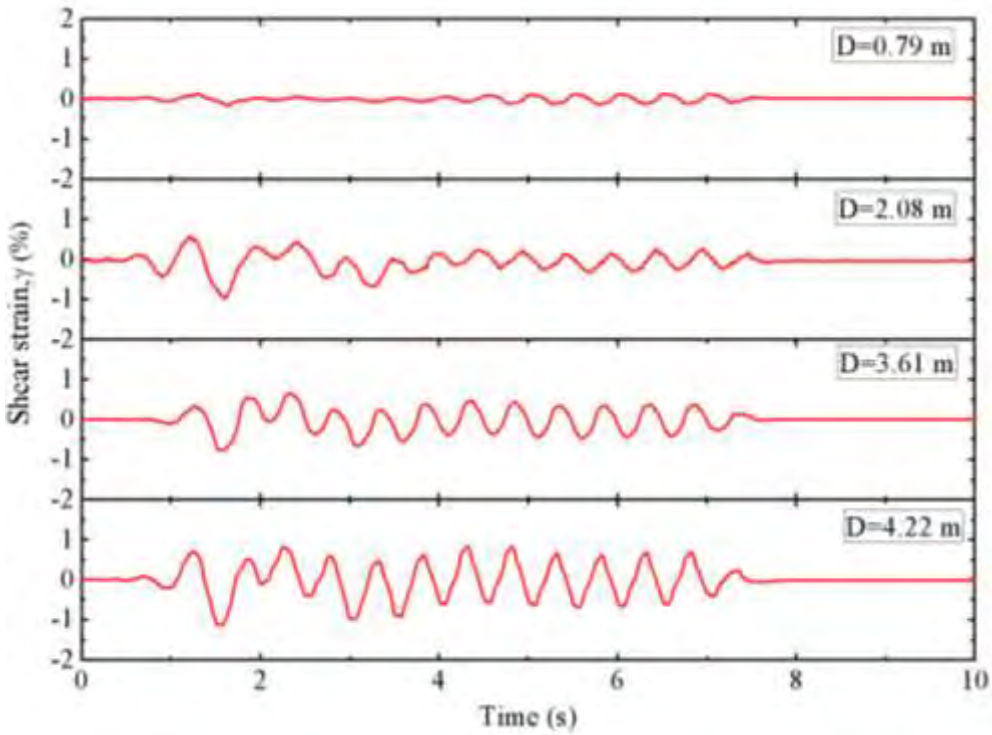

(a) Shear strain

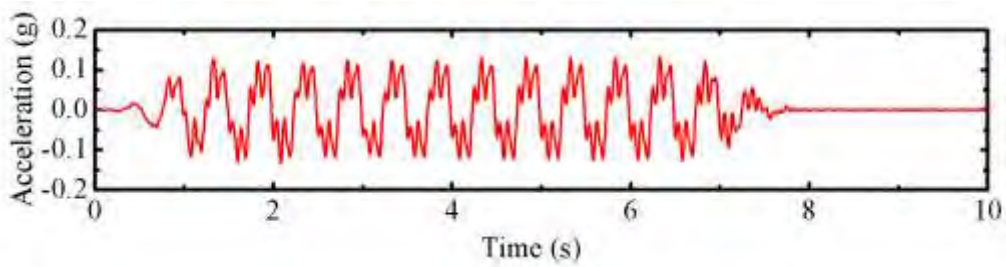

(b) B3X

Fig.E. 77 Time history of shear strain of T31 (a_{max}=0.10 g/15 cyc)

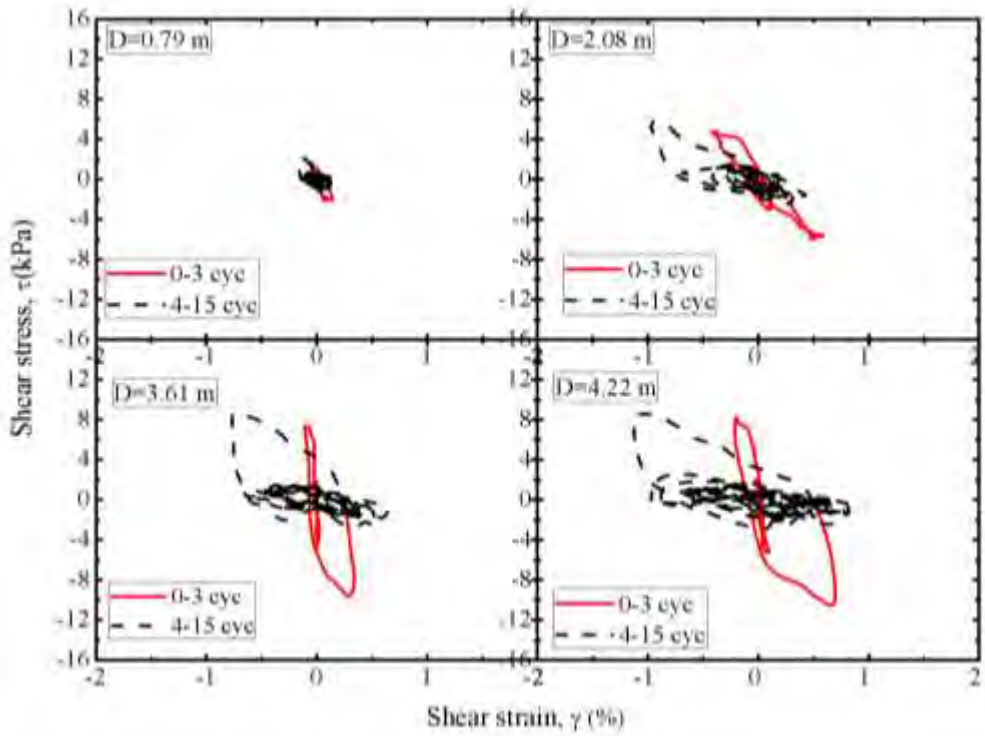

Fig.E. 78 Shear stress- strain loop of T31 (a_{max}=0.10 g/15 cyc)

E.4 Liquefaction tests-shaking series 6

This shaking series consists of T32a (IM1), T32 through T36 (IM4), T37 (IM2) and T38 (IM3)-refer to Fig. 7.24 and Table 7.8 for details. Only T37 and T38 are presented in this section.

E.4.1 Base shaker

E.4.1.1 T37-IM2 (a_{max}=0.03 g/15 cyc)

Fig.E. 79 compares the recorded base acceleration at different locations for both x-(shaking) and y-(non-shaking) direction of T44 (a_{max}=0.03 g/15 cyc).

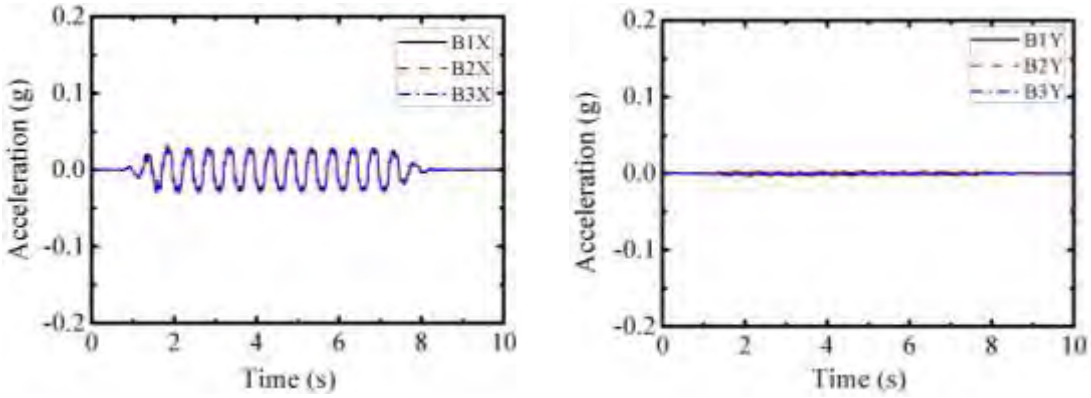

(a) x-direction (b) y-direction

Fig.E. 79 Base shaker of T37 (a_{max}=0.03 g/15 cyc)

E.4.1.2 T38-IM3 (a_{max}=0.10 g/15 cyc)

Fig.E. 80 compares the recorded base acceleration at different locations for both x-(shaking) and y-(non-shaking) direction of T38 (a_{max}=0.10 g/15 cyc).

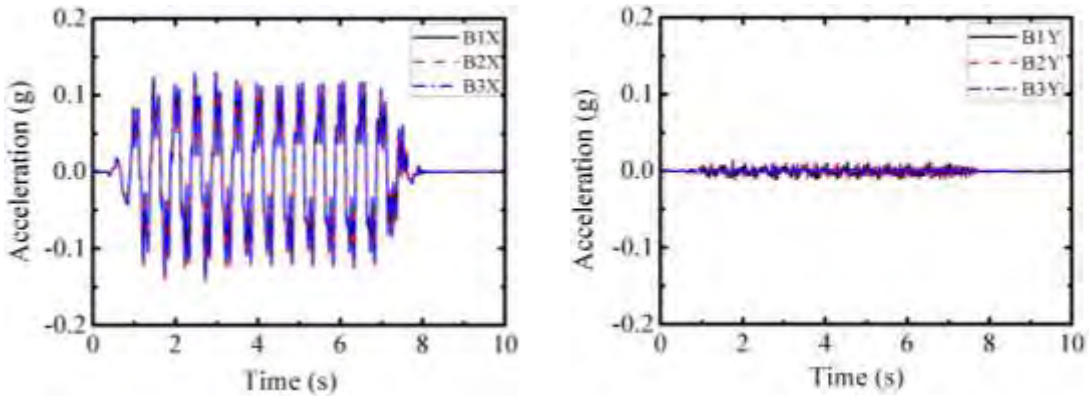

(a) x-direction (b) y-direction

Fig.E. 80 Base shaker of T38 (a_{max}=0.10 g/15 cyc)

E.4.2 Acceleration response

E.4.2.1 T37-IM2 (a_{max}=0.03 g/15 cyc)

Fig.E. 81 compares the acceleration from selected accelerometers as the base motion of T37 (a_{max}=0.03 g/15 cyc) is input. It is noticed that the accelerometer located at laminate 27 instead of laminate 30 is extracted to be the surface acceleration recorder because of post liquefaction densification of soil after series of shaking. The amplification factor of soil at different depths is

shown in Fig.E. 82.

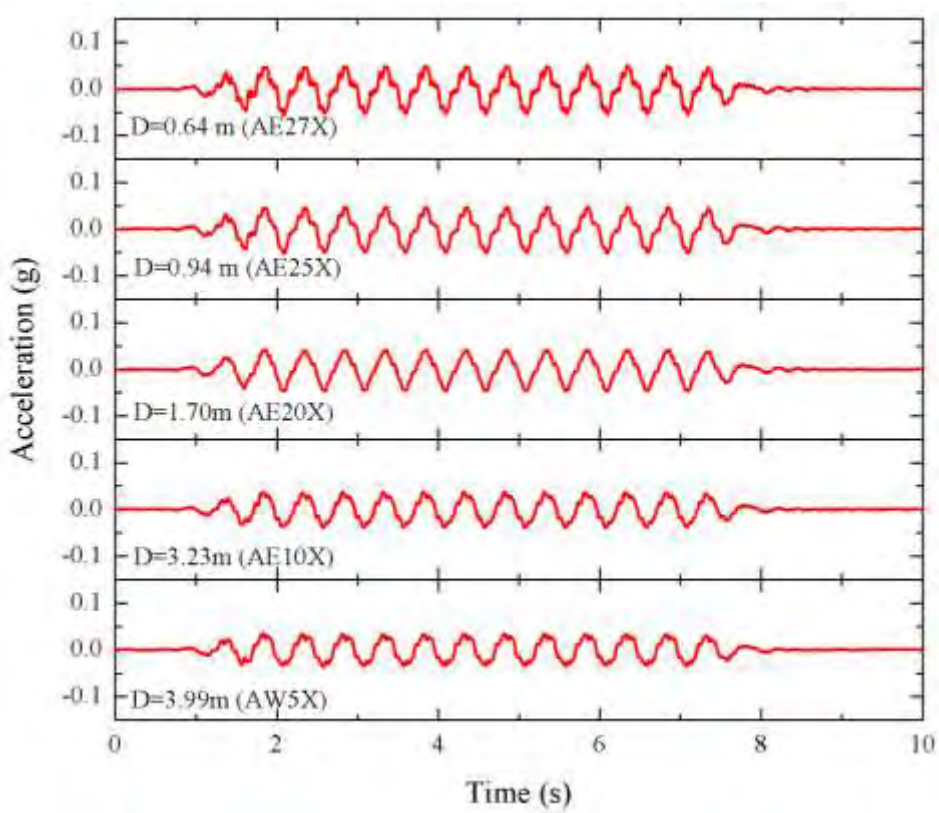

(a) Laminate acceleration

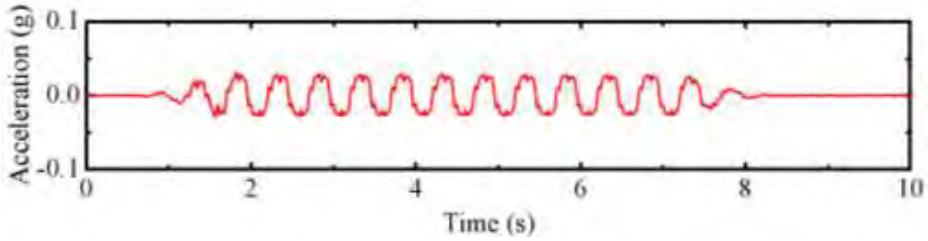

(b) B3X

Fig.E. 81 x-acceleration at different depths and base of T37 (a_{max}=0.03g/15 cyc)

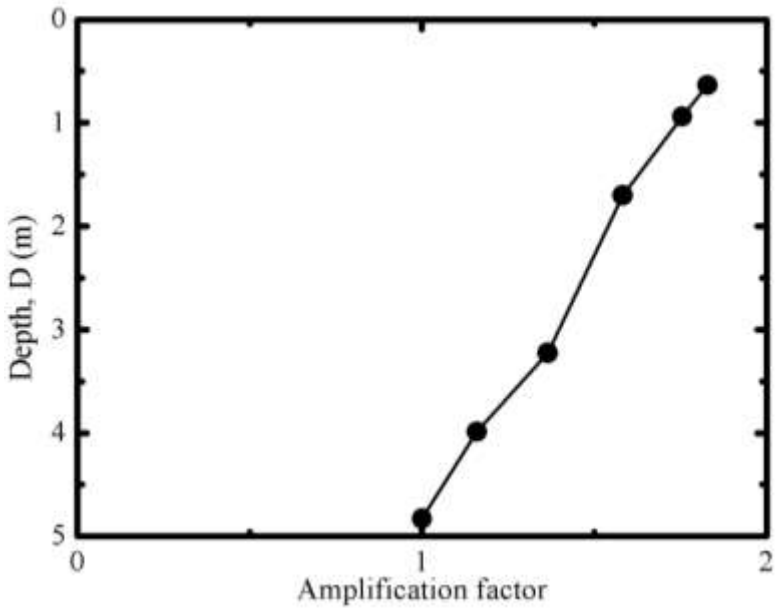

Fig.E. 82 Amplification factor profile of T37 (a_{max}=0.03 g/15 cyc)

E.4.2.2 T38-IM3 (a_{max}=0.10 g/15 cyc)

Fig.E. 83 compares the acceleration from selected accelerometers as the base motion of T38 (a_{max}=0.10 g/15 cyc) is input. It is noticed that the accelerometer located at laminate 27 instead of laminate 30 is extracted to be the surface acceleration recorder because of post liquefaction densification of soil after series of shaking. The amplification factor of soil at different depths is shown in Fig.E. 84.

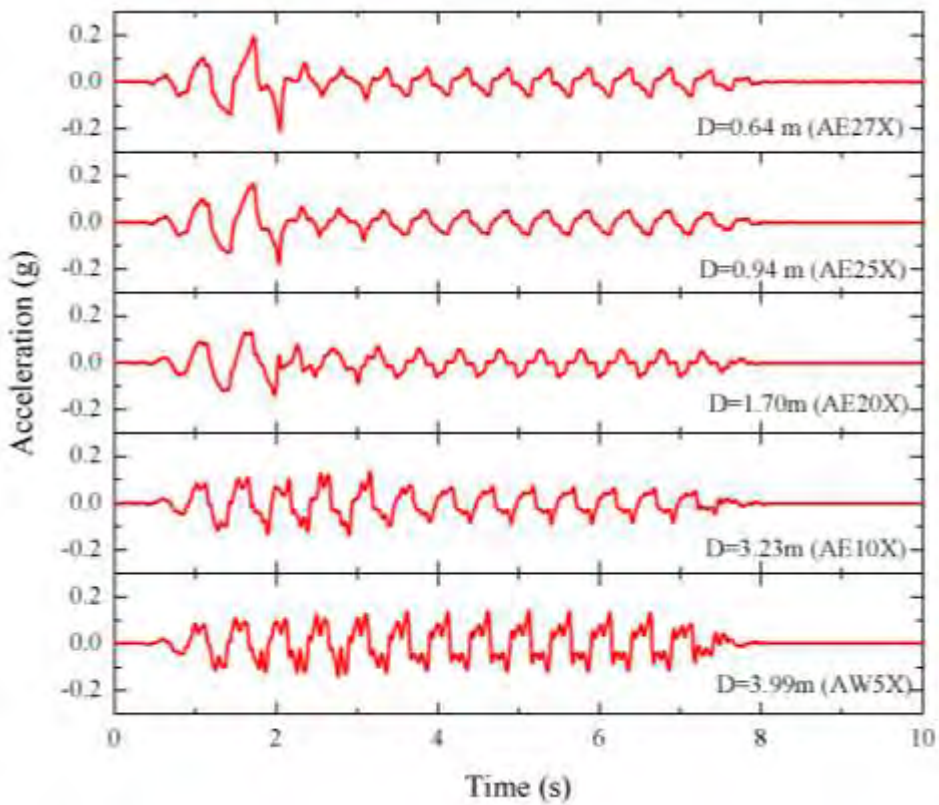

(a) Laminate acceleration

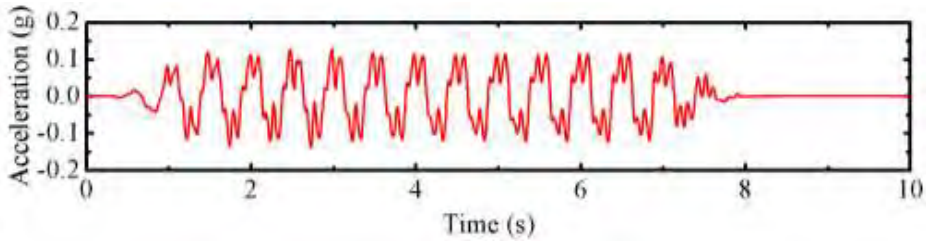

(b) B3X

Fig.E. 83 x-acceleration at different depths and base of T38 (a_{max}=0.10 g/15 cyc)

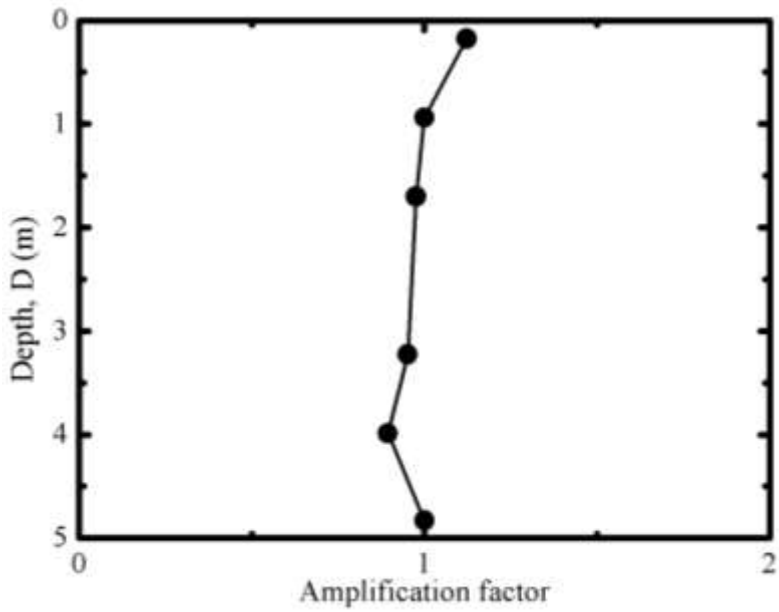

Fig.E. 84 Amplification factor profile of T38 (a_{max}=0.10 g/15 cyc)

E.4.3 Excess pore water pressure (Δu) response

E.4.3.1 T37-IM2 (a_{max}=0.03 g/15 cyc)

Fig.E. 85 presents the time history of normalized excess pore water pressure r_u and base acceleration during shaking of T37 (a_{max}=0.03 g/15 cyc), to better observe whether and when liquefaction occurs (i.e., r_u reaches unity) at different soil depths. Fig.E. 86 shows the time history of the excess pore water pressure (EPWP) Δu of the soil profile recorded by piezometers of T37. Fig.E. 87 plots the Δu as well as r_u with respect to depth at various shaking cycle for T37.

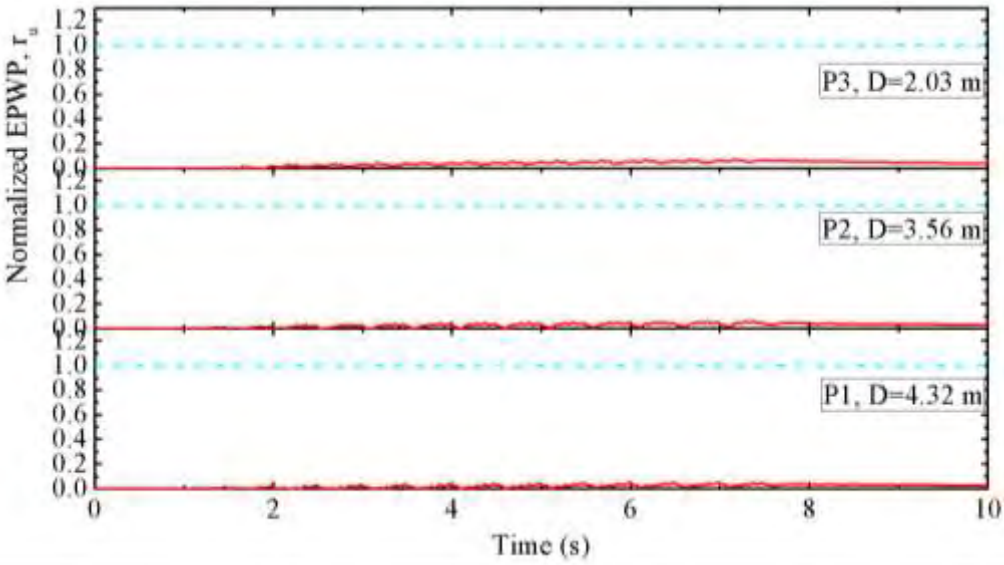

(a) r_u

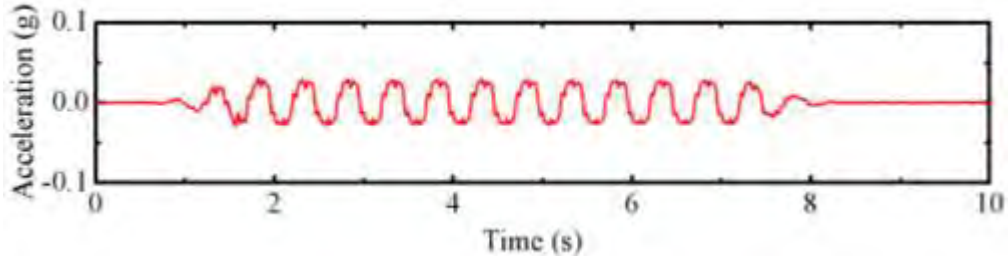

(b) B3X

Fig.E. 85 Time history of r_u and base acceleration of T37 (a_{max}=0.03 g/15 cyc)

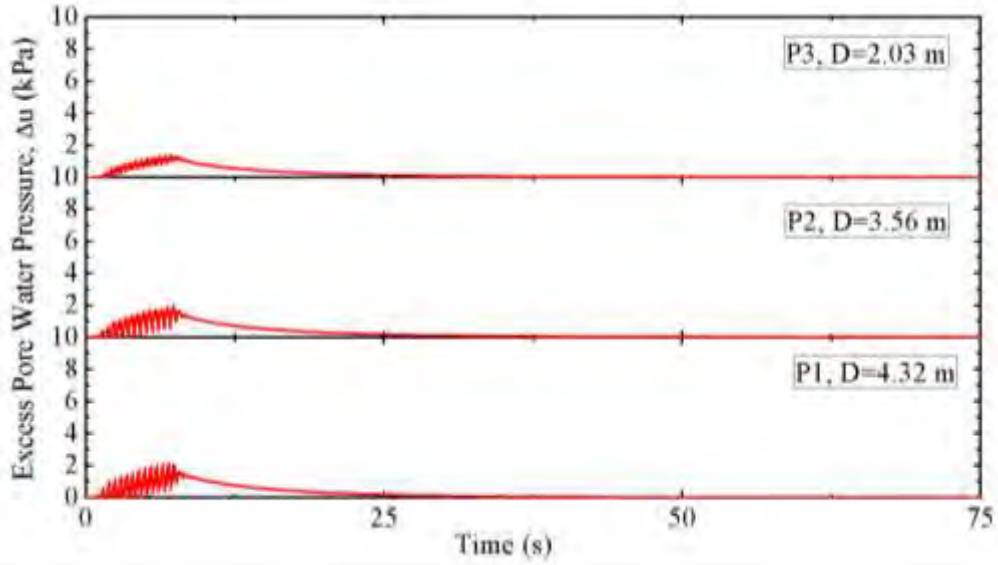

Fig.E. 86 Time history of Δu of T37 (a_{max}=0.03 g/15 cyc)

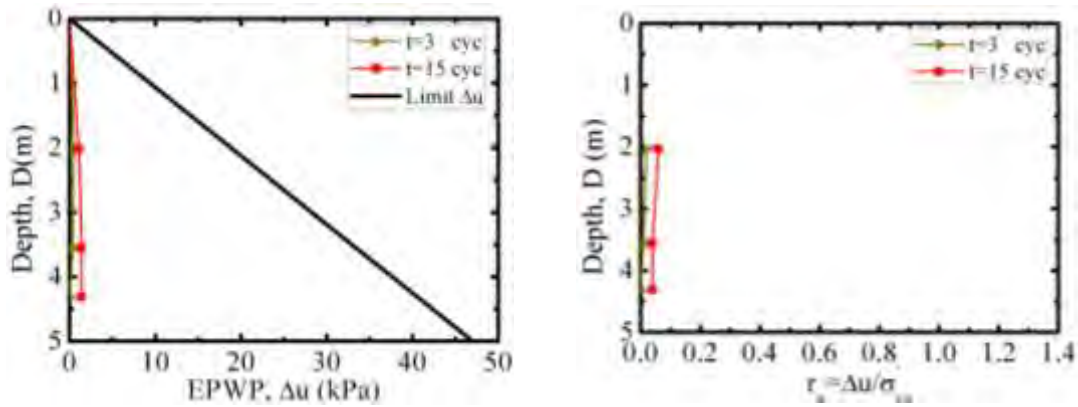

(a) Δu vs D (b) r_u vs D

Fig.E. 87 EPWP profiles of T37 (a_{max}=0.03 g/15 cyc)

E.4.3.2 T38-IM3 (a_{max}=0.10 g/15 cyc)

Fig.E. 88 presents the time history of normalized excess pore water pressure r_u and base acceleration during shaking of T38 (a_{max}=0.10 g/15 cyc), to better observe whether and when liquefaction occurs (i.e., r_u reaches unity) at different soil depths. Fig.E. 89 shows the time history of the excess pore water pressure (EPWP) Δu of the soil profile recorded by piezometers of T38. Fig.E. 90 plots the Δu as well as r_u with respect to depth at various shaking cycle for T38.

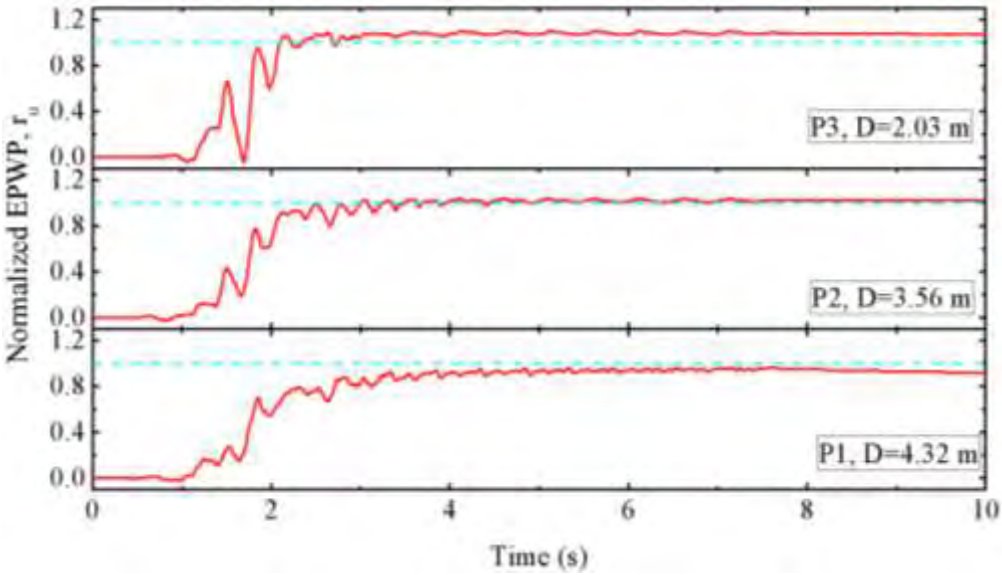

(a) r_u

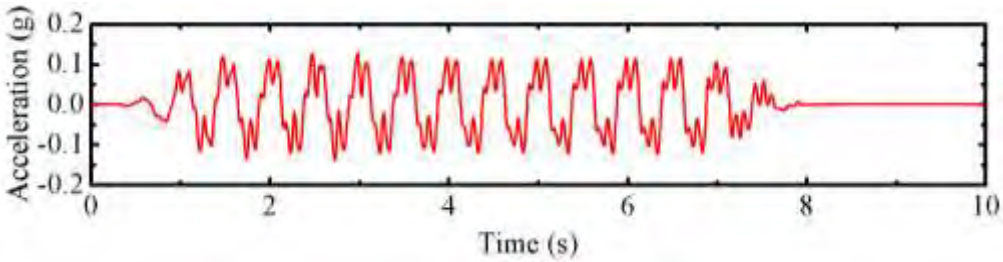

(b) B3X

Fig.E. 88 Time history of r_u and base acceleration of T38 (a_{max}=0.10 g/15 cyc)

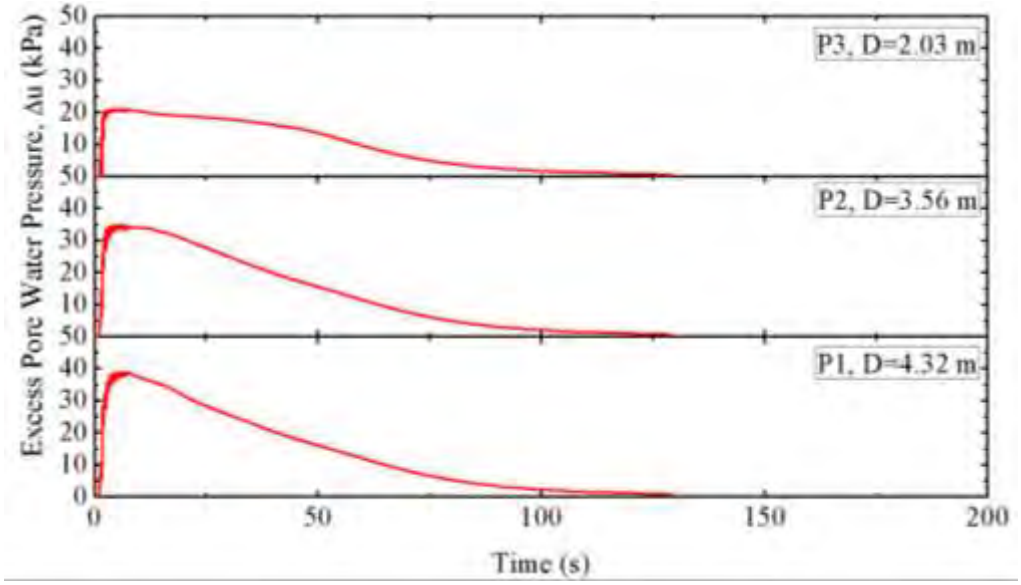

Fig.E. 89 Time history of Δu of T38 (a_{max}=0.10 g/15 cyc)

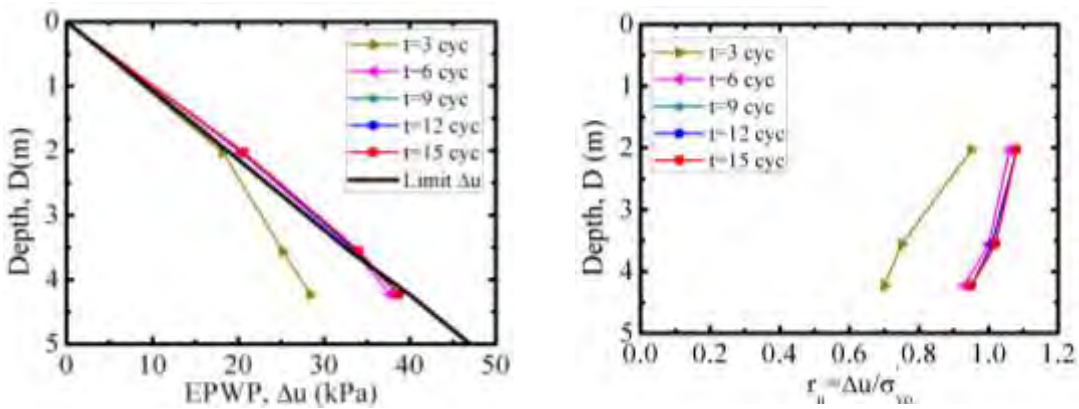

(a) Δu vs D (b) r_u vs D

Fig.E. 90 EPWP profiles of T38 (a_{max}=0.10 g/15 cyc)

E.4.4 Horizontal displacement

E.4.4.1 T37-IM2 (a_{max}=0.03 g/15 cyc)

Fig.E. 91(a) plots the time history of horizontal displacement of the soil at selected depths in T37 (a_{max}=0.03 g/15 cyc). Fig.E. 91(b) and (c) plot the time history of relative horizontal displacement of the soil at selected depths in T37.

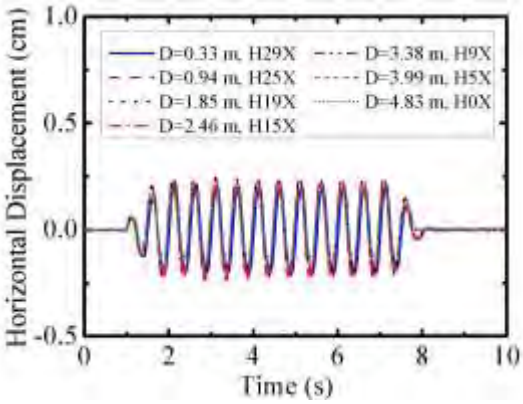

(a) Horizontal displacement

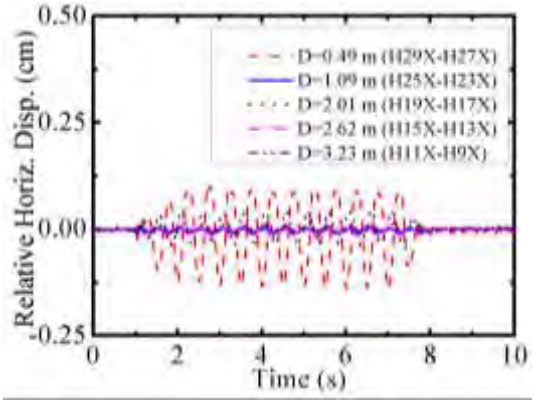

(b) Relative horiz. disp. b/w every other ring

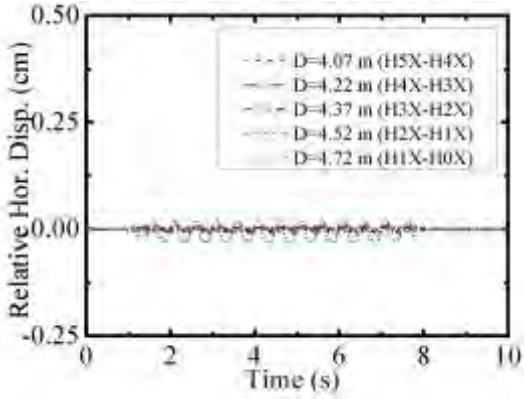

(c) Relative horiz. disp. b/w every ring

Fig.E. 91 Time history of horizontal displacement of T37 (a_{max}=0.03 g/15 cyc)

E.4.4.2 T38-IM3 (a_{max}=0.10 g/15 cyc)

Fig.E. 92(a) plots the time history of horizontal displacement of the soil at selected depths in T38 (a_{max}=0.10 g/15 cyc). Fig.E. 92(b) and (c) plot the time history of relative horizontal displacement of the soil at selected depths in T38.

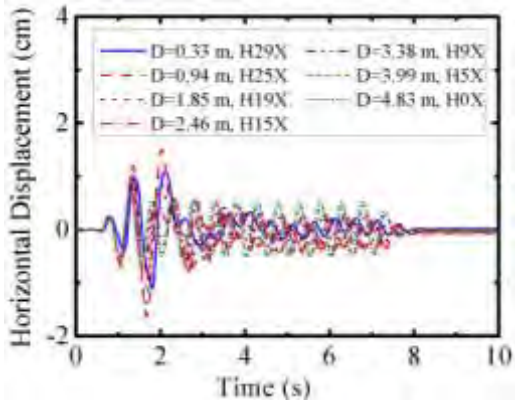

(a) Horizontal displacement

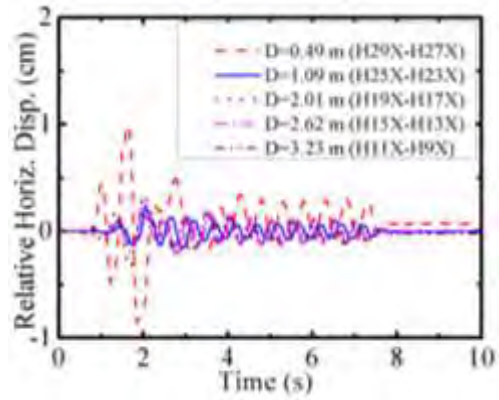

(b) Relative horiz. disp. b/w every other ring

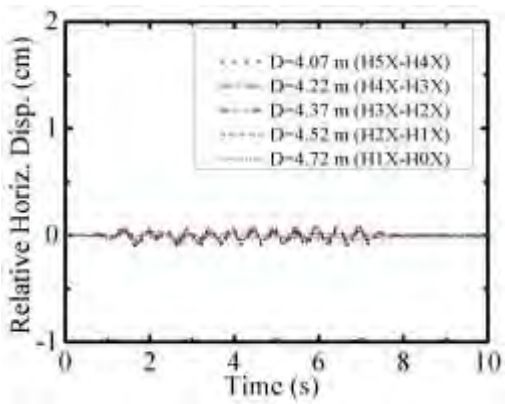

(c) Relative horiz. disp. b/w every ring

Fig.E. 92 Time history of horizontal displacement of T38 (a_{max}=0.10 g/15 cyc)

E.4.5 Ground settlement

Fig.E. 93 plots the time history of incremental ground settlement in shaking series 6 while Table E. 4 summarizes the incremental and total ground settlement of liquefaction tests in shaking series 6. The average incremental settlement of each liquefaction test is based on the incremental settlement of V1 and V3 because V2 was buried in the soil after T2.

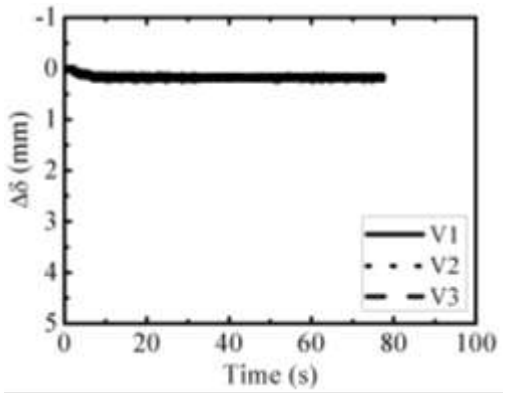

(a) T37 (a_{max}=0.03 g/15 cyc)

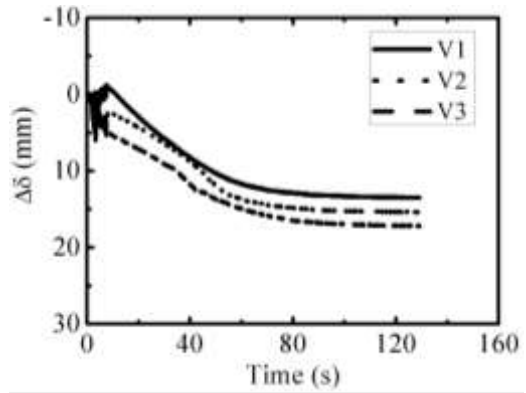

(c) T38 (a_{max}=0.10 g/15 cyc)

Fig.E. 93 Time history of incremental ground settlement in shaking series 6

Table E. 4 Ground settlement of liquefaction tests-shaking series 6

Shaking series	Test No.	Input Motion	Δδ for each shaking test			$\Delta\delta_{ave.}$	Cumulative Settlement δ
			V1	V2	V3		
			(mm)	(mm)	(mm)	(mm)	(mm)
6	T32a	IM1 (a_{max}=0.015 g/5 cyc)	0	0	0	0	375
	T32	IM4 (a_{max}=0.03 g/5 cyc)	3	3	3	3	378
	T33	IM4 (a_{max}=0.03 g/5 cyc)	3	3	3	3	381
	T34	IM4 (a_{max}=0.03 g/5 cyc)	0	0	0	0	381
	T35	IM4 (a_{max}=0.03 g/5 cyc)	0	0	0	0	381
	T36	IM4 (a_{max}=0.03 g/5 cyc)	0	0	0	0	381
	T37	IM2 (a_{max}=0.03 g/15 cyc)	0	0	0	0	381
	T38	IM3 (a_{max}=0.10 g/15 cyc)	14	16	18	16	397

E.4.6 Stress-strain response

E.4.6.1 T37-IM2 (a_{max}=0.03 g/15 cyc)

The time history of shear stress of the soil at different depths in T37 (a_{max}=0.03 g/15 cyc) is plotted in Fig.E. 94. Fig.E. 95 shows the time history of shear strain of the soil at different depths in T37. The shear stress-strain response of the soil at different depths in T37 is plotted in Fig.E. 96.

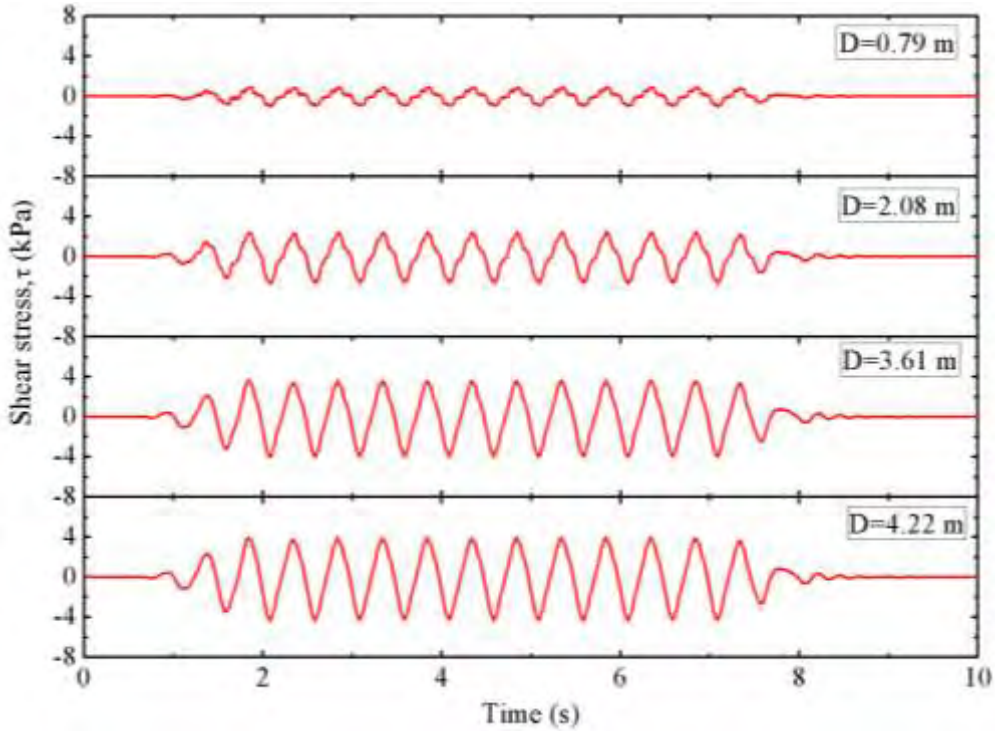

(a) Shear stress

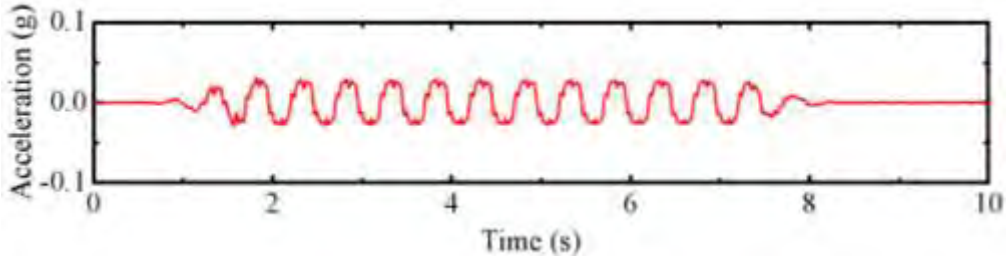

(b) B3X

Fig.E. 94 Time history of shear stress of T37 (a_{max}=0.03 g/15 cyc)

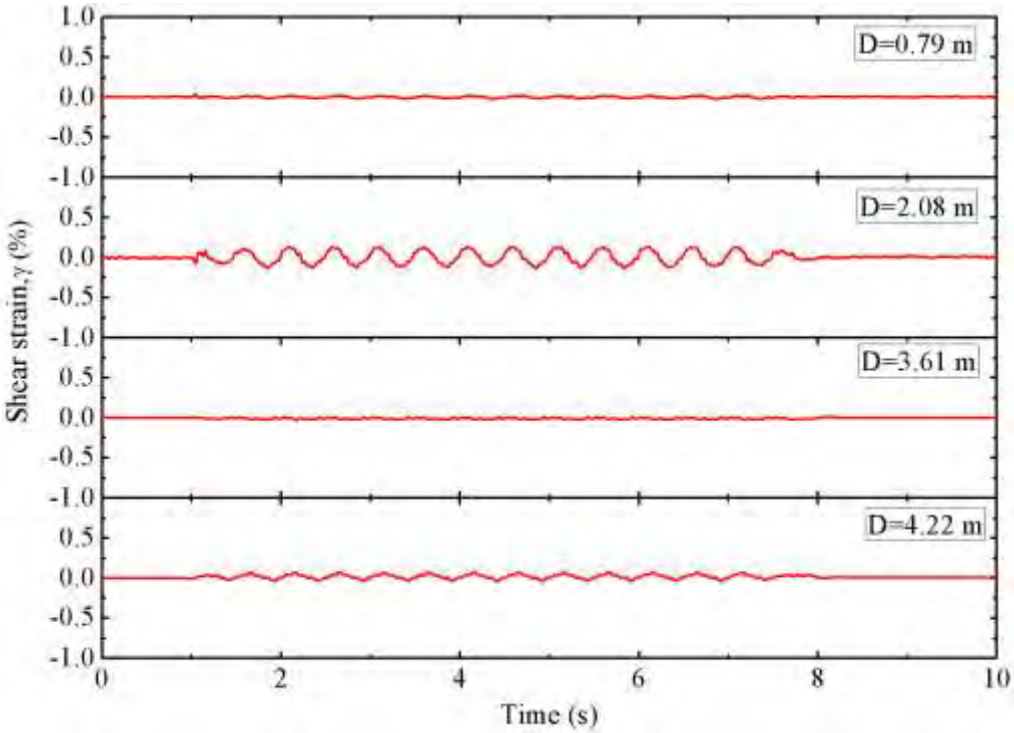

(a) Shear strain

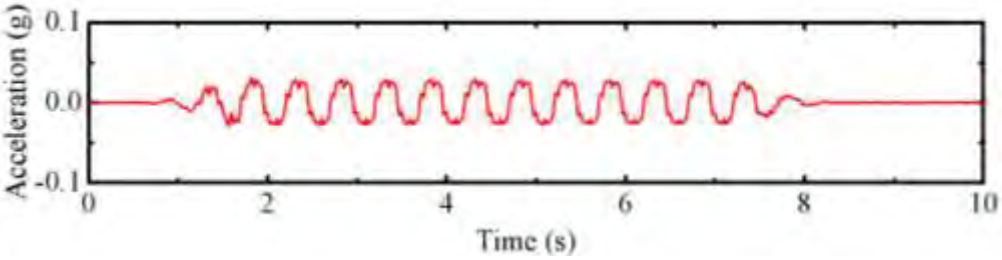

(b) B3X

Fig.E. 95 Time history of shear strain of T37 (a_{max}=0.03 g/15 cyc)

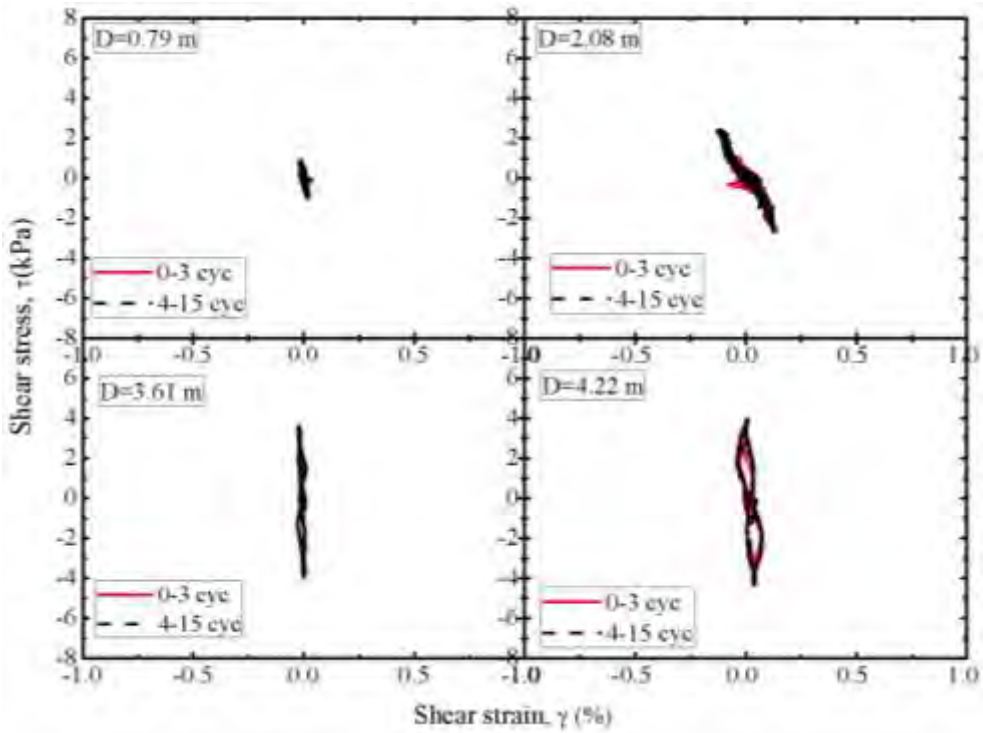

Fig.E. 96 Shear stress- strain loop of T37 (a_{max}=0.03 g/15 cyc)

E.4.6.2 T38-IM3 (a_{max}=0.10 g/15 cyc)

The time history of shear stress of the soil at different depths in T38 (a_{max}=0.10 g/15 cyc) is plotted in Fig.E. 76. Fig.E. 77 shows the time history of shear strain of the soil at different depths in T38. The shear stress-strain response of the soil at different depths in T38 is plotted in Fig.E. 78.

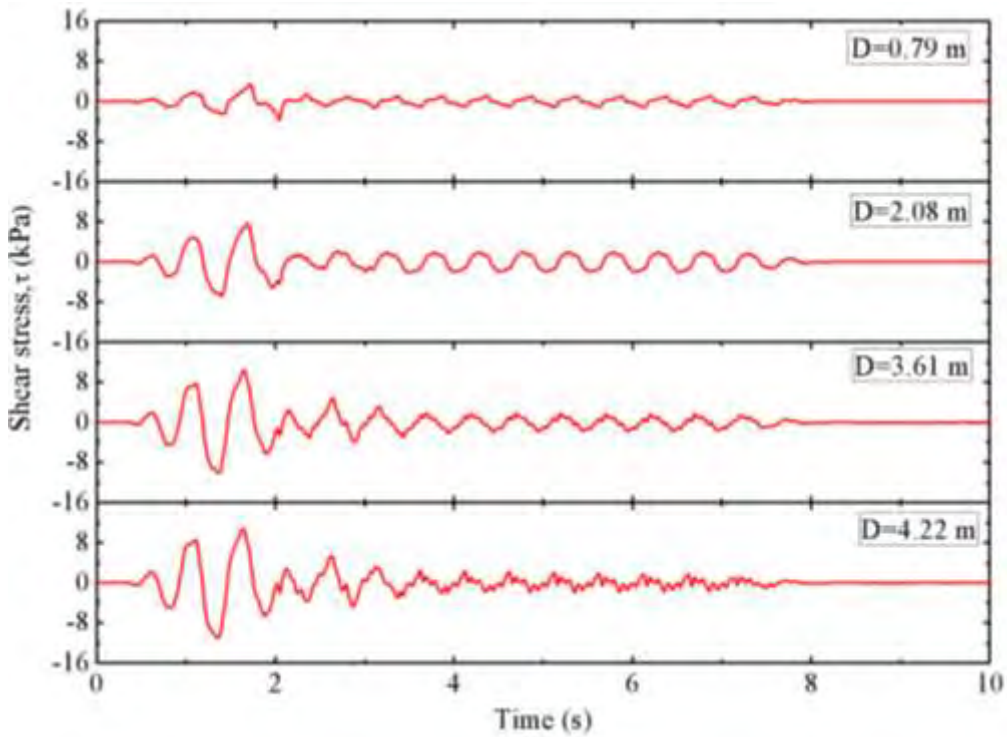

(a) Shear stress

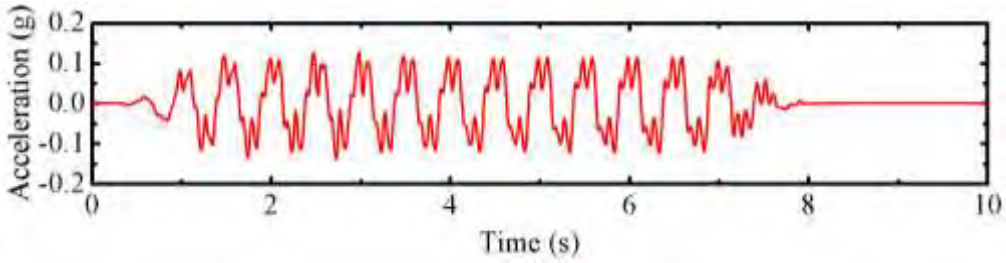

(b) B3X

Fig.E. 97 Time history of shear stress of T38 (a_{max}=0.10 g/15 cyc)

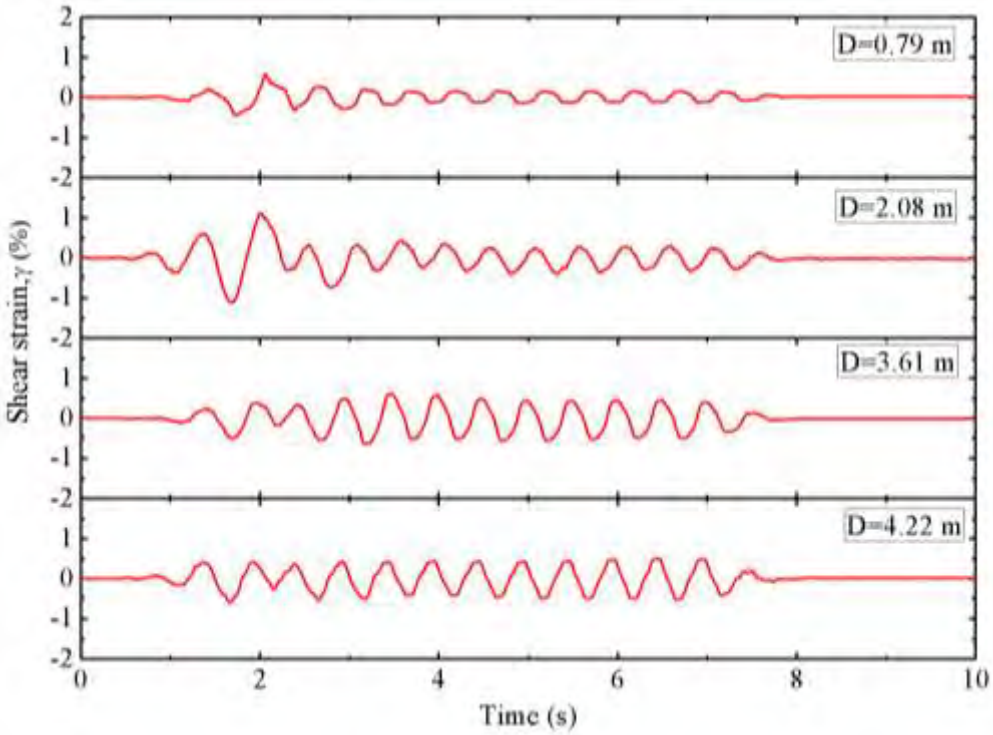

(a) Shear strain

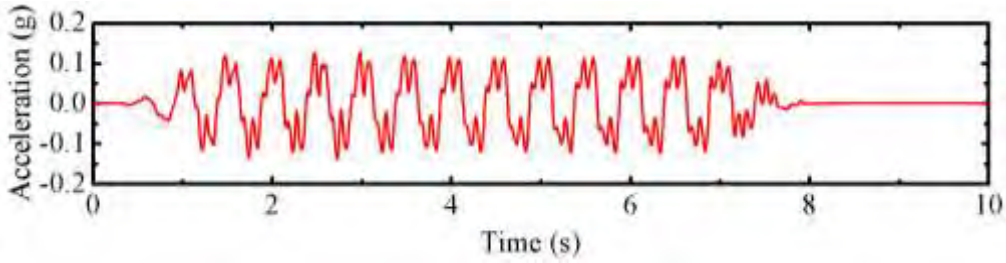

(b) B3X

Fig.E. 98 Time history of shear strain of T38 (a_{max}=0.10 g/15 cyc)

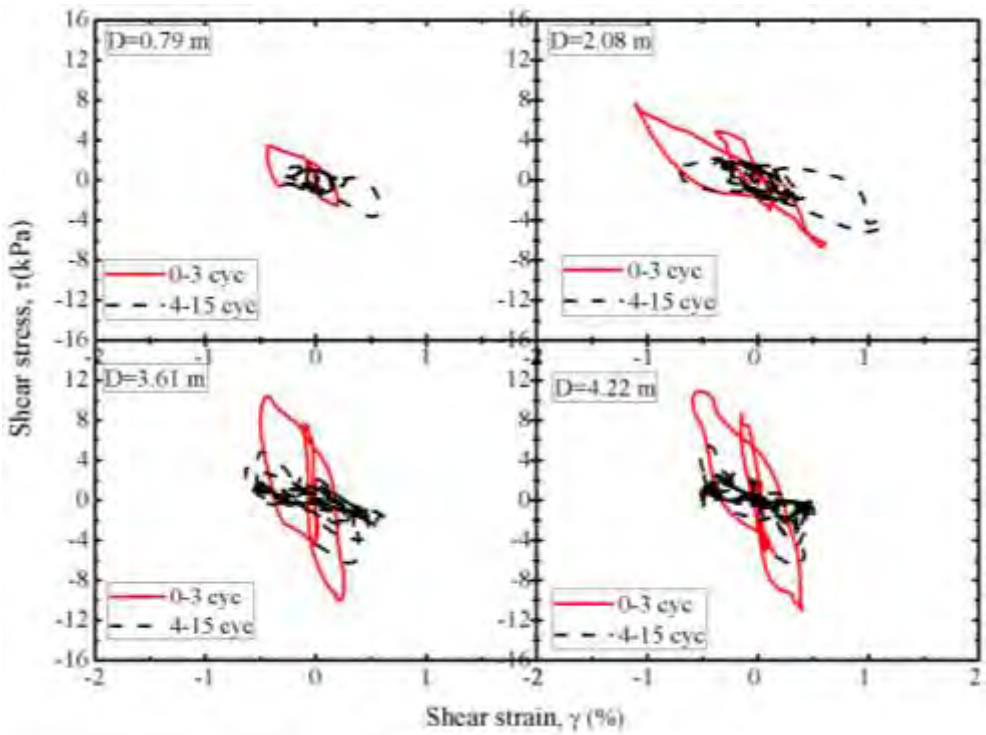

Fig.E. 99 Shear stress- strain loop of T38 (a_{max}=0.10 g/15 cyc)

E.5 Liquefaction tests-shaking series 7

This shaking series consists of T39a (IM1), T39 through T43 (IM4), T44 (IM2) and T45 (IM3)-refer to Fig. 7.24 and Table 7.8 for details. Only T44 and T45 are presented in this section.

E.5.1 Base shaker

E.5.1.1 T44-IM2 (a_{max}=0.03 g/15 cyc)

Fig.E. 100 compares the recorded base acceleration at different locations for both x-(shaking) and y-(non-shaking) direction of T44 (a_{max}=0.03 g/15 cyc).

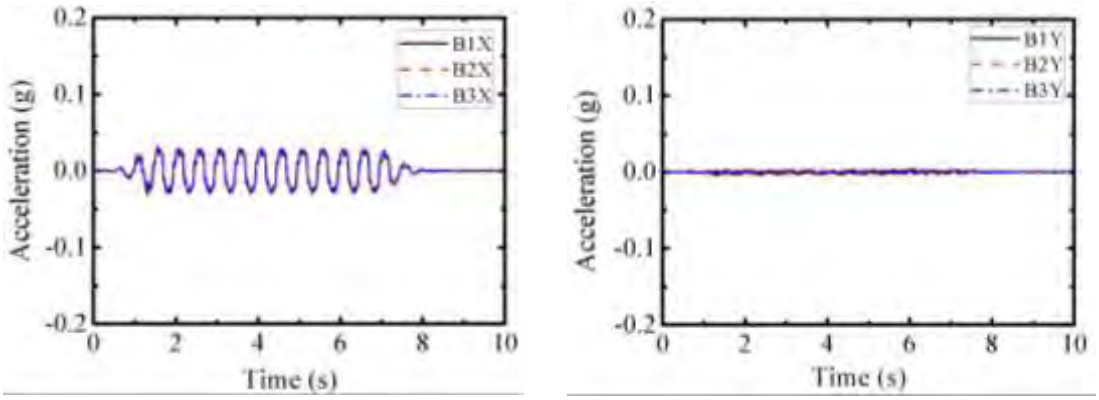

(a) x-direction (b) y-direction

Fig.E. 100 Base shaker of T44 (a_{max}=0.03 g/15 cyc)

E.5.1.2 T45-IM3 (a_{max}=0.10 g/15 cyc)

Fig.E. 101 compares the recorded base acceleration at different locations for both x-(shaking) and y-(non-shaking) direction of T45 (a_{max}=0.10 g/15 cyc).

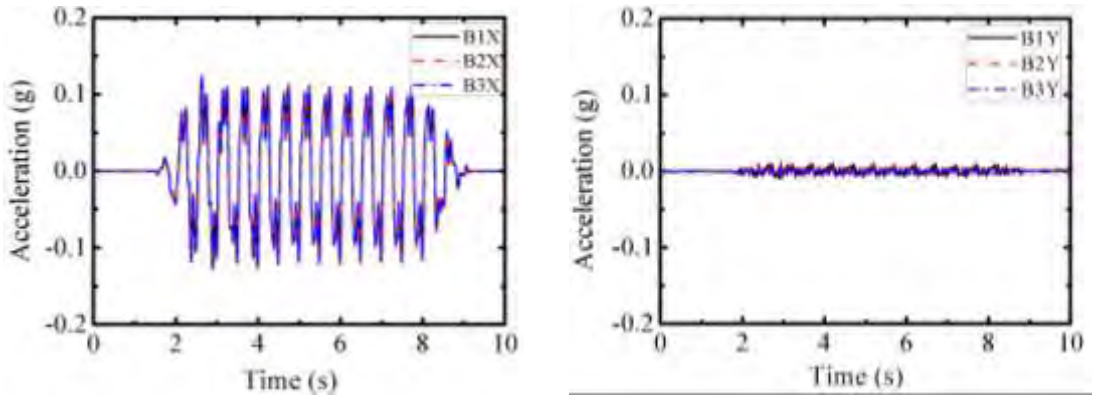

(a) x-direction (b) y-direction

Fig.E. 101 Base shaker of T45 (a_{max}=0.10 g/15 cyc)

E.5.2 Acceleration response

E.5.2.1 T44-IM2 (a_{max}=0.03 g/15 cyc)

Fig.E. 102 compares the acceleration from selected accelerometers as the base motion of T44 (a_{max}=0.03 g/15 cyc) is input. It is noticed that the accelerometer located at laminate 27 instead of laminate 30 is extracted to be the surface acceleration recorder because of post liquefaction densification of soil after series of shaking. The amplification factor of soil at different depths is

shown in Fig.E. 103.

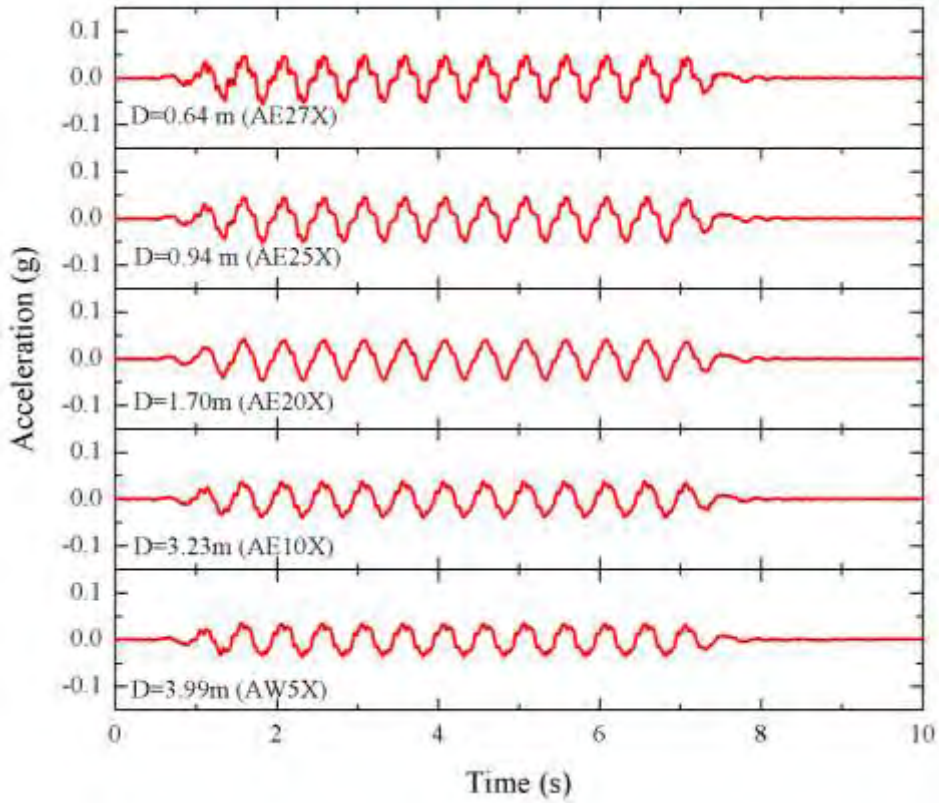

(a) Laminate acceleration

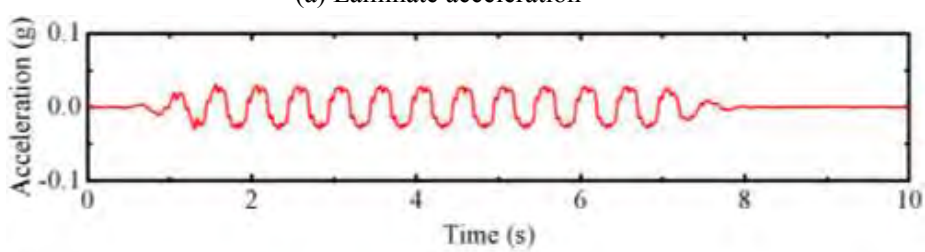

(b) B3X

Fig.E. 102 x-acceleration at different depths and base of T44 (a_{max}=0.03g/15 cyc)

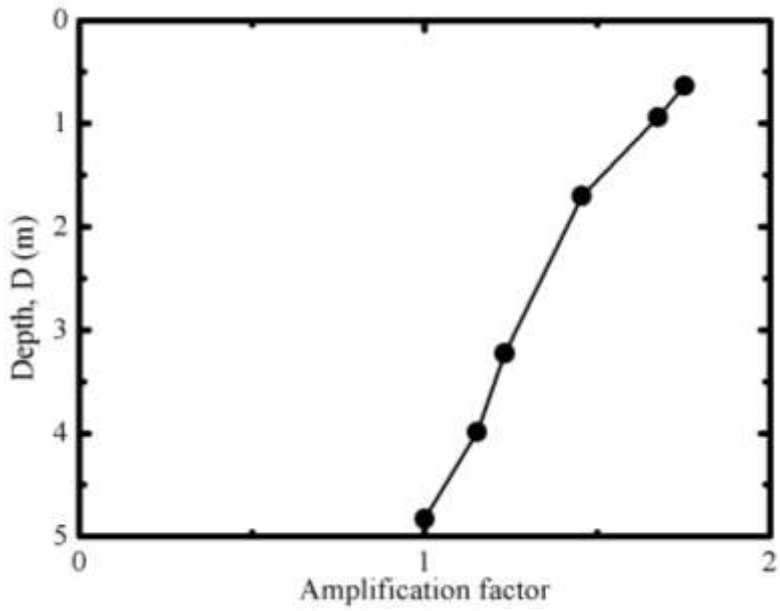

Fig.E. 103 Amplification factor profile of T44 (a_{max}=0.03 g/15 cyc)

E.5.2.2 T45-IM3 (a_{max}=0.10 g/15 cyc)

Fig.E. 104 compares the acceleration from selected accelerometers as the base motion of T45 (a_{max}=0.10 g/15 cyc) is input. It is noticed that the accelerometer located at laminate 27 instead of laminate 30 is extracted to be the surface acceleration recorder because of post liquefaction densification of soil after series of shaking. The amplification factor of soil at different depths is shown in Fig.E. 105.

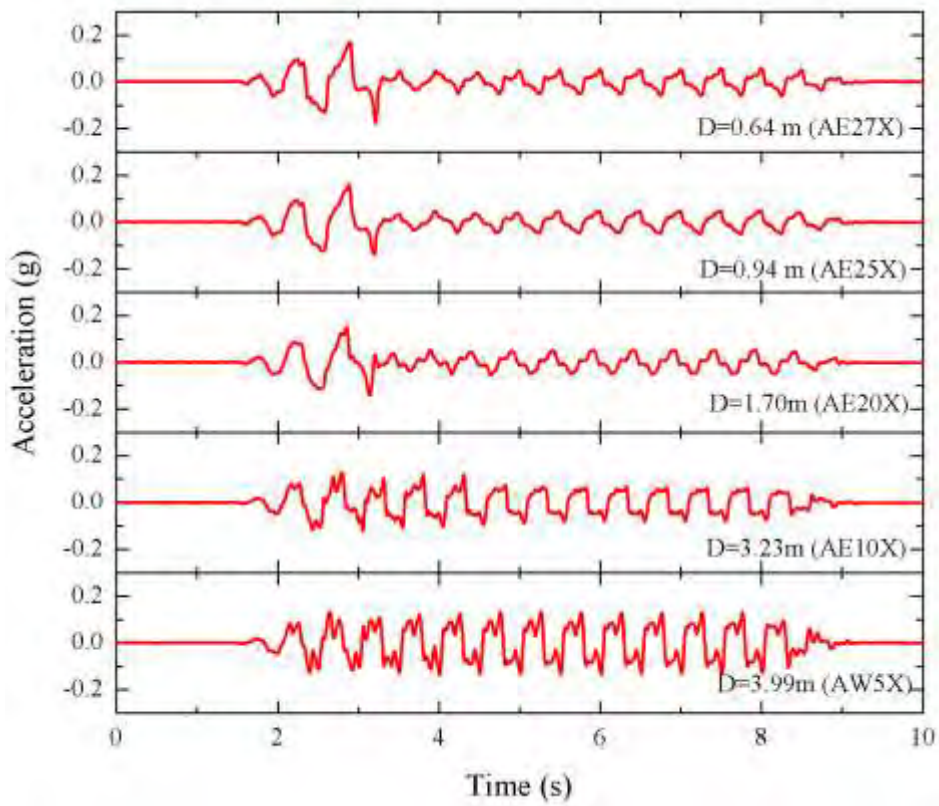

(a) Laminate acceleration

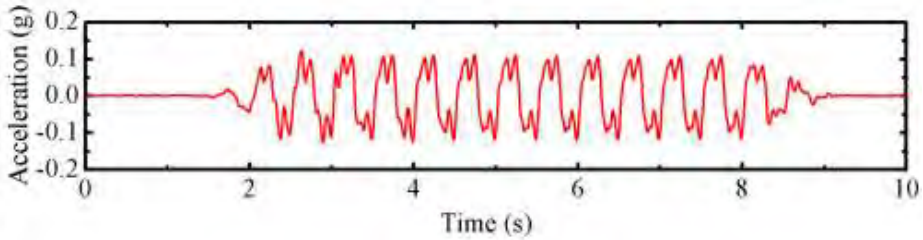

(b) B3X

Fig.E. 104 x-acceleration at different depths and base of T45 (a_{max}=0.10 g/15 cyc)

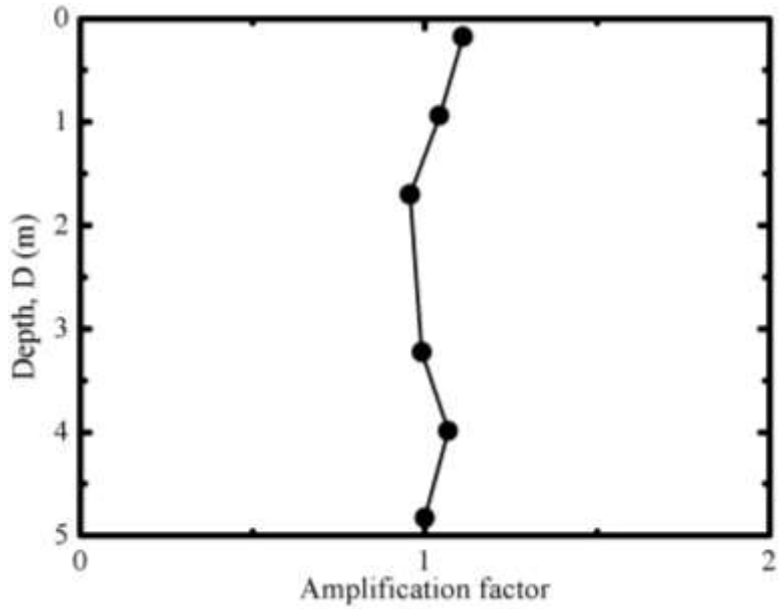

Fig.E. 105 Amplification factor profile of T45 (a_{max}=0.10 g/15 cyc)

E.5.3 Excess pore water pressure (Δu) response

E.5.3.1 T44-IM2 (a_{max}=0.03 g/15 cyc)

Fig.E. 106 presents the time history of normalized excess pore water pressure r_u and base acceleration during shaking of T44 (a_{max}=0.03 g/15 cyc), to better observe whether and when liquefaction occurs (i.e., r_u reaches unity) at different soil depths. Fig.E. 107 shows the time history of the excess pore water pressure (EPWP) Δu of the soil profile recorded by piezometers of T44. Fig.E. 108 plots the Δu as well as r_u with respect to depth at various shaking cycle for T44.

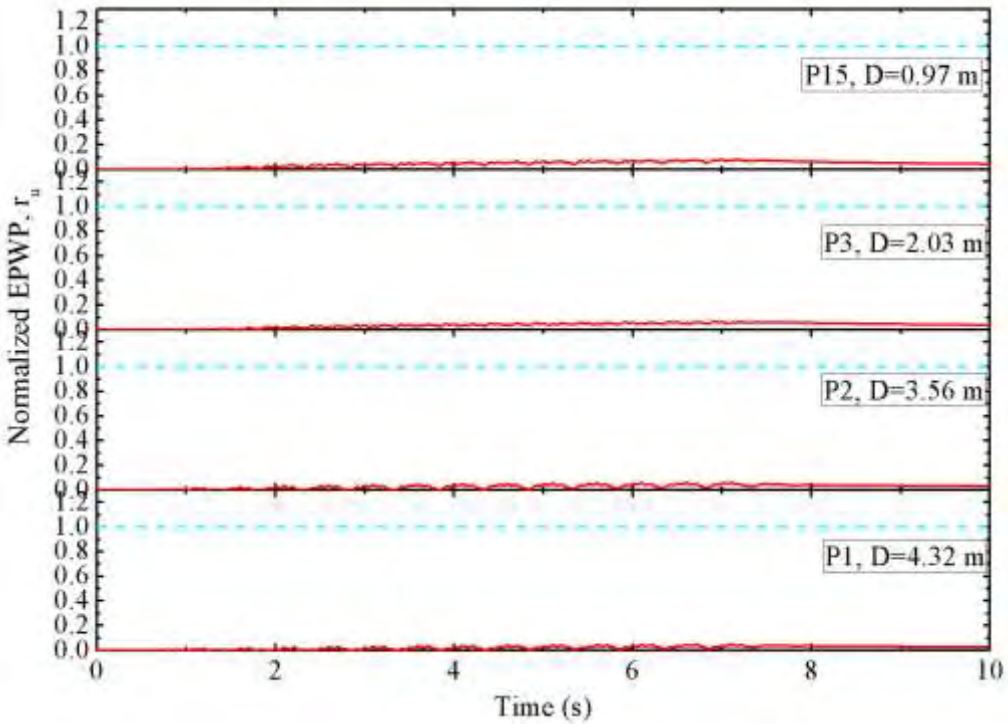

(a) r_u

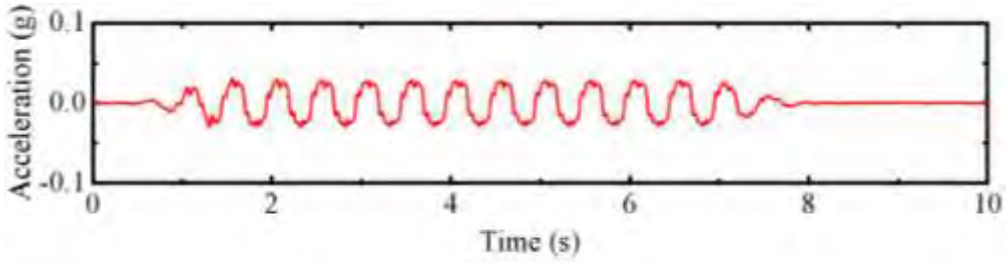

(b) B3X

Fig.E. 106 Time history of r_u and base acceleration of T44 (a_{max}=0.03 g/15 cyc)

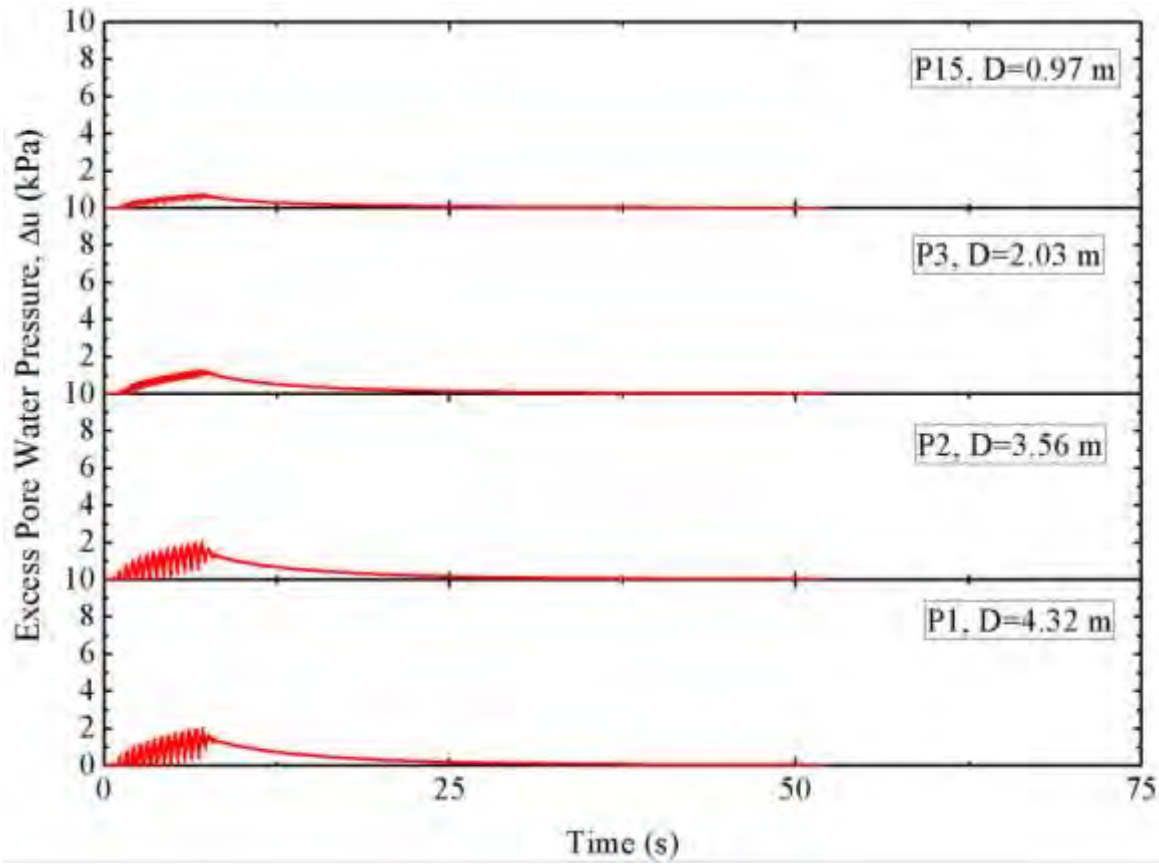

Fig.E. 107 Time history of Δu of T44 (a_{max}=0.03 g/15 cyc)

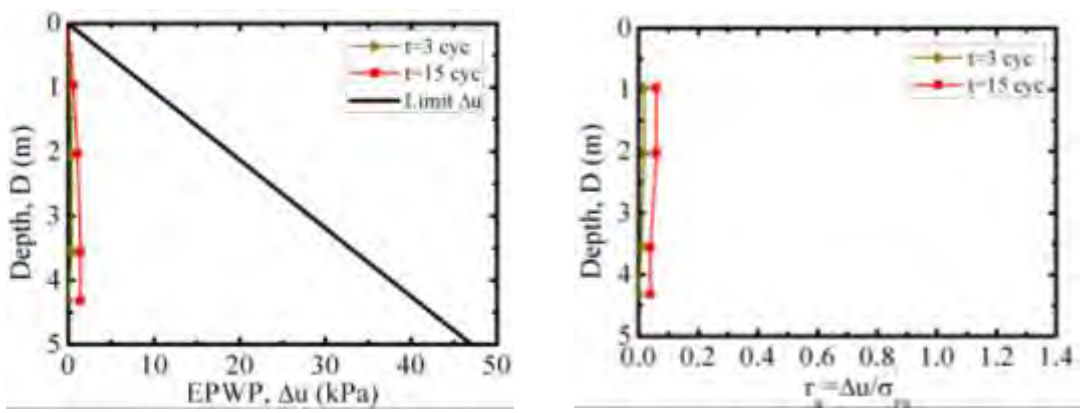

(a) Δu vs D (b) r_u vs D

Fig.E. 108 EPWP profiles of T44 (a_{max}=0.03 g/15 cyc)

E.5.3.2 T45-IM3 (a_{max}=0.10 g/15 cyc)

Fig.E. 109 presents the time history of normalized excess pore water pressure r_u and base acceleration during shaking of T45 (a_{max}=0.10 g/15 cyc), to better observe whether and when liquefaction occurs (i.e., r_u reaches unity) at different soil depths. Fig.E. 110 shows the time history

of the excess pore water pressure (EPWP) Δu of the soil profile recorded by piezometers of T45. Fig.E. 111 plots the Δu as well as r_u with respect to depth at various shaking cycle for T45.

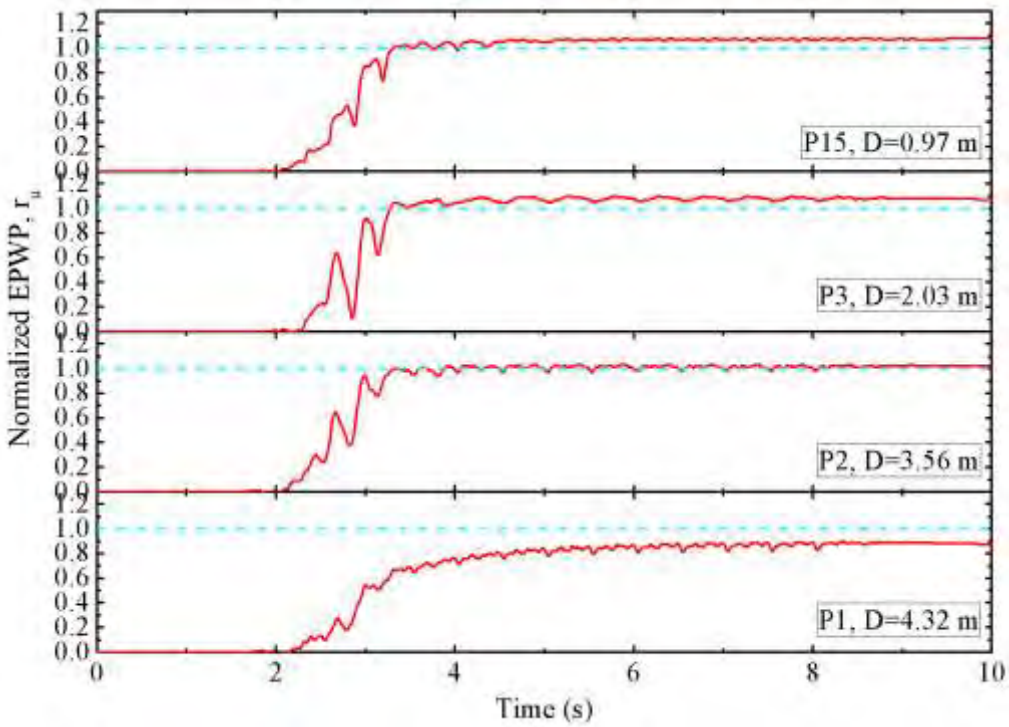

(a) r_u

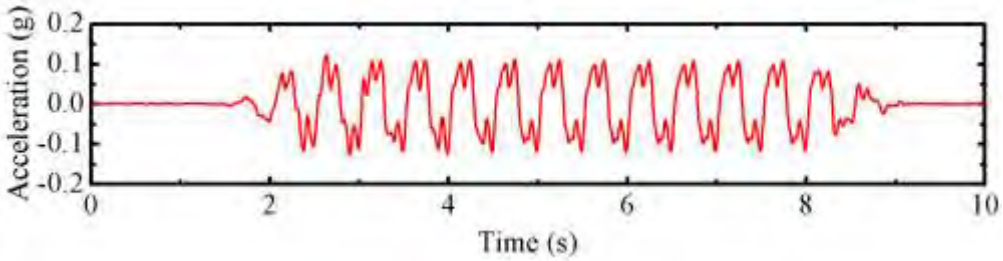

(b) B3X

Fig.E. 109 Time history of r_u and base acceleration of T45 (a_{max}=0.10 g/15 cyc)

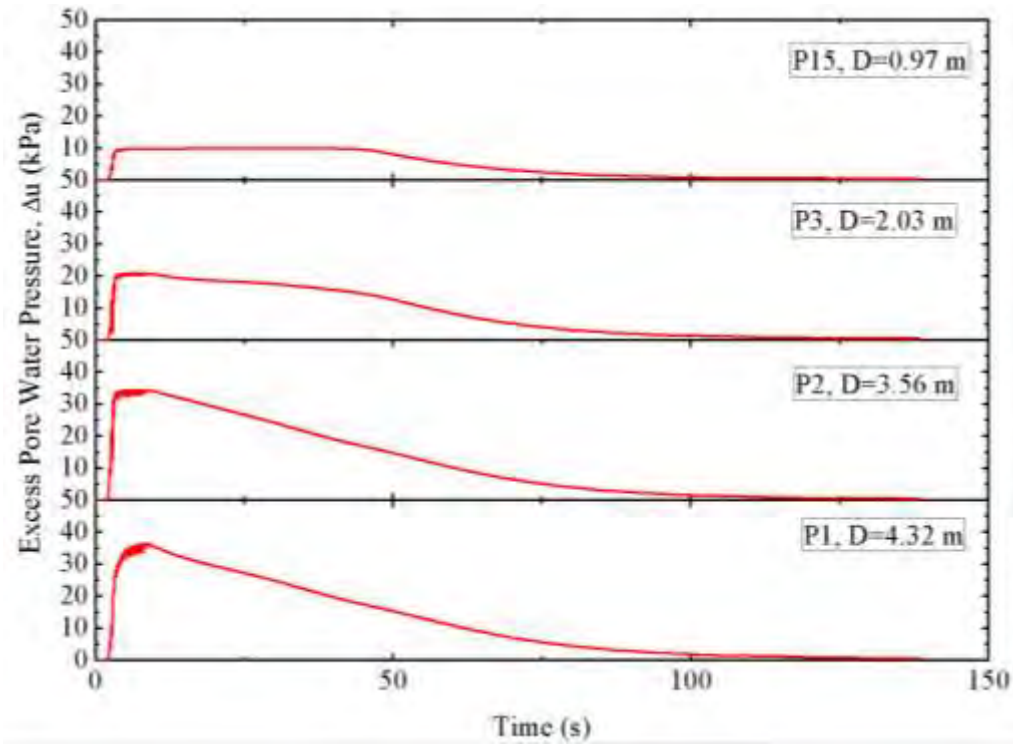

Fig.E. 110 Time history of Δu of T45 (a_{max}=0.10 g/15 cyc)

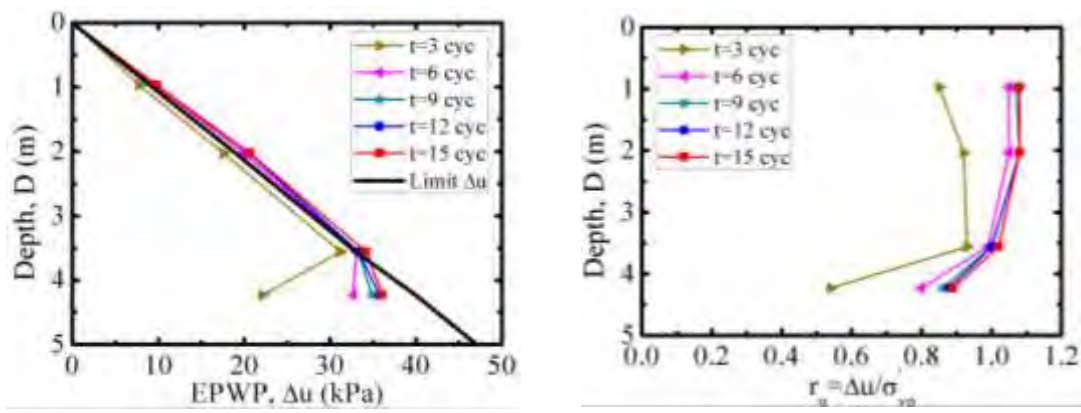

(a) Δu vs D (b) r_u vs D

Fig.E. 111 EPWP profiles of T45 (a_{max}=0.10 g/15 cyc)

E.5.4 Horizontal displacement

E.5.4.1 T44-IM2 (a_{max}=0.03 g/15 cyc)

Fig.E. 112(a) plots the time history of horizontal displacement of the soil at selected depths in T44 (a_{max}=0.03 g/15 cyc). Fig.E. 112(b) and (c) plot the time history of relative horizontal displacement of the soil at selected depths in T44.

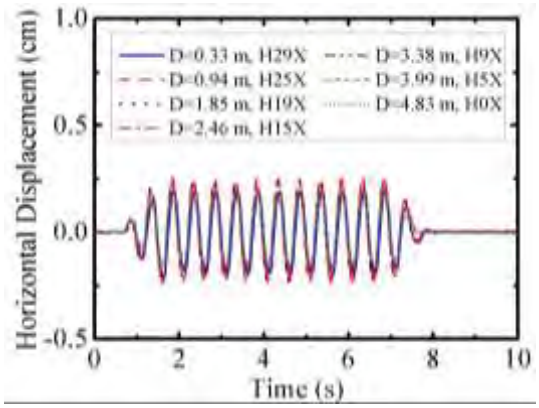

(a) Horizontal displacement

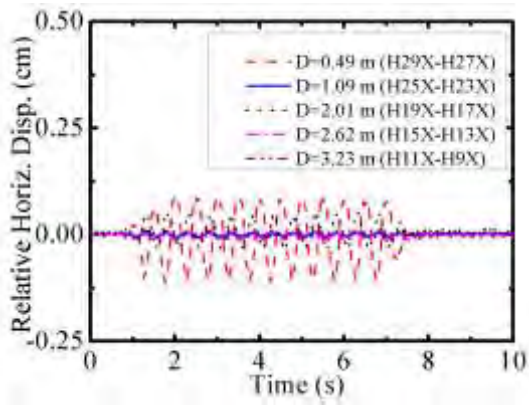

(b) Relative horiz. disp. b/w every other ring

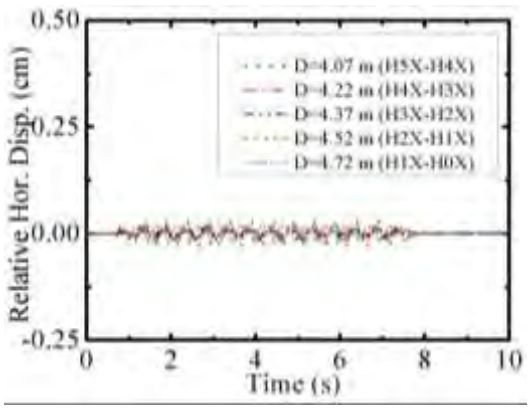

(c) Relative horiz. disp. b/w every ring

Fig.E. 112 Time history of horizontal displacement of T44 (a_{max}=0.03 g/15 cyc)

E.5.4.2 T45-IM3 (a_{max}=0.10 g/15 cyc)

Fig.E. 113(a) plots the time history of horizontal displacement of the soil at selected depths in T45 (a_{max}=0.10 g/15 cyc). Fig.E. 113(b) and (c) plot the time history of relative horizontal displacement of the soil at selected depths in T45.

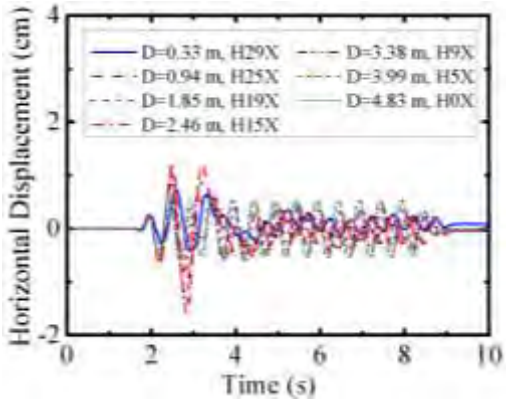

(a) Horizontal displacement

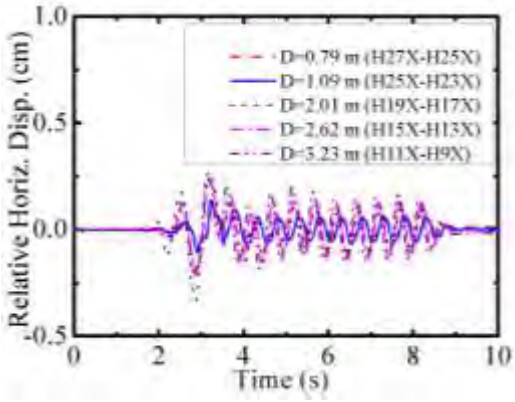

(b) Relative horiz. disp. b/w every other ring

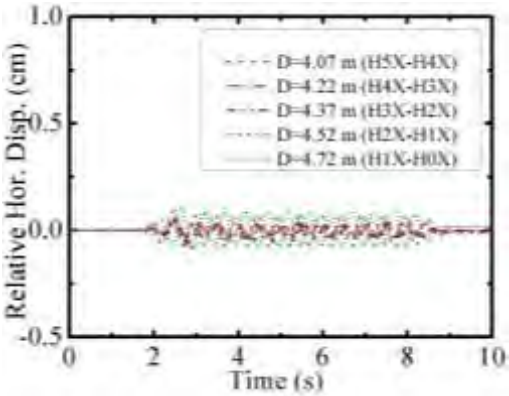

(c) Relative horiz. disp. b/w every ring

Fig.E. 113 Time history of horizontal displacement of T45 (a_{max}=0.10 g/15 cyc)

E.5.5 Ground settlement

Fig.E. 114 plots the time history of incremental ground settlement in shaking series 7 while Table E. 5 summarizes the incremental and total ground settlement of liquefaction tests in shaking series 7. The average incremental settlement of each liquefaction test is based on the incremental settlement of V1 and V3 because V2 was buried in the soil after T2.

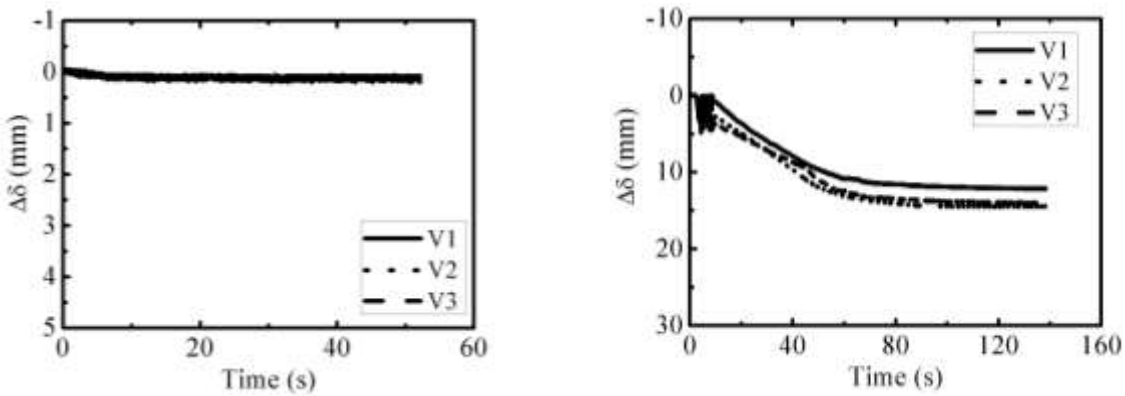

(a) T44 (a_{max}=0.03 g/15 cyc) (c) T45 (a_{max}=0.10 g/15 cyc)

Fig.E. 114 Time history of incremental ground settlement in shaking series 7

Table E. 5 Ground settlement of liquefaction tests-shaking series 7

Shaking series	Shaking event	Input Motion	Δδ for each shaking test			$\Delta\delta_{ave.}$	Cumulative Settlement δ
			V1	V2	V3		
			(mm)	(mm)	(mm)	(mm)	(mm)
7	T39a	IM1 (a_{max}=0.015 g/5 cyc)	0	0	0	0	397
	T39	IM4 (a_{max}=0.03 g/5 cyc)	2	2	1	2	398
	T40	IM4 (a_{max}=0.03 g/5 cyc)	0	0	0	0	398
	T41	IM4 (a_{max}=0.03 g/5 cyc)	0	0	0	0	398
	T42	IM4 (a_{max}=0.03 g/5 cyc)	0	0	0	0	398
	T43	IM4 (a_{max}=0.03 g/5 cyc)	0	0	0	0	398
	T44	IM2 (a_{max}=0.03 g/15 cyc)	0	0	0	0	398
	T45	IM3 (a_{max}=0.10 g/15 cyc)	12	14	14	13	411

E.5.6 Stress-strain response

E.5.6.1 T44-IM2 (a_{max}=0.03 g/15 cyc)

The time history of shear stress of the soil at different depths in T44 (a_{max}=0.03 g/15 cyc) is plotted in Fig.E. 115. Fig.E. 116 shows the time history of shear strain of the soil at different depths in T44. The shear stress-strain response of the soil at different depths in T44 is plotted in Fig.E. 117.

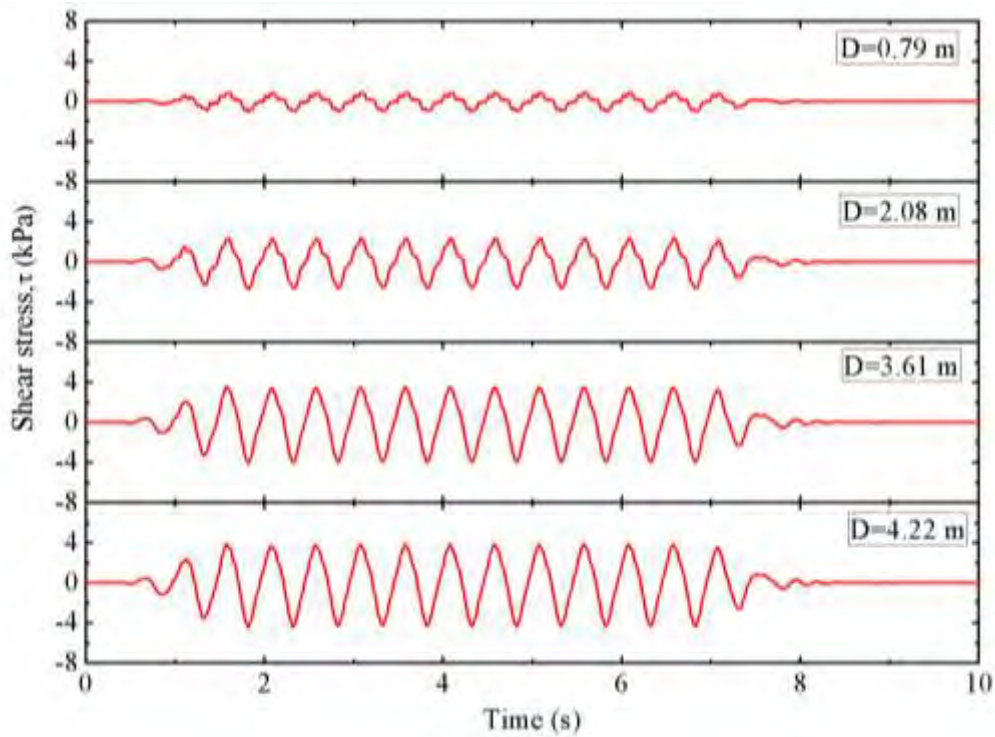

(a) Shear stress

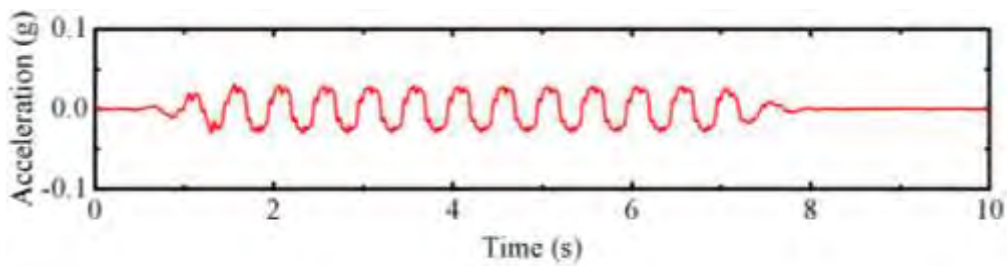

(b) B3X

Fig.E. 115 Time history of shear stress of T44 (a_{max}=0.03 g/15 cyc)

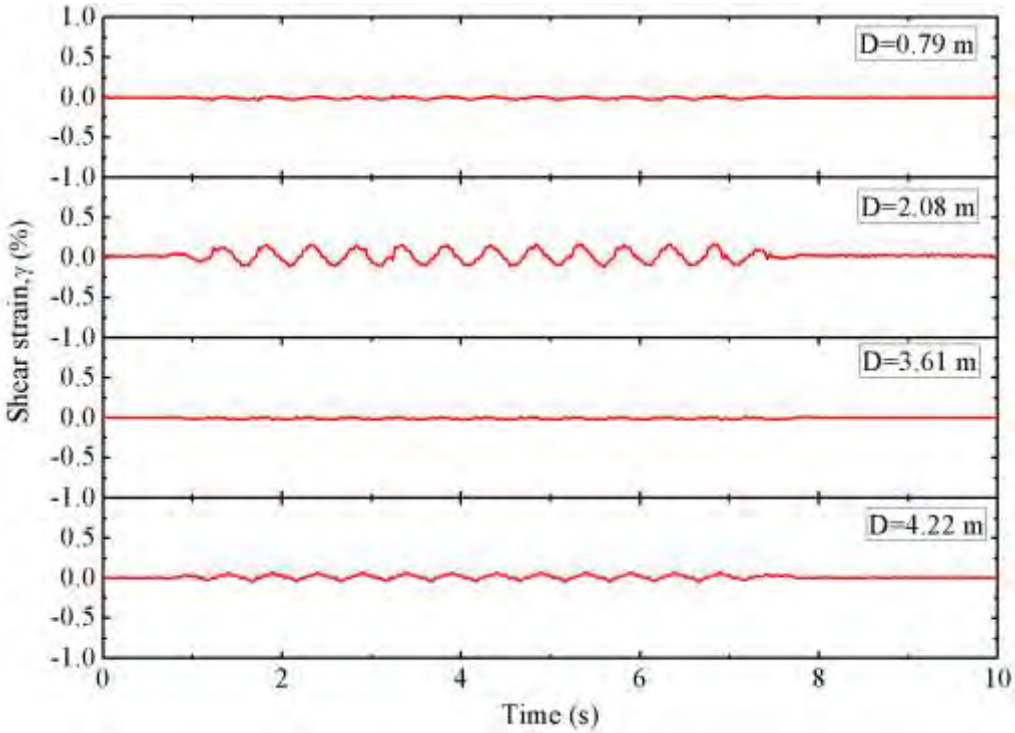

(a) Shear strain

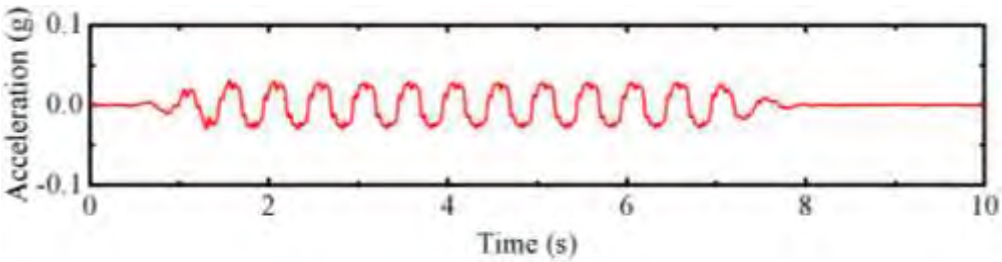

(b) B3X

Fig.E. 116 Time history of shear strain of T44 (a_{max}=0.03 g/15 cyc)

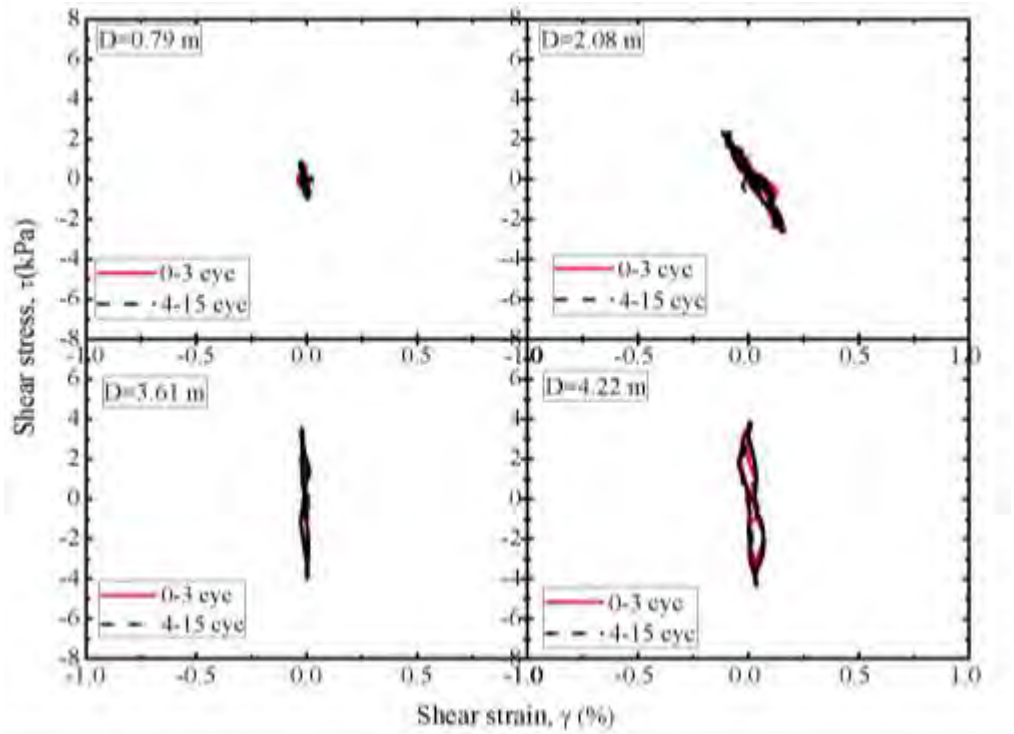

Fig.E. 117 Shear stress- strain loop of T44 (a_{max}=0.03 g/15 cyc)

E.5.6.2 T45-IM3 (a_{max}=0.10 g/15 cyc)

The time history of shear stress of the soil at different depths in T45 (a_{max}=0.10 g/15 cyc) is plotted in Fig.E. 118. Fig.E. 119 shows the time history of shear strain of the soil at different depths in T45. The shear stress-strain response of the soil at different depths in T45 is plotted in Fig.E. 120.

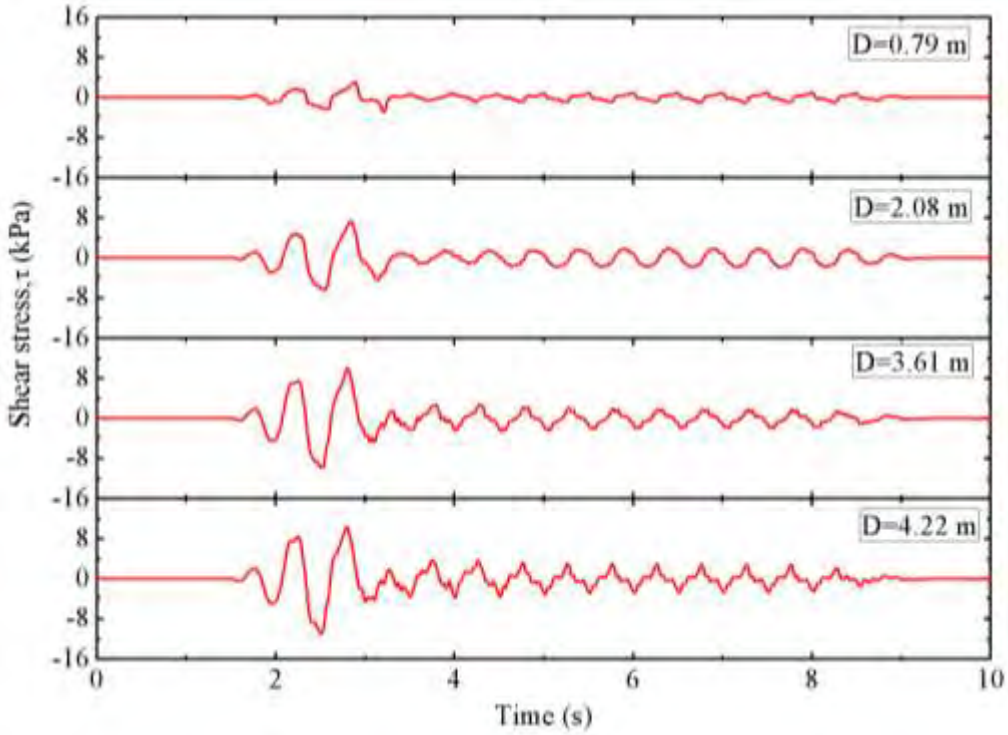

(a) Shear stress

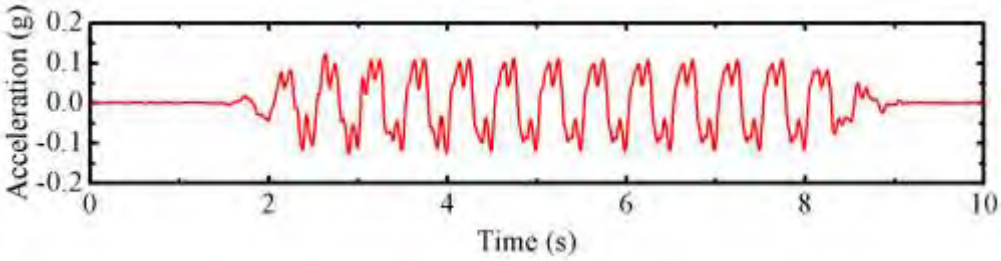

(b) B3X

Fig.E. 118 Time history of shear stress of T45 (a_{max}=0.10 g/15 cyc)

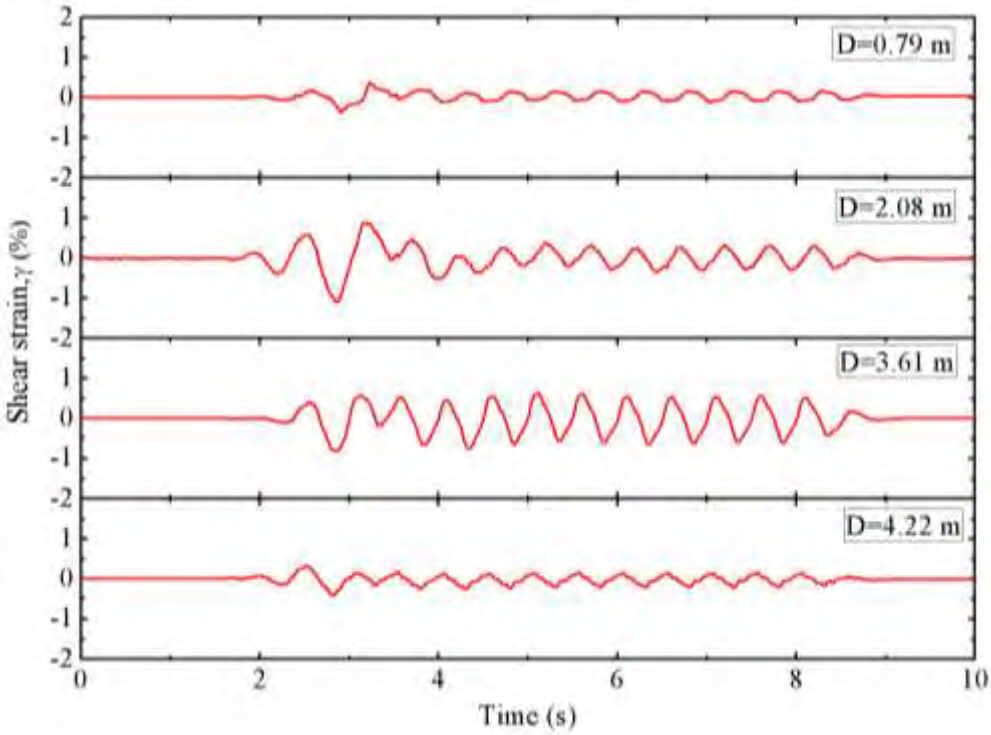

(a) Shear strain

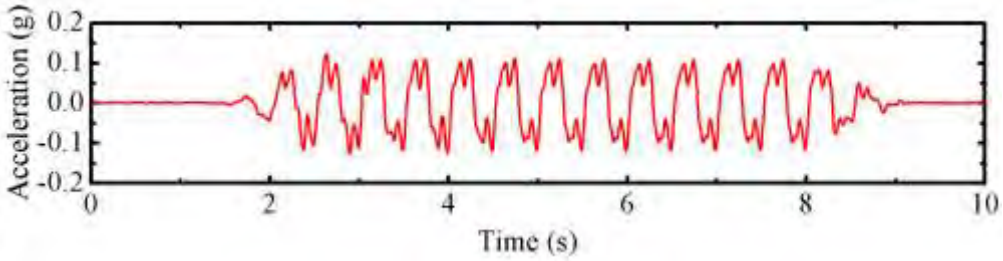

(b) B3X

Fig.E. 119 Time history of shear strain of T45 (a_{max}=0.10 g/15 cyc)

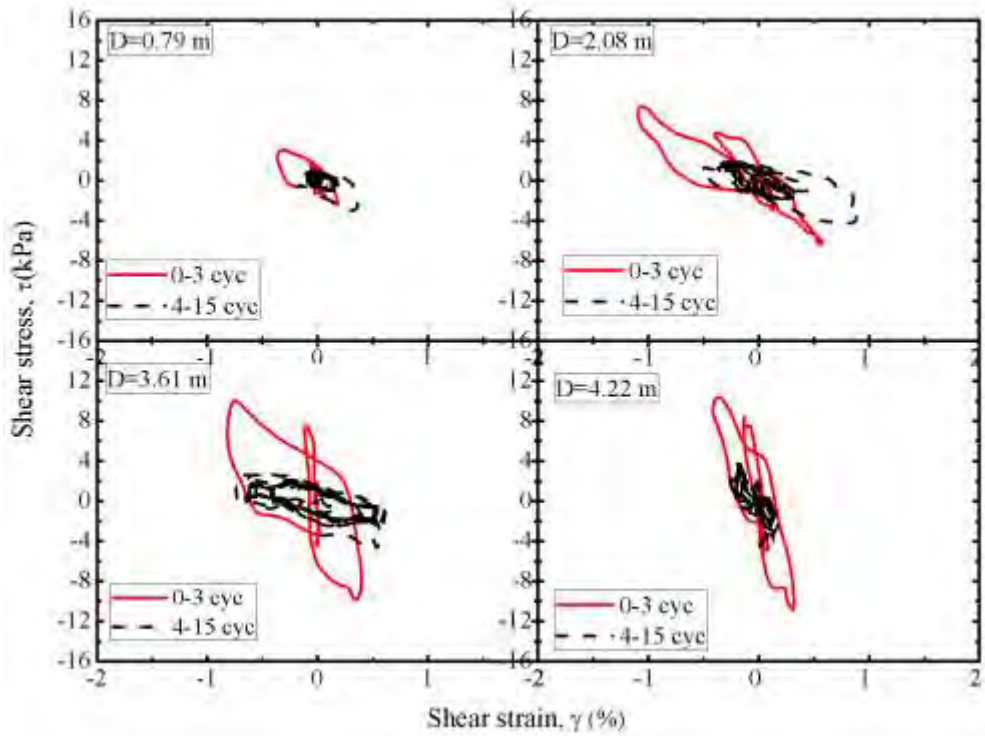

Fig.E. 120 Shear stress- strain loop of T45 (a_{max}=0.10 g/15 cyc)

E.6 Liquefaction tests-shaking series 8

This shaking series consists of T46a (IM1), T46 through T50 (IM4), T51a (IM1), T51 (IM2) and T52 (IM3)-refer to Fig. 7.24 and Table 7.8 for details. The soil response of T46a and T51a are similar to that of T1. Only T51 and T52 are analyzed in this section.

E.6.1 Base shaker

E.6.1.1 T51-IM2 (a_{max}=0.03 g/15 cyc)

Fig.E. 121 compares the recorded base acceleration at different locations for both x-(shaking) and y-(non-shaking) direction of T51 (a_{max}=0.03 g/15 cyc).

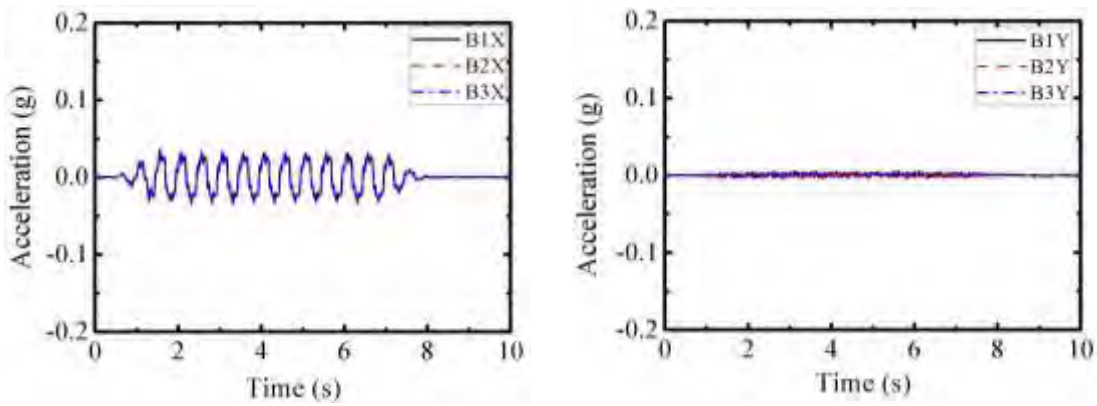

(a) x-direction (b) y-direction

Fig.E. 121 Base shaker of T51 (a_{max}=0.03 g/15 cyc)

E.6.1.2 T52-IM3 (a_{max}=0.10 g/15 cyc)

Fig.E. 122 compares the recorded base acceleration at different locations for both x-(shaking) and y-(non-shaking) direction of T52 (a_{max}=0.10 g/15 cyc).

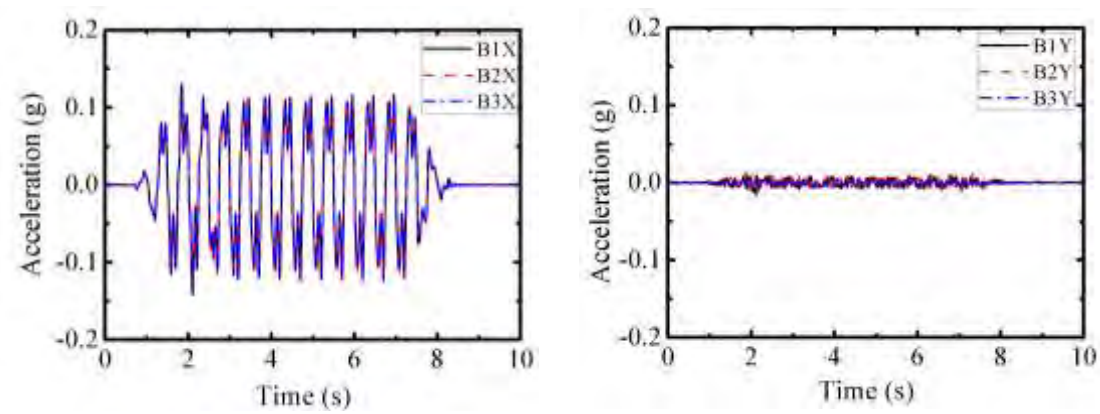

(a) x-direction (b) y-direction

Fig.E. 122 Base shaker of T52 (a_{max}=0.10 g/15 cyc)

E.6.2 Acceleration response

E.6.2.1 T51-IM2 (a_{max}=0.03 g/15 cyc)

Fig.E. 123 compares the acceleration from selected accelerometers as the base motion of T51 (a_{max}=0.03 g/15 cyc) is input. It is noticed that the accelerometer located at laminate 27 instead of laminate 30 is extracted to be the surface acceleration recorder because of post liquefaction densification of soil after series of shaking. The amplification factor of soil at different depths is

shown in Fig.E. 124.

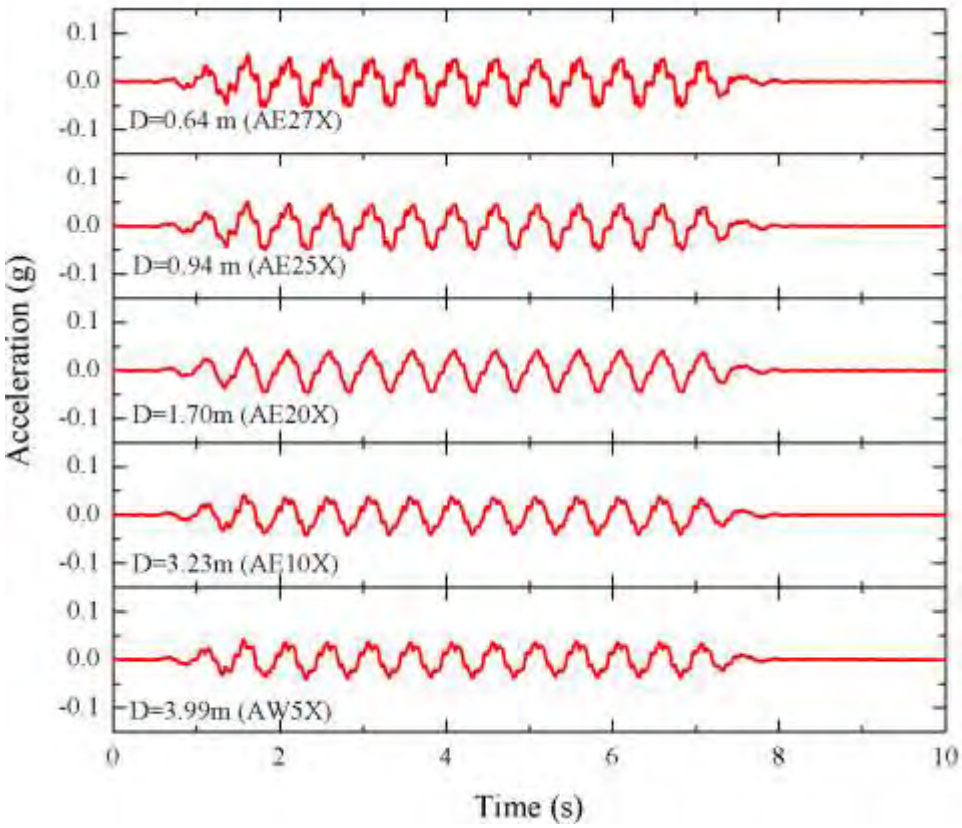

(a) Laminate acceleration

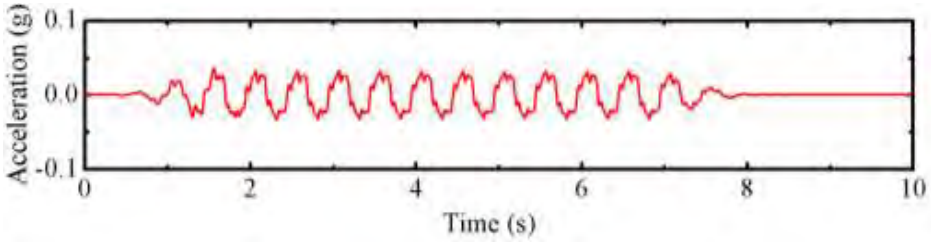

(b) B3X

Fig.E. 123 x-acceleration at different depths and base of T51 (a_{max}=0.03g/15 cyc)

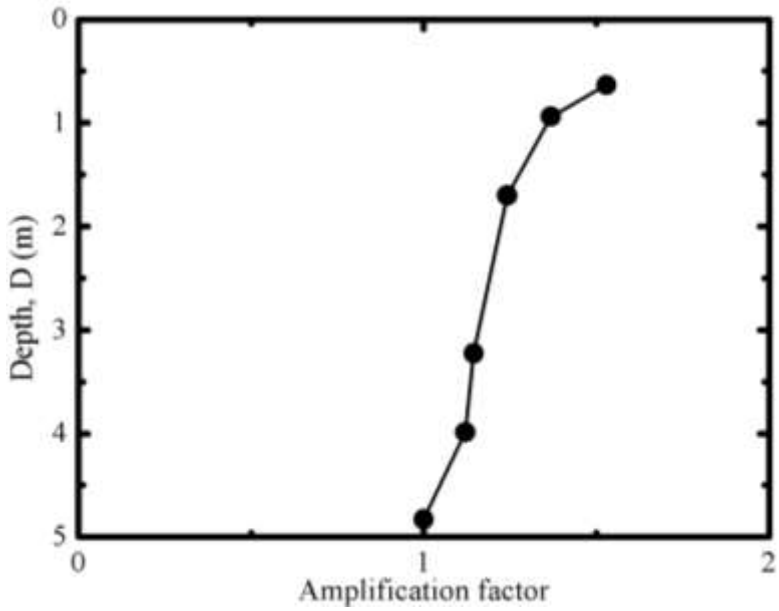

Fig.E. 124 Amplification factor profile of T51 (a_{max}=0.03 g/15 cyc)

E.6.2.2 T52-IM3 (a_{max}=0.10 g/15 cyc)

Fig.E. 125 compares the acceleration from selected accelerometers as the base motion of T52 (a_{max}=0.10 g/15 cyc) is input. It is noticed that the accelerometer located at laminate 27 instead of laminate 30 is extracted to be the surface acceleration recorder because of post liquefaction densification of soil after series of shaking. The amplification factor of soil at different depths is shown in Fig.E. 126.

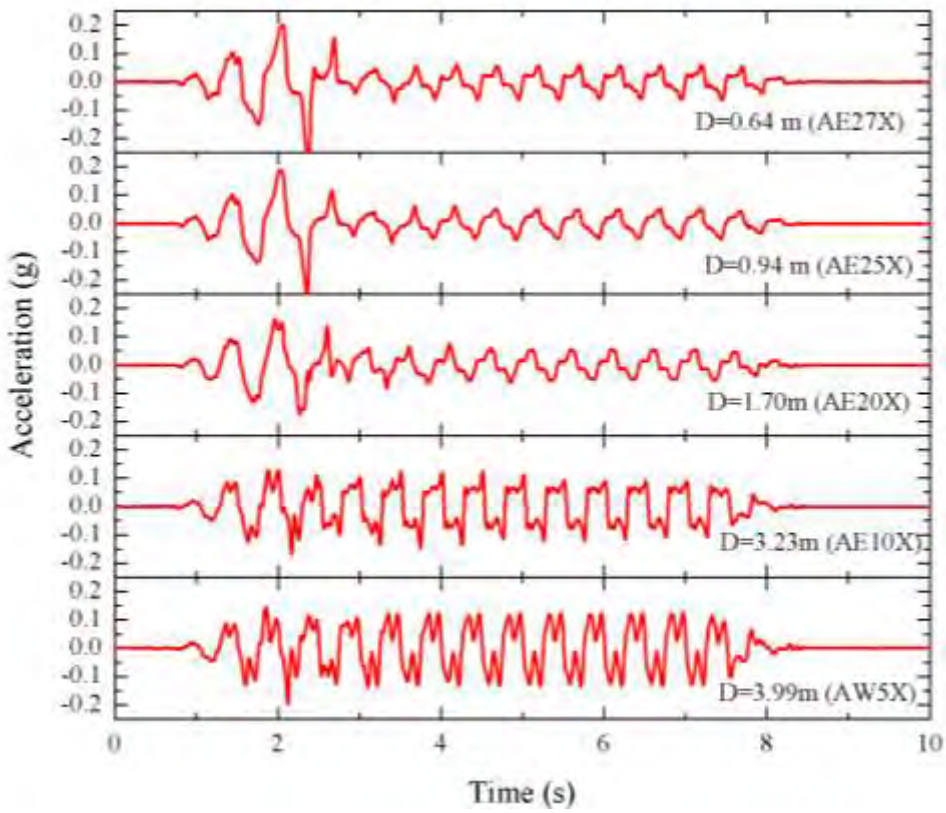

(a) Laminate acceleration

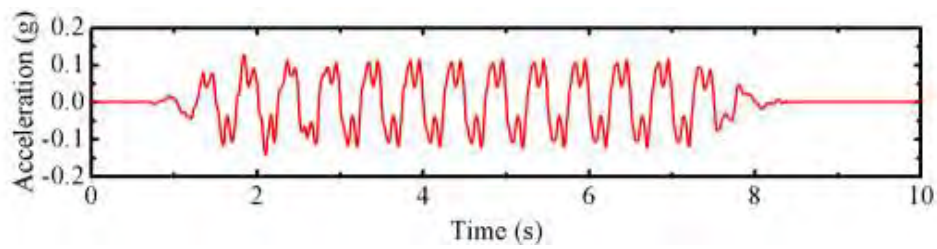

(b) B3X

Fig.E. 125 x-acceleration at different depths and base of T52 (a_{max}=0.10 g/15 cyc)

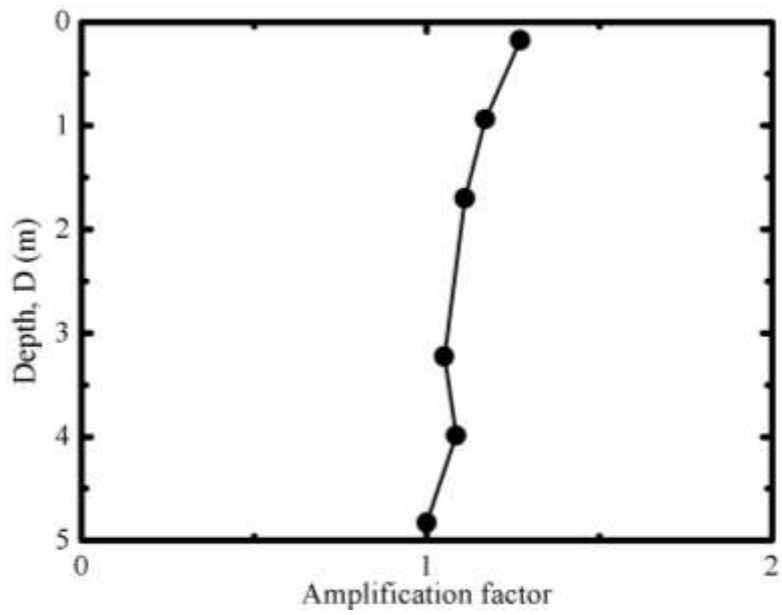

Fig.E. 126 Amplification factor profile of T52 (a_{max}=0.10 g/15 cyc)

E.6.3 Excess pore water pressure (Δu) response

E.6.3.1 T51-IM2 (a_{max}=0.03 g/15 cyc)

Fig.E. 127 presents the time history of normalized excess pore water pressure r_u and base acceleration during shaking of T51 (a_{max}=0.03 g/15 cyc), to better observe whether and when liquefaction occurs (i.e., r_u reaches unity) at different soil depths. Fig.E. 128 shows the time history of the excess pore water pressure (EPWP) Δu of the soil profile recorded by piezometers of T51. Fig.E. 129 plots the Δu as well as r_u with respect to depth at various shaking cycle for T51.

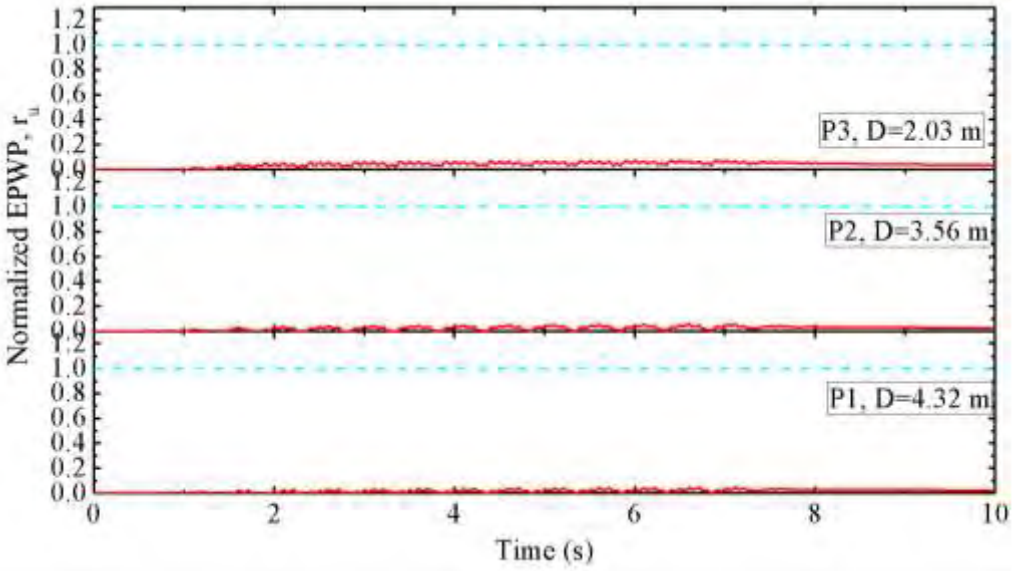

(a) r_u

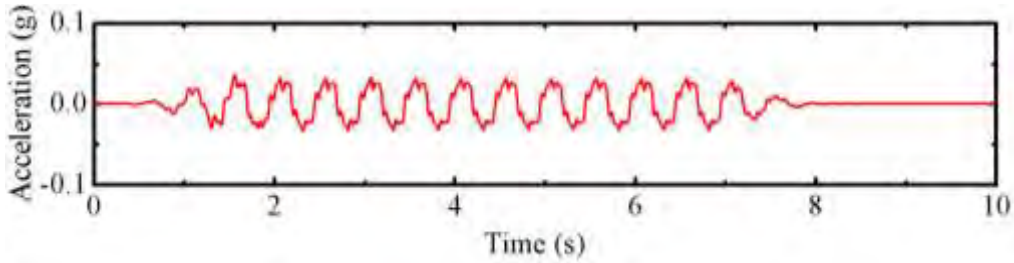

(b) B3X

Fig.E. 127 Time history of r_u and base acceleration of T51 (a_{max}=0.03 g/15 cyc)

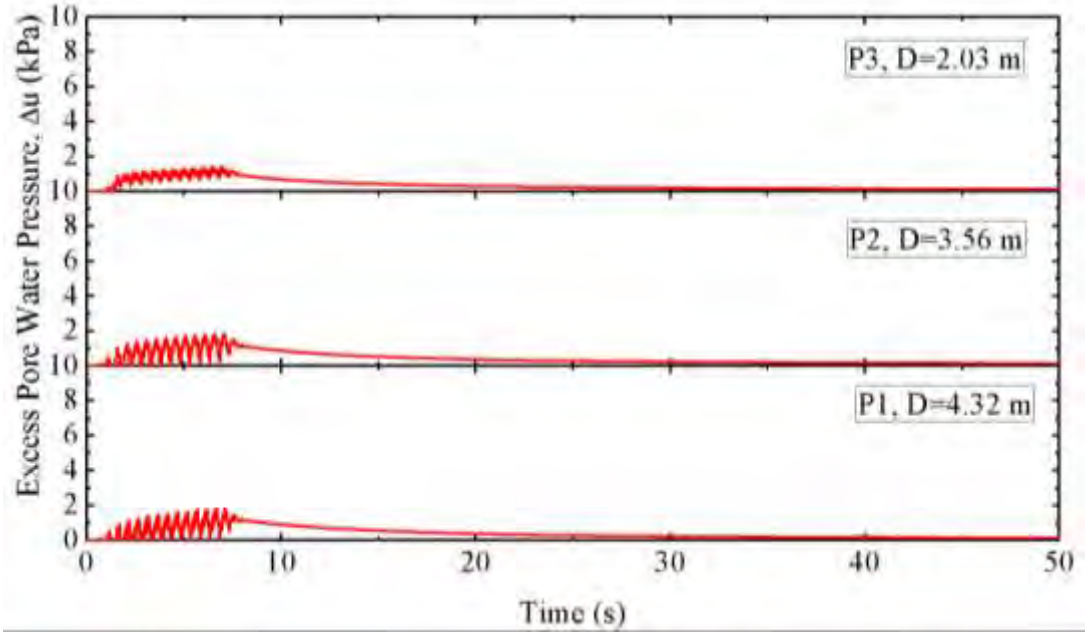

Fig.E. 128 Time history of Δu of T51 (a_{max}=0.03 g/15 cyc)

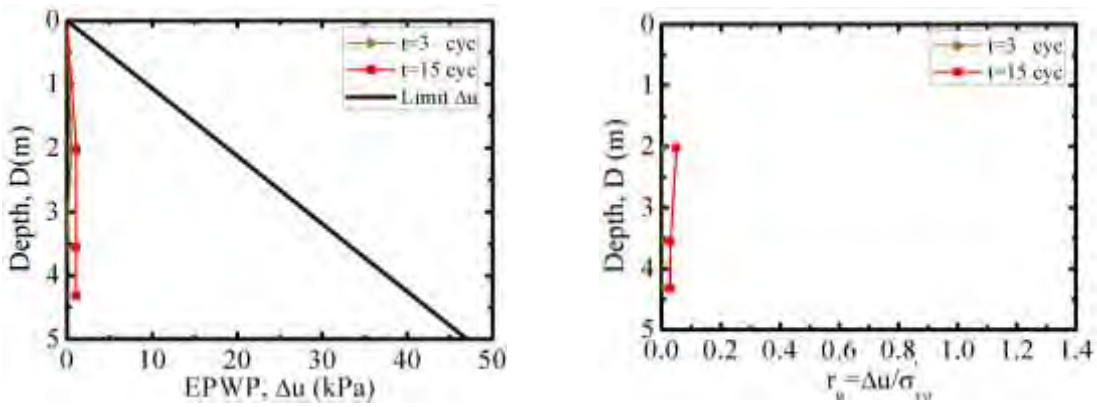

(a) Δu vs D (b) r_u vs D

Fig.E. 129 EPWP profiles of T51 (a_{max}=0.03 g/15 cyc)

E.6.3.2 T52-IM3 (a_{max}=0.10 g/15 cyc)

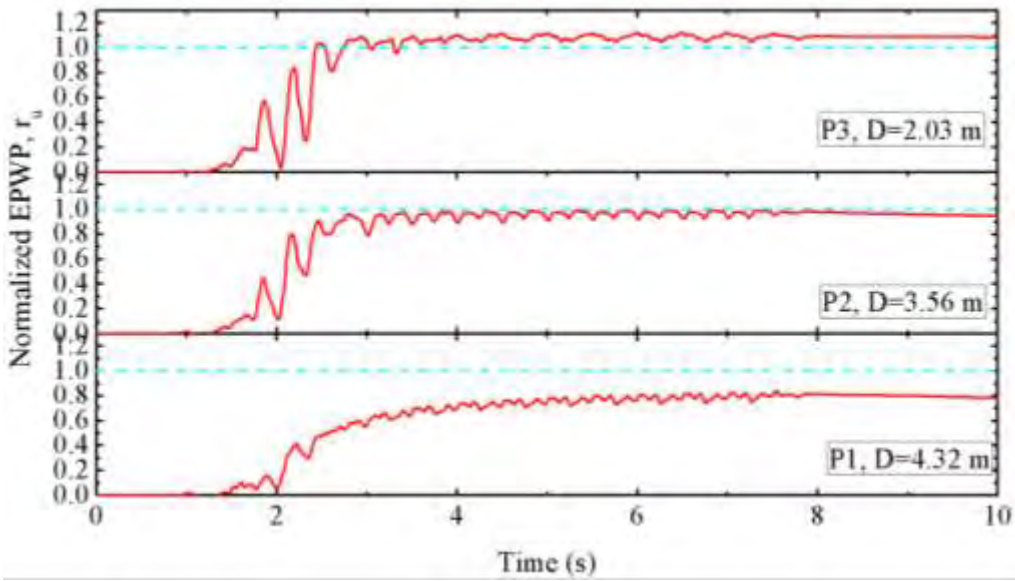

(a) r_u

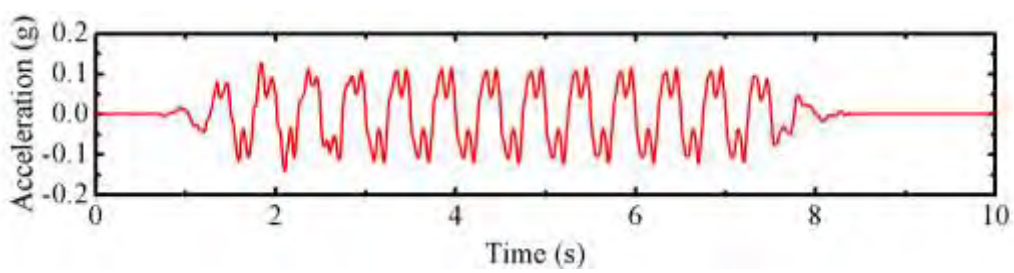

(b) B3X

Fig.E. 130 Time history of r_u and base acceleration of T45 (a_{max}=0.10 g/15 cyc)

Fig.E. 130 presents the time history of normalized excess pore water pressure r_u and base acceleration during shaking of T52 (a_{max}=0.10 g/15 cyc), to better observe whether and when

liquefaction occurs (i.e., r_u reaches unity) at different soil depths. Fig.E. 131 shows the time history of the excess pore water pressure (EPWP) Δu of the soil profile recorded by piezometers of T52. Fig.E. 132 plots the Δu as well as r_u with respect to depth at various shaking cycle for T52.

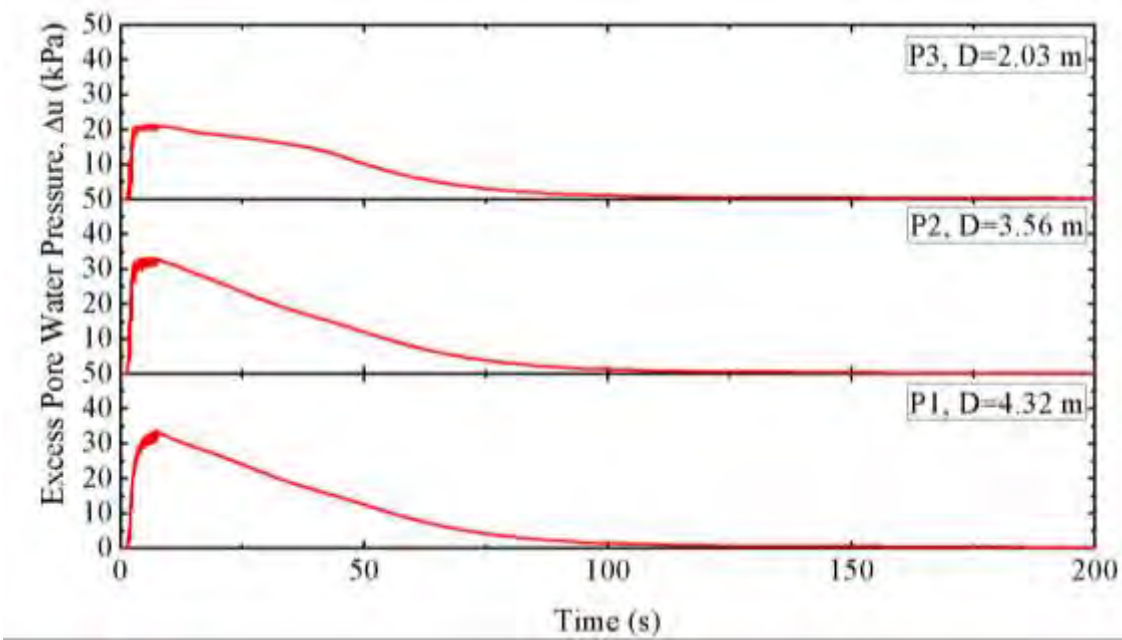

Fig.E. 131 Time history of Δu of T52 (a_{max}=0.10 g/15 cyc)

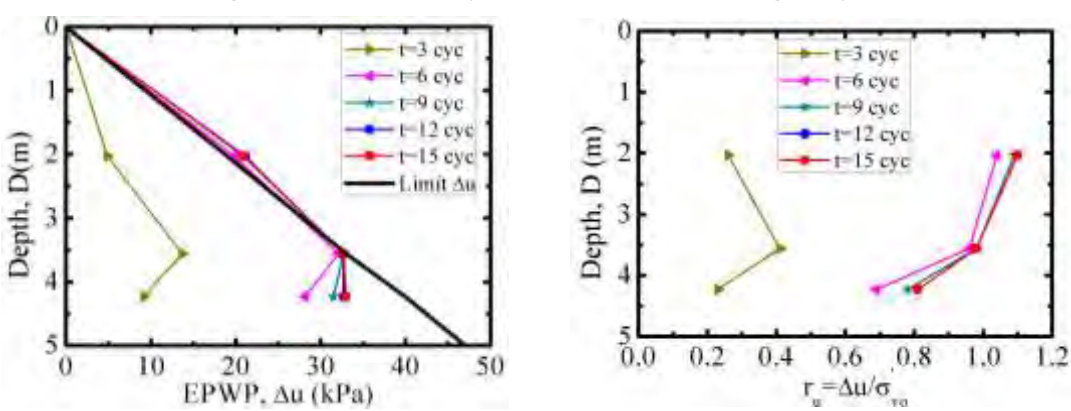

(a) Δu vs D (b) r_u vs D

Fig.E. 132 EPWP profiles of T52 (a_{max}=0.10 g/15 cyc)

E.6.4 Horizontal displacement

E.6.4.1 T44-IM2 (a_{max}=0.03 g/15 cyc)

Fig.E. 133(a) plots the time history of horizontal displacement of the soil at selected depths

in T51 (a_{max}=0.03 g/15 cyc). Fig.E. 133(b) and (c) plot the time history of relative horizontal displacement of the soil at selected depths in T51.

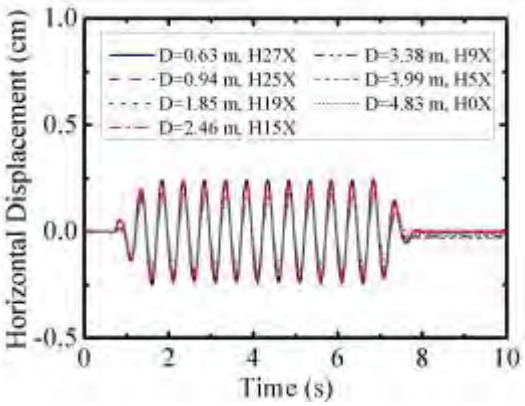

(a) Horizontal displacement

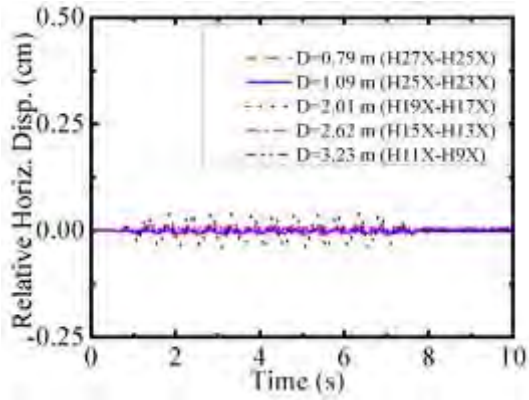

(b) Relative horiz. disp. b/w every other ring

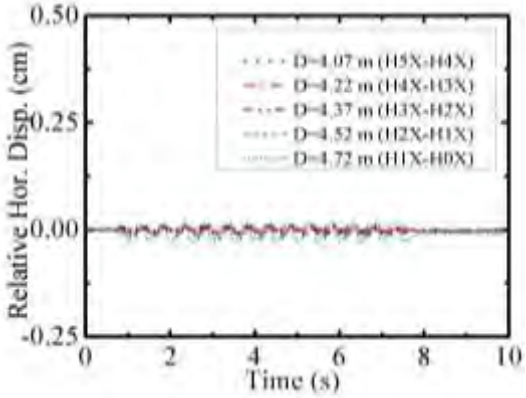

(c) Relative horiz. disp. b/w every ring

Fig.E. 133 Time history of horizontal displacement of T51 (a_{max}=0.03 g/15 cyc)

E.6.4.2 T52-IM3 (a_{max}=0.10 g/15 cyc)

Fig.E. 134(a) plots the time history of horizontal displacement of the soil at selected depths in T52 (a_{max}=0.10 g/15 cyc). Fig.E. 134(b) and (c) plot the time history of relative horizontal displacement of the soil at selected depths in T52.

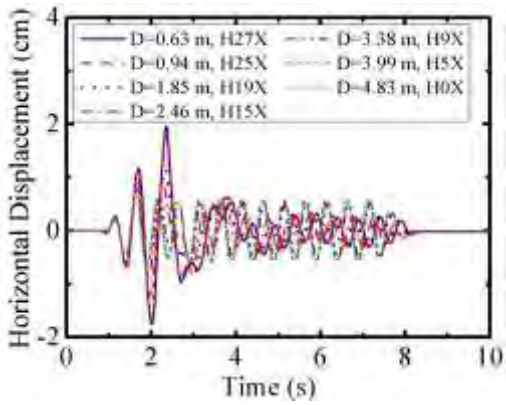

(a) Horizontal displacement

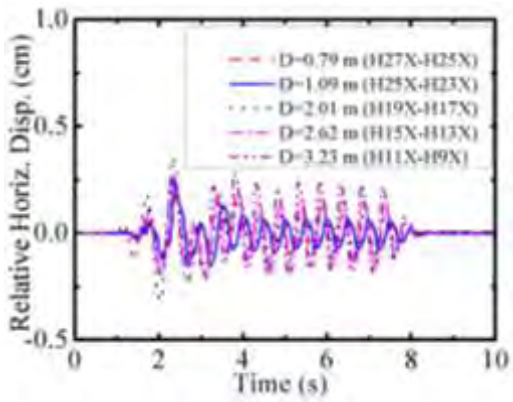

(b) Relative horiz. disp. b/w every other ring

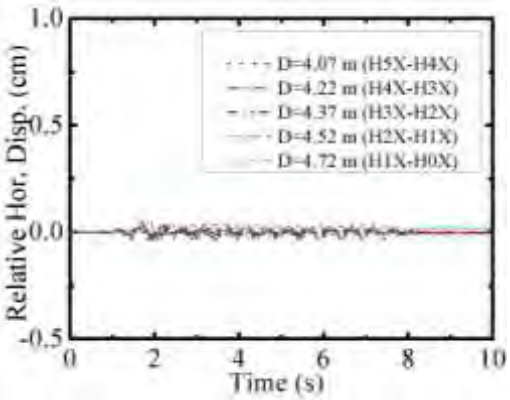

(c) Relative horiz. disp. b/w every ring

Fig.E. 134 Time history of horizontal displacement of T52 (a_{max}=0.10 g/15 cyc)

E.5.6 Ground settlement

Fig.E. 135 plots the time history of incremental ground settlement in shaking series 8 while Table E. 6 summarizes the incremental and total ground settlement of liquefaction tests in shaking series 8. The average incremental settlement of each liquefaction test is based on the incremental settlement of V1 and V3 because V2 was buried in the soil after T2.

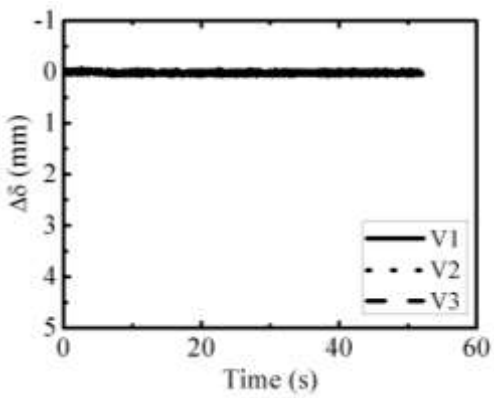

(a) T51 (a_{max}=0.03 g/15 cyc)

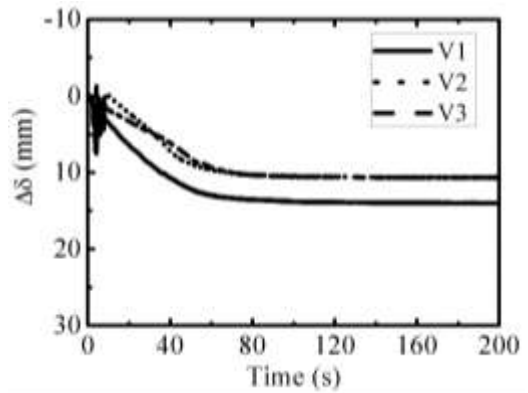

(c) T52 (a_{max}=0.10 g/15 cyc)

Fig.E. 135 Time history of incremental ground settlement in shaking series 8

Table E. 6 Ground settlement of liquefaction tests-shaking series 8

Shaking series	Shaking event	Input Motion	Δδ for each shaking test			$\Delta\delta_{ave.}$	Cumulative Settlement δ
			V1	V2	V3		
			(mm)	(mm)	(mm)	(mm)	(mm)
8	T46a	IM1 (a_{max}=0.015 g/5 cyc)	0	0	0	0	411
	T46	IM4 (a_{max}=0.03 g/5 cyc)	1	1	1	1	412
	T47	IM4 (a_{max}=0.03 g/5 cyc)	1	1	1	1	413
	T48	IM4 (a_{max}=0.03 g/5 cyc)	0	0	0	0	413
	T49	IM4 (a_{max}=0.03 g/5 cyc)	0	0	0	0	413
	T50	IM4 (a_{max}=0.03 g/5 cyc)	0	0	0	0	413
	T51a	IM1 (a_{max}=0.015 g/5 cyc)	0	0	0	0	413
	T51	IM2 (a_{max}=0.03 g/15 cyc)	0	0	0	0	413
	T52	IM3 (a_{max}=0.10 g/15 cyc)	14	10	10	12	425

E.5.6 Stress-strain response

E.5.6.1 T51-IM2 (a_{max}=0.03 g/15 cyc)

The time history of shear stress of the soil at different depths in T51 (a_{max}=0.03 g/15 cyc) is plotted in Fig.E. 136. Fig.E. 137 shows the time history of shear strain of the soil at different depths in T51. The shear stress-strain response of the soil at different depths in T51 is plotted in Fig.E. 138.

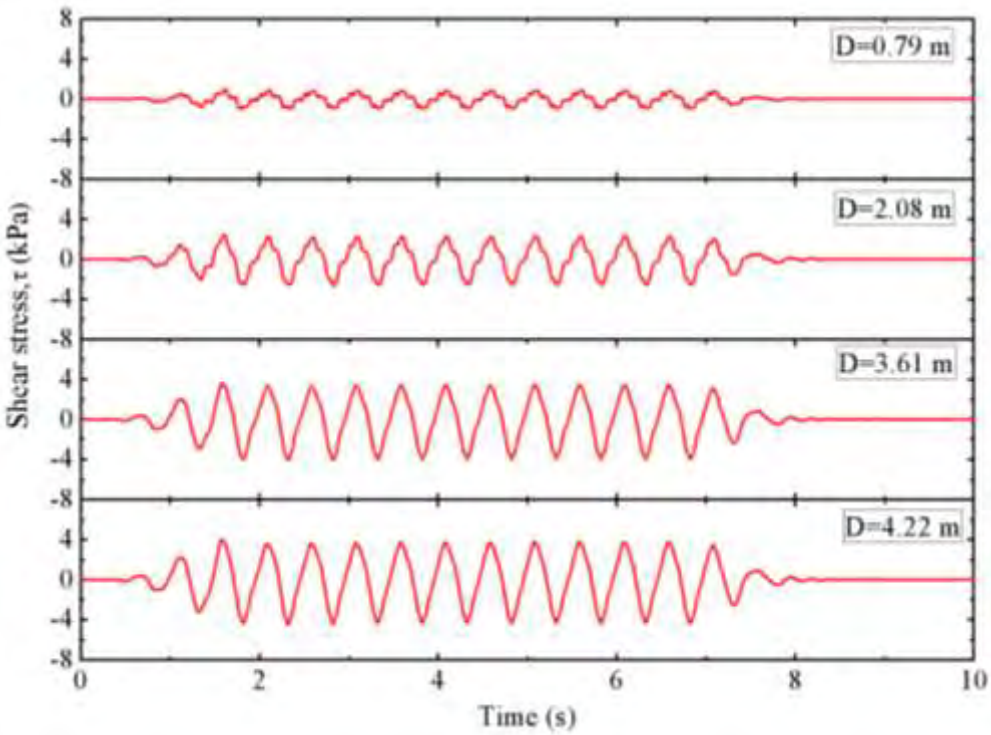

(a) Shear stress

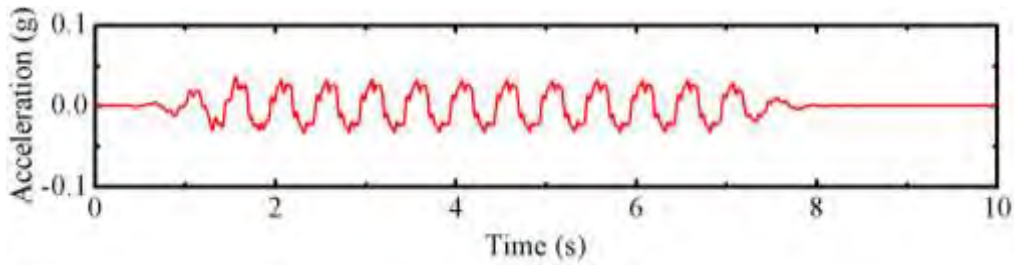

(b) B3X

Fig.E. 136 Time history of shear stress of T51 (a_{max}=0.03 g/15 cyc)

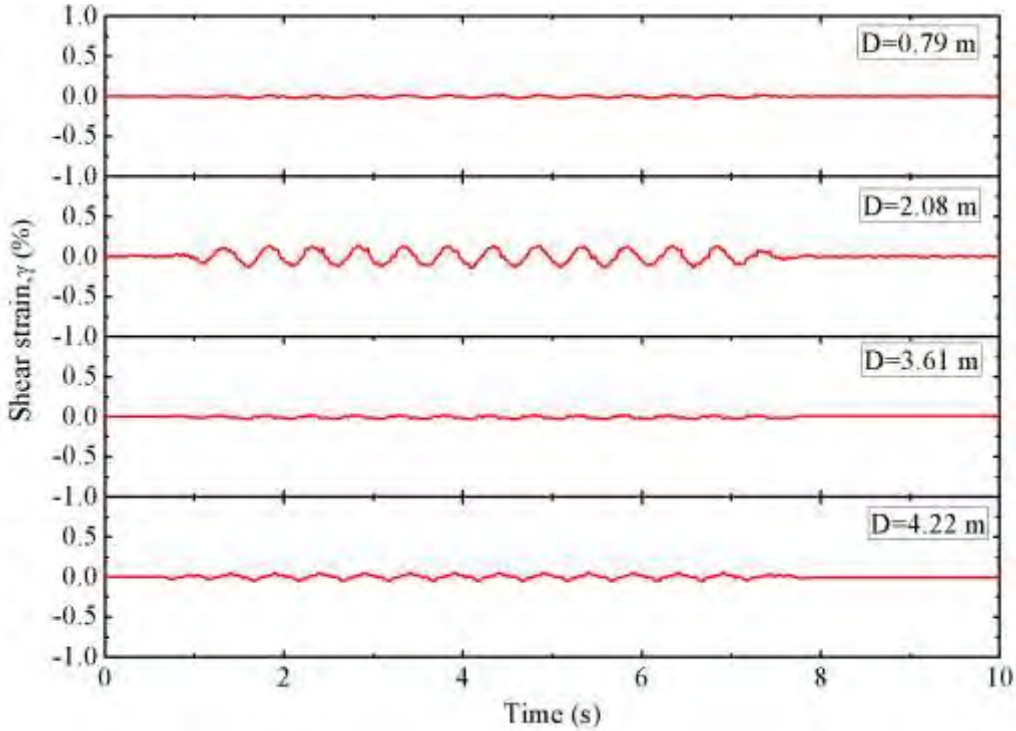

(a) Shear strain

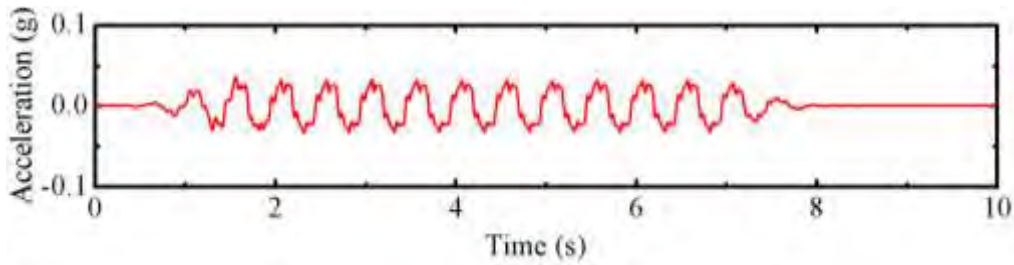

(b) B3X

Fig.E. 137 Time history of shear strain of T51 (a_{max}=0.03 g/15 cyc)

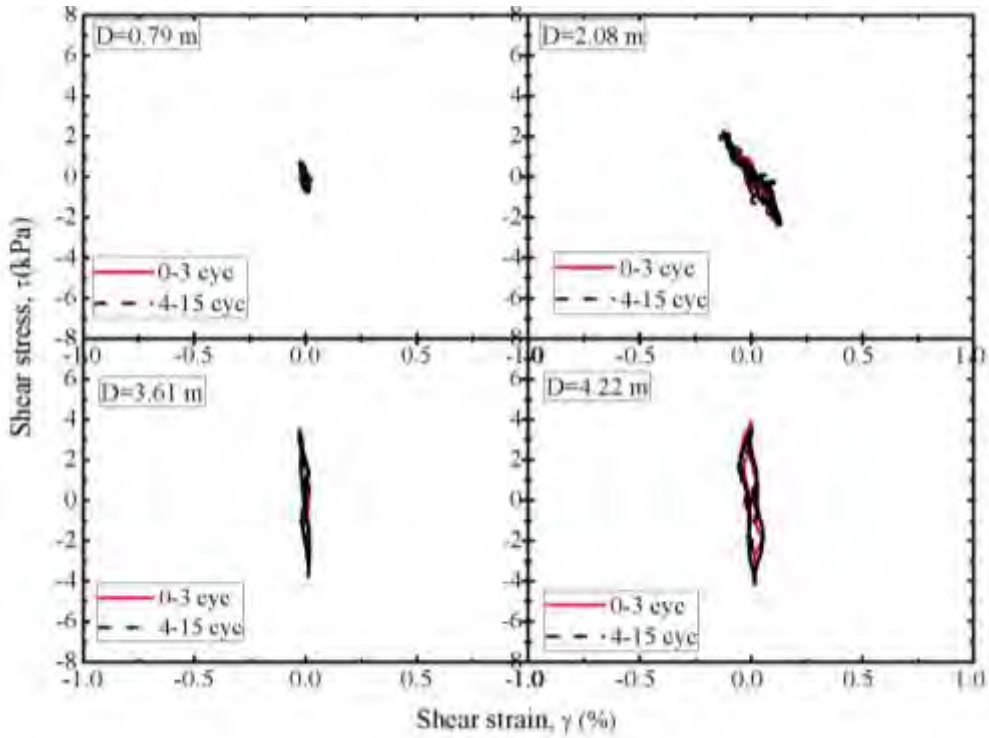

Fig.E. 138 Shear stress- strain loop of soil at different depths of T51 (a_{max}=0.03 g/15 cyc)

E.5.6.2 T52-IM3 (a_{max}=0.10 g/15 cyc)

The time history of shear stress of the soil at different depths in T52 (a_{max}=0.10 g/15 cyc) is plotted in Fig.E. 139. Fig.E. 140 shows the time history of shear strain of the soil at different depths in T52. The shear stress-strain response of the soil at different depths in T52 is plotted in Fig.E. 141.

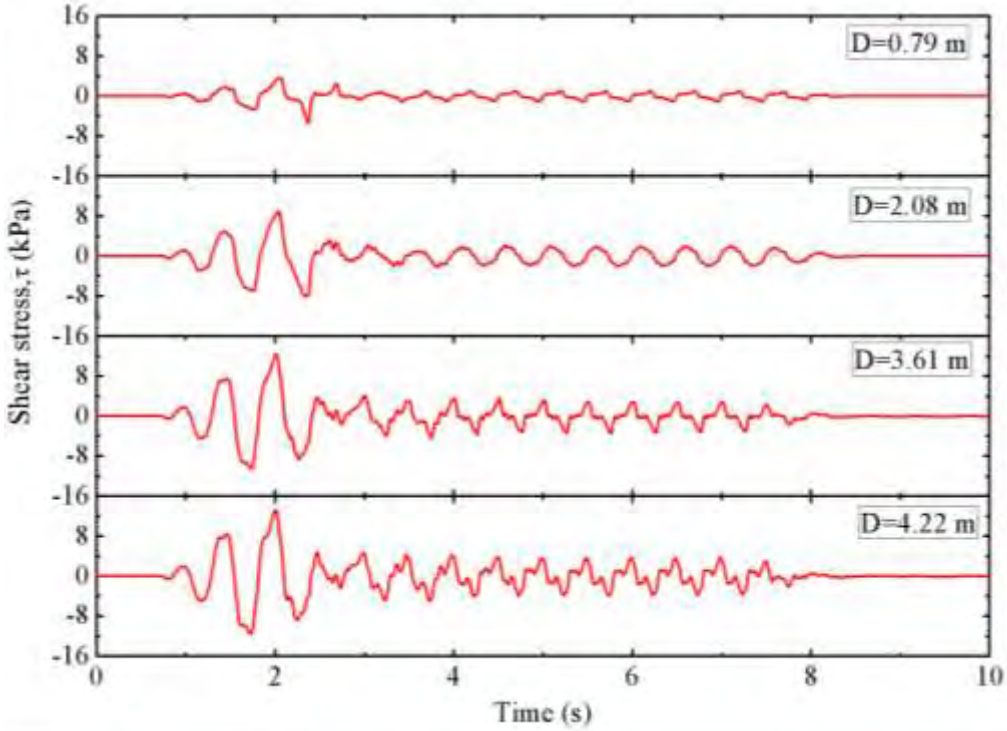

(a) Shear stress

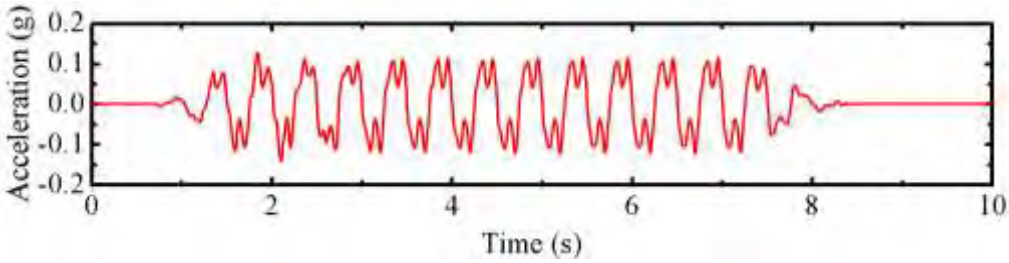

(b) B3X

Fig.E. 139 Time history of shear stress of T52 (a_{max}=0.10 g/15 cyc)

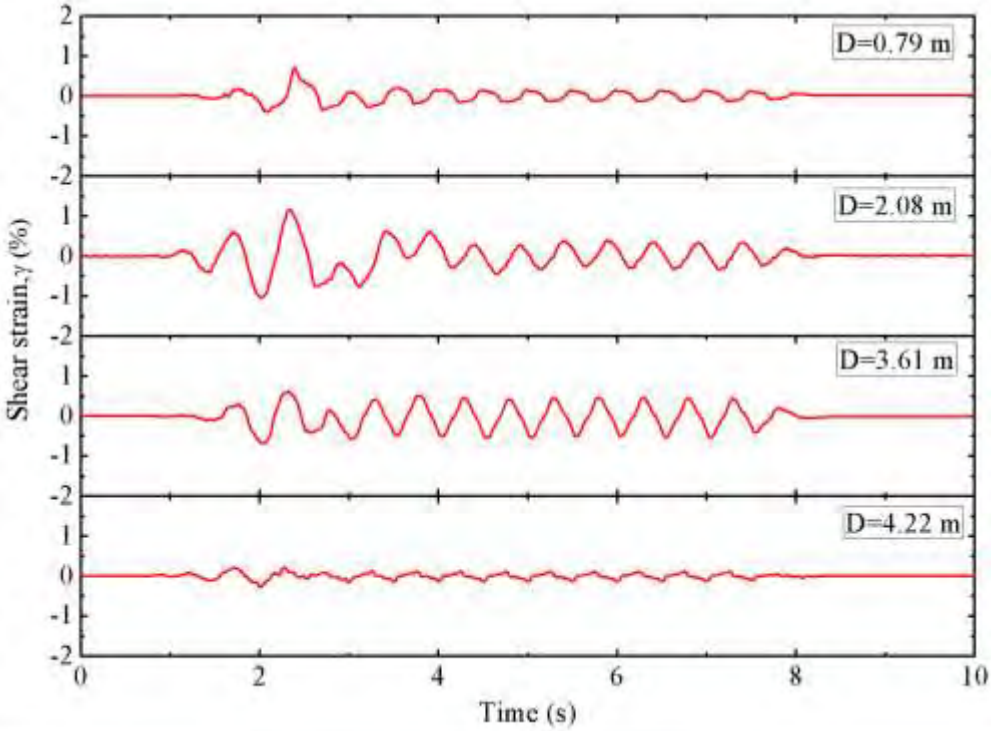

(a) Shear strain

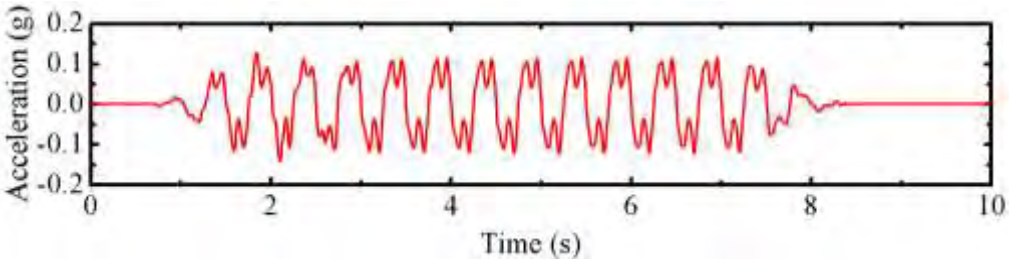

(b) B3X

Fig.E. 140 Time history of shear strain of T52 (a_{max}=0.10 g/15 cyc)

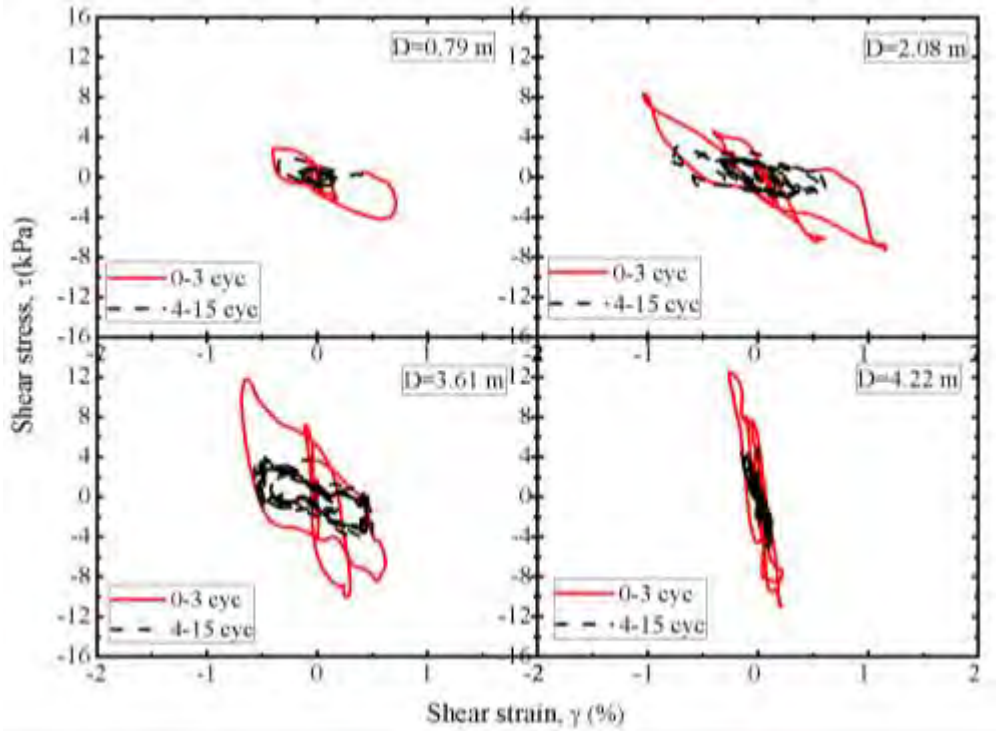

Fig.E. 141 Shear stress- strain loop of T52 (a_{max}=0.10 g/15 cyc)

E.7 Raw data for shear wave velocity tets

This section includes the raw data for the performed shear wave velocity tests. The horizontal distance from the hitting spot to the cone (receiver) is 0.609 m (2 ft).

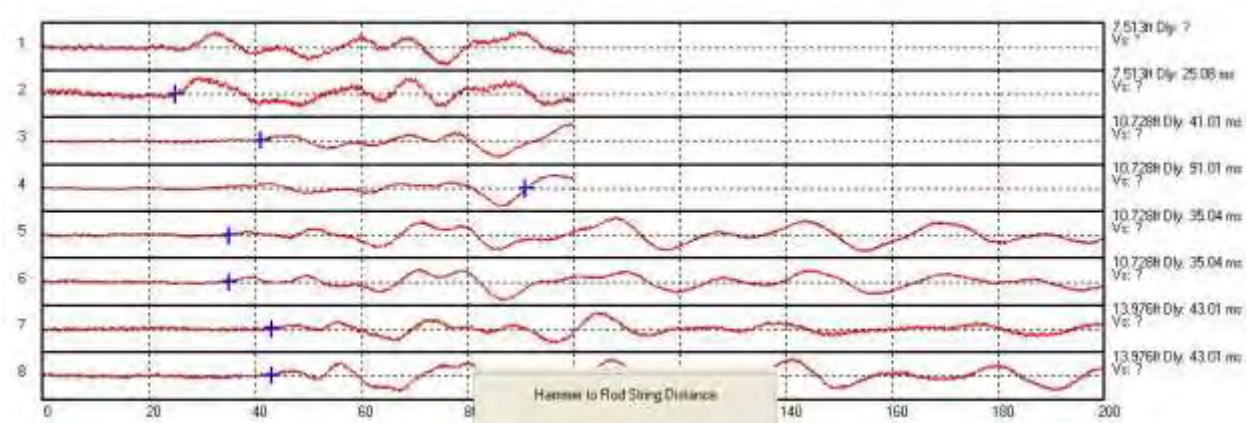

Fig.E. 142 Arrival times of shear wave of C0

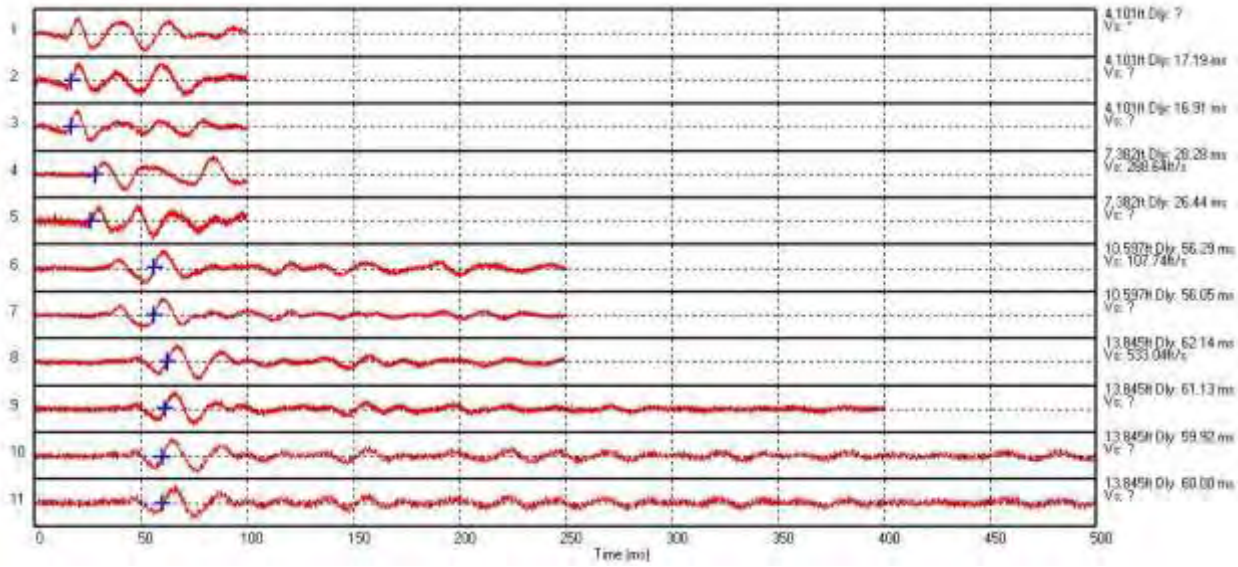

Fig.E. 143 Arrival times of C3

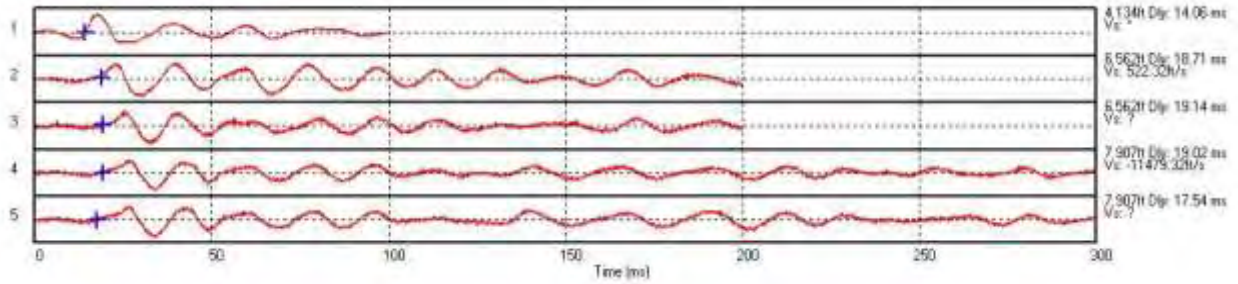

Fig.E. 144 Arrival times of shear wave of C29

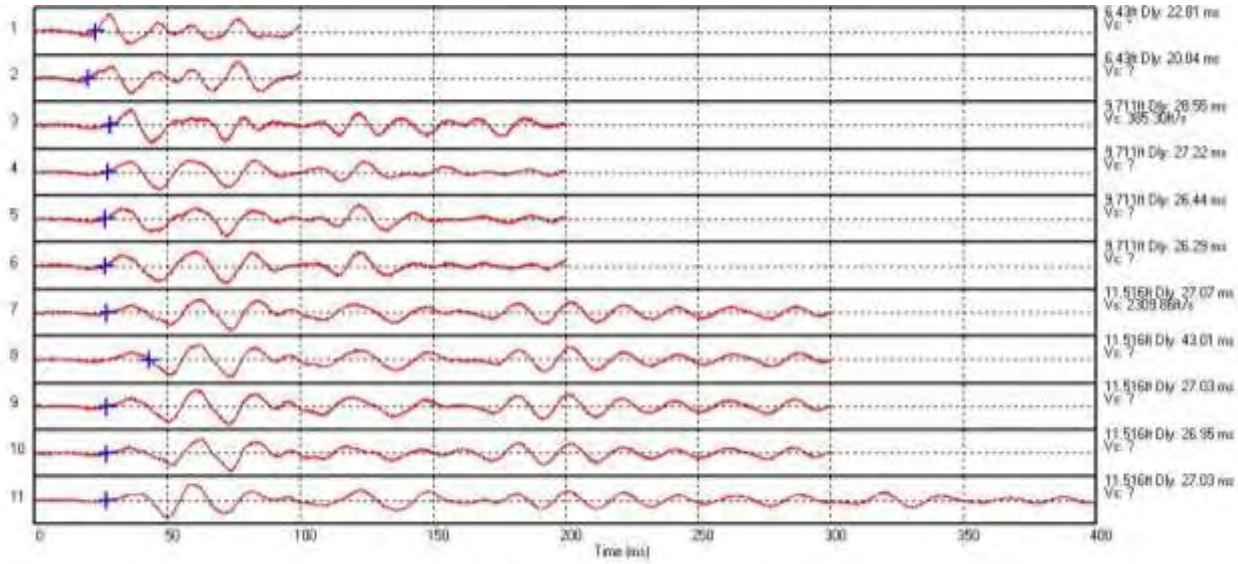

Fig.E. 145 Arrival times of shear wave of C31

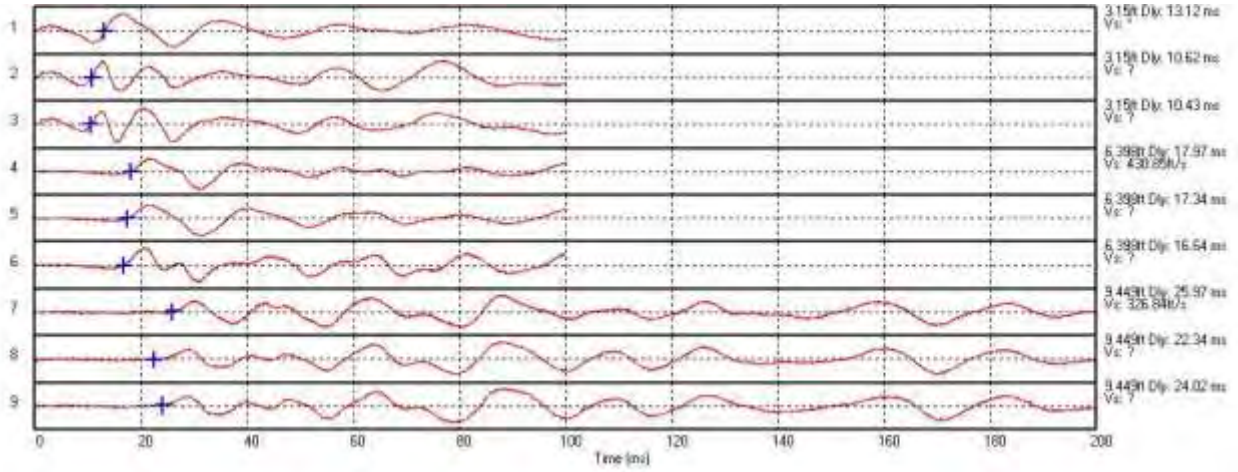

Fig.E. 146 Arrival times of shear wave of C38

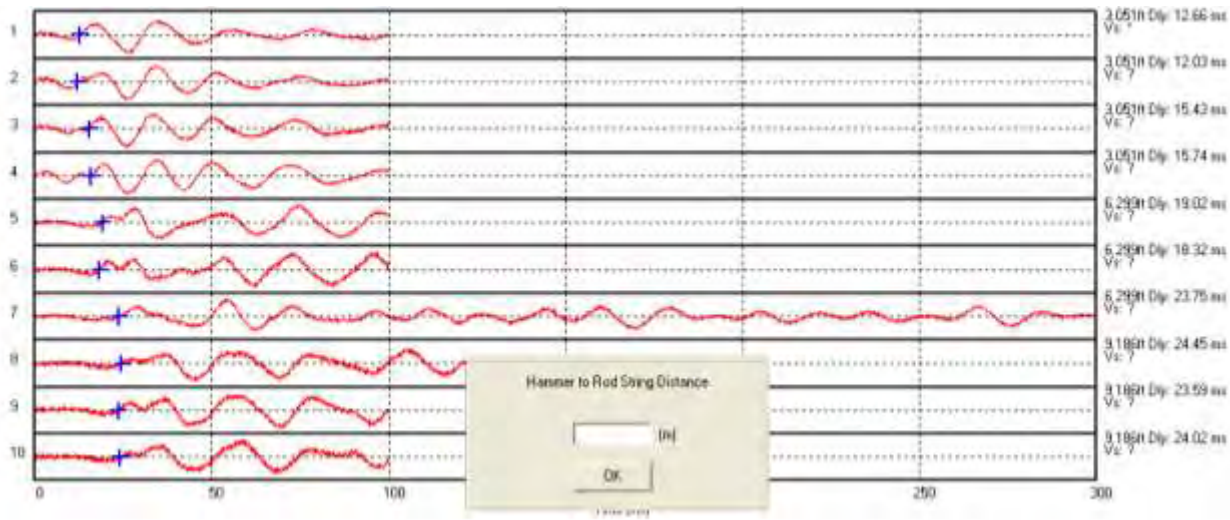

Fig.E. 147 Arrival times of shear wave of C50